SEISMIC PERFORMANCE

OF

STEEL-ENCASED

CONCRETE PILES

A Thesis

submitted in partial fulfillment of the requirements

for the degree of

Doctor of Philosophy in Civil Engineering

at the

University of Canterbury

by

ROBERT JAMES THOMAS PARK

University of Canterbury

Christchurch, New Zealand

1986

ABSTRACT

This thesis investigates the seismic performance of circular-sectioned steel-encased reinforced concrete bridge piles.

Constitutive models which account for lateral interaction of tube and concrete under monotonic loading were developed and calibrated against test data. Steel-encased reinforced concrete members, with casing diameter to thickness ratios in the range of 34 to 214, were tested under longitudinal and cyclic lateral load. Sound performance was displayed under the simulated seismic attack. Despite the formation at relatively low ductility levels of local buckles in the tube; strength, ductility and energy-dissipating characteristics were found to be equal or superior to those of conventionally designed ductile reinforced concrete members. Good agreement was obtained between the experimental results and predictions based on moment-curvature analyses. Steel-encased reinforced concrete members with casing circumferential discontinuities in the plastic hinge zones also behaved in a ductile fashion.

Soil-pile interaction under monotonic and cyclic lateral load was investigated by conducting tests on small-scale (diameter = 115mm) piles. Non-linear lateral load-deflection responses were obtained and ultimate loads were not reached despite imposed lateral displacements of up to 2.6 pile diameters. Soil lateral pressures of up to 15 times passive pressure were obtained and a large reserve of hysteretic damping was available in the soil. For the pile which formed a plastic hinge at depth in the ground, pile plasticity was well-developed over a considerable length. Thus it is recommended that piles which form plastic hinges in the ground be designed for full ductility. Due to lateral interaction between piles and pile head rotation under the overturning effect of lateral load, twin-capped piles were found to have only 1.5 times the lateral load-carrying capacity of similar single piles with free heads. A method was described in which the differential equation governing pile-soil interaction under lateral load is solved using a finite difference approach to allow for non-linear pile and soil behaviour and P-Δ effect. This method was used to calibrate simple tri-linear soil models, and subsequently the performance of a prototype pile under large lateral displacement was theoretically analysed.

ACKNOWLEDGEMENTS

The investigation described in this thesis was conducted in the Civil Engineering Department of the University of Canterbury under the overall guidance of my father Professor R. Park. I gratefully acknowledge the assistance that I have received during the course of this project and extend my thanks to the following groups of people:

(i) Drs. M.J.N. Priestley and J.B. Berrill, supervisors of this study, for their valued encouragement and guidance throughout the length of the project, and also to Dr. A.J. Carr for the use of his computer programs;

(ii) the technical staff of the Civil Engineering Department, under the leadership of Mr. N.W. Prebble, in particular special thanks are due to Messrs. P.F. Coursey, A.M. Bell, G.E. Hill and A.J. Stokes for their advice and assistance during construction and testing of the model piles;

(iii) Mrs A. Watt and Mrs D.E. Ball for typing the manuscript, Mrs V.J. Grey for tracing diagrams and Mr. L.H. Gardner for providing photographic services;

(iv) the New Zealand Railways Corporation and the National Roads Board for their generous financial assistance;

(v) Mr. P. S. Holmes (Bridge Engineer) and Mr. R.W. Fisher (Assistant Bridge Engineer) of the New Zealand Railways Corporation for providing me with the opportunity to start this project and their interest throughout the course of the project;

(vi) my wife, children, father, mother, father-in-law and mother-in-law for their constant support and encouragement;

(vii) fellow past and present postgraduate students, especially Dr. John Mander, Mr. David Whittaker, Dr. John Goodsir, Dr. Franz Zahn and Associate Professor Jin Tanaka for their fellowship and advice over the years of this study; and

(viii) Mr. R.G. Davies (District Engineer, Wanganui), Mr. P.G. Miskell (Assistant District Engineer, Wanganui) and Mr. J. Revington (Bridging Engineer on the Hapuawhenua and Taonui Railway Viaduct Construction Projects) for allowing me to work part-time whilst completing the thesis preparation.

TABLE OF CONTENTS

NOTATION

A = area of section

A_c = area of concrete inside tube ($= \frac{1}{4}\pi(D - 2t)^2$)

A_{cc} = area of concrete to outside of spiral reinforcement

A_g = gross area of reinforced concrete section

A_{sp} = area of spiral reinforcement

A_t = area of tube ($= \pi(D - t)t$)

A_{vf} = area of shear-friction reinforcement

A_1, A_2, A_3, A_4, A_5 = coefficients in finite difference equation

a = coefficient in third order polynomial

B = first moment of area of section about $x = 0$

b = width of element

b = coefficient in third order polynomial

C = coefficient in Reese et al (1.37) soil model

C = ratio defining ε_L at peak of concrete $f_L - \varepsilon_L$ relationship

$C_{H\mu}$ = coefficient of horizontal acceleration

$C_{\Delta\mu}$ = basic displacement coefficient

$C_0, C_1, C_2, C_3, C_4, C_5$ = coefficients in fifth order polynomial

c = coefficient in a third order polynomial

c = depth of longitudinal-compression strain on the section

D = steel tube outside diameter

D_{sp} = centre to centre diameter across spiral reinforcement

d = coefficient in third order polynomial

d_b = diameter of longitudinal reinforcing bar

d_s = outside diameter across the spiral reinforcement

E = modulus of elasticity

E = actual energy dissipated

E_c = initial modulus of concrete ($= 5000\sqrt{f'_c}$, MPa units)

E_{EP} = energy dissipated by an elastic-plastic system

E_R = energy dissipation ratio ($= E/E_{EP}$)

E_s = steel elastic modulus

E_{sec} = secant modulus of concrete at peak of stress-strain curve ($= f'_{cc}/\varepsilon'_{cc}$)

E_t = tangent modulus of steel

$(E_t)_i$ = tangent slope of the stress-strain curve at the ith discretisation

EI = pile flexural rigidity

F_L = longitudinal force

$f(x)$ = longitudinal stress at a distance x from the centroid

f'_c = longitudinal-compression strength of unconfined concrete

f'_{cc} = longitudinal-compression strength of confined concrete

f_L = longitudinal stress on concrete

f_R = radial pressure on concrete

f_R^{max} = peak value of radial pressure on concrete

f_t = tensile strength of concrete

f_2^{max} = concrete strength in the direction of compressive load

g = acceleration due to gravity (= 9.81 m/s^2)

H = lateral load

H = seismic horizontal inertia force

H_i = theoretical ultimate flexural load (based on $\varepsilon_c = 0.003$)

H_i^+ = value of H_i for positive deflection

H_i^- = value of H_i for negative deflection

H_1 = lateral load carried by pile 1

H_2 = lateral load carried by pile 2

h = height

h = spacing of nodes in finite difference method

h_i = spacing from spline endpoints i to i + 1

I = second moment of area

K = empirical factor representing strength enhancement due to confinement

K' = empirical factor representing stress enhancement due to confinement

K_a = active pressure coefficient (= $\tan^2(45^o - \phi/2)$)

K_i = stiffness of inner struts

K_o = stiffness of outer struts

K_o = at-rest pressure coefficient (taken as 0.4 in Reese et al (1.37) model)

K_1, K_2, K_3, K_4 = coefficients in the Desayi et al (2.22) concrete $f_L - \varepsilon_L$ relationship

K_{σ_L} = $\sigma_L/|\sigma_y|$ for $\varepsilon_L > 0.002$

$K_{\sigma_{L\infty}}$ = $\sigma_L/|\sigma_y|$ for $\varepsilon_L > 0.01$

k = modulus of horizontal subgrade reaction [F/L^2 units]

k_e = elastic stiffness

k_t = tangent value of k

L = length

L_D = depth-to-fixity (beneath ground level) for determining lateral deflection at level of lateral load application

L_e = length of equivalent pin-ended strut

L_{emb} = embedded length of pile

L_M = depth-to-fixity (beneath ground level) for determining maximum pile moment

L_r = ratio of length in the prototype to length in the model

ℓ_p = idealised plastic hinge length

M = moment on pile

M(x) = moment as a function of depth x

M_{cr} = moment at which concrete cracks

M_e = equivalent lumped mass of the bridge acting at its centre of mass

M_{exp} = maximum experimentally obtained moment

M_i = theoretical ultimate strength (based on $\varepsilon_c = 0.003$)

M_i = moment at ith spline endpoint

M_i'' = second derivative of moment at ith spline endpoint

M_t = maximum moment carried by empty tube

M_y = moment at first yield of steel

MOR = concrete modulus of rupture

n_h = coefficient of horizontal subgrade reaction [F/L^3 units]

n_{ht1} = tangent value of n_h for lateral deflections < 1% of pile diameter

n_{ht2} = tangent value of n_h for lateral deflections > 1% of pile diameter and < 10% of pile diameter

n_{ht3} = tangent value of n_h for lateral deflections > 10% of pile diameter

P = overall longitudinal load

P_c = longitudinal load carried by concrete

P_H = ultimate load, for tube in uniaxial-hoop-tension stress

P_L = ultimate load, for tube in uniaxial-longitudinal-compression stress

P_t = longitudinal load carried by tube

P_u^{exp} = maximum load attained in experiment

P_u^{SEN} = ultimate load predicted by Sen (2.33) formulae

p(x) = change in lateral pressure on the pile, from the at-rest conditions, as a function of depth x

$Q_{11}, Q_{12}, Q_{21}, Q_{22}, Q_{31}, Q_{32}$ = matrix coefficients relating ΔP and ΔM to $\Delta\varepsilon_o$ and $\Delta\psi$

q = vertical soil pressure beneath strip footing

R = ratio of tube yield strength to sum of tube yield strength plus unconfined concrete strength

R_ψ = radius of curvature of local buckle

r = constant in Popovics equation ($= E_c/(E_c - E_{sec})$)

r_g = radius of gyration of the section

S_H = sign of tube hoop stress σ_H

S_L = sign of tube longitudinal stress σ_L

S_R = strength ratio ($= P_u^{SEN}/(f_c'.A_c + |\sigma_y|.A_t)$)

s = centre to centre pitch of spiral reinforcement

T = natural period of vibration of the structure based on elastic first-mode response

t = tube wall thickness

u = equivalent effective bond stress between tube and concrete

u_{max} = bond strength (maximum value of u)

V(x) = shear force on pile as a function of depth x

V_c = shear force carried by concrete

V_{sp} = shear force carried by spiral reinforcement

V_t = shear force carried by tube

V_u = ultimate shear force

v_c = concrete shear stress capacity

w = distributed load on pile [F/L units] (i.e. soil lateral pressure times pile diameter)

w_c = smaller of w_{ct} or w_{cd}, Reese et al (1.37) soil model

w_{cd} = theoretical ultimate soil resistance for horizontal flow failure [F/L units] Reese et al (1.37) soil model

w_{ct} = theoretical ultimate soil resistance for passive wedge failure [F/L units] Reese et al (1.37) soil model

w_k = soil resistance at point k on w-y curve [F/L units] Reese et al (1.37) soil model

w_m = soil resistance at point m on w-y curve [F/L units] Reese et al (1.37) soil model

w_u = recommended ultimate soil resistance [F/L units] Reese et al (1.37) soil model

X = variable in Popovic's equation (= $\varepsilon_L/\varepsilon'_{cc}$)

x = distance from centroid of section

x = depth at a position on pile axis

x_b = depth at pile base

x_i = depth at ith strain gauge or spline endpoint

y = lateral deflection

$y(x)$ = lateral deflection as a function of x

y_i = lateral deflection at ith strain gauge pair

y_k = lateral deflection at point k on w-y curve (Reese et al (1.37) soil model

y_m = lateral deflection at point m on w-y curve (Reese et al (1.37) soil model

y_u = lateral deflection at point u on w-y curve (Reese et al (1.37) soil model

Z_H = return period coefficient

α = f_L/f'_{cc} at a control point on the falling branch of the f_L-ε_L relationship

α = half of soil angle ϕ of internal friction

β = $\varepsilon_L/\varepsilon'_{cc}$ at a control point on the falling branch of the f_L-ε_L relationship

β = $\alpha + 45^o$

γ = empirical constant in Sen (2.33) formulae (= $(25-L_e/D)/50$)

γ^p_{oct} = plastic component of octahedral shear strain

Δ = lateral deflection

Δ^+ = lateral deflection at positive peak of first cycle to $\mu = \pm 3/4$

Δ^- = lateral deflection at negative peak of first cycle to $\mu = \pm 3/4$

ΔL = length of element

ΔT = temperature change

ΔM = increment of pile moment (= $E_t\ I_t \cdot d^2(\Delta_y)/dx^2$)

Δp = increment of soil lateral pressure

ΔV = increment of pile shear force

Δy = increment of pile lateral deflection

$(\Delta A)_i$ = area lumped to the ith discretisation

$(\Delta I)_i$ = local second moment of area of the material represented by the ith discretisation

$\Delta\varepsilon_L^p$ = increment of plastic strain, in the longitudinal direction

$\Delta\varepsilon_H^p$ = increment of plastic strain, in the hoop direction

Δ_μ = seismic displacement at bridge centre of mass

$\Delta\psi$ = increment of pile curvature

$\varepsilon(x)$ = longitudinal strain at a distance x from centroid of section

ε_c = maximum longitudinal-compression strain on section

ε'_{cc} = ε_L at peak of confined concrete stress-strain curve

ε_{co} = ε_L at peak of unconfined concrete stress-strain curve

ε_{eff} = effective strain

ε_{eff}^e = effective elastic strain

ε_{eff}^p = effective plastic strain

ε_H = tube strain, in the hoop direction

ε_H^e = tube elastic strain, in the hoop direction

ε_H^p = tube plastic strain, in the hoop direction

ε'_H = apparent tube hoop strain

ε_L = tube (or concrete) strain, in the longitudinal direction

ε_L^e = tube elastic strain, in the longitudinal direction

ε_L^p = tube plastic strain, in the longitudinal direction

ε'_L = apparent tube longitudinal strain

ε_o = longitudinal strain at centroid of section

ε_{RC} = concrete strain, in the radial direction

ε_{RT} = tube strain, in the radial direction

ε_{RT}^e = tube elastic strain, in the radial direction

ε_{RT}^p = tube plastic strain, in the radial direction

ε_{sh} = steel strain at commencement of strain-hardening (uniaxial stress)

ε_u = steel strain at ultimate strength (uniaxial stress)

ε_y = steel yield strain (uniaxial stress)

ε_v = volumetric strain

ε_1 = concrete strain in the direction of tensile load

θ = rotation of test unit at midheight

θ = rotation of rosette from preperly aligned orientation

$\theta(x)$ = slope of pile

θ_i = slope at ith strain gauge pair

κ = empirical constant in Sen (2.33) formulae ($=\sqrt{1+\gamma+\gamma^2}$)

λ = variable which is a function of the loading history

μ = empirical constant in Sen (2.35) formulae ($=(25 - L_e/D)/4$)

μ = displacement ductility factor

μ_{BOT} = displacement ductility factor based on bottom half of test unit

μ_f = coefficient of friction

μ_{TOP} = displacement ductility factor based on top half of test unit

ν_c = initial value of concrete Poisson's ratio

ν_s = elastic value of Poisson's ratio for steel

ρ = soil density

ρ_s = ratio of volume of transverse steel to volume of confined concrete

$\sum|\mu|$ = cumulative displacement ductility factor

$\sum|\mu_{BOT}|$ = cumulative displacement ductility factor, based on bottom half of test unit

$\sum|\mu_{TOP}|$ = cumulative displacement ductility factor, based on top half of test unit

σ_{cr} = critical (buckling) stress

σ_{eff} = effective stress

σ_H = tube stress, in the hoop direction

σ_H^{max} = value of σ_H at $P = P_u^{exp}$

σ_{HV} = average hoop-tension stress in tube due to shear force

σ_L = tube stress, in the longitudinal direction

σ_L^{max} = value of σ_L at $P = P_u^{exp}$

σ_R = tube stress, in the radial directiom

σ_{sp} = stress in spiral reinforcement

σ_y = steel yield stress (from uniaxial stress test)

σ_{yh} = yield strength of spiral reinforcement

σ_u = steel ultimate stress (from uniaxial stress test)

τ = shear stress

τ_{oct} = octahedral shear stress

ϕ = capacity reduction factor

ϕ = soil angle of internal friction

ψ = curvature

ψ_i = curvature at ith strain gauge pair

ψ_y = yield curvature (based on elasto-plastic idealisation of moment-curvature behaviour)

Chapter One

INTRODUCTION AND SCOPE OF RESEARCH

1.1 INTRODUCTION

The use of steel-encased reinforced concrete piles of circular section in the foundations of bridges is common both in New Zealand and overseas. A typical two-span railway bridge using such piles is illustrated in Figure 1.1. The substructure consists of twin-pile bents. For the pier, shown in view B-B, permanent steel casing extending to just above river bed level has been used to form the piles. In the bridge abutments, shown in view A-A, the casing extends some 50 mm into the pile cap. Railway bridge pile designs have utilised ratios of steel tube outside diameter, D, to tube wall thickness, t, ratios in the range of $60 \leq D/t \leq 180$. Typically t has a value of 10 mm in New Zealand. Highway bridge substructures frequently consist of single or multiple steel-encased reinforced concrete piles beneath ground level, with a reinforced concrete pier above ground, as shown in Figure 1.2.

Steel-encased piles are particularly convenient for construction purposes. The steel tube stabilises excavation of the pile hole as auguring into the ground proceeds. When excavation is completed, the tube provides an impermeable formwork which facilitates the easy placing of a reinforcing cage and a sound concrete pour. The steel tube also improves the structural behaviour of the pile, as the casing is located at the perimeter of the section where it is most efficient in providing concrete confinement and resisting bending moment, shear force and column buckling. Thus the presence of steel encasement implies that provided corrosion of the casing is not excessive, little structural reliance needs to be placed on internal longitudinal and transverse reinforcing steel.

In earthquake-prone countries like New Zealand, seismic design usually governs the design of bridge substructures. In New Zealand, current design philosophy (1.1) requires that bridges of normal importance subjected to an earthquake with a return period of 150 percent of the bridge design-life may sustain damage, but should be subsequently available for use by emergency traffic. For crucial bridges on life-line routes, a lower probability of damage is required. It might appear that the collapse of a small bridge, such as that shown in Figure 1.1, is not as severe as the collapse of a major bridge or viaduct. However, the collective collapse of a number of small bridges may be just as damaging (1.2) to the operation of a transport network as the collapse of a major bridge. Also where alternative routing is not possible, collapse of a single, minor bridge may isolate an earthquake-stricken area from ground access.

Despite the large financial investment (1.2) in bridges, only a small amount of relevant research (1.3) has been conducted on the seismic performance of steel-encased reinforced concrete bridge piles. The study described in this thesis was performed to gain a more complete understanding of the behaviour of such piles during seismic attack.

1.2 ANALYSIS AND DESIGN OF PILES UNDER LATERAL LOAD

1.2.1 Lateral Load and Ductility Level

It is generally uneconomic to design bridge substructures to remain elastic under design-level earthquakes. Thus reliance has to be placed on dissipating seismic energy by either allowing stable plastic hinges to form or by providing special mechanical-energy-dissipating devices. Recommendations for the design of mechanical-energy-dissipating systems are available in the summary by Blakeley et al (1.4).

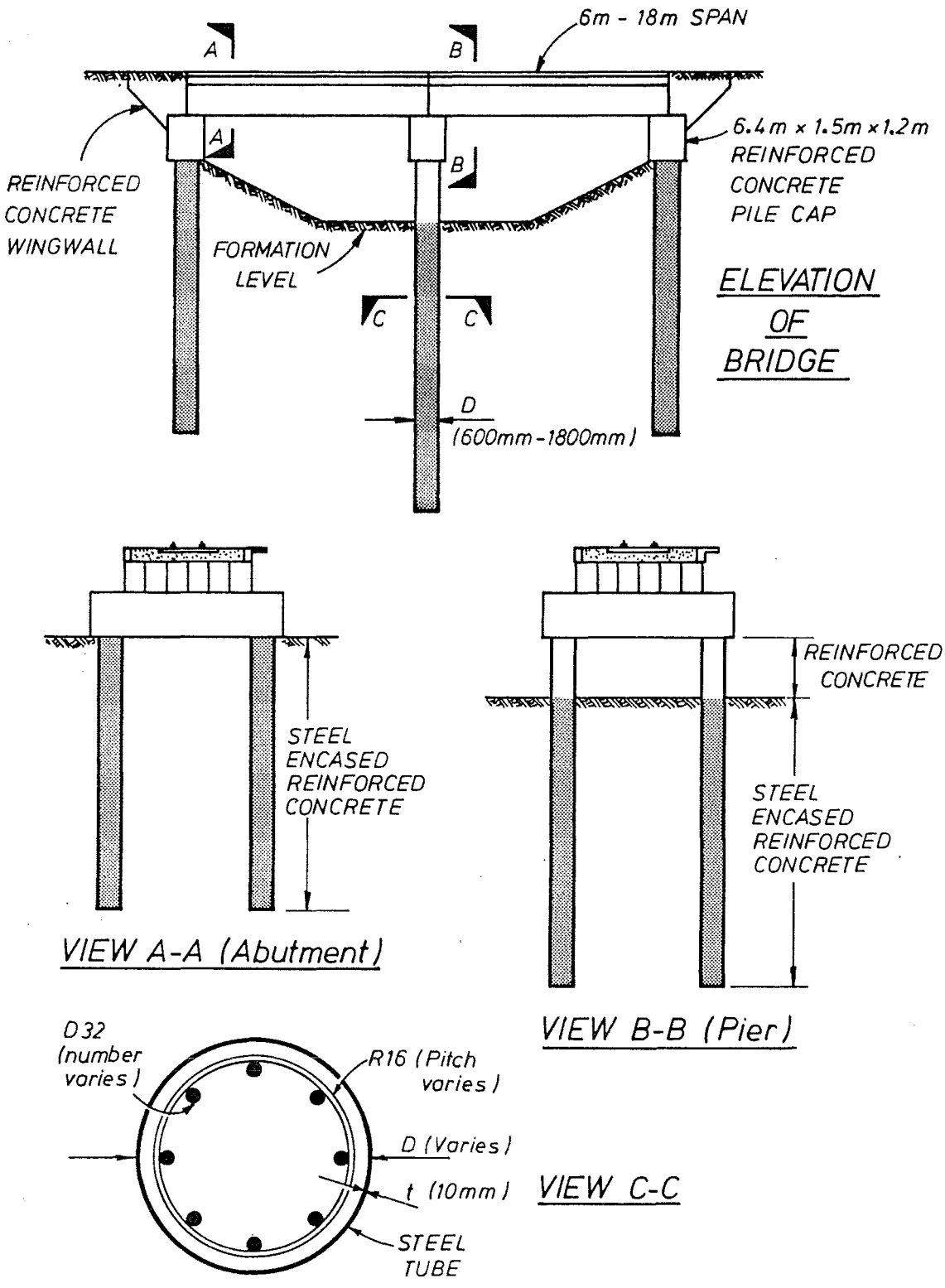

FIGURE 1.1 TYPICAL TWO-SPAN RAILWAY BRIDGE.

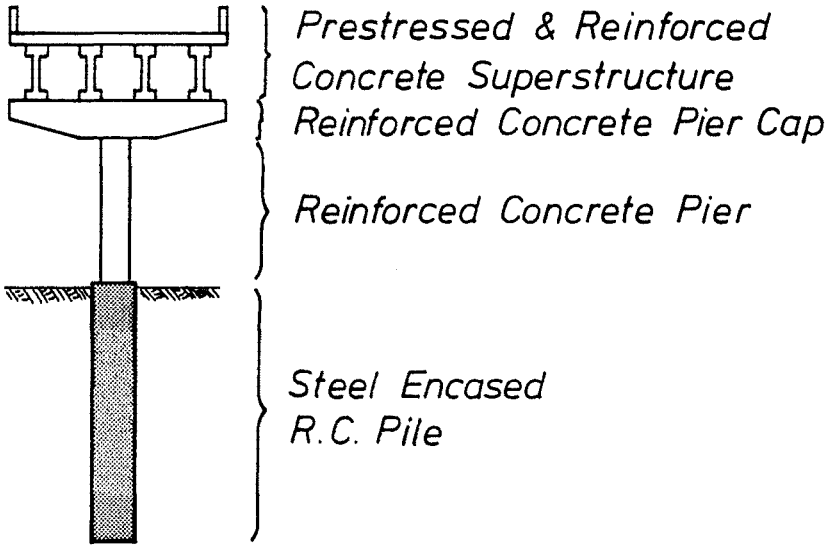

(a) Single Pile Substructures

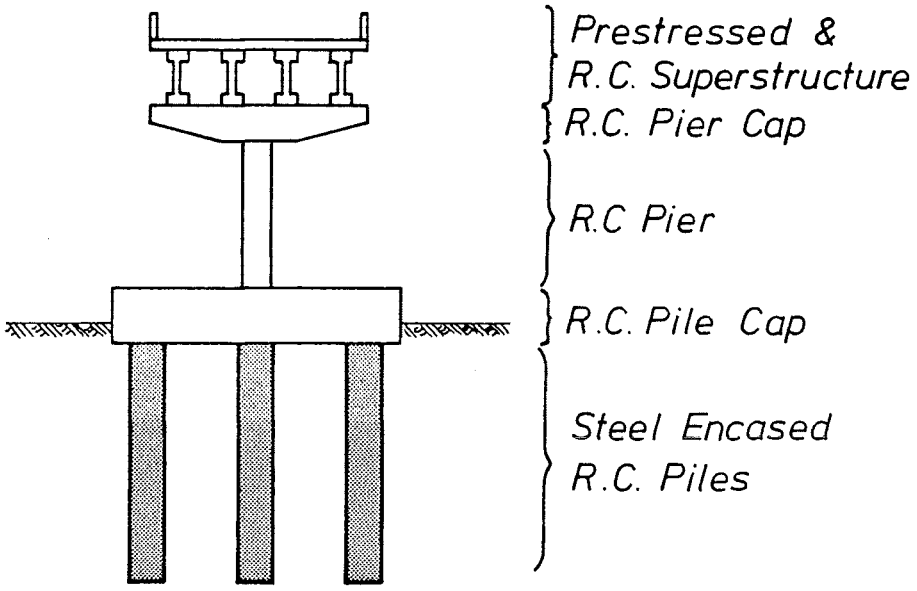

(b) Multi-pile Substructures

FIGURE 1.2 TYPICAL HIGHWAY BRIDGE SUBSTRUCTURE.

In New Zealand, for designs which require formation of plastic hinges, current seismic design philosophy (1.5, 1.6) relates the level of seismic inertia load, for a given seismic zone and design-earthquake return period, to three factors:

(i) The natural period of vibration, T, of the structure based on elastic first-mode response.

(ii) The assumed level of viscous damping on the structure (commonly taken as 5% of critical).

(iii) The displacement ductility level, μ, chosen on the basis of the position of the plastic hinges (discussed later in this section).

Figure 1.3, from Berrill et al (1.5, 1.6), shows how the coefficient of horizontal acceleration, $C_{H\mu}$, is obtained for New Zealand seismic zone A, as a function of T and μ. Note that in this figure five percent damping is assumed, and also a comparison of the lateral force values required by Berrill et al (1.5, 1.6) and the New Zealand Ministry of Works and Development (1.7) is made. The design curves of Berrill et al imply that for $T > 0$, increasing μ decreases $C_{H\mu}$. For $T > 0.7$ seconds, $C_{H\mu}$ is inversely proportional to μ which is in accordance with the equal displacement principle. At $T = 0$, $C_{H\mu}$ is independent of μ, as could be predicted from the equal acceleration principle. For T, in the range of 0 to 0.7 seconds, a linear variation between the equal displacement and acceleration principles has been used in predicting $C_{H\mu}$ from μ. Structures which form plastic hinges below ground level are currently designed (1.2) for lower values of μ, and hence higher seismic forces, than structures which form plastic hinges above ground level, as illustrated in Figure 1.4. There are two main reasons for penalising the formation of plastic hinges beneath ground level:

(i) the uncertain effects of fluctuation in river bed level and of pile-soil interaction make this a less reliable mechanism for dissipating seismic energy;

and (ii) plastic hinges should preferably be located in areas where damage can be readily inspected and, if necessary, repaired.

The highway bridge substructures shown in Figure 1.2 are generally designed to form plastic hinges just above ground level in the reinforced concrete pier, with the steel-encased reinforced concrete pile remaining substantially elastic. Thus for these highway bridges, a design incorporating $\mu \leq 6$ can be performed. The rail bridge, shown in Figure 1.1, is likely to form plastic hinges at depth in the ground and so a design incorporating $\mu \leq 3$ is required. One aim of the research described in this thesis was to investigate whether steel-encased reinforced concrete piles possess adequate ductility to design for $\mu \leq 6$ in all cases.

1.2.2 Soil-Pile Interaction

Bridge substructures under seismic attack are generally analysed in a pseudo-static fashion. The seismic horizontal intertia force, H, which is assumed to act through the centre of mass of the bridge is calculated as:

$$H = C_{H\mu} \times M_e \times g \qquad (1.1)$$

where M_e = equivalent lumped mass of the bridge acting at its centre of mass
g = acceleration due to gravity (9.81 m/s^2).

There are many methods (1.8), at a variety of levels of sophistication, for analysing the response of piles to lateral loads. Generally it is assumed that both pile and soil behave in a linearly elastic fashion. Five methods of analysis are described below and illustrated in Figure 1.5.

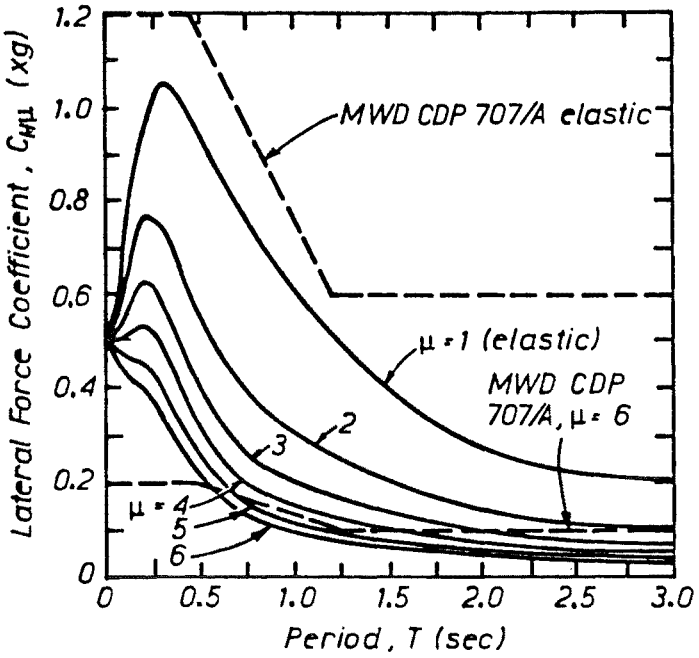

FIGURE 1.3 : ZONE A INELASTIC DESIGN SPECTRA - FROM BERRILL ET AL (1.5, 1.6).

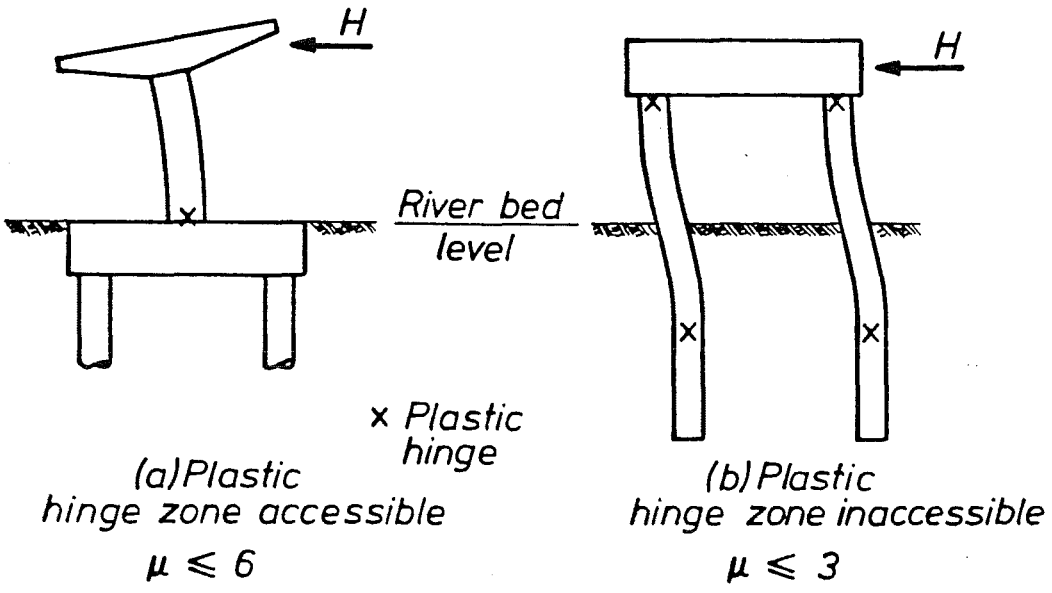

FIGURE 1.4 ASSESSING DUCTILITY LEVEL μ .

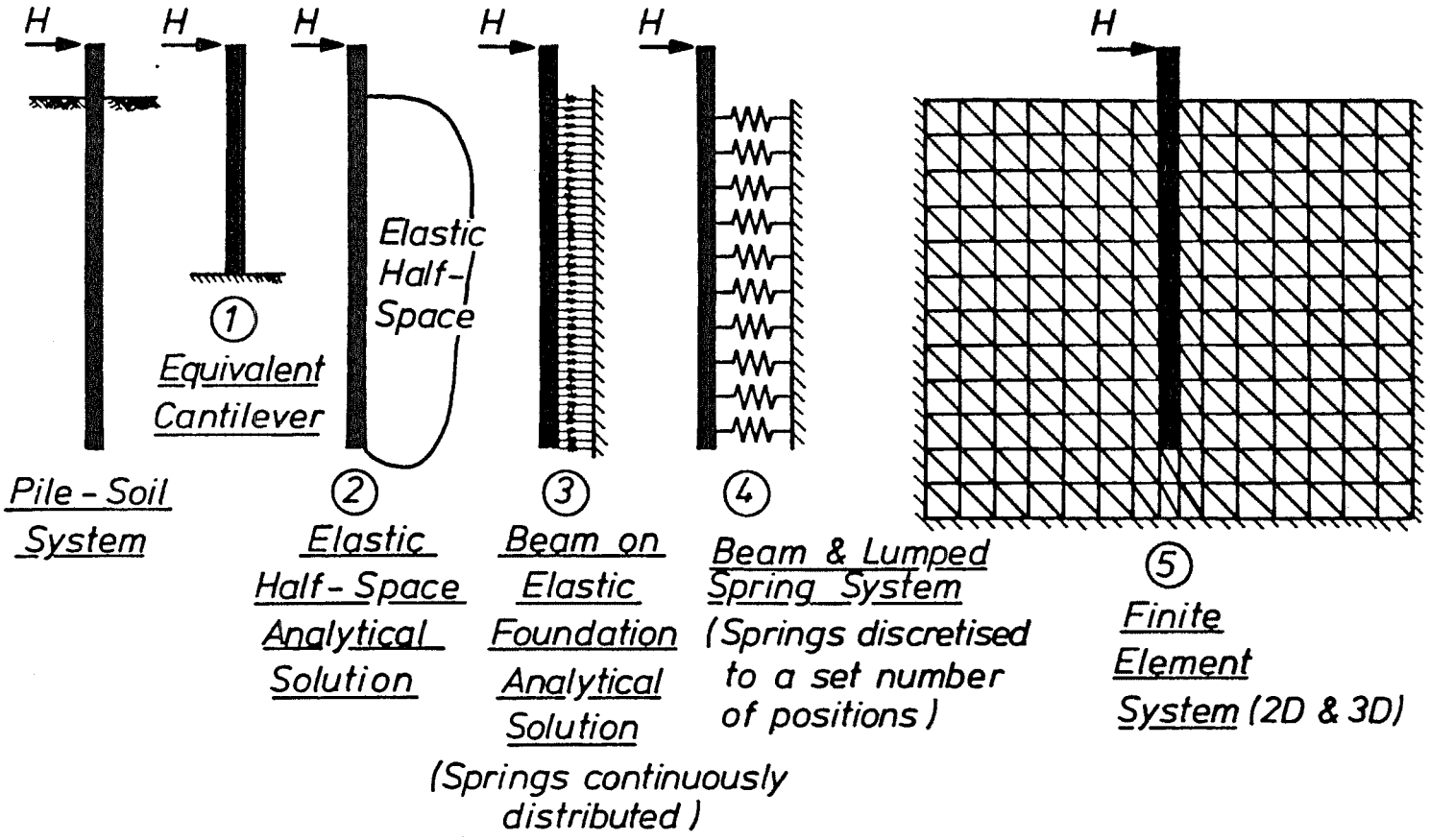

FIGURE 1.5 ANALYSIS OF SOIL-PILE INTERACTION.

1.2.2.1 Equivalent Cantilever Method

In this method the pile-soil system is assumed to be equivalent to a vertically standing cantilever. The depth-to-fixity of the cantilever beneath ground level is a function (1.8) of the relative pile and soil stiffnesses. Care must be exercised in using this method as the depth-to-fixity used in calculating the maximum pile moment and the lateral deflection at the level of lateral load application, L_M and L_D respectively, are different. For cohesionless soils these depths (1.8) are:

$$L_M = 0.78\left(\frac{EI}{n_h}\right)^{0.2} \tag{1.2}$$

$$L_D = 1.8\left(\frac{EI}{n_h}\right)^{0.2} \tag{1.3}$$

where EI = pile flexural rigidity [$F.L^2$ units]

n_h = constant of horizontal subgrade reaction [F/L^3 units].

The method also severely misrepresents equilibrium and compatibility conditions between the soil and the pile. This results in the distributions of moment, shear, distributed load, curvature, slope and lateral deflection along the length of the pile for the equivalent cantilever and the real pile-soil system being quite different. Thus analysis using the equivalent cantilever method gives only a very rough estimate of true behaviour.

1.2.2.2 Elastic Half-Space Solutions

Analytical solutions (1.9) for the application of point loads to an elastic half-space can be used. These solutions are limited to the case of constant soil stiffness. Since, in general, soil stiffness increases with pile depth, the solution results of this approach will be approximate.

1.2.2.3 Beam-on-Elastic-Foundation Solutions

Analytical solutions of the fourth order differential equation which governs beam-on-elastic-foundation behaviour are available (1.10). The governing equation is:

$$EI\ d^4y/dx^4 + k.y = w \tag{1.4}$$

where y = lateral pile deflection

x = distance along pile axis

k = modulus of horizontal subgrade reaction [F/L^2 units]

w = distributed load on pile [F/L units]

However as for the elastic half-space method, analytical solutions are not available for arbitrary distributions of soil or pile stiffness.

1.2.2.4 Beam and Lumped Spring System

A more versatile elastic method for coping with the depth dependence of soil stiffness utilises a beam and lumped spring model. In this method the soil lateral stiffness is lumped to a number of discrete springs along the length of the pile as shown in Figure 1.5. Thus any arbitrary variation of soil stiffness with depth can be analysed. This method is particularly suitable for use by design engineers, since the analysis can be accomplished with the aid of a simple two-dimensional frame analysis computer program. However, the method has the disadvantage of assuming that each layer of soil behaves independently of adjacent soil layers which misrepresents the continuum nature of the soil mass, since in

general shear transfer between adjacent soil layers will occur.

1.2.2.5 Finite Element System

The most sophisticated and realistic method for determining pile-soil interaction uses a finite element mesh to model the soil as shown in Figure 1.5. This method can readily allow for spatial variations in the soil stiffness due to the heterogeneous nature of the soil mass. However it should be noted that soil displacement around a pile is 3-dimensional. Thus ideally a 3-dimensional rather than a 2-dimensional finite element model should be employed. Because of the large number of degrees of freedom in a 3-dimensional model, analysis will be very costly in terms of both human and computer time.

1.2.2.6 Summary of Analysis Methods

When any of the five methods shown in Figure 1.5 is used, care must be taken to select soil and pile stiffnesses that are sufficiently close to the true behaviour over the anticipated range of soil and pile strains. If significant pile or soil plasticity occurs when for example linear elastic constitutive relationships have been assumed, then the results of analysis will be unreliable. However it is possible to allow for soil and pile non-linearity by extending the methods previously outlined in Sections 1.2.2.1, 1.2.2.4 and 1.2.2.5, and adopting an incremental solution technique which allows for the progressive softening of both soil and pile. Time-history analyses may also be attempted by further modifying the methods contained in Sections 1.2.2.1, 1.2.2.4 and 1.2.2.5 to allow for damping and the hysteretic behaviour of both soil and pile.

Thus it is possible to use numerical analytical methods with a high degree of refinement to solve pile-soil interaction problems. However, in-situ soil properties are usually very difficult to define accurately and are often very sensitive to local site conditions. Thus the analytical precision given by the above methods is usually not justified by the accuracy to which the soil properties are known. There are also many analytical complexities and uncertainties in modelling some of the following effects:

(i) crushing and ultimate strength of soil;
(ii) soil hysteretic behaviour;
(iii) skin friction between pile and soil; and
(iv) the separation of soil from the pile near the ground surface.

Hence designers generally analyse a pile-soil system using the simple beam and lumped spring model, and adopt the most conservative solution obtained from a number of analyses based on the likely range of soil parameters. One of the aims of this thesis was to develop a simple computer program to solve the problem of a pile under lateral load allowing for material non-linearity in the soil and the pile by solving equation 1.4 incrementally using a finite difference approach.

1.2.2.7 Free-Field Induced Pile Deformations

Regardless of the method employed for application of pile and soil stiffness characteristics to determine earthquake-induced pile bending moments using a pseudo-static approach, it is generally assumed that pile moments are only induced by loads resulting from the inertia of the bridge superstructure. However the inertia response of the superstructure is generated by interaction of the free-field earthquake motion with the piles; and the free-field displacements can themselves influence pile bending moments.

Near ground level, pile moments will be dominated by the lateral inertia loads on the bridge. Martin (1.11) states that at depths of greater than ten pile diameters beneath ground level the stiffness of the soil is high with respect to that of the pile, and hence the pile is constrained to deform in a similar manner to that of the free field. Thus at large depths in the soil, pile moments are

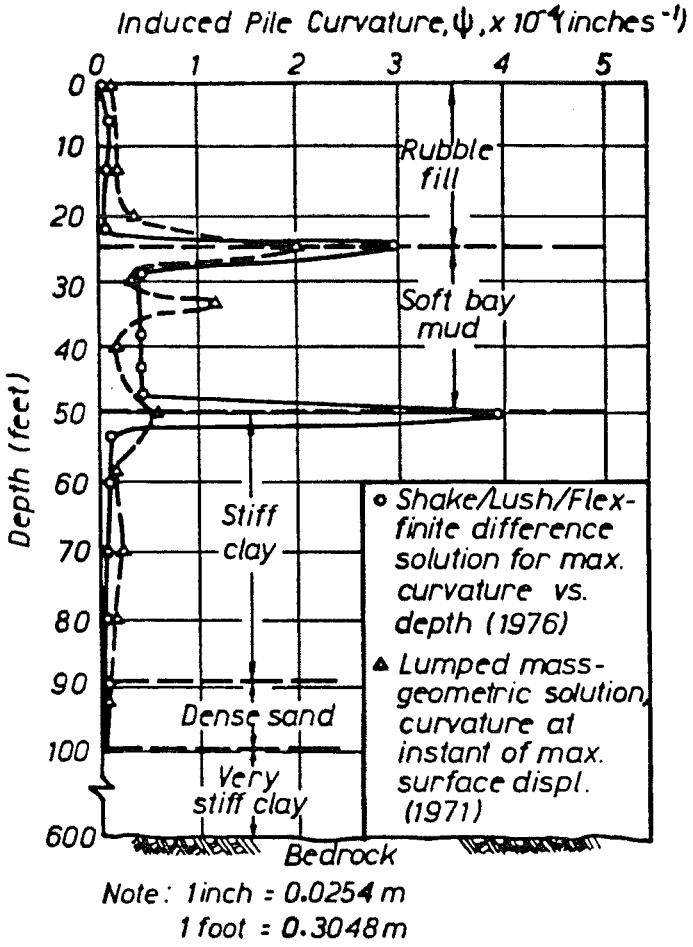

FIGURE 1.6 CALCULATED PILE CURVATURE AT DEPTH FOR A SAN FRANCISCO BAYSHORE SITE, AND AN 8+ MAGNITUDE EARTHQUAKE 16 MILES AWAY - FROM MARGASON AND HOLLOWAY (1.12).

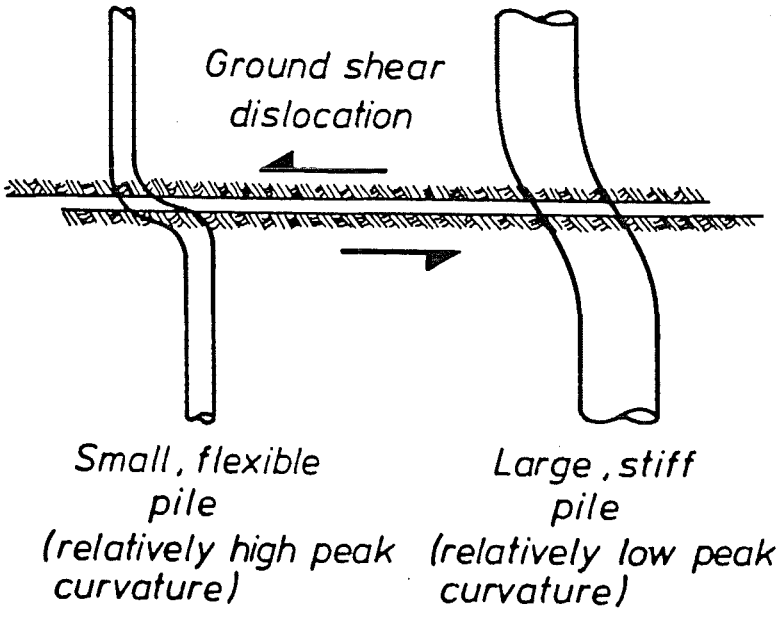

FIGURE 1.7 EFFECT OF PILE STIFFNESS ON PILE CURVATURE.

largely a function of the curvature induced by the free field motion. At such depths the inertial load approach would erroneously predict negligible curvatures and hence moments on the pile.

Margason and Holloway (1.12) have conducted time-history dynamic analyses to determine the free-field response to strong motion earthquakes of soil layers which overlay bedrock in the San Francisco Bay area. They have assumed that at large depths in the foundation soil, piles have negligible stiffness when compared with the stiffness of the soil. This implies that the lateral deformation of the pile and the soil are identical, and allows the curvature distribution on the pile deep in the foundation to be calculated from the free-field response of the soil. Typical peak pile curvature results, taken from Margason and Holloway (1.12) are shown in Figure 1.6. The results from two analyses are indicated. The first analysis (1971) used a crude lumped mass and shear spring model. The second analysis (1976) used a more rigorous 2-dimensional finite element model of the soil and hence is more accurate. The induced pile curvatures are shown to clearly peak at positions where the soil stiffness is changing rapidly, such as at the interface of hard and soft soil layers. They concluded that under a "maximum credible" earthquake, pile curvatures of up to 0.024 rads/m could be induced at depth in the foundation, although if the soil fails due to shear or liquefaction, even higher pile curvatures will be induced. Based on their analyses, they recommend that in general piles should be ductile enough to sustain a curvature of 0.024 rads/m without suffering excessive structural distress.

It should be noted that this curvature recommendation is conservative because it neglects the reduction in pile curvature, from that imposed by the free-field motion, due to the stiffness of the pile. The flexible 300 mm diameter prestressed concrete piles, with which Margason and Holloway were mainly concerned, would not significantly resist the ground deformation deep in the foundation. However since pile stiffness is proportional to D^4, significant resistance to ground motion could be expected from the steel-encased reinforced concrete bridge piles used in New Zealand which, with diameters in the range of 600 - 1800 mm , will have 16 - 1296 times the stiffness of a 300 mm diameter pile. Also in California, piles with diameters of 3000 mm have been constructed which have 10000 times the stiffness of a 300 mm diameter pile. Thus at depth in the foundation these large diameter piles will significantly resist following the ground motion which will result in large diameter piles being subjected to a lower curvature than are small diameter piles, as shown in Figure 1.7. This point is neither recognised nor discussed by Margason and Holloway.

It is interesting to estimate the maximum longitudinal compressive strain, ε_c, associated with Margason and Holloway's 0.024 rads/m design curvature recommendation. Pile curvature, ψ, is equal to the magnitude of the longitudinal strain gradient on the section:

$$\psi = \varepsilon_c / c \qquad (1.5)$$

where c = depth of longitudinal compressive strain on the section.
Typically, piles are under low levels of axial load and c can be estimated as being equal to $D/3$; thus:

$$\varepsilon_c = \psi . D/3 \qquad (1.6)$$

For ψ = 0.024 rads/m, then :

$$\varepsilon_c = 0.008D \qquad (1.7)$$

This means that typical piles of 0.6 - 1.8 m diameter would have to sustain ε_c of 0.0048 - 0.0144. These compressive strain levels are well above the yield strain, ε_y, of mild steel (approximately 0.0015) and the strain at peak stress of unconfined concrete (approximately 0.002). Thus Margason and Holloway's conservative recommendation that all piles, at positions deep in the foundation irrespective of diameter, be designed to resist a curvature of 0.024 rads/m, would require piles in the 600 - 1800 mm diameter range to possess ductility well into the inelastic range. Although the level of curvature recommended appears unrealistic for large diameter piles, Margason and Holloway's work indicates that accidental plastic hinging of piles at depth is a real possibility.

Clearly then, allowance in pile design should be made for both the effects of superstructure inertia loads which will dominate the pile response down to a depth of approximately ten pile diameters; and for the free field motion which will govern pile response at greater depths.

1.2.3 Pile Detailing

After the design pile moments, shear forces, and curvatures have been determined, the detailing of the steel-encased reinforced concrete section can be performed. The New Zealand Concrete Code (1.13), NZS 3101, provides some incomplete guidance on how this can be achieved.

Structural use of the casing is permitted, but conservative allowance has to be made for loss of steel tube thickness due to corrosion. In the Commentary to Clause 12.4.1.3 it is suggested that an average loss of tube thickness of 0.05 mm/year is appropriate, although a higher rate of loss should be assumed in a more aggressive environment.

In the Commentary to Clause 6.4.12.2 it is stated that: "The same rules used for computing the load-moment interaction strength for reinforced concrete sections can be applied to composite sections". This is taken to mean that the tube can be idealised as an equivalent array of reinforcing bars equally spaced around the perimeter of the section, with the total area of this equivalent array of bars being equal to the area of the casing. Design would then proceed in accordance with normal rules for reinforced concrete.

Clause 6.4.12.6 provides a criterion for the minimum thickness of tube, t, to be used in design for non-seismic applications. No guidance is given for seismic applications. The criterion given below as equation 1.8, is based on an empty tube yielding, before local buckling develops, under monotonically and concentrically applied longitudinal load. Local buckling can be observed as the local corrugating of a thin steel surface which is under compression. To avoid local buckling the Code (1.13) requires:

$$t \geq D \sqrt{\frac{\sigma_y}{8E_s}} \qquad (1.8)$$

where σ_y = steel yield stress
E_s = steel elastic modulus.

Equation 1.8 requires that typically for mild steel, with σ_y = 275 MPa, and E_s = 205,000 MPa, the casing D/t ratio should be less than or equal to 77. It was mentioned in Section 1.1 that piles have been constructed with casing D/t ratios of up to 180. Thus the application of equation 1.8 may severely reduce the design flexural strength of prototype steel-encased concrete sections from that predicted assuming no loss of tube stability. However the appropriateness of equation 1.8 to steel-encased concrete piles under seismic attack is doubtful for three reasons:

(i) Equation 1.8 was developed from the results of monotonic loading tests. Earthquakes impose cyclic and not monotonic loading on structures. Cyclic loading is likely to be more severe than monotonic loading; since under cyclic loading, strength and stiffness degradation of the pile will occur. This implies that the application of equation 1.8 may not be conservative in seismic situations.

(ii) Equation 1.8 was developed from empty tube tests which showed that once local buckling occurs the tube quickly loses load-carrying capacity. However concrete-filled tubes should behave in a more stable fashion once local buckling occurs, since the concrete partially restrains inward movement and local shortening of the tube. This suggests that the application of equation 1.8 may be too conservative.

(iii) Equation 1.8 was developed from concentric compression test results. Pile response under earthquake loading is generally dominated by flexural rather than axial load effects. This would also suggest that equation 1.8 is too conservative, as instability is less likely to occur in flexure than in compression.

These arguments indicate that the application of equation 1.8 to pile design is of doubtful validity, and it is also unclear as to whether equation 1.8 is conservative or non-conservative for the design of steel-encased reinforced concrete bridge piles for seismic applications.

If plastic hinges occur at positions where compatibility of longitudinal strains between tube and concrete cannot be guaranteed, due to inadequate anchorage of the tube, then the tube should not be assumed to contribute to flexural strength. However, the Commentary to Clause 12.5.2.1 allows the designer to use the tube as confinement reinforcing in such cases. No guidance is given as to the bond strength between tube and concrete. Thus it is not possible to calculate the length the tube needs to develop its yield strength. This could cause a serious problem in assessing the flexural strength of the pier pile (shown in view B-B of Fig. 1.1) if plastic hinging occurred close to ground level.

Specific guidelines as to the shear capacity of steel-encased concrete members or the design of internal longitudinal or transverse reinforcing steel are not given in the Code. Another design uncertainty can be related to the method of fabricating the steel tubes. Typically cylinders of three metres length are prefabricated by rolling flat plate into tubes of circular section and then welding up a longitudinal seam. In the field, adjacent lengths of tube are welded together along a circumferential seam. Currently it is New Zealand Railways practice to check only the quality of the longitudinally running shop weld. Doubt exists with regard to the development of tube flexural strength across the circumferentially running weld. However it should still be possible to rely on the tube to confine the concrete even in cases of poor circumferentially running welds.

Japanese and U.S.A. requirements concerning the structural detailing of steel-encased reinforced concrete members are also incomplete. The design procedures outlined for such members in NZS 3101 are very similar to those of ACI 318-83 (1.14), and in particular equation 1.8 was originally developed by ACI. In Japan the design of steel-encased reinforced concrete members subjected to axial load and flexure is achieved in the following fashion (1.15). Axial load is divided between the reinforced concrete and the tube, on the basis of their relative axial stiffnesses. Then the tube plastic moment and the reinforced concrete ultimate moment are computed independently of each other, taking into account the appropriate axial loads. For the reinforced concrete a maximum

concrete compressive strain of 0.003 is assumed. The total moment taken by the section is then assumed to be equal to the sum of the independently calculated tube and reinforced concrete moments. It should be noted that this method assumes that incompatibility of tube and concrete strains will occur. However it is unlikely that the flexural strength calculated by the Japanese method will be significantly different from that of the method outlined in NZS 3101 (1.13) which assumes composite behaviour with a maximum concrete compression strain of 0.003.

The discussion in this section has indicated that current design guidelines for steel-encased reinforced concrete piles are incomplete, and (as in the case of equation 1.8) sometimes inappropriate. A further aim of this study was to critically examine current design requirements by an experimental programme designed to check strength and ductility of typical pile designs, and to make recommendations based on the results.

1.3 REPORTED SEISMIC DAMAGE TO PILES

Martin (1.11), Margason and Holloway (1.12) and Sheppard (1.16) discuss foundation failures at bridge sites which have been reported after major earthquakes. Liquefaction of saturated cohesionless foundation soils has been the major source of bridge foundation failure during earthquakes. At sites where liquefaction has not occurred, pile failures have not been common.

After the 1964 earthquakes at Alaska and Nigata, the 1967 earthquake at Caracus, and the 1971 San Fernando earthquake, damaged foundation structures were exposed for inspection. The observations indicated that deep in the foundation, piles tended to move with the soil mass, while close to the ground piles tended to cut through the soil during the earthquake. These observations are in accordance with the design requirements noted at the end of Section 1.2.2.7.

Two instances of evidence of structural damage to piles are given in Figures 1.8 and 1.9. At the Showa Bridge, which collapsed due to soil liquefaction during the Nigata earthquake of 1964, a steel shell pile with D = 650 mm and t = 9 mm (D/t = 72) was extracted from the ground and found to have formed a local buckle at a section of high pile curvature, as shown in Figure 1.8. It should be noted from Figure 1.8 that the indicated local buckling is shown at a position which after the pile was removed from the ground is under high longitudinal compressive strain. However, prior to removing the pile from the ground that position would have been in a state of longitudinal tensile strain. Thus care needs to be taken in relating the damage to piles which have been extracted from the ground, with the damage to the pile that occurs during the earthquake. Figure 1.9, taken from Ref. 1.7, shows an uncovered pile to pile-cap system which, in responding to the vibrational characteristics of the bridge, has displaced through the soil during the 1971 San Fernando earthquake. The piles, which consisted of concrete cast inside corrugated steel pipe, show evidence of plastic hinging just beneath the pile-cap.

It should also be noted that a large number of bridges have collapsed during earthquakes due to poor structural detailing of piers and superstructures. Such failures cannot be directly attributed to foundation deficiencies. For example during the San Fernando earthquake (1.17), a large number of reinforced concrete piers failed due to inadequate provision of lateral reinforcement, and bridge spans fell from piers due to poor attachment and seating of spans to the tops of piers.

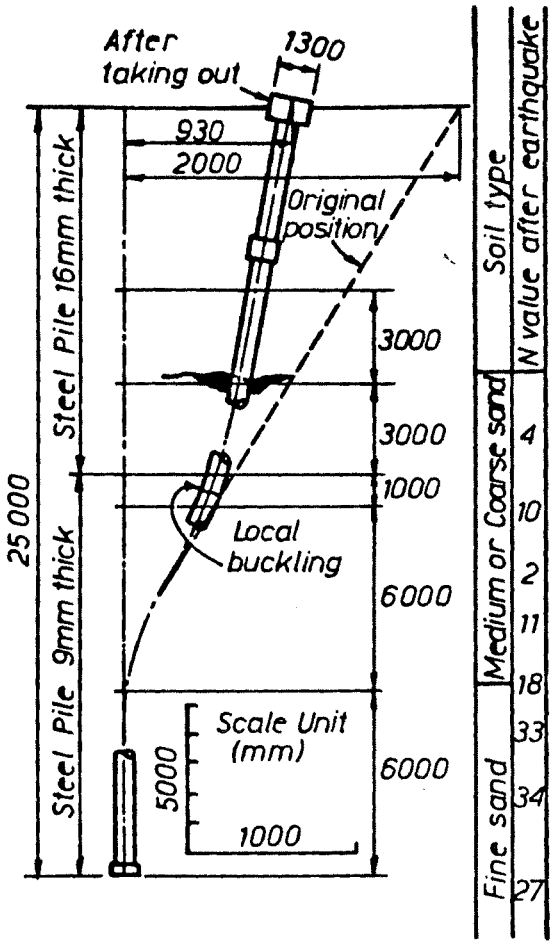

FIGURE 1.8 PILE DISPLACEMENT AT SHOWA BRIDGE - FROM MARTIN (1.11).

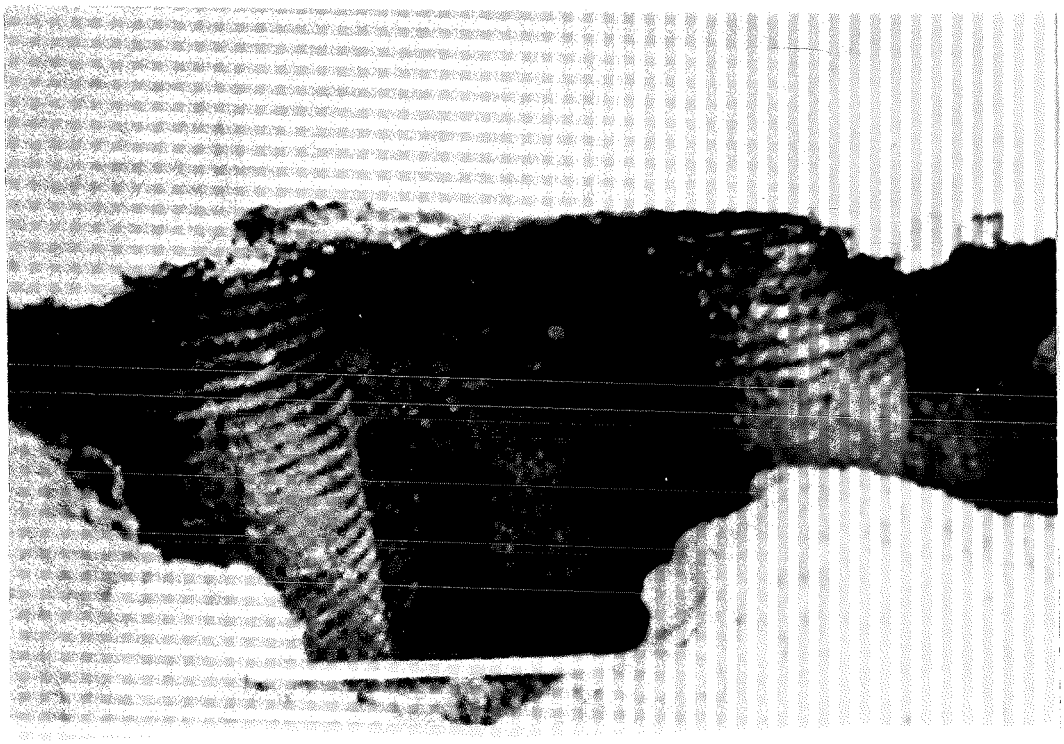

FIGURE 1.9 PILING DAMAGE DURING 1971 SAN FERNANDO EARTHQUAKE - FROM REFERENCE 1.17.

1.4 PREVIOUS RESEARCH WORK AND FUTURE NEEDS

The previous sections indicate that both strength and ductility characteristics of steel-encased reinforced concrete members, and aspects of soil-pile interaction are of importance in the design of bridge foundations. Sections 1.4.1 and 1.4.2 discuss previous relevant research and then proceed to identify the specific areas still requiring additional research.

1.4.1 Strength and Ductility Characteristics of Steel-Encased Concrete

The value of confining concrete has been realised since 1898 when Consideré (1.18) performed compression tests on concrete cylinders which were subjected to lateral fluid pressures. These early tests showed:

$$f'_{cc} = f'_c + 4.8f_R \qquad (1.9)$$

where f'_{cc} = longitudinal compressive strength of confined concrete
f'_c = longitudinal compressive strength of unconfined concrete
f_R = radial pressure on concrete.

Hence Consideré's tests indicated that the provision of lateral (radial) pressure to concrete is a very efficient way of increasing the longitudinal compressive strength of the concrete. Later researchers, including Richart et al (1.19), confirmed this behaviour and also showed that under longitudinal compressive load the ductility of concrete is markedly improved by lateral confinement.

The testing of empty tubes under longitudinal compressive load has shown that rapid failure of the tube results when local buckling occurs. Hence designers generally provide internal or external stiffening elements to thin-walled vessels, so that material yielding will occur before local buckling failure.

Thus structural advantages to both tube and concrete exist in providing a composite concrete-filled tube. Concrete benefits from the confinement offered by the tube, while it is reasonable to assume that tube local buckling will be stabilised by the internal restraint provided by the concrete.

Kloppel and Goder (1.20), Salani and Sims (1.21), Gardner and Jacobson (1.22), Furlong (1.23), Knowles and Park (1.24), Neogi et al (1.25), and Tomii et al (1.26) have tested concrete-filled tubes. However this research has concentrated on the behaviour of concrete-filled tubes with relatively thick walls ($D/t < 100$) when compared with the thin-walled concrete-filled tubes (D/t of up to 180) sometimes used in bridge piles. In the tests, longitudinal compressive load was applied either concentrically or eccentrically until failure occurred. The main conclusions from these tests of circular-sectioned concrete-filled tubes are listed below:

(i) The composite concrete-filled tube has vastly superior ductility to that of either the empty tube or unconfined concrete. Stable load-carrying capacity was in evidence long after local buckling first occurred.

(ii) Short concrete-filled tubes possess strength in excess of that offered by the sum of the independent strengths of an empty tube and unconfined concrete. However, similar tests of square-sectioned concrete-filled tubes indicated no such excess strength.

(iii) The strength of long columns can be satisfactorily estimated by first assuming that composite behaviour occurs between tube and concrete, and then analysing as an "equivalent" reinforced concrete section, as was previously outlined in Section 1.2.3.

The only previous investigation of steel-encased reinforced concrete members, under conditions likely to be appropriate to the seismic loading of piles, was the preliminary investigation (1.3) to this thesis. In this investigation, half-scale

models of steel-encased reinforced concrete piles were tested essentially as vertical beams with a low level of constant vertical longitudinal load. Cyclic horizontal lateral load was applied at midheight to simulate seismic loading. The tubes used in the tests had D = 360 mm and t = 5 mm (D/t = 72). Based on the measured steel properties, σ_y = 370 MPa and E_s = 206,000 MPa, the casing D/t ratio should have been less than 67 according to the criterion represented by equation 1.8. Thus the models were marginally in violation of equation 1.8. Despite this design violation and the local buckling that was observed in the casing, under the simulated seismic loading ductile behaviour was observed and full flexural strength based on compatible behaviour between tube and concrete was attained. The main recommendations for further research based on this preliminary investigation are listed below:

(i) Additional tests and theoretical analyses of model piles with casing D/t ratios in the range of those currently used in practice (60 - 180) should be conducted so that the actual strength and ductility characteristics of all prototype steel-encased piles can be assessed.

(ii) Tests and theoretical analyses should be conducted to assess the strength and ductility characteristics of piles with circumferential discontinuities in the casing, representing the worst case of defective circumferentially running welds.

(iii) A study of the flexural bond characteristics between casing and core concrete under cyclic loading conditions should be conducted.

1.4.2 Pile-Soil Interaction

Full-scale lateral load testing of prototype piles has been performed at a variety of sites. For example, Carter (1.27) lists a total of six pile tests which were performed in either uniform sand, uniform clay, or a layered soil. In all of the tests, lateral load and the lateral deflection and slope at the level of application of lateral load were measured. In two of the tests, Mangere Bridge (1.28) and Mustang Island (1.29) which involved piles with diameters of 1370 mm and 610 mm respectively, strain gauges were mounted along two vertical lines on opposite sides of the pile to enable the curvature, $\psi(x)$, as a function of distance along the pile, x, to be calculated. By using the following elementary beam theory it was then possible to determine the deformations and actions imposed on the pile:

$$M(x) = EI.\psi(x) \tag{1.10}$$

$$V(x) = EI.\psi'(x) \tag{1.11}$$

$$p(x) = EI.\psi''(x)/D \tag{1.12}$$

$$\theta(x) = \int \psi(x).dx \tag{1.13}$$

$$y(x) = \iint \psi(x).dx.dx \tag{1.14}$$

where $\psi'_{(x)} = d\psi(x)/dx$

$\psi''_{(x)} = d^2\psi(x)/dx^2$

$M(x)$ = moment on pile

$V(x)$ = shear force on pile

$p(x)$ = change in lateral pressure on the pile, from the original unloaded condition.

$\theta(x)$ = slope of pile

$y(x)$ = lateral deflection of pile.

Thus, in principle, at any given depth, x, the pressure-deflection or $p(x) - y(x)$ relationship in the soil can be calculated. In practice the calculation of $\theta(x)$ and $y(x)$ by the successive numerical integration of $\psi(x)$ is stable. However the calculation of $V(x)$ and $p(x)$ by successive numerical differentiation of $M(x)$ is potentially unstable, and considerable judgement has to be exercised to achieve physically reasonable results. Nevertheless, both the Mangere Bridge and Mustang Island tests have shown that soil behaves in a non-linear fashion even at very low strain levels. It should be noted that the full-scale pile tests were limited to the elastic range of pile behaviour which is a necessary condition for equations 1.10 to 1.12 to be valid. Thus an in-situ study of the behaviour of full-scale piles in the plastic range has not been attempted.

On the basis of the $p(x) - y(x)$ soil relationships found from full-scale tests, models for sand and clay behaviour have been proposed. These models allow for the reduction in soil stiffness which occurs as the magnitude of strain increases. Scott (1.30) has formulated a simple bi-linear model, Reese et al (1.29) have formulated a relationship consisting of two straight lines and two parabolas, Parker (1.31) and Pender (1.32) have modelled behaviour using hyperbolic functions. Figure 1.10 illustrates these relationships. All of the above theoretical models are semi-empirical, as they have some theoretical justification. For example the Reese et al method derives an ultimate soil strength, at a given depth, on the basis of the weaker of two possible failure mechanisms. The first mechanism which tends to dominate behaviour close to the ground surface, involves the formation of a passive wedge in front of the pile. The second mechanism which tends to dominate soil behaviour at greater depths involves horizontal flow of the soil in the vicinity of the pile. Both possible soil failure mechanisms are illustrated in Figure 1.11. Despite this rational basis for determining soil ultimate strength, Reese et al still found it necessary to include empirical constants in their soil models to provide a match with the results of the Mustang Island tests.

Small-scale model tests have also been performed, but these have also been limited to the elastic range of pile behaviour. Goldsmith (1.33) has investigated soil displacement around rigid poles, and Fendall (1.34) has investigated the reduction of pile group lateral stiffness due to interaction effects. However both of these investigations employed very small model piles, with diameters of less than or equal to 20 mm, embedded in dry sand under normal gravity conditions. The mechanical properties of soils depend upon the gravity induced stresses within the soil. Therefore if the prototype soil is to be used the model soil bed should be subjected to a larger gravitational field (L_r, where L_r = the ratio of length in the prototype to length in the model) than the prototype to satisfy the laws of similitude, and to achieve the same soil stresses in the model as in the prototype. For the tests of Goldsmith (1.33) and Fendall (1.34), which were performed under normal gravity conditions, model pile-soil behaviour is overly dominated by the soil wedge type failure shown in Figure 1.11; whereas the prototype pile would tend to be more dominated by horizontal shear failure in the soil, also shown in Figure 1.11. Thus model tests such as these which do not correctly model soil stresses can only be used to crudely indicate soil behaviour. However certain aspects of pile behaviour such as the magnitude of stress and strain in the pile which do not depend directly on the scaling of gravity are modelled accurately.

To generate a properly scaled gravity field when using small-scale models, it is necessary to resort to centrifuge testing (1.35) in which artificially high gravity fields can be produced. Scott (1.36) has satisfactorily reproduced the results from the full-scale pile test performed at Mustang Island by using this method. However he did not achieve a perfect match between his 1/100 scale model and the prototype due to difficulties in exactly reproducing the layering of soil from prototype to model.

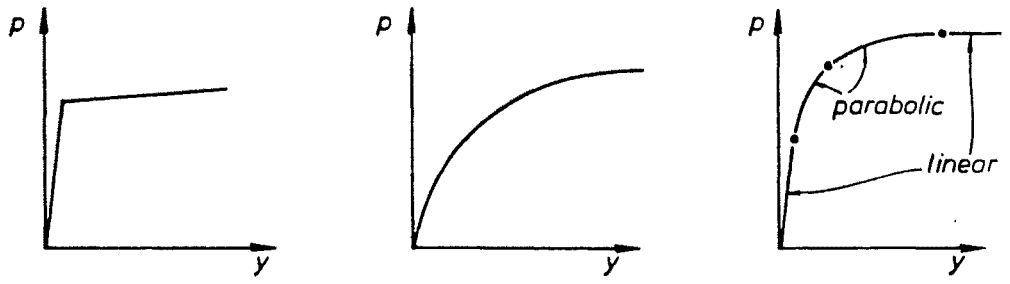

FIGURE 1.10 TYPICAL SOIL PRESSURE-DEFLECTION, P-Y, RELATIONSHIPS.

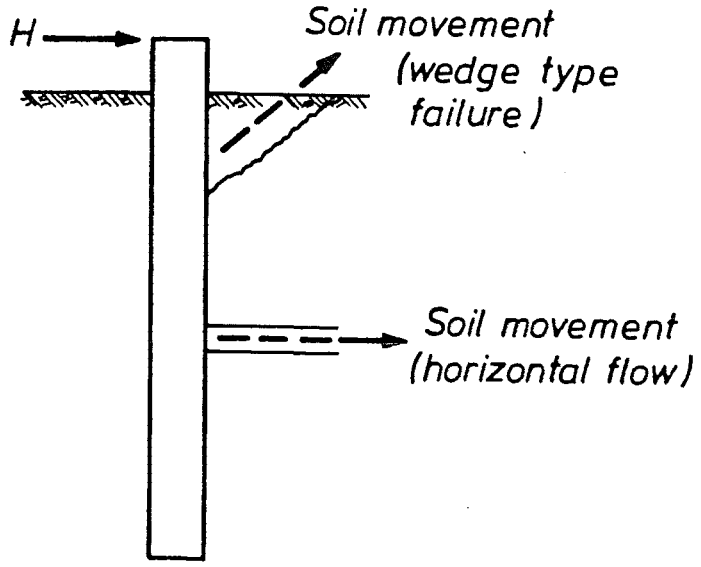

FIGURE 1.11 MODES OF SOIL FAILURE.

Computer programs which utilise non-linear depth-dependent soil p-y relationships have been developed. Reese et al (1.37) have used a finite difference technique to solve the governing fourth order differential equation equation 1.4). Carter (1.27) has used a matrix displacement method to solve the same problem. However soil p-y relationships which have been empirically calibrated against specific test results may give poor results when applied to different soil profiles than the one from which they were originally calibrated. The analyses also do not allow for non-linear behaviour of the pile itself. Caution should thus be used in extrapolating the results from such analyses to real design situation.

Douglas (1.38) has conducted ambient vibration tests, and pull-back-and-quick-release tests on bridge structures to determine foundation stiffness and damping properties. He obtained good correlation between his experimental results and predictions based on existing analytical methods. However the experiments were conducted in the small vibration range and thus his results may not be valid for large earthquake-induced vibrations.

Soil-pile interaction effects have been identified as a major uncertainty in recent U.S.A./N.Z. cooperative workshops into the earthquake resistance of highway bridges (1.38 and 1.39). From these workshops, recommendations of topics for on-going and future study of pile-soil interaction under earthquake loading have been made:

(i) More earthquake ground motion records at a variety of different sites should be obtained.

(ii) The soil stiffnesses used in analyses should be correlated with the results of in-situ soil tests and field tests of piles under lateral load.

(iii) More field tests into the plastic range of soil and pile behaviour should be conducted.

(iv) The influence of scale effects on soil stiffness should be investigated.

(v) Analytical studies of the effect of earthquake-induced ground motion, as distinct from inertial response, on bridge foundations should be undertaken.

(vi) The use of realistic soil stiffness and damping values in pile-soil interaction analyses, and the verification of results with data from experiments, field tests and actual response in earthquakes.

1.5 SCOPE AND FORMAT OF REPORT

The investigation described in this thesis has two main aims:

(i) The evaluation of strength and ductility characteristics of steel-encased reinforced concrete members under axial load and cyclically varying bending moment, which are investigated in Chapters 2-5.

(ii) The determination of the likely behaviour of bridge piles in a major earthquake, due to inertia loading of the bridge structure which is covered in Chapters 6-7.

These two main aims have been previously identified in Sections 1.4.1 and 1.4.2 as important. The effects of curvatures imposed on a pile at great depth in the foundation due to the soil free-field motion, and the effects of liquefaction on piles are considered to be outside the scope of this research.

The thesis comprises eight chapters. Chapter 1 represents an introduction to the subject matter, Chapter 8 contains conclusions and recommendations for future research. The remaining chapters 2-7 address the individual studies within the overall investigation.

1.5.1 Chapter 2 - Multi-Axial Stress-Strain Response of Steel-Encased Concrete

In the moment-curvature analysis of sections subjected to longitudinal load and bending moment, it is common to utilise material stress-strain laws which have been derived from longitudinal-load tests. In Chapter 2, the response of short circular-sectioned steel-encased concrete members to both tensile and compressive monotonically applied longitudinal load is investigated. Lateral interaction between tube and concrete results in the response of the composite member being different to the sum of the independent responses of tube and concrete. For both tensile and compressive load, analytical stress-strain laws for the tube and concrete which account for this lateral interaction are developed. For compressive loading, predictions from these stress-strain laws are compared with the experimental results of previous researchers.

1.5.2 Chapter 3 - Longitudinal-Load Tests of Short Thick-Walled Steel-Encased Concrete Members

In Chapter 3, an experimental investigation into the response to longitudinal load of short circular-sectioned thick-walled (casing D/t ratio = 25.6) steel-encased concrete members is described. Three types of longitudinal loading were employed: monotonic tension, monotonic compression, and cyclic tension and compression. Experimental load-stress-strain responses were determined from these tests and compared with predictions based on the constitutive models described in Chapter 2.

1.5.3 Chapter 4 - Flexural Strength and Ductility Characteristics of Steel-Encased Concrete

Chapter 4 describes the construction and simulated seismic response of approximately half-scale models of steel-encased reinforced concrete bridge piles, tested under a constant level of longitudinal load with pseudo-static cyclic reversals of lateral displacement at high ductility levels. The main variable considered in these tests was the influence of the casing D/t ratio. The influence of a circumferential discontinuity in the casing in the plastic hinge zone was also examined.

Strain and curvature profiles in the vicinity of the critical plastic regions were plotted to indicate the damage resulting from the cyclic loading. Flexural strength, ductility and energy-dissipating characteristics of the model piles were examined and compared with those obtained from conventionally designed reinforced concrete members. Finally the magnitude of flexural bond between tube and concrete under cyclic loading was investigated.

1.5.4 Chapter 5 - Moment-Curvature and Load-Deformation Analyses of Steel-Encased Concrete Members

Analytical predictions of the moment-curvature and lateral load-lateral deflection responses of steel-encased reinforced concrete piles to monotonic loading are described in Chapter 5. The material stress-strain relationship used for the internal longitudinal reinforcing bars was based on the results of tensile testing of bar samples. The constitutive laws developed in Chapter 2 were used to model concrete and casing behaviour. A comparison of the analytical predictions was then made with the experimental results which were described in Chapter 4.

1.5.5 Chapter 6 - Model Tests of Steel-Encased Concrete Piles in a Dry Sand Foundation

The pseudo-static - lateral-load testing of 115 mm diameter steel-encased concrete model piles embedded up to 20 pile diameters in a steel tank containing dry sand is described in Chapter 6. Two experiments involved the testing of piles under capped-head conditions, and nine experiments involved piles under free-head conditions. In the tests, the sand density and the pattern of lateral displacement application were varied.

Pile strain and deflection measurements were taken during testing. This enabled the curvature ductility factor on the pile to be calculated and compared with a theoretical prediction based on equivalent cantilever behaviour. Soil lateral pressure-lateral deflection responses were also calculated at varying depths of the pile and compared with predictions based on an existing analytical model.

1.5.6 Chapter 7 - Finite Difference Analysis of Free-Head Piles under Lateral Load

In Chapter 7, a solution technique for solving the pile-soil interaction problem, for monotonically applied lateral load, is described. Solutions are achieved by using a finite difference approximation to the governing fourth order differential equation (Equation 1.4). Non-linearities in the pile moment-curvature and soil lateral pressure-lateral deflection-depth relationships are taken into account by using tangential stiffness properties and an incremental solution technique. The responses of pile-soil systems were analysed using this technique.

Chapter Two

MULTI-AXIAL STRESS-STRAIN RESPONSE OF STEEL-ENCASED CONCRETE

2.1 INTRODUCTION

This chapter describes theoretical and experimental investigations into the response of circular-sectioned concrete-filled tubes to tensile and compressive longitudinal loads. Previous investigators, including Tomii et al (2.1), have shown that when a composite concrete-filled tube is loaded longitudinally, concrete and tube interact laterally due to the difference in Poisson's ratio between concrete and steel. The result is a state of triaxial stress in both concrete and tube. At large values of longitudinal-compression strain, behaviour is further complicated by the presence of local buckling in the tube. The purpose of the investigation described in this chapter is to develop and calibrate constitutive models which trace satisfactorily the multi-axial stress-strain paths of both tube and concrete, in composite concrete-filled tubes subjected to monotonically increasing longitudinal tensile and compressive loads. The constitutive models developed in this chapter are used in subsequent chapters to obtain moment-curvature relationships for steel-encased reinforced concrete model piles.

The stress-strain models for concrete and longitudinal reinforcing bars which have been used in moment-curvature analyses of reinforced concrete sections have usually been deduced (2.2) from the results of concentric longitudinal-load tests. This approach ignores the effect of shear force and strain gradient which are known (2.3) to modify stress-strain characteristics. Nevertheless, this method has been shown by Mander et al (2.2) to give accurate results in moment-curvature analyses of reinforced concrete sections. The same approach was adopted in this investigation to derive constitutive models for concrete-filled tubes which may be considered to be similar in many respects to conventionally reinforced concrete members.

The following topics are covered in the remaining sections of this chapter:

(i) a review of the behaviour of empty tubes and unconfined concrete subjected to monotonically increasing longitudinal load;

(ii) the applicability of existing concrete and steel constitutive laws to describe the composite behaviour of concrete-filled tubes;

(iii) a literature review of research concerning the longitudinal-load testing of concrete-filled tubes;

(iv) the development of simple concrete and steel constitutive models to describe the response of concrete-filled tubes to monotonically increasing tensile and compressive longitudinal loads ; and

(v) a comparison of experimental results with theoretical predictions.

In this chapter the sign convention used for loads, stresses and strains is positive represents compression.

2.2 REVIEW OF RELEVANT THEORY AND PREVIOUS RESEARCH

In order to describe the behaviour of circular-sectioned concrete-filled tubes, it is first necessary to consider the behaviour of empty tubes and concrete which are acting separately, and then to consider the interactive effects which occur when tube and concrete act compositely. Hence the following sections (2.2.1 - 2.2.6.3) contain a discussion of the behaviour and constitutive modelling of concrete and empty tubes, followed by a literature review of research concerning longitudinal-load tests of circular-sectioned concrete-filled tubes.

2.2.1 Empty Tube Behaviour

Empty tubes under longitudinal-tension load will fail when the ultimate tensile strength of the steel is reached. However only very short thick-walled tubes will fail under longitudinal-compression load due to steel crushing. Generally under longitudinal-compression load, behaviour will be governed by one of two types of instability:

(i) The first type of instability is referred to as column buckling, as shown in Fig. 2.1(a), where for elastic buckling the maximum steel stress is given by the Euler buckling formula:

$$\sigma_{cr} = \frac{\pi^2 E_s}{(L_e/r_g)^2} \tag{2.1}$$

where σ_{cr} = critical (buckling) stress
E_s = steel elastic modulus
L_e = length of equivalent pin-ended strut
r_g = radius of gyration of the section.

For an empty tube:

$$r_g = 0.354(D - t) \tag{2.2}$$

(ii) The second type of instability is caused by local buckling of the tube wall which involves inward and outward corrugation of the tube as shown in Fig. 2.1(b). In 1908, Lorenz (2.4) obtained a theoretical solution for this type of instability:

$$\sigma_{cr} = \frac{1.2\ E_s}{(D/t)} \tag{2.3}$$

In developing equation 2.3 it was assumed that the tube is linearly elastic and has no imperfections. The equation indicates that σ_{cr} is inversely proportional to the tube D/t ratio. For typical mild steel, with for example E_s = 205 000 MPa and σ_y (yield stress) = 300 MPa, equation 2.3 predicts that local buckling will occur before tube yielding when the tube D/t ratio exceeds 820. However as described by Troitsky (2.5), there is poor correlation between equation 2.3 and experimental evidence, since small imperfections in test specimens, non-uniformity in loading, and small uncertainties in the control of boundary conditions have a large effect. Typically (2.5) loads at which elastic local buckling occurs have been in the range of 10% to 30% of the Lorenz solution (equation 2.3). Thin-walled tubes are more susceptible to imperfections than are thick-walled tubes. Hence thin-walled tubes tend to give poorer agreement with the theoretical Lorenz solution than do thick-walled tubes. Wilson and Newmark's (2.6) tests of tubular steel compression members, with large tube D/t ratios, implied actual local

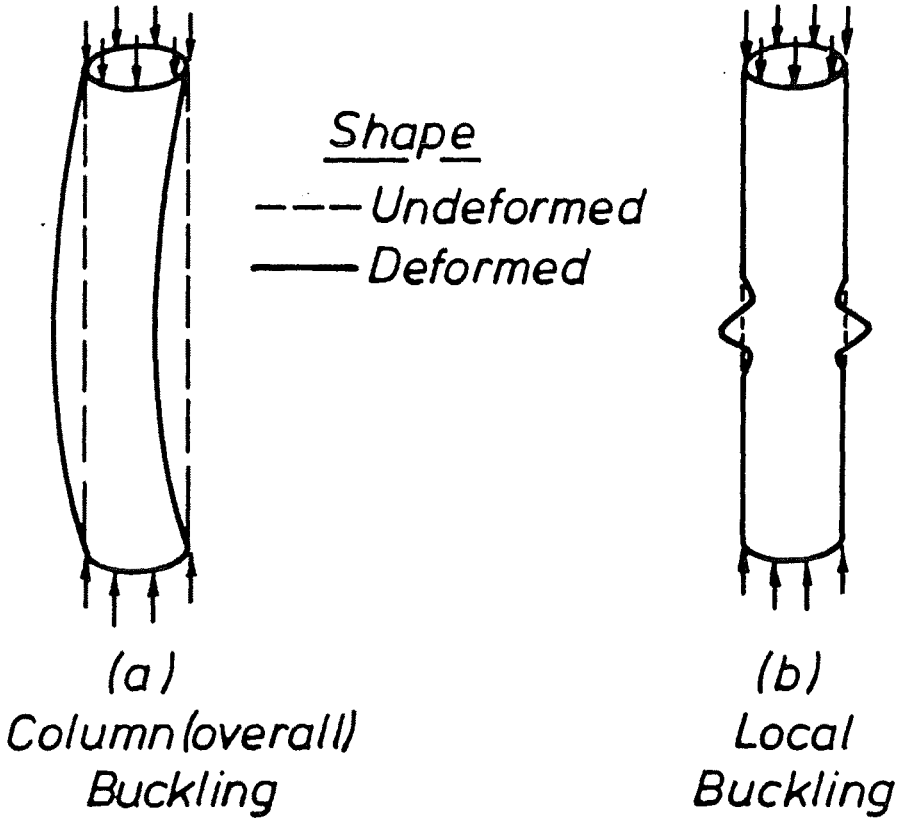

FIG. 2.1 : BUCKLING FAILURE OF EMPTY TUBES

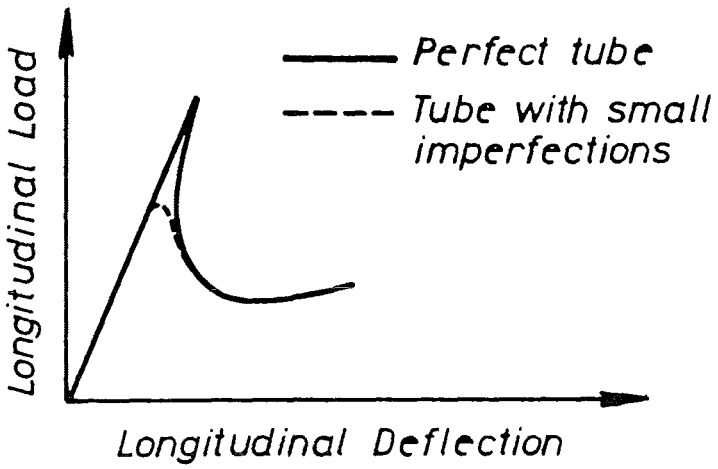

FIG. 2.2 : BEHAVIOUR OF EMPTY TUBES WHICH FORM LOCAL BUCKLES - FROM McGUIRE (2.7).

buckling stresses assuming linear elastic behaviour of:

$$\sigma_{cr} = \frac{55000}{(D/t)} \text{ MPa} \qquad (2.4)$$

For steel with σ_y = 300 MPa, equation 2.4 predicts that local buckling will occur before tube yielding when the tube D/t ratio exceeds 183. Rapid strength degradation occurs when an empty tube develops local buckling, as is illustrated in Fig. 2.2. Thus design codes give larger factors of safety against local buckling than against material failure.

The elastic solutions to column and local buckling given by equations 2.1, 2.3 and 2.4 are sufficient for indicating if the tube will yield before it buckles. Therefore these equations are suitable for a design philosophy in which ductility, the ability to deform plastically without excessive strength degradation, is not necessary. However current seismic design philosophy generally relies on ductility provided by post-elastic response of steel reinforcement or structural steel members. In the post-elastic range of steel response, the stiffness of the steel is much lower than its stiffness in the elastic range. In the yield range of behaviour the tangent modulus, E_t, of the steel is zero, while in the strain-hardening range E_t is typically less than $0.05E_s$ (2.2). Thus it is inevitable that unless extremely short thick-walled tubes are used, either inelastic column or local buckling will limit both the strength and ductility capacity of empty tubes.

2.2.2 Constitutive Modelling of Steel

In the following sections the background theory necessary to describe the three-dimensional stress-strain behaviour of steel is outlined, and manipulated to formulate simple constitutive laws which describe the response of the tube in a composite concrete-filled tube to tensile and compressive longitudinal loads. These laws assume isotropic steel properties and monotonic loading.

2.2.2.1 Elastic Range

In the elastic range of steel behaviour a knowledge of the values of the elastic constants E_s (typically 205000 MPa) and ν_s (elastic value of Poisson's ratio for steel, typically 0.3) is sufficient to enable the strain field in the tube to be determined from the stress field (2.8) using Hooke's Law as follows:

$$\varepsilon_L = \frac{\sigma_L - \nu_s (\sigma_H + \sigma_R)}{E_s} \qquad (2.5)$$

$$\varepsilon_H = \frac{\sigma_H - \nu_s (\sigma_L + \sigma_R)}{E_s} \qquad (2.6)$$

$$\varepsilon_{RT} = \frac{\sigma_R - \nu_s (\sigma_L + \sigma_H)}{E_s} \qquad (2.7)$$

where ε_L, ε_H, ε_{RT} = tube strains, in the longitudinal, hoop and radial directions respectively

and σ_L, σ_H, σ_R = tube stresses, in the longitudinal, hoop and radial directions, respectively.

Alternatively if the strain field has been measured and the stress field is required, equations 2.5 to 2.7 can be inverted to give:

$$\sigma_L = \left(\frac{E_s}{1 + \nu_s}\right)\varepsilon_L + (\varepsilon_L + \varepsilon_H + \varepsilon_{RT}) \frac{\nu_s E_s}{(1 + \nu_s)(1 - 2\nu_s)} \quad (2.8)$$

$$\sigma_H = \left(\frac{E_s}{1 + \nu_s}\right)\varepsilon_H + (\varepsilon_L + \varepsilon_H + \varepsilon_{RT}) \frac{\nu_s E_s}{(1 + \nu_s)(1 - 2\nu_s)} \quad (2.9)$$

$$\sigma_R = \left(\frac{E_s}{1 + \nu_s}\right)\varepsilon_{RT} + (\varepsilon_L + \varepsilon_H + \varepsilon_{RT}) \frac{\nu_s E_s}{(1 + \nu_s)(1 - 2\nu_s)} \quad (2.10)$$

Although under longitudinal load concrete bearing radially on to the tube will result in a finite value for tube σ_R, this value will generally be small and can be ignored without significant error. Then for a biaxial stress field ($\sigma_R = 0$) equations 2.8 - 2.10 can be rearranged and solved for tube σ_L and σ_H:

$$\sigma_L = \frac{E_s}{1 - \nu_s^2} (\varepsilon_L + \nu_s.\varepsilon_H) \quad (2.11)$$

$$\sigma_H = \frac{E_s}{1 - \nu_s^2} (\varepsilon_H + \nu_s.\varepsilon_L) \quad (2.12)$$

The tube σ_L/σ_H ratio can be determined by dividing equation 2.11 by 2.12 and rearranging to give:

$$\frac{\sigma_L}{\sigma_H} = \frac{1 + \nu_s (\varepsilon_H/\varepsilon_L)}{(\varepsilon_H/\varepsilon_L) + \nu_s} \quad (2.13)$$

Equation 2.13 is in a form suitable for direct comparison with the equation governing the tube σ_L/σ_H ratio in the plastic range which is developed subsequently (see equation 2.20).

2.2.2.2 Plastic Range

The elastic range of material behaviour is only the prelude to the inelastic response of a concrete-filled tube, and after yielding has occurred the elastic relationships between stresses and strains (equations 2.5 - 2.13) are no longer valid. To calculate response in the plastic range of behaviour, it is necessary to use other relationships such as those discussed in the following sections (a)-(d).

In the plastic range of steel behaviour it is convenient to separate strain into elastic and plastic components. The elastic component of strain in the longitudinal, hoop and radial directions; ε_L^e, ε_H^e and ε_{RT}^e respectively; are related to σ_L, σ_H and σ_R by Hooke's Law (equations 2.5-2.7) where ε_L^e, ε_H^e and ε_{RT}^e are substituted for ε_L, ε_H and ε_{RT} respectively in equations 2.5-2.7. Hence the plastic components of strain in the longitudinal, hoop and radial directions; ε_L^p, ε_H^p and ε_{RT}^p respectively, can be determined from:

$$\varepsilon_L^p = \varepsilon_L - \varepsilon_L^e = \varepsilon_L - \frac{\sigma_L - \nu_s(\sigma_H + \sigma_R)}{E_s} \quad (2.14)$$

$$\varepsilon_H^p = \varepsilon_H - \varepsilon_H^e = \varepsilon_H - \frac{\sigma_H - \nu_s(\sigma_L + \sigma_R)}{E_s} \quad (2.15)$$

$$\varepsilon_{RT}^p = \varepsilon_{RT} - \varepsilon_{RT}^e = \varepsilon_{RT} - \frac{\sigma_R - \nu_s(\sigma_L + \sigma_H)}{E_s} \quad (2.16)$$

(a) Prandtl-Reuss Relationships

On the basis of test results (2.8), it has been shown that in the plastic range of steel behaviour, stresses are related to the increments of plastic strain by the following Prandtl-Reuss relationships:

$$\frac{d\varepsilon_L^p}{\sigma_L - 1/3(\sigma_L + \sigma_H + \sigma_R)} = d\lambda \qquad (2.17)$$

$$\frac{d\varepsilon_H^p}{\sigma_H - 1/3(\sigma_L + \sigma_H + \sigma_R)} = d\lambda \qquad (2.18)$$

$$\frac{d\varepsilon_{RT}^p}{\sigma_R - 1/3(\sigma_L + \sigma_H + \sigma_R)} = d\lambda \qquad (2.19)$$

where $d\varepsilon_L^p$, $d\varepsilon_H^p$ and $d\varepsilon_{RT}^p$ = infinitesimal increments of tube plastic strain in the longitudinal, hoop and radial directions, respectively

and $d\lambda$ = variable, which is a function of the loading history.

It should be noted that the denominators of the expressions in equations 2.17-2.19 are the deviatoric stresses in the longitudinal, hoop and radial directions respectively.

For $\sigma_R = 0$ which is correct for empty tubes and approximately correct for concrete-filled tubes under longitudinal load, equations 2.17-2.18 can be rearranged to eliminate $d\lambda$ and solved for the tube σ_L/σ_H ratio:

$$\frac{\sigma_L}{\sigma_H} = \frac{1 + 1/2\ (d\varepsilon_H^p/d\varepsilon_L^p)}{(d\varepsilon_H^p/d\varepsilon_L^p) + 1/2} \qquad (2.20)$$

The σ_L/σ_H relationships in the elastic (equation 2.13) and plastic (equation 2.20) ranges are similar in form since equation 2.20 could be derived from equation 2.13, by substituting $d\varepsilon_H^p$, $d\varepsilon_L^p$ and 0.5 for ε_H, ε_L and ν_s respectively.

(b) Mean Stress-Volumetric Strain Relationship

Despite the fact that in the plastic range stresses cannot be determined from strains using Hooke's Law (equations 2.8-2.10), it has been demonstrated that the relationship between the mean stress and the volumetric strain is linear throughout the elastic and plastic ranges of steel behaviour (2.9), and is given by:

$$\frac{1/3(\sigma_L + \sigma_H + \sigma_R)}{\varepsilon_L + \varepsilon_H + \varepsilon_{RT}} = \frac{E_s}{3(1 - 2\nu_s)} \qquad (2.21)$$

The right hand side, numerator of the left hand side and denominator of the left hand side of equation 2.21 represents the bulk modulus, the mean stress and the volumetric strain respectively in the steel. Because volume changes are elastic, equations 2.22 and 2.23, which represent the experimental result (2.9) that plastic strains do not alter the volume, also hold.

$$\varepsilon_L^p + \varepsilon_H^p + \varepsilon_{RT}^p = 0 \qquad (2.22)$$

$$d\varepsilon_L^p + d\varepsilon_H^p + d\varepsilon_{RT}^p = 0 \qquad (2.23)$$

(c) Yield, Strain-Hardening and Ultimate Strength Criteria

Under loading which results in uniaxial stress (σ_L), stress-strain response in the plastic range of steel behaviour can be defined by the $\sigma_L - \varepsilon_L^p$ relationship which is determined from the $\sigma_L - \varepsilon_L$ response as shown in Fig. 2.3. Since $\sigma_H = \sigma_R = 0$, then from $\varepsilon_L^e = \sigma_L/E_s$ and equation 2.14, ε_L^p can be calculated as:

$$\varepsilon_L^p = \varepsilon_L - \sigma_L/E_s \tag{2.24}$$

Figure 2.3 also shows that typically steel exhibits three zones of behaviour: an elastic range (0 - X), a yield range (X - Y), and a strain-hardening range (Y - Z). The ε_L at points X,Y and Z are known as the yield strain, ε_y, the strain at commencement of strain-hardening ε_{sh}, and the ultimate strain ε_u, respectively.

Loading which results in a multi-axial state of stress can be treated in a similar fashion. This is achieved by using an effective stress-effective plastic strain, $\sigma_{eff} - \varepsilon_{eff}^p$, relationship for the multi-axial stress state (2.8), in place of the $\sigma_L - \varepsilon_L^p$ relationship which is used in the uniaxial stress state. For the longitudinal, hoop and radial directions of the tube corresponding to the principal directions of stress and strain, then σ_{eff} and ε_{eff}^p are defined (2.8) by:

$$\sigma_{eff} = [(\sigma_L - \sigma_H)^2 + (\sigma_H - \sigma_R)^2 + (\sigma_R - \sigma_L)^2\ ]^{\frac{1}{2}}/\sqrt{2} \tag{2.25}$$

$$\varepsilon_{eff}^p = \int d\varepsilon_{eff}^p \tag{2.26}$$

$$\text{where } d\varepsilon_{eff}^p = \frac{\sqrt{2}}{3}\ [(d\varepsilon_L^p - d\varepsilon_H^p)^2 + (d\varepsilon_H^p - d\varepsilon_{RT}^p)^2 + (d\varepsilon_{RT}^p - d\varepsilon_L^p)^2\ ]^{\frac{1}{2}} \tag{2.27}$$

The values of effective strain ε_{eff}, effective elastic strain ε_{eff}^e, and effective plastic strain ε_{eff}^p, in the multi-axial stress field which are analagous to ε_L, ε_L^e and ε_L^p respectively in a uniaxial stress (σ_L) field can also be calculated from:

$$\varepsilon_{eff} = \varepsilon_{eff}^e + \varepsilon_{eff}^p \tag{2.28}$$

$$\text{where } \varepsilon_{eff}^e = \sigma_{eff}/E_s \tag{2.29}$$

$$\text{and hence } \varepsilon_{eff} = \varepsilon_{eff}^p + \sigma_{eff}/E_s \tag{2.30}$$

The more widely known octahedral shear stress, τ_{oct}, and plastic component of octahedral shear strain, γ_{oct}^p, are related (2.8) to σ_{eff} and ε_{eff}^p respectively by:

$$\tau_{oct} = \frac{\sqrt{2}}{3}\ \sigma_{eff} \tag{2.31}$$

$$\gamma_{oct}^p = \varepsilon_{eff}^p/\sqrt{2} \tag{2.32}$$

It should be noted that for uniaxial stress (σ_L), $\sigma_{eff} = |\sigma_L|$ and $\varepsilon_{eff}^p = |\varepsilon_L^p|$. This can be verified by substituting $\sigma_H = \sigma_{RT} = 0$ into equation 2.25, to show that $\sigma_{eff} = |\sigma_L|$. Substitution of $\sigma_H = \sigma_R = 0$ into the Prandtl-Reuss

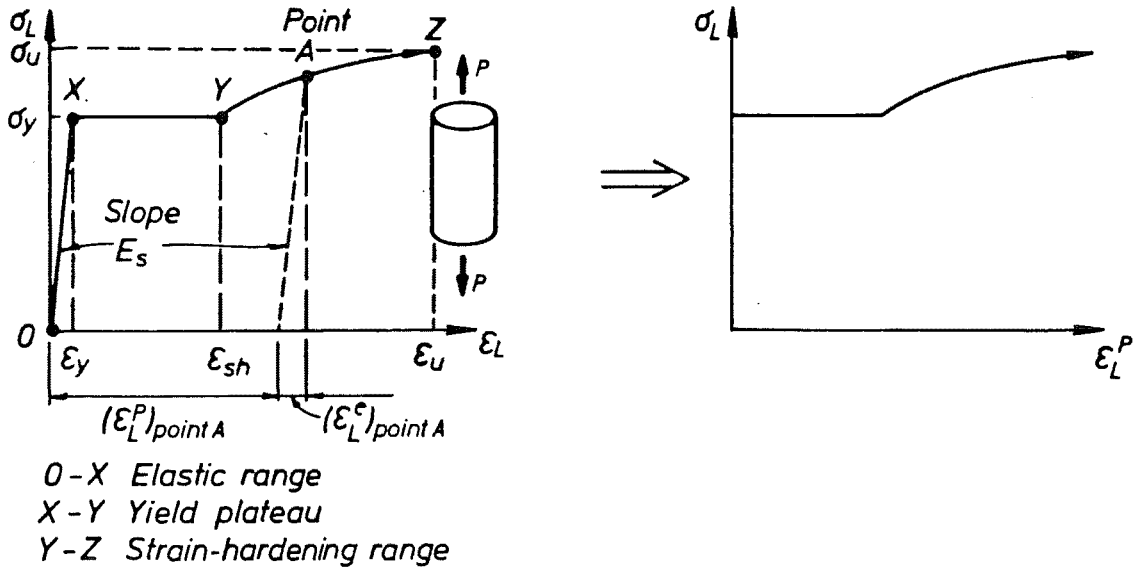

FIG. 2.3 : DERIVING THE LONGITUDINAL STRESS-PLASTIC LONGITUDINAL STRAIN RELATIONSHIP FROM A UNIAXIAL STRESS TEST

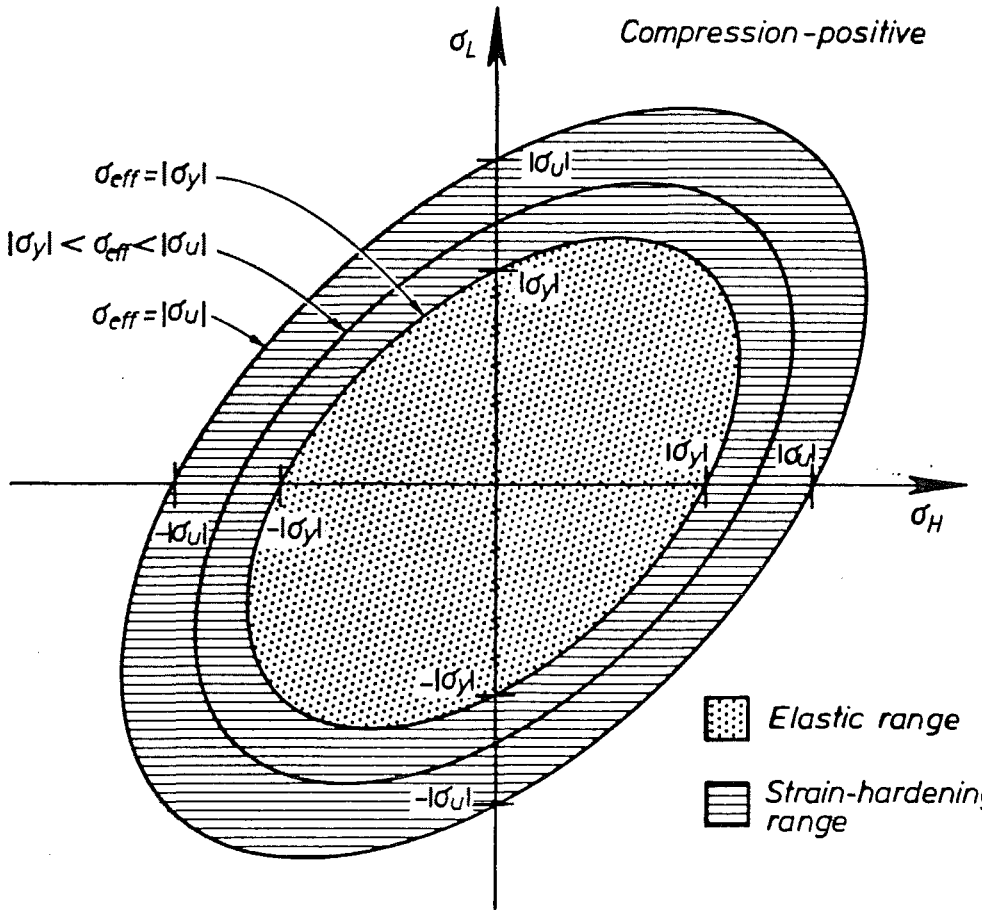

FIG. 2.4 : YIELD, STRAIN-HARDENING, AND ULTIMATE STRENGTH CURVES

relationships (equations 2.17-2.19) gives:

$$\frac{d\varepsilon_L^p}{2/3\sigma_L} = d\lambda \tag{2.33}$$

$$\frac{d\varepsilon_H^p}{-1/3\sigma_L} = d\lambda \tag{2.34}$$

$$\frac{d\varepsilon_{RT}^p}{-1/3\sigma_L} = d\lambda \tag{2.35}$$

Elimination of $d\lambda$ between equations 2.33-2.35 gives: $d\varepsilon_H^p = d\varepsilon_{RT}^p = -0.5d\varepsilon_L^p$ Then substituting $-0.5d\varepsilon_L^p$ for $d\varepsilon_H^p$ and $d\varepsilon_{RT}^p$ into equations 2.26 and 2.27 results in $\varepsilon_{eff}^p = |\varepsilon_L^p|$.

Thus the $\sigma_{eff} - \varepsilon_{eff}^p$ relationship for applying to multi-axial stress-strain behaviour can conveniently be taken as equivalent to the $|\sigma_L| - |\varepsilon_L^p|$ relationship derived from a uniaxial stress (σ_L) test, as shown in Fig. 2.3. This is the reason for using a $\sigma_{eff} - \varepsilon_{eff}^p$ formulation rather than the more conventional $\tau_{oct} - \gamma_{oct}^p$ formulation.

For a stress field in the tube, with $\sigma_R = 0$, the square of equation 2.25 simplifies to:

$$\sigma_{eff}^2 = \sigma_L^2 + \sigma_H^2 - \sigma_L.\sigma_H \tag{2.36}$$

In the yield range of steel behaviour, $\sigma_{eff} = |\sigma_y|$ the magnitude of the yield stress established from a uniaxial stress test. Substituting $\sigma_{eff} = |\sigma_y|$ into equation 2.36 results in the Von Mises yield criterion (2.8) where σ_L and σ_H correspond to the principal stresses:

$$\sigma_y^2 = \sigma_L^2 + \sigma_H^2 - \sigma_L.\sigma_H \tag{2.37}$$

Equation 2.37 represents an ellipse in the two-dimensional stress space, $\sigma_L - \sigma_H$. Successively large ellipses in the stress space may be used to represent possible (σ_L, σ_H) coordinates up to and including the ultimate strength of the steel as shown in Fig. 2.4. At ultimate strength in the $\sigma_L - \sigma_H$ field $\sigma_{eff} = |\sigma_u|$, the magnitude of the ultimate strength of steel established from a uniaxial stress test. In the strain-hardening range of steel behaviour, as ε_{eff}^p increases from $|\varepsilon_{sh} - \varepsilon_y|$ to $|\varepsilon_u - \varepsilon_y|$, σ_{eff} increases from $|\sigma_y|$ to $|\sigma_u|$.

Figure 2.4 also shows that a biaxial tension-tension or compression-compression stress field results in enhanced strength for the larger of $|\sigma_L|$ or $|\sigma_H|$, from its magnitude in a uniaxial stress field at the same σ_{eff}. Peak strength enhancement from the uniaxial to the biaxial stress field occurs when $\sigma_L = 2\sigma_H$ (or $\sigma_H = 2\sigma_L$) in which case $|\sigma_L| = 1.155\ \sigma_{eff}$ (or $|\sigma_H| = 1.155\ \sigma_{eff}$). However for a biaxial tension-compression stress field, $|\sigma_L|$ and $|\sigma_H|$ are always less than the magnitude of stress present in a uniaxial stress field at the same σ_{eff}. For example if $\sigma_L = -\sigma_H$, then $|\sigma_L| = |\sigma_H| = 0.577\ \sigma_{eff}$.

Equations 2.20 and 2.36 represent functions for σ_L and σ_H in terms of $d\varepsilon_H^p/d\varepsilon_L^p$ and σ_{eff} respectively. It is possible to solve for σ_L and σ_H from these two equations to give:

$$\sigma_L = \frac{\left| \left(\frac{d\varepsilon_H^p}{d\varepsilon_L^p} \right) + 2 \right|}{\sqrt{3} \cdot \sqrt{1 + \left(\frac{d\varepsilon_H^p}{d\varepsilon_L^p} \right) + \left(\frac{d\varepsilon_H^p}{d\varepsilon_L^p} \right)^2}} S_L \cdot \sigma_{eff} \qquad (2.38)$$

$$\sigma_H = \frac{\left| 2 \left(\frac{d\varepsilon_H^p}{d\varepsilon_L^p} \right) + 1 \right|}{\sqrt{3} \cdot \sqrt{1 + \left(\frac{d\varepsilon_H^p}{d\varepsilon_L^p} \right) + \left(\frac{d\varepsilon_H^p}{d\varepsilon_L^p} \right)^2}} S_H \cdot \sigma_{eff} \qquad (2.39)$$

where $$S_L = \frac{2\, d\varepsilon_L^p + d\varepsilon_H^p}{\left| 2\, d\varepsilon_L^p + d\varepsilon_H^p \right|} \qquad (2.40)$$

and $$S_H = \frac{2\, d\varepsilon_H^p + d\varepsilon_L^p}{\left| 2\, d\varepsilon_H^p + d\varepsilon_L^p \right|} \qquad (2.41)$$

Thus it is possible to determine the stresses in a biaxial stress (σ_L and σ_H) field in the plastic range of steel behaviour provided:

(i) the three-dimensional strain history is known; and

(ii) a uniaxial stress (coupon) test on a representative sample of the steel has been performed.

An incremental solution technique should be adopted, since in the plastic range the tube stresses depend on the strain path. To evaluate tube stresses ($(\sigma_L)_{i+1}$ and $(\sigma_H)_{i+1}$) at step $i + 1$, given that step i has been previously solved, the procedure outlined below should be followed:

Step 1: Guess $(\sigma_L)_{i+1} = (\sigma_L)_i$ and $(\sigma_H)_{i+1} = (\sigma_H)_i$

Step 2: Calculate $(\varepsilon_L^p)_{i+1}$, $(\varepsilon_H^p)_{i+1}$ and $(\varepsilon_{RT}^p)_{i+1}$ from equations 2.14-2.16 using the values of E_s, ν_s, $(\sigma_L)_{i+1}$, $(\sigma_H)_{i+1}$ and $(\sigma_R)_{i+1}$ (= zero)

Step 3: Calculate

$$\left.\begin{aligned} (d\varepsilon_L^p)_{i+1} &= (\varepsilon_L^p)_{i+1} - (\varepsilon_L^p)_i \\ (d\varepsilon_H^p)_{i+1} &= (\varepsilon_H^p)_{i+1} - (\varepsilon_H^p)_i \\ (d\varepsilon_{RT}^p)_{i+1} &= (\varepsilon_{RT}^p)_{i+1} - (\varepsilon_{RT}^p)_i \end{aligned}\right\} \qquad (2.42)$$

Step 4: Calculate $(d\varepsilon_{eff}^p)_{i+1}$ from the values of $(d\varepsilon_L^p)_{i+1}$, $(d\varepsilon_H^p)_{i+1}$, $(d\varepsilon_{RT}^p)_{i+1}$ and equation 2.27.

Step 5: Calculate $(\varepsilon_{eff}^p)_{i+1} = (\varepsilon_{eff}^p)_i + (d\varepsilon_{eff}^p)_{i+1}$ (2.43)

Step 6: Obtain $(\sigma_{eff})_{i+1}$ from the values of $(\varepsilon^p_{eff})_{i+1}$ and the $\sigma_{eff} - \varepsilon^p_{eff}$ relationship (equivalent to the $\sigma_L - \varepsilon^p_L$ response obtained in a uniaxial stress (σ_L) test).

Step 7: Recalculate $(\sigma_L)_{i+1}$ and $(\sigma_H)_{i+1}$ from equations 2.38 and 2.39 and the values of $(d\varepsilon^p_L)_{i+1}$, $(d\varepsilon^p_H)_{i+1}$ and $(\sigma_{eff})_{i+1}$.

Step 8 : Do the values of $(\sigma_L)_{i+1}$ and $(\sigma_H)_{i+1}$ which were used in Step 2 agree with those recalculated in Step 7?

Yes - Convergence achieved, go to the next increment (i + 2)

No - Using the later values of $(\sigma_L)_{i+1}$ and $(\sigma_H)_{i+1}$ go to Step 2.

This iterative procedure which is used in determining σ_L and σ_H is relatively slow to converge. Also for accurate results, it is recommended that a large number of increments should be used, which implies a solution by computer or programmable calculator is appropriate.

(d) Theoretical Variation of Tube Poisson's Ratio with Strain Level

In this section, an expression for the theoretical variation, in the plastic range, of the Poisson's ratio for steel in a uniaxial stress (σ_L) field is derived. Subsequently in Chapter 3 this theoretical variation is compared with experimentally obtained variations.

For a uniaxial stress (σ_L) field in the tube, Poisson's ratio can be expressed as $-\varepsilon_H/\varepsilon_L$. In the plastic range of steel behaviour, ε_L can be divided into two components (ε^e_L and ε^p_L):

$$\varepsilon^e_L = \sigma_L/E_s \tag{2.44}$$

$$\varepsilon^p_L = \varepsilon_L - \sigma_L/E_s \tag{2.45}$$

(Similarly $\varepsilon_H = \varepsilon^e_H + \varepsilon^p_H$)

Now ε^e_H can be calculated from:

$$\varepsilon^e_H = -\nu_s \varepsilon^e_L = -\nu_s \sigma_L/E_s \tag{2.46}$$

Also as shown previously in Section 2.2.2.2(c):

$$\varepsilon^p_H = -1/2\ \varepsilon^p_L = -1/2\ (\varepsilon_L - \sigma_L/E_s) \tag{2.47}$$

Hence $\varepsilon_H = -\nu_s\sigma_L/E_s - 0.5(\varepsilon_L - \sigma_L/E_s)$ (2.48)

Dividing equations 2.48 by $-\varepsilon_L$ and simplifying gives:

$$\left(\frac{-\varepsilon_H}{\varepsilon_L}\right)_{\sigma_H = \sigma_R = 0} = 0.5 + \frac{(\nu_s - 0.5)\sigma_L}{E_s \cdot \varepsilon_L} \quad (2.49)$$

The variation of steel Poisson's ratio ($-\varepsilon_H/\varepsilon_L$ for $\sigma_H = \sigma_R = 0$) with ε_L for an idealised elastic-perfectly plastic sample of steel (with $\nu_s = 0.3$, $\sigma_y = 300$ MPa and $E_s = 200000$ MPa) in a uniaxial stress (σ_L) field is shown in Fig. 2.5. It can be seen that as $\varepsilon_L \to \infty$, Poisson's ratio tends asymptotically to a value of 0.5.

2.2.3 Unconfined Concrete Behaviour

The response of concrete to loading which produces uniaxial stress f_L (concrete longitudinal stress) is well understood (2.10) and is illustrated in Fig. 2.6.

The plot of f_L versus ε_L (concrete longitudinal strain, also used previously for tube longitudinal strain) for longitudinal-compression load shows that concrete reaches its peak value of f_L, the unconfined compression strength f'_c, at $\varepsilon_L = \varepsilon_{co} \simeq 0.002$. For $\varepsilon_L > \varepsilon_{co}$, as ε_L increases, f_L reduces rapidly in value. The volumetric strain, ε_v, in a uniaxial-stress (f_L) test can be calculated from:

$$\varepsilon_v = \varepsilon_L + 2\,\varepsilon_{RC} \quad (2.50)$$

where ε_{RC} = concrete strain, in the radial (perpendicular to the longitudinal) direction.

Typically for concrete under uniaxial-compression stress, f_L, the initial value (ν_c) of concrete Poisson's ratio ($= -\varepsilon_{RC}/\varepsilon_L$, in a uniaxial stress f_L field) is equal to 0.15 - 0.20. From equation 2.50 this means that initially the concrete decreases in volume as the compressive load increases. As ε_L increases to a value close to ε_{co}, the Poisson's ratio also increases due to the formation of cracks parallel to the direction of loading. At this stage Poisson's ratio ($-\varepsilon_{RC}/\varepsilon_L$) exceeds 0.5. Hence, the volume of concrete increases with increasing compressive load. For $\varepsilon_L > \varepsilon_{co}$, it is not possible to determine accurately Poisson's ratio, since the concrete loses its cohesion.

For concrete under uniaxial-tension stress, f_L, the $f_L - \varepsilon_L$ response is linear with a stiffness approximately equal to the value appropriate for compressive loading at small values of strain. Brittle failure occurs generally at an f_L of between $-0.1f'_c$ and $-0.3f'_c$. Typically Poisson's ratio ($= -\varepsilon_{RC}/\varepsilon_L$ for uniaxial stress f_L) has a constant value of between 0.15 and 0.20. Hence from equation 2.50, the concrete is expanding in volume throughout the application of longitudinal-tension load.

2.2.4 Constitutive Modelling of Concrete

Many theoretical models have been developed to describe the multi-axial stress-strain behaviour of concrete. Individual models have usually been verified and calibrated by using experimental results from a specific series of tests. However predictions based on the use of a particular theoretical model may give poor agreement with experimental results when the experimental stress or strain path is different from that used in calibrating the theoretical model.

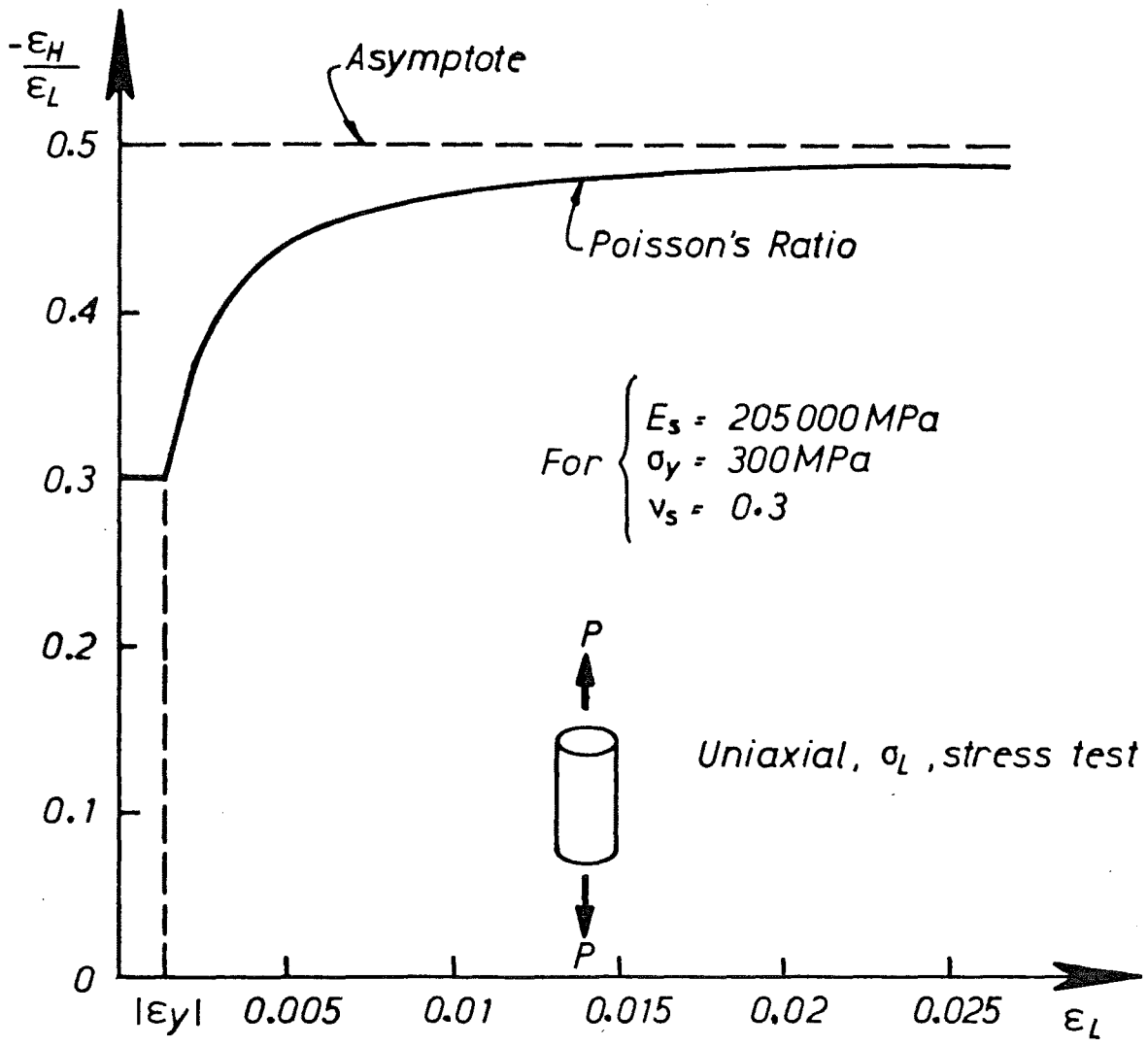

FIG. 2.5 : TYPICAL VARIATION OF POISSON'S RATIO FOR STEEL WITH STRAIN LEVEL

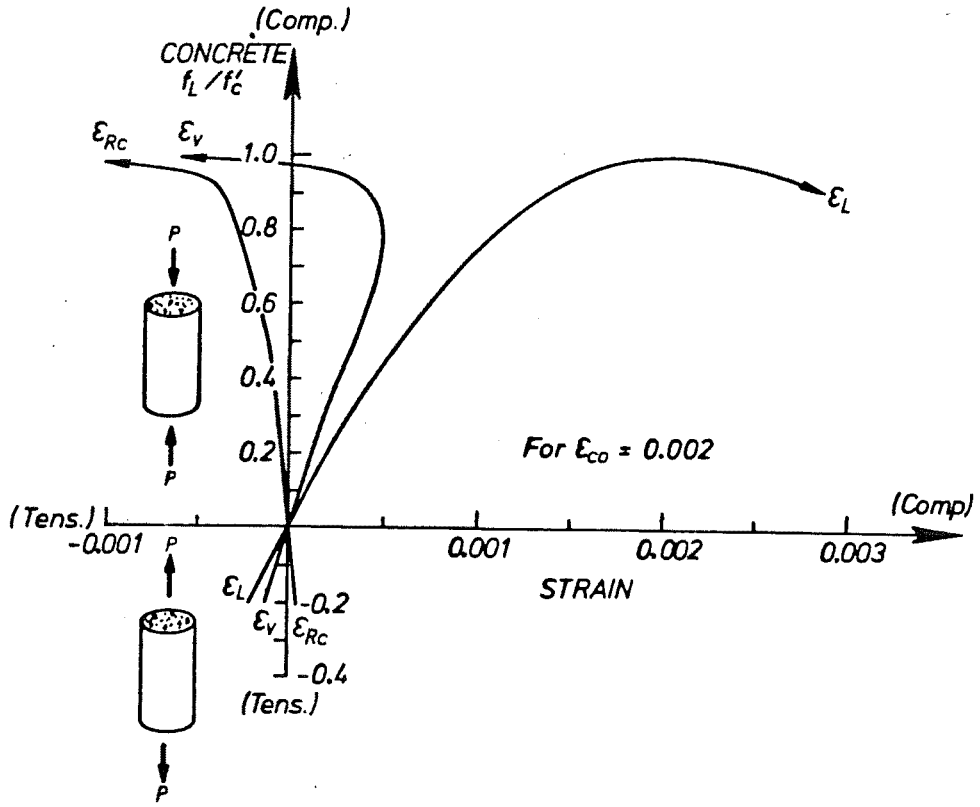

FIG. 2.6 : TYPICAL UNCONFINED CONCRETE BEHAVIOUR

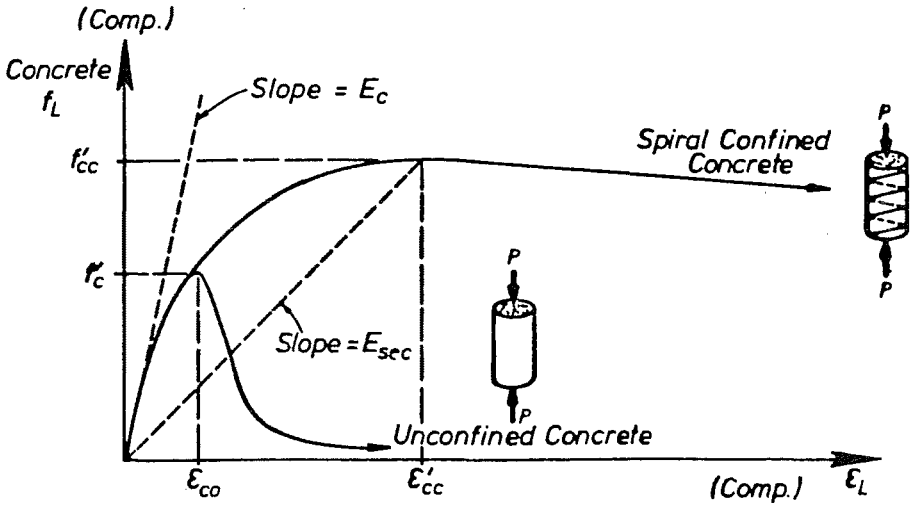

FIG. 2.7 : MANDER ET AL (2.2) CONFINED CONCRETE STRESS-STRAIN MODEL

Existing constitutive laws can be categorised into the following six groups, with at least one example from each group provided:

(i) Non-linear elastic - Kupfer and Gerstle (2.11), Liu et al (2.12) and Palaniswamy and Shah (2.13);

(ii) Hypoelastic - Elwi and Murray (2.14);

(iii) Octahedral - Cedolin et al (2.15);

(iv) Plastic - Chen and Chen (2.16);

(v) Endochronic - Bazant and Bhat (2.17,2.18), Bazant and Shieh (2.19), Bazant and Burrow (2.20);

and (vi) Equivalent uniaxial - Mander et al (2.2), Leslie and Park (2.21), Desayi et al (2.22).

Constitutive laws from the first of the five categories mentioned above were developed using data contained in the literature based on tests with biaxial or triaxial stress fields. In these tests, confinement to the concrete was generally applied in an active fashion by mechanical means. Thus the resulting constitutive laws do not realistically simulate the passive confinement offered by the tube to the concrete, since the tube only confines the concrete when the concrete presses radially on to the tube.

An an example consider the three-dimensional hypoelastic constitutive relationship of Elwi and Murray (2.14). In this model it is assumed that the maximum value of Poisson's ratio in the concrete is 0.5. This has been found to be appropriate for an actively applied triaxial-compression-stress field where the microcracks which develop in the concrete are kept closed. However, it is unlikely that the tube will keep microcracks in the concrete closed, since the tube itself is expanding laterally in the presence of longitudinal-compression stress due to Poisson's ratio effect. At large values of plastic strain, the Poisson's ratio of the tube is approximately equal to 0.5, which is equivalent to the maximum value of Poisson's ratio in the concrete assumed in the Elwi and Murray (2.14) model. Thus for a composite concrete-filled tube at large values of ε_L under longitudinal-compression load, this concrete model would result in a prediction of no lateral interaction between tube and concrete. Later (in Section 2.2.6.2) it is shown that this is not the case, since values of tube $|\varepsilon_H|$ in a concrete-filled tube, under longitudinal-compression loading, are in excess of those obtained in an empty tube at the same value of ε_L (≥ 0.002). This evidence emplies that at large values of ε_L, the Poisson's ratio of the infill concrete is in excess of 0.5.

The sixth category of constitutive models, mentioned above, was classified as equivalent uniaxial. These models which are appropriate for confined concrete under uniaxial-compression loading, trace only the one-dimensional stress-strain response of the concrete in the direction of loading. Tests of concrete confined passively by lateral spiral reinforcement have been used to empirically calibrate these models. However as discussed in the following section, there are significant differences between concrete confined by a tube and concrete confined by spiral reinforcement. The result is that, as shown later in Section 2.4.2.3 the experimental f_L- ε_L response of concrete confined by a tube is, in general, poorly predicted by models which have been calibrated from tests of concrete confined by spiral reinforcement. Also by definition, category (vi) constitutive models are only of limited use, since no direct prediction of concrete or confining steel stress-strain response in the plane perpendicular to the loading axis is provided.

It thus appears that no currently available constitutive law is adequate for describing the multi-axial stress-strain response of concrete confined by a tube. In Section 2.4 proposed methods for modelling the behaviour of concrete inside a tube are described.

2.2.5 Confined Concrete Behaviour

In Section 2.2.3 the rather brittle behaviour of unconfined concrete was mentioned. In structures which are required to respond in a ductile fashion to seismic attack, brittle material behaviour is unacceptable. Thus establishing ways of improving the ductility of concrete are important.

Consideré (2.23) conducted tests involving the monotonic longitudinal loading of concrete cylinders subjected to a constant level of radial fluid pressure. His results indicated that concrete longitudinal strength was enhanced in proportion to the value of radial fluid pressure:

$$f'_{cc} = f'_c + K \cdot f_R^{max} \tag{2.51}$$

where f'_{cc} = peak value of f_L, for confined concrete
f'_c = peak value of f_L, for unconfined concrete
f_R^{max} = peak value of concrete stress, in the radial (perpendicular to the longitudinal) direction
K = empirically determined constant.

Consideré found that K was equal to 4.8 in his tests. Similar tests conducted by Richart et al (2.24) gave an average value of $K = 4.1$, although at small values of f_R^{max} ($\leq$ 7 MPa) results implied K as large as 5.1, while at large values of f_R^{max} ($\geq f'_c$) results implied K as low as 3.5. The tests of Balmer et al (2.25) also implied a range of values for K ranging from 6 at small values of f_R^{max} to 2 at large values of f_R^{max}. Thus the efficiency of the confining stress, in increasing the longitudinal-compression strength of the concrete, decreases as the magnitude of the confining stress increases. However just as significantly, Richart et al and Balmer et al found the ductility of confined concrete was improved markedly from that of unconfined concrete; as evidenced by the higher value of ε_L at $f_L = f'_{cc}$ than at $f_L = f'_c$, and the flattening of the falling branch of the concrete $f_L - \varepsilon_L$ relationship.

In practice lateral confinement of concrete, under longitudinal-compression load, is generally provided by lateral reinforcing steel. This steel applies a gradually increasing level of lateral pressure to the concrete, as the concrete expands laterally under longitudinal-compression load due to Poisson's ratio effect. Thus the confinement offered by the lateral steel to the concrete is passively applied, as opposed to the application of lateral fluid pressure to the concrete which is a case of actively applied confinement.

Mander et al (2.2), Leslie and Park (2.21) and Desayi et al (2.22) have derived empirical models based on experimental data to deduce the $f_L - \varepsilon_L$ response of concrete confined by spiral reinforcement. To facilitate later comparisons between the $f_L - \varepsilon_L$ response of concrete confined by a tube and concrete confined by an equivalent volume of extremely closely spaced spiral reinforcement, the model of Mander et al,which is the most generally applicable, is briefly described below.

The analytical model, which is illustrated in Fig. 2.7, is based on an equation suggested by Popovics (2.26):

$$f_L = \frac{f'_{cc} \cdot X \cdot r}{r - 1 + X^r} \tag{2.52}$$

The confined strength of the concrete is given by:

$$f'_{cc} = f'_c \left[2.254 \left(1 + 7.94 \left(\frac{f_R^{max}}{f'_c} \right) \right)^{\frac{1}{2}} - 2 \left(\frac{f_R^{max}}{f'_c} \right) - 1.254 \right] \tag{2.53}$$

The value of f_R^{max} can be found from the requirement of lateral equilibrium between the confining steel and the concrete. For example for a tube (or an equivalent tube which occupies the same volume as the spiral reinforcement), from Fig. 2.8:

$$f_R = \frac{-2t \cdot \sigma_H}{D - 2t} \tag{2.54}$$

where f_R = concrete stress, in the radial direction.
Mander et al (2.2) assumed that at $f_R = f_R^{max}$, σ_H was equal to $-|\sigma_y|$ (i.e. strain-hardening of the confining steel was ignored) and hence:

$$f_R^{max} = \frac{2t \cdot |\sigma_y|}{D - 2t} \tag{2.55}$$

In equation 2.52, X is given by:

$$X = \varepsilon_L / \varepsilon'_{cc} \tag{2.56}$$

where ε'_{cc} is the value of ε_L corresponding to $f_L = f'_{cc}$:

$$\varepsilon'_{cc} = \varepsilon_{co} \left[C \left(\frac{f'_{cc}}{f'_c} - 1 \right) + 1 \right] \tag{2.57}$$

where C is an empirical constant found by Mander et al to be about 5 for concrete confined by spiral reinforcement.

In equation 2.52, r is given by:

$$r = E_c / (E_c - E_{sec}) \tag{2.58}$$

where E_c, the initial modulus of the concrete is calculated from an empirical relationship:

$$E_c = 5000 \sqrt{f'_c} \quad \text{[MPa units]} \tag{2.59}$$

where E_{sec} represents the secant modulus of the confined concrete at $\varepsilon_L = \varepsilon'_{cc}$:

$$E_{sec} = f'_{cc} / \varepsilon'_{cc} \tag{2.60}$$

Figure 2.7 illustrates typical responses of confined and unconfined concrete which have been predicted using the Mander et al model. The diagram clearly shows the enhancement to concrete strength and ductility gained by the presence of concrete confinement. A typical value (2.2) of spiral reinforcement in reinforced concrete columns will result in f_R^{max} being approximately equal to $0.1f'_c$. For this value of f_R^{max} from equation 2.53: $f'_{cc} = 1.565f'_c$.

Equation 2.51 can be rearranged to solve for

$$K = (f'_{cc} - f'_c) / f_R^{max} \tag{2.61}$$

Solving equation 2.61, for $f_R^{max} = 0.1f'_c$ and $f'_{cc} = 1.565f'_c$ gives K = 5.65. However for a value of $f_R^{max} = 0.5f'_c$, similar analysis gives $f'_{cc} = 2.771f'_c$ and K = 3.54. Thus the Mander et al model implies the efficiency of lateral reinforcement, in enhancing concrete ductility, decreases as the volume of the lateral reinforcement and hence f_R^{max} increases. This conclusion is in agreement with the experimental results of Richart et al (2.24) and Balmer et al (2.25) which were described earlier in this section, and is of significance to

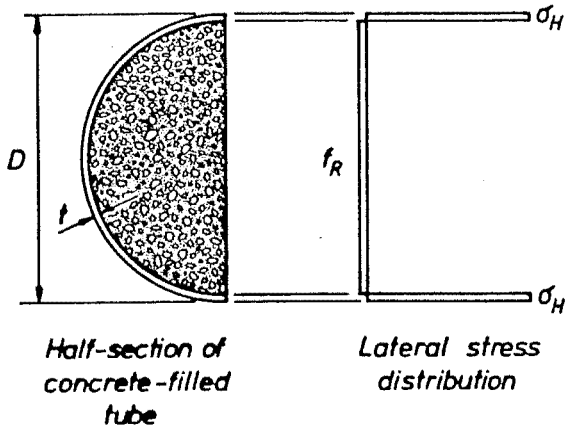

FIG. 2.8 : LATERAL EQUILIBRIUM IN A CONCRETE-FILLED TUBE

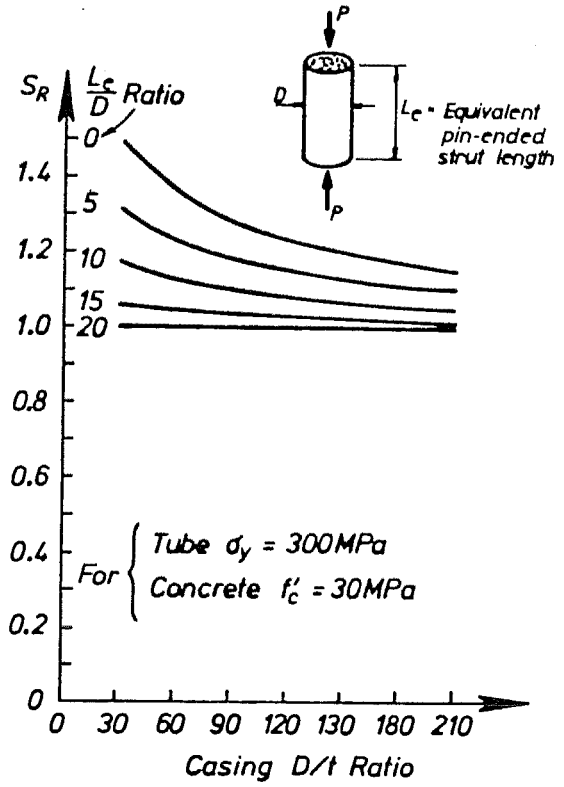

FIG. 2.9 : STRENGTH ENHANCEMENT OF CONCRETE-FILLED TUBES PREDICTED BY SEN (2.33)

steel-encased concrete piles where the potential lateral confining stresses may be very large.

It should be noted that under longitudinal-compression load, the confinement offered to concrete by equivalent volumes of spiral reinforcement and steel casing is, in general, not the same for the following reasons:

(i) The tube offers continuous lateral support to the whole concrete mass, whereas spiral reinforcement does not restrain the cover and part of the core concrete from spalling at large values of ε_L .

(ii) Spiral reinforcement is in a state of uniaxial-hoop-tension stress, whereas the steel tube has longitudinal-compression stress and hoop-tension stress. The biaxial strength criteria indicated in equation 2.36 and Fig. 2.4 mean that in the plastic range at a given σ_{eff}, the resulting hoop-tension stress in the tube will be lower than the hoop-tension stress in the spiral reinforcement.

(iii) Hoop strain in the spiral reinforcement is due to Poisson's ratio lateral expansion of concrete which is under longitudinal-compression stress. However because of longitudinal-compression stress in the tube from the action of bending moment and longitudinal load, Poisson's ratio lateral expansion will also occur in the tube. This will reduce the hoop stiffness of the tube for resisting concrete lateral expansion, with the result that the tube has a delayed confining effect on the concrete relative to the confining effect offered by spiral reinforcement.

The implication of the above discussion is that, in general, the direct use of the Mander et al (2.2) model to predict stress-strain behaviour of concrete confined by a tube is inappropriate, and some modification is necessary. This point is further demonstrated later in this chapter.

2.2.6 Previous Tests of Circular-Sectioned Concrete-Filled Tubes

A literature search failed to reveal research results concerning the testing of concrete-filled tubes under longitudinal-tension load. However over the last 30 years there has been many reports (2.1, 2.27— 2.42) published concerning the behaviour of concrete-filled tubes under monotonically increasing longitudinal-compression load. Long and short column behaviour under concentrically and eccentrically applied load have been studied. However the research has concentrated on the behaviour of concrete-filled tubes with casing $D/t \leq 100$, and thus little information is available on the behaviour of concrete-filled tubes with casing D/t ratio approaching the upper limit of 180 used for piling in New Zealand. In the following sections, the main findings from these reports (2.1, 2.27— 2.42) are described and discussed.

2.2.6.1 Tests of Sen et al

Based on experimental results from concrete-filled tubes with casing D/t ratios of 17 - 37, Sen (2.33) has proposed a design formula for the ultimate compressive strength, P_u^{SEN} of such members which empirically allows for:

(i) long and short column (variable L_e/D) behaviour;

(ii) triaxial-compression stress in the concrete;

(iii) longitudinal-compression and hoop-tension stresses in the tube; and

(iv) stabilising of tube local buckling, due to the internal restraint provided by the concrete.

The formula is given as:

$$P_u^{SEN} = A_t \cdot \frac{|\sigma_y|}{\kappa} + A_c \cdot \left(f'_c + 2\mu.\gamma.\frac{t}{D} \cdot \frac{|\sigma_y|}{\kappa}\right) \quad (2.62)$$

where A_t = area of tube = $\pi(D - t).t$ (2.63)

A_c = area of concrete = $\frac{1}{4}\pi(D - 2t)^2$ (2.64)

and μ, γ, and κ are functions of the column slenderness ratio:

$\mu = (25 - L_e/D)/4$ (2.65)

$\gamma = (25 - L_e/D)/50$ (2.66)

$\kappa = (1 + \gamma + \gamma^2)^{\frac{1}{2}}$ (2.67)

The first and second terms, on the right hand side of equation 2.62, represent the longitudinal load carried by tube and concrete respectively, after allowance has been made for lateral interaction between tube and concrete. For $L_e/D = 0$, equation 2.62 gives tube $\sigma_L = 0.756|\sigma_y|$ and concrete $f_L = f'_c + 4.725|\sigma_y| \cdot t/D$. Thus lateral interaction results in a reduction in the longitudinal load carried by the tube, and an increase in the longitudinal load carried by the concrete.

Equation 2.62 is used in Great Britain as a design equation (2.43). A strength ratio, S_R, which represents the ratio between P_u^{SEN} and the sum of the yield strength of the tube and the unconfined-compression strength of the concrete may be expressed as:

$$S_R = \frac{P_u^{SEN}}{|\sigma_y| \cdot A_t + f'_c \cdot A_c} \quad (2.68)$$

Values of S_R as a function of casing D/t ratio and member L_e/D slenderness ratio (for $L_e/D \leq 20$, since the formula is inappropriate at higher L_e/D), for $|\sigma_y| = 300$ MPa and $f'_c = 30$ MPa are plotted in Fig. 2.9. The figure shows that the ultimate load of a concrete-filled tube predicted by equation 2.62 is usually substantially higher than the sum of the unconfined-compression strength of the concrete and the tube yield strength. Clearly thick-walled (low casing D/t ratio) concrete-filled tubes have higher S_R values than do thin-walled concrete-filled tubes. For example at $L_e/D = 5$, $S_R = 1.31$ for $D/t = 30$ and $S_R = 1.10$ for $D/t = 210$. Also from Fig. 2.9, as L_e/D increases, S_R decreases due to the increasing dominance of long column over short column behaviour.

Sen et al (2.34) also calculated the variation of tube σ_L and σ_H and concrete f_L and f_R with ε_L, from the values of ε_L, ε_H and P (overall longitudinal load) obtained during longitudinal-compression-load testing of short ($L_e/D = 4$) thick-walled ($17 \leq D/t \leq 37$) concrete-filled tubes. They achieved this by using plasticity theory and assuming that the steel behaved in an elastic-perfectly plastic (i.e. ignoring strain hardening) manner. On the basis of these tests they calibrated tube $\sigma_L - \varepsilon_L$ and concrete $f_L - \varepsilon_L$ relationships which represent the responses of concrete and tube in a concrete-filled tube:

For $\varepsilon_L \leq |\varepsilon_y|$: $\sigma_L = 0.95\, E_s.\varepsilon_L$ (2.69)

For $\varepsilon_L > |\varepsilon_y|$: $\sigma_L = \dfrac{1.063\varepsilon_L/|\varepsilon_y| - 0.113}{1.417\varepsilon_L/|\varepsilon_y| - 0.417}\ |\sigma_y|$ (2.70)

$$\text{For } \varepsilon_L > 0 : \quad f_L = \frac{2.41\ \varepsilon_L/\varepsilon_{co}}{1 + 1.105\ \varepsilon_L/\varepsilon_{co}}\ f'_c \qquad (2.71)$$

Figures 2.10 and 2.11 show a comparison of the above relationships, in non-dimensional form, with the experimental data from which they were calibrated. A large amount of scatter is evident in the experimental data. However it is apparent that lateral interaction effects do not significantly influence the stress fields in the tube and concrete until the steel yields. As ε_L increases, concrete f_L steadily increases and tube σ_L (for $\varepsilon_L > |\varepsilon_y|$) steadily decreases. As $\varepsilon_L \to \infty$, the above relationships give tube $\sigma_L \to 0.75|\sigma_y|$ and concrete $f_L \to 2.18f'_c$. Thus the lateral interaction which implies radial-compression stress in the concrete and hoop-tension stress in the tube, results in a redistribution of longitudinal-compression stress from the steel to the concrete. However Sen et al (2.34) have warned that it is not appropriate to use equations 2.69-2.71 in deriving stress-strain relations for concrete-filled tubes with casing D/t ratios outside the range of 17-37 (cf. prototype piles $60 \leq D/t \leq 180$), since the equations have only been calibrated for members within that range.

2.2.6.2 Tests of Tomii et al and Sakino et al

In this section, the experimental results of Tomii et al (2.1) and Sakino et al (2.41) are described and discussed in some detail, since these results are used subsequently (Section 2.4.2.3) in deriving constitutive relationships which model the behaviour of concrete and steel in composite concrete-filled tubes under longitudinal-compression loading.

Tomii et al (2.1) performed an extensive number of longitudinal-compression-load tests on short ($L_e/D = 3$) thick-walled ($19 \leq D/t \leq 75$) concrete-filled tubes. The $P - \varepsilon_L$ responses obtained from some of these tests are shown in Fig. 2.12. For the results shown tubes had $D = 150$ mm, and were of mild steel which strain-hardened at an ε_L of approximately 0.02 under uniaxial stress (σ_L) conditions. The main parameters investigated in the indicated tests were concrete f'_c (18, 22 and 29 MPa) and tube t (2.0, 3.2 and 4.3 mm). These values of t give casing D/t ratios of 75.0, 46.9 and 34.9 respectively. To estimate the range of statistical scatter, three tests were performed for each of the above nine combinations of f'_c and t. In Fig. 2.12, the ε_L at which local buckling of the tube wall was first observed is also indicated.

Local buckling effects are more important in thin-walled than in thick-walled concrete-filled tubes, and as discussed previously in Section 2.2.1, it is difficult to predict accurately the load-deflection behaviour of tubes after local buckling occurs. Thus the significant scatter which is shown in Fig. 2.12 to occur between the three tests at each combination of f'_c and t, especially for thin-walled concrete-filled tubes, is not surprising.

Figure 2.12 also shows that most of the concrete-filled tubes behave in a ductile fashion up to $\varepsilon_L = 0.04$, and in all cases ductile behaviour is indicated for ε_L substantially in excess of the ε_L at which local buckling was initiated. However there is a trend which indicates that ductile behaviour is harder to achieve in concrete-filled tubes with small values of t and large values of f'_c. For example, for concrete-filled tubes with $t = 2.0$ mm and $f'_c = 29$ MPa, the $P - \varepsilon_L$ response is indicated to terminate at an ε_L of between 0.01 and 0.02. Tomii et al (2.1) state that this termination is at the stage of "crushing failure". However it is unclear as to whether this refers to concrete crushing, tube local buckling, or tube crushing; and $P - \varepsilon_L$ responses for ε_L in excess of ε_L at "crushing failure" are not given.

Figure 2.13 shows the $\varepsilon_H - \varepsilon_L$ response of concrete-filled tubes with $D = 150$ mm and $t = 2.0$, 3.2 and 4.3 mm (concrete f'_c was not stated) obtained

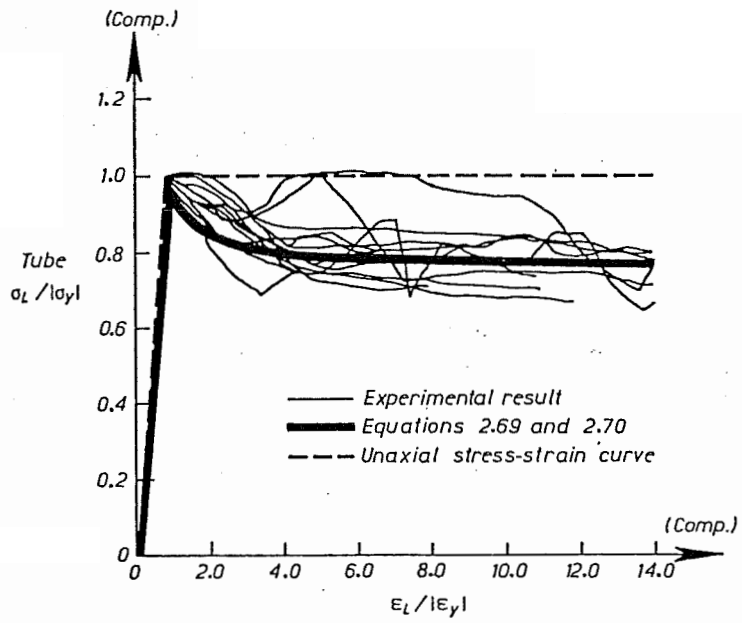

FIG. 2.10 : TUBE LONGITUDINAL STRESS-LONGITUDINAL STRAIN RESPONSE FROM SEN ET AL (2.34) TESTS

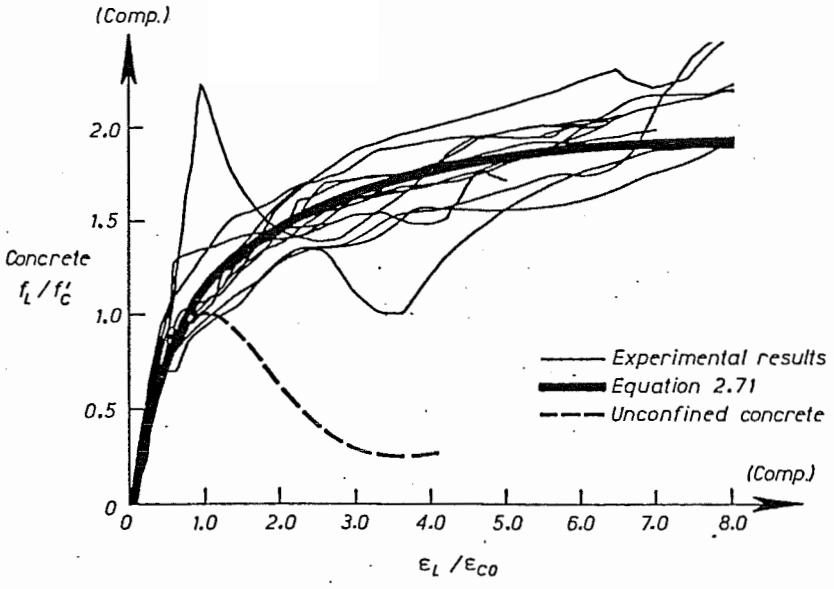

FIG. 2.11 : CONCRETE LONGITUDINAL STRESS-LONGITUDINAL STRAIN RESPONSE - FROM SEN ET AL (2.34) TESTS

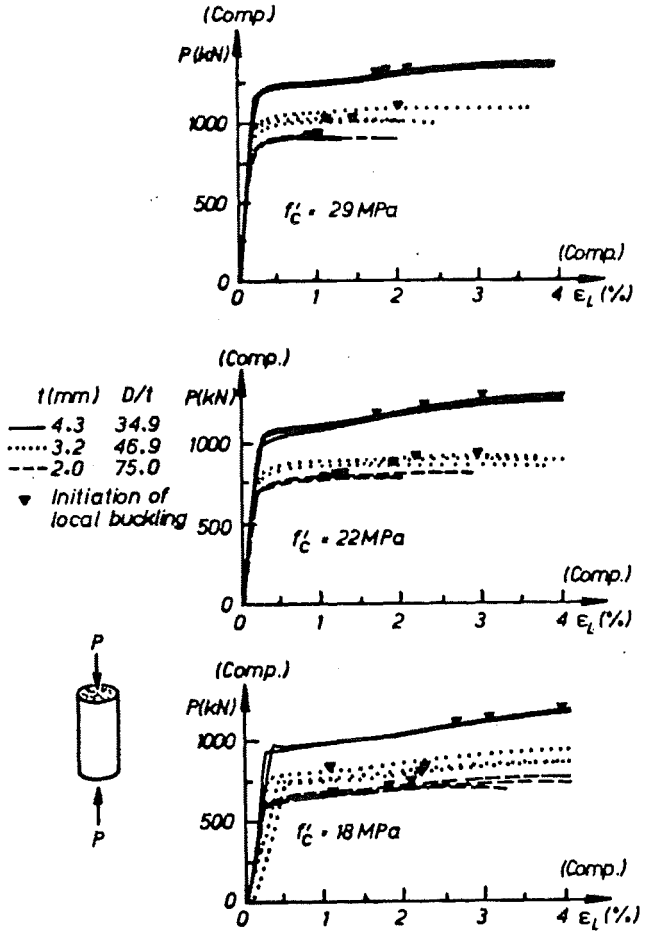

FIG. 2.12 : LONGITUDINAL LOAD-LONGITUDINAL STRAIN RESPONSE FROM TOMII ET AL (2.1) TESTS

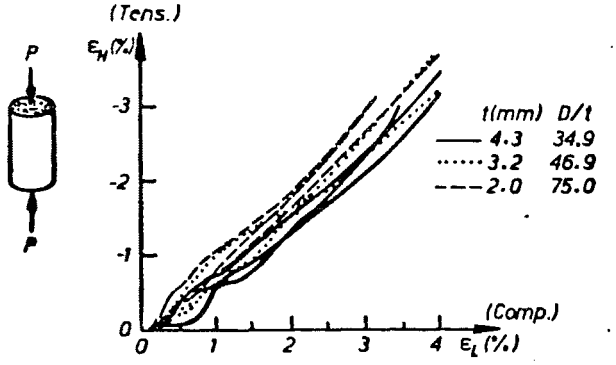

FIG. 2.13 : HOOP STRAIN-LONGITUDINAL STRAIN RESPONSE FROM TOMII ET AL (2.1) TESTS

from the longitudinal-compression-load tests of Tomii et al (2.1). Three tests at each value of t are indicated. The figure shows that considerable scatter was present in the data. Nevertheless the trend of behaviour indicates that $d\varepsilon_H/d\varepsilon_L$ increases with ε_L, although at a gradually decreasing rate. The trend also indicates that for a given $\varepsilon_L \geq 0.002$, thick-walled concrete-filled tubes which tend to be dominated by tube behaviour have smaller values of tube $|\varepsilon_H|$ than do thin-walled concrete-filled tubes, which tend to be dominated by concrete behaviour. This indicates that:

(i) thin-walled concrete-filled tubes will have a larger tube $|\sigma_H/\sigma_L|$ ratio than will thick-walled concrete-filled tubes, at the same value of ε_L; and

(ii) for $\varepsilon_L \geq 0.002$, Poisson's ratio for concrete is in excess of Poisson's ratio for steel.

For their concrete-filled tube tests, Tomii et al (2.1) also deduced the tube $\sigma_L - \sigma_H - \sigma_L$ response from the $\varepsilon_L - \varepsilon_H - P$ data obtained during testing, and the results of coupon (uniaxial-tension stress) tests. However they achieved this relatively crudely by assuming that:

(i) in the plastic range $\sigma_{eff} = |\sigma_y|$;

(ii) in the plastic range $d\varepsilon_L$ (infinitesimal increment of tube strain in the longitudinal direction) = $d\varepsilon_L^p$ and $d\varepsilon_H$ (infinitesimal tube strain in the hoop direction) = $d\varepsilon_H^p$; and

(iii) for $\varepsilon_L > 6|\varepsilon_y|$ which for their steel approximately implies $\varepsilon_L > 0.01$, $d\varepsilon_H/d\varepsilon_L$ is constant.

The above point (i) results in an underestimation of tube strength in the strain-hardening range of steel behaviour which would be expected to become significant for ε_L approximately > 0.02. Point (ii) is an approximation because it implies that $d\varepsilon_L^e$ and $d\varepsilon_H^e$, the increments of tube elastic strain in the longitudinal and hoop directions respectively, are both zero. This is strictly not the case, since even in the plastic range redistribution of tube σ_H and σ_L stresses will result in changes to the elastic strains, ε_L^e and ε_H^e . The above point (iii) is also an approximation since from Fig. 2.13 it is clear that $d\varepsilon_H/d\varepsilon_L$ is slowly increasing with increasing ε_L. This approximation would result in tube σ_H being underestimated at large values of ε_L, and overestimated at small values of ε_L. Conversely the approximation will result in tube σ_L being overestimated at large values of ε_L, and underestimated at small values of ε_L.

On the basis of the above three assumptions, Tomii et al manipulated the Von Mises yield criterion (equation 2.37) and the Prandtl-Reuss relationships (equations 2.17 - 2.19) to calculate tube σ_L and σ_H, in the plastic range of steel behaviour from:

$$\sigma_L = \frac{(d\varepsilon_H/d\varepsilon_L) + 2}{\sqrt{3}.\sqrt{1 + (d\varepsilon_H/d\varepsilon_L) + (d\varepsilon_H/d\varepsilon_L)^2}} |\sigma_y| \qquad (2.72)$$

$$\sigma_H = \frac{2(d\varepsilon_H/d\varepsilon_L) + 1}{\sqrt{3}.\sqrt{1 + (d\varepsilon_H/d\varepsilon_L) + (d\varepsilon_H/d\varepsilon_L)^2}} |\sigma_y| \qquad (2.73)$$

Equations 2.72 and 2.73 are similar in form to the more correct equations 2.38 and 2.39 which were presented previously in Section 2.2.2.2. The differences are a direct consequence of the approximations made by Tomii et al.

Based on a statistical analysis of their results, Tomii et al derived an empirical equation relating the $d\varepsilon_H/d\varepsilon_L$ value, at $\varepsilon_L \geq 6|\varepsilon_y|$, to the section geometry and strength properties of the concrete-filled tube:

$$d\varepsilon_H/d\varepsilon_L = 0.9R - 1.4 \tag{2.74}$$

$$\text{where} \quad R = \frac{|\sigma_y| \cdot A_t}{|\sigma_y| \cdot A_t + f'_c \cdot A_c} \tag{2.75}$$

It is interesting to calculate the values of $d\varepsilon_H/d\varepsilon_L$ given by equations 2.74 and 2.75, at casing D/t ratios of 2 and ∞, although clearly these two cases are outside the range of concrete-filled tubes from which equation 2.74 was calibrated. A casing D/t ratio of 2 corresponds to a solid steel member in which case R = 1, and hence for $\varepsilon_L \geq 6|\varepsilon_y|$ then $d\varepsilon_H/d\varepsilon_L = -0.5$. Since in a solid steel member uniaxial-longitudinal stress conditions will apply, then $d\varepsilon_H/d\varepsilon_L = -0.5$ approximately corresponds to a steel Poisson's ratio of 0.5 as could be expected in the plastic range of steel behaviour. A casing D/t ratio of ∞ corresponds to an unconfined concrete member in which case R = 0, and for $\varepsilon_L \geq 6|\varepsilon_y|$ then $d\varepsilon_H/d\varepsilon_L = -1.4$. Since in an unconfined concrete member uniaxial-longitudinal stress conditions will apply, then $d\varepsilon_H/d\varepsilon_L = -1.4$ approximately corresponds to a concrete Poisson's ratio of 1.4. This value (= 1.4) may be compared with Elwi and Murray (2.14) limiting the theoretical value to 0.5 on the basis of tests of concrete subjected to an actively applied triaxial-compression-stress field, an experimental value of 2 at large levels which can be deduced from the tests of Mander et al (2.2) of spirally confined concrete, and an apparently unlimited value for unconfined concrete at large strain levels. Thus it appears that the apparent large strain value of concrete Poisson's ratio depends on the extent to which concrete micro-cracks are prevented from opening. However, for concrete-filled tubes ($2 \leq D/t \leq \infty$) equations 2.74 and 2.75 imply that $d\varepsilon_H/d\varepsilon_L$ is within the limits of -0.5 and -1.4 when $\varepsilon_L > 0.01$.

Best fit curves for the tube $\sigma_L/|\sigma_y| - \varepsilon_L/|\varepsilon_y|$ and $\sigma_H/|\sigma_y| - \varepsilon_L/|\varepsilon_y|$ relationships which resulted from the data reduction of their experimental results performed by Tomii et al are given in Fig. 2.14. The results imply that in the elastic range ($\varepsilon_L < |\varepsilon_y|$) no lateral interaction of tube and concrete occurs, and thus tube $\sigma_L = E_s\varepsilon_L$ and $\sigma_H = 0$. As ε_L increases between $|\varepsilon_y|$ and $6|\varepsilon_y|$, the values of $|\sigma_H|$ and σ_L steadily increase and decrease respectively. For $\varepsilon_L \geq 6|\varepsilon_y|$, σ_L and σ_H are constant in value and can be predicted by substituting for $d\varepsilon_H/d\varepsilon_L$ from equation 2.74 into equations 2.72 and 2.73 respectively which gives:

$$\sigma_L = \frac{0.9R + 0.6}{\sqrt{3} \cdot \sqrt{(0.9R - 0.4) + (0.9R - 1.4)^2}} \cdot |\sigma_y| \tag{2.76}$$

$$\sigma_H = \frac{1.8R - 1.8}{\sqrt{3} \cdot \sqrt{(0.9R - 0.4) + (0.9R - 1.4)^2}} \cdot |\sigma_y| \tag{2.77}$$

For a solid steel member (R = 1) the stress field is shown to be uniaxial-longitudinal-compression with tube $\sigma_H = 0$. At a given ε_L ($> |\varepsilon_y|$) as R decreases the tube stress field is increasingly dominated by hoop-tension stress at the expense of longitudinal-compression stress. However it is significant to note that even for extremely thin-walled concrete-filled tubes ($R \cong 0$) the statistical analysis by Tomii et al of their experimental data implied a residual longitudinal-compression stress of at least $0.28|\sigma_y|$ is carried by the tube.

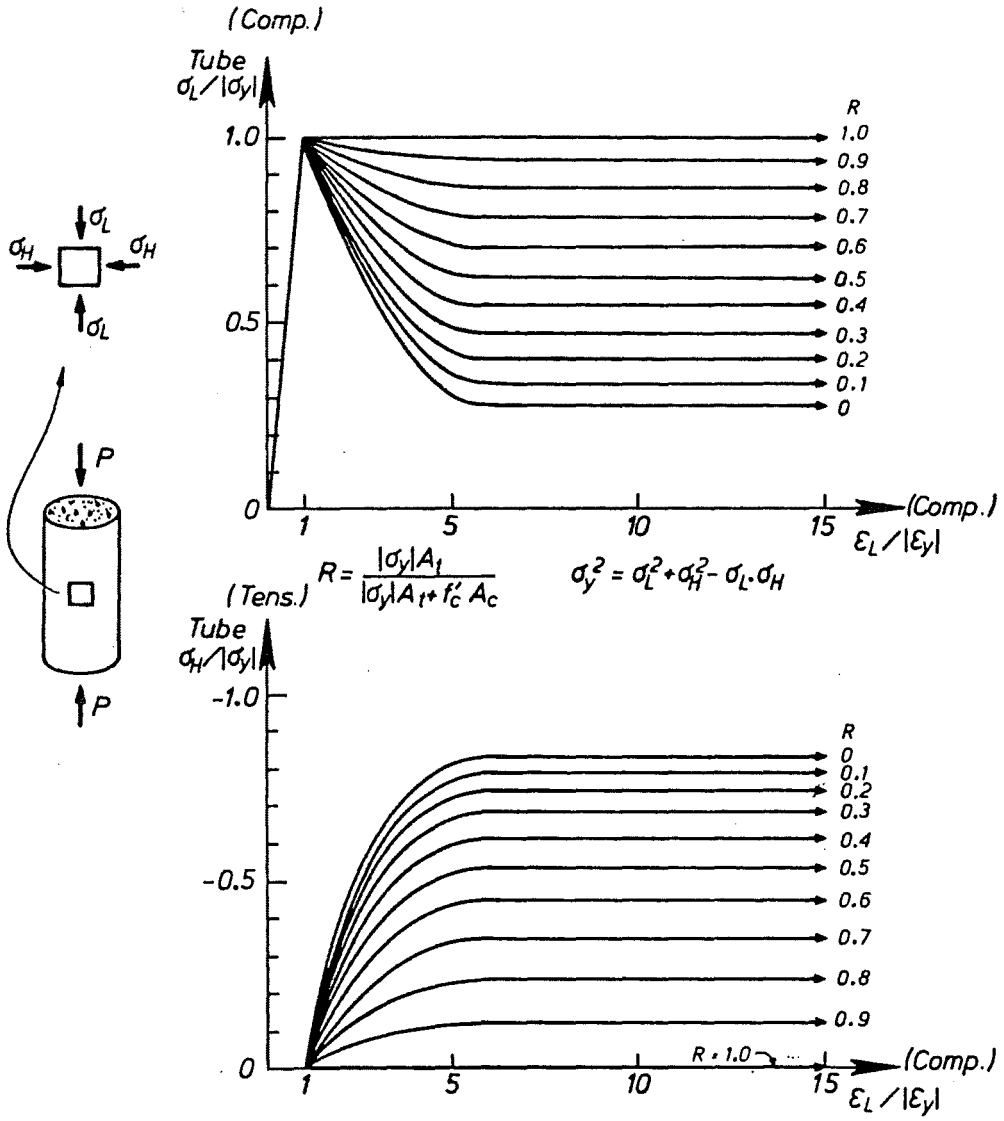

FIG. 2.14 : TUBE BIAXIAL STRESS-LONGITUDINAL STRAIN RELATIONSHIPS FROM TOMII ET AL (2.1) DATA REDUCTION

The tube $\sigma_L - \varepsilon_L$ responses obtained by Sen et al (2.34) and Tomii et al (2.1) show some similarities, as can be seen by comparing Figs.2.10 and 2.14. The comparison shows the general shapes of the tube $\sigma_L - \varepsilon_L$ responses are the same. The average value of R from the 14 tests of Sen et al was equal to 0.50. At large ε_L for this value of R, the results of Tomii et al would predict tube $\sigma_L = 0.62\ |\sigma_y|$. In comparison Sen et al found $\sigma_L = 0.75|\sigma_y|$.

Tomii et al (2.1) also calculated the value of the empirical coefficient K (see equation 2.51) which is appropriate for concrete confined by a circular tube from:

$$K = \left(\frac{\sigma_L^{max} \cdot A_t - P_u^{exp}}{A_c} + f_c'\right) \cdot \left(\frac{D - 2t}{\sigma_H^{max} \cdot 2t}\right) \qquad (2.78)$$

where P_u^{exp} = maximum experimentally obtained longitudinal load

$\sigma_L^{max}, \sigma_H^{max}$ = values of σ_L and σ_H respectively at $P = P_u^{exp}$

The mean value of K, determined by Tomii et al (2.1) from their tests was 2.6, which appeared to be independent of the casing D/t ratio and material strength, although there were large fluctuations in K from test to test.

Figure 2.15 shows a comparison of the K value obtained by Tomii et al (2.1) for concrete confined by a tube with K values calculated from tests with lateral confinement provided by either spiral reinforcement or a constant level of fluid pressure. Clearly in a role of increasing concrete strength by providing lateral confinement the tube is relatively inefficient (low K value), as could be implied from the discussion contained in Section 2.2.5. However Fig. 2.15 does show that at large values of f_R^{max}/f_c', the K values appropriate for concrete confined by spiral reinforcement and tube are similar, although it should be noted that the spiral reinforcement results are highly extrapolated as they were only calibrated for $f_R^{max}/f_c' < 0.15$.

At a particular value of K, it is shown (see below) that the tube in a composite concrete-filled tube is equally efficiently utilised in resisting longitudinal-compression load by:

(i) uniaxial-hoop-tension stress (i.e. only providing concrete confinement); or

(ii) uniaxial-longitudinal-compression stress (i.e. only providing direct resistance to longitudinal load).

For uniaxial-hoop-tension stress, the maximum load carrying capacity, P_H, of the concrete-filled tube is given by:

$$P_H = (f_c' + K \cdot f_R^{max}) \cdot \tfrac{1}{4}\pi (D - 2t)^2 \qquad (2.79)$$

From the lateral equilibrium requirement:

$$f_R^{max} = \frac{2t\ |\sigma_u|}{D - 2t} \qquad (2.80)$$

Substituting for f_R^{max} from equation 2.80 into equation 2.79 gives:

$$P_H = \left(f_c' + \frac{2Kt|\sigma_u|}{D - 2t}\right) \tfrac{1}{4}\pi (D - 2t)^2 \qquad (2.81)$$

For uniaxial-longitudinal-compression stress in the tube, the maximum load-carrying capacity, P_L, of the concrete-filled tube is given by:

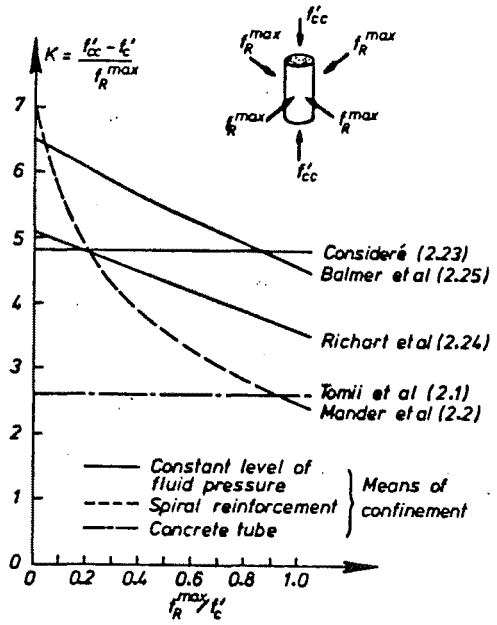

FIG. 2.15 : EXPERIMENTALLY DETERMINED VALUES OF LONGITUDINAL STRENGTH ENHANCEMENT FACTOR K

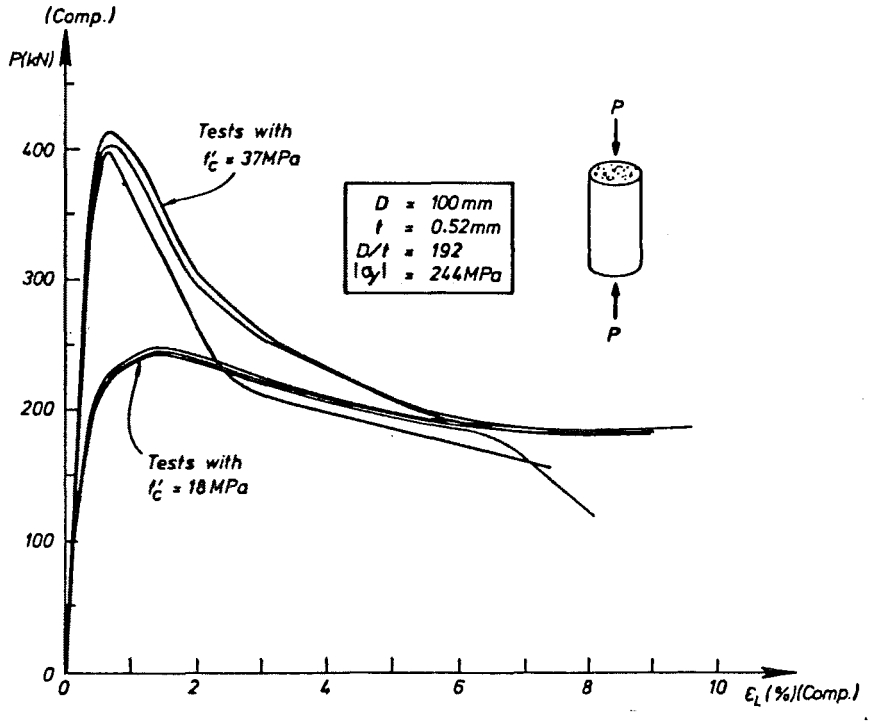

FIG. 2.16 : LONGITUDINAL LOAD-LONGITUDINAL STRAIN RESPONSE FROM SAKINO ET AL (2.41) TESTS

$$P_L = |\sigma_u| \cdot \pi(D - t).t + f'_c \cdot \tfrac{1}{4}\pi (D - 2t)^2 \qquad (2.82)$$

For the tube to be equally efficient in a uniaxial-hoop-tension stress role as in a uniaxial-longitudinal-compression stress role, then $P_L = P_H$. Thus equating the right hand sides of equations 2.81 and 2.82, it can be shown that:

$$K = \frac{2(D/t - 1)}{(D/t - 2)} \qquad (2.83)$$

From equation 2.83 for comparatively thick-walled (e.g. D/t = 30) and thin-walled (e.g. D/t = 210) concrete-filled tubes under longitudinal-compression load, for overall compressive strength the tube is utilised equally efficiently in a role of longitudinal-compression stress as in a role of uniaxial-hoop-tension stress at a K of approximately 2, or more exactly for K = 2.01 to 2.07 (for D/t = 210 to 30). For K less than that defined by equation 2.83, uniaxial-longitudinal-compression stress in the tube is more efficient for longitudinal-compression-load strength of the concrete-filled tube than is uniaxial-hoop-tension stress in the tube. The reverse applies for K greater than that defined by equation 2.83.

Since Tomii et al (2.1) have found that K for concrete inside tubes is 2.6 and the tube develops large values of hoop-tension stress, this explains why the composite strength of concrete-filled tubes is greater than the sum of the independent strengths of the concrete and the tube.

The literature review revealed only one set of well-documented test results concerning the behaviour of short concrete-filled tubes with casing D/t ratio in excess of 100 (cf. prototype piles have been built with $60 \leq D/t \leq 180$). These were a later series of tests performed by Sakino, Tomii and Watanabe (2.41), and involved concrete-filled tubes with $L_e/D = 2$, $D/t = 192$ and tube $|\sigma_y| = 254$ MPa. Three tests were performed for each of concrete strengths $f'_c = 18$ MPa and 37 MPa. The $P - \varepsilon_L$ responses obtained from the six tests are shown in Fig. 2.16.

As ε_L increases the results show an early peak in strength and then a gradual degradation of load-carrying capacity for tests with $f'_c = 18$ MPa and a more rapid degradation in load-carrying capacity for tests with $f'_c = 37$ MPa. This peaked $P - \varepsilon_L$ response is in contrast with the $P - \varepsilon_L$ responses obtained from the earlier tests of thick-walled concrete-filled tubes (see Fig. 2.12) which, in general, show $dP/d\varepsilon_L \geq 0$ within the indicated range of measured ε_L ($0 \leq \varepsilon_L \leq 0.04$). It should be noted that the longitudinal strain, plotted for the thin-walled concrete-filled tube tests (Fig. 2.16), was based on longitudinal deflection measured over the full specimen height, whereas the earlier tests of thick-walled concrete-filled tubes (Fig. 2.12) relied on longitudinal strain indicated by strain gauges at the midheight of the specimen. Since in general local buckling did not occur at the midheight of the specimens, at a given stage of testing after maximum load had been reached, the ε_L indicated at the midheight of the test specimen would be lower than the average ε_L measured over the total height of the test specimen.

2.2.6.3 General Results from Tests

In general, tests (2.1, 2.27 - 2.42) of long columns under eccentric and concentric longitudinal-compression load have demonstrated that behaviour can be modelled adequately by using conventional reinforced concrete theory, in which uniaxial stress-strain characteristics are assumed to apply for the tube and the concrete. For short columns under concentrically applied longitudinal-compression loading, many investigators (2.1, 2.28-2.30, 2.33-2.42) have demonstrated that the performance of concrete-filled tubes, in terms of both strength and ductility, is superior to the independent responses of the empty tube and the unconfined concrete. This is due to the internal concrete stabilising

local buckling in the tube, while the tube confines the concrete which enhances the concrete strength and ductility.

The above discussion of long and short column behaviour reveals an apparent contradiction concerning stress-strain modelling of concrete in long (unconfined behaviour assumed) and short (confined behaviour assumed) columns. The difference occurs because for long columns a gradient in the ε_L distribution across the section occurs, while for short columns an approximately zero gradient is present. For concrete with symmetrically placed reinforcing steel, and a large gradient in ε_L across the section, it has been shown (2.10) that overall strength depends primarily on the behaviour of steel in tension, and response is comparatively insensitive to concrete strength and behaviour. Also in the presence of a gradient in ε_L, the average Poisson's ratio expansion of the concrete is not as large as it is for a zero gradient in ε_L, given the same value of maximum ε_L in both cases. Thus the lateral interaction of tube and concrete which results in augmented concrete strength and ductility becomes less important as the magnitude of the gradient in ε_L increases. Therefore it is not surprising that researchers have been able to satisfactorily predict the overall behaviour of long concrete-filled tubes by conservatively assuming that the concrete behaves in an unconfined manner.

2.3 THEORETICAL MODELLING OF LONGITUDINAL-TENSION LOADING

In Section 2.2.6, it was noted that the behaviour of circular-sectioned concrete-filled tubes subjected to longitudinal-tension loading appears to have received no previous research attention. In the following sections, a model which assumes uniaxial stress-strain behaviour in the concrete and the tube, and a further more realistic model which allows for the effect of lateral interaction on behaviour of tube and concrete are outlined. In Chapter 3, experimental results are compared with predictions based on these two models.

2.3.1 Uniaxial Model

In this model it is assumed that the overall $P - \varepsilon_L$ response of a concrete-filled tube can be obtained by superposing the independent $P - \varepsilon_L$ response of the plain concrete and the empty tube. This model ignores any restraint to Poisson's ratio hoop-compression strains in the steel tube provided by the concrete core, and is developed to enable the significance of lateral interaction to be investigated.

2.3.1.1 Concrete Response

The concrete $f_L - \varepsilon_L$ response to longitudinal-tension load is assumed to be identical to that illustrated previously in Fig. 2.6. Response is linearly elastic up to brittle failure which occurs at the tensile strength, f_t, of the concrete which can be assumed to occur at 60% of the modulus of rupture (MOR) (2.10) or at $-0.5\sqrt{f'_c}$ (2.44). The concrete modulus, E_c, is taken to be:

$$E_c = 5000\sqrt{f'_c} \quad \text{[MPa units]} \tag{2.84}$$

Concrete f_L is then related to ε_L as follows:

For $f_t/E_c \leq \varepsilon_L \leq 0$: $f_L = E_c \cdot \varepsilon_L$ (2.85)

and for $\varepsilon_L \leq f_t/\varepsilon_L$: $f_L = 0$ (2.86)

(Note in the above equations, f_t has a tensile and hence negative value).

2.3.1.2 Tube Response

The tube uniaxial $\sigma_L - \varepsilon_L$ characteristics, as determined from a coupon test of a sample of the tube are used in assessing the response of the tube. For example for typical mild steel, the response of which was illustrated previously in Fig. 2.3:

$$\text{For } -|\varepsilon_y| \leq \varepsilon_L \leq 0 \quad : \quad \sigma_L = E_s.\varepsilon_L \tag{2.87}$$

$$\text{For } -|\varepsilon_{sh}| \leq \varepsilon_L \leq -|\varepsilon_y| \quad : \quad \sigma_L = -|\sigma_y| \tag{2.88}$$

$$\text{For } -|\varepsilon_u| \leq \varepsilon_L \leq -|\varepsilon_{sh}| : \quad \sigma_L = -|\sigma_y| + \int E_t.d\varepsilon_L \tag{2.89}$$

where E_t = tangent modulus of the tube, which is an experimentally determined function of ε_L

For steel which does not exhibit the above elastic-plastic-strain-hardening stress-strain characteristics, then the actual $\sigma_L - \sigma_L$ response as determined from the coupon test should be used.

2.3.2 Lateral Interaction Model

The composite response of concrete-filled tubes to longitudinal-tension loading will be different to that predicted by the "Uniaxial Model" in two respects:

(i) Under longitudinal-tension load, the tube will attempt to contract laterally more than the concrete, particularly after the concrete has cracked, and is no longer carrying longitudinal stress. Prior to concrete cracking, the difference in Poisson's ratio contraction of tube and concrete will not be so pronounced since $\nu_s \cong 0.3$ and $\nu_c \cong 0.15$ implies that for compatibility of tube and concrete ε_L, the unrestrained (Poisson's ratio) lateral contraction of the concrete would be equal to half that of the tube.
Hence for compatible tube and concrete behaviour (i.e. tube ε_H = concrete ε_{RC} and tube ε_L = concrete ε_L, where concrete ε_L is assessed over a gauge length containing several cracks since strictly at a crack tube and concrete longitudinal strains are not compatible), the Poisson's ratio lateral contraction of the tube will be at least partially restrained by the concrete core. The result is hoop-tension stress in the tube and radial-compression stress in the concrete. The effect of these lateral stresses is ignored in the "Uniaxial Model" (see Section 2.3.1).

(ii) For $\varepsilon_L < f_t/E_c$, the proposed "Uniaxial Model" for concrete $f_L - \varepsilon_L$ (Section 2.3.1.1) effectively uses a cracked section analysis, and thus ignores the presence of concrete tensile stress in the zones between concrete cracks. As shown in Fig. 2.17, longitudinal-tension stress in the concrete between the cracks will cause local reductions to the longitudinal-tension stress carried by the tube. For a given longitudinal load, the average ε_L (measured over a gauge length containing several cracks) in the tube will thus be reduced, from that predicted on the basis of a cracked section, resulting in an apparent stiffening of the tube compared with that predicted by the "Uniaxial Model". This tension-stiffening effect will clearly increase in significance as the casing D/t ratio and hence A_c/A_t ratio increases.

The model outlined in Sections 2.3.2.1 - 2.3.2.3 allows for these two effects.

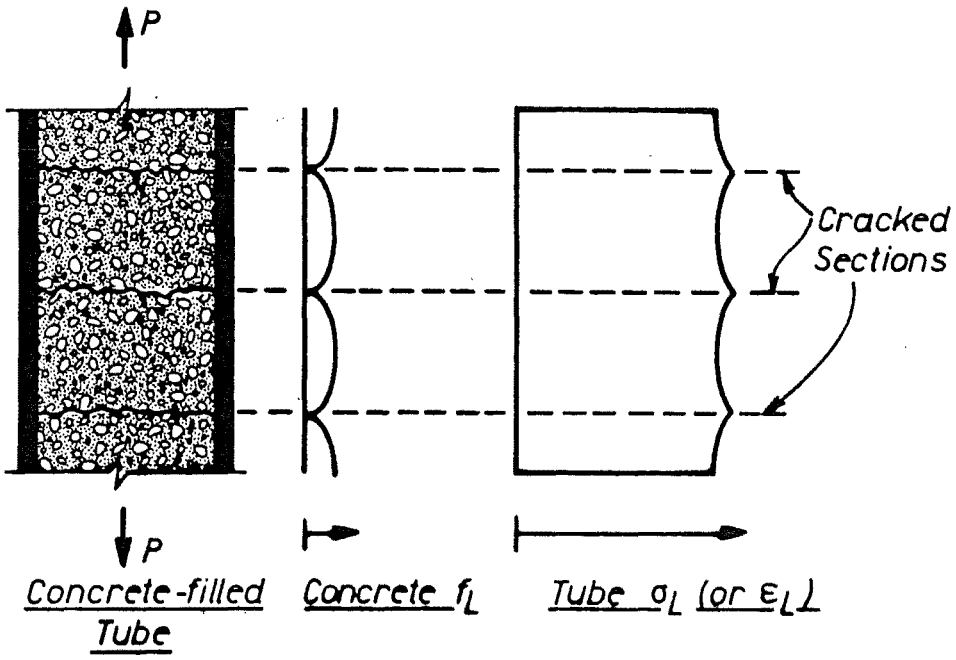

FIG. 2.17 : CONCRETE AND STEEL STRESS DISTRIBUTIONS AFTER CONCRETE CRACKING

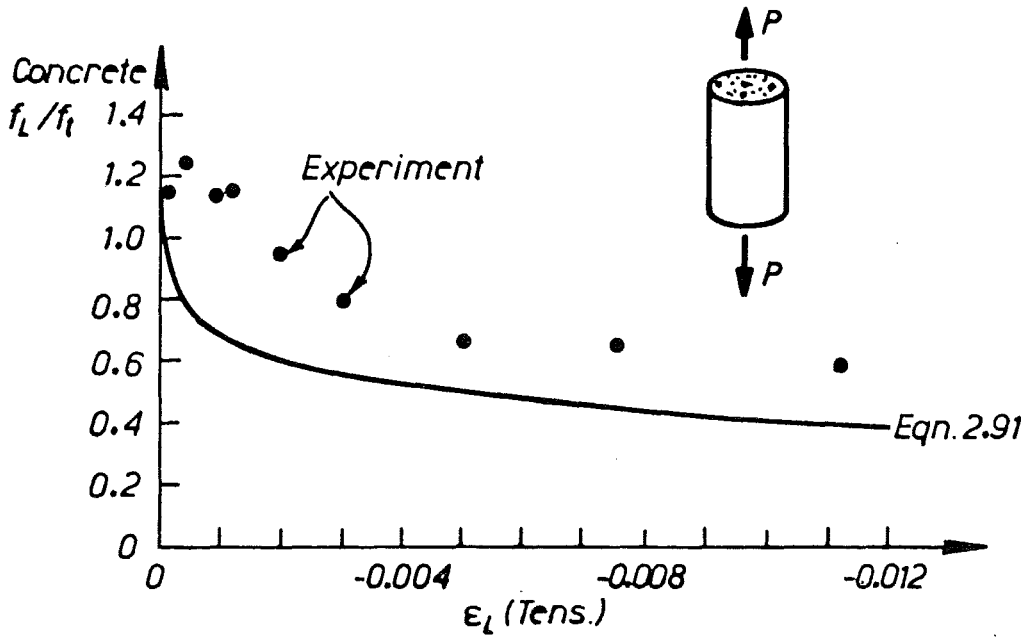

FIG. 2.18 : VECCHIO AND COLLINS (2.45) STRESS-STRAIN RELATIONSHIP FOR CONCRETE WHICH ALLOWS FOR THE TENSION-STIFFENING EFFECT

2.3.2.1 Concrete Response

To model the concrete $f_L - \varepsilon_L$ response allowing for the effect of concrete tension-stiffening between cracks, the relationship of Vecchio and Collins (2.45) was used, as shown below in equation 2.91. This equation was developed from longitudinal-tension-load tests of concrete reinforced with longitudinally orientated steel deformed bars. The steel area, in these tests, was approximately equal to 1% of the concrete area. For strains below the cracking strain, linear elastic behaviour was assumed.

$$\text{For } f_t/E_c \leq \varepsilon_L \leq 0 \quad : \quad f_L = E_c \cdot \varepsilon_L \tag{2.90}$$

$$\text{and for } \varepsilon_L \leq f_t/E_c \quad : \quad f_L = \frac{f_t}{1 + \sqrt{\varepsilon_L/-0.005}} \tag{2.91}$$

Steel stress (σ_L), based on load-sharing with concrete where the concrete stress is given by equation 2.91, can be considered to be the average steel stress over a gauge length containing several cracks. At a cracked section, the steel stress will be larger than the average steel stress, and a check must be made at each given load to ensure yield of the steel at the cracked section (where concrete $f_L = 0$) has not occurred. If yield has occurred f_L should be taken as being equal to zero and equation 2.91 should not be used. A further consequence of the tension-stiffening of the tube by the cracked concrete will be that the steel ε_L at the crack is significantly larger than the average steel ε_L, particularly after yield has occurred. The consequence is an apparent reduction in ductility caused by the reduced average tensile strain in the steel at fracture.

Figure 2.18 represents a comparison between equation 2.91 and typical Vecchio and Collins (2.45) experimental results. It is apparent that predictions based on equation 2.91 generally underestimate the experimentally obtained concrete f_L values. This is probably because the tension-stiffening phenomenon is related to the average tensile strength of the concrete, whereas typically tensile tests (e.g. split cylinder tests) of plain concrete give the tensile strength of the concrete at a position of weakness in the concrete sample. For this reason in this model f_t was chosen to be equal to the MOR (cf. the "Uniaxial Model" where it was suggested that f_t = 60% of MOR). Figure 2.18 also indicates that a substantial value of average tensile stress exists in the concrete at large values of $|\varepsilon_L|$. For example at $\varepsilon_L = -0.0015$ (assuming yield of the steel at the crack has not occurred), equation 2.91 gives concrete $f_L = 0.65 f_t$.

The application of equation 2.91 to concrete encased by a tube is not strictly appropriate, since the equation was developed from tests of deformed bars embedded in concrete. Bond conditions between a smooth steel surface and concrete would not be expected to be as good as those between a deformed steel surface and concrete, resulting in the cracks in the steel-encased concrete member occurring at a wider spacing than the cracks in a reinforced concrete member. However for concrete surrounding a reinforcing bar and a tube surrounding concrete, Poisson's ratio contraction of the steel under tensile stress will reduce and improve respectively the bond conditions. Thus it is probable that the application of equation 2.91 to steel-encased concrete is satisfactory.

2.3.2.2 Tube Response in the Elastic Range

The tube response is computed from the assumption that the concrete is infinitely rigid in the lateral direction, and hence concrete $\varepsilon_{RC} = 0$. It is shown later that this assumption which is relatively crude does not result in significant errors, and makes the development of a theoretical model relatively straightforward. Lateral compatibility of tube and concrete then require that $\varepsilon_H = 0$.

For $\varepsilon_H = 0$, the biaxial stress constitutive equations 2.11 and 2.12 then simplify to:

$$\sigma_L = E_s.\varepsilon_L/(1 - \nu_s^2) \tag{2.92}$$

and $$\sigma_H = \nu_s\, \sigma_L \tag{2.93}$$

Equations 2.92 and 2.93 may be compared with $\sigma_L = E_s.\varepsilon_L$ and $\sigma_H = 0$ which are the constitutive relations applying to the empty tube. Thus for a typical value of $\nu_s = 0.3$, equation 2.92 indicates that the steel in a concrete-filled tube has a 9.9% increase in longitudinal stiffness when compared with the steel in an empty tube. Equation 2.93 shows that the assumption of the concrete core being laterally rigid implies hoop-tension stress in the tube, and hence from lateral equilibrium of tube and concrete (equation 2.54), radial-compression stress in the concrete.

At the elastic-plastic boundary, from the Von Mises yield criterion (equation 2.37) with $\sigma_H = \nu_s\sigma_L$, it can be shown that

$$\sigma_L = \frac{-|\sigma_y|}{\sqrt{1 + \nu_s^2 - \nu_s}} \tag{2.94}$$

Substituting $\nu_s = 0.3$ gives $\sigma_L = -1.125|\sigma_y|$ and $\sigma_L = -0.338|\sigma_y|$.
Thus the apparent magnitude of the yield strength of the steel in a concrete-filled tube is predicted to be 12.5% larger than that of the steel in an empty tube. From equating the right hand sides of equations 2.92 and 2.94 and since $|\varepsilon_y| = |\sigma_y|/E_s$, it can be shown that at the elastic-plastic boundary:

$$\varepsilon_L = \frac{-|\sigma_y|}{\sqrt{1 + \nu_s^2 - \nu_s}} \cdot \frac{1 - \nu_s^2}{E_s} = -|\varepsilon_y| \cdot \frac{1 - \nu_s^2}{\sqrt{1 + \nu_s^2 - \nu_s}} \tag{2.95}$$

Thus at yield in the biaxial stress field with $\nu_s = 0.3$, $\varepsilon_L = -1.024|\varepsilon_y|$.

2.3.2.3 Tube Response in the Plastic Range

The tube response in the plastic range of material behaviour is also assessed on the basis that $\varepsilon_H = 0$. Since tube σ_L and σ_H are dependent on the strain path, it is necessary to use an iterative and incremental procedure to solve for these stresses. Given the following information:

(i) the values of E_s and ν_s and the $\varepsilon^p_{eff} - \sigma_{eff}$ relationship;

(ii) the values of $(\sigma_L)_i$, $(\sigma_H)_i$, $(\varepsilon^p_L)_i$, $(\varepsilon^p_H)_i$ and $(\varepsilon^p_{RT})_i$ (e.g. at step 0, which corresponds to the elastic-plastic boundary, $(\sigma_{eff})_o = |\sigma_y|$, $(\sigma_L)_o$ is defined by equation 2.94, $(\sigma_H)_o = \nu_s(\sigma_L)_o$, $(\varepsilon^p_L)_o = (\varepsilon^p_H)_o = (\varepsilon^p_H)_o = (\varepsilon^p_{RT})_o = 0$) ; and

(iii) the value of $(\varepsilon_L)_{i+1}$

then the procedure outlined below should be followed to solve for increment i + 1, where it is assumed that the size of the increments is small. If larger increments are used,the procedure below is potentially unstable, since convergence is very sensitive to the guessed value of $(\sigma_H)_{i+1}$.

Step 1 : Guess $(\sigma_L)_{i+1} = (\sigma_L)_i$, and $(\sigma_H)_{i+1} = (\sigma_H)_i$

Step 2 : Calculate $(\varepsilon_{RT})_{i+1}$ from equation 2.21 and the values of $(\sigma_L)_{i+1}$, $(\sigma_H)_{i+1}$, $(\sigma_R)_{i+1}$ (= zero), $(\varepsilon_L)_{i+1}$, $(\varepsilon_H)_{i+1}$ (= zero), E_s and ν_s.

Step 3 : Calculate $(\varepsilon^p_L)_{i+1}$, $(\varepsilon^p_H)_{i+1}$ and $(\varepsilon^p_{RT})_{i+1}$ from the values of $(\varepsilon_L)_{i+1}$, $(\varepsilon_H)_{i+1}$ (= zero), $(\varepsilon_{RT})_{i+1}$, $(\sigma_L)_{i+1}$, $(\sigma_H)_{i+1}$, $(\sigma_R)_{i+1}$ (= zero), E_s and ν_s and equations 2.14 - 2.16.

Step 4 : Calculate $(d\varepsilon^p_L)_{i+1} = (\varepsilon^p_L)_{i+1} - (\varepsilon^p_L)_i$, $(d\varepsilon^p_H)_{i+1} = (\varepsilon^p_H)_{i+1} - (\varepsilon^p_H)_i$ and $(d\varepsilon^p_{RT})_{i+1} = (\varepsilon^p_{RT})_{i+1} - (\varepsilon^p_{RT})_i$.

Step 5 : Calculate $(d\varepsilon^p_{eff})_{i+1}$ from the values of $(d\varepsilon^p_L)_{i+1}$, $(d\varepsilon^p_H)_{i+1}$ and $(d\varepsilon^p_{RT})_{i+1}$ and equation 2.27, and hence $(\varepsilon^p_{eff})_{i+1} = (\varepsilon^p_{eff})_i + (d\varepsilon^p_{eff})_{i+1}$.

Step 6 : Obtain $(\sigma_{eff})_{i+1}$ from the $\varepsilon^p_{eff} - \sigma_{eff}$ relationship and the value of $(\varepsilon^p_{eff})_{i+1}$.

Step 7 : Calculate $(\sigma_L)_{i+1}$ and $(\sigma_H)_{i+1}$ from equations 2.38 and 2.39 and the values of $(\sigma_{eff})_{i+1}$, $(d\varepsilon^p_L)_{i+1}$ and $(d\varepsilon^p_H)_{i+1}$.

Step 8 : Do the values of $(\sigma_L)_{i+1}$ and $(\sigma_H)_{i+1}$ obtained in Step 7 agree with those used earlier?

Yes - Convergence achieved for $(\sigma_L)_{i+1}$ and $(\sigma_H)_{i+1}$, go to increment i + 2.

No - Using the later values of $(\sigma_L)_{i+1}$ and $(\sigma_H)_{i+1}$, go to Step 2.

For $|\varepsilon_L| >> |\varepsilon_y|$ where $d\varepsilon^e_L \cong d\varepsilon^e_H \cong d\varepsilon^p_H \cong d\varepsilon_H = 0$ and $d\varepsilon^p_L \cong d\varepsilon_L$, then

$$d\varepsilon^p_H/d\varepsilon^p_L \cong 0 \qquad (2.96)'$$

Substituting equation 2.96 into equations 2.38 and 2.39 and noting that $d\varepsilon^p_H \cong 0$ and $d\varepsilon^p_L$ has a tensile and hence a tensile value gives:

$$\sigma_L = -1.155\ \sigma_{eff} \qquad (2.97)$$

$$\sigma_H = -0.577\ \sigma_{eff} \qquad (2.98)$$

From equations 2.97 and 2.98 $\sigma_L/\sigma_H = 2$, which as noted previously in Section 2.2.2.2 results in the maximum possible enhancement (15.5%) of σ_L in the biaxial-stress field relative to its uniaxial-stress value at the same σ_{eff}.

From Section 2.3.2.2, it was predicted that (for $\nu_s = 0.3$) tube $\sigma_L = -1.125\sigma_{eff}$ and $\sigma_H = -0.338\sigma_{eff}$ at the elastic-plastic boundary where $\sigma_{eff} = |\sigma_y|$, while at large $|\varepsilon_L|$ from equations 2.97 and 2.98 it is predicted that $\sigma_L = -1.155\sigma_{eff}$ and $\sigma_H = -0.578\sigma_{eff}$. Thus at the start of the plastic range there will be a transition zone where as ε_L increases, tube σ_L varies from $-1.125\sigma_{eff}$ to $-1.155\sigma_{eff}$ and σ_H varies from $-0.338\sigma_{eff}$ to $-0.578\sigma_{eff}$. This transition zone does not have a great deal of practical importance, since overall $P-\varepsilon_L$ response of the concrete-filled tubes depends primarily on σ_L

and the value of σ_H is of limited relevance to the proposed model.

For $|\varepsilon_L| >> |\varepsilon_y|$ where $d\varepsilon_H^p \cong 0$, then from equation 2.23 $d\varepsilon_{RT}^p = -d\varepsilon_L^p$. Now substituting $d\varepsilon_H^p = 0$ and $d\varepsilon_{RT}^p = -d\varepsilon_L^p$ into equations 2.27 results in:

$$d\varepsilon_{eff}^p = 1.155\ |d\varepsilon_L^p| \tag{2.99}$$

This implies that the steel in a concrete-filled tube will commence strain-hardening and reach ultimate strength at a smaller value of $|\varepsilon_L|$ than will the steel in an empty tube. This and the similar result occurring due to concrete tension-stiffening mentioned previously in Section 2.3.2.1 imply that the steel in a concrete-filled tube has apparently less ductility than the steel in a similar empty tube.

2.3.2.4 Possible Limitations to Theory

Two possible limitations to the proposed lateral interaction model, for concrete-filled tubes under longitudinal-tension load are discussed below.

(a) Effect of Concrete Lateral Flexibility and a Tube-Concrete Gap

Concrete lateral flexibility and the possibility of an initial gap between the tube and the core concrete will cause violations of the assumptions used in the "Lateral Interaction Model" that tube and concrete lateral strains are compatible (i.e. tube ε_H = concrete ε_{RC}) and that tube $\varepsilon_H = 0$.

To illustrate the effect of lateral flexibility of the concrete, an elastic range analysis was conducted in which it was assumed that the concrete and the steel are in a state of biaxial stress (f_R - f_R and σ_L - σ_H respectively). This assumed biaxial-stress state in the concrete ignores the effect of tensile values of concrete f_L and the resulting Poisson's ratio contraction of the concrete in the radial direction which would have a diminishing effect as the strain level increases.

Similarly to equation 2.12 and assuming lateral compatibility of tube and concrete (i.e. concrete ε_{RC} = tube ε_H), the constitutive relationship for the concrete can thus be expressed as:

$$f_R = \frac{E_c}{1 - \nu_c^2}\left(\varepsilon_{RC} + \nu_c\, \varepsilon_{RC}\right) = \frac{E_c \varepsilon_{RC}}{1 - \nu_c} = \frac{E_c \varepsilon_H}{1 - \nu_c} \tag{2.100}$$

Equating the right hand sides of equation 2.54 (the lateral equilibrium relationship) and equation 2.100, rearranging and solving for tube σ_H gives:

$$\sigma_H = \frac{2 - D/t}{2} \cdot \frac{E_c \varepsilon_H}{1 - \nu_c} \tag{2.101}$$

Equating the right hand sides of equation 2.12 (tube constitutive relationship) and equation 2.101, rearranging and solving for $-\varepsilon_H/\varepsilon_L$ gives

$$\frac{-\varepsilon_H}{\varepsilon_L} = \frac{\nu_s}{\left[\frac{E_c}{E_s} \cdot \frac{1 - \nu_s^2}{1 - \nu_c} \cdot \frac{D/t - 2}{2} + 1\right]} \tag{2.102}$$

Solving for ε_H from equation 2.102, substituting this into equation 2.11 (tube constitutive relationship) and rearranging gives:

$$\sigma_L = E_s.\varepsilon_L \frac{1}{1-\nu_s^2}\left[1 + \frac{\nu_s^2}{\frac{E_c}{E_s}\cdot\frac{1-\nu_s^2}{1-\nu_c}\cdot\frac{2-D/t}{2} - 1}\right] \quad (2.103)$$

Similarly solving for ε_H from equation 2.102, substituting this into equation 2.12 (constitutive relationship) and rearranging gives:

$$\sigma_H = E_s.\varepsilon_L \frac{\nu_s}{1-\nu_s^2}\left[1 + \frac{1}{\frac{E_c}{E_s}\cdot\frac{1-\nu_s^2}{1-\nu_c}\cdot\frac{2-D/t}{2} - 1}\right] \quad (2.104)$$

In the elastic range typical values of E_c, E_s, ν_c and ν_s are 25000 MPa, 200000 MPa, 0.15 and 0.3 respectively. Substituting these values into equations 2.102 - 2.104 gives:

$$\frac{-\varepsilon_H}{\varepsilon_L} = \frac{4.484}{12.95 + D/t} \quad (2.105)$$

$$\sigma_L = E_s\varepsilon_L\left[1.099 - \frac{1.478}{12.95 + D/t}\right] \quad (2.106)$$

$$\sigma_H = E_s\varepsilon_L\left[0.3297 - \frac{4.927}{12.95 + D/t}\right] \quad (2.107)$$

Figure 2.19 shows the variation of $-\varepsilon_H/\varepsilon_L$ with casing D/t ratio as defined by equation 2.105. The figure shows that as the casing D/t increases from 2 (solid steel member) to infinity, the $-\varepsilon_H/\varepsilon_L$ ratio decreases from 0.3 (assumed value of ν_s) to 0. Thus the assumption of the concrete being laterally rigid is more satisfactory at large than at small casing D/t ratios, since for large D/t ratios the ratio of concrete lateral stiffness to tube lateral stiffness is larger than it is for small casing D/t ratios.

Figure 2.20 shows the variations of $\sigma_L/(E_s\varepsilon_L)$ and $\sigma_H/(E_s.\varepsilon_L)$ with casing D/t ratio, where σ_L and σ_H are determined from equations 2.106 and 2.107 respectively and $E_s\varepsilon_L$ represents the value of σ_L in a uniaxial-stress field. Asymptotes which represent behaviour for $\varepsilon_H = 0$ (i.e. laterally rigid concrete are also indicated). Clearly the lateral flexibility of the concrete reduces the potential enhancement of tube σ_L which occurs in the biaxial-tension-stress field. However for large casing D/t ratios, the assumption of the concrete being laterally rigid is reasonable. For example at D/t = 100, $\sigma_L = 1.086E_s\varepsilon_L$ (cf. for $\varepsilon_H = 0, \sigma_L = 1.099E_s\varepsilon_L$). Thus typically the error in assessing tube σ_L, from the assumption that $\varepsilon_H = 0$, will be small. Figure 2.20 also shows that tube σ_H increases with the casing D/t ratio.

The specific results from the above analysis cannot be extrapolated into either the inelastic range of tube or concrete behaviour where different constitutive laws will govern behaviour, or the elastic range of material behaviour before the concrete cracks, where the $-\varepsilon_H/\varepsilon_L$ ratio will lie somewhere between ν_c and ν_s (e.g. 0.15 and 0.3) However it is subsequently demonstrated experimentally (Chapter 3) that the assumption of the concrete being laterally rigid is reasonable even for thick-walled concrete-filled tubes (D/t = 25.6). Thus from the trend indicated in Figs. 2.19 and 2.20, the assumption will be reasonable for all prototype piles ($60 \leq D/t \leq 180$).

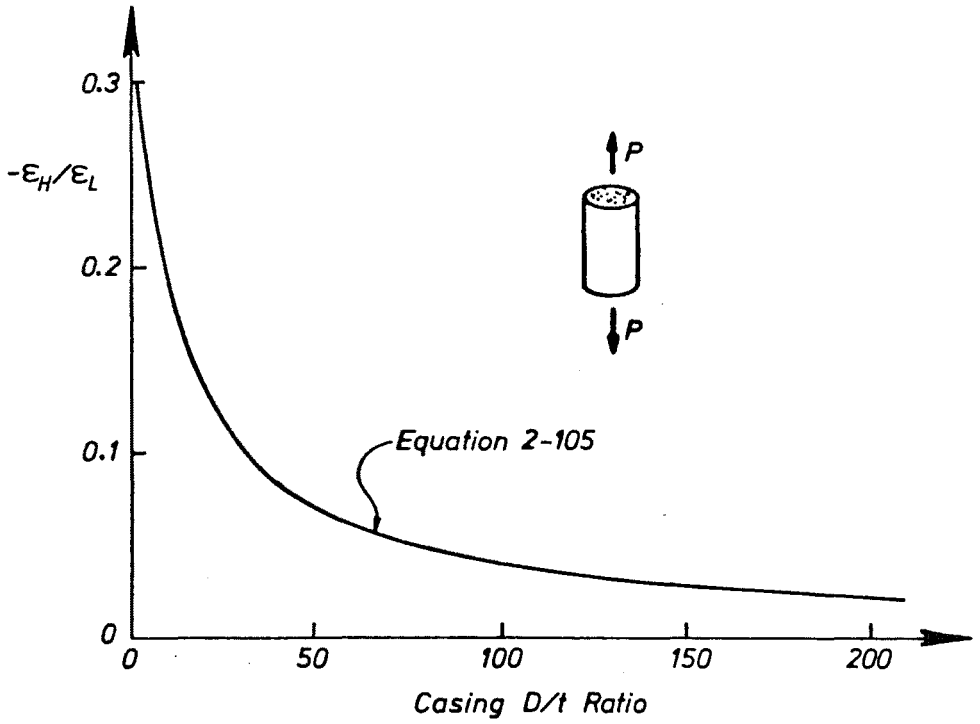

FIG. 2.19 : VARIATION OF HOOP STRAIN/LONGITUDINAL STRAIN WITH CASING DIAMETER/THICKNESS RATIO

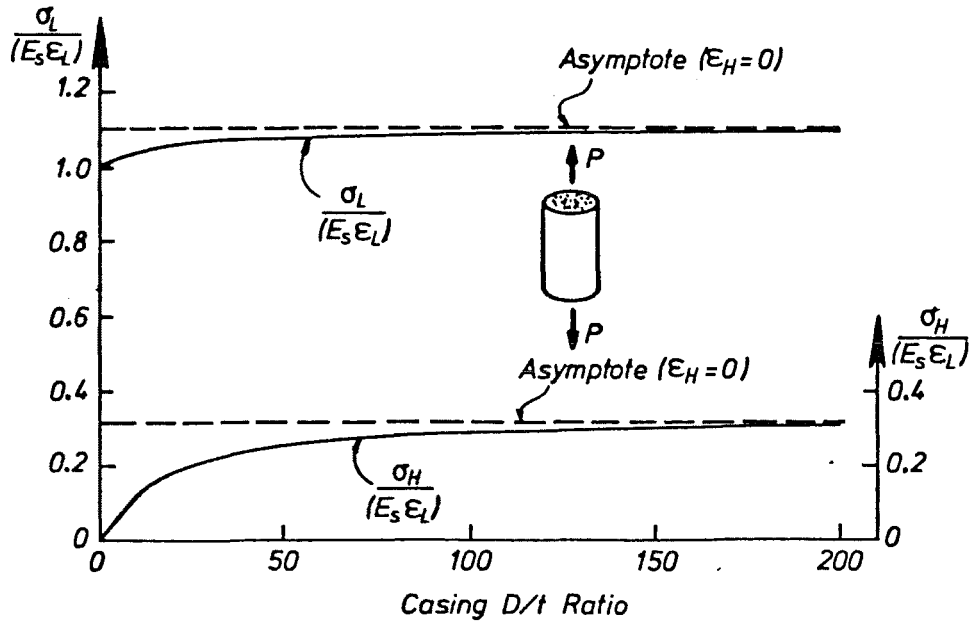

FIG. 2.20 : VARIATION OF TUBE BIAXIAL STRESSES WITH CASING DIAMETER/THICKNESS RATIO

It is also possible that prior to testing, a gap between tube and concrete may be present. Such a gap, which may develop when the concrete contracts after the initial rise in temperature associated with heat of hydration, can be expected to be small. However until this gap is closed the concrete and tube will not be compatible laterally (tube $\varepsilon_H \neq$ concrete ε_{RC}), and the steel in a concrete-filled tube will respond in the same fashion as does the steel in an empty tube, with the result that no enhancement of tube σ_L from biaxial-tension stress will occur at this stage. For realistic situations this effect should be negligible.

(b) Concrete Radial Strength

The assumption that the concrete is rigid in the lateral direction also implies the concrete is strong enough to equilibrate the tube σ_H which is predicted by the proposed tube constitutive model. For a concrete-filled tube subjected to longitudinal-tension load, for $|\varepsilon_L| >> |\varepsilon_y|$, tube $\varepsilon_H = 0$ has been shown (Section 2.3.2.3) to imply that $\sigma_H = \sigma_L/2$, $\sigma_L = -1.155\sigma_{eff}$ and $\sigma_H = -0.577\sigma_{eff}$. The largest value of concrete f_R, f_R^{max}, will occur at tube ultimate strength where $\sigma_{eff} = |\sigma_u|$ and $\sigma_H = \sigma_H^{max}$, and thus:

$$\sigma_H^{max} = -0.577|\sigma_u| \tag{2.108}$$

Substituting $f_R = f_R^{max}$ and $\sigma_H = \sigma_H^{max} = -0.577|\sigma_u|$ into equation 2.54 and rearranging gives:

$$f_R^{max} = \frac{1.155|\sigma_u|}{D/t - 2} \tag{2.109}$$

For typical material strength parameters of $f'_c = 30$ MPa and $|\sigma_u| = 450$ MPa, equation 2.109 indicates that f_R^{max} exceeds f'_c for $D/t \leq 19.3$ (cf. prototype piles : $60 \leq D/t \leq 180$). It should, however, be noted that the radial-compression strength of the concrete will, in general, differ from f'_c because of the triaxial-stress state involving longitudinal tension and radial compression in the concrete.

Tests of reinforced concrete panels subject to in-plane loading have been conducted by Vecchio and Collins (2.45). These tests have shown that for compressive load in one direction and tensile load in the direction transverse to the compressive load, the compressive strength of the concrete is reduced appreciably by the presence of transverse tensile strain, as indicated by equation 2.110.

$$f_2^{max} = \frac{f'_c}{0.8 - 170\varepsilon_1} \leq f'_c \tag{2.110}$$

where ε_1 = concrete strain, in the direction of the tensile load

f_2^{max} = concrete strength, in the direction of the compressive load.

For example, at $\varepsilon_1 = -0.01$, equation 2.110 gives $f_2^{max} = 0.40f'_c$, indicating a marked reduction in compressive strength. However the work of Vecchio and Collins related to a biaxial-tension-compression-stress field and in the triaxial-tension-compression-compression stress field of concrete encased by a tube, the strength reduction should be less significant. It thus appears that except for tubes with very small values of either casing D/t ratio or concrete f'_c, the radial strength of the concrete should not limit the potential 15.5% enhancement of tube σ_L which occurs as a result of the assumed lateral rigidity of the concrete.

2.4 THEORETICAL MODELLING OF LONGITUDINAL-COMPRESSION LOADING

The work described in the previous sections has indicated that there has been no consistent model developed to describe the compressive load-strain behaviour of concrete-filled steel tubes. Although Tomii et al (2.1) developed a model that considered the lateral interaction between tube and concrete, it ignored the influence of tube strain-hardening and did not consider the stress-strain characteristics of the confined concrete beyond determining an empirical value of $K = 2.6$ for the strength enhancement of concrete due to confining stress (see equation 2.51).

However the considerable body of well reported test data of Tomii et al (2.1) and Sakino et al (2.41) provides a potential for more detailed analysis. In this section the development of a model, which was calibrated from this test data, to allow for lateral interaction between the tube and concrete is described. A further, simplified, model based on uniaxial stress-strain behaviour in the steel and concrete was developed and for comparative purposes is also described in this section.

2.4.1 Uniaxial Model

In this model it is assumed that the overall $P - \varepsilon_L$ response of a concrete-filled tube can be obtained by addition of the independent $P - \varepsilon_L$ responses of the plain concrete and the empty tube. This model ignores the effect of composite and laterally compatible behaviour in the tube and concrete, and is developed to enable the significance of lateral interaction to be identified by comparison with the more realistic model which is described in later sections.

2.4.1.1 Tube Response

The tube uniaxial $\sigma_L - \varepsilon_L$ characteristics, as determined from a coupon test of a sample of the tube are used in assessing the response of the tube. It should be noted that the coupon test is a tensile test, and thus will not take into account the probable unstable performance, in the plastic range of steel behaviour, of the empty tube. Thus it is implicit in this "Uniaxial Model" that the internal concrete stabilises the tube, resulting in the tensile and compressive longitudinal-load behaviour of the tube being approximately identical.

2.4.1.2 Concrete Response

In the uniaxial model the concrete is assumed to respond in accordance with a prediction based on the Popovics (2.16) relationship which was given previously for confined concrete in equation 2.52. For unconfined concrete where it can be considered that $\varepsilon'_{cc} = \varepsilon_{co}$, $f'_{cc} = f'_c$ and $E_{sec} = f'_c/\varepsilon_{co}$, the relationship can be rewritten as:

$$f_L = \frac{f'_c \cdot X \cdot r}{r - 1 + X^r} \qquad (2.111)$$

$$\text{where } X = \varepsilon_L/\varepsilon_{co} \qquad (2.112)$$

$$r = E_c/(E_c - E_{sec}) \qquad (2.113)$$

$$\text{and as before } E_c = 5000\sqrt{f'_c} \text{ [MPa] units} \qquad (2.114)$$

It is also assumed that $\varepsilon_{co} = 0.002$.

2.4.2 Lateral Interaction Model

At very small values of ε_L (<< 0.002), Poisson's ratio for steel and concrete are approximately equal to 0.3 and 0.15 respectively. This implies that under longitudinal-compression load either a small level of radial-tension stress in the concrete and hoop-compression stress in the tube are present, or more likely a small gap between tube and concrete will develop. There is also the possibility of a small gap at the tube-concrete interface being present at the start of testing due to the concrete contracting after the initial rise of temperature associated with heat of hydration. Thus at small values of ε_L, tube and concrete are unlikely to interact laterally.

As ε_L increases from 0 to 0.002, the Poisson's ratio for concrete increases from 0.15 to a value in excess of 0.5, as was mentioned previously in Section 2.2.3. From the results of Tomii et al (2.1) it was deduced previously (see Section 2.2.6.2) that the large strain ($\varepsilon_L > 0.01$) value of Poisson's ratio for concrete confined by a tube was 1.4. For the tube, Poisson's ratio has a value of typically 0.3 throughout the elastic range of steel behaviour (typically $\varepsilon_L \leq 0.0016$ for mild steel with σ_y = 320 MPa). In the plastic range of steel behaviour, Poisson's ratio for the tube gradually increases from a value of 0.3 to 0.5, as was shown in Fig. 2.5.

The result for concrete-filled tubes is that as longitudinal-compression load increases and ε_L approaches 0.002, the Poisson's ratio lateral expansion of the concrete equals that of the tube. Hence for ε_L in the vicinity of and greater than 0.002, lateral interaction of tube and concrete will occur. In the concrete and tube models which are described subsequently, it is assumed that lateral interaction which results in radial-compression stress in the concrete and hoop-tension stress in the tube occurs for $\varepsilon_L \geq 0.002$.

2.4.2.1 Tube Response

In this section, tube $\sigma_L - \varepsilon_L$ and $\sigma_H - \varepsilon_L$ relationships are proposed which model biaxial-stress behaviour of the steel in a concrete-filled tube under longitudinal-compression loading. These relationships are similar to those derived by Tomii et al (2.1) and presented previously in Sections 2.2.6.2 and Fig. 2.14. The stress-strain behaviour is divided into three stages:

(i) Initial Stage

For $\varepsilon_L \leq 0.002$, no lateral interaction between tube and concrete is assumed to occur. Uniaxial tube $\sigma_L - \varepsilon_L$ (i.e. tube $\sigma_H = 0$) response is assumed in accordance with the "Uniaxial Model" for the tube which was outlined previously in Section 2.4.1.1.

(ii) Final Stage

For $\varepsilon_L \geq 0.01$, full lateral interaction between tube and concrete is assumed to occur, resulting in a constant level of longitudinal-compression stress being present in the tube:

$$\sigma_L = K_{\sigma_{L^\infty}} |\sigma_y| \qquad (2.115)$$

where $K_{\sigma_{L^\infty}} = \dfrac{0.9R + 0.6}{\sqrt{3}\sqrt{0.9R - 0.4 + (0.9R - 1.4)^2}}$ (2.116)

The value of R which represents the relative strengths of the tube and concrete is given by equation 2.75, and $K_{\sigma_{L^\infty}} |\sigma_y|$ corresponds to the value of the tube σ_L at $\varepsilon_L > 6|\varepsilon_y|$ as derived by Tomii et al (see equation 2.76). Since in the proposed model for $\varepsilon_L > 0.01$, it is assumed that σ_L is constant, then in the strain-hardening range, the subsequent increase in σ_{eff} results only in an increase in the magnitude of tube σ_H and hence in the confinement of the concrete.

(iii) Transition Stage

For $0.002 \leq \varepsilon_L \leq 0.01$, a transition stage occurs during which tube σ_L steadily decreases and tube $|\sigma_H|$ and hence concrete f_R steadily increase with increasing ε_L. During this stage σ_L is defined by:

$$\sigma_L = K_{\sigma_L} |\sigma_y| \tag{2.117}$$

where K_{σ_L} is a parabolic function of ε_L (and at $\varepsilon_L = 0.01$, $K_{\sigma_L} = K_{\sigma_L^\infty}$):

$$K_{\sigma_L} = K_{\sigma_L^\infty} + (1 - K_{\sigma_L^\infty}) \left[\frac{0.01 - \varepsilon_L}{0.008} \right]^2 \tag{2.118}$$

Figure 2.21 shows the relationship between K_{σ_L}, R and ε_L.

In the plastic range at a given σ_{eff} and σ_L, σ_H can then be determined by rearranging equation 2.36 to give:

$$\sigma_H = \sigma_L/2 - \sqrt{\sigma_{eff}^2 - 0.75\, \sigma_L^2} \tag{2.119}$$

However since σ_{eff} is a function of ε^p_{eff} and hence the strain history, it is necessary to use an incremental and iterative solution to determine σ_H.

At increment $i = 0$, which represents the commencing point of lateral interaction $(\varepsilon_L)_o = 0.002$, and for typical mild steel $(\sigma_L)_o = |\sigma_y|$. Then for the uniaxial stress conditions which exist at this point $(\varepsilon^p_L)_o = 0.002 - |\sigma_y|/E_s$, $(\varepsilon^p_H)_o = -\frac{1}{2}(\varepsilon^p_L)_o$ and $(\varepsilon^p_{RT})_o = (\varepsilon^p_H)_o$. To solve for $(\sigma_H)_{i+1}$, it is necessary to have the following information:

(i) the values of E_s and ν_s and the $\varepsilon^p_{eff} - \sigma_{eff}$ relationship as determined from a coupon test.

(ii) the values of $(\varepsilon^p_L)_i$, $(\varepsilon^p_H)_i$, $(\varepsilon^p_{RT})_i$, $(\varepsilon^p_{eff})_i$ and $(\sigma_H)_i$. (e.g. these values are given for Step 0, as above), and

(iii) the value of $(\varepsilon_L)_{i+1}$ and hence from equations 2.115 or 2.117 the value of $(\sigma_L)_{i+1}$.

The procedure outlined below may be followed to solve for increment $i+1$.

Step 1 : Guess $(\sigma_H)_{i+1} = (\sigma_H)_i$

Step 2 : Calculate $(\varepsilon^e_L)_{i+1}$, $(\varepsilon^e_H)_{i+1}$ and $(\varepsilon^e_{RT})_{i+1}$ from the values of E_s, ν_s, $(\sigma_L)_{i+1}$, $(\sigma_H)_{i+1}$ and $(\sigma_R)_{i+1}$ (= zero) and equations 2.5-2.7 (where ε^e_L, ε^e_H and ε^e_{RT} are substituted for ε_L, ε_H and ε_{RT} respectively).

Step 3 : Calculate $(\varepsilon^p_L)_{i+1} = (\varepsilon_L)_{i+1} - (\varepsilon^e_L)_{i+1}$

Step 4 : Calculate $(d\varepsilon^p_L)_{i+1} = (\varepsilon^p_L)_{i+1} - (\varepsilon^p_L)_i$

Step 5 : Calculate $(d\varepsilon^p_H)_{i+1}$ by rearranging the Prandtl-Reuss relationships (equations 2.17 - 2.18) to eliminate $d\lambda$ and substituting $\sigma_R = 0$:

$$(d\varepsilon^p_H)_{i+1} = \frac{2(\sigma_H)_{i+1} - (\sigma_L)_{i+1}}{2(\sigma_L)_{i+1} - (\sigma_H)_{i+1}} (d\varepsilon^p_L)_{i+1} \tag{2.120}$$

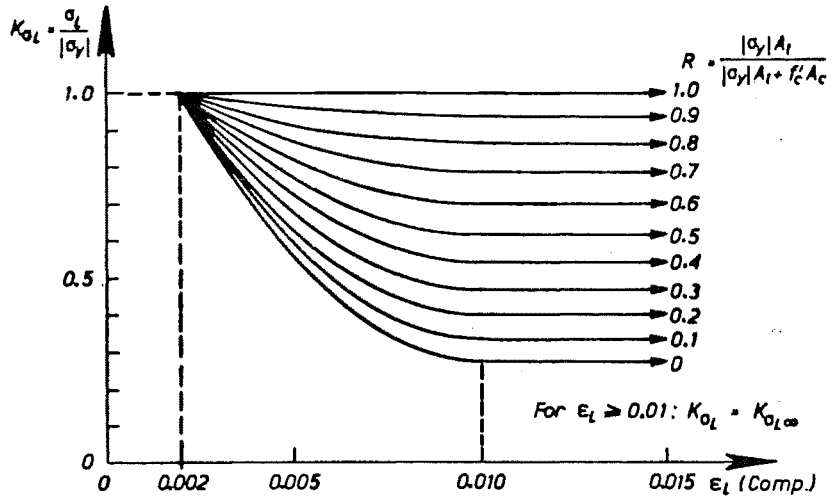

FIG 2.21 : INFLUENCE OF RELATIVE CONCRETE AND TUBE STRENGTH ON THE LONGITUDINAL STRESS IN THE TUBE

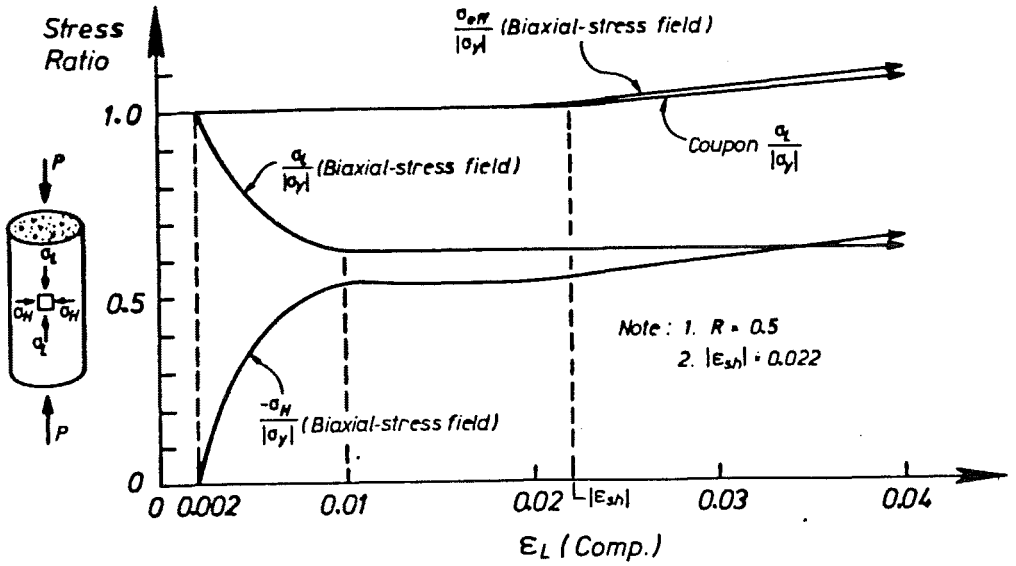

FIG. 2.22 : TYPICAL VARIATION OF TUBE BIAXIAL STRESSES WITH LONGITUDINAL STRAIN

Step 6 : Similarly calculate $(d\varepsilon^p_{RT})_{i+1}$:

$$(d\varepsilon^p_{RT})_{i+1} = \frac{-(\sigma_L)_{i+1} - (\sigma_H)_{i+1}}{2(\sigma_L)_{i+1} - (\sigma_H)_{i+1}} (d\varepsilon^p_L)_{i+1} \qquad (2.121)$$

Step 7 : Calculate $(d\varepsilon^p_{eff})_{i+1}$ from the value of $(d\varepsilon^p_L)_{i+1}$, $(d\varepsilon^p_H)_{i+1}$ and $(d\varepsilon^p_{RT})_{i+1}$ and equation 2.27.

Step 8 : Calculate $(\varepsilon^p_{eff})_{i+1} = (\varepsilon^p_{eff})_i + (d\varepsilon^p_{eff})_{i+1}$

Step 9 : Obtain $(\sigma_{eff})_{i+1}$ from the $\varepsilon^p_{eff} - \sigma_{eff}$ relationship and the value of $(\varepsilon^p_{eff})_{i+1}$.

Step 10 : Calculate $(\sigma_H)_{i+1}$ from the values of $(d\varepsilon^p_L)_{i+1}$, $(d\varepsilon^p_H)_{i+1}$, $(\sigma_{eff})_{i+1}$ and equation 2.39.

Step 11 : Check if the value of $(\sigma_H)_{i+1}$ obtained in Step 10 is in close agreement with the value used in Step 2.
Yes - Convergence achieved for $(\sigma_H)_{i+1}$, proceed to increment i + 2.
No - Using the later value of $(\sigma_H)_{i+1}$, go to Step 2.

If the tube strain history is required then $(\varepsilon_H)_{i+1}$ and $(\varepsilon_{RT})_{i+1}$ can be calculated from:

$$(\varepsilon_H)_{i+1} = (\varepsilon^e_H)_{i+1} + (\varepsilon^p_H)_i + (d\varepsilon^p_H)_{i+1} \qquad (2.122)$$

$$(\varepsilon_{RT})_{i+1} = (\varepsilon^e_{RT})_{i+1} + (\varepsilon^p_{RT})_i + (d\varepsilon^p_{RT})_{i+1} \qquad (2.123)$$

From the above procedures it can be shown that the biaxial-stress field in the tube wall will result in the steel strain-hardening and reaching ultimate strength at a smaller value of ε_L than will the steel in an empty tube which is also subjected to longitudinal-compression loading. To illustrate this point consider a typical concrete-filled tube with $R = 0.5$ and $\varepsilon_L > 0.01$. From equation 2.74, $d\varepsilon_H$ is equal to $-0.95d\varepsilon_L$. Since at this stage $d\varepsilon^e_L \cong d\varepsilon^e_H \cong d\varepsilon^e_{RT} \cong 0$, then $d\varepsilon^p_H \cong -0.95d\varepsilon^p_L$ and from equation 2.23 $d\varepsilon^p_{RT} \cong -0.05d\varepsilon^p_L$. From equation 2.27 and $d\varepsilon^p_H = -0.95d\varepsilon^p_L$ and $d\varepsilon^p_{RT} = -0.05d\varepsilon^p_L$, $d\varepsilon^p_{eff} = 1.127d\varepsilon^p_L$ and hence at large strains $\varepsilon^p_{eff} \cong \varepsilon_{eff} \cong 1.127\varepsilon^p_L \cong 1.127\varepsilon_L$.

Concrete-filled tubes which attain large σ_H/σ_L ratio have very thin walls ($R \cong 0$). For such members it can similarly be shown that for $\varepsilon_L > 0.01$, $d\varepsilon^p_{eff} = 1.442d\varepsilon^p_L$. Thus the earlier onset of strain-hardening and ultimate strength, and hence loss of ductility which occurs in the concrete-filled tube relative to the empty tube is particularly pronounced for concrete-filled tubes with small values of R.

Figure 2.22 shows typical biaxial-stress field variations of tube $\sigma_{eff}/|\sigma_y|$, $\sigma_L/|\sigma_y|$ and $-\sigma_H/|\sigma_y|$ with ε_L which are plotted for $R = 0.5$ and $|\varepsilon_{sh}| = 0.022$. Also indicated on the figure is the variation of coupon (uniaxial-stress conditions) $\sigma_L/|\sigma_y|$ with ε_L. A comparison of the biaxial-stress field $\sigma_{eff}/|\sigma_y|$ and the coupon $\sigma_L/|\sigma_y|$ variations emphasises the effect of the earlier onset of strain-hardening under longitudinal-compression loading which occurs in the steel in a concrete-filled tube relative to the steel in an empty tube.

These biaxial-stress field variations of $\sigma_L/|\sigma_y|$ and $\sigma_H/|\sigma_y|$ are similar to those shown in Fig. 2.14 which represented the statistical smoothing of their experimental results by Tomii et al (2.1). The differences which occur are due to two causes:

(i) Tomii et al (2.1) defined the ε_L at which biaxial-stress effects first occur as equal to $|\varepsilon_y|$, whereas in the proposed model the effects are assumed to first occur at $\varepsilon_L = 0.002$. Also the results of Tomii et al imply that $K_{\sigma_L} = K_{\sigma_{L\infty}}$ applies for $\varepsilon_L \geq 6|\varepsilon_y|$, whereas the writer proposes $K_{\sigma_L} = K_{\sigma_{L\infty}}$ applies for $\varepsilon_L \geq 0.01$. For typical mild steel with for example $|\varepsilon_y| = 0.0016$, there is little practical difference between the K_{σ_L} values predicted by Tomii et al and the proposed model. However concrete dilatancy, which is the main cause of concrete-tube lateral interaction, was considered to be more properly related to the value of ε_L than to the ratio of $\varepsilon_L/|\varepsilon_y|$. Thus for steel with ε_y different to that used by Tomii et al (2.1), a variation of $\sigma_L/|\sigma_y|$ based on a function of $\varepsilon_L/|\varepsilon_y|$, as used by Tomii et al, could give poor results.

(ii) As was stated previously in Section 2.2.6.2, in interpreting their experimental data Tomii et al (2.1) assumed that $d\varepsilon_H/d\varepsilon_L$ was equal to $d\varepsilon_H^p/d\varepsilon_L^p$ and of constant value for $\varepsilon_L > 6|\varepsilon_y|$. For $|\varepsilon_{eff}^p| > |\varepsilon_{sh} - \varepsilon_y|$, they also ignored strength increase in the steel due to strain-hardening. The result was that Tomii et al predicted constant values of σ_L and σ_H for $\varepsilon_L > 6|\varepsilon_y|$ and a given value of R, as shown in Fig. 2.14. The proposed model for tube $\sigma_L - \varepsilon_L$ makes allowance for the experimental observation that $|d\varepsilon_H/d\varepsilon_L|$ increases with ε_L (see Fig. 2.13) and for increase in steel strength due to strain-hardening by allowing σ_H to increase with ε_L, in the strain-hardening range, as shown in Fig. 2.22.

Finally it should also be noted that the above procedure for determining the variation of tube σ_H with ε_L will also give indirectly the variation of concrete f_R with ε_L from the requirement of lateral equilibrium between tube and concrete (equation 2.54).

2.4.2.2 Concrete Response

The concrete longitudinal stress (f_L) will be a function of both the longitudinal strain (ε_L) and the lateral confining stress (f_R) which results from concrete-tube lateral interaction. Existing models for confined concrete based on a constant confining stress are unlikely to be appropriate because of the gradual increase in confining stress (since concrete f_R is proportional to tube $|\sigma_H|$) indicated by Fig. 2.22.

For $\varepsilon_L \leq 0.002$, the response of the concrete is assumed to be in accordance with the "Uniaxial Model" which was outlined previously in Section 2.4.1.2.

For $\varepsilon_L \geq 0.002$, the longitudinal-stress in the concrete is determined in non-dimensionalised form from:

$$f_L/f'_c = \text{Function } (f_R/f'_c , \varepsilon_L) \qquad (2.124)$$

where f_R is the radial stress in the concrete corresponding to the longitudinal strain ε_L. Existing data do not permit development of equation 2.124 as a unique relationship. Consequently this equation will be developed in terms of a family of curves for constant concrete radial stress. It is assumed that concrete f_L will then be given by the curve for the current value of f_R/f'_c. Since f_R varies during the loading of the member, this implies a $f_L/f'_c - \varepsilon_L$ curve that moves between the family of curves, as illustrated conceptually in Fig. 2.23 for a thick-walled and a thin-walled concrete-filled tube.

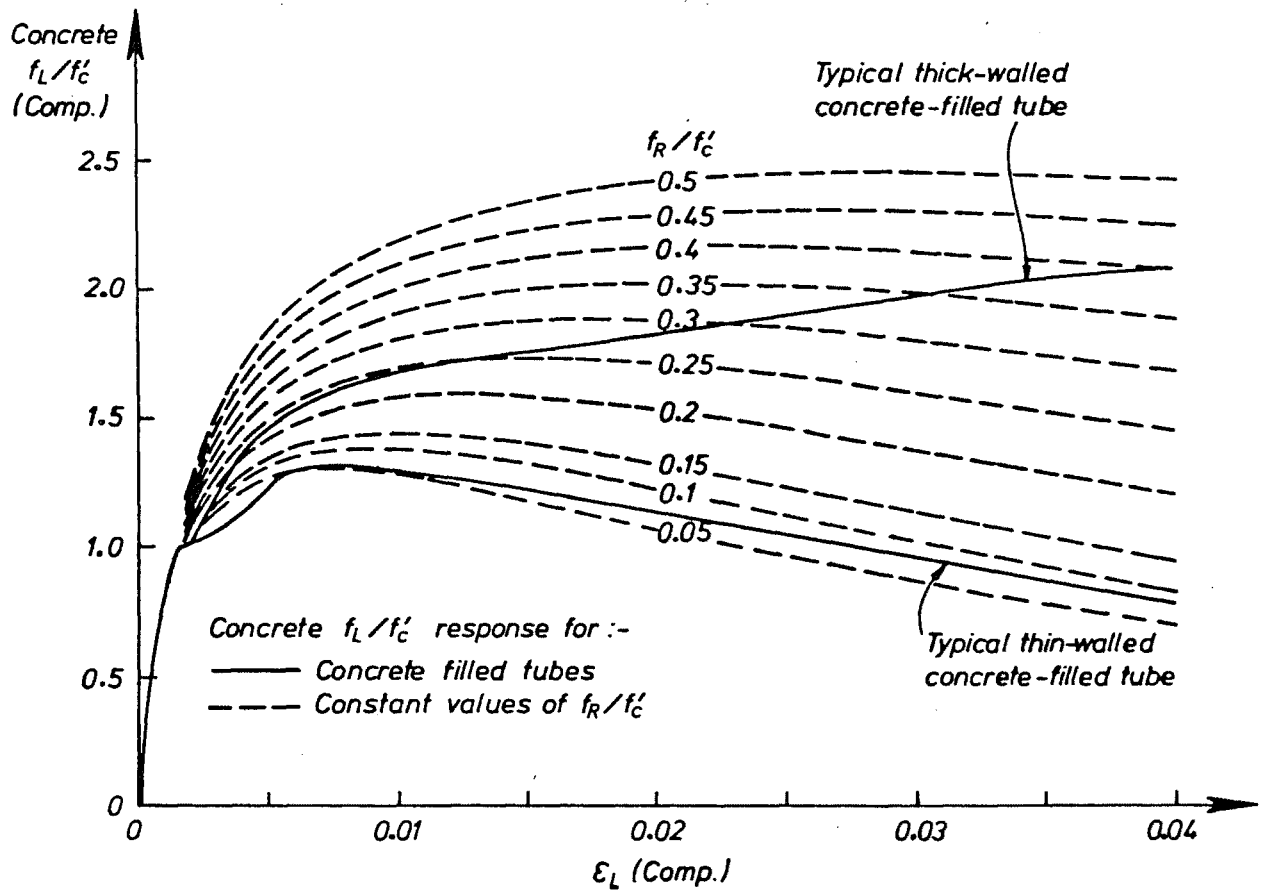

FIG. 2.23 : PREDICTION OF CONCRETE LONGITUDINAL STRESS-LONGITUDINAL STRAIN BEHAVIOUR FOR VARIABLE RADIAL STRESS, FROM CONSTANT RADIAL STRESS CURVES

The procedure to be used in solving the concrete f_L vs ε_L response for $\varepsilon_L \geq 0.002$ is as follows:

(i) Determine the tube $\sigma_H - \varepsilon_L$ response from the method outlined in the previous section.

(ii) Determine the concrete $f_R - \varepsilon_L$ response from the tube $\sigma_H - \varepsilon_L$ response and the requirement of concrete and tube lateral equilibrium (equation 2.54).

(iii) From the $f_R - \varepsilon_L$ relationship determine the concrete $f_L - \varepsilon_L$ response using the family of stress-strain curves representing equation 2.124.

2.4.2.3 Derivation of Stress-Strain Relationship for Concrete Confined by a Tube

As discussed earlier in Section 2.2.4, existing stress-strain curves for concrete confined by transverse reinforcement such as the model of Mander et al (2.2) are not expected to be representative of concrete confined by a tube, because of the interaction of tube σ_L, σ_H, $\varepsilon_L, \varepsilon_H$ and ε_{RT} which occurs in the steel. Consequently an attempt was made to extract the stress-strain behaviour of concrete confined by a tube using relevant test data. To this end, the relationships represented by equation 2.124 and Fig. 2.23 were obtained by analysis of the 33 test results of Tomii et al (2.1) and Sakino et al (2.41), described previously in Section 2.2.6.2, and the theoretical response of the tube allowing for lateral interaction effects, described in Section 2.4.2.1. It is recalled that the 33 tests involved three specimens at each of 11 different values of R (the ratio of the tube yield strength to the sum of the tube yield strength and the unconfined strength of the concrete) between 0.12 and 0.66. In comparison for prototype piles (with for example $|\sigma_y| = 300$ MPa, $f'_c = 30$ MPa and $60 \leq D/t \leq 180$), R will range from 0.18 to 0.41. Thus the following deduced results from the tests of Tomii et al (2.1) and Sakino et al (2.41) should be suitable for application to prototype piles.

Tomii et al and Sakino et al used four different thicknesses of tubes in their 33 tests, and the uniaxial stress-strain characteristics of these four types of steel which were used in predicting the theoretical response of the tube are listed in Table 2.1. As can be seen from the table, Tomii et al and Sakino et al did not give complete information on the stress-strain characteristics of the tube steel, and in particular the tangent modulus of the steel in the strain-hardening range was not given. Thus the strain-hardening characteristics of the cold-formed steel (t = 0.52 mm) and the hot-formed steel (t = 2.0 mm, 3.2 mm and 4.3 mm) were estimated as shown in Table 2.1. The estimated values of E_t in the strain-hardening range are of the same order as those which were found from coupon testing plate samples as described in Chapters 3 and 4. Although the assumed strain-hardening behaviour was only crudely estimated, it was anticipated that for $\varepsilon_L \leq 0.04$, the $P - \varepsilon_L$ response of the concrete-filled tubes would not be too sensitive to the guessed steel strain-hardening characteristics. It was also assumed that tube ν_s was equal to 0.3.

The following procedure was then adopted at each of the 11 values of R which were used in the tests of Tomii et al (2.1) and Sakino et al (2.41):

(i) The average (of the three tests at the given value of R) $P - \varepsilon_L$ response was determined from either of figure 2.12 or 2.16.

(ii) Tube $\sigma_L - \varepsilon_L$ and $\sigma_H - \varepsilon_L$ responses were then calculated using the "Lateral Interaction Model" for the tube which was outlined in Section 2.4.2.1. These responses allowed the concrete $f_R - \varepsilon_L$ (from equation 2.54) and $P_t - \varepsilon_L$ responses to be calculated, where P_t the longitudinal load carried by the tube comes from:

$$P_t = A_t \cdot \sigma_L = \pi(D - t).t.\sigma_L \qquad (2.125)$$

TABLE 2.1 : UNIAXIAL STRESS-STRAIN PARAMETERS OF THE TUBES OF TOMII ET AL (2.1) AND SAKINO ET AL (2.41)

t (mm)	$\lvert\varepsilon_y\rvert$	$\lvert\varepsilon_{sh}\rvert$	$\lvert\sigma_y\rvert$ (MPa)	$\lvert\sigma_u\rvert$ (MPa)	σ_L (MPa)		
					$\varepsilon_L \leq \lvert\varepsilon_y\rvert$	$\lvert\varepsilon_y\rvert \leq \varepsilon_L \leq \lvert\varepsilon_{sh}\rvert$	$\varepsilon_L \geq \lvert\varepsilon_{sh}\rvert$
0.52 (2.41)	-	-	244	350	$205000\varepsilon_L$	244	$244 + 1073(\varepsilon_L - 0.001190)$
2.0 (2.1)	0.001590	0.0194	337	464	$212000\varepsilon_L$	337	$337 + 2120(\varepsilon_L - 0.0194)$
3.2 (2.1)	0.001516	0.0225	288	413	$190000\varepsilon_L$	288	$288 + 1900(\varepsilon_L - 0.0225)$
4.3 (2.1)	0.001333	0.0212	280	414	$210000\varepsilon_L$	280	$280 + 2100(\varepsilon_L - 0.0212)$

Note: Values of $\lvert\varepsilon_y\rvert$, $\lvert\varepsilon_{sh}\rvert$, $\lvert\sigma_y\rvert$ and $\lvert\sigma_u\rvert$ are as given by Tomii et al and Sakino et al, and $\sigma_L - \varepsilon_L$ relationships are given from these values or estimated in the absence of information.

(iii) The longitudinal load carried by the concrete was then determined from:

$$P_c = P - P_t \tag{2.126}$$

and hence concrete f_L from:

$$f_L = \frac{P_c}{A_c} = \frac{P_c}{\frac{1}{4}\pi(D - 2t)^2} \tag{2.127}$$

At each value of ε_L from 0.003 to 0.040 by increments of 0.001, a diagram of concrete f_L/f'_c vs f_R/f'_c was drawn, and the results from each of the 11 values of R were plotted. Typical examples for ε_L = 0.005, 0.020 and 0.040 are shown in Fig. 2.24. Linear regression equations to the data are also plotted on the diagrams. From these regression equations, f_L/f'_c vs ε_L responses at a variety of constant values of f_R/f'_c (0.05, 0.1, 0.15, ... 0.45, 0.5) were plotted as shown in Fig. 2.25. In the figure interpolated results from the data are shown as solid lines, and extrapolated results from the data which were used subsequently for the purpose of curve-fitting are shown as dashed lines. The peaks of the curves are also indicated in the figure. Figure 2.25 clearly shows the enhancement to concrete strength and ductility which results from the confinement offered by the tube.

The Mander et al (2.2) $f_L - \varepsilon_L$ relationship for concrete confined by spiral reinforcement, which was outlined previously in Section 2.2.5, can be used to produce similar curves to those shown in Fig. 2.25. In Fig. 2.26, a family of curves for f_L/f'_c vs ε_L at given values of f_R^{max}/f'_c as predicted by the Mander et al model are shown. Since the shape of these curves is slightly dependent on the value of f'_c, the curves were derived on the basis that f'_c = 24 MPa, which corresponds to the average value of f'_c from the 33 tests of Tomii et al (2.1) and Sakino et al (2.41).

It should be noted that in the Mander et al (2.2) model, f_R^{max}, is based on the yield strength of the confining steel. This implies that at small values of ε_L before the confining steel has yielded, $f_R < f_R^{max}$, while at large values of ε_L after the confining steel has strain-hardened $f_R > f_R^{max}$. Thus is is not strictly appropriate to compare the results from Figs. 2.25 and 2.26. Nevertheless the comparison between Figs. 2.25 and 2.26 shows that the Mander et al model generally overestimates f_L for concrete confined by a tube, particularly at small values of strain. It is also obvious that for a given value of f_R/f'_c (or f_R^{max}/f'_c) that the peak of the f_L/f'_c vs ε_L curve in Fig. 2.25 generally occurs at a larger value of ε_L than does the peak of the Mander et al curve. This is because the tube has a delayed confining effect on the concrete relative to that provided by spiral reinforcement, due to the lateral expansion of the tube under

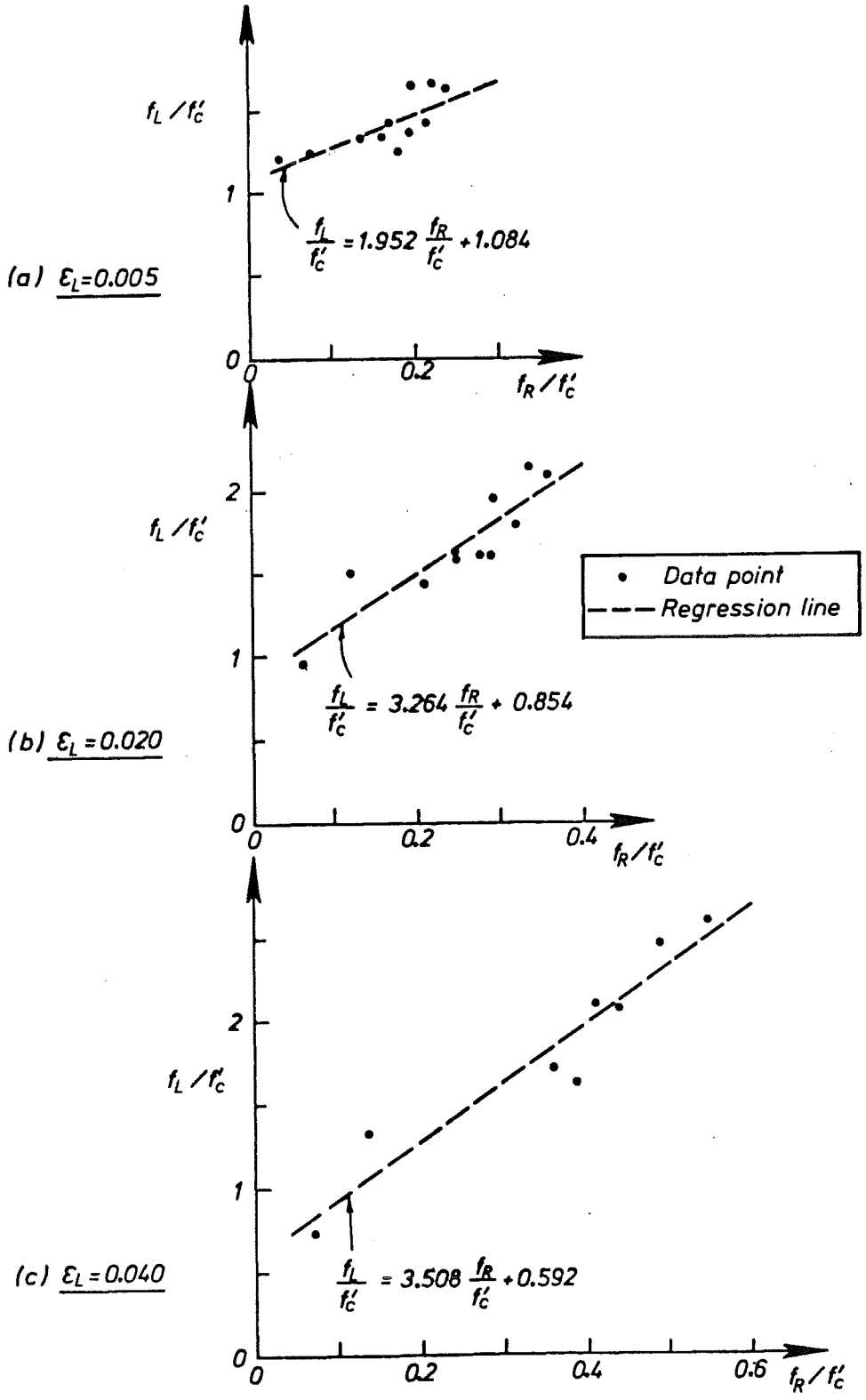

FIG. 2.24 : TYPICAL RELATIONSHIPS BETWEEN LONGITUDINAL AND RADIAL CONCRETE STRESS RATIOS, AT CONSTANT VALUES OF LONGITUDINAL STRAIN FROM TOMII ET AL (2.1) AND SAKINO ET AL (2.41) DATA

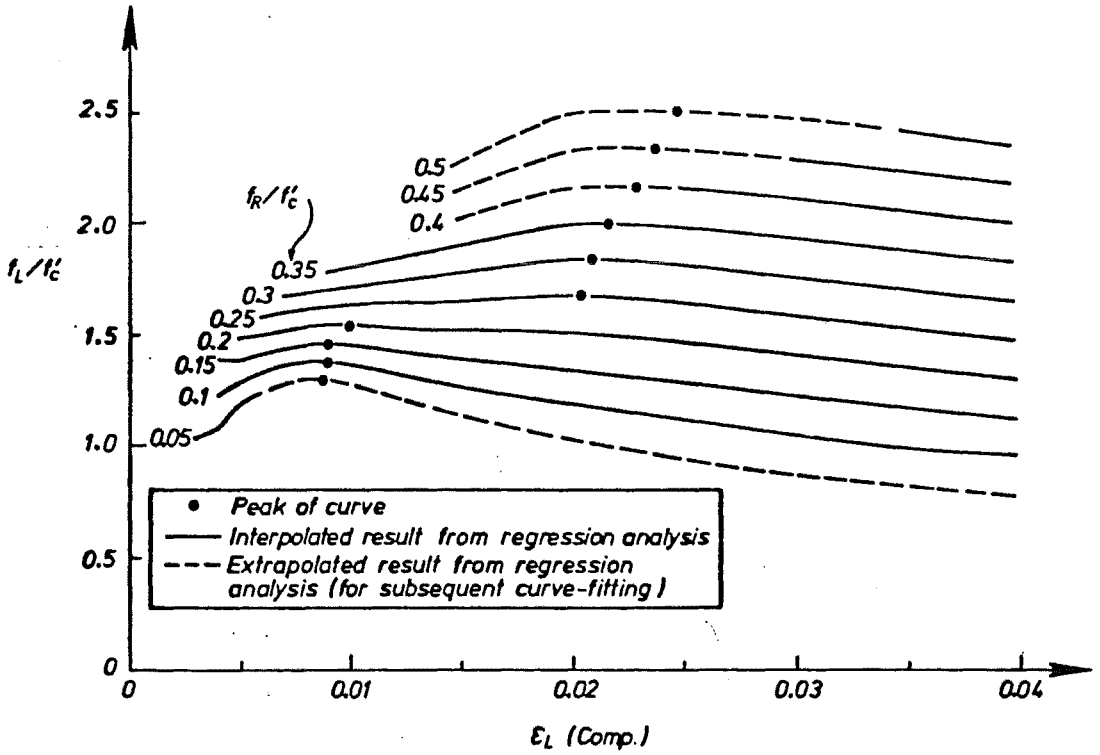

FIG. 2.25 : INFERRED CONCRETE LONGITUDINAL STRESS-LONGITUDINAL STRAIN RELATIONSHIPS FOR CONCRETE CONFINED BY A TUBE

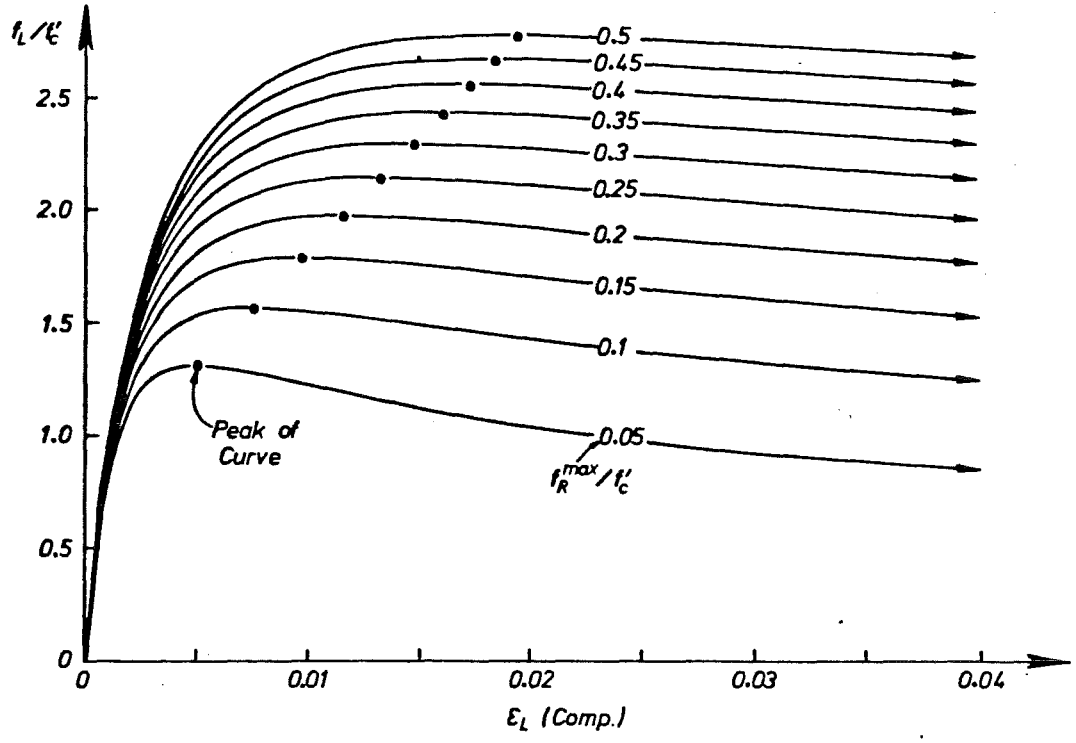

FIG. 2.26 : MANDER ET AL (2.2) STRESS-STRAIN CURVES FOR CONCRETE CONFINED BY SPIRAL REINFORCEMENT

longitudinal-compression stress. Since the curves of Fig. 2.25 indicate that, as expected, the Mander et al model could not be used for this study, an attempt was made to obtain a suitable function for equation 2.124 directly from the results shown in Fig. 2.25.

It was found that a modified form of the Popovics (2.26) equation (given previously as equation 2.52) to allow for the differences in ε'_{cc} and f'_{cc} which occur between concrete confined by spiral reinforcement and a tube would not accurately model the falling branch characteristics of the curves shown in Fig. 2.25. This is because the Popovics' equation is defined by three parameters, E_c, f'_{cc} and ε'_{cc} and it is not possible to alter the falling branch characteristics at given values of these three parameters.

The equation used by Desayi et al (2.22) for modelling the $f_L - \varepsilon_L$ relationship of confined concrete does allow the falling branch characteristics to be independently modified, since the relationship is defined by five parameters, E_c, f'_{cc}, ε'_{cc}, $\alpha f'_{cc}$ and $\beta\varepsilon'_{cc}$, where $(\beta\varepsilon'_{cc}, \alpha f'_{cc})$ are (ε_L, f_L) coordinates at a control point on the falling branch of the curve. The equation can be defined by:

$$f_L = \frac{K_1 \cdot \varepsilon_L}{1 + K_2 \cdot \varepsilon_L + K_3 \cdot \varepsilon_L^2 + K_4 \cdot \varepsilon_L^3} \qquad (2.128)$$

where $K_1 = E_c$ $(= 5000\sqrt{f'_c}$ as before) (2.129)

$$K_2 = \left[\frac{1 - 2\alpha\beta + \alpha\beta^2}{\alpha(\beta - 1)^2} \cdot \frac{E_c}{E_{sec}} - \frac{2\beta + 1}{\beta}\right] \cdot \frac{1}{\varepsilon'_{cc}} \qquad (2.130)$$

$$K_3 = \left[\frac{\beta + 2}{\beta} - \frac{2(1 - \alpha)}{\alpha(\beta - 1)^2} \cdot \frac{E_c}{E_{sec}}\right] \cdot \frac{1}{(\varepsilon'_{cc})^2} \qquad (2.131)$$

$$K_4 = \left[\frac{1 - \alpha}{\alpha(\beta - 1)^2} \cdot \frac{E_c}{E_{sec}} - \frac{1}{\beta}\right] \frac{1}{(\varepsilon'_{cc})^2} \qquad (2.132)$$

and $E_{sec} = f'_{cc}/\varepsilon'_{cc}$ (2.133)

Desayi et al (2.22) recommended that the control point on the falling branch was chosen at $f_L = 0.85f'_{cc}$ which implies $\alpha = 0.85$.

To define equation 2.128 for concrete confined by a tube, it was thus necessary to develop relationships for f'_{cc}, ε'_{cc} and β :

(a) Determining f'_{cc}

The peak value of concrete f_L/f'_c $(= f'_{cc}/f'_c)$ at a given value of f_R/f'_c can be expressed as:

$$\frac{f'_{cc}}{f'_c} = 1 + K' \frac{f_R}{f'_c} \qquad (2.134)$$

where K' = an empirically determined constant. The above equation is similar in form to equation 2.51 divided by f'_c, since equation 2.134 could be derived from equation 2.51 by replacing K with K' and f_R^{max} with f_R. Equation 2.134 can also be rearranged to solve for K' :

$$K' = \frac{(f'_{cc}/f'_c) - 1}{(f_R/f'_c)} \qquad (2.135)$$

From the results of the linear regression analysis of concrete-filled tube data shown in Fig. 2.25, the values of K' for $0.05 \leq f_R/f'_c \leq 0.50$ were determined as shown in Fig. 2.27(a). A proposed empirical relationship for K' vs f_R/f'_c and the K vs f_R^{max}/f'_c relationship predicted using the Mander et al (2.2) model are also shown in Fig. 2.27(a). From the empirical fit it is proposed that:

$$\text{for } \frac{f_R}{f'_c} \leq 0.12 : \quad K' = 8 - 42.5 \frac{f_R}{f'_c} \qquad (2.136)$$

$$\text{and for } \frac{f_R}{f'_c} \geq 0.12 : \quad K' = 2.9 \qquad (2.137)$$

For $f_R/f'_c > 0.05$, the Mander et al method would clearly result in an overestimate of the K' and hence f'_{cc} for concrete confined by a tube. For $f_R/f'_c > 0.12$, the empirical relationship gives $K' = 2.9$ which is a little larger than the K of 2.6 which was derived by Tomii et al (2.1) from their tests of thick-walled concrete-filled tubes.

(b) Determining ε'_{cc}

In the Mander et al (2.2) model, ε'_{cc} for concrete confined by spiral reinforcement is calculated from equation 2.57 which can be rearranged to give:

$$C = \frac{(\varepsilon'_{cc}/\varepsilon_{co}) - 1}{(f'_{cc}/f'_c) - 1} \qquad (2.138)$$

From the results of the linear regression analyses of concrete-filled tube data shown in Fig. 2.25, the values of C for $0.05 \leq f_R/f'_c \leq 0.5$ can be determined as shown in Fig. 2.27(b), where it is assumed that $\varepsilon_{co} = 0.002$. The results show a considerable degree of scatter, but it is recommended that for concrete confined by a tube C is taken as 9.5. This compares with the value of 5 that Mander et al (2.2) recommend for concrete confined by spiral reinforcement, and again it is illustrated that relative to spiral reinforcement the tube has a delayed confining effect on the concrete.

(c) Determining β

From the results of the linear regression analyses of the concrete-filled tube data which are shown in Fig. 2.25, the values of β (which correspond to $\alpha = 0.85$) at $0.05 \leq f_R/f'_c \leq 0.50$ were determined as shown in Fig. 2.27(c). The results show a considerable degree of scatter, but it is recommended that the average value, obtained from the 10 data points, which was 2.45 is used.

(d) Resulting Equation

From the preceding section (c) $\beta = 2.45$ and $\alpha = 0.85$, thus the expressions for K_2, K_3 and K_4 (see equations 2.130, 2.131 and 2.132 respectively) can be simplified to give:

$$K_2 = (1.084E_c/E_{sec} - 2.408)/\varepsilon'_{cc} \qquad (2.139)$$

$$K_3 = (1.816 - 0.1679E_c/E_{sec})/(\varepsilon'_{cc})^2 \qquad (2.140)$$

$$K_4 = (0.08393E_c/E_{sec} - 0.4082)/(\varepsilon'_{cc})^3 \qquad (2.141)$$

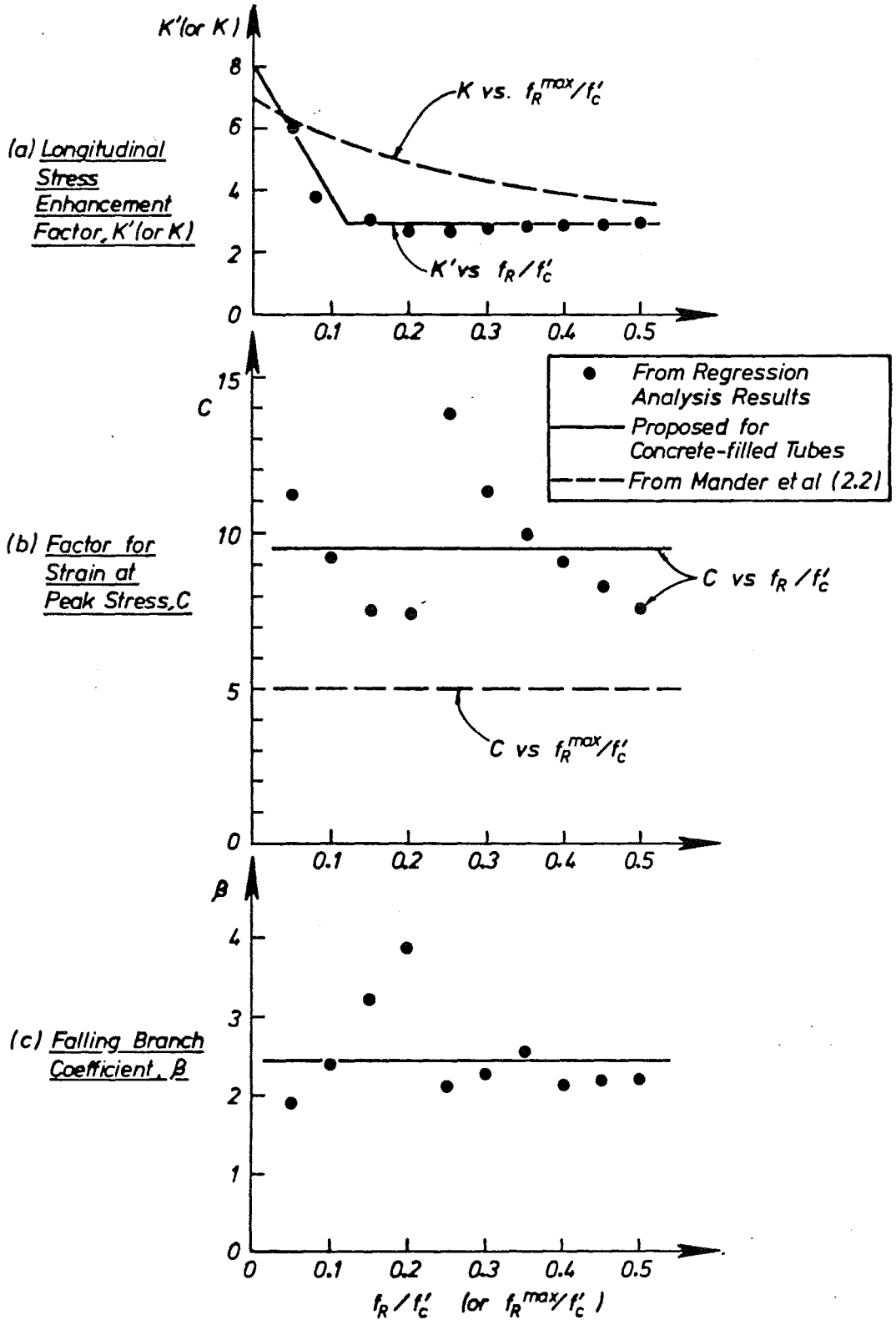

FIG. 2.27 : DETERMINING EMPIRICAL RELATIONSHIPS FOR K', C and β

The resulting f_L/f'_c vs ε_L relationships at a variety of constant values of f_R/f'_c are shown in Fig. 2.28, plotted for f'_c = 24 MPa which corresponds to the average value of f'_c used in the 33 tests of Tomii et al (2.1) and Sen et al (2.41).

In Fig. 2.29, plots of f_L/f'_c vs ε_L predicted by the proposed model, and the model of Mander et al are compared with data points from the linear regression analyses, at constant values of f_R/f'_c (or f_R^{max}/f'_c for Mander et al model) of 0.05, 0.25 and 0.50. Clearly the proposed model closely matches the results from the regression analyses, while the model of Mander et al generally overestimates the concrete $f_L - \varepsilon_L$ response.

2.4.3 Comparison Between Experiment and Theory

A comparison between the experimental results of Tomii et al (2.1) and Sakino et al (2.41) and predictions based on the "Uniaxial Model" (see Section 2.4.1) and the "Lateral Interaction Model" (see Section 2.4.2) is presented in Figs. 2.30 to 2.40. Since the "Lateral Interaction Model" was calibrated from these experimental results, its average agreement with the experimental results is expected to be good, and this model is primarily tested by its ability to predict behaviour over a wide range of casing D/t ratios.

In determining the $\sigma_L - \sigma_H - f_L - f_R - \varepsilon_L$ responses predicted by the "Lateral Interaction Model", prior to calculating overall $P - \varepsilon_L$ response, the large effect of lateral interaction on the stress-strain behaviour of the concrete and the tube was noticed. For example for these tests at 11 different values of R (0.12 to 0.66) at ε_L = 0.04, tube σ_L varied from $0.34|\sigma_y|$ to $0.74|\sigma_y|$, tube σ_H varied from $-1.02|\sigma_y|$ to $-0.59|\sigma_y|$, concrete f_R from $0.07f'_c$ to $0.56f'_c$, and concrete f_L from $0.84f'_c$ to $2.67f'_c$.

Figures 2.30 to 2.40 present the comparison in order of increasing R, from R = 0.12 (concrete-dominated response) to R = 0.66 (tube-dominated response). The theoretical ultimate load, P_u^{SEN}, predicted by the formula of Sen (see equation 2.62) and the concrete $P_c - \varepsilon_L$ and tube $P_t - \varepsilon_L$ responses predicted by the two models are also shown. The following comments can be made from these figures:

(i) For $\varepsilon_L \leq 0.002$, the experimental $P - \varepsilon_L$ response lies between the theoretical $P - \varepsilon_L$ and $P_t - \varepsilon_L$ responses. This difference between experimental and theoretical $P - \varepsilon_L$ responses is possibly due to the concrete being slightly withdrawn inside the tube due to shrinkage, which would result in a delayed loading of the concrete relative to that of the tube.

(ii) The $P - \varepsilon_L$ responses predicted from the "Lateral Interaction Model" give generally a good approximation to the experimental $P - \varepsilon_L$ responses for the full range of R. A comparison of the $P - \varepsilon_L$ responses predicted from the "Uniaxial Model" and the experimental $P - \varepsilon_L$ responses shows that the response of the concrete-filled tubes is considerably stronger and more ductile that the sum of the responses of the unconfined concrete and the empty tube.

(iii) The maximum loads predicted by the formula of Sen, P_u^{SEN}, were on average 2% larger than the maximum experimental loads, P_u^{exp}, with a coefficient of variation of 10% for P_u^{exp}/P_u^{SEN}. In eight of the 11 tests (those with R > 0.46), P vs ε_L response was still rising at ε_L = 0.04 which implies that a low estimate of P_u^{exp} was obtained. Thus it appears that the ultimate load formula of Sen which was developed from concrete-filled tube tests with $17 \leq D/t \leq 37$, could be used to give a generally conservative estimate of the ultimate load for all prototype piles ($60 \leq D/t \leq 180$).

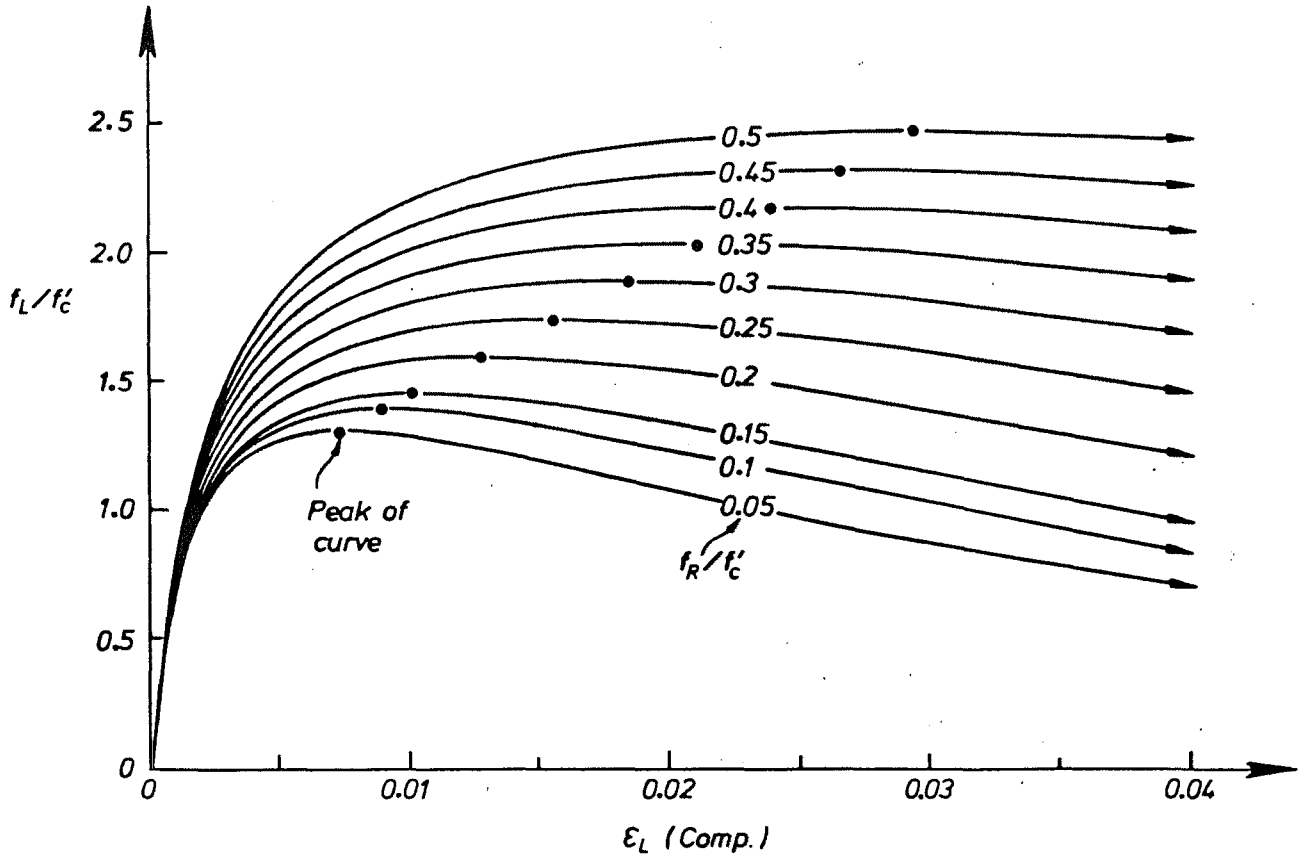

FIG.2.28 : PROPOSED STRESS-STRAIN CURVES FOR CONCRETE CONFINED BY A TUBE

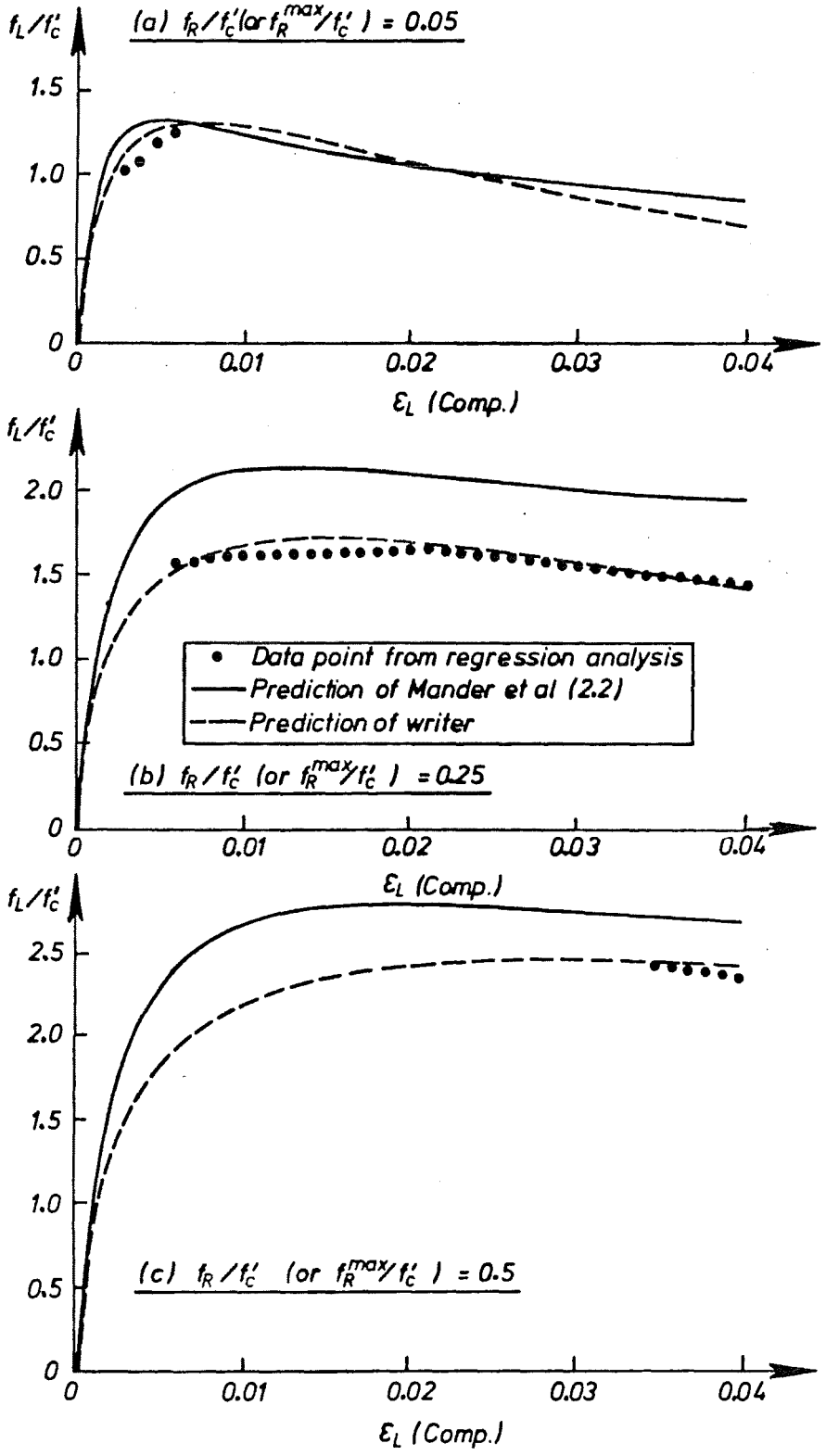

FIG. 2.29 : COMPARISON OF CONCRETE LONGITUDINAL STRESS-LONGITUDINAL STRAIN RESPONSES, AT CONSTANT RADIAL STRESS

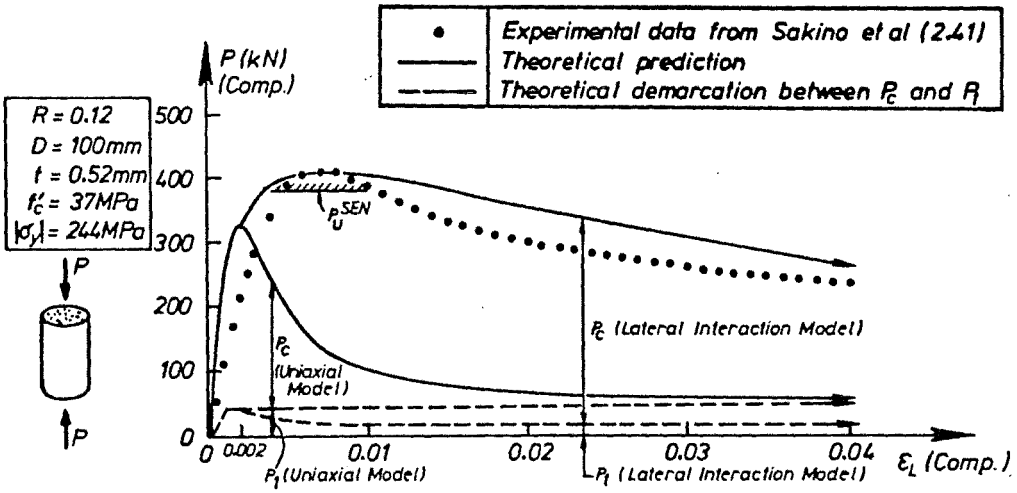

FIG. 2.30 : LONGITUDINAL LOAD-LONGITUDINAL STRAIN COMPARISON (R = 0.12)

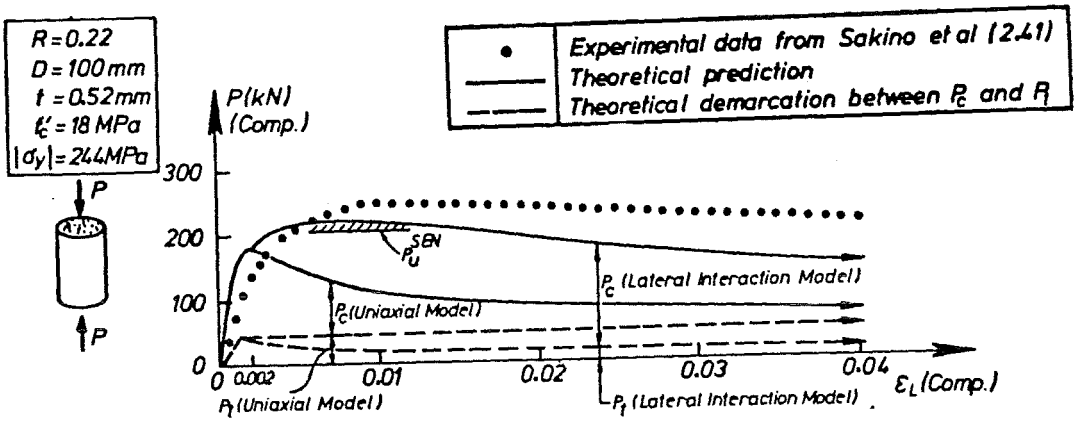

FIG. 2.31 : LONGITUDINAL LOAD-LONGITUDINAL STRAIN COMPARISON (R = 0.22)

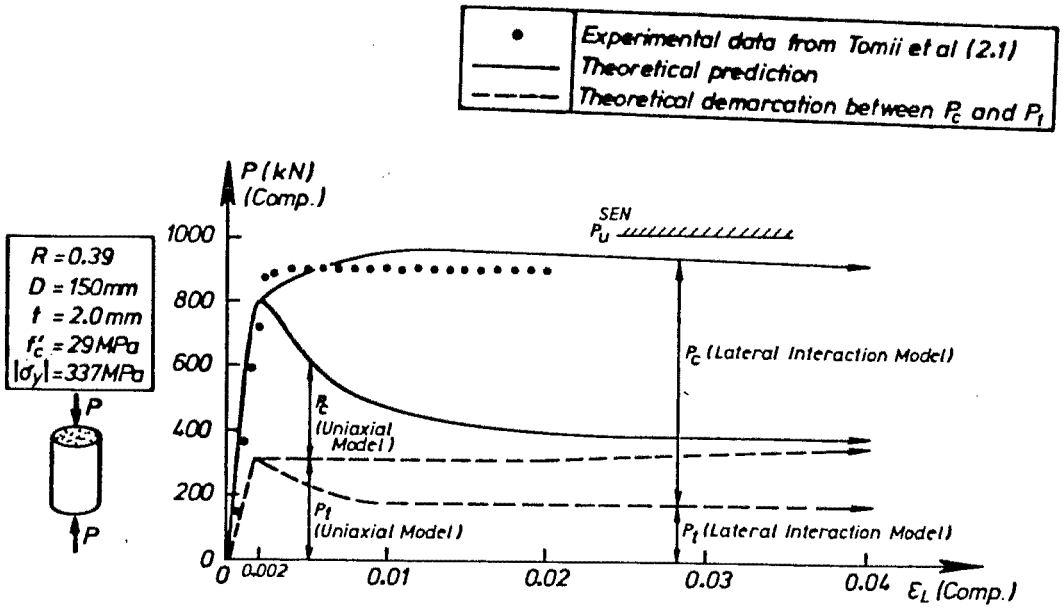

FIG. 2.32 : LONGITUDINAL LOAD-LONGITUDINAL STRAIN COMPARISON (R = 0.39)

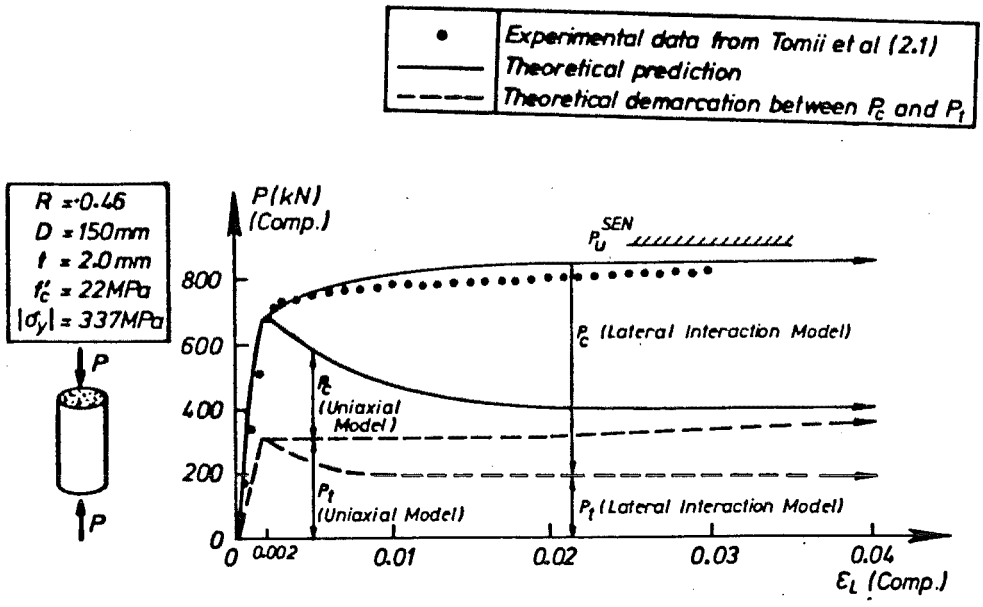

FIG. 2.33 : LONGITUDINAL LOAD-LONGITUDINAL STRAIN COMPARISON (R = 0.46)

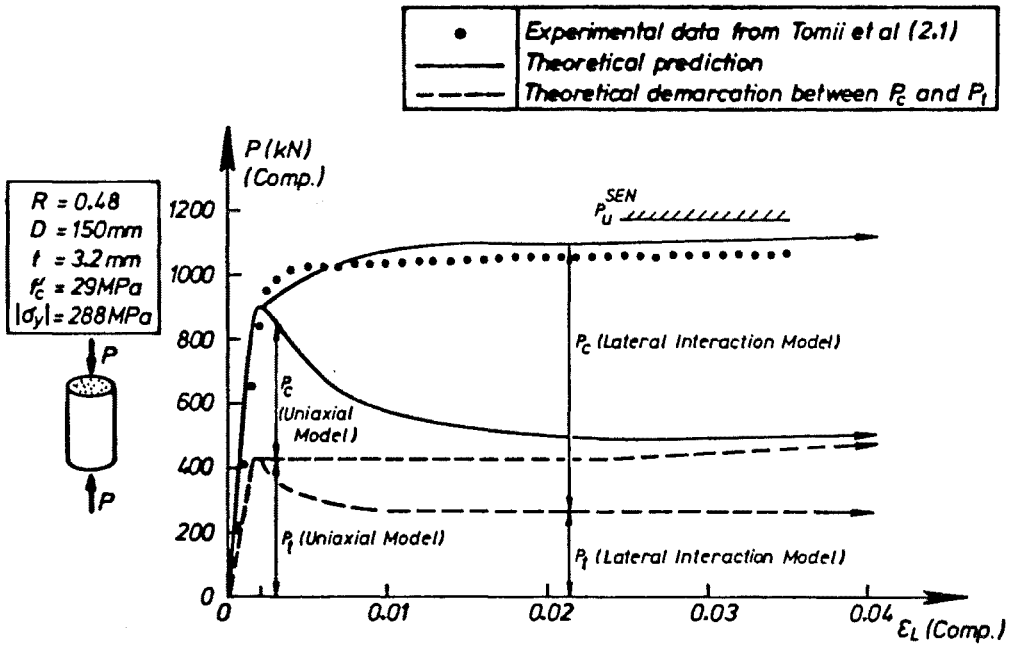

FIG. 2.34 : LONGITUDINAL LOAD-LONGITUDINAL STRAIN COMPARISON (R = 0.48)

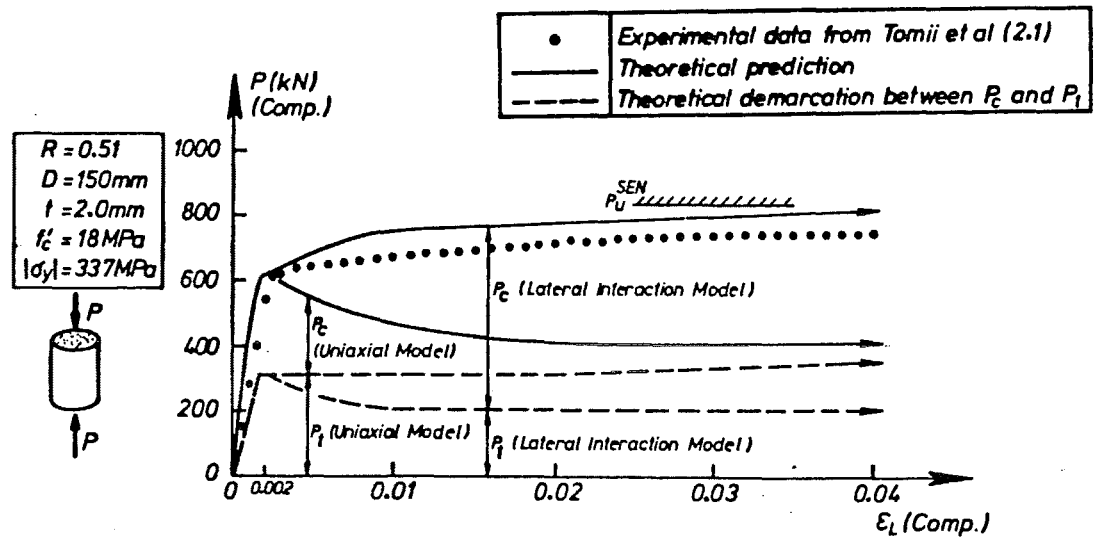

FIG. 2.35 : LONGITUDINAL LOAD-LONGITUDINAL STRAIN COMPARISON (R = 0.51)

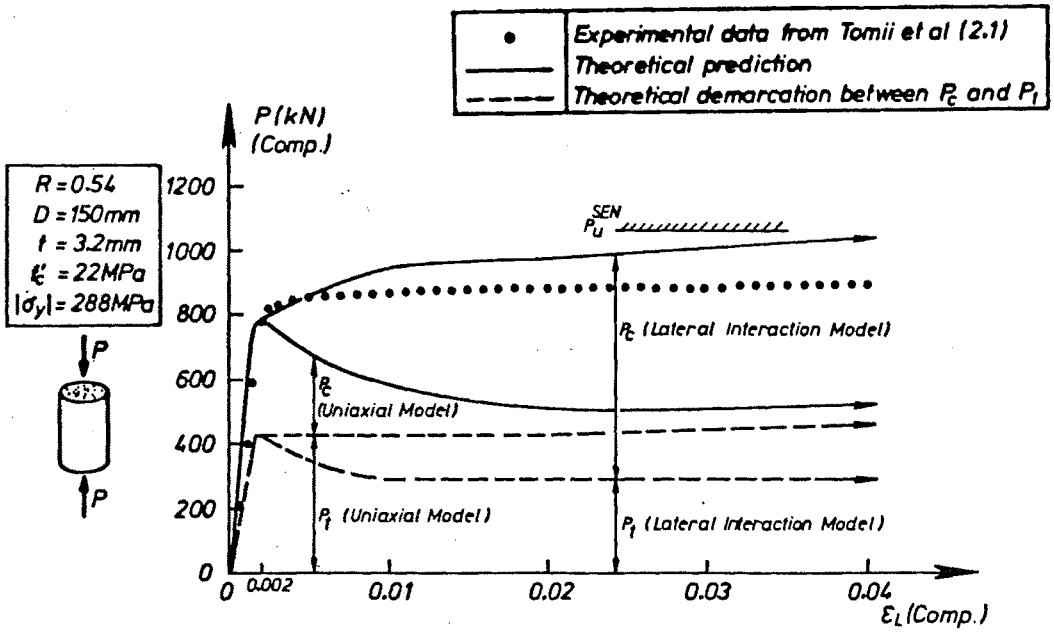

FIG. 2.36 : LONGITUDINAL LOAD-LONGITUDINAL STRAIN COMPARISON (R = 0.54)

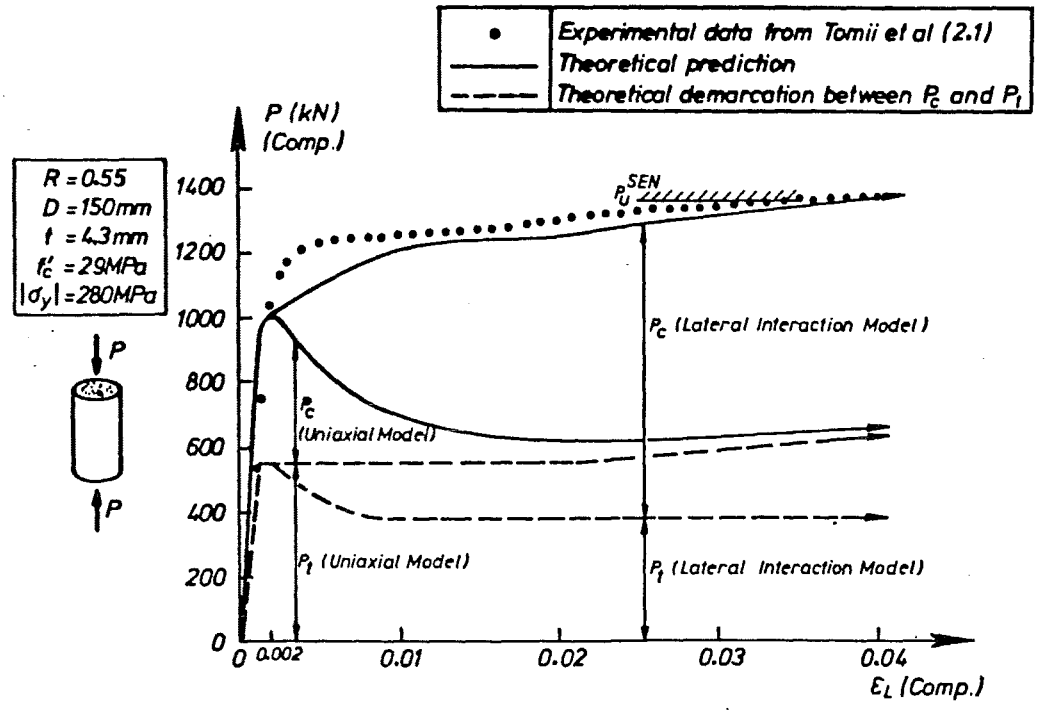

FIG. 2.37 : LONGITUDINAL LOAD-LONGITUDINAL STRAIN COMPARISON (R = 0.55)

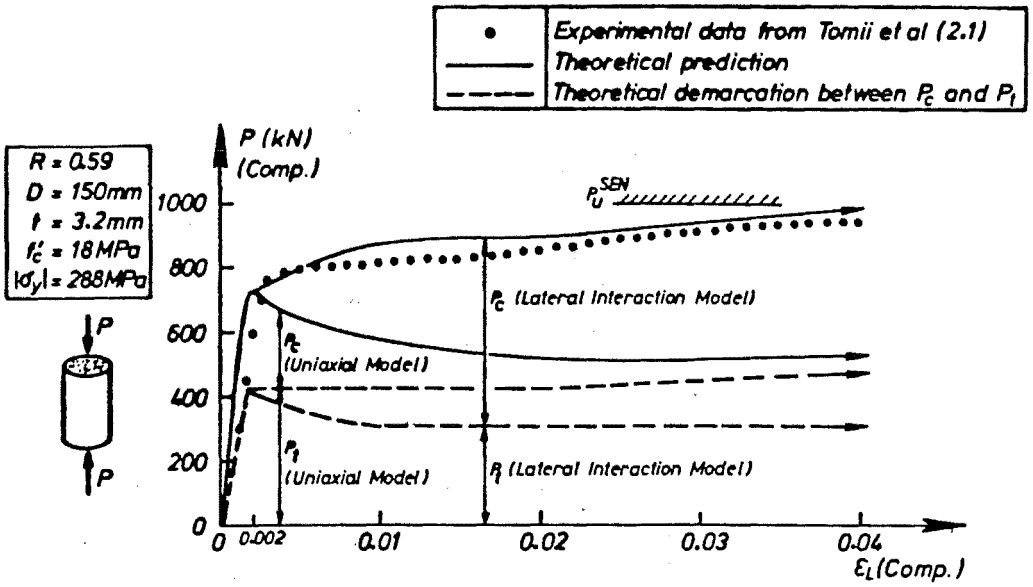

FIG. 2.38 : LONGITUDINAL LOAD-LONGITUDINAL STRAIN COMPARISON (R = 0.59)

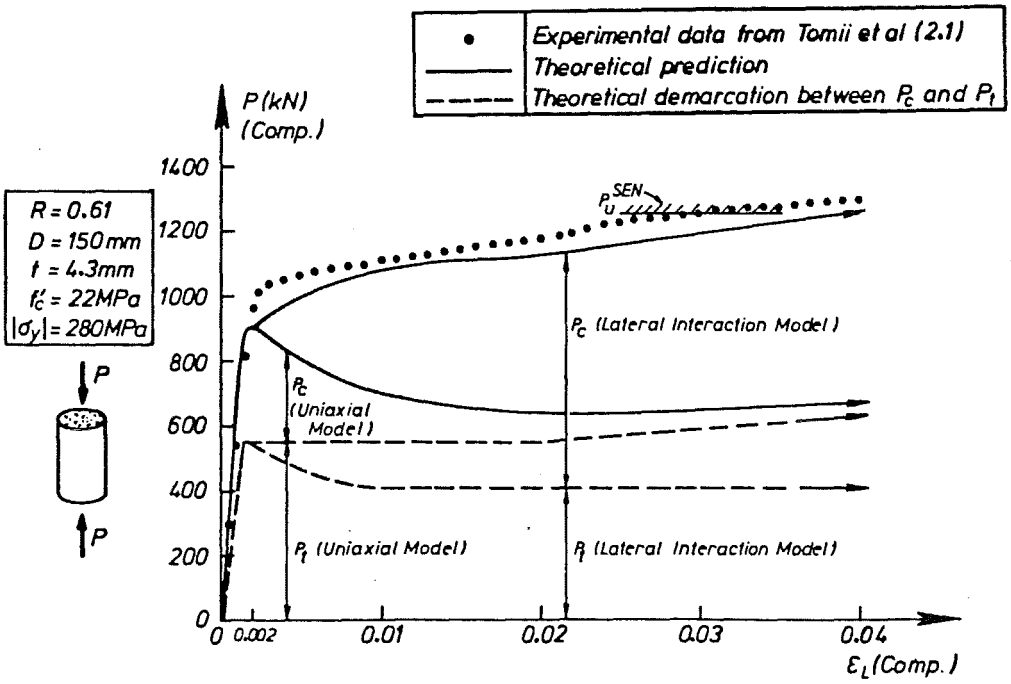

FIG. 2.39 : LONGITUDINAL LOAD-LONGITUDINAL STRAIN COMPARISON (R = 0.61)

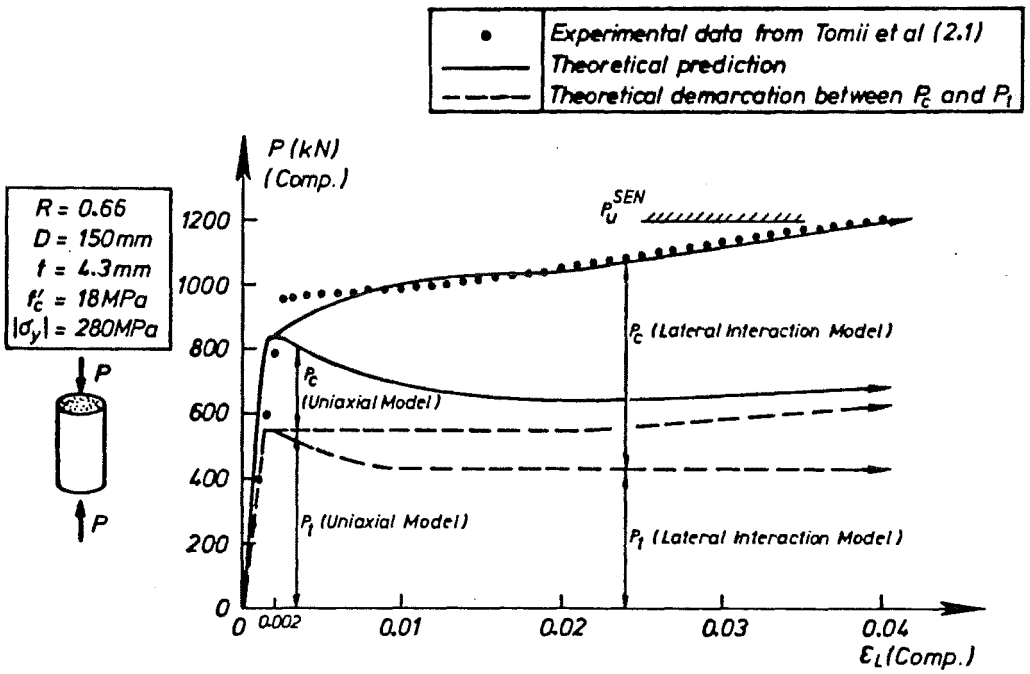

FIG. 2.40 : LONGITUDINAL LOAD-LONGITUDINAL STRAIN COMPARISON (R = 0.66).

2.5 CONCLUSIONS

For both tensile and compressive longitudinal loading, lateral interaction of tube and concrete will occur due to their different values of Poisson's ratio. This results in radial-compression stress in the concrete and hoop-tension stress in the tube, and the composite response of concrete-filled tubes being stronger and generally stiffer than that predicted from the sum of the independent responses of tube and concrete.

2.5.1 Longitudinal-Compression Load

Due to lack of confinement the response of unconfined concrete to compressive load is brittle, while empty tubes generally behave in an unstable fashion due to inelastic buckling. However the composite response of tube and concrete is strong and ductile since the concrete stablises tube local buckling and the concrete strength and ductility is enhanced by the confining influence of the tube.

It was found that existing stress-strain relationships for concrete confined by transverse reinforcement do not adequately describe behaviour of concrete confined by a tube. Thus a "Lateral Interaction Model" was developed from the experimental data of Tomii et al (2.1) and Sakino et al (2.41). This model allows for the presence of a biaxial-stress field (σ_L - σ_H) in the tube and a triaxial-stress field (f_L - f_R - f_R) in the concrete, and has been demonstrated to predict satisfactorily the P - ε_L response of concrete-filled tubes with casing D/t ratios in the range of 35 to 192 (cf. prototype piles $60 \leq D/t \leq 180$).

2.5.2 Longitudinal-Tension Load

A "Lateral Interaction Model" for concrete-filled tubes under longitudinal-tension load has also been developed.

Tube response is predicted on the basis that due to restraint from the concrete core, tube hoop strains cannot develop ($\varepsilon_H = 0$). This has been demonstrated theoretically to increase both the longitudinal strength and stiffness of the steel in a concrete-filled tube, relative to the steel in an empty tube. For example, in the elastic range the increase in stiffness is typically equal to 10%, while the ultimate strength is increased by 15.5%. Although the actual tube hoop strain will not equal zero, since the concrete is not infinitely rigid in the lateral direction, investigations have shown that the influence of concrete lateral flexibility on the predicted stress-strain behaviour is likely to be small.

Concrete response is predicted to allow for the concrete carrying tensile stress in the zones between cracks, which has the effect of stiffening the tube in these zones. The formula of Vecchio and Collins (2.45) was used to allow for this "concrete-tension-stiffening" phenomenon.

Chapter Three

LONGITUDINAL-LOAD TESTS OF SHORT THICK-WALLED STEEL-ENCASED CONCRETE MEMBERS

3.1 INTRODUCTION

In this chapter observations and results from the longitudinal-load testing of short circular-sectioned steel-encased concrete members with D = 115 mm and t = 4.5 mm (D/t = 25.6) are described. Predictions to the experimental results, based on the constitutive models which were outlined in Chapter 2, are also described in Chapter 3. Three types of longitudinal loading were used: monotonic tension, monotonic compression and cyclic tension and compression.

This chapter has two main purposes:

(i) to enable the calibration of a moment-curvature relationship which would be appropriate for the small-scale model piles, also with D = 115 mm and t = 4.5 mm, which were tested in a dry sand foundation as described subsequently in Chapter 6; and

(ii) to enable the constitutive models, which were outlined in Chapter 2, for tensile and compressive longitudinal load to be further checked against experimental evidence.

Similarly to Chapter 2, a sign convention for loads, stresses and strains of positive representing compression is used.

3.2 TEST PROGRAMME DESCRIPTION

3.2.1 General Description

The materials used in this set of experiments were similar to those used in the sand tank experiments described subsequently in Chapter 6. Two series of tests were performed. The first series was performed in an AVERY Testing Machine (type 7104 DCJ) of 1000 kN capacity, and the second series in a DARTEC Universal Testing Machine of 10000 kN capacity.

Six types of tests were performed as summarised in Table 3.1. Designations A and D refer to tests performed in the AVERY Test Machine and the DARTEC Test Machine respectively. The 15 tests undertaken involved the concentric longitudinal loading of either empty or concrete-filled tubes. For concrete-filled tubes, no internal reinforcing steel was provided within the concrete core. Three of the test units, as shown in Table 3.1, also had 10 mm thick endplates welded to the top and bottom of the tubes which was done in an attempt to force local buckling to occur close to the midheight of the test units. The concentrically applied longitudinal loading consisted of either monotonic tension, monotonic compression or cyclic tension and compression to successively larger strain amplitudes.

3.2.2 Mild Steel Tubes

The dimensions of the mild steel hot-formed tubes used in the experiments were:

height h	=	230 mm
outside diameter D	=	115 mm
wall thickness t	=	4.5 mm
steel area/gross area	=	0.15

TABLE 3.1 : SUMMARY OF TEST TYPES

Tests	Concrete-Filled or Empty Tube	Concentric Longitudinal Loading
A6, A7*, D4	Filled	Monotonic Compression
D5	Filled	Monotonic Tension
D6, D8	Filled	Cyclic Tension and Compression
A1*, A2*, A3, A4, A5, D3	Empty	Monotonic Compression
D1	Empty	Monotonic Tension
D2, D7	Empty	Cyclic Tension and Compression

Note: (1) * Includes 10 mm thick welded endplates.
(2) Designation A refers to AVERY test
(3) Designation D refers to DARTEC test.

From these figures, the test units under longitudinal-compression load would be expected to exhibit short column behaviour.

In Fig. 3.1 the stress-strain (σ_L vs ε_L or σ_H vs ε_H) responses obtained from tensile testing coupon samples of the tube with load applied in either the longitudinal (L) or hoop (H) directions of the tube are shown. Strain was measured over a 50.8 mm gauge length using a Baty extensometer. Three tests in each of the L and H directions were performed. A negligible amount of scatter was observed within each set of three tests.

Results from the coupon tests in the L direction indicated $|\sigma_y|$ = 308 MPa, elongation at fracture (50.8 mm gauge length) = 48%, $|\varepsilon_{sh}|$ = 0.009, and $|\sigma_u|$ = 361 MPa. While the results for $|\sigma_y|$ and elongation at fracture are quite typical of mild steel behaviour, the $|\varepsilon_{sh}|$ and $|\sigma_u|$ results are smaller than are typical for New Zealand mild steel where values of $|\varepsilon_{sh}|$ = 0.02 to 0.03 and $|\sigma_u|$ = 400 to 500 MPa are normally attained.

In preparing a coupon test for loading in the hoop direction, it was necessary to straighten a sample of the tube. This straightening process involves considerable work-hardening of the steel, as shown in Fig. 3.2, with residual strains of up to ± 0.041 (= ± t/(D - t)) being induced in the tube prior to tensile testing. This results in minor modification to the stress-strain curves with the lack of a sharply defined yield stress or a clear yield plateau. Since the tubes were hot-formed it is probable that actual stress-strain behaviour in the hoop direction, before straightening, was similar to that in the longitudinal direction.

3.2.3 Concrete

For test units which were concrete-filled, concrete was supplied by a ready-mix contractor. The target strength was 28 MPa at 28 days, and the concrete was specified to have a 100 mm slump. Ordinary Portland Cement was used, and the aggregate was a graded Greywacke with a maximum size of 13.2 mm.

Samples of the concrete for uniaxial-compression-stress testing were cast into 200 mm long x 100 mm diameter cylinders. Modulus of rupture (MOR) tests were also performed on concrete prisms which had a square cross-section of 150 mm x 150 mm. All concrete samples were cured in a fog room at a temperature of 20°C and a relative humidity of 100%.

It should be noted that the concrete cast inside the tubes had a height of 230 mm and a diameter of 106 mm. These dimensions are only marginally larger

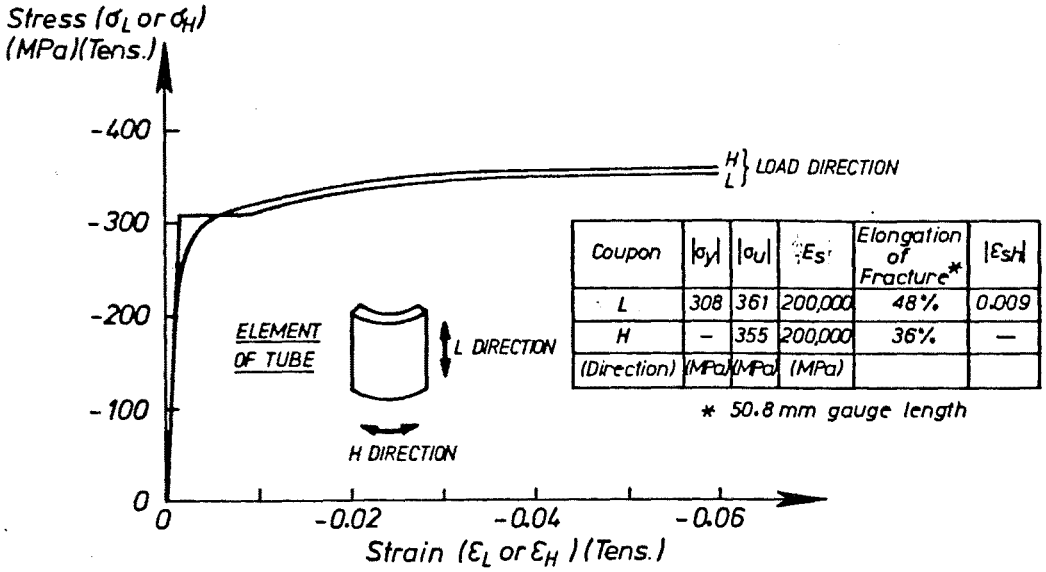

Coupon	$\lvert\sigma_y\rvert$	$\lvert\sigma_u\rvert$	E_s	Elongation of Fracture*	$\lvert\varepsilon_{sH}\rvert$
L	308	361	200,000	48%	0.009
H	–	355	200,000	36%	—
(Direction)	(MPa)	(MPa)	(MPa)		

FIG. 3.1 : COUPON STRESS-STRAIN RESULTS

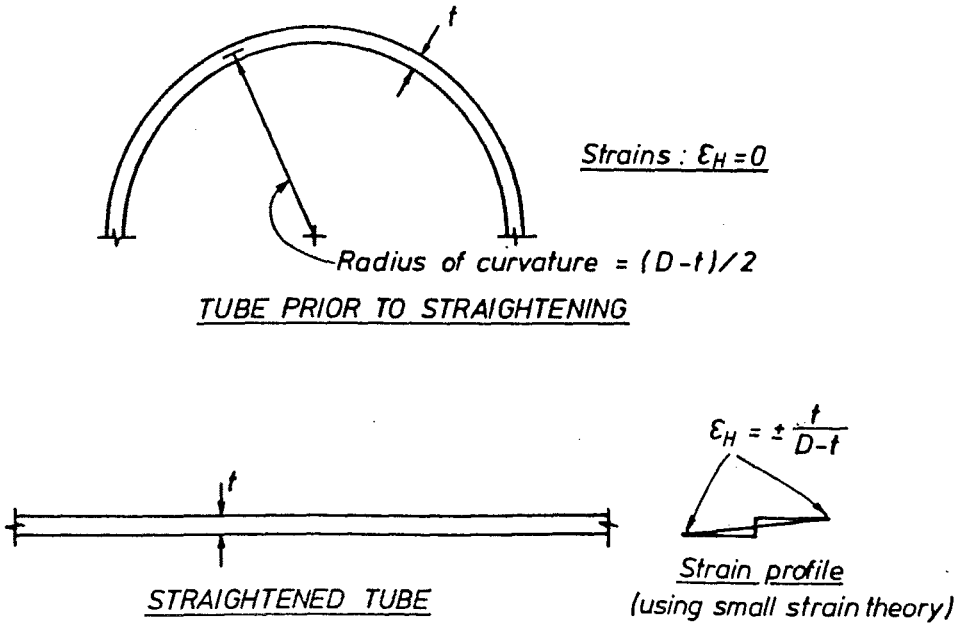

FIG. 3.2 : WORK-HARDENING DUE TO STRAIGHTENING PROCESS

than those of the concrete samples taken for uniaxial-compression-stress testing. Thus negligible distortion of results due to scale effects was expected. Since the concrete-filled tubes were also left in a fog room until testing, it was likely that curing conditions for the concrete samples and the concrete inside the concrete-filled tubes were similar.

Results of uniaxial-compression-stress and modulus of rupture tests on the concrete samples are given in Table 3.2. In each case, the average of three tests is indicated. Scatter of results within each of the three tests was less than 1 MPa for f'_c and less than 0.3 MPa for MOR. These concrete sample tests were performed at approximately the same time as the corresponding longitudinal-load tests in the AVERY and DARTEC test machines. A relationship between MOR and f'_c from the sample tests is given below:

$$MOR = -0.79\sqrt{f'_c} \qquad (3.1)$$

The coefficient of 0.79 is significantly larger than the value of 0.5 which is recommended by the New Zealand Concrete Code (3.1).

TABLE 3.2 : CONCRETE SAMPLE TESTS

Test Series	AVERY (A)	DARTEC (D)
Approximate age at testing (months)	3	6
f'_c (MPa)	32	24
MOR (MPa)	-4.6	-3.8

3.2.4 AVERY Test Set-Up

For tests in the AVERY machine a uniform longitudinal-compression strain was applied to the test units by thick platens above and beneath the test units. Connection of the test units to the AVERY cross-head was only by direct bearing, and thus only compression testing was possible in the AVERY series of tests.

3.2.5 DARTEC Test Set-Up

Figure 3.3 gives details of units tested in the DARTEC machine and Fig. 3.4 shows a typical instrumented test unit assembly in the DARTEC. The indicated method of connection allowed both tension and compression loading to be applied. The same two sets of 100 mm diameter shaft and attached 180 mm diameter discs were used in all of the tests in the DARTEC series. Thus at the conclusion of each test, in which longitudinal-tension load was applied, it was necessary to cut through the fillet welds connecting the 180 mm diameter discs to the test unit and then to reface the discs prior to preparing the next test unit. For longitudinal-compression-load tests, fillet welds between the test unit and the 180 mm diameter discs were not utilised, since the test units were located in 5 mm deep recesses in the discs and the connections were only required to transfer longitudinal-compression force.

3.2.6 Construction

Test units were cut in 240 mm lengths from 3 m lengths of tube. The 240 mm lengths of tube were then machined to the 230 mm length required for testing. Care was taken to ensure that the ends of the test units were square with the longitudinal direction of the tube, so as to avoid undesirable eccentric loading during testing.

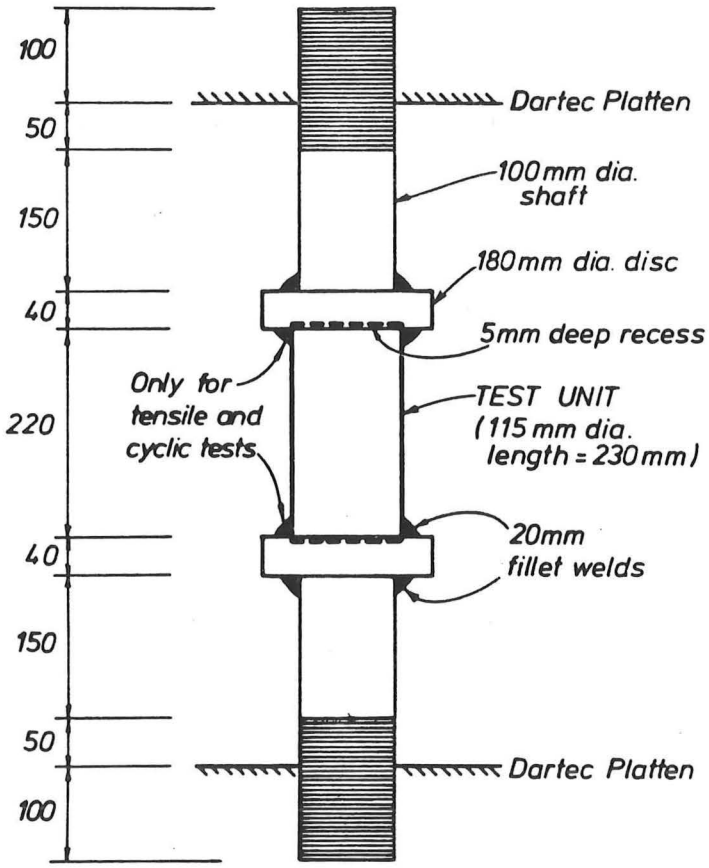

FIG. 3.3 : TEST UNIT ASSEMBLY FOR DARTEC TESTS

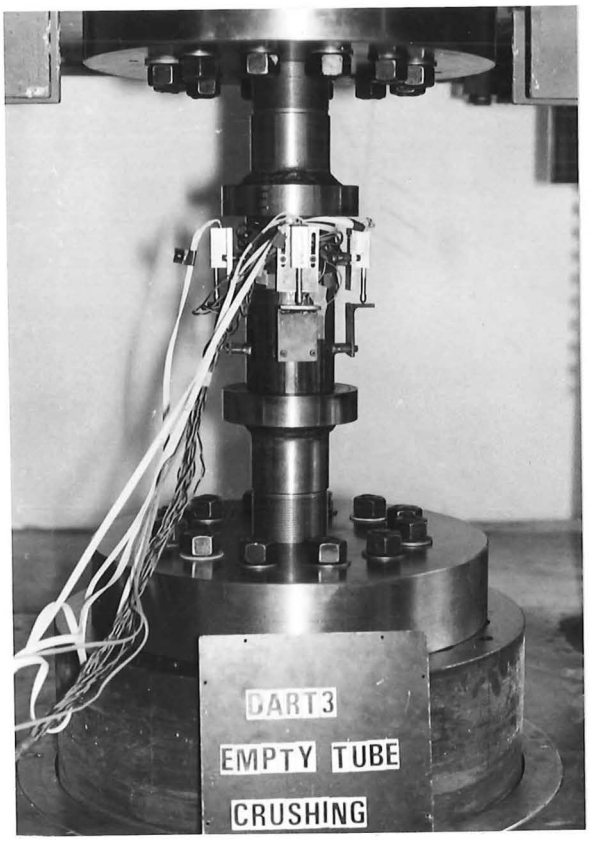

FIG. 3.4 : INSTRUMENTED TEST UNIT ASSEMBLY IN DARTEC TEST MACHINE

The tubes that were to be tested full of concrete were poured to a slightly overtopped state, and then left to cure in a fog room at 20°C and 100% relative humidity, until the day before testing. After curing excess concrete was ground off the top end of the test unit, and at the bottom end high strength dental plaster was cast inside and flush with the end of the tube to compensate for any surface irregularities which had occurred in the concrete.

For three of the test units (A1, A2 and A7) 10 mm thick end plates were then welded on to the top and bottom of the tubes.

For units tested in the DARTEC, under tensile or cyclic longitudinal load, a large amount of welding was necessary (see Fig. 3.3) to ensure that the strength of the welded connections was superior to the strength of the test units. Welds are generally considered to be susceptible to fatigue failure. Thus the four rings of fillet weld shown in Fig. 3.3 were all stipulated to have relatively large leg lengths of 20 mm. During welding, particular care was taken to ensure accurate concentric alignment of the test unit assembly. Welding of the tubes to the discs was performed in short runs with long spells in between runs to keep the heat generated during welding to a minimum.

Despite these precautions, as discussed later in Section 3.5.4.3, it is probable that for test units subjected to tensile or cyclic longitudinal load, the welding resulted in significant residual longitudinal-tension stress in the tube and longitudinal-compression stress in the concrete.

3.2.7 Instrumentation

3.2.7.1 Load

For the AVERY tests, longitudinal load was read off a graduated scale. The manufacturers regularly check the calibration of the test machine and accuracy is certified to ± 1% of the maximum load shown on the scale. The load exerted by the DARTEC machine on the test units was measured by load cells installed on the four columns of the DARTEC machine. In the range of the anticipated longitudinal loads, approximately ± 1000 kN, the load cells are accurate to within ± 3 kN.

3.2.7.2 Longitudinal Displacements

Longitudinal displacements over the central 115 mm length of the test units were measured by four 15 mm travel Sakae linear potentiometers at 90° intervals around the circumference. These potentiometers had a strain range of 0.13 assessed on the 115 mm gauge length. The potentiometers were mounted on stands that had been tack-welded on to the outsides of the tubes. The layout of the potentiometers is shown in Fig. 3.5

For the DARTEC tests, the movement of the DARTEC ram was also monitored. This gave an indication of the longitudinal deformation over the total 230 mm length of the test unit. However, as this deformation also included "take-up" and flexibility of the DARTEC machine and the 100 mm diameter threaded shafts (see Fig. 3.3), it was not directly useful.

3.2.7.3 Strains

To measure directly strains on the test units, electrical resistance strain gauges were bonded on to the outside surface of the tubes. The casing was anticipated to be in a state of biaxial stress (σ_L and σ_H) during testing. Thus at each position requiring gauging, a rectangular rosette (0°, 45° and 90°) aligned in in the longitudinal (0°) and hoop (90°) directions was used.

The rosettes used were Showa type N31-FA-5-120-11. The manufacturers claim these gauges have ± 1% accuracy up to a strain of 0.04, and a fatigue life of 10^5 cycles from 0 to 0.001 strain. However strain gauge reliability for a small number of high intensity strain cycles which was the condition for the cyclic loading tests in the DARTEC machine is not stated. The three gauges making up each rosette were located on a grid of approximately 10 mm x 10 mm dimensions. Strain gradients at the rosette locations were expected to be small, unless local buckling occurred in the vicinity of the strain gauges. Thus it was assumed that the three gauges making up the rosette were located at the same point.

On units A3, A4 and D8 rosettes were placed at 90° intervals around the central section and sections at 38 mm above and beneath the central section. As results from gauges at these three sections were found to be similar, all other test units were gauged with four rosettes at the central section only. The strain gauge patterns and designations are illustrated in Fig. 3.6.

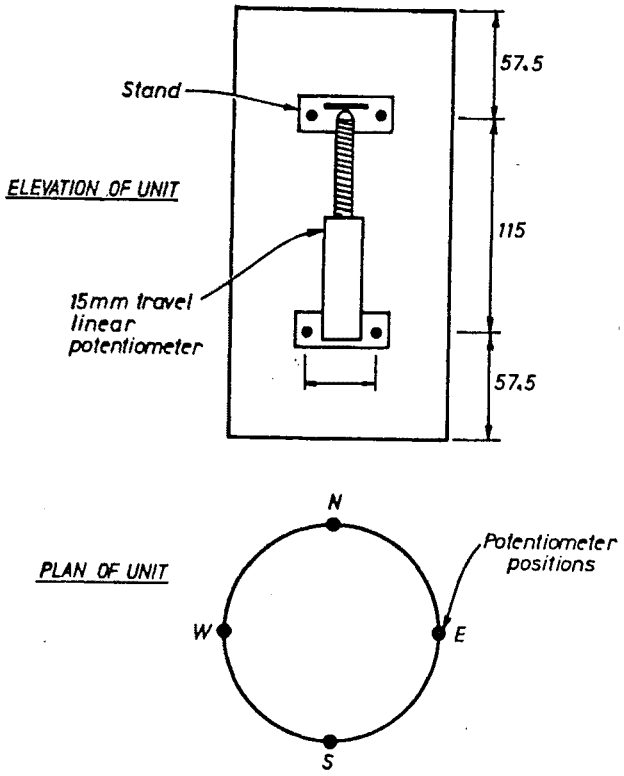

FIG. 3.5 : POSITION OF LINEAR POTENTIOMETERS

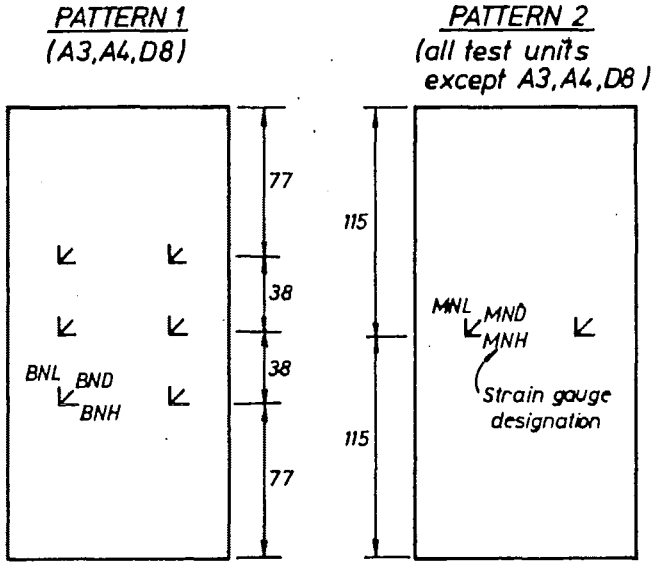

Strain gauge designation : XYZ

X = section (B = Bottom, M = Middle, T = Top)
Y = compass position (N,S,E or W)
Z = orientation (L = Longitudinal, D = Diagonal, H = Hoop)

FIG. 3.6 : STRAIN ROSETTE PATTERNS

3.2.7.4 Data Acquisition and Reduction

All data (except the load in the AVERY tests, which was read off a graduated scale) were recorded by a Solartron Data Transfer Unit. In addition during the DARTEC tests, an X-Y plot of the longitudinal load-longitudinal strain response was obtained, based on a single linear potentiometer output, to give a visual record of test progress. Data were recorded at regular intervals during testing. The number of data scans per test varied from 30 (for longitudinal-compression loading of empty tubes) to almost 800 (for cyclic longitudinal loading of concrete-filled tubes). These raw voltage data from the tests were subsequently processed by computer to give values of strain, displacement, stress and load.

3.2.8 Test Procedure

For tests involving monotonically increasing load, the experiments continued until either:

(i) The load-carrying capacity of the unit was greatly reduced due to local buckling or fracturing of the tube; or

(ii) The load or displacement capacity of the test machine was reached.

For the cyclic loading tests, two cycles to each of the following nominal ε_L levels: $\mp$ 0.001, $\mp$ 0.002, $\mp$ 0.005, $\mp$ 0.01, $\mp$ 0.02, $\mp$ 0.03, $\mp$ 0.04, and $\mp$ 0.05 were successively performed. The sign $\mp$ means that first tensile (-) and then compressive (+) values of ε_L were imposed during each cycle. Cycling was strain-controlled by monitoring the average ε_L measured over the 115 mm gauge length of a single linear potentiometer, which in general was slightly different to the ε_L given by the average of the four potentiometers located around the test unit.

All test units were loaded in a pseudo-static fashion. This implies an extremely low strain rate when compared with the maximum strain rate that would be experienced by a pile under seismic loading. In an earthquake strain rates of the order of 0.01/second are expected. Mander et al (3.2) have demonstrated that at this dynamic strain rate, steel and concrete are approximately 7% and 17% respectively stronger than they are under static loading. However Mander et al (3.2) have also shown that these increases in strength are accompanied by reductions in ductility. Thus strictly, if the results from this and the previous chapter are to be applied to dynamic strain rates, modifications to the shape of the steel and concrete curves similar to those adopted by Mander et al (3.2) should be followed.

3.3 EXPERIMENTAL RESULTS AND OBSERVATIONS

Test results are presented primarily as longitudinal load vs longitudinal strain plots (see Figs. 3.7-3.12) for each of the six types of test performed. The condition of typical test units at the end of testing is shown in Fig. 3.13.

3.3.1 Empty Tubes under Monotonic Longitudinal-Compression Load

Six empty tubes were tested under montonically increasing longitudinal-compression load. Test units A3, A4, A5 and D3 were plain tubes, while units A1 and A2 were tubes with 10 mm thick endplates welded on to their ends as described previously in Section 3.2.1.

Failure, characterised by rapid loss of load-carrying capacity, occurred when local buckles formed at the top and bottom of the test units. Figure 3.13(a) shows a typical test unit, with instrumentation removed, after testing. The visible extent, in the longitudinal direction, of each local buckle was approximately 30 mm.

Table 3.3 indicates the maximum attained (ultimate) load (P_u^{exp}) and corresponding stress (σ_u) for each test unit, as well as the values of ε_L at $P = P_u^{exp}$. The values of ε_L were obtained from both the average reading

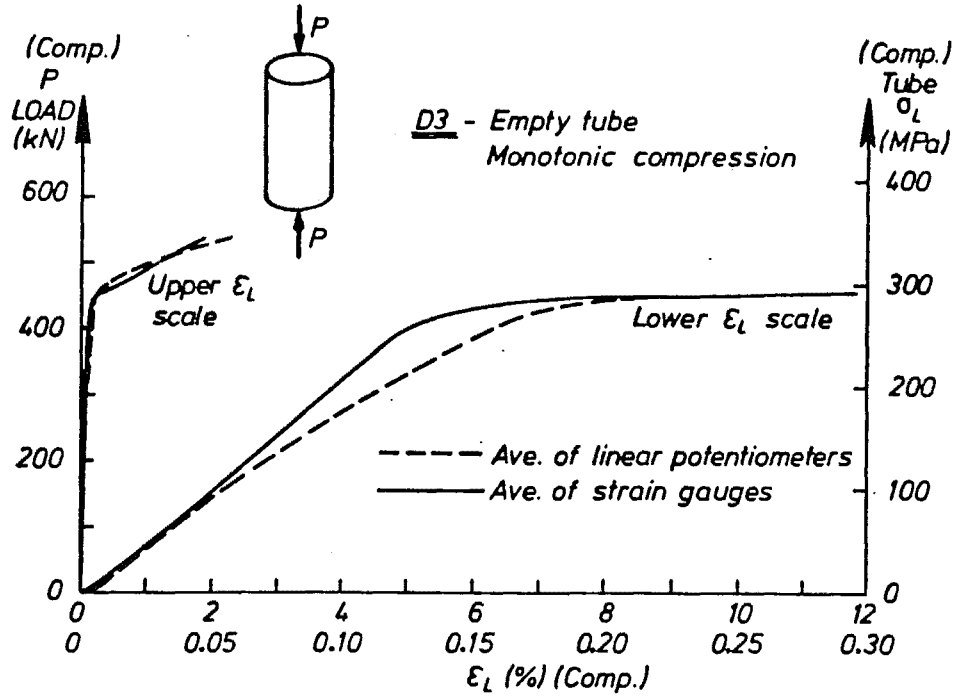

FIG. 3.7 : MONOTONIC COMPRESSION LOAD-LONGITUDINAL STRAIN RESPONSE OF AN EMPTY TUBE (D3)

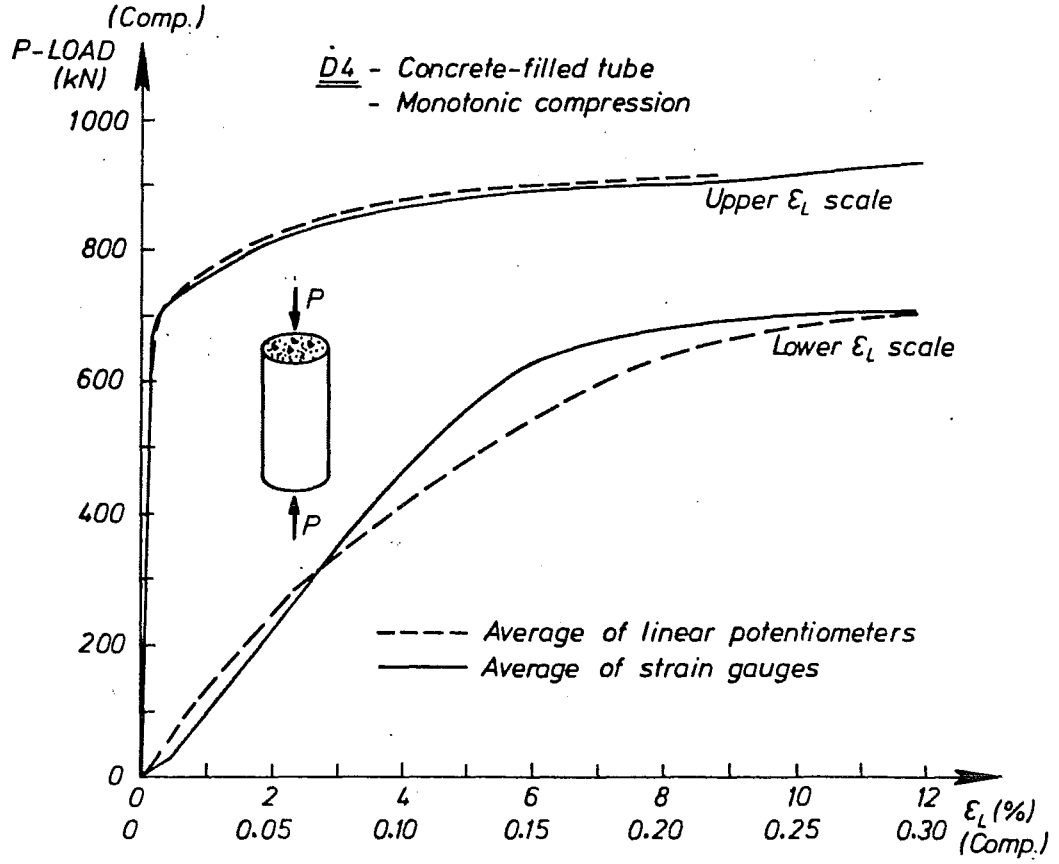

FIG. 3.8 : MONOTONIC COMPRESSION LOAD-LONGITUDINAL STRAIN RESPONSE OF A CONCRETE-FILLED TUBE (D4)

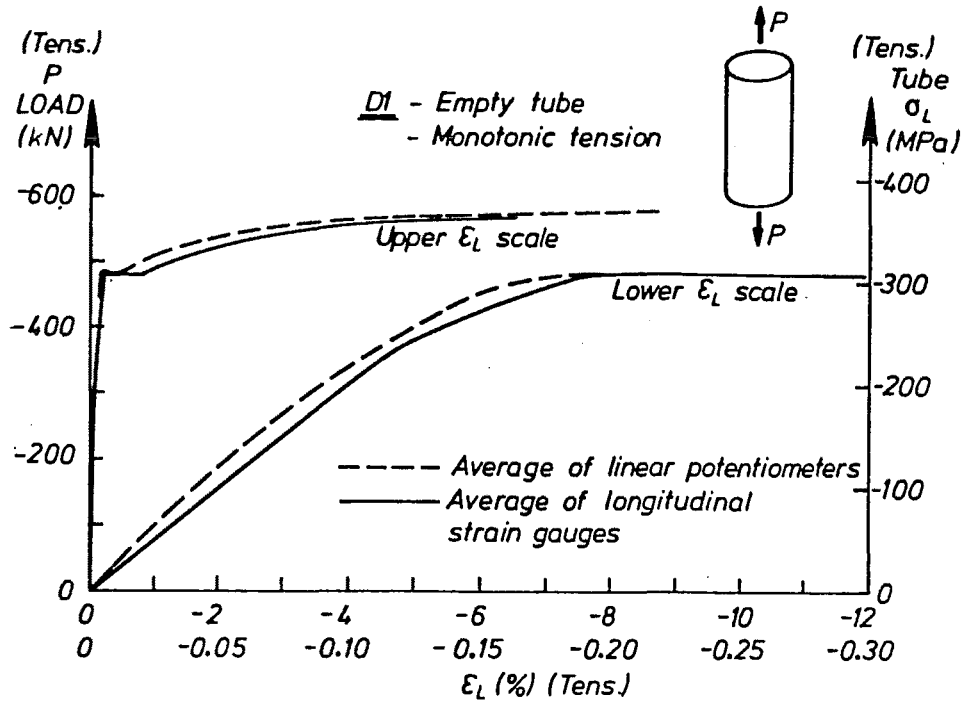

FIG. 3.9 : MONOTONIC TENSION LOAD-LONGITUDINAL STRAIN RESPONSE OF AN EMPTY TUBE (D1)

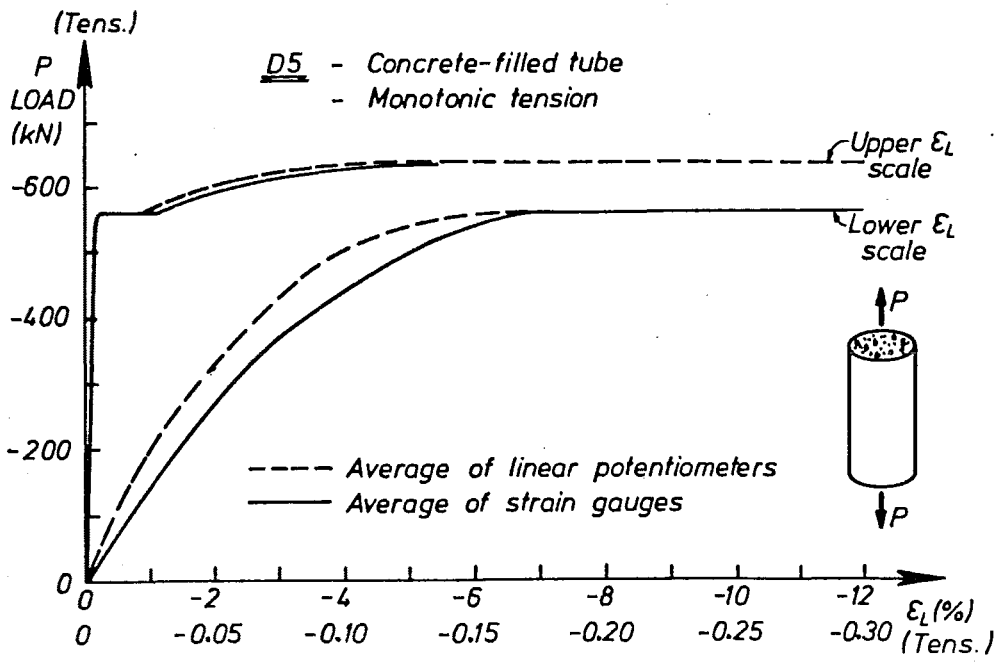

FIG. 3.10 : MONOTONIC TENSION LOAD-LONGITUDINAL STRAIN RESPONSE OF A CONCRETE-FILLED TUBE (D5)

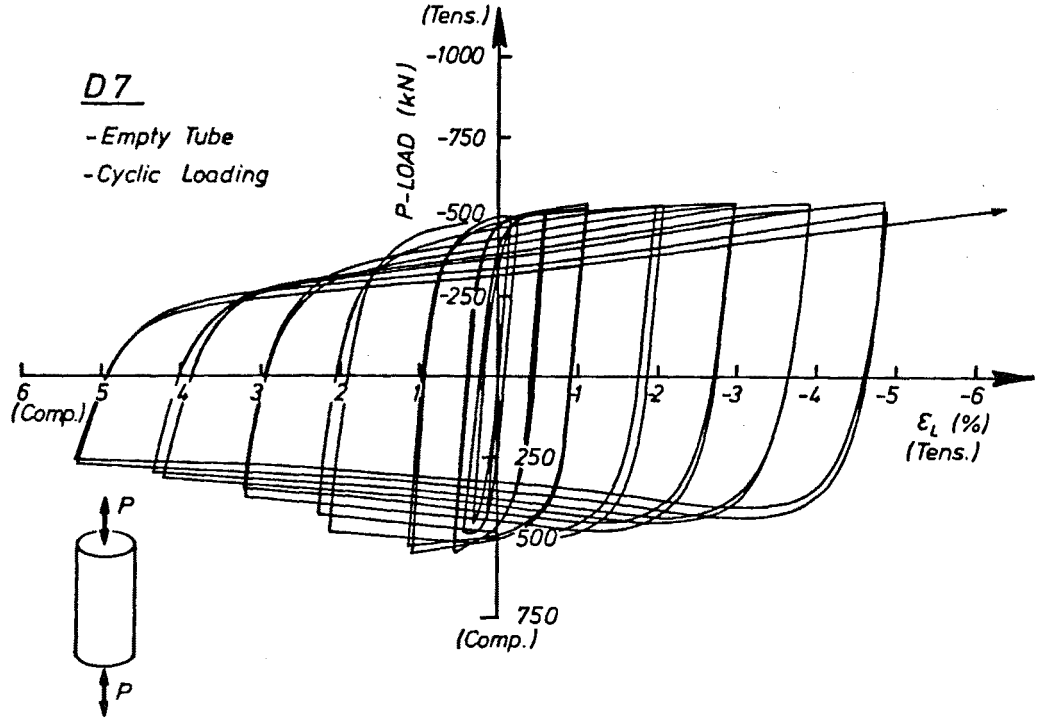

FIG. 3.11 : CYCLIC LOAD-LONGITUDINAL STRAIN RESPONSE OF EN EMPTY TUBE (D7)

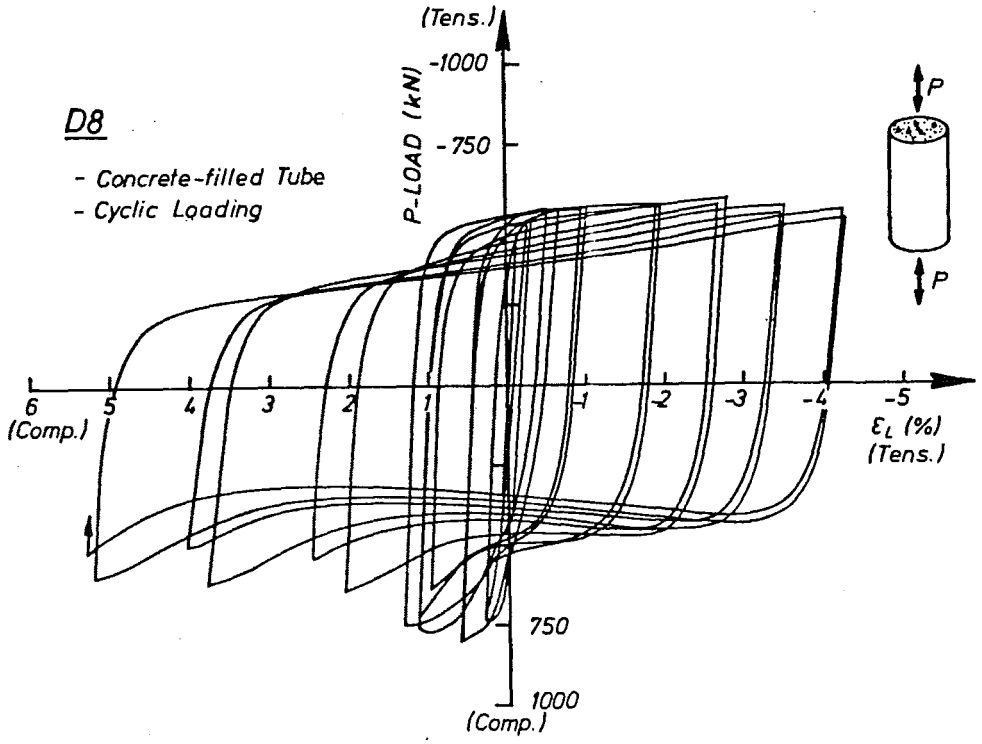

FIG. 3.12 : CYCLIC LOAD-LONGITUDINAL STRAIN RESPONSE OF A CONCRETE-FILLED TUBE (D8)

(a) LOCAL BUCKLING AT ENDS OF EMPTY TUBE (A1) AFTER COMPRESSION TEST

(b) POST-MORTEM TO COMPRESSION TEST OF A CONCRETE-FILLED TUBE (D4)

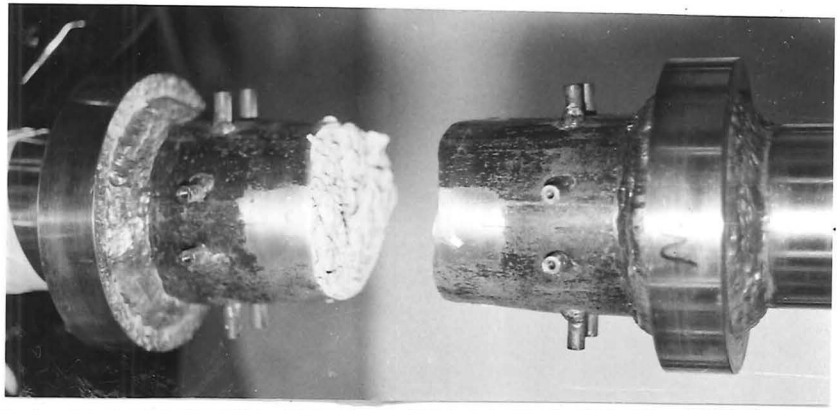

(c) FRACTURING OF A CONCRETE-FILLED TUBE (D5) DURING TENSION TEST

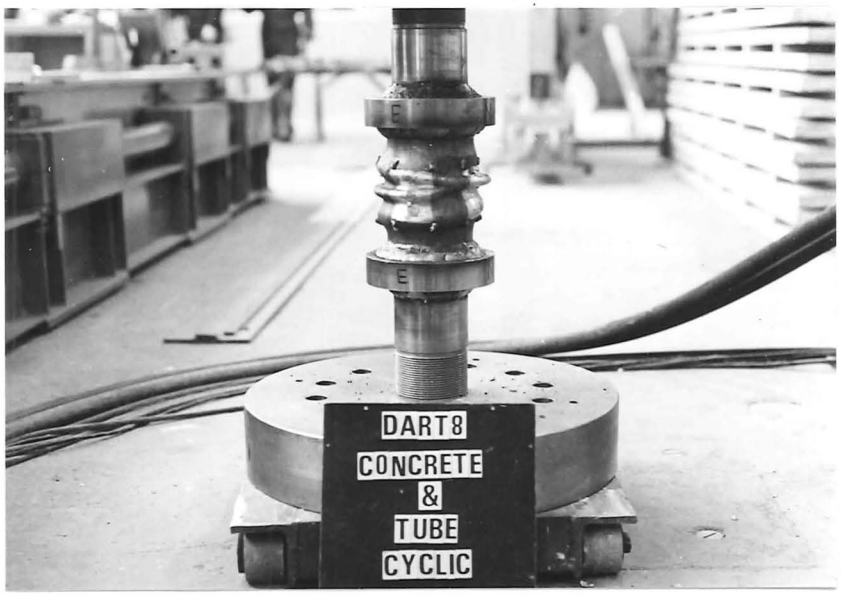

(d) LOCAL BUCKLING OF A CONCRETE-FILLED TUBE (D8) AT LARGE COMPRESSIVE ε_L (> 26%)

FIG. 3.13

indicated by the longitudinally orientated strain gauges and the average reading indicated by the four linear potentiometers. As could be expected with failure occurring as a result of local buckling there is a significant amount of scatter between the results for the six tests. The scatter is larger in the ε_L (at $P = P_u^{exp}$) than it is in the σ_u results, as can be seen from the values of standard deviation divided by the mean which are shown in Table 3.3. The average compressive strength of the tubes was 363 MPa which is approximately equal to the tensile strength ($|\sigma_u|$ = 361 MPa) found from coupon tests of tube samples. On average, local buckling resulted in failure of the tubes at ε_L = 0.0201 or 0.0268 for strain measured by the electrical resistance strain gauges or the linear potentiometers respectively. At strains of this order, the strain gauges read more accurately, as could be inferred from the smaller standard deviation values shown in Table 3.3. However as failure occurred close to the ends of the tubes, away from the strain rosette positions, it is probable that the magnitude of ε_L at the critical sections for $P = P_u^{exp}$ was larger than both 0.0201 or 0.0268. From Table 3.3, P_u^{exp} and ε_L (at $P = P_u^{exp}$) for tubes with endplates are, in general, of slightly larger value than they are for plain tubes. Thus although the end rotational and translational restraint offered to the tube by the endplates did not force local buckling to occur at the midheight of the test unit, the endplates did improve the performance of the tube.

TABLE 3.3 : MONOTONIC LONGITUDINAL-COMPRESSION LOAD TEST RESULTS FOR EMPTY TUBES

Test Unit	P_u^{exp} (kN)	σ_u (MPa)	ε_L at $P = P_u^{exp}$	
			(i) Strain Gauges	(ii) Linear Potentiometers
A1*	572	366	0.0227	0.0364
A2*	604	387	0.0188	0.0355
A3	568	364	0.0199	0.0233
A4	570	365	0.0201	0.0212
A5	542	347	0.0201	0.0221
D3	540	346	0.0188	0.0224
Average	566	363	0.0201	0.0268
(Standard Deviation / Average)	0.04	0.04	0.07	0.26

* Includes 10 mm thick welded endplates.

The P vs ε_L (and corresponding σ_L vs ε_L) response obtained from Test D3 is shown in Fig. 3.7, the other five tests indicated similar, although not identical, responses as is subequently shown in Fig. 3.19. The responses indicated by linear potentiometers and electrical resistance strain gauges show a small but significant difference. This is especially so in the elastic range of steel behaviour where stress is sensitive to variations in strain. In this range the strain gauges give the more accurate measure of strain and indicate that E_s (average of six empty tube tests) was equal to 206 GPa. In the plastic range of steel behaviour, there is little apparent difference in the response indicated by potentiometers and strain gauges, since at this stage stress is relatively insensitive to strain. It was not possible to trace the P vs ε_L response of the tubes after local buckling occurred, since the critical sections were not

strain-gauged, and over the central gauged region of the tube elastic unloading took place immediately after P_u^{exp} had been reached.

3.3.2 Concrete-Filled Tubes under Monotonic Longitudinal-Compression Load

Three concrete-filled tubes were tested under monotonically increasing longitudinal-compression load. Test unit A7 had 10 mm thick welded endplates, and units D4 and A6 were tested without endplates. Local buckles of approximately 30 mm longitudinal extent formed at the top and bottom of the test units by an ε_L of approximately 0.02, as measured by the average of the longitudinally orientated strain gauges. However, unlike the empty tubes under longitudinal-compression load, failure did not occur at this stage. Test units A6 and A7 reached the 1000 kN capacity of the AVERY test machine, at longitudinal strains of 0.05 and 0.09 respectively as indicated by the average of the longitudinally orientated strain gauges and approximately confirmed by the average of the potentiometers. Test unit D4 reached a load of 1066 kN by the end of testing. At this stage the length of D4 had reduced by 48 mm, implying an average ε_L over the original 230 mm length of the test unit of 0.21, although the peak ε_L at the critical sections would clearly have been considerably larger. For all three tests, test machine displacement (DARTEC test) or load (AVERY tests) limitation meant that the ultimate loads could not be determined.

By the end of testing three bulges in the tube were visible, as a long central bulge had formed in addition to the short bulges at the top and bottom of the test unit. As a post-mortem to test D4, a length of tube was removed to reveal the condition of the concrete as shown in Fig. 3.13(b). It was observed that the concrete had flowed radially in the vicinity of the midheight of the test unit, and at this position a Schmidt hammer test of the exposed concrete showed that even though the concrete had retained its cohesion, it had an unconfined-compression strength of less than 7 MPa. Underneath the local buckles at the ends of the tubes to a depth of 20 mm, the concrete had lost its cohesion and been reduced to rubble.

A typical (test unit D4) P vs ε_L response is shown in Fig. 3.8. As for empty tubes (see Fig. 3.7), there are small differences between the P vs ε_L responses derived from strain gauge and linear potentiometer readings. At large values of ε_L (>> 0.04) the potentiometers are the more accurate measure of strains, while at small values of ε_L the strain gauges are more reliable. A comparison of Figs. 3.7 and 3.8 indicates that under longitudinal-compression load, the presence of concrete inside the tube results in a stronger and considerably more ductile structural member.

3.3.3 Empty Tube under Monotonic Longitudinal-Tension Load

The only test of an empty tube under monotonically increasing longitudinal-tension load involved unit D1. Ductile failure occurred in this test when the tube necked and finally fractured at the midheight of the test unit. At failure, the average ε_L (230 mm gauge length) was -0.18, and a reduction of 31 mm in the diameter of the tube had occurred at the midheight of the test unit. An ultimate tensile strength of -596 kN corresponding to $|\sigma_u|$ = 382 MPa was achieved. This strength is 5% larger than the average ultimate compressive strength of the empty tubes reported in Table 3.3. It is to be expected that the tube tensile strength would exceed the compressive strength, since for compressive load inelastic instability occurs before material failure.

The P vs ε_L (and σ_L vs ε_L) response of unit D1 is shown in Fig. 3.9. The stress-strain characteristics are similar to those obtained from tensile testing longitudinally orientated coupon samples of the tube (see Fig. 3.1). For example, E_s = 200,000 MPa in both cases, although the tensile strength of D1 is 6% larger than the strength of the coupon. A comparison of Figs. 3.7 and 3.9 indicates that the tensile response of the empty tube is considerably more ductile than the compressive response of similar tubes.

3.3.4 Concrete-Filled Tube under Monotonic Longitudinal-Tension Load

The only test of a concrete-filled tube under monotonically increasing longitudinal-tension load was D5. The longitudinal load vs longitudinal strain response of this unit, which showed ductile characteristics, is shown in Fig. 3.10. An ultimate load of -640 kN was achieved in this test. Failure by tube fracturing occurred at the midheight of D5 at an average ε_L (230 mm gauge length) of -0.09, compared with -0.18 for the empty tube (see the previous section). Thus as was discussed previously in Section 2.3.2, under longitudinal-tension load the presence of internal concrete reduces the ductility of the test units, since at a given ε_L the value of steel ε^p_{eff} is larger in the concrete-filled tube than it is in the empty tube and the concrete-tension-stiffening effect also reduces the apparent ductility of the steel.

At fracture the diameter of the concrete-filled tube at the midheight section had reduced by 7 mm compared with 31 mm for the empty tube. Thus the restraint of the lateral contraction of the tube by the concrete core, which was assumed to be total when modelling longitudinal-tension-load behaviour (see Section 2.3.2), was in fact only partial. However, a comparison of Figs. 3.1 and 3.10 indicates the concrete-filled tube is 16% stronger at ε_L = -0.2% and 13% stronger at ultimate than is the plain steel which are close to the values predicted in Section 2.3.2 on the basis of full radial restraint provided by the concrete. Thus the effect of concrete lateral flexibility on the predicted behaviour of the tube is small.

Figure 3.13(c) shows the condition of D5 at the conclusion of testing. Concrete inside the tube, adjacent to the section where tube fracturing had occurred had been reduced to rubble due to lateral contraction of the tube.

3.3.5 Empty Tubes under Cyclic Longitudinal Load

Tests D2 and D7 involved cyclic tensile and compressive longitudinal loading of empty tubes. Due to a malfunction of the data acquisition system, most data from D2 was lost. However overall behaviour of D2 was similar to the behaviour of D7 which is described below.

The monotonically applied longitudinal-compression-load tests of empty tubes indicated that failure occurred with local buckling at the ends of the tubes, while the monotonically applied longitudinal-tension-load test of an empty tube indicated that failure occurred due to necking and eventual fracturing of the tube at its midheight. In the cyclic tests of empty tubes, alternate local buckling under compressive load and necking under tensile load developed at sections approximately 40 mm above and beneath the midheight of the test unit. Thus in the cyclic load tests, the critical sections were located at positions which were intermediate to the critical sections found in the monotonic compression and tension tests.

Local buckling was first observed at the end of the second cycle to a nominal ε_L of $\mp$ 0.01. In the monotonic longitudinal-compression-load tests of both empty and concrete-filled tubes, local buckling was first observed at an ε_L of 0.02. This difference in the strain at which local buckling occurs is probably due to stiffness degradation of the steel under cyclic loading, which at a given ε_L results in a lower tangent modulus for the steel in the cyclic tests when compared with the steel in monotonic tests. Local buckles were of approximately 30 mm length in the longitudinal direction, which is the same length as reported earlier for local buckles in both empty and concrete-filled tubes under compressive load. Despite the presence of local buckling, cycling up to a nominal ε_L of $\mp$ 0.05 was achieved without drastic loss of strength in the tube, although significant degradation did occur particularly under compressive loading. This good performance, up to ε_L of $\mp$ 0.05, is surprising when it is considered that monotonic compression testing resulted in

failure at an ε_L of approximately 0.02. However as was mentioned in Section 3.3.1, it is probable that an underestimate of ε_L at failure in the monotonic compression testing of empty tubes was obtained, due to the instrumentation being located in the central regions of the tubes and not in the failure zones at the ends of the tubes.

Figure 3.11 shows the P vs ε_L response of an empty tube (D7) to the cyclic loading. For cycles to nominal ε_L of up to and including $\mp$ 0.5%, excellent hysteretic behaviour is shown with little apparent strength and stiffness degradation occurring in the steel. However for cycles to ε_L of and in excess of the $\mp$ 1%, at which local buckling was first observed, gradually degrading performance is evident as the ε_L level to which cycling was performed is increased. The degrading performance is especially noticeable under compressive load, due to the increasing influence of local buckling.

After the conclusion of the intended cyclic testing, with nominal ε_L of up to and including $\mp$ 5%, the test unit (D7) was subjected to an increasing level of tensile ε_L until fracture occurred. During this final stage of testing, an ultimate tensile strength of -543 kN (-347 MPa) and an ε_L (assessed on a 230 mm gauge length) of -0.05 were recorded, although clearly from Fig. 3.11, the peak $|\varepsilon_L|$ at the critical section would have been considerably larger. These values of tensile strength and $|\varepsilon_L|$ (230 mm gauge length) at fracture were only 91% and 28% respectively of the values obtained from the monotonic tension-load testing of empty tube D1. Thus the previous cyclic loading had reduced the strength and severely reduced the ductility of test unit D7 in resisting a large amplitude longitudinal-tension strain.

3.3.6 Concrete-Filled Tubes under Cyclic Longitudinal Load

Test units D6 and D8 were concrete-filled tubes tested under cyclic tensile and compressive longitudinal load. Local buckling was first observed during the cycling to a nominal ε_L of $\mp$ 1%, as for the cyclic loading tests of empty tubes. However despite the formation and growth of large local buckles, units D6 and D8 did not suffer a drastic loss of strength at any stage of the cycling up to and including a nominal ε_L of $\mp$ 5%. At this stage three distinct local buckles, all within the central 115 mm height of the test unit, were visible.

Unit D6 was then subjected to an increasing level of tensile ε_L until fracture occurred at its midheight. During this final stage of testing, an ultimate tensile strength of -607 kN and an ε_L of -0.09 (230 mm gauge length) were recorded. These values of tensile strength and ε_L (230 mm gauge length) were 95% and 100% respectively of the values obtained from the monotonic tensile testing of a concrete-filled tube (D5). This indicates that the previous cyclic loading had only reduced marginally the strength and not reduced the ductility of unit D6 in resisting a large amplitude tensile ε_L.

After the cyclic testing of unit D8 to a nominal ε_L of $\mp$ 5% was completed, D8 was then subjected to an increasing level of compressive ε_L. During this final stage of testing, the load-carrying capacity of the unit increased continuously, and thus the ultimate compressive strength could not be determined. At the conclusion of testing an ε_L (230 mm gauge length) of 0.26 and a load of 1228 kN were measured. In comparison the concrete-filled tube (D4) which was subjected to monotonically increasing longitudinal-compression load reached ε_L (230 mm gauge length) of 0.21 and a load of 1066 kN. Thus the previous cyclic loading did not appear to have significantly reduced the strength and ductility of unit D8 in resisting a large amplitude compressive ε_L.

The condition of D8 at the conclusion of testing is shown in Fig. 3.13(d). Three very pronounced local buckles, all within the central 115 mm of the test unit were visible, and a small longitudinally orientated split in the tube had

developed near the midheight of the unit. This split indicated local failure of the tube under hoop-tension stress.

Under monotonically applied longitudinal-compression load, both empty and concrete-filled tubes formed local buckles near the ends of the test unit, while for cyclic loading test units formed local buckles near their midheight. This difference in position of local buckles was due to tensile loading, for cyclic tests, causing a reduction of the area of the tube near its midheight. A smaller reduction of area occurs at the ends since test machine restraint results in a longitudinal strength enhancing biaxial-tension-stress ($\sigma_L - \sigma_H$) field at the ends of the tube which means that plastic behaviour concentrates near the tube midheight. Thus when loading was reversed to compression, the middle of the tube was not as stiff as the ends. Hence as was observed for units subjected to cyclic loading, the tube was more prone to forming local buckles at its midheight than at its ends.

In Fig. 3.12, the P vs ε_L response of a concrete-filled tube (D8) to cyclic loading is shown. A comparison of Figs. 3.11 and 3.12 shows that the cyclic loading responses of empty and concrete-filled tubes are similar in shape over three of the four quadrants. However, there is a large difference in shape for the quadrant which contains compressive (+) values of both P and ε_L. In this quadrant, the concrete-filled tube has markedly superior strength and stiffness to that of the empty tube. This difference, between empty and concrete-filled behaviour, is due to the longitudinal-compression stress carried in the concrete since for compressive values of P and ε_L the cracks which opened in the concrete under longitudinal-tension load will have closed and the tube is providing effective lateral confinement to the concrete.

3.3.7 Variation of Hoop and Longitudinal Strains

In the following sections, the experimentally determined variations of tube hoop strain with longitudinal strain from the rosettes are shown. However before this is done, a short discussion of the effect of mounting rosettes at a slightly skew angle is given.

Although considerable care was taken in orientating the rosettes squarely with the hoop and longitudinal directions of the tube, it is inevitable that the rosettes were mounted slightly skew to these directions. If the apparent hoop and longitudinal strains measured by a rosette are designated as ε'_H and ε'_L respectively, and the rosette had been rotated anti-clockwise through an angle of θ with respect to its correct orientation, then ε'_H and ε'_L are related to the true hoop and longitudinal strains (ε_H and ε_L respectively) by

$$\begin{pmatrix} \varepsilon'_H \\ \varepsilon'_L \end{pmatrix} = \begin{bmatrix} \cos\theta & \sin\theta \\ -\sin & \cos\theta \end{bmatrix} \begin{pmatrix} \varepsilon_H \\ \varepsilon_L \end{pmatrix} \tag{3.2}$$

From the above $\varepsilon'_H/\varepsilon'_L$ can be expressed as:

$$\frac{\varepsilon'_H}{\varepsilon'_L} = \frac{\varepsilon_H/\varepsilon_L \cdot \cos\theta + \sin\theta}{-\varepsilon_H/\varepsilon_L \cdot \sin\theta + \cos\theta} \tag{3.3}$$

At large values ($>> |\varepsilon_y|$) of $|\varepsilon_L|$ in a uniaxial-stress (σ_L) field, Poisson's ratio is equal to $-\varepsilon_H/\varepsilon_L$ and approximately equal to 0.5 (see Section 2.2.2.2(d)), substituting this into equation 3.3 and rearranging gives:

$$-\frac{\varepsilon'_H}{\varepsilon'_L} = \frac{\cos\theta - 2\sin\theta}{2\cos\theta + \sin\theta} \qquad (3.4)$$

This apparent (large strain) value of Poisson's ratio $(-\varepsilon'_H/\varepsilon'_L)$ as a function of θ is plotted in Fig. 3.14. Clearly $-\varepsilon'_H/\varepsilon'_L$ is very sensitive to even a small error in placing the rosette, for example at $\theta = 5°$, $-\varepsilon'_H/\varepsilon'_L$ is only 0.395 compared with the true $-\varepsilon_H/\varepsilon_L$ of 0.5.

Thus appreciable scatter in the experimental results will occur due to the out-of-alignment condition of the rosettes. To reduce the effect of this scatter, the results described subsequently use the average hoop and longitudinal strains obtained from all of the rosettes mounted on a given test unit, unless stated otherwise.

3.3.7.1 Monotonic Tests of Empty Tubes

The experimentally determined variations of Poisson's ratio $(-\varepsilon_H/\varepsilon_L)$ with longitudinal strain for the empty tube tests are shown in Fig. 3.15. For each test the average of readings of the strain gauges orientated in the hoop and longitudinal directions were used in determining the values of ε_H and ε_L respectively. In the elastic range of steel behaviour, $|\varepsilon_L| < 0.001540$, an average value of $-\varepsilon_H/\varepsilon_L$ of 0.28 is indicated by the experimental results. For the presumed uniaxial-stress (σ_L) conditions this gives a value of $\nu_s = 0.28$.

Results show considerable scatter, particularly in the inelastic range of steel behaviour. This is probably due to the results being sensitive to the exact positioning of the rosettes as discussed in the previous section. Figure 3.15 also represents a comparison of experimental results with a prediction based on equation 2.49. This equation represents the theoretical variation of Poisson's ratio with longitudinal strain in a uniaxial-stress (σ_L) field. In using this equation it was assumed that the stress-strain characteristics determined from coupon tests of tube samples in the longitudinal direction represented the "true" uniaxial-stress condition of the empty tube. Thus in using equation 2.49, values of $E_s = 200000$ MPa and $\nu_s = 0.28$ were used, and the $\sigma_L - \varepsilon_L$ variation was taken directly from Fig. 3.1.

At a given value of $|\varepsilon_L|$ $(> |\varepsilon_y|)$, Fig. 3.15 indicates that tension and compression test results have smaller and larger values respectively of $-\varepsilon_H/\varepsilon_L$ than they should have under "true" uniaxial-stress conditions. The result of this is that at the strain-gauged positions, for the tension test the tube is in a state of longitudinal-tension and hoop-tension stress, while for the compression tests the tube is in a state of longitudinal-compression and hoop-tension stress. This means (see equation 2.36 or Fig. 2.4) that at the strain-gauged sections, for compression and tension testing of the empty tubes, σ_L vs ε_L responses are weaker and stronger respectively than they are under "true" uniaxial-stress (σ_L) conditions.

In Fig. 3.16, deflected shapes (to a distorted scale) of empty tubes under both tensile and compressive load are shown. During testing, large lateral forces and moments are generated at the tube ends, due to:

(i) The tube (D1) tested under tensile load was welded to the test machine assembly which effectively fixes the ends of the tube against rotation and lateral translation.

(ii) For tubes (A3, A4, A5 and D3), without welded endplates, under compressive load large frictional forces develop between the tube ends and the test machine platens. The result is that rotation and lateral translation of the tube ends are largely prevented.

(iii) For tubes (A1 and A2), with welded endplates, under compressive load frictional forces (as for (ii)) and endplate stiffness mean that the ends of the tube are effectively fixed against rotation and lateral translation.

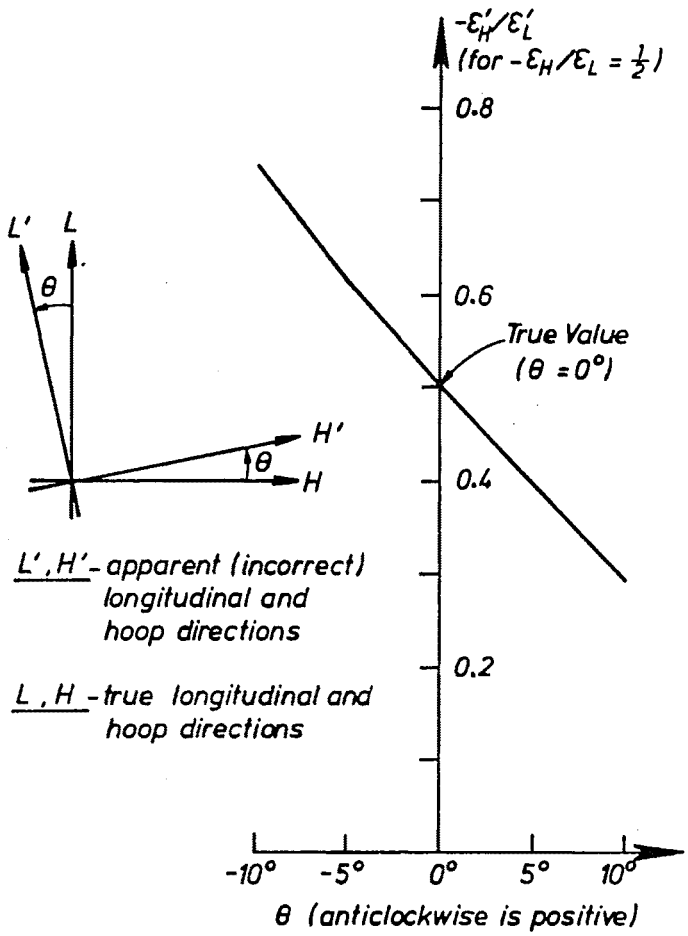

FIG. 3.14 : INFLUENCE OF A ROSETTE PLACING ERROR ON APPARENT VALUE OF POISSON'S RATIO

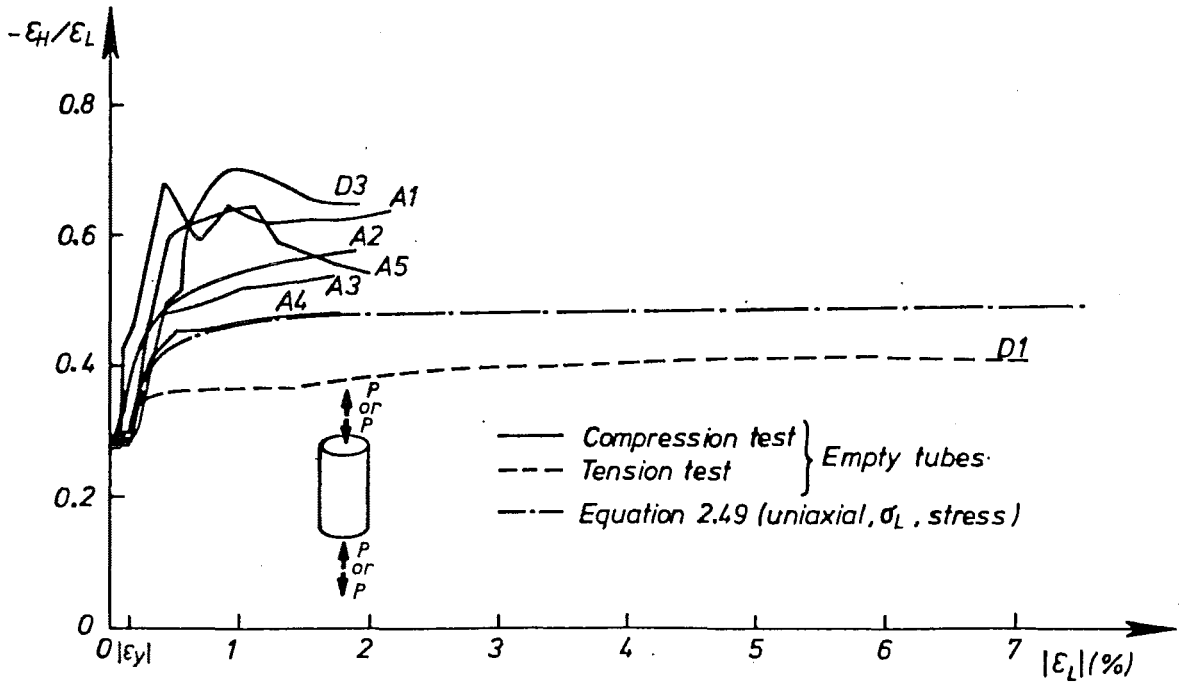

FIG. 3.15 : VARIATION OF POISSON'S RATIO WITH LONGITUDINAL STRAIN FOR EMPTY TUBE TESTS

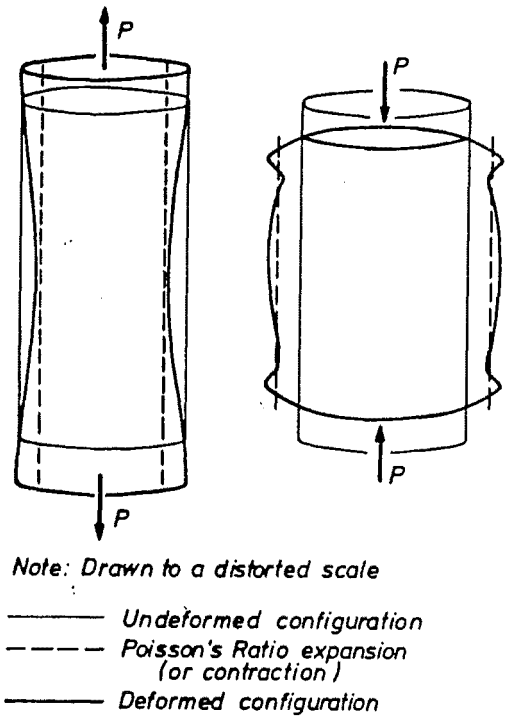

FIG. 3.16 : DEFLECTED SHAPES OF EMPTY TUBES UNDER LONGITUDINAL LOAD

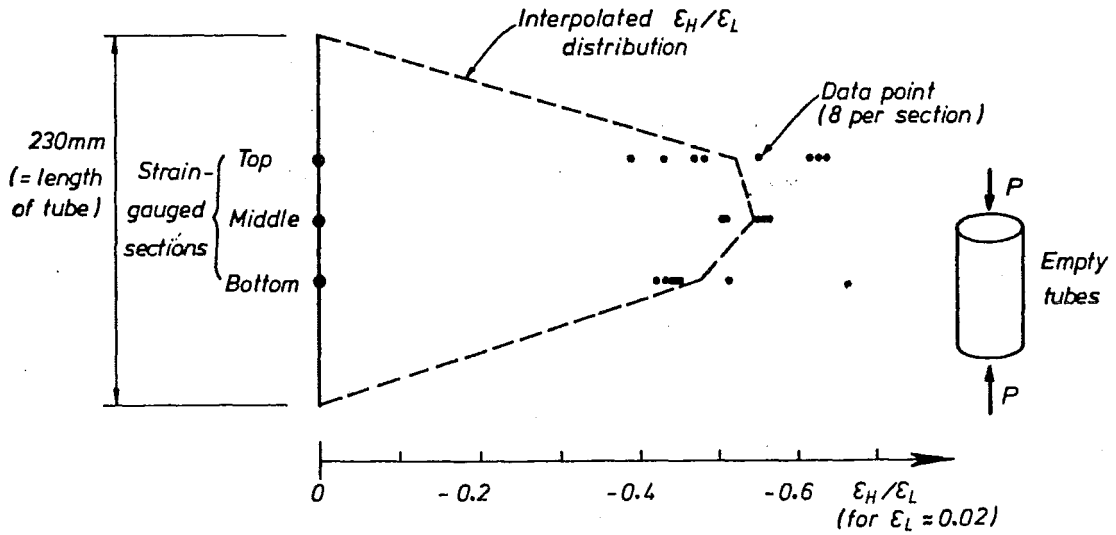

FIG. 3.17 : DISTRIBUTION OF HOOP STRAIN/LONGITUDINAL STRAIN WITH DISTANCE ALONG THE TUBE (TESTS A3 AND A4)

Under tensile (or compressive) longitudinal load, the tube is trying to contract (or expand) laterally due to Poisson's ratio effect. Thus the restraint to the ends of the tube results in the perturbations to the deflected shape of the empty tube which are shown in Fig. 3.16.

For two of the empty tubes (A3 and A4) tested under compressive load, 4 strain rosettes were located at each of three sections (see Fig. 3.6). The interpolated distribution of $\varepsilon_H/\varepsilon_L$ along the length of these tubes, just before local buckling occurs ($\varepsilon_L \simeq 0.02$), based on data from these two tests is shown in Fig. 3.17. In this figure, it is assumed that at the ends of the tubes due to lateral restraint $\varepsilon_H = 0$ (hence $\varepsilon_H/\varepsilon_L = 0$). As expected (see Section 3.3.7), a large amount of scatter is shown between the eight (four rosettes for each of tests A3 and A4) data points at each section. However the interpolated $\varepsilon_H/\varepsilon_L$ distribution which is based on the average of the eight data points at each section, indicates average values of $\varepsilon_H/\varepsilon_L$ of 0.52, 0.54 and 0.48 at the top, middle and bottom sections respectively. These compare with a predicted value (using equation 2.49) of 0.48 for uniaxial-stress conditions. Thus it appears that lateral restraint of the tube at its ends changes the distribution of $\varepsilon_H/\varepsilon_L$, from that expected under uniaxial-stress conditions, throughout the length of the tube.

3.3.7.2 Monotonic Tests of Concrete-Filled Tubes

In Fig. 3.18, the experimentally obtained variations of tube $\varepsilon_H/\varepsilon_L$ with ε_L from monotonically applied tensile and compressive longitudinal-load tests of concrete-filled tubes are compared with the theoretical variation (equation 2.49) of $\varepsilon_H/\varepsilon_L$ with ε_L in a uniaxial-stress (σ_L) field. For small strains ($|\varepsilon_L| < |\varepsilon_y|$), the experimental responses of the concrete-filled tubes are predicted reasonably well by equation 2.49, indicating the tube is in a uniaxial-stress state at this stage. However at large values of $|\varepsilon_L|$, the lateral movement of the tube is affected by lateral interaction of tube and concrete. For compressive load, concrete dilation results in $-\varepsilon_H/\varepsilon_L$ being larger than that predicted by equation 2.49, while for tensile load, partial radial restraint from the concrete results in $-\varepsilon_H/\varepsilon_L$ being smaller than that predicted from equation 2.49. Thus for both tensile and compressive load, lateral interaction results in hoop-tension stress in the tube and hence radial-compression stress in the concrete.

3.4 DISCUSSION OF EXPERIMENTAL RESULTS

3.4.1 Longitudinal Stress-Strain Response of Empty Tubes and Coupons

Figure 3.19 summarises the longitudinal stress-strain results from the tensile and compressive longitudinal-load testing of empty tubes, and the coupon testing of longitudinally orientated tube samples.

The coupon tests approximate uniaxial-stress conditions and since for $|\varepsilon_L| < 0.03$ there is no practical difference in the $|\sigma_L|$ vs $|\varepsilon_L|$ response to tensile load between the empty tube and the coupons, it appears that the influence of end effects on the stress field over the central (instrumented) region of the tube can be neglected for $|\varepsilon_L| < 0.03$. At larger strains, the response of D1 is stronger than the response of the coupon due to end effects which results in a biaxial-tension-stress field in the tube, as mentioned previously in Section 3.3.7.1.

The $|\sigma_L|$ vs $|\varepsilon_L|$ responses obtained from tensile and compressive longitudinal-load tests of empty tubes show significant differences, even before $|\varepsilon_L| \simeq 2\%$ which corresponded to the onset of local buckling in the compressive tests. The tensile tests of empty tubes indicated distinct elastic, yield and strain-hardening regions, which cannot be identified in the compressive test results (see Fig. 3.19).

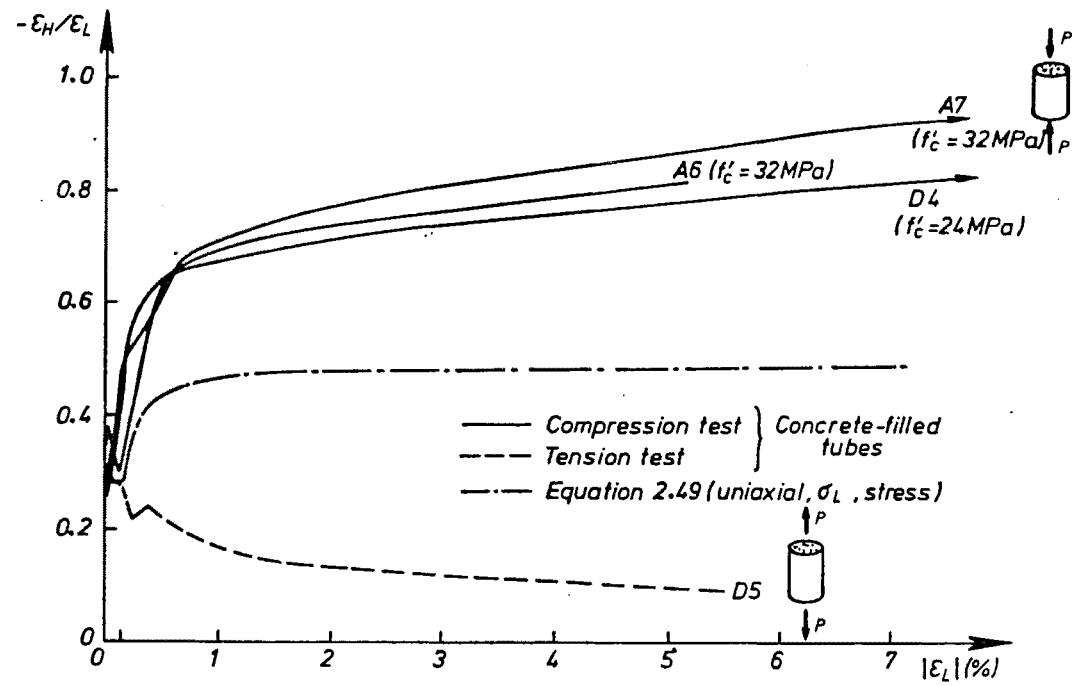

FIG. 3.18 : VARIATION OF HOOP STRAIN/LONGITUDINAL STRAIN WITH LONGITUDINAL STRAIN FOR CONCRETE-FILLED TUBE TESTS

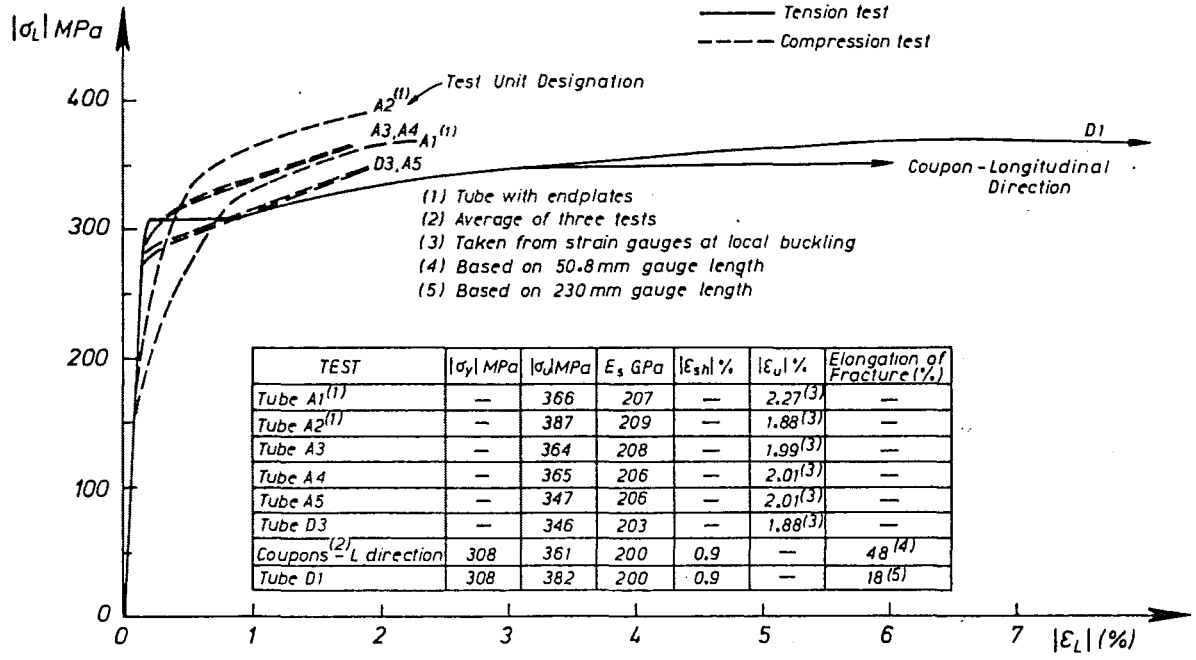

TEST	$\lvert\sigma_y\rvert$ MPa	$\lvert\sigma_u\rvert$ MPa	E_s GPa	$\lvert\varepsilon_{sh}\rvert$ %	$\lvert\varepsilon_u\rvert$ %	Elongation at Fracture (%)
Tube A1 (1)	—	366	207	—	2.27 (3)	—
Tube A2 (1)	—	387	209	—	1.88 (3)	—
Tube A3	—	364	208	—	1.99 (3)	—
Tube A4	—	365	206	—	2.01 (3)	—
Tube A5	—	347	206	—	2.01 (3)	—
Tube D3	—	346	203	—	1.88 (3)	—
Coupons (2) L direction	308	361	200	0.9	—	48 (4)
Tube D1	308	382	200	0.9	—	18 (5)

FIG. 3.19 : LONGITUDINAL STRESS-LONGITUDINAL STRAIN RESPONSE FROM EMPTY TUBE AND COUPON TESTS

For the compression-load tests of tubes without endplates (A3, A4, A5 and D3) the onset of $|\sigma_L|$ vs $|\varepsilon_L|$ non-linearity occurs at a stress of approximately 93% of the steel yield stress obtained from the tensile tests. This early onset of non-linearity in the compression-load tests is presumed to be a result of minor eccentricity in the application of longitudinal load, resulting in premature yielding. Mander et al (3.2) have reported a similar result in longitudinal-load tests of reinforcing bars. In the compression-load tests of tubes with endplates (A1 and A2), non-linear $|\sigma_L|$ vs $|\varepsilon_L|$ behaviour was first obtained at a $|\sigma_L|$ of approximately 150 MPa which is approximately half the $|\sigma_y|$ measured in the tension-load tests. Furthermore, tests A1 and A2 have quite different responses to those of the other four compression-load tests A3, A4, A5 and D3. Thus it is probable that despite the care taken to weld the endplate square on to the tubes, a square connection was not achieved and as a result tubes A1 and A2 were subsequently loaded eccentrically.

From Fig. 3.19, the average $|\sigma_u|$ from the tensile tests of an empty tube, coupon tests of tube samples and the compressive tests of empty tubes were 382 MPa, 361 MPa and 363 MPa respectively. The small differences between these three values of $|\sigma_u|$ also indicates that the complicated stress field which is set-up by end restraint of the tube results in only a small difference to the longitudinal strength of the tube.

From tensile testing of the steel an E_s of 200 GPa was found to be appropriate, while compressive testing gave E_s in the range of 203 - 209 GPa. Mander et al (3.2) found a similar difference between compressive and tensile load behaviour of reinforcing bars.

3.4.2 Comparison of Longitudinal Load vs Longitudinal Strain Response

3.4.2.1 Monotonic Compression

Figure 3.20 shows a comparison of the P vs ε_L results for longitudinal-compression-load tests of both empty and concrete-filled tubes. Also indicated are the values of $f'_c A_c$ for the two grades of concrete that were used in the concrete-filled tube tests. Clearly in terms of both strength and ductility, the composite response of the concrete-filled tubes is superior to the sum of the independent responses of the empty tubes and the unconfined concrete.

3.4.2.2 Monotonic Tension

Figure 3.21 shows a comparison of the P vs ε_L results obtained from longitudinal-tension-load tests of empty tubes, concrete-filled tubes, and coupon samples of the empty tube.

It is recalled that from Fig.3.18 for a given value of $|\varepsilon_L|$ approximately less than $|\varepsilon_y|$, hoop strains in empty and concrete-filled tubes are practically identical, which indicates that a negligible amount of lateral interaction between tube and concrete is occurring at this stage. Thus for $|\varepsilon_L|$ approximately less than $|\varepsilon_y|$ uniaxial-stress fields are present in tube and concrete, and hence the difference in P vs ε_L response for concrete-filled and empty tubes is due to longitudinal stress carried by the concrete. From Fig. 3.18 for $|\varepsilon_L|$ approximately greater than $|\varepsilon_y|$ lateral interaction occurs, hence the difference in P vs ε_L response for empty and concrete-filled tubes, at this stage, is due to the tube biaxial-tension-stress field and the concrete-tension-stiffening effect.

In Section 3.3.7, it was mentioned that restraint to the ends of the empty tubes disturbes the σ_L vs ε_L response of the tubes from that expected under uniaxial (σ_L) - stress (i.e. coupon test) conditions. From Fig. 3.18, at a given value of $|\varepsilon_L| > |\varepsilon_y|$, hoop-tension strains in the tube which is infilled with concrete are relatively small when compared with hoop-tension strains in the empty tube. Thus, in a concrete-filled tube, it was anticipated that the effects of

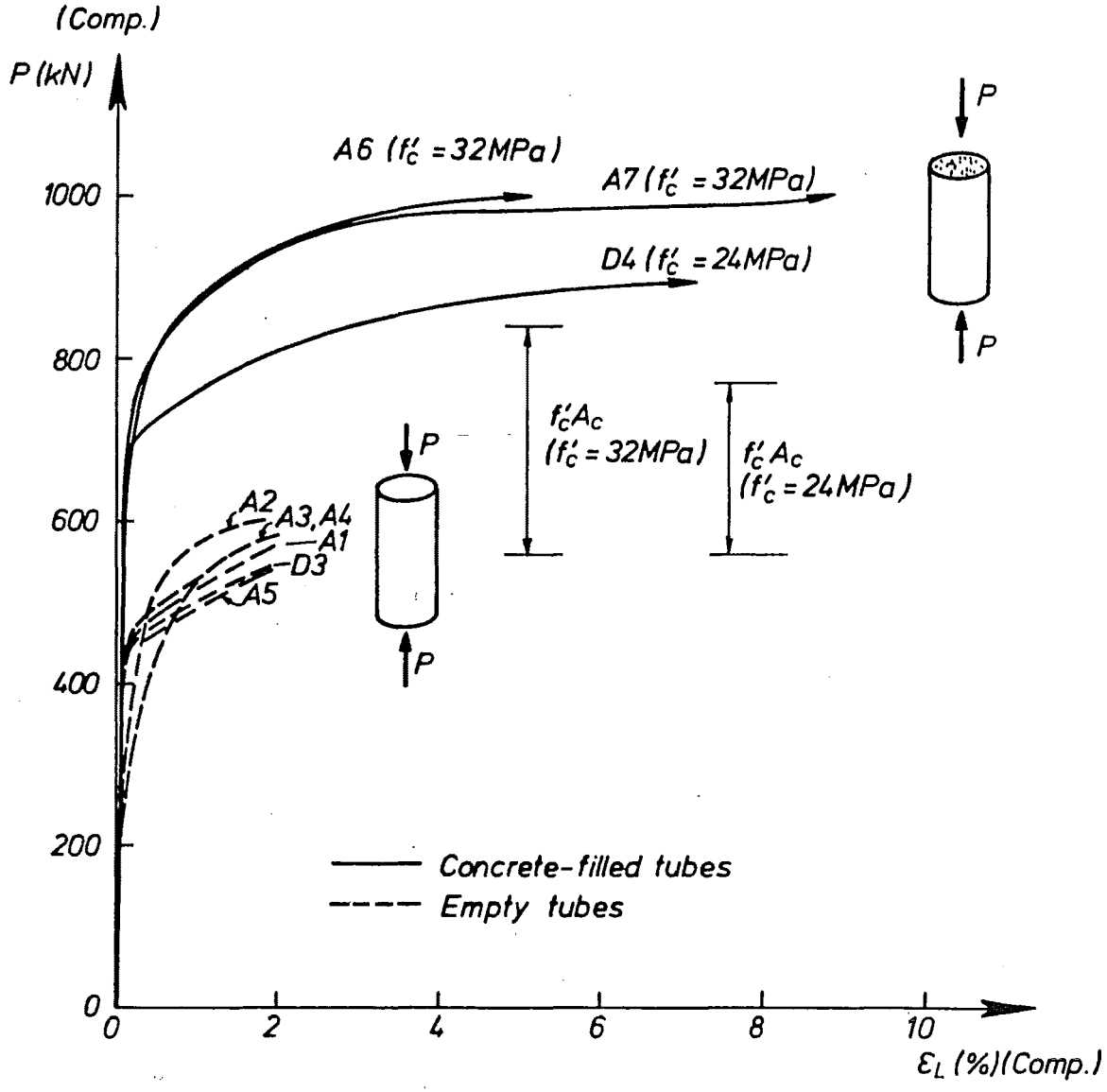

FIG. 3.20 : COMPARISON OF LOAD-LONGITUDINAL STRAIN RESULTS FOR MONOTONIC COMPRESSION LOAD TESTS

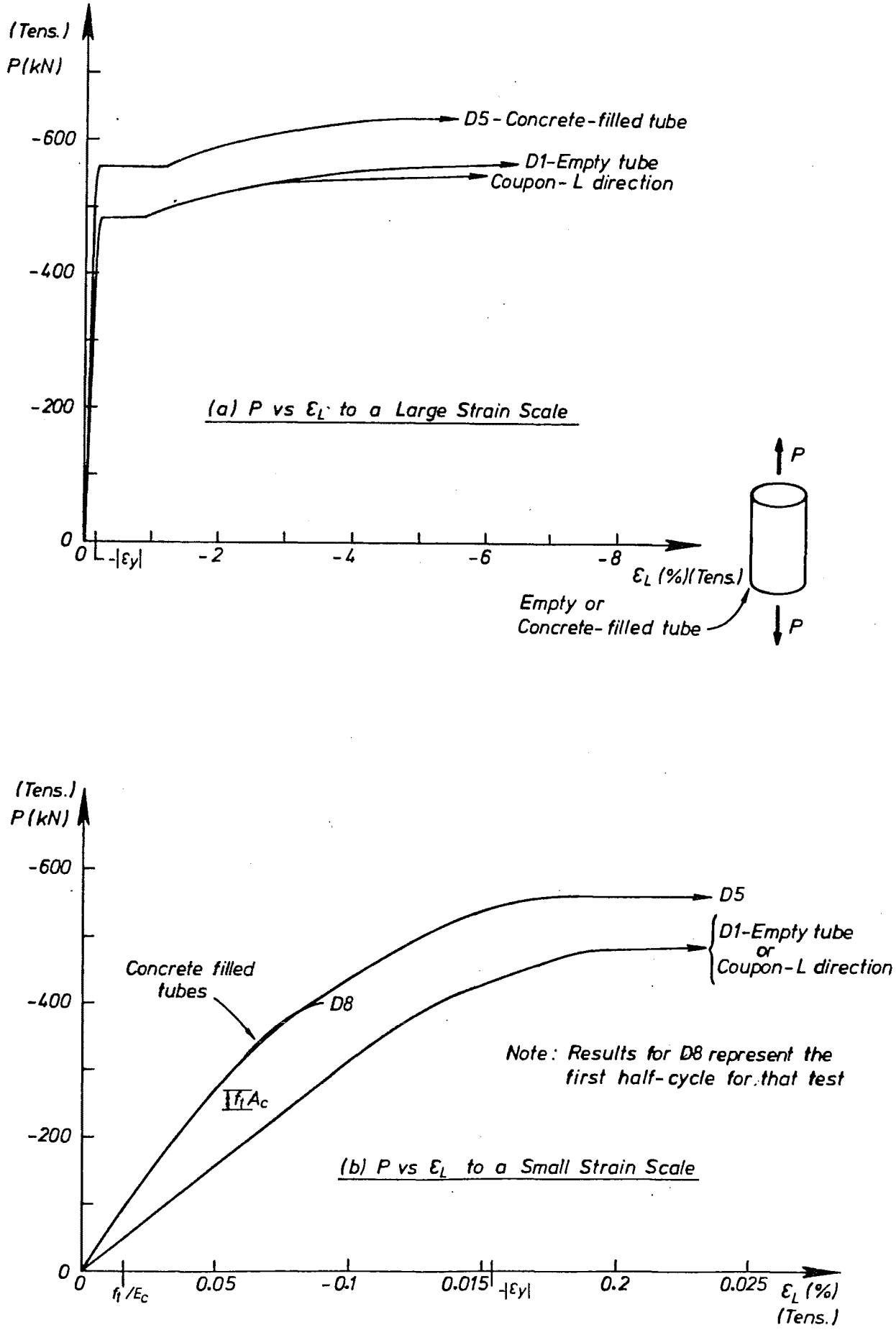

FIG. 3.21 : COMPARISON OF LOAD-LONGITUDINAL STRAIN RESULTS FOR MONOTONIC TENSION LOAD TESTS

end restraint, which arise as a direct consequence of hoop strain in the tube, will also be relatively small. Hence since end effects are negligible in the tensile tests of coupons and concrete-filled tubes, a direct comparison of the effect of infill concrete on tube performance between these two tests is valid. Conversely a direct comparison between the P vs ε_L responses of empty and concrete-filled tubes is not as good because of the small but significant influence of end effects on the measured σ_L vs ε_L response of the empty tube.

Figure 3.21 shows that the concrete-filled tube has an appreciably stronger response than either the empty tube or the coupon. For $|\varepsilon_L| < |\varepsilon_y|$ where the difference between empty and concrete-filled tube response is due to the concrete-tension-stiffening effect, the average load carried by the concrete over a gauge length containing several cracks is shown to be many times the value of $f_t A_c$ (f_t = MOR -3.8 MPa). This large value of average load is thought to be due to the inadvertently introduced thermal prestressing of the concrete which occurred during welding of the test unit to the test machine assembly which is discussed later in Section 3.5.4.5.

3.4.2.3 Cyclic Tension and Compression

In Fig. 3.22, a comparison of typical P vs ε_L results from the six types of test (see Table 3.1) is shown. Envelopes to the cyclic response of an empty tube and a concrete-filled tube are given along with the responses of concrete-filled and empty tubes to tensile and compressive monotonic longitudinal loading. The comparison shows:

(i) In the quadrant with tensile (-) P and ε_L, the monotonic curve and the envelope to the cyclic response of the empty tubes are very similar. This indicates that negligible strength and stiffness degradation of the empty tubes occurs in this quadrant due to cyclic loading. However, in the same quadrant, the envelope to the cyclic response of concrete-filled tubes is inferior to the monotonic response of concrete-filled tubes. For $\varepsilon_L < -2.5\%$, the envelopes of the cyclic responses of empty and concrete-filled tubes are practically identical. This occurs because under compressive load the concrete is crushed, which under reversed tensile load diminishes greatly the longitudinal and radial stiffness of the concrete. Thus negligible concrete-tension-stiffening between concrete cracks will occur, and since an insignificant level of hoop-tension stress can develop in the tube, the longitudinal-tension strength of the tube will not be significantly enhanced by the presence of a biaxial-tension-stress field.

(ii) In the quadrant with compressive (+) P and ε_L for both concrete-filled and empty tubes, the envelopes to the cyclic loading response are not as strong as the monotonic responses. This indicates that the cyclic loading causes a deterioration of performance under compressive load. The envelope to the cyclic response of the empty tube is shown to larger strains than is the monotonic response of the empty tube. This is because as mentioned previously in Section 3.3.5, in the cyclic tests the critical sections were instrumented, while in the monotonic tests the critical sections were located at the ends of the tubes away from the instrumented areas. This emphasises that the estimates (see Table 3.3) of ε_L at failure for compression-load testing of empty tubes are too small.

(iii) A comparison of the envelopes to the cyclic responses of concrete-filled tubes clearly shows that the dominant effect of the concrete is to enhance the strength and stiffness of the tube under compressive (+) values of both P and ε_L.

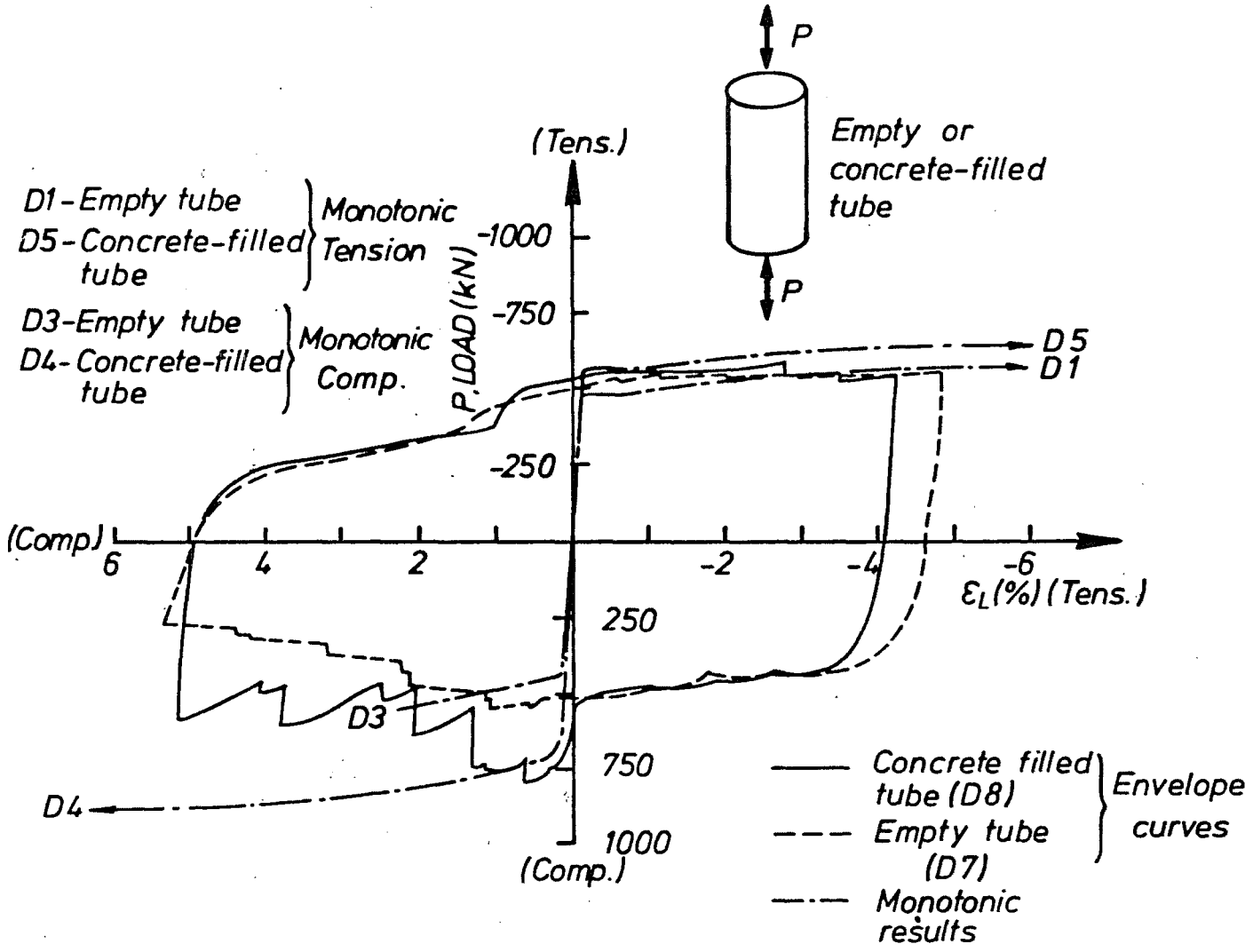

FIG. 3.22 : COMPARISON OF LOAD-LONGITUDINAL STRAIN RESULTS

(iv) The core concrete has a negligible effect on the strength and stiffness of the concrete in the quadrants with P and ε_L having opposite signs, since the envelopes of the empty and concrete-filled tubes are approximately identical in these two quadrants. This occurs because as load reverses from tension to compression, the concrete will not take longitudinal-compression stress until the cracks are closed, while as the load reverses from compression to tension the crushed concrete will neither take significant longitudinal-tension stress nor permit appreciable hoop-tension stresses in the tube to develop.

3.4.3 Influence of Core Concrete on Lateral Strains

Figures 3.23 and 3.24 show the influence of core concrete on the tube $-\varepsilon_H/\varepsilon_L$ vs ε_L responses for compressive and tensile longitudinal loading respectively. Under compressive load for a given value of ε_L approximately greater than 0.002, concrete dilation results in $-\varepsilon_H/\varepsilon_L$ being larger for the concrete-filled tubes than for the empty tubes. Under tensile load for a given value of $|\varepsilon_L|$ approximately greater than $|\varepsilon_y|$, concrete radial stiffness results in $-\varepsilon_H/\varepsilon_L$ being smaller for the concrete-filled tube than the empty tube.

3.4.4 Effect of End Restraint on Displaced Shape

Priestley (3.3) has developed a two-dimensional frame analogy to enable the analysis of shells, which have axi-symmetric loading and geometry, to be achieved without recourse to a more expensive and complicated finite element analysis. In this section the analogy is used to demonstrate quantitatively the effects of end restraint on the response of empty tubes to tensile and compressive longitudinal load.

The analogy is demonstrated in Fig. 3.25. The structural properties of the shell in the longitudinal and hoop directions are simulated by the beam-column members and the pin-ended strut members respectively in the analogy. For analysing a unit width of the shell the beam-column properties are:

A = section area of beam-column = t (shell) (3.5)

I = second moment of area of beam-column = $t^3/12$ (shell) (3.6)

E = modulus of beam-column = E (shell) (3.7)

The stiffness (load for unit deflection) of the inner (K_i) and outer (K_o) struts are:

$$K_i = \frac{4 E t h}{(D-t)^2 n} \quad \text{(shell)} \tag{3.8}$$

$$K_o = K_i/2 \tag{3.9}$$

where h = length of shell

n + 1 = number of pin-ended struts in the analogous frame.

In interpreting the results from the two-dimensional frame analyses:

$$y(\text{frame analogy}) = \left[(\varepsilon_H)_{\sigma_H = \sigma_R = 0} - (\varepsilon_H)\right] \frac{D-t}{2} \quad \text{(shell)} \tag{3.10}$$

In equation 3.10, ε_H represents the actual tube hoop strain, $(\varepsilon_H)_{\sigma_H = \sigma_R = 0}$ represents the tube hoop strain in a uniaxial-stress (σ_L) field, and y represents the lateral deflection of the beam-column which is a function of distance along the longitudinal axis of the shell.

Two-dimensional frame analyses were performed to indicate the effect of non-linearities in both geometry (P-Δ effects) and material (plastic behaviour) on the distribution of $-\varepsilon_H/\varepsilon_L$ with position along the length of the tube.

To simulate geometric non-linearity, it is necessary for the geometry of the structure (which needs to be defined before structural analysis can be commenced) to be identical to the deflected shape of the structure (which is not known until the end of the analysis). Thus an iterative procedure needs to be adopted with

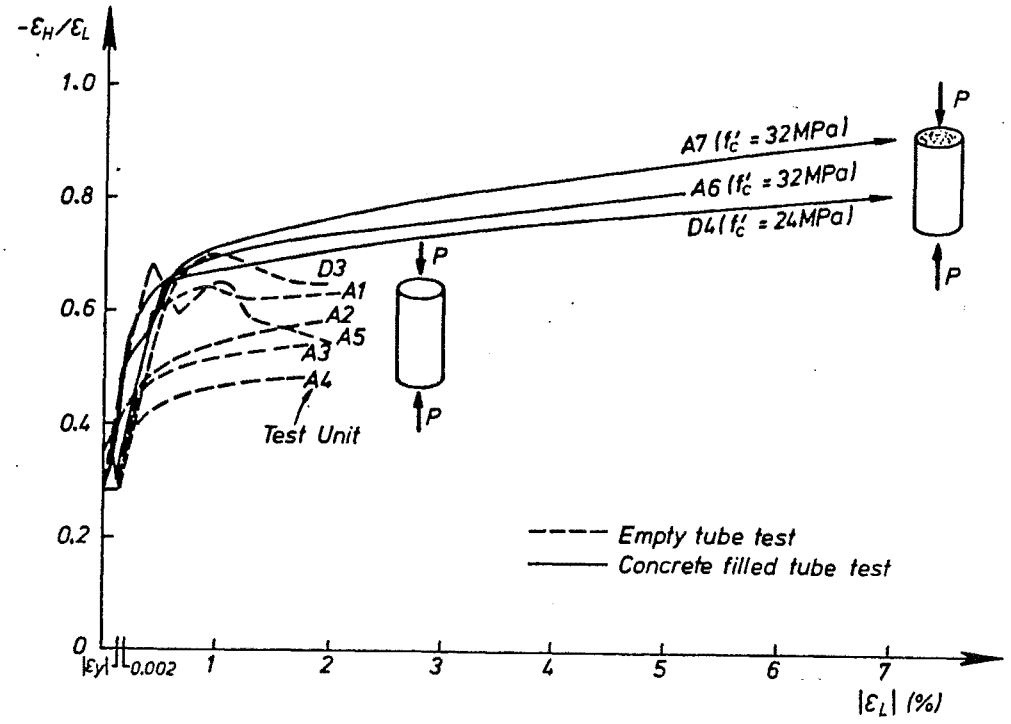

FIG. 3.23 : INFLUENCE OF CORE CONCRETE ON LATERAL STRAINS FOR MONOTONIC COMPRESSION LOAD TESTS

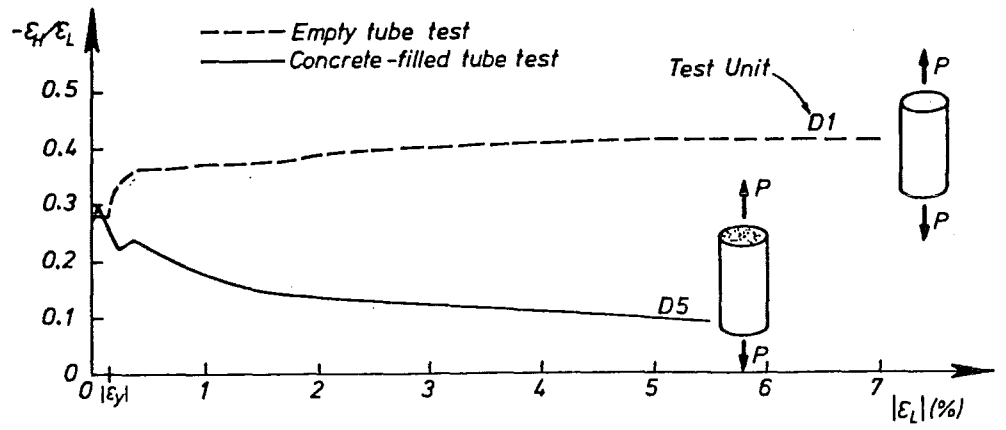

FIG. 3.24 : INFLUENCE OF CORE CONCRETE ON LATERAL STRAINS FOR MONOTONIC TENSION LOAD TESTS

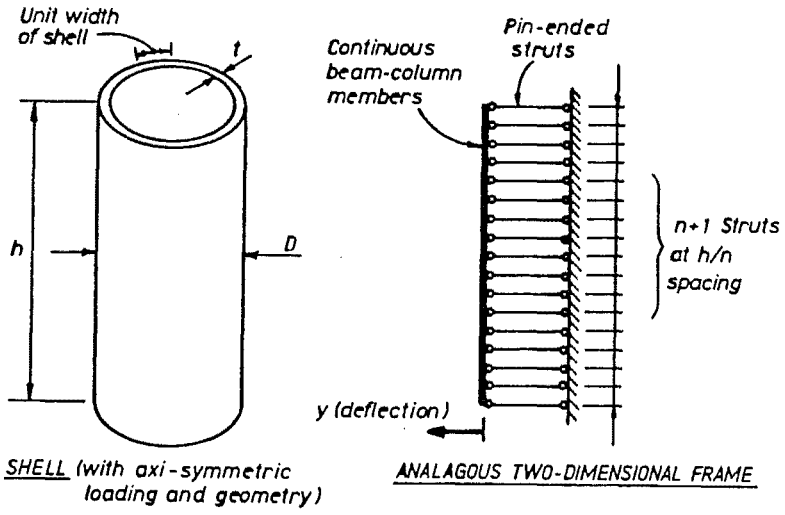

FIG. 3.25 : SHELL AND ANALOGOUS TWO-DIMENSIONAL FRAME

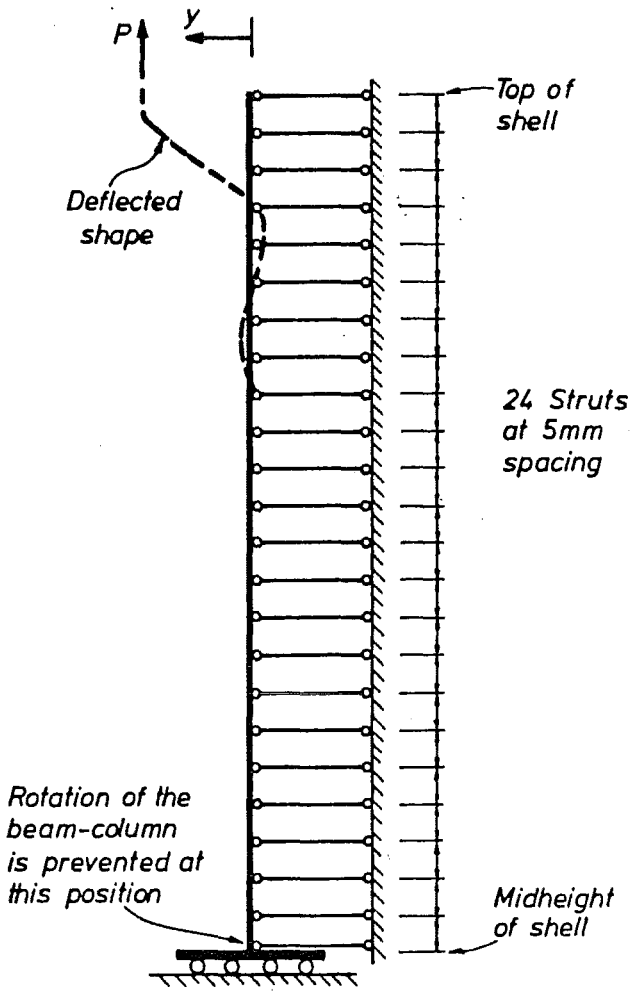

FIG. 3.26 : FRAME MODEL ADOPTED

successively better guesses at the deformed configuration being used in defining the geometry until convergence is achieved. In performing these iterative analyses, convergence was found to be relatively slow, with typically more than 10 iterations being required before satisfactory convergence was achieved.

Material non-linearity was simulated relatively crudely by using the secant modulus of the steel (i.e. σ_L/ε_L) at a given value of ε_L, in place of E in equations 3.7 and 3.8. This assumption also implies crudely that in the plastic range of steel behaviour, the secant modulii in the longitudinal and hoop directions are identical.

By symmetry, only the top (or bottom) half of the tube needs to be considered in the simulation, as the midheight of the tube can be considered to be fixed against rotation. Figure 3.26 shows the two-dimensional frame model which contained 24 strut and 23 beam-column members that was used in the analyses. An example deflected shape is also shown. At a given level of ε_L and P (evaluated as longitudinal load/unit width of the shell) displacements and rotations of:

$$y = \varepsilon_L \cdot \left(\frac{\varepsilon_H}{\varepsilon_L}\right)_{\sigma_H = \sigma_R = 0} \cdot \left(\frac{D - t}{2}\right)$$

$y' = 0$ = rotation of beam-column

were applied at the top of the analogous two-dimensional frame to simulate zero rotational and translational movement at the top of the tube due to end restraint. The load P was also applied to the top of the frame to allow P-Δ effects to be evaluated.

Results of the analyses for $-\varepsilon_H/\varepsilon_L$ distribution with height; for $|\varepsilon_L| = |\varepsilon_y|$, 0.01, 0.02 and 0.03; are shown in Fig. 3.27. Also indicated are the positions where strain gauges were mounted on the tubes. Three theoretical results (solid lines) are indicated at each of the levels of $|\varepsilon_L|$. The first result represents the effect of end restraint where P-Δ effects are ignored. The second and third results represent the effect of end restraint, with P-Δ effects included, under tensile and compressive longitudinal loads respectively. These theoretical results are compared with the distribution of $-\varepsilon_H/\varepsilon_L$ in a uniaxial-stress field (i.e. $-\varepsilon_H/\varepsilon_L$ equals Poisson's ratio, see the dashed lines).

As $|\varepsilon_L|$ increases, the effect of geometric non-linearity (P-Δ effect) becomes more significant. Under compressive loads, P-Δ effects exaggerate the effect of end restraint on the deflected shape of the shell, while under tensile loads, P-Δ effects tend to straighten the deflected shape of the tube. Results from the analyses under tensile and compressive loads simulate the experimentally observed deflected shapes (see Fig. 3.16) reasonably well. In particular, considering the results at an $|\varepsilon_L|$ of 0.02 which corresponds to the strain at which local buckling was observed in the compression-load tests, local buckling of the tube adjacent to its ends is shown by the theoretical results. The largest value of $-\varepsilon_H/\varepsilon_L$ occurs at the local buckle, and is substantially larger than Poisson's ratio. This explains why failure occurs at the local buckle, since at this section the longitudinal strength of the tube is reduced by the biaxial-compression-tension-stress field and the bending stresses which are present in this zone of high curvature.

In hindsight it would appear that to avoid the effect of end restraint on the envisaged uniaxial-stress field near the midheight of the tube, longer tubes should have been utilised in the experiments. However under longitudinal-compression loading, this measure would still not prevent local buckling occurring near the end regions of the tube. Also the analyses results shown in Fig. 3.27 indicate an extreme case, since a relaxation to the translational and rotational fixity conditions at the end of the tube would result in the reduced influence of end effects. However it is significant to note that from Table 3.3, empty tubes with

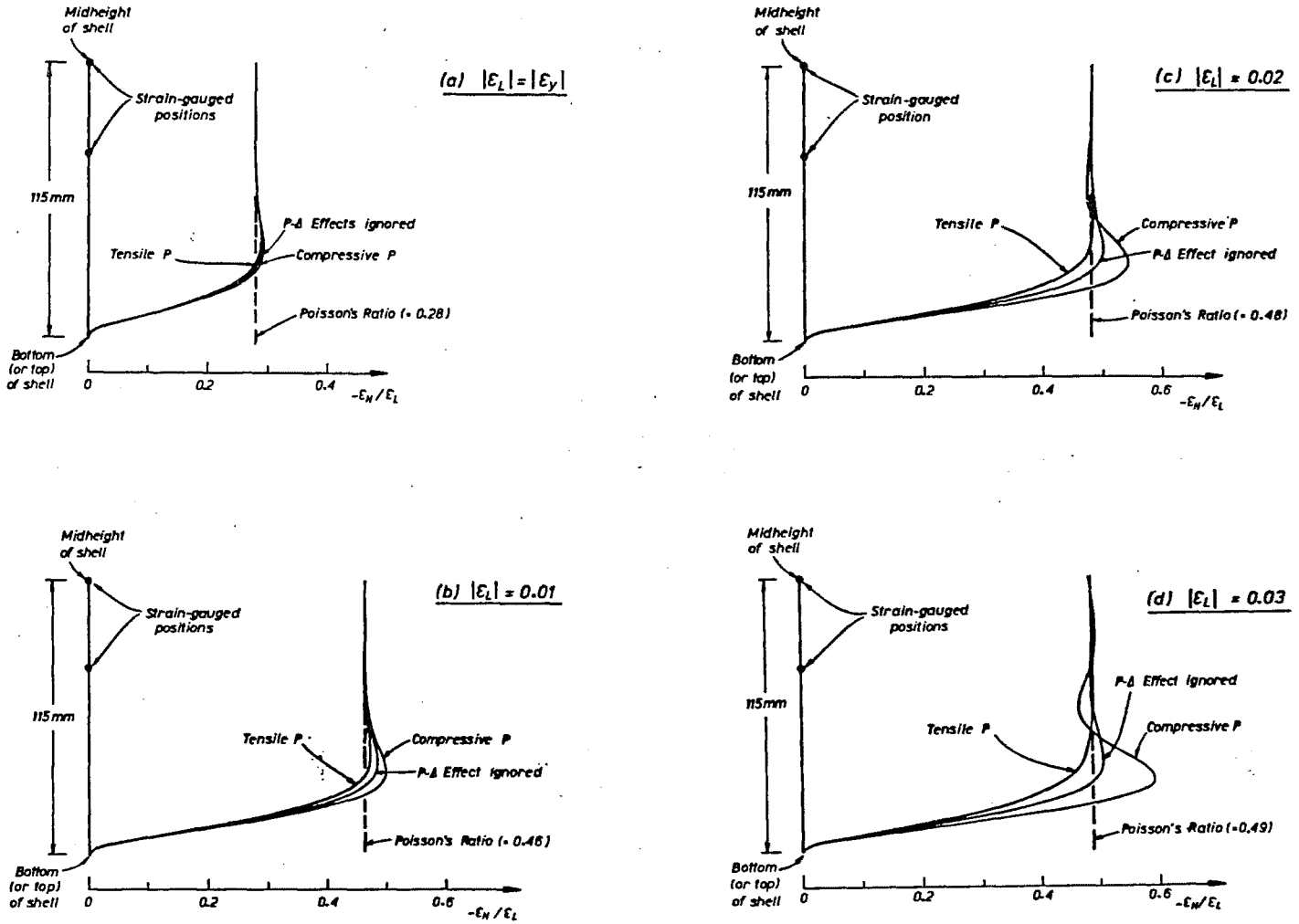

FIG. 3.27 : THEORETICAL DISTRIBUTION OF HOOP STRAIN/LONGITUDINAL STRAIN

welded end plates did have slightly larger values of P and ε_L at failure than did empty tubes without welded end plates. Thus stiff end restraint does appear to slightly enhance the performance of the empty tube.

3.4.5 Tube Local Buckling Characteristics

In this section the inelastic local buckling characteristics of a tube infilled with concrete are examined. In such members local buckling of the tube is a complex phenomenon, as the boundary conditions on the tube make it difficult to determine if behaviour is closest to that of a tube, a column or a plate. Figure 3.28 shows the post-buckling behaviour of these three types of members. Plates exhibit a large reserve of post-buckling strength, columns have stable post-buckling strength and shells only have a small reserve of post-buckling strength. Since the post-buckling load-carrying capacity of concrete-filled tubes is quite stable, due to the concrete stabilising tube local buckling, it appears that a conservative prediction of behaviour should be obtained by assuming column buckling of the tube in the vicinity of the local buckle.

In 1947, Shanley (3.4) showed that column buckling could be predicted satisfactorily in the inelastic as well as the elastic range of material behaviour by replacing the elastic modulus, E_s, in the Euler buckling formula with the tangent modulus, E_t :

$$\sigma_{cr} = \frac{\pi^2 E_t}{(L_e/r_g)^2} \qquad (3.11)$$

Local buckling of the tube wall will involve outward movement in the radial direction of the tube wall for which $r_g = 0.29t$. The deformed shape of a thin strip of tube that has formed a local buckle is shown in Fig. 3.29. It is assumed that a negligible amount of sway occurs between the top and bottom of the local buckle. Hence the visible length of local buckling is just less than $2L_e$. Rearranging equation 3.11 and substituting $r = 0.29t$, then the length $(2L_e)$ of visible local buckling can be expressed as:

$$2L_e = 1.82t\sqrt{\frac{E_t}{\sigma_{cr}}} \qquad (3.12)$$

In the yield range of steel behaviour $E_t = 0$, and hence from equation 3.12 theoretically $2L_e = 0$. However at this level of strain, local buckling of the tube is generally too small to be visible. The coupon tests (see Fig. 3.1) indicated that E_t varied from $0.015E_s$ at the commencement of strain-hardening to 0 at ultimate strength. Thus at the commencement of strain-hardening with $E_t = 3000$ MPa, $\sigma_{cr} = |\sigma_y| = 308$ MPa and $t = 4.5$ mm (from equation 3.12), the visible length of local buckling is equal to $5.7t$ or 26 mm, compared with the experimentally observed length of 30 mm which was reported (see Section 3.3) for both empty and concrete-filled tubes. For ε_L greater than that at which strain-hardening commences, equation 3.12 implies that the length of local buckling will progressively reduce to zero, since E_t is also reducing to zero. However, as was observed experimentally the length of visible local buckling stays at the level predicted at the commencement of strain-hardening, since P-Δ effects on the tube wall and internal concrete pressure will prevent the length of tube which has already bent outwards from restraightening.

3.5 COMPARISON OF EXPERIMENTAL RESULTS WITH THEORETICAL PREDICTIONS

In the following sections, the experimental results for longitudinal load, tube longitudinal strain and tube hoop strain are manipulated to give tube stresses, concrete stresses, tube load and concrete load. These stresses and loads are compared with predictions based on the proposed "Uniaxial Model" and "Lateral Interaction Model"

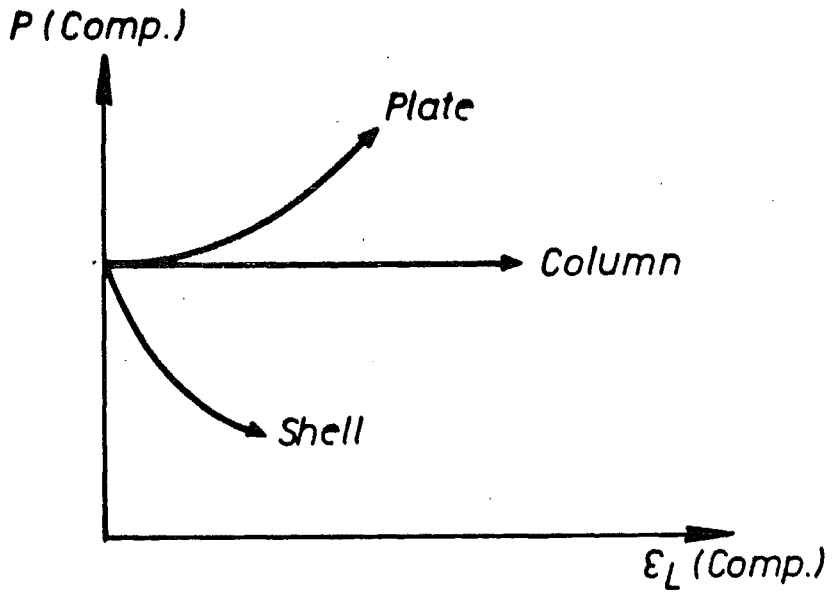

FIG. 3.28 : POST-BUCKLING BEHAVIOUR OF PERFECT SHELLS, COLUMNS AND PLATES

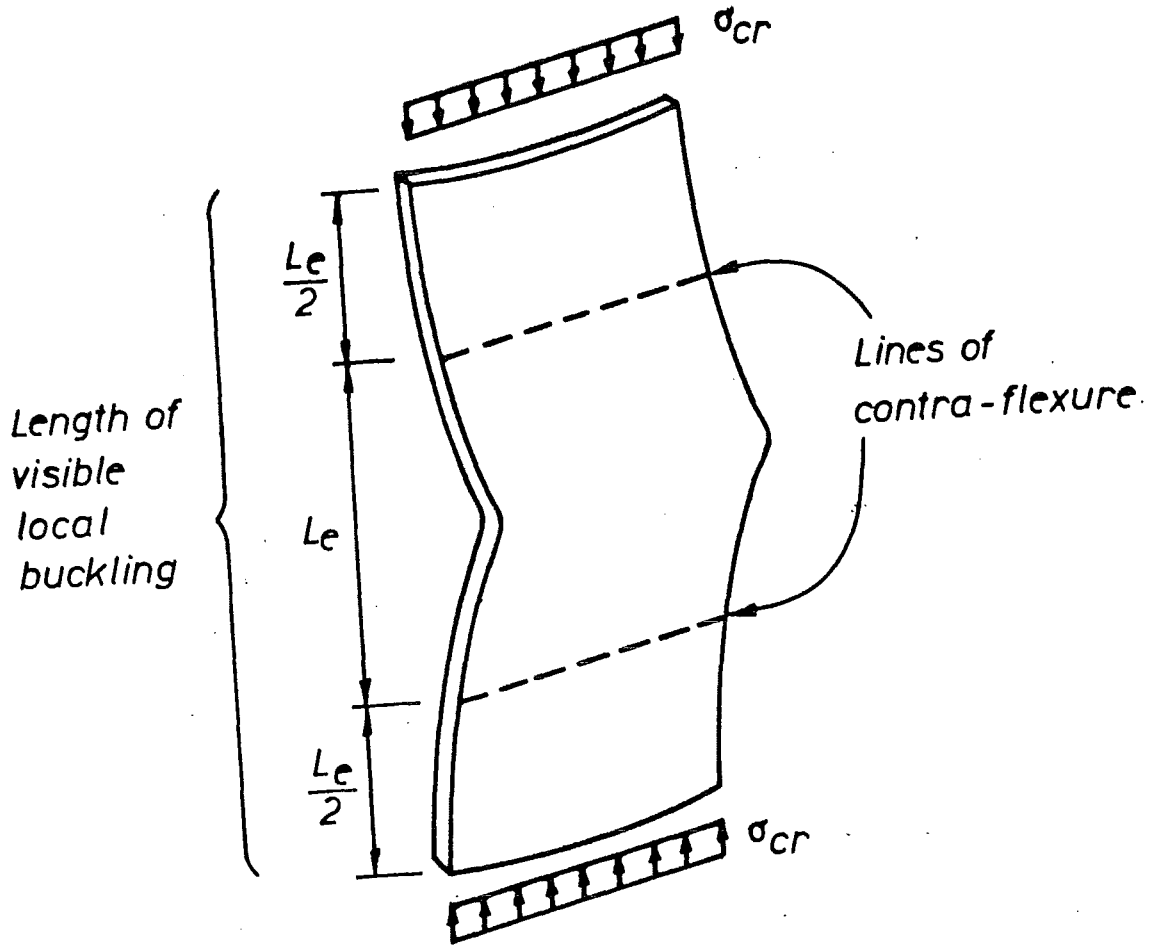

FIG. 3.29 : CONFIGURATION OF A LOCAL BUCKLE

(see Chapter 2 for outlines of these models). Values of tube longitudinal and hoop strain used in the data manipulation process were the average strains indicated by the electrical resistance strain gauges orientated in the longitudinal and hoop directions respectively.

3.5.1 Determination of Loads and Stresses Carried by Steel and Concrete

In determining tube and concrete stresses from the experimental load and strain data the following assumptions were made:

(i) The constitutive laws for steel outlined previously in Section 2.2.2 apply.

(ii) Deformations of concrete and tube are compatible. This implies that longitudinal strains, ε_L, in the tube and concrete are identical, and that the tube hoop strain, ε_H, is equal to the concrete radial strain, ε_{RC}.

(iii) Lateral equilibrium between tube and concrete occurs as defined by equation 2.54.

(iv) Tube σ_R can be neglected.

3.5.1.1 Elastic Range

From the measured tube ε_L and ε_H, it is possible to calculate directly the tube σ_L and σ_H by using equations 2.11 and 2.12 and the values of E_s which can be determined from a uniaxial-stress test of a coupon sample of the tube. Thus P_t can be calculated from:

$$P_t = A_t \cdot \sigma_L \tag{3.13}$$

Equilibrium of P with P_c and P_t gives:

$$P_c = P - P_t \tag{3.14}$$

and concrete f_L from:

$$f_L = P_c/A_c \tag{3.15}$$

Finally concrete f_R can be calculated from the lateral equilibrium requirement as:

$$f_R = \frac{-2t \cdot \sigma_H}{D - 2t} \tag{3.16}$$

3.5.1.2 Plastic Range

In the plastic range of steel behaviour, stresses are related to the increments of plastic strain as was shown previously in equations 2.38 and 2.39. Thus it is convenient to use an incremental solution in solving for σ_L, σ_H, f_L, f_R, P_c and P_t. Increment $i = 0$ corresponds to the elastic-plastic boundary where $(\varepsilon^p_L)_o = (\varepsilon^p_H)_o = (\varepsilon^p_{RT})_o = (\varepsilon^p_{eff})_o = 0$ and $(\sigma_L)_o$ and $(\sigma_H)_o$ can be calculated from the elastic constitutive laws (equations 2.11 and 2.12) and the von Mises yield criterion (equation 2.37). Assuming that increment i has been solved to give $(\varepsilon^p_L)_i$, $(\varepsilon^p_H)_i$, $(\varepsilon^p_{RT})_i$, $(\varepsilon^p_{eff})_i$, $(\sigma_L)_i$ and $(\sigma_H)_i$, then from the measured $(\varepsilon_L)_{i+1}$, $(\varepsilon_H)_{i+1}$ and $(P)_{i+1}$ solutions for $(\sigma_L)_{i+1}$, $(\sigma_H)_{i+1}$, $(f_L)_{i+1}$, $(f_R)_{i+1}$, $(P_t)_{i+1}$, and $(P_c)_{i+1}$ may be obtained as follows:

Step 1: Guess values of tube $(\sigma_L)_{i+1}$ and $(\sigma_H)_{i+1}$, for example $(\sigma_L)_{i+1} = (\sigma_L)_i$ and $(\sigma_H)_{i+1} = (\sigma_H)_i$.

Step 2: Use the mean stress-volumetric strain relationship (equation 2.21) and the values of E_s, ν_s, $(\varepsilon_L)_{i+1}$, $(\varepsilon_H)_{i+1}$, $(\sigma_L)_{i+1}$ and $(\sigma_H)_{i+1}$ to solve for $(\varepsilon_{RT})_{i+1}$.

Step 3: Calculate: $(\varepsilon^p_L)_{i+1}$, $(\varepsilon^p_H)_{i+1}$ and $(\varepsilon^p_{RT})_{i+1}$ from equations 2.14 to 2.16 respectively and the values of E_s, ν_s, $(\sigma_L)_{i+1}$, $(\sigma_H)_{i+1}$ and $(\sigma_R)_{i+1}$ (= zero).

Step 4: Calculate the increments of plastic strain in the tube:

$$(d\varepsilon_L^p)_{i+1} = (\varepsilon_L^p)_{i+1} - (\varepsilon_L^p)_i \tag{3.17}$$

$$(d\varepsilon_H^p)_{i+1} = (\varepsilon_H^p)_{i+1} - (\varepsilon_H^p)_i \tag{3.18}$$

$$(d\varepsilon_{RT}^p)_{i+1} = (\varepsilon_{RT}^p)_{i+1} - (\varepsilon_{RT}^p)_i \tag{3.19}$$

Step 5: Calculate $(d\varepsilon_{eff}^p)_{i+1}$ from equation 2.27 and the values of $(d\varepsilon_L^p)_{i+1}$, $(d\varepsilon_H^p)_{i+1}$ and $(d\varepsilon_{RT}^p)_{i+1}$

Step 6: Calculate $(\varepsilon_{eff}^p)_{i+1}$:

$$(\varepsilon_{eff}^p)_{i+1} = (\varepsilon_{eff}^p)_i + (d\varepsilon_{eff}^p)_{i+1} \tag{3.20}$$

Step 7: Obtain the effective stress, $(\sigma_{eff})_{i+1}$, from the $\varepsilon_{eff}^p - \sigma_{eff}$ relationship (equivalent to the $\varepsilon_L^p - \sigma_L$ relationship obtained in a uniaxial-stress (σ_L) test) and the value of $(\varepsilon_{eff}^p)_{i+1}$.

Step 8: Recalculate $(\sigma_L)_{i+1}$ and $(\sigma_H)_{i+1}$ from equations 2.38 and 2.39 and the values of $(d\varepsilon_L^p)_{i+1}$, $(d\varepsilon_H^p)_{i+1}$ and $(\sigma_{eff})_{i+1}$.

Step 9: Compare the values of $(\sigma_L)_{i+1}$ and $(\sigma_H)_{i+1}$ used in Step 2 with those calculated in Step 8. If the differences are negligible go to Step 10. If the differences are not negligible, use the Step 8 values of $(\sigma_L)_{i+1}$ and $(\sigma_H)_{i+1}$ and go to Step 2.

Step 10: The procedure adopted for the elastic range (see equations 3.13 to 3.16) may then be adopted to solve for $(P_t)_{i+1}$, $(P_c)_{i+1}$, $(f_L)_{i+1}$, and $(f_R)_{i+1}$.

3.5.2 Tube Stress Paths

In Fig. 3.30, tube biaxial-stress paths (σ_L vs σ_H) for the concrete-filled tubes under monotonically applied tensile and compressive longitudinal load are shown. These stress paths are compared with the elliptical-shaped curves which represent possible (σ_H, σ_L) coordinates at yield (σ_{eff} = 308 MPa) and ultimate strength (σ_{eff} = 361 MPa, based on the coupon test from the longitudinal direction of the tube). Also indicated are the ultimate strengths of the empty tubes and the coupons where it is assumed that $\sigma_H = 0$.

For $|\varepsilon_L| \leq |\varepsilon_y|$, Figs. 3.23 and 3.24 indicated that under both tensile and compressive longitudinal loads, ε_H vs ε_L responses for concrete-filled and empty tubes were practically identical, and hence at that stage a negligible level of lateral interaction occurred between tube and concrete. Thus as shown in Fig. 3.30 as $|\varepsilon_L|$ increased from 0 to $|\varepsilon_y|$ tube $\sigma_H = 0$, and tube $|\sigma_L|$ increased from 0 to $|\sigma_y|$ for both tensile and compressive longitudinal load.

In the yield and strain-hardening ranges ($\sigma_{eff} \geq |\sigma_y|$ = 308 MPa) of tube behaviour, the level of tube $|\sigma_H|$ increased as testing proceeded for both tensile and compressive longitudinal load. For tensile loading this clearly enhanced the longitudinal stress carried by the tube, as could be predicted from the "Lateral Interaction Model" (see Section 2.3.2), while for compressive loading this reduced the longitudinal stress carried by the tube. For the largest recorded value of compressive ε_L (= 12%): tube σ_L = 150 MPa and σ_H = -255 MPa. Thus at large values of ε_L, the response of the concrete-filled tube under longitudinal-compression load is dominated by restraint of concrete dilation. In Figs. 3.23, test units A6 and A7 (both with f_c' = 32 MPa) were shown to have larger hoop-tension strains than was D4 (with f_c' = 24 MPa). This observation is reflected in Fig. 3.30 where test units A6 and A7 are shown to be more dominated by hoop-tension stress than is D4.

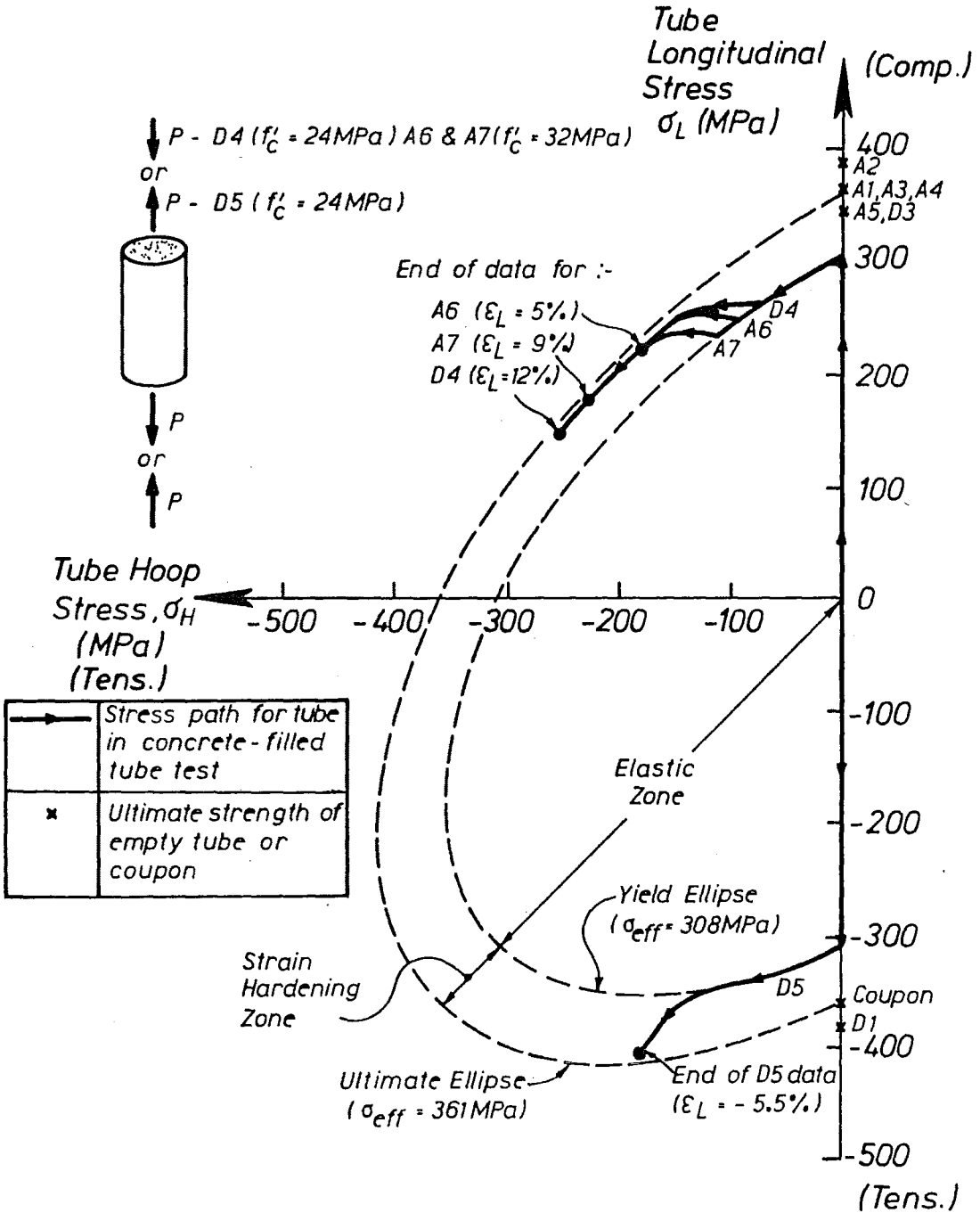

FIG. 3.30 : TUBE BIAXIAL-STRESS PATHS

3.5.3 Monotonic Longitudinal-Compression-Load Tests of Concrete-Filled Tubes

3.5.3.1 Longitudinal Load vs Longitudinal Strain Comparisons

Figure 3.31 shows comparisons of the theoretical and experimental P vs ε_L response of test units D4 (f'_c = 24 MPa), A6 (f'_c = 32 MPa) and A7 (f'_c = 32 MPa) to longitudinal-compression load. The ultimate loads predicted by the formula of Sen (equation 2.62) are also indicated.

For $\varepsilon_L \leq$ 8%, the "Lateral Interaction Model" gives good predictions to the experimental responses. However for $\varepsilon_L \geq$ 8%, the "Lateral Interaction Model" underestimates the experimental P vs ε_L response. This discrepancy arises because the "Lateral Interaction Model" (see Section 2.4.2) was calibrated from the test data of Tomii et al (2.1) and Sen et al (2.41) which were only available for $\varepsilon_L \leq$ 4%. The "Uniaxial Model" is again shown to underestimate the response of concrete-filled tubes which implies that lateral interaction between tube and concrete increases greatly the strength and ductility of the composite member. For $\varepsilon_L \leq$ 12%, the experimental longitudinal load does not exceed the ultimate load predicted by the formula of Sen.

Table 3.4 shows a comparison of the experimentally obtained maximum load with ultimate loads predicted from the formula of Sen, the "Lateral Interaction Model", and the "Uniaxial Model". Since due to test machine constraints the maximum experimentally obtained loads were probably substantially smaller than the test units actual ultimate loads, it is apparent from Table 3.4 that the theoretical predictions will give a conservative estimate of the ultimate loads of the concrete-filled tubes. However it should be noted that maximum experimental loads were obtained at very large longitudinal strains (5% to 12%), and thus have little significance for real engineering design situations. Hence from this data the formula of Sen could be considered to be non-conservative for design. It is also shown in the table that the "Lateral Interaction Model" gives an ultimate load which is approximately 34% larger than that predicted from the "Uniaxial Model".

TABLE 3.4 : ULTIMATE LOAD COMPARISONS

Test	Ultimate Load (kN)				(1)/(2)	(1)/(3)	(1)/(4)	(3)/(4)
	Experiment (1)	Sen (2.33) (2)	Lateral Interaction Model (3)	Uniaxial Model (4)				
D4	≥ 1066	1048	934	693	≥1.02	≥1.14	≥1.54	1.35
A6 and A7	≥ 1000	1119	1012	763	≥0.89	≥0.99	≥1.31	1.33

3.5.3.2 Tube Longitudinal Stress vs Longitudinal Strain Comparisons

Figure 3.32 shows comparisons of the experimental and theoretical tube σ_L (and P_t) vs ε_L responses of test units D4, A6 and A7. The experimental response shows that for $\varepsilon_L \geq$ 0.2%, tube σ_L decreases with ε_L to a value of the order of $0.5|\sigma_y|$ at ε_L = 10%. The "Lateral Interaction Model" clearly gives a better prediction to tube σ_L vs ε_L response than does the "Uniaxial Model". However at large strains, the "Lateral Interaction Model" overestimates the level of σ_L carried by the tube. This occurs because in the "Lateral Interaction Model", which was calibrated from the tests of Tomii et al (2.1) with data for $\varepsilon_L \leq$ 4%, it is assumed that tube σ_L is constant for $\varepsilon_L >$ 1%. From the test results of Tomii et al (2.1) and Fig. 3.32 (tests D4, A6 and A7), this assumption appears reasonable for $\varepsilon_L <$ 4%, but at larger strains as shown in Fig. 3.32 the assumption is crude.

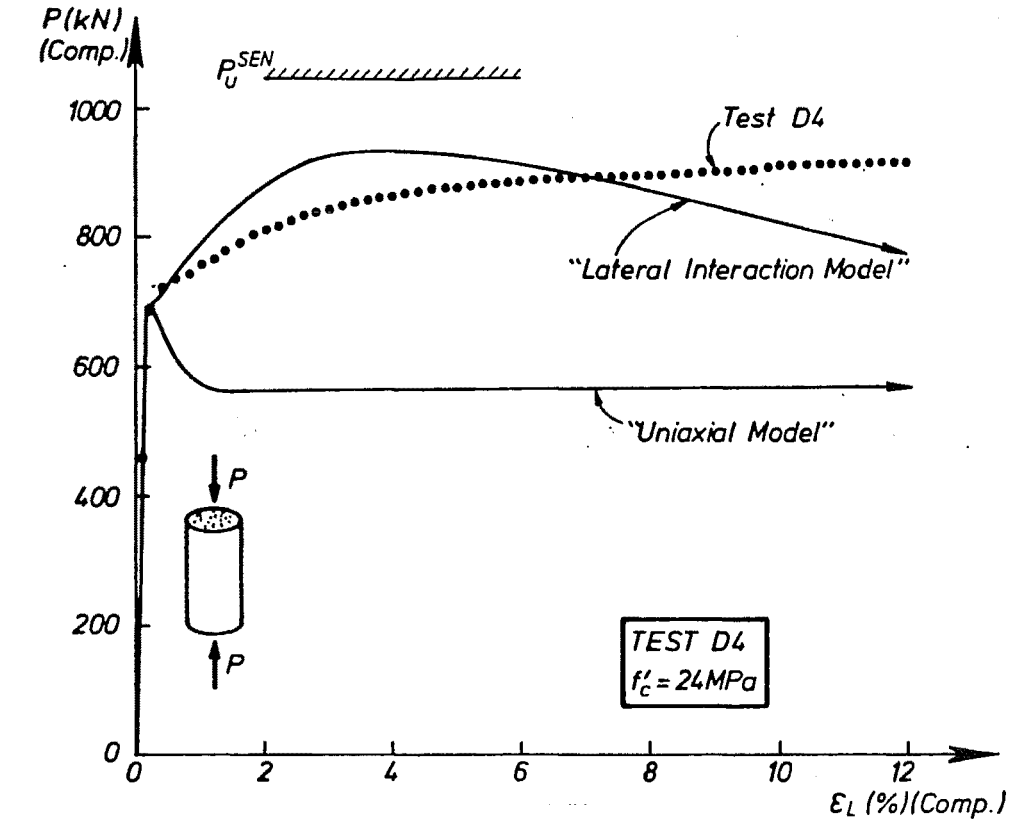

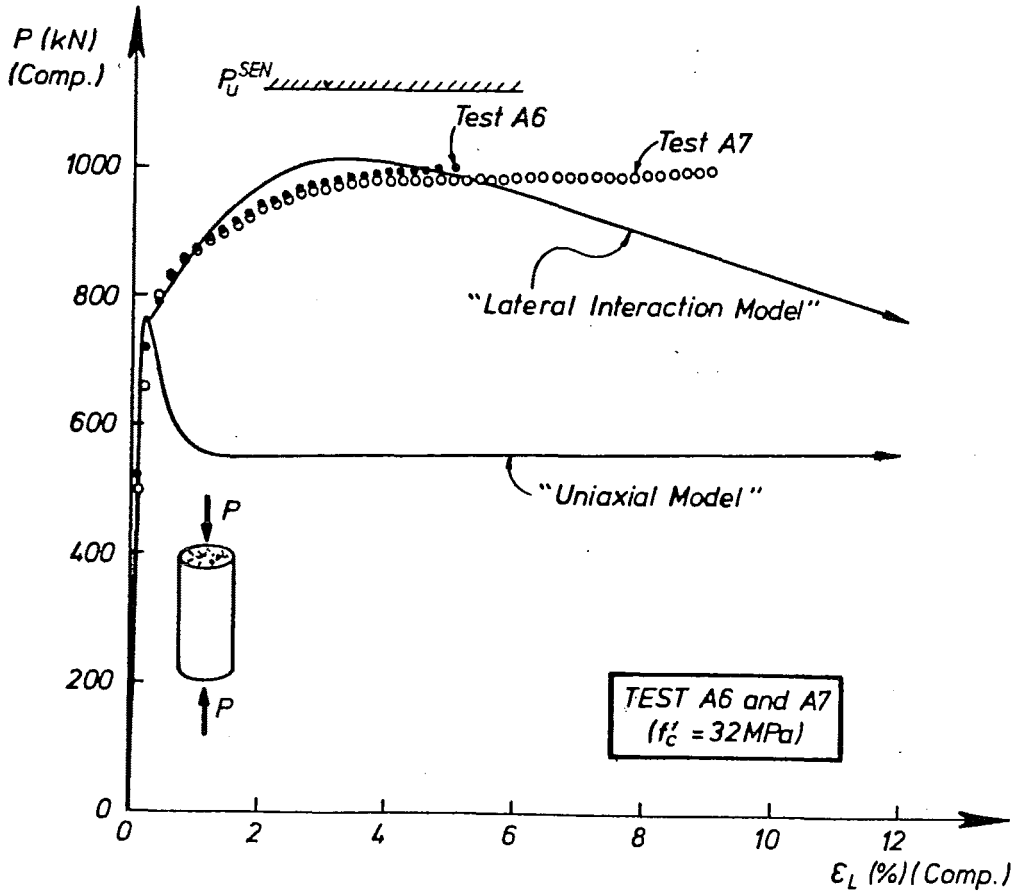

FIG. 3.31 : LONGITUDINAL LOAD-LONGITUDINAL STRAIN COMPARISONS FOR MONOTONIC COMPRESSION-LOAD TESTS

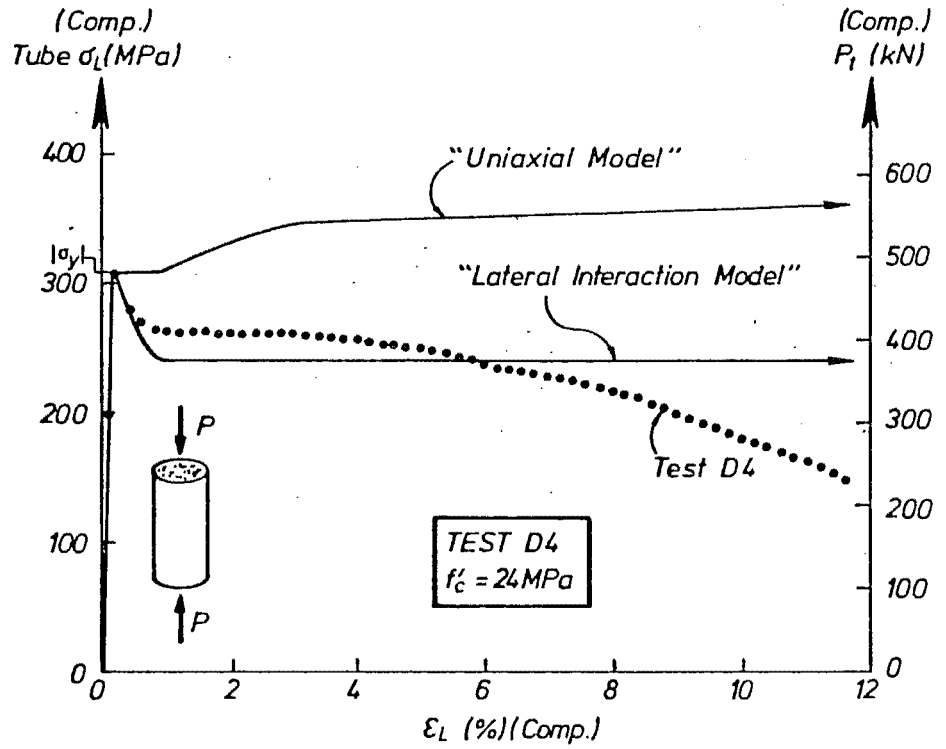

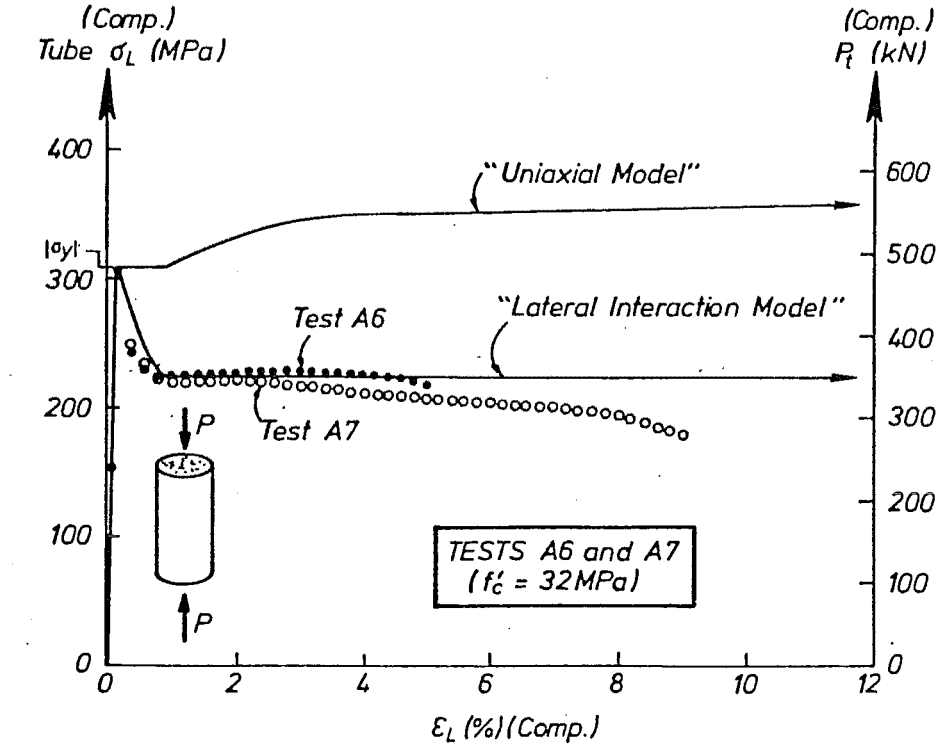

FIG. 3.32 : TUBE LONGITUDINAL STRESS-LONGITUDINAL STRAIN COMPARISONS FOR MONOTONIC COMPRESSION-LOAD TESTS

3.5.3.3 Tube Hoop Stress and Concrete Radial Stress vs Longitudinal Strain Comparisons

Figure 3.33 shows comparisons of the theoretical and experimental tube σ_L (and concrete f_R) vs ε_L responses of test units D4, A6 and A7. For comparative purposes, the uniaxial stress-strain characteristics of a coupon sample of the tube are also shown. For $\varepsilon_L > 0.002$, experimental values of tube $|\sigma_H|$ and concrete f_R are shown to increase continuously with ε_L. Large lateral stresses occur due to concrete-tube lateral interaction, for example for unit D4 at $\varepsilon_L = 12\%$, tube $\sigma_H = -0.83\ |\sigma_y|$ (= -255 MPa) and concrete $f_R = 0.9f'_c$ (= 22 MPa). The "Lateral Interaction Model" generally gives a good prediction to the experimental response (cf. the "Uniaxial Model" predictions and the coupon response). However at large values of ε_L, the "Lateral Interaction Model" does tend to underestimate the values of tube $|\sigma_H|$ and concrete f_R. This is a direct consequence of the overestimation of tube σ_L which was described in the previous section, since at a given value of σ_{eff}, σ_L and σ_H are related through equation 2.36.

3.5.3.4 Concrete Longitudinal Stress vs Longitudinal Strain Comparisons

Figure 3.34 shows comparisons of the theoretical and experimental concrete f_L (and P_c) vs ε_L responses of test units D4, A6 and A7. The experimental f_L vs ε_L responses are shown to increase continuously with ε_L. For D4 (f'_c = 24 MPa) by an ε_L of 12% an experimental f_L of 79 MPa (= $3.3f'_c$) was obtained, while for A7 (f'_c = 32 MPa) by an ε_L of 9%, an experimental f_L of 86 MPa (= $2.7f'_c$) was achieved. Thus substantial enhancement to concrete strength and ductility (cf. "Uniaxial Model" predictions) occurred due to confinement provided by the tube. The "Lateral Interaction Model" generally gave a satisfactory prediction of the experimental response for $\varepsilon_L < 6\%$, which covers and exceeds the strain range from which this model was calibrated. However at larger strains, this model underestimated the longitudinal stress carried by the concrete. This is a direct consequence of the overestimation of tube σ_L and hence underestimation of tube $|\sigma_H|$ and concrete confining stress f_R which were discussed in the previous sections.

3.5.3.5 General Discussion

This series of tests has shown that the stress-strain responses of thick-walled (D/t = 25.6) concrete-filled tubes can be predicted satisfactorily by the "Lateral Interaction Model" for $\varepsilon_L \leq 4\%$, which corresponded to the level of strain from which this model (see Section 2.4.2) was calibrated. However at strains much larger than 4%, tube σ_L was generally overestimated, and tube σ_H, concrete f_L and f_R were generally underestimated. Despite this observation for $\varepsilon_L < 8\%$, the "Lateral Interaction Model" gave good predictions to the overall P vs ε_L response, while for $\varepsilon_L > 8\%$, the "Lateral Interaction Model" is conservative.

The main reason for this conservatism at large strains is the assumption that for $\varepsilon_L \geq 1\%$, the longitudinal stress in the tube is constant. The experimental results show a significant reduction to the longitudinal-compression stress in the tube occurs as ε_L increases above 4%, with a corresponding increase in hoop-tension stress in the tube which also increases the level of confining stress in the concrete above the predicted level. The result (for $\varepsilon_L > 4\%$) is an underestimation of the longitudinal load carried by the concrete. Since the tube is more efficiently utilised confining the concrete than directly resisting the longitudinal load (see Section 2.2.6.2), the result was the observed underestimation of the overall load carried by the concrete-filled tube at large strains. It should be noted that this modified behaviour could be included in the "Lateral Interaction Model" by redefining the longitudinal stress-strain relationship assumed for the tube at ε_L larger than 4%. However, the experimental data produced by the test programme was insufficient to justify such a modification to the theory. Further, since the P vs ε_L prediction is satisfactory for $\varepsilon_L < 8\%$, there is little engineering significance in modelling experimental behaviour at larger strains.

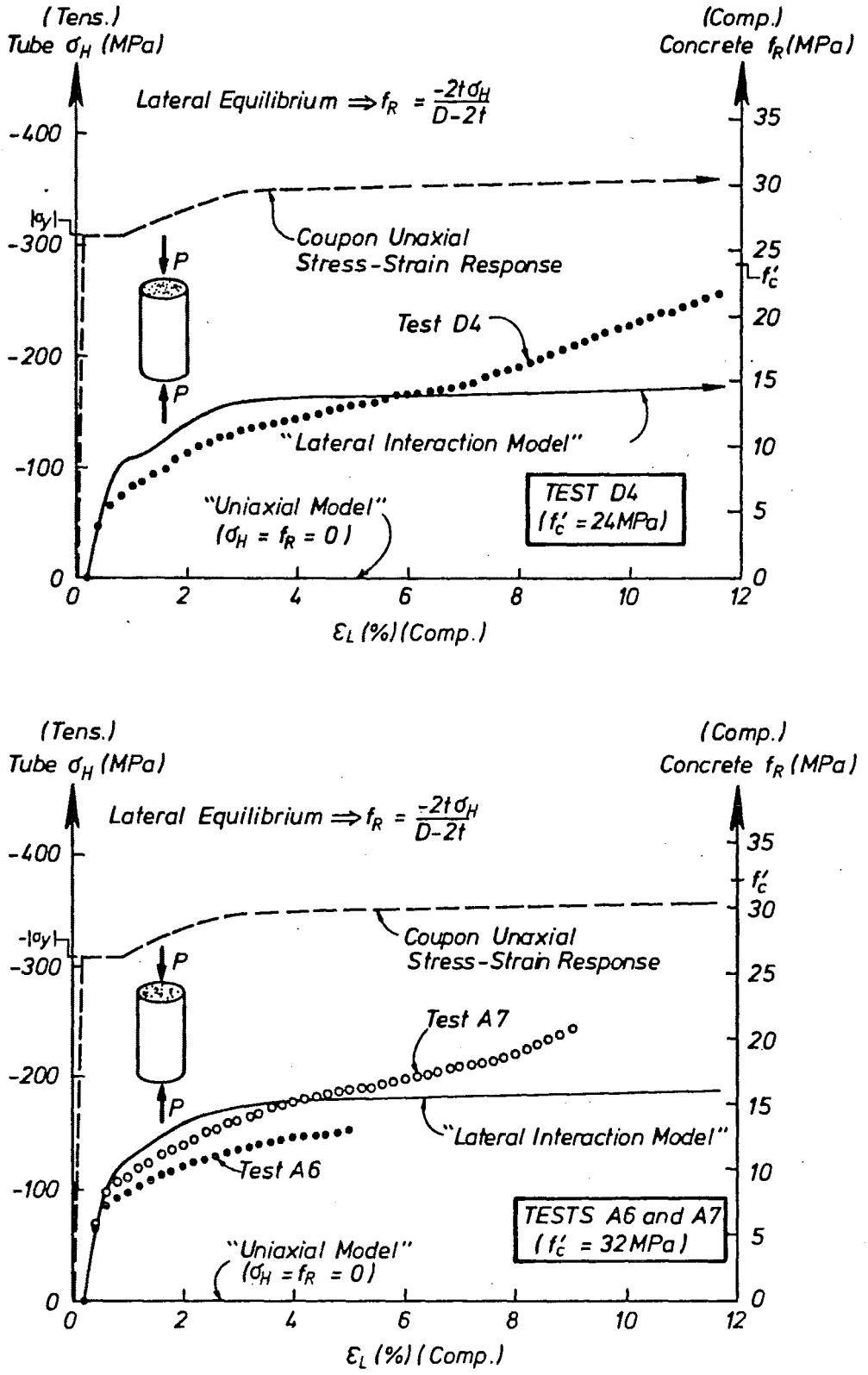

FIG. 3.33 : TUBE HOOP (AND CONCRETE RADIAL) STRESS-LONGITUDINAL STRAIN COMPARISONS FOR MONOTONIC COMPRESSION-LOAD TESTS

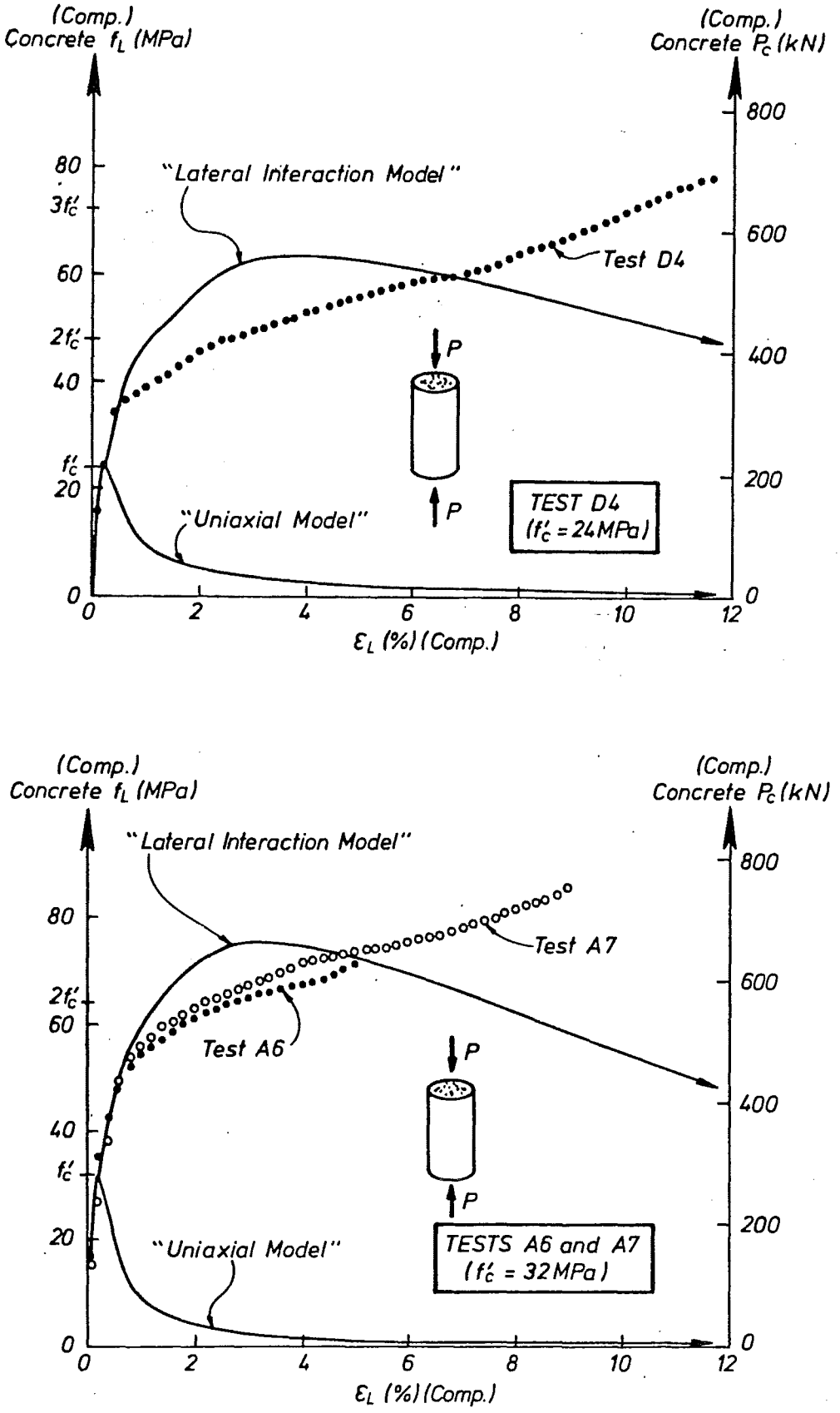

FIG. 3.34 : CONCRETE LONGITUDINAL STRESS-LONGITUDINAL STRAIN COMPARISONS FOR MONOTONIC COMPRESSION-LOAD TESTS

Although the comparisons contained in Figs. 3.31 - 3.34 are valid, they represent behaviour at sections away from the regions of local buckling. At a local buckle the longitudinal strains in the concrete will be very large, and it is likely that the longitudinal-compression stress carried by the tube is negligible. Assuming the tube $\sigma_H = -|\sigma_u| = -361$ MPa, then from lateral equilibrium of concrete and tube (equation 2.54) concrete $f_R = 30.65$ MPa. The concrete f_L vs ε_L (and hence P_c vs ε_L and P vs ε_L) responses predicted by the "Lateral Interaction Model" for tests with $f'_c = 24$ MPa (D4) and 32 MPa (A6 and A7) and $f_R = 30.65$ MPa are shown in Fig. 3.35. These predictions represent envelopes to possible concrete f_L vs ε_L response since in general tube $|\sigma_H| \leq |\sigma_u|$ and hence concrete $f_R \leq 30.65$ MPa. These predictions also represent a substantial extrapolation of the data from which the "Lateral Interaction Model" was calibrated, since the curves plotted represent response for $f_R/f'_c = 0.958$ or 1.277 and the model was only calibrated for $f_R/f'_c \leq 0.5$. In tests D4, A6 and A7, local buckles occurred adjacent to the tube ends. Thus there is also additional confinement to the concrete at these positions due to restraint of lateral strains at the ends of the test unit caused by the attachment to the test machine. Nevertheless from Fig. 3.35 large longitudinal loads are predicted to be carried at the sections of local buckling, as can be seen by a comparison with Fig. 3.31 which represents behaviour away from the regions of local buckling. This helps to provide an explanation for why the load-carrying capacity continues to rise despite the presence of extensive local buckling on the tube.

It is also significant to note that in test D8, which involved cyclic tensile and compressive longitudinal loading followed by a large amplitude of compressive ε_L, a longitudinal load of 1228 kN was recorded at an ε_L of 26% (assessed on a 230 mm gauge length). From the trend indicated in the plot of tube biaxial-stress paths (Fig. 3.30), it can be assumed that at this level of ε_L, tube $\sigma_L = 0$ and hence concrete $f_L = 139$ MPa ($= 5.8f'_c$). This concrete stress is larger than the value of $4.7f'_c$ which could be predicted from the "Lateral Interaction Model" (assuming tube $\sigma_L = 0$) and thus again it is indicated that this model is conservative at $\varepsilon_L > 8\%$.

3.5.4 Monotonic Longitudinal-Tension-Load Test of a Concrete-Filled Tube

3.5.4.1 Longitudinal Load vs Longitudinal Strain Comparison

Figure 3.36 shows a comparison of the experimental and theoretical variations of longitudinal load (P) with longitudinal strain (ε_L).

Results plotted to the full strain scale indicate that excellent agreement occurs between experimental results and a prediction based on the "Lateral Interaction Model" with the experimental response being appreciably stiffer and stronger than that predicted from the "Uniaxial Model". For example at $\varepsilon_L = -3\%$, the actual load carried was equal to 114% of the load predicted from the "Uniaxial Model".

Results plotted to the expanded strain scale indicate that response in the elastic range of tube behaviour is better predicted by the "Lateral Interaction Model" than it is by the "Uniaxial Model", although predictions by both models underestimate the experimental load at a given strain. The discontinuities in load for the predictions correspond to the tube yielding at a crack in the "Lateral Interaction Model", at which stage it is assumed that the concrete has no further tension-stiffening effect, and to the concrete cracking in the "Uniaxial Model". The indicated initial experimental stiffness is approximately 10% greater than the initial stiffness predicted by the "Lateral Interaction Model" which implies that basing the concrete modulus on $E_c = 5000\sqrt{f'_c}$ provides a low estimate to the actual initial concrete stiffness. After concrete cracking, the level of indicated longitudinal strain (measured from the average of the longitudinally

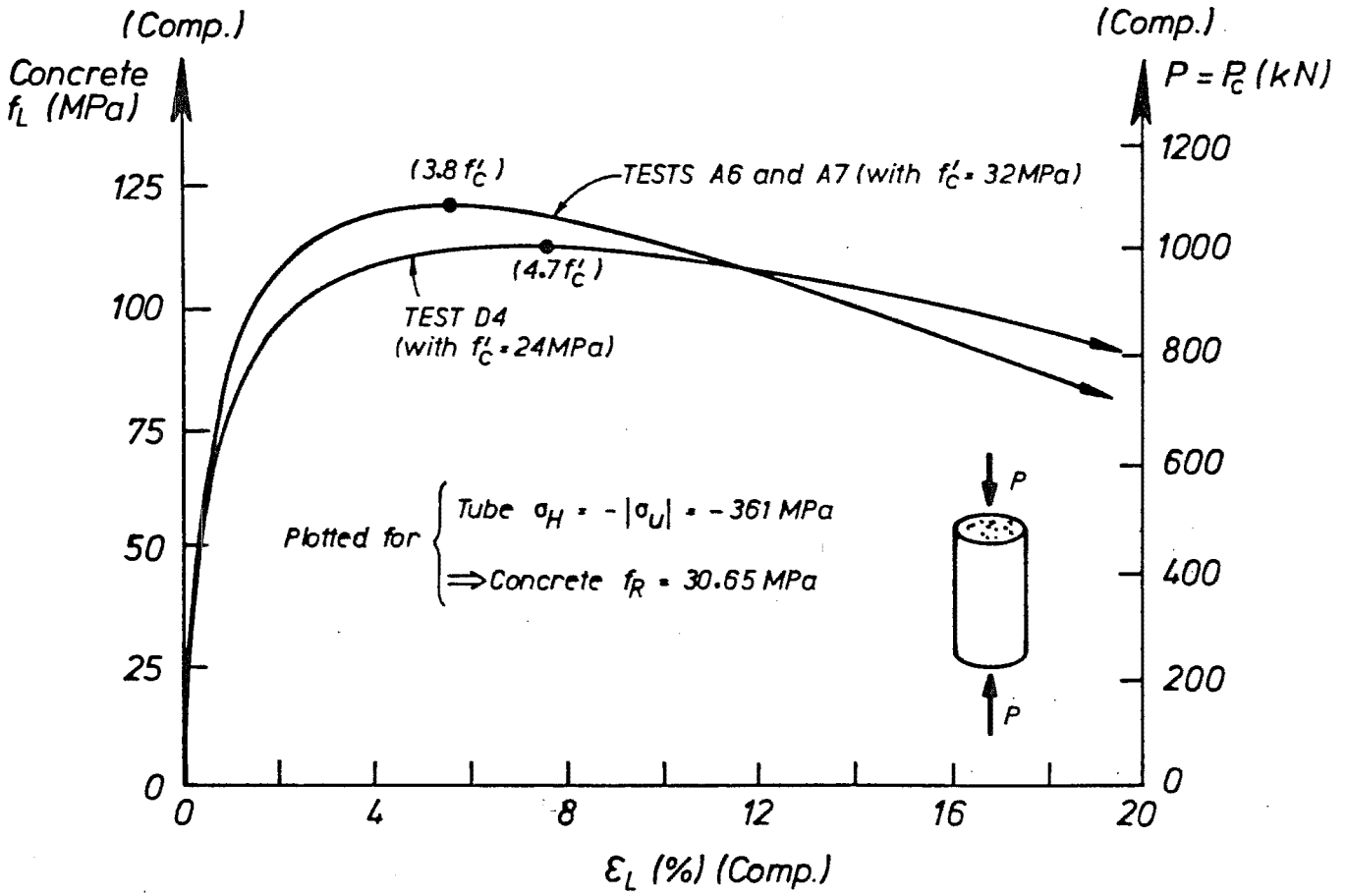

FIG. 3.35 : THEORETICAL LONGITUDINAL-COMPRESSION STRESS-STRAIN RESPONSE OF THE CONCRETE (ASSUMING TUBE HOOP-TENSION STRESS IS EQUAL TO ITS ULTIMATE STRESS)

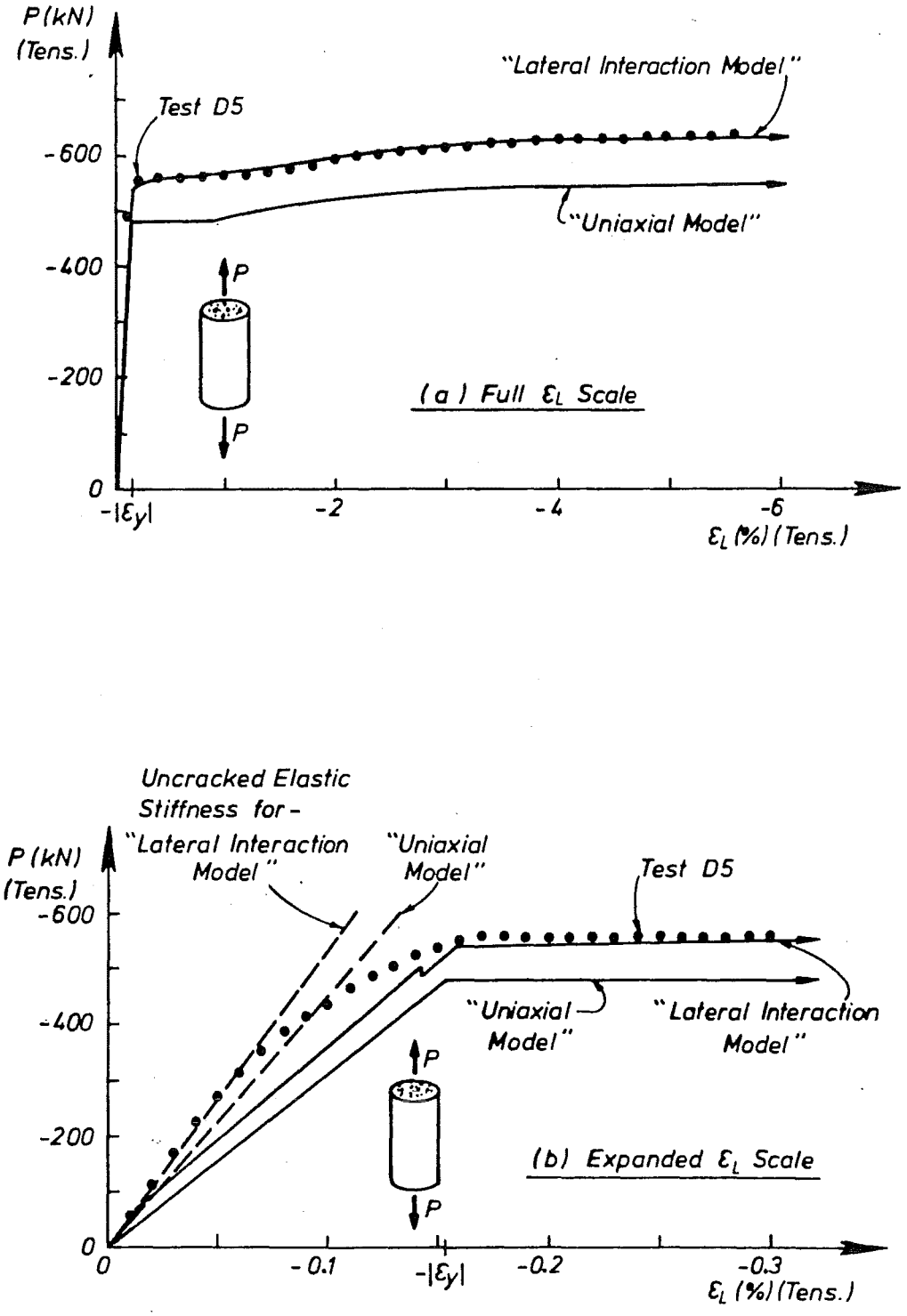

FIG. 3.36 : LONGITUDINAL LOAD-LONGITUDINAL STRAIN COMPARISON FOR MONOTONIC TENSION-LOAD TEST

orientated strain gauges) is sensitive to the position of the strain gauges relative to the position of the concrete cracks, since at a crack the tube ε_L will be larger than the tube ε_L half-way between the crack as was shown in Fig. 2.17. A comparison of the P vs ε_L responses indicated by the strain gauges (very short gauge lengths < 10 mm) and the linear potentiometers (115 mm gauge length) for concrete-filled tube D4 (see Fig. 3.10) at $|\varepsilon_L| < |\varepsilon_y|$ shows the potentiometers indicate a stiffer response which implies the strain gauges were located close to concrete cracks.

3.5.4.2 Tube Longitudinal Stress vs Longitudinal Strain Comparison

In Fig. 3.37, the deduced tube σ_L (and P_t) vs ε_L experimental response is compared with theoretical predictions.

In the elastic range of tube behaviour it is shown that response is correctly predicted by the "Uniaxial Model", since at this stage lateral interaction of tube and concrete has not occurred, as was shown previously in Fig. 3.24 where both empty and concrete-filled tubes have similar values of ε_H for $|\varepsilon_L| \leq |\varepsilon_y|$. Thus the prediction from the "Lateral Interaction Model", which is based on lateral interaction producing an enhancement of tube σ_L from the presence of a biaxial-tension-stress field in the tube, is shown to overestimate the actual tube response since at this stage the tube is behaving in a uniaxial-tension-stress fashion.

In the strain-hardening range of tube behaviour, the "Lateral Interaction Model" closely predicts the experimental response which indicates at this stage that a biaxial-tension-stress field with large values of hoop-tension stress ($\sigma_H \cong 0.5\sigma_L$) has developed.

In the yield range of tube behaviour, experimental response gradually increases from that predicted by the "Uniaxial Model" to that predicted by the "Lateral Interaction Model".

3.5.4.3 Tube Hoop Stress and Concrete Radial Stress vs Longitudinal Strain Comparison

In Fig. 3.38 the deduced tube σ_H (and concrete f_R) vs ε_L experimental response is compared with the theoretical predictions, and also with the uniaxial-stress-strain (σ_L vs ε_L) response of a coupon sample of the tube. For $|\varepsilon_L| < |\varepsilon_y|$, due to concrete Poisson's ratio contraction and an initial small gap between tube and concrete, which was probably caused when the concrete cooled down after the initial rise in temperature associated with heat of hydration, negligible interaction occurs resulting in zero values for concrete f_R and tube σ_H. For $|\varepsilon_L| > |\varepsilon_y|$, as $|\varepsilon_L|$ increases concrete f_R and tube $|\sigma_H|$ also increase. At an ε_L of -5.5%, a tube σ_H of -200 MPa and a concrete f_R of 17 MPa were reached, indicating a large level of lateral interaction between tube and concrete.

Although the "Lateral Interaction Model" overestimates the experimental response, it gives a reasonable prediction when compared with the response indicated by the coupon and the "Uniaxial Model". It should again be noted that in the "Lateral Interaction Model" it is assumed that the concrete is laterally rigid, with the consequence that the actual concrete and tube lateral stresses are overestimated as discussed previously in Section 2.3.2.4.

3.5.4.4 Tube Hoop Stress and Concrete Radial Stress vs Concrete Radial Strain Comparison

Figure 3.39 shows the deduced radial stress-strain (f_R vs ε_{RC}) response of the concrete where it is assumed that from lateral compatibility of concrete and tube, concrete ε_{RC} is equal to the measured tube ε_H, although strictly at small levels of strain ($|\varepsilon_L| < |\varepsilon_y|$ or $\varepsilon_H < \nu_s |\varepsilon_y|$) before the tube and concrete interact $\varepsilon_{RC} < \varepsilon_H$. Also shown in the figure are predictions

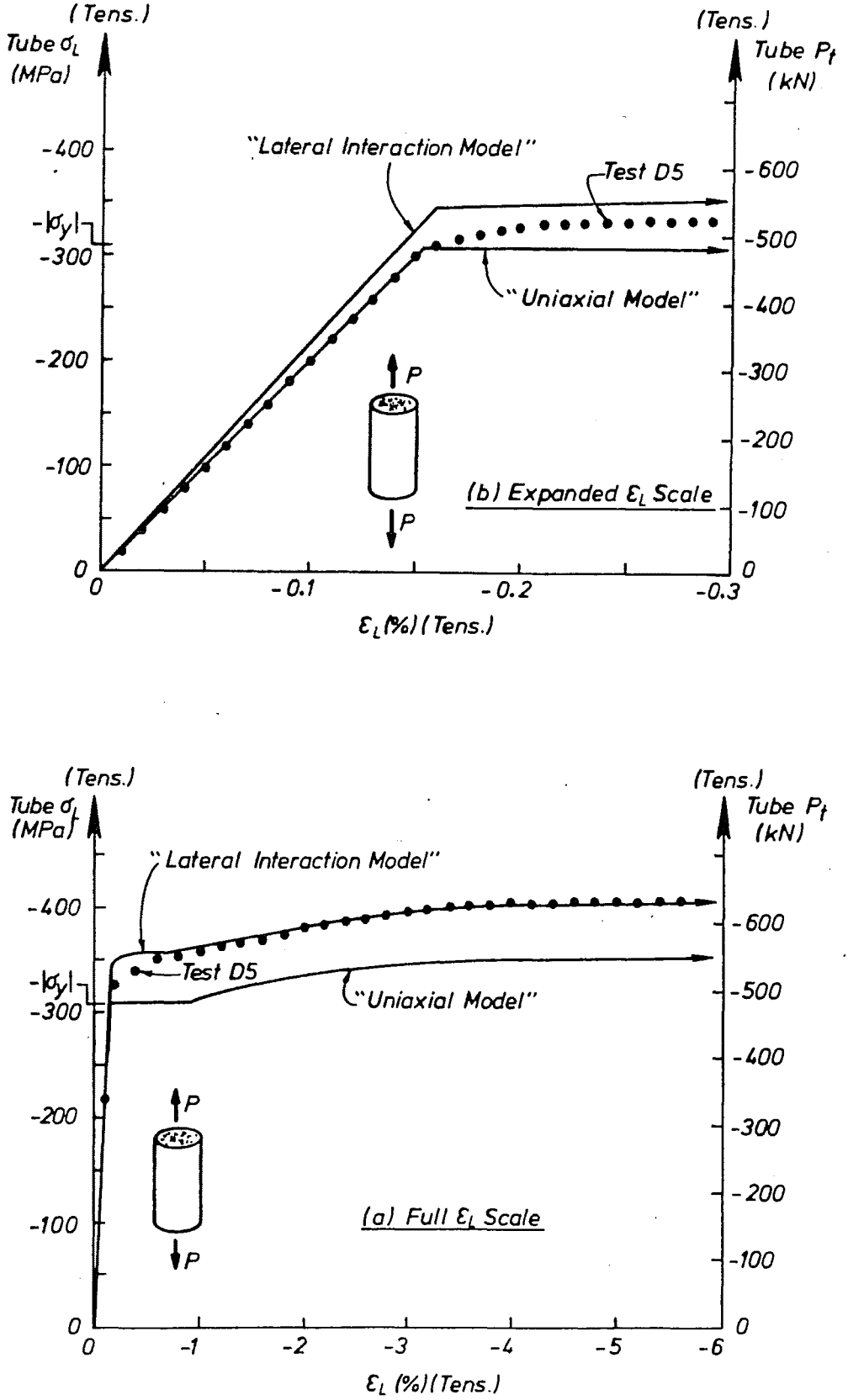

FIG. 3.37 : TUBE LONGITUDINAL STRESS-LONGITUDINAL STRAIN COMPARISON FOR MONOTONIC TENSION-LOAD TEST

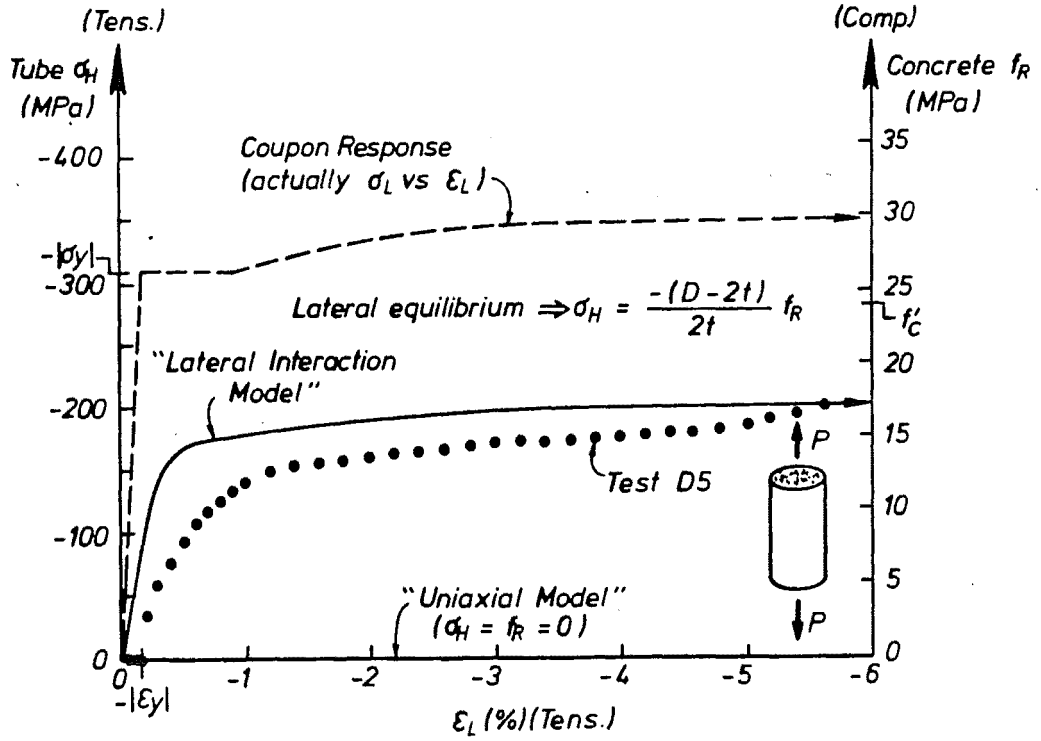

FIG. 3.38 : TUBE HOOP (AND CONCRETE RADIAL) STRESS-LONGITUDINAL STRAIN COMPARISON FOR MONOTONIC TENSION-LOAD TEST

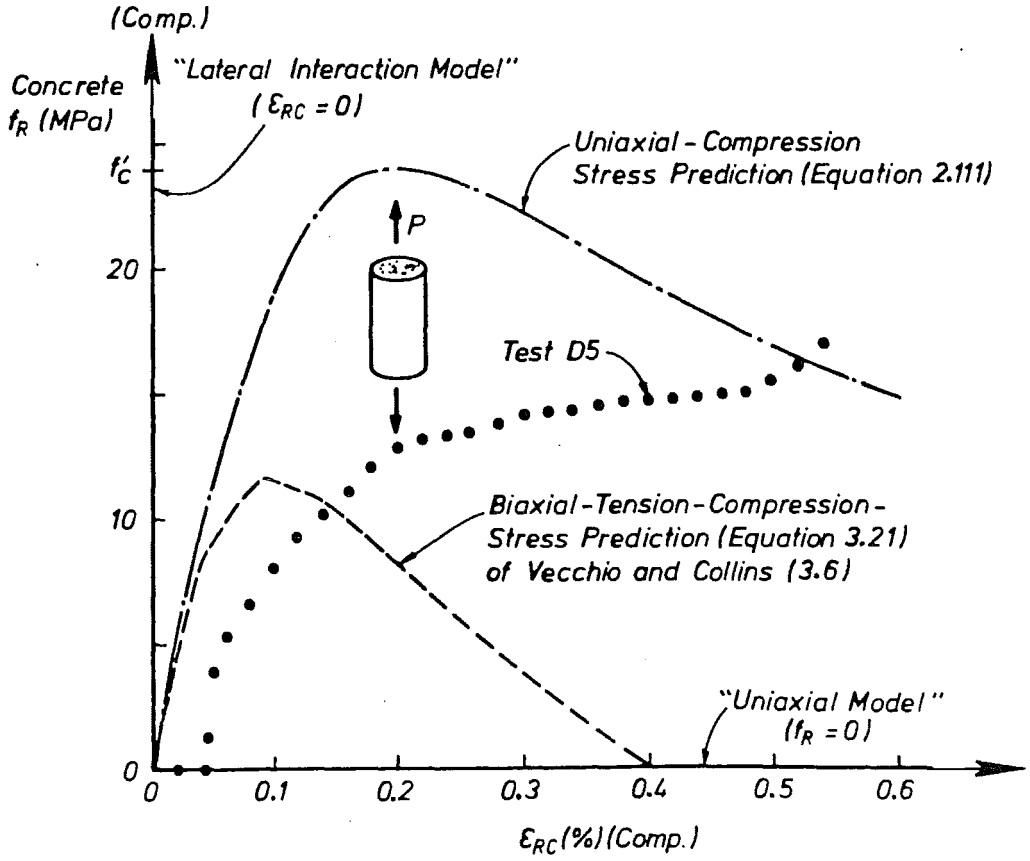

FIG. 3.39 : CONCRETE RADIAL STRESS-CONCRETE RADIAL STRAIN COMPARISON FOR MONOTONIC TENSION-LOAD TEST

based on the "Uniaxial Model" ($f_R = 0$) and the "Lateral Interaction Model" ($\varepsilon_{RC} = 0$), together with the theoretical uniaxial stress-strain response of the concrete (as described by equation 2.111 with f_R and ε_{RC} substituted for f_L and ε_L respectively) and the empirical relationship of Vecchio and Collins (3.6) which was calibrated from biaxial-tension-compression-stress tests of reinforced concrete panels as described previously in Section 2.3.2.4. This relationship can be expressed as:

$$f_R = \frac{f'_c \left[2(\varepsilon_{RC}/0,002) - (\varepsilon_{RC}/0.002)^2\right]}{0.8 - 170\varepsilon_L} \qquad (3.21)$$

The experimental results indicate that negligible lateral interaction (i.e. $f_R = 0$) occurs between tube and concrete for $\varepsilon_{RC} < 0.043\% \cong \nu_s |\varepsilon_y|$ (where $\nu_s = 0.28$ and $|\varepsilon_y| = 0.001540$). None of the theoretical predictions give good agreement with the experimental response. However it is shown that the triaxial-compression-compression-tension-stress state of the concrete inside the tube results in the concrete having a stronger and more ductile performance, in the radial direction, than that which would be predicted from the biaxial-compression-tension-stress relationship of Vecchio and Collins. Thus the presence of a third principal stress as compression clearly enhances the performance of the concrete. Nevertheless comparison with the uniaxial-compression-stress-strain curve indicates a very significant decrease in radial-compression strength results from the presence of longitudinal-tension strain which confirms the trend of strength reduction predicted by the use of the Vecchio and Collins relationship.

3.5.4.5 Concrete Longitudinal Stress vs Longitudinal Strain Comparison

In Fig. 3.40, the deduced concrete f_L (and P_c) vs ε_L experimental response is compared with theoretical predictions. The comparison shows that for $|\varepsilon_L| < |f_t|/E_c$, a good match between experiment and theory is obtained. However for $|\varepsilon_L| > |f_t|/E_c$, experimental and theoretical responses are greatly divergent. The experimentally obtained peak value of f_L is -15.4 MPa which is 4.1 times as large as the value of f_t which is used in the "Latest Interaction Model". Since in test unit D5 for $|\varepsilon_L| < |\varepsilon_y| = 0.001540$, concrete and tube do not interact laterally, the only plausible explanation for this wide divergence of theory and experiment is that prestress was inadvertently applied to the concrete during welding of the concrete-filled tube in the test machine assembly (see Fig. 3.3). It is probable that despite the care taken during welding to avoid overheating the test unit, residual pretension-longitudinal stress in the tube and precompression-longitudinal stress in the concrete were present immediately prior to testing.

The thermal conductivity of steel is approximately 600 times that of the concrete (3.5). Thus after welding of the test unit, heat is predominantly transferred longitudinally out of the test unit through the tube. The coefficients of linear expansion of concrete and tube are similar (3.5) at approximately 0.000012/°C. Hence the result of the greater conductivity of the steel than of the concrete is that during cooling the tube attempts to shorten by a large amount while the concrete has a negligible tendency to shorten. Compatibility of longitudinal strains between tube and concrete results in longitudinal-tension stress in the tube and longitudinal-compression stress in the concrete.

The difference between the peak experimental and theoretical concrete f_L was 11.6 MPa. For this difference to be attributed to thermal prestress, then a residual tube σ_L of -66 MPa ($= -f_L.A_c/A_t$) was present immediately prior to testing. The longitudinal strain in the concrete immediately prior to testing will be equal to

$$\varepsilon_L = \frac{f_L}{E_c} = \frac{11.6}{5000\sqrt{24}} = 0.000474$$

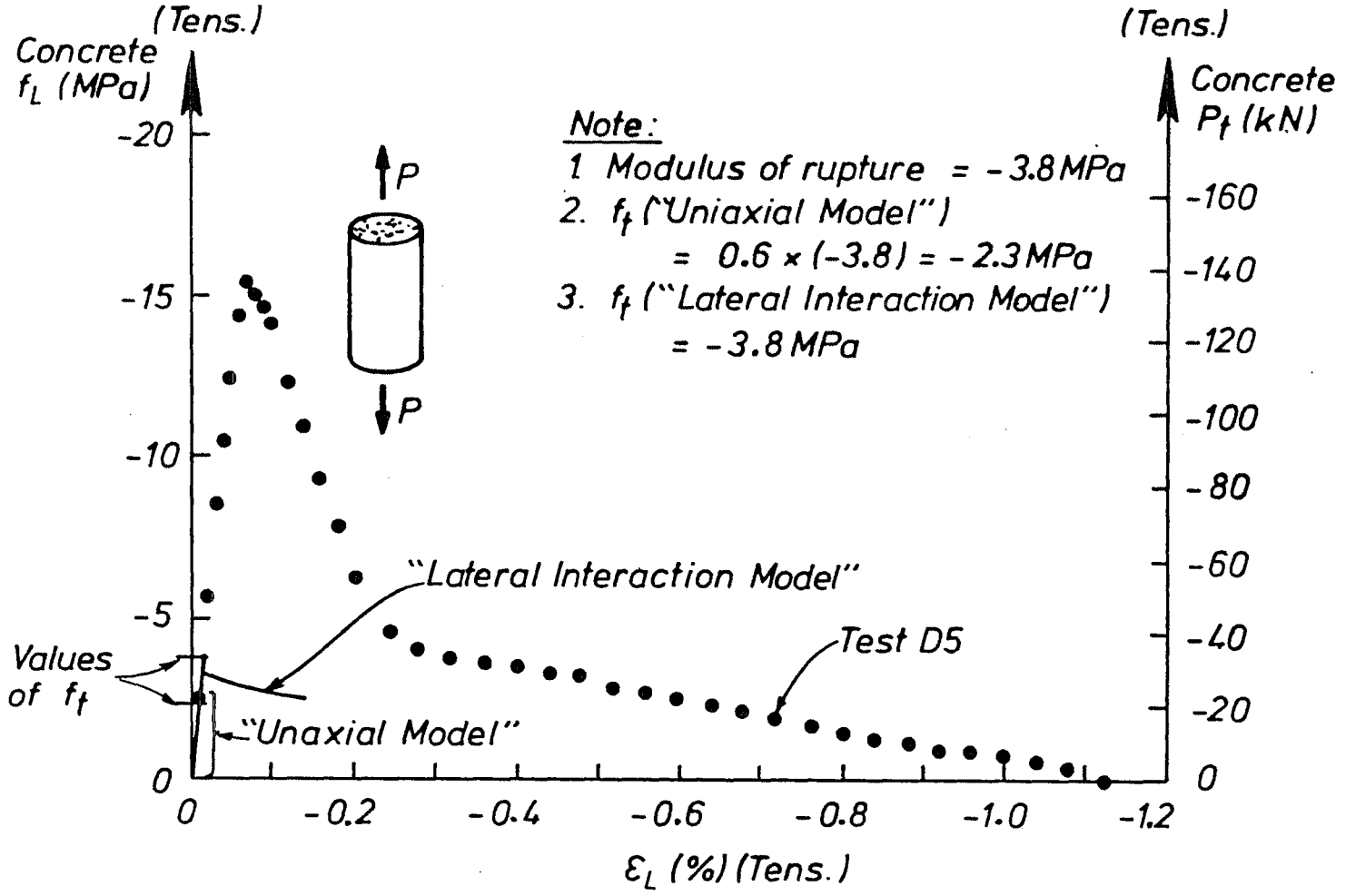

FIG. 3.40 : CONCRETE LONGITUDINAL STRESS-LONGITUDINAL STRAIN COMPARISON FOR MONOTONIC TENSION-LOAD TEST

Longitudinal stress in the tube can be expressed as:

$$\sigma_L = E_s (\varepsilon_L - 0.000012 \cdot \Delta T) \qquad (3.22)$$

where ΔT is the difference between ambient temperature and temperature of the test unit at the cessation of welding and 0.000012 is the coefficient of linear expansion. Equation 3.22 can be solved to give $\Delta T = 67°$.

The above analysis greatly simplifies the actual behaviour of the concrete-filled tube both during and after welding, for example as time proceeds, creep will reduce the prestress effect and thus a larger value of ΔT would be needed to achieve the same values of residual stress in tube and concrete. Nevertheless, it has been demonstrated that the stiffer than anticipated experimental P vs ε_L response, for $|f_t|/E_c < |\varepsilon_L| < |\varepsilon_y|$ is probably due to the inadvertently introduced presence of precompression stress in the concrete.

The gradual decay of the concrete f_L vs ε_L response (see Fig. 3.40) occurs because of the stiffening of the tube between concrete cracks, as discussed previously in Section 2.3.2.1.

3.5.4.6 General Discussion

Despite the simplifying assumption in the "Lateral Interaction Model" (see Section 2.3.2) that tube $\varepsilon_H = 0$, the experimental P vs ε_L response was predicted satisfactorily by this model for $|\varepsilon_L| > |\varepsilon_y|$ and underestimated for $|\varepsilon_L| < |\varepsilon_y|$. The underestimate at low strains could be explained by thermally introduced prestress in the concrete-filled tubes.

In Section 2.3.2.4, two possible limitations to the "Lateral Interaction Model" were discussed which involved:

(i) the effect of concrete lateral flexibility and a tube-concrete gap; and

(ii) concrete radial strength.

These points were shown in Section 2.3.2.4 to reduce the potential enhancement of tube σ_L which occurs in a biaxial-tension-stress field. The experimental results discussed previously indicated that for $|\varepsilon_L| < |\varepsilon_y|$, concrete Poisson's ratio lateral contraction and the initial presence of a tube-concrete gap resulted in tube $\sigma_H = 0$ and hence a uniaxial stress response from the tube. For $|\varepsilon_y| < |\varepsilon_L| < |\varepsilon_{sh}|$, concrete lateral flexibility prevented the full 15.5% enhancement of tube σ_L. However for $|\varepsilon_L| > |\varepsilon_{sh}|$, concrete lateral flexibility did not prevent tube σ_L from equalling $-1.155\sigma_{eff}$. Furthermore in this concrete-filled tube test, concrete radial strength was shown to be adequate to equilibrate the large values of tube $|\sigma_H|$ (up to $0.5777|\sigma_u|$) which occur in the tube.

Since for thick-walled concrete-filled tubes, concrete radial strength and stiffness have been shown to be adequate in developing the large values of hoop-tension stress (i.e. $\sigma_H = -0.577\sigma_{eff}$) in the tube which are necessary to give enhanced tube σ_L (i.e. $\sigma_L = -1.155\sigma_{eff}$); it is also clear from Section 2.3.2.4 that thin-walled concrete-filled tubes, for which concrete radial stresses will be smaller, will be even better predicted by the "Lateral Interaction Model".

In deducing tube (σ_L and σ_H) and concrete (f_L and f_R) stresses as discussed in previous sections (3.5.4.2 - 3.5.4.5) and shown in Figs. 3.37 - 3.40, it was assumed that at the commencement of testing concrete and tube were free of residual stresses. However as demonstrated in Section 3.5.4.5 residual stresses were present due to welding. Thus strictly the deduced stresses should be corrected to allow for these residual stresses, as is shown in Fig. 3.41 for the σ_L and f_L vs ε_L responses. Small and less significant corrections should also be made to the σ_H and f_R vs ε_L responses. From Fig. 3.41, it can be

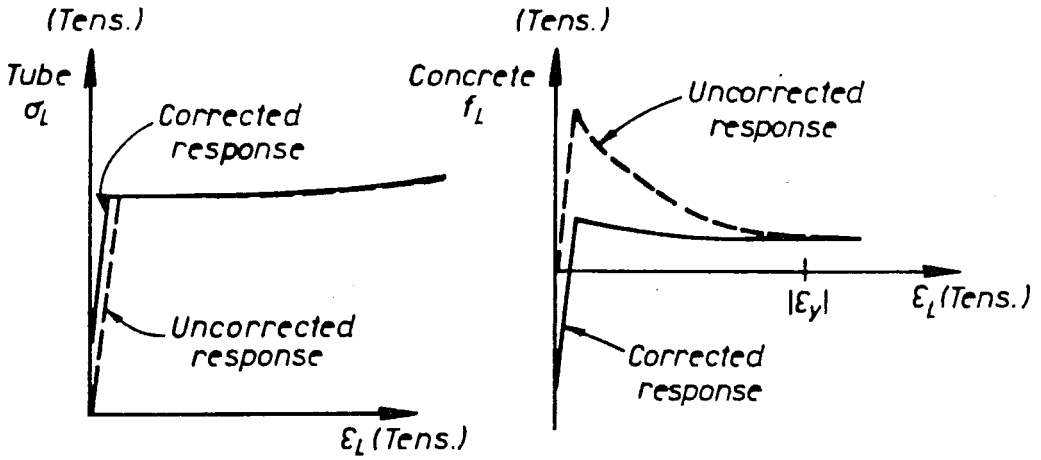

FIG. 3.41 : ALLOWING FOR RESIDUAL LONGITUDINAL STRESSES IN TUBE AND CONCRETE

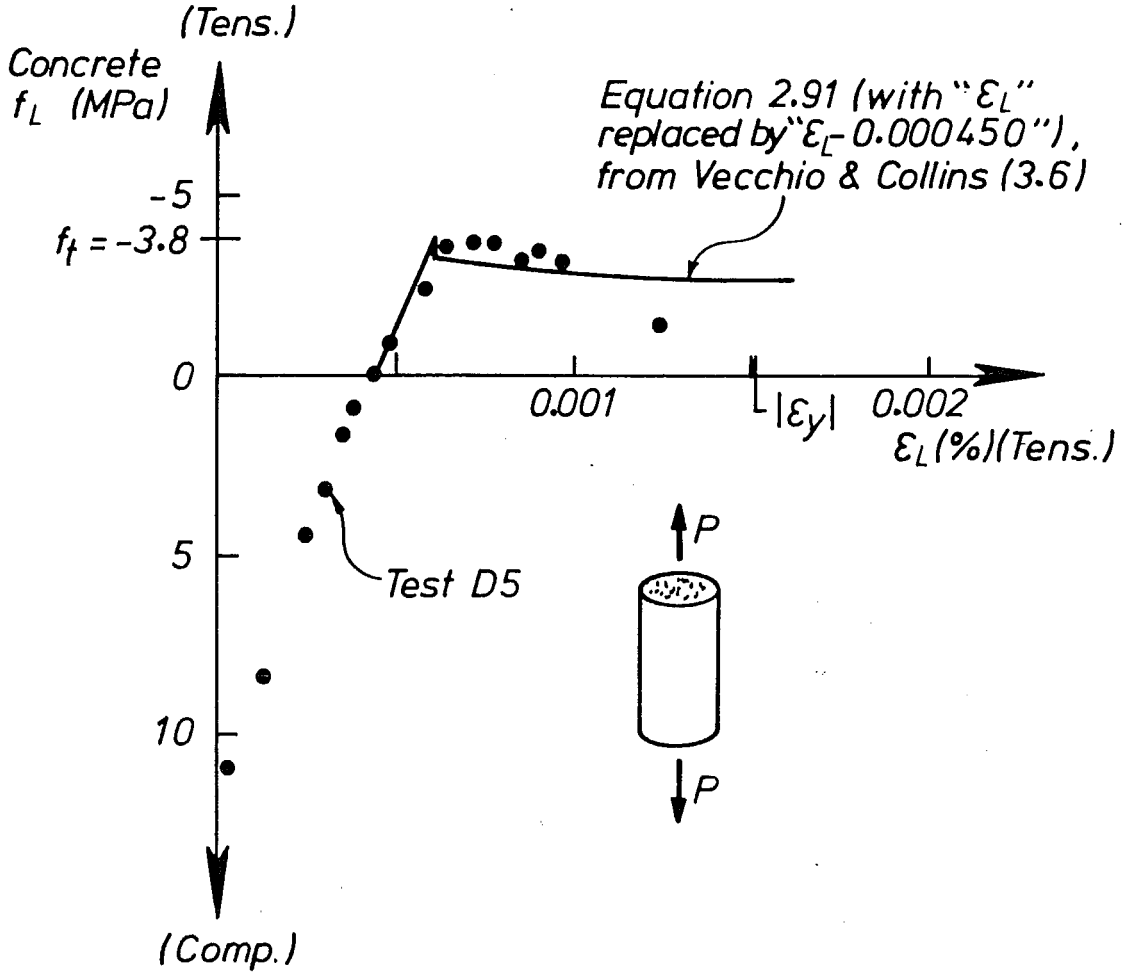

FIG. 3.42 : COMPARISON OF CORRECTED CONCRETE LONGITUDINAL STRESS-LONGITUDINAL STRAIN RESPONSE WITH VECCHIO AND COLLINS (3.6) RELATIONSHIP FOR MONOTONIC TENSION-LOAD TEST

seen that at large strains ($|\varepsilon_L| > |\varepsilon_y|$) the correction makes little difference. However for $|\varepsilon_L| < |\varepsilon_y|$ the correction makes a substantial difference to both the peak concrete stress and the shape of the f_L vs ε_L relationship. In Fig. 3.42 the corrected concrete f_L vs ε_L response is compared with a modified form (i.e. replacing "ε_L" with "ε_L - 0.000450") of the Vecchio and Collins (3.6) empirical relationship (see equation 2.91) for the concrete-tension-stiffening effect. Clearly the corrected response gives good agreement with the modified form of the empirical relationship.

3.6 CONCLUSIONS

In this chapter experimental results from the longitudinal-load testing of short thick-walled concrete-filled tubes were described and compared with theoretical predictions. The main conclusions from this work are described below.

3.6.1 Monotonic Compression Tests

Despite the occurrence of local buckling at a longitudinal strain of approximately 2%, the concrete-filled tubes showed a large reserve of ductility, with load-carrying capacity still increasing at a longitudinal strain of greater than 21%. In comparison, the empty tubes failed due to local buckling at a measured longitudinal strain of 2% and unconfined concrete reaches peak load at a longitudinal strain of approximately 0.2%.

At a given longitudinal strain greater than 0.2%, restraint of concrete dilation resulted in the steel in a concrete-filled tube being subjected to a larger hoop-tension strain than is the steel in an empty tube. This lateral interaction of tube and concrete resulted in increasing levels, as loading proceeded, of hoop-tension stress in the tube and radial-compression stress in the concrete. At a longitudinal strain of 12%, a tube hoop-tension stress of 83% of the yield stress, and a concrete radial-compression stress of 90% of the unconfined-compression strength were deduced to be present. Accompanying these lateral stresses were a concrete longitudinal-compression stress of 330% of the unconfined-compression strength and a tube longitudinal-compression stress of 50% of the yield stress. Thus the lateral interaction resulted in a redistribution of longitudinal load-carrying capacity from the tube to the concrete.

Theoretically predicted longitudinal load vs longitudinal strain responses based on the "Lateral Interaction Model" were found to be in generally good agreement with the experimentally obtained responses for longitudinal strains less than 8%. Predicted responses based on the "Uniaxial Model" underestimated the experimentally obtained responses.

The longitudinal extent of local buckling was predicted satisfactorily by using a tangent modulus buckling formula and assuming the local buckle could be analysed as an equivalent column. In the tests local buckles were observed to form at the ends of the test units. An "equivalent frame analogy" analysis of the tube successfully predicted the position of these local buckles which occur at the ends due to the effect of test machine introduced lateral restraint of the test units.

Predictions to the experimental ultimate load based on the formula of Sen, the "Uniaxial Model" and the "Lateral Interaction Model" were found to be conservative. However the formula of Sen predicted a level of longitudinal load which was obtained at longitudinal strains appreciably in excess of 9%, implying that serviceability limitations would govern design rather than this formula.

3.6.2 Monotonic Tension Test

The longitudinal load vs longitudinal strain response of the concrete-filled tube was stronger and stiffer but less ductile than that of the empty tube.

In the elastic range of tube behaviour, the tube response tended to follow that predicted by the "Uniaxial Model", while in the strain-hardening range of tube behaviour, the tube response tended to follow that predicted by the "Lateral Interaction Model". In the yield range of tube behaviour, the tube response was intermediate between those predicted by the two models.

The response of the concrete was satisfactorily predicted by the "Lateral Interaction Model" which allowed for the effect of tension-stiffening of the tube between concrete cracks. However to achieve this good comparison it was necessary to allow for the effect of residual stresses due to welding.

In the plastic range of tube behaviour, the core concrete was shown to significantly restrict the Poisson's ratio hoop contraction of the tube. This resulted in large values of both hoop-tension stress in the tube ($|\sigma_H| \leq 200$ MPa) and radial-compression stress in the concrete ($f_R \leq 17$ MPa). The hoop-tension stress resulted in an enhancement to the longitudinal-tension stress in the tube above that present at the same longitudinal strain for zero hoop-tension stress.

3.6.3 Cyclic Tension and Compression Tests

The main difference between the envelopes to the cyclic longitudinal load vs longitudinal strain responses of the empty and concrete-filled tubes occurred in the quadrant with compressive values of load and strain. In this quadrant the concrete-filled tube had a markedly stronger response than did the empty tube, since the concrete stabilised tube local buckling and the tube confined the concrete. In the quadrant with tensile values of load and strain, empty and concrete-filled tube responses were similar, particularly at large strain levels, since the cyclic loading severely deteriorated the radial strength and stiffness of the concrete and also the ability of the concrete to carry tensile stress between the cracks.

Chapter Four

FLEXURAL STRENGTH AND DUCTILITY CHARACTERISTICS OF STEEL-ENCASED CONCRETE

4.1 INTRODUCTION

The importance of stable ductile performance in steel-encased concrete piles under lateral seismic-induced loading was established in Chapter 1. In Chapter 4, the following topics are covered:

(i) Previous research which is relevant to the flexural strength and ductility characteristics of steel-encased concrete piles is reviewed.

(ii) The design, construction, instrumentation and testing of nine circular-sectioned model piles are described. The main factors investigated in the tests were: (a) the effect of the casing D/t ratio (within the range of 34 to 214); and (b) the effect of the continuity of the casing in the plastic hinge zone (7 models with continuous casing and 2 models with circumferential discontinuities in the casing).

(iii) Results from the tests are presented in the form of hysteresis loops of lateral load-lateral deflection and lateral load-plastic hinge rotation responses. The distribution of curvature along the length of the test units, and strain in the vicinity of the critical plastic sections are also given. Experimentally obtained strengths are compared with theoretical ultimate strengths predicted on the basis of the steel-encased reinforced concrete member behaving as an equivalent reinforced concrete member.

(iv) Investigations of the effect of shear force on flexural behaviour, the possibility of strain-age embrittlement of the casing, and the bond strength between tube and concrete are described.

(v) The strength, ductility and energy-dissipating characteristics of the steel-encased reinforced concrete members and conventionally designed reinforced concrete members are compared.

(vi) Recommendations for the design of steel-encased reinforced concrete members are given.

Tables (4.1-4.9) of results for this chapter are contained immediately after Section 4.13.2.

4.2 PREVIOUS RESEARCH

Due to soil-bearing stress considerations, the longitudinal load on a pile is generally small when compared with the ultimate strength of the pile member. Thus in analysing piles for local and overall buckling effects it can be assumed that behaviour is dominated by flexural rather than longitudinal loads.

4.2.1 Empty Tubes Under Flexural Loading

Only a small amount of theoretical work has been performed concerning the problem of local buckling of thin cylinders under pure bending, and contradictory experimental evidence exists. Gerard and Becker (4.1) have suggested that the elastic buckling stress for empty tubes subjected to flexure is 1.3 times the value appropriate for longitudinal-compression loading. This has been verified by some experiments, for example those of Brazier (4.2) and Chwalla (4.3) and justified theoretically by Flugge (4.4). However other experimental results such as those of Dinnick (4.5) gave critical stresses that were smaller than those appropriate for longitudinal-compression load. Schilling (4.6) has commented that when the plastic

moment is attained the gradient in tube σ_L is practically zero over most of the critical section. Thus at this stage of well-developed plasticity over the section, local buckling behaviour of members under flexural or longitudinal-compression load are essentially identical.

Little (4.7) as a result of his and other investigators' work (4.6, 4.8 and 4.9) has prepared a design chart (see Fig. 4.1) for the value of design stress to be used in calculating the ultimate moment of a member as a function of casing D/t ratio and casing σ_y for the case where local buckling is critical. For mild steel, with for example σ_y = 250 MPa, it appears that the full plastic moment cannot be attained for casing D/t ratios which exceed 50, and for a casing D/t ratio of 150 the design moment will be only 66% of the plastic moment. High strength steels are affected by local buckling at smaller casing D/t ratios than are low strength steels.

Sherman (4.8) conducted monotonically increasing flexural load tests on empty tubes with yield stresses of up to 420 MPa and casing D/t ratios in the range of 18 to 102. His main aim was to determine if tubes had sufficient rotational ductility to permit plastic mechanisms to form before the tube became locally unstable. The main conclusions from these tests were:

(i) For a fixed-end tube with $D/t < 35$, under uniformly distributed lateral load, the plastic moment was achieved at the three plastic hinges. At this stage tube local buckling had not occurred and the peak curvature was equal to 10 times the curvature at first yield of the steel.

(ii) Tubes with $D/t > 35$ could not develop their full plastic moment. In particular the tube, with $D/t = 102$, could only attain a moment equivalent to that at first yield of the steel. At that stage local buckling developed and load-carrying capacity reduced rapidly.

(iii) Shear force of up to 28% of the theoretical capacity (in pure shear) of the tube, did not have a significantly adverse influence on the development of the plastic moment.

These results imply that for typical prototype piles ($60 \leq D/t \leq 180$), the presence of the internal concrete which should stabilise tube local buckling is of vital importance to the ductile behaviour of composite steel-encased concrete members.

Cyclic loading which simulates the action of earthquakes on members is more severe than monotonic loading, since high amplitude cyclic loading causes strength and stiffness degradation of the structure and eventually fatigue failure. A literature search failed to reveal any information concerning the cyclic flexural loading of steel tubes.

4.2.2 Reinforced and Prestressed Concrete Members under Longitudinal and Cyclic Flexural Loading

A large number of experimental projects at the University of Canterbury have investigated the longitudinal and cyclic lateral load performance of reinforced and prestressed concrete members. The main conclusion from these tests (4.10 - 4.16) is that structural integrity of such members can be maintained, even under severe earthquakes, providing detailing of the transverse reinforcement is performed in accordance with the New Zealand Concrete Code (4.17).

The Code (4.17) specifies that transverse reinforcement should be provided to satisy three requirements:

(i) The lateral restraint of longitudinal reinforcement;

(ii) The prevention of shear failure in the member; and

(iii) The confinement of concrete, so as to guarantee its ductile performance.

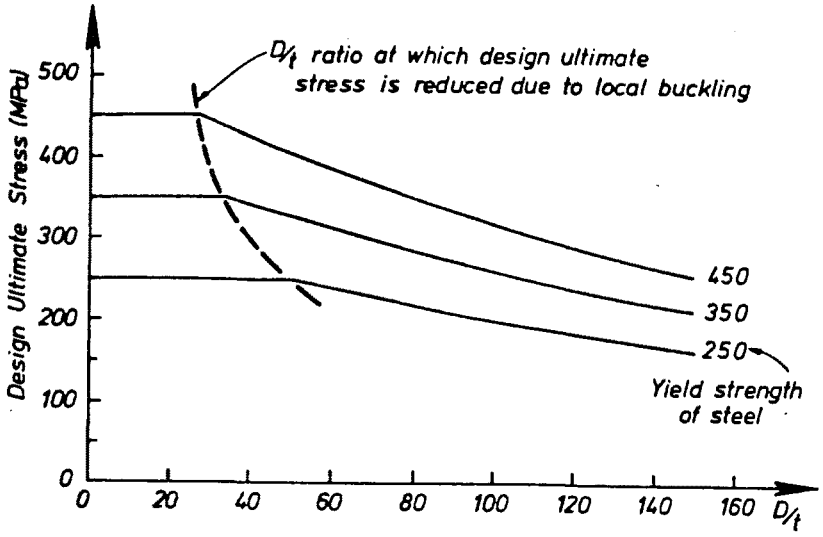

FIG. 4.1 : G.H. LITTLE (4.7) DESIGN CURVES FOR THE ULTIMATE STRESS IN AN EMPTY TUBE SUBJECTED TO PURE FLEXURE

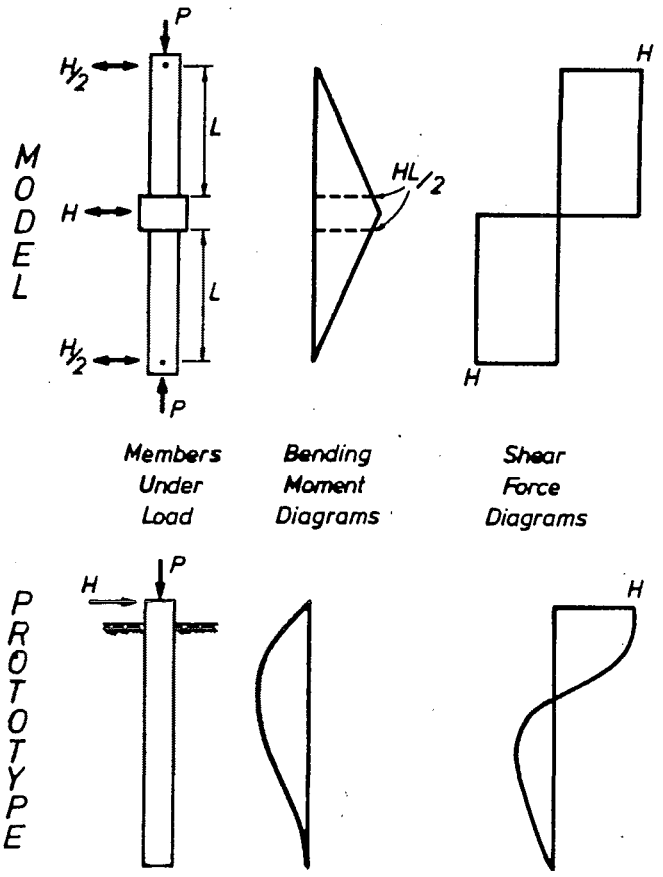

FIG. 4.2 : COMPARISON BETWEEN MODEL AND PROTOTYPE

Dealing with the implication of each of the above three requirements for steel-encased reinforced concrete piles:

(i) Longitudinal reinforcing bars are unlikely to buckle, since the presence of the steel tube means that the cover concrete (i.e. concrete between the tube and spiral reinforcement) cannot spall. Hence even at large values of longitudinal-compression strain the concrete surrounding the bars will restrain bar buckling. For the tube the internal concrete has been shown (see Chapters 2 and 3) to result in stabilising of tube local buckling.

(ii) The presence of shear force is unlikely to significantly affect the flexural performance of steel-encased reinforced concrete members, since tests of empty tubes (see previous section) have shown that the tube can sustain a shear force of up to 28% of its theoretical capacity (under pure shear) without significantly influencing the flexural capacity of the tube.

(iii) For piles a typical level of longitudinal-compression load is $0.1f'_c(A_c + A_t)$. For reinforced concrete members, under this longitudinal load, the Code (4.17) would typically require a ρ_s (volumetric ratio of transverse steel to concrete core) of just less than 0.01. For prototype piles, the largest value of casing D/t ratio used is 180 which corresponds to a ρ_s due to the tube of 0.022. It was shown previously (see Section 2.2.6.2) that in concrete-filled tubes with large casing D/t ratios, at large strains under longitudinal-compression load the tube is acting predominantly in a hoop-tension stress role in a similar fashion to an equivalent volume of closely spaced spiral reinforcement. Thus even for the thinnest-walled prototype concrete-filled tube, at the low level of longitudinal load typical for piles, the level of confining stress on the concrete is of the order of twice that provided in conventionally designed reinforced concrete members (4.17). Thus the tube should more than adequately confine the core concrete.

4.2.3 Steel-Encased Reinforced Concrete Members Under Longitudinal and Cyclic Flexural Loading

As discussed in Chapter 2, an extensive amount of research concerning steel-encased concrete members under longitudinal-compression load has been performed. However relatively little work has been undertaken concerning the response of such members to lateral load.

Research of direct relevance to flexural loading has generally consisted of longitudinal-compression loading which was monotonically and eccentrically applied. Bridge (4.18), Furlong (4.19) and Knowles (4.20) have tested members with square sections under such loading, while Neogi et al (4.21), Knowles (4.20) and Furlong (4.19) have investigated circular sections. Design methods for longitudinal load-moment interaction taking into account the effect of member slenderness have been formulated by Furlong (4.22) and the British Steel Corporation (4.23). A literature review revealed the only previous study of the performance of steel-encased reinforced concrete members to longitudinal load and cyclically varying load, simulating seismic attack of piles, was the preliminary study (4.24) to this investigation. Since the preliminary investigation was of direct relevance to the investigation presented in this chapter, a brief review of the preliminary investigation is provided below.

In the preliminary investigation (4.24) six half-scale models of circular-sectioned steel-encased reinforced concrete members were tested, with a constant level of longitudinal-compression load and a cyclically varying midspan lateral load. The longitudinal load was of a magnitude to represent the dead and earthquake vertical loads from a bridge superstructure on the pile, while the lateral load was representing horizontal seismic loading of the pile. However as

shown in Fig. 4.2, this is strictly not an accurate representation of the bending moment and shear force distributions which are likely to exist in a prototype pile. The model piles can be considered to have been more severely tested than prototype piles, since when the suitably scaled results from the models are applied to prototypes:

(i) The level of shear force present in the plastic hinge zone of the prototype is negligible when compared with that applying to the model. For example, at the position of peak moment in the prototype, the shear force is zero.

(ii) In the vicinity of the section of maximum moment, the moment gradients are relatively large and small for the model and the prototype respectively. Thus taking into account scale effects, the plastic hinge length will be larger for the prototype than the model. Thus at a given value of load-level displacement the critical section in the prototype will be subjected to a lower level of curvature and hence damage, than will the critical section in the model.

(iii) In the prototype, the presence of soil may help to stabilise local buckling of the tube. This effect is not simulated in the model.

Test units had an overall length of 3.9 m, casing diameter D of 360 mm and thickness t of 5 mm (casing D/t ratio = 72). Test unit details are given at the end of the chapter in Table 4.1. Thus the test series enabled the significance of the level of longitudinal load, inclusion or exclusion of an internal reinforcing cage, and the casing anchorage of the critical sections to be investigated. Hysteresis loops for the test units are given in Fig. 4.3. Theoretical predictions to behaviour as discussed later in this section are also shown in Fig. 4.3.

Satisfactory behaviour was observed in all six tests, in terms of the performance criteria used in New Zealand. The first criterion (4.25) which is part of seismic design philosophy for ductile bridge systems is that significant strength degradation does not occur between displacement ductility factors (ratio of displacement to displacement at yield of structure) of $\mu = 1$ and 6. The second criterion is contained in the New Zealand Loadings Code for Buildings (4.26). This criterion requires four complete cycles to $\mu = \pm 4$ (equivalent to a cumulative displacement ductility level of $\Sigma|\mu| = 32$), with strength degradation not exceeding 20% of the maximum strength attained.

For units 1-4 (see Table 4.1) which contained casing which was well anchored at the critical flexural sections, overstrength of approximately 22% was available above the ideal strength (indicated as H_i in Fig. 4.3) taking into account P-Δ effect. For this purpose, ideal strength was calculated by a strain compatibility approach, with the casing assumed to act as an equivalent array of reinforcing bars around the perimeter of the concrete core. The measured steel yield strengths, concrete cylinder strength, an ultimate compression strain of 0.003, a rectangular stress block for concrete in compression, and a linear distribution of longitudinal strain across the section were used in calculating this ideal strength. An example of these calculations is given in Ref. 4.24.

For units 5 and 6 which possessed inadequately anchored casing at the critical flexural sections, ideal strength was assessed as for units 1 - 4 except that the contribution of the casing was ignored. This was in accordance with the Commentary to Clause 12.5.2.1 of the New Zealand Concrete Code (4.17). For these two units, an overstrength of 78% was available above the ideal strength taking into account P-Δ effect.

The level of longitudinal load modified the available flexural strength in a similar fashion to that found in reinforced concrete (i.e. since the levels of longitudinal-compression load were small, increasing the longitudinal load increases

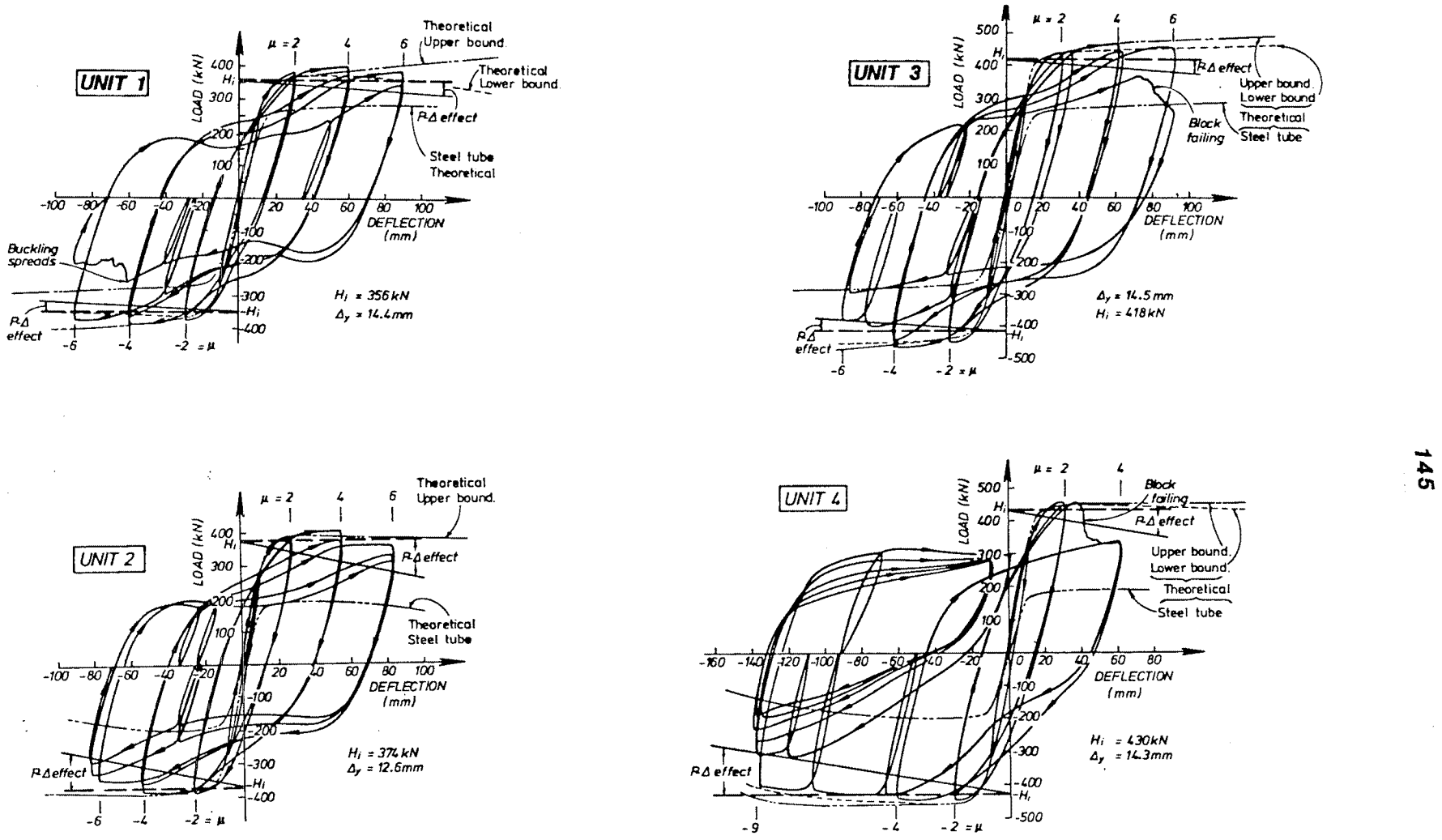

FIG. 4.3 : LATERAL LOAD-LATERAL DEFLECTION RESPONSES FROM THE PRELIMINARY INVESTIGATION (4.24)

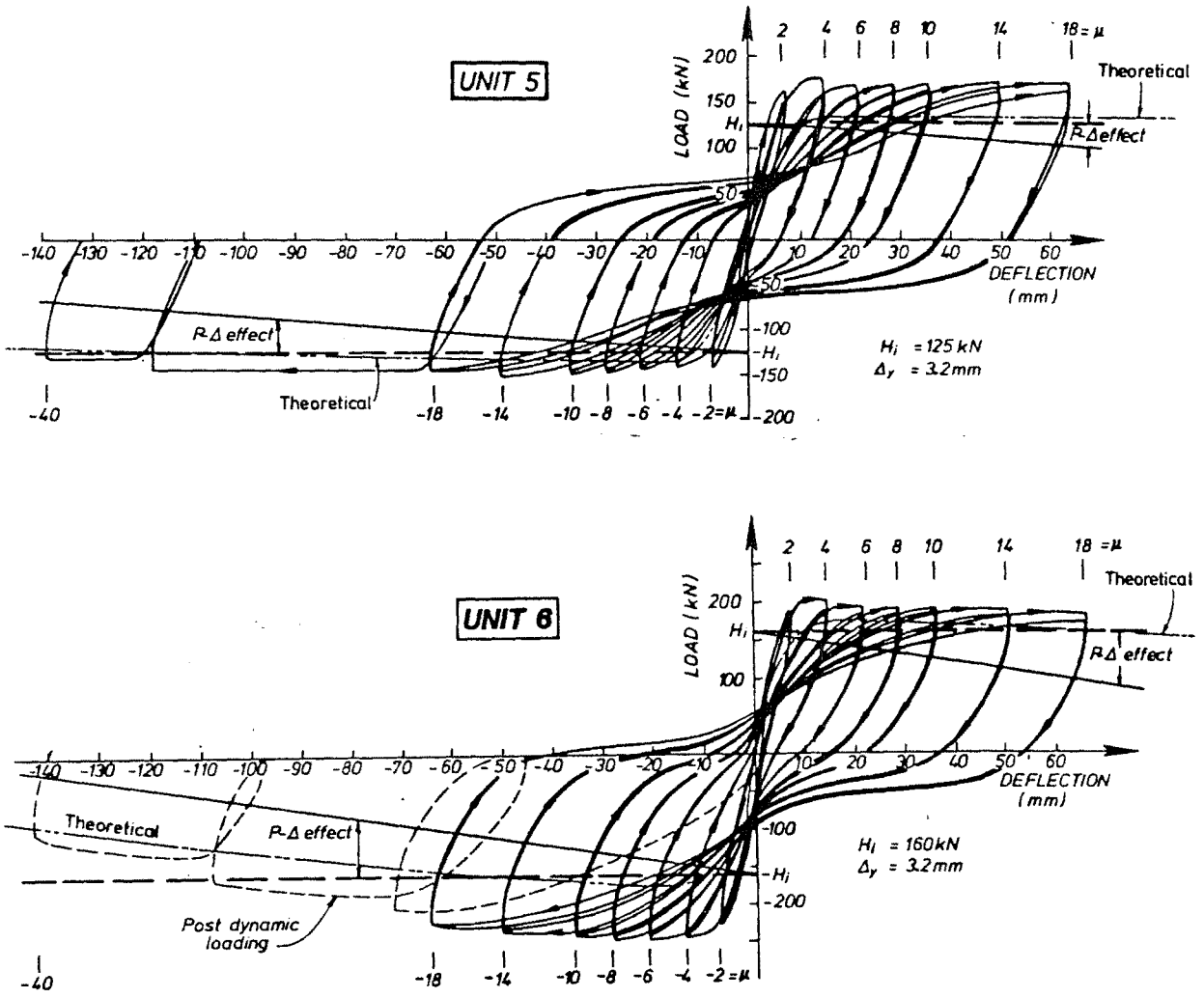

FIG. 4.3 (CONTINUED)

the flexural strength). In reinforced concrete columns, the level of longitudinal load significantly affects the ductility characteristics of the member. In these tests of steel-encased reinforced concrete members, this was not evident because the tubes, which occupied 5.6% of the volume of the member, were more than capable of providing the confinement to the concrete which is necessary for ductile performance. Internal longitudinal reinforcement increased the flexural strength, but internal transverse reinforcement did not significantly enhance the ductility of the test units since the confining effect of the reinforcement was small when compared with that of the tube.

In the preliminary study, the difficulties in theoretically modelling behaviour were described, in particular the uncoupling of the concrete-confining role of the tube which results in hoop-tension stress and the direct response of the tube to longitudinal and flexural loading, which results in longitudinal stress in the tube. For units 1 - 4 which had continuous casing, moment-curvature analyses for monotonic loading based on theoretical upper and lower bound approaches were found to bracket closely the experimental response (see Fig. 4.3). In the theoretical upper bound approach it was assumed that the casing could develop simultaneously its uniaxial longitudinal stress-longitudinal strain characteristics in resisting flexural and longitudinal loads, and in addition the tube was assumed to act as an equivalent volume of closely spaced spiral reinforcement with the resulting benefits to concrete strength and ductility. Thus this upper bound approach crudely allowed for the effect of concrete-tube lateral interaction on the stress-strain response of the tube in the longitudinal and hoop directions. However from the results of Chapters 2 and 3, the upper bound approach could be expected to give a good approximation to overall behaviour under flexural load, since under tensile and compressive longitudinal stress lateral interaction enhances and reduces respectively the longitudinal strength of the tube in a crudely self-compensating fashion. In the theoretical lower bound approach it was assumed that the tube had its uniaxial longitudinal stress-longitudinal strain characteristics in resisting flexural and longitudinal loads, and the concrete behaviour was unmodified by the presence of the tube. Similar moment-curvature analyses of units 5 and 6 which had discontinuous casing showed that a large proportion of the observed 78% overstrength was due to the presence of the tube which had been ignored in calculating the ideal strength of these units, since the tube develops longitudinal-compression stress in end-bearing and also provides confinement to the concrete.

Although satisfactory seismic performance was observed in all of these tests, for the four test units with continuous casing, local buckling of the tube was observed at displacement ductility levels of $\mu \geq 4$. This resulted in some degradation of performance as plastic rotation concentrated at the local buckles, which had a longitudinal extent of approximately 30 mm. This concentration of local buckling resulted in a large curvature ductility demand at the critical flexural sections.

As mentioned previously in Chapter 1, for non-seismic (i.e. monotonic loading) design, the New Zealand Concrete Code (4.17) has a requirement for the minimum thickness of steel tubes in composite columns:

$$t \geq D \sqrt{\frac{\sigma_y}{8E_s}} \qquad (4.1)$$

This criterion is based on the attainment of yield stress in an empty tube under monotonic longitudinal-compression load before local buckling forms. The tests of Sakino et al (2.41) which were described previously in Section 2.2.6.2, had $D = 100$ mm, $t = 0.52$ mm ($D/t = 192$), $\sigma_y = 244$ MPa, $E_s \cong 205000$ MPa and concrete with f'_c of either 18 MPa or 37 MPa. The above value of t violates equation 4.1 which would require that $t \geq 1.22$ mm should be used. However despite the presence of local buckling, as shown previously in Fig. 2.16, reasonably ductile behaviour was obtained in these tests and the ultimate loads, P_u^{exp}, attained were appreciably in excess

of the sum of the unconfined strength of the concrete, $f'_c A_c$, and the yield strength of the tube, $\sigma_y A_t$. For the tests with f'_c = 18 MPa:

$$\frac{P_u^{exp}}{f'_c A_c + \sigma_y A_t} = 1.38$$

while for tests with f'_c = 37 MPa:

$$\frac{P_u^{exp}}{f'_c A_c + \sigma_y A_t} = 1.24$$

Thus from this evidence, equation 4.1 is an unnecessary restriction on steel-encased concrete members subjected to monotonic loading (i.e. non-seismic applications).

However it was of interest to establish if equation 4.1 was appropriate for the more severe case of seismic loading. In the six model tests conducted in the preliminary investigation (4.24): D = 360 mm, t = 5 mm (D/t = 72), σ_y = 370 MPa and E_s = 205000 MPa. Thus from equation 4.1, t should have been greater than or equal to 5.4 mm. Hence from the sound performance of these models, equation 4.1 was established to be conservative for seismic design, at least for the low levels of longitudinal-compression load ($P < 0.3f'_c(A_c + A_t)$) which are present in piles.

The tests performed in the preliminary investigation indicated satisfactory ductility and predictable flexural strengths. However the applicability of the results was limited due to the single value of D/t = 72 which was investigated. One of the recommendations of the preliminary study was that additional tests be carried out of units with casing D/t ratio encompassing the entire range (60 - 180) commonly used in practice.

4.3 DESIGN OF THE MODEL PILES

4.3.1 Test Rig

The test rig illustrated in Fig. 4.4 was used for testing the model piles. This rig was designed and first used by Ang et al (4.12). For this series of tests minor alterations were necessary to cope with the changes in section diameter that occurred from test to test, as the rig had been originally designed for test units with a diameter of 400 mm. Vertical longitudinal loads were applied by a ± 10 MN capacity DARTEC universal testing machine and horizontal lateral loads were applied by a ± 500 kN MTS actuator. Without reblocking the actuator was limited to displacements of ± 75 mm, although larger displacements could be achieved by unloading and subsequently reblocking the actuator. From Fig. 4.4 it can be seen that the actuator also induces vertical longitudinal loads in the test units through the inclined arms of the loading frame. Thus to maintain a constant nett longitudinal load on the unit during testing it was necessary to adjust the DARTEC longitudinal load as the MTS horizontal load varied.

The test rig was the same as that used in the preliminary study (4.24) to this investigation. Thus the same observations concerning the shear force and bending moment distributions on model and prototype apply. In particular, the loading system on the model can be considered to be more severe than that present on a prototype pile which is subjected to horizontal inertia loads through the bridge centre of mass (see Fig. 4.2).

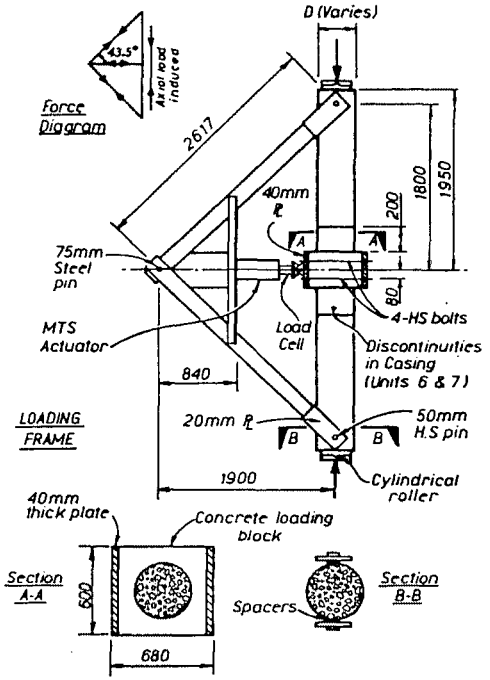

FIG. 4.4 : TEST UNIT IN THE REACTION FRAME

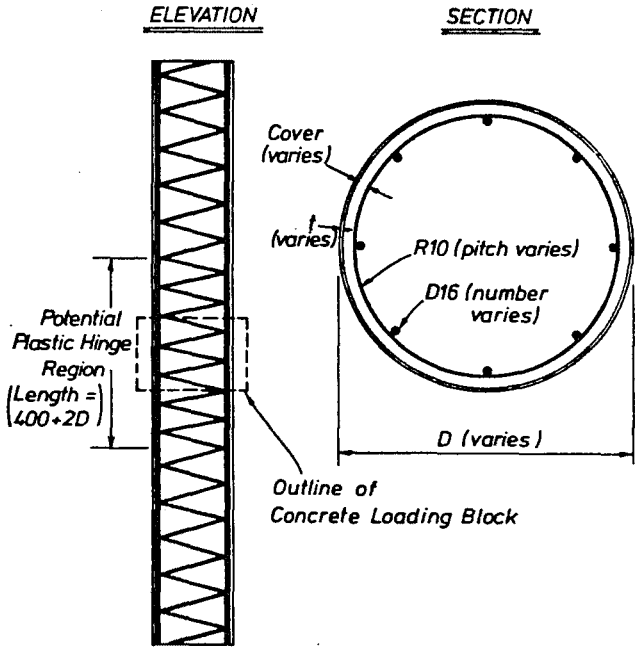

FIG. 4.5 : REINFORCING CAGE DETAILS

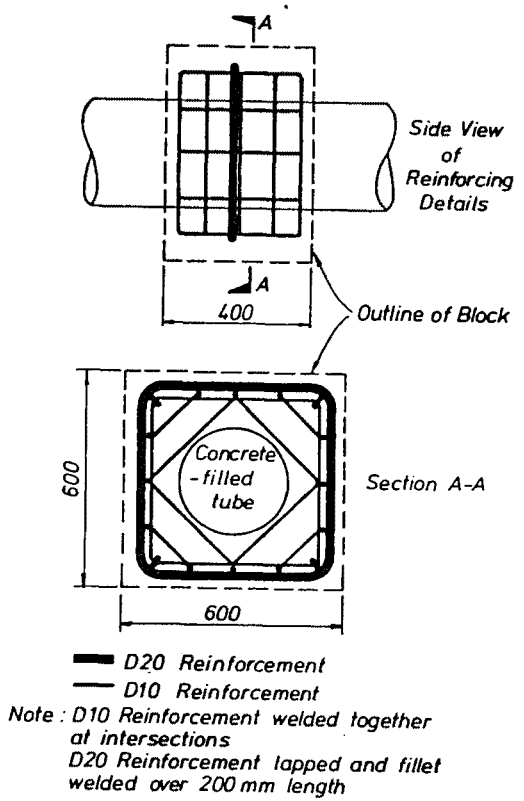

FIG. 4.6 : TYPICAL DETAILING OF A CONCRETE LOADING BLOCK

4.3.2 Test Unit Dimensions

The maximum lateral force of ± 500 kN and the 3.9 m maximum height of the test units were the factors which limited the dimensions of the test units. The bending moment distribution (see Fig. 4.2) on the model was designed to produce critical sections, in the pile, at the top and bottom faces of the concrete loading block close to the midheight of the test unit. Thus from consideration of equilibrium at the faces of the concrete loading block, the moment capacity of the test units could not exceed 400 kNm (= HL/2 from Fig. 4.2, where H = 500 kN, L = 1.6 m) plus any secondary moments from P-Δ effect.

One of the conclusions reached in the preliminary study (4.24) to this investigation, was that apart from its effect on flexural strength the level of longitudinal-compression load on the pile was not an important parameter. Thus it was decided that for the series of tests described subsequently in this chapter, a load of $0.1f'_c(A_c + A_t)$ would be used. This load is typical of the small loads generally present on bridge piles, due to soil bearing stress considerations.

Since prototype piles have generally been constructed with $60 \leq D/t \leq 180$, it was decided to test 7 model piles with nominal tube D/t ratios of 30, 60, 90, 120, 150, 180 and 210 to investigate the effect of the tube D/t ratio on seismic behaviour. Two other units which simulated the effect of a circumferential discontinuity in the casing in the plastic hinge zone of the pile were also tested. As discussed previously in Section 1.2.3, a discontinuity in the casing could be present due to poor workmanship in the welding together of adjacent lengths of tube. For these models the discontinuities were located at distances of 200 mm above and beneath the concrete loading block as shown in Fig. 4.4. In the models with discontinutities, a tube diameter of 400 mm and thickness of 5 mm (D/t = 80) were used. Table 4.2 gives the values of D,t, nominal and actual D/t ratio, and scale factor used in the nine model tests. The average scale factor utilised was 0.42 which was felt to be large enough to avoid severe distortion of behaviour between model and prototype.

4.3.3 Tubes

Test unit 1 was constructed using a mild steel hot-formed seamless boiler tube. The tubes used in units 2-9 were specified to be made from mild steel plate which was cold-rolled into a circular shape and then welded along a longitudinally running seam. Due to variations between test units in the amount of cold-working and in tube wall thickness, it was not possible to ensure that all units had the same material properties.

Units 1-5, 8 and 9 contained a continuous length of tube throughout their height. Units 6 and 7 were made from three lengths of tube, with nominal tack-welding connecting the lengths of tube together at the two positions of circumferential discontinuity. The tack welding was present to facilitate the concentric alignment of the three lengths of tube during construction.

For concrete-filled tubes with assumed mild steel properties of σ_y = 300 MPa and E_s = 200 000 MPa, equation 4.1 implies that the design longitudinal stress in the tube should be less than the yield stress for test units 3, 4, 5, 8 and 9 which all had casing D/t ratios in excess of 73. For units 6 and 7 which contained circumferential discontinuities in the tubes, clearly the tube is not able to contribute fully to flexural strength of the composite member at the discontinuity. However, in practice end-bearing of the tube either side of the discontinuity, and the confinement offered to the concrete by the tube at the discontinuity, will increase the flexural strength of the member above that calculated ignoring the presence of the tube.

4.3.4 Longitudinal Reinforcement

Figure 4.5 and Table 4.3 show the reinforcing cage details for units 1-9. Longitudinal reinforcing bars occupied approximately 1.1% of the gross section area. This percentage was considered to be typical of that used in prototype piles. The cover dimensions, from the outside of the reinforcing cage to the inside of the casing, in the test units generally modelled a prototype value of 50 mm. The longitudinal reinforcing bars used in the test units were D16 (deformed bars of 16 mm diameter) which modelled the D32 bars used typically in prototype piles. The longitudinal reinforcing bars and the tubes were welded on to 10 mm thick endplates at the top and bottom of the test units. This was to ensure sound anchorage of the tube and the longitudinal reinforcing bars during the subsequent testing.

4.3.5 Transverse Reinforcement

From the results of the preliminary investigation (4.24), it was clear that spiral reinforcement inside the tubes made little difference to the performance of the test units. Nevertheless for units 1-5, 8 and 9 spiral reinforcement, in the potential plastic hinge zone (the length of which is defined later in this section), was provided conservatively in accordance with the confinement requirements of the New Zealand Concrete Code (4.17). This requires the volumetric ratio of transverse confining reinforcement (ρ_s) to be not less than the greater of the values given by the following equations:

$$\rho_s = 0.45 \left(\frac{A_c}{A_{cc}} - 1\right) \frac{f'_c}{\sigma_{yh}} \left(0.5 + 1.25 \frac{P}{\phi f'_c (A_c + A_t)}\right) \quad (4.2)$$

$$\rho_s = 0.12 \frac{f'_c}{\sigma_{yh}} \left(0.5 + 1.25 \frac{P}{\phi f'_c (A_c + A_t)}\right) \quad (4.3)$$

where $$\rho_s = \frac{4A_{sp}}{s.d_s} \quad (4.4)$$

A_c = total section area of the concrete inside the tube
A_{cc} = section area of concrete to the outside of the spiral reinforcement
σ_{yh} = yield strength of spiral reinforcement
A_{sp} = area of spiral reinforcement
s = centre to centre pitch of spiral reinforcement
d_s = outside diameter across the spiral reinforcement
ϕ = capacity reduction factor (see Ref. 4.17).

In using equations 4.2 and 4.3, nominal values of f'_c = 28 MPa and σ_{yh} = 316 MPa were assumed. The longitudinal load ratio $P/(f'_c(A_c + A_t))$ was equal to 0.1 and ϕ was taken as 0.75. This value of ϕ was taken in accordance with an early draft of the Code (4.17). In the final form of the Code a value of 0.9 is specified for columns complying with equations 4.2 or 4.3. However this discrepancy in the design makes less than 5% difference to ρ_s and thus is unlikely to be significant.

Units 6 and 7 possessed circumferential discontinuities in the casing. Spiral reinforcement for unit 7 was designed at a spacing of 110 mm, which was in accordance with equations 4.2 and 4.3. However on the basis that the tube would adequately confine the concrete, unit 6 was arbitrarily designed with spiral reinforcement at a greater spacing of 200 mm.

The preliminary tests (4.24) of concrete-filled tubes, with D/t = 72, had indicated that the presence of shear force resulted in strains very much less than the yield strain. Thus in the subsequent series of tests, it was decided not to follow the provisions of the Concrete Code (4.17) for designing transverse

reinforcement to resist shear forces. The Code also limits the pitch of spiral reinforcement to the smaller of D/5, $6d_b$ (where d_b is the diameter of the longitudinal reinforcing bars) or 200 mm. No attempt was made to comply with these requirements, which are primarily designed to prevent bar buckling in reinforced concrete members, since in steel-encased reinforced concrete members there is little likelihood of bars buckling as the cover concrete is kept in place by the outside steel casing.

Spiral reinforcement outside the potential plastic hinge zone was spaced at the larger of D/2 or the spacing in the potential plastic hinge zone. A length of 2 pile diameters plus 400 mm (which was the length of the concrete loading block) at the centre of the test units was defined as the potential plastic hinge zone. For some test units (i.e. those with D > 320 mm), this violated the Concrete Code (4.17) criterion that sections where moments exceed 80% of the moment at the critical flexural section should be detailed as part of the potential plastic hinge zone. This criterion was not followed as from the preliminary investigation (4.24) the plastic rotation was observed to concentrate at the local buckles over a very short length adjacent to the concrete loading block.

Table 4.3 and Fig. 4.5 also summarise the spiral reinforcement details. The RI0 bars (plain bars of 10 mm diameter) that were used modelled R16 bars which are typically used in prototype piles. Table 4.3 also indicates the dominance of the tube over the spiral reinforcement, since for a thick-walled tube (e.g. unit 1 with D/t = 34) ρ_s for the tube is 21.7 times ρ_s for the spiral, while for a thin-walled tube (e.g. unit 9 with D/t = 214) ρ_s for the tube is 3.2 times ρ_s for the spiral.

Where necessary adjacent spiral reinforcement windings were lapped and welded together over a length of 100 mm. Laps were restricted to areas outside the potential plastic hinge zone.

4.3.6 Concrete Loading Blocks

For units 1-5, 8 and 9 loading was intended to produce critical flexural sections in the pile at the top and bottom faces of the concrete loading block, while for units 6 and 7 critical flexural sections were expected at the positions of casing discontinuity. However as shown in Fig. 4.2, the maximum moment on the test unit occurs within the zone of the loading block. Thus to achieve the desired unobtrusive behaviour of the block, the block was constructed using high strength concrete ($f'_c \geq 40$ MPa) and a large quantity of reinforcing steel.

In the preliminary investigation (4.24) to this investigation, D24 hoop reinforcement was placed within the concrete loading block. On the basis of a steel truss mechanism distributing the concentrated forces from the MTS actuator through the block into the model pile, this hoop reinforcement was theoretically strong enough for the anticipated loading. However as testing had proceeded, large cracks had developed in the concrete loading block, and in one of the test units failure of the block had occurred.

For this subsequent series of tests, a large amount of smaller diameter D10 and D20 reinforcement was placed in the block surrounding the pile, with the aim of controlling cracking in the block as well as providing adequate strength for the resistance of the concentrated loads applied by the MTS actuator to the test unit. A typical arrangement of reinforcing steel within the concrete loading block is shown in Fig. 4.6. For simplicity of construction the reinforcing steel was placed surrounding but not through the model pile. This meant that the length of model pile surrounded by the concrete loading block was relatively free to slide inside the block due to limited bond between the concrete and the steel tube.

4.4 CONSTRUCTION OF THE TEST UNITS

Construction of the steel-encased reinforced concrete test units was achieved with relative ease when compared with the equivalent reinforced concrete or pretensioned concrete alternatives. The steel tube acted as formwork for the bulk of each unit, and the only special formwork necessary was that used to form the concrete loading block.

A commercial steel fabricator rolled and welded the tube steel to the required form and bent all reinforcement to a specified schedule. The construction sequence was then as follows:

(i) The reinforcing cages were tied.

(ii) Electrical resistance strain gauges required for the reinforcing bars were placed on the outside of the cage, to lessen the risk of subsequent damage when concrete was poured through the inside of the cage.

(iii) For units 6 and 7 which had the casing in three lengths, small tack welds connecting the adjacent lengths of tube together were made at the two positions of casing discontinuity. This was done to align the casing for the subsequent stages of construction.

(iv) The reinforcing cages were then placed inside the tubes with tack-welded blocks to maintain the appropriate cover between the cages and the tube.

(v) A 10 mm thick endplate was then welded onto the end of the casing and the reinforcing cage that was to be at the base of the test unit during concrete pouring.

(vi) The tubes, of 50 mm inside diameter, to locate the pin connections with the loading frame, were then inserted and welded to the test unit.

(vii) Wiring for the strain gauges, which were located on the reinforcing cage, was passed through a number of 25 mm diameter holes in the tube. These holes were located approximately 700 mm away from the concrete loading block.

(viii) The test units were then erected so that their longitudinal direction was vertical, and they were braced against surrounding scaffolding.

(ix) Concrete was provided by a local ready-mix contractor, and the tubes were filled to the top by using six lifts of concrete per test unit. Following each lift of concrete, vibration was applied down the middle of the tube.

(x) The test units were left to cure for a week. Damp hessian was placed over the top of the units to prevent loss of moisture from the concrete.

(xi) Endplates were welded onto the casing and the longitudinal reinforcement at the top of the test units.

(xii) The test units were then laid so that their longitudinal direction was horizontal. Then each unit had the D10 and D20 reinforcement for the concrete loading block, tubes for locating the four high strength bolts to the MTS actuator, and the surrounding plywood formwork placed in position.

(xiii) The loading block concrete was poured and vibrated, then screed and later floated off.

(xiv) The loading block concrete was then left to cure for one week with damp hessian placed over the exposed concrete.

(xv) Plywood formwork was stripped and rosettes of electrical resistance strain gauges, for measuring strains on the outside of the casing, were fixed in position.

Figure 4.7(a) shows the assembly of a typical reinforcing cage. Typical centre block reinforcement and the four tubes for positioning of high strength connecting bolts to the MTS actuator are shown in Fig. 4.7(b).

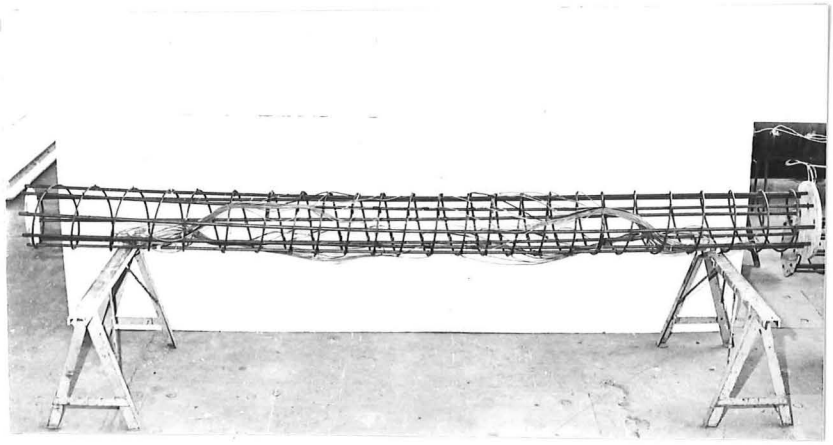

FIG. 4.7a : TYPICAL REINFORCING CAGE

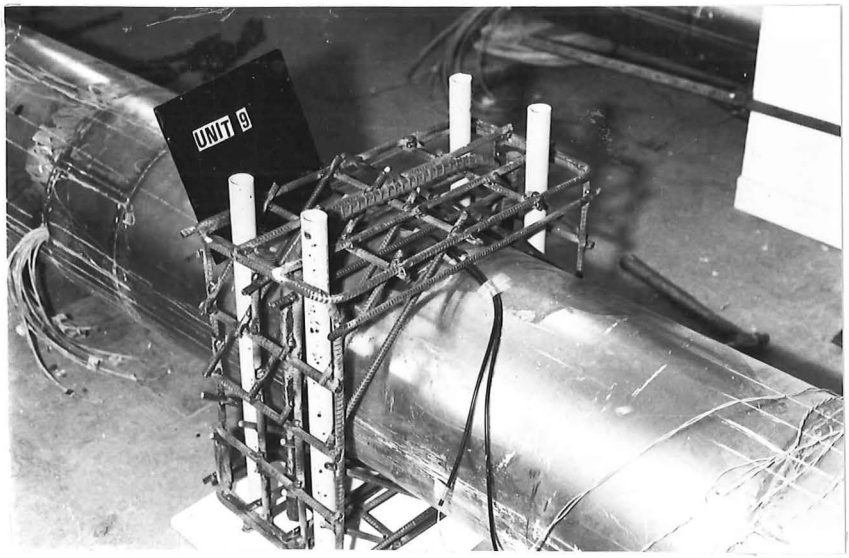

FIG. 4.7b : TYPICAL CONCRETE LOADING BLOCK REINFORCEMENT

4.5 INSTRUMENTATION

4.5.1 Lateral Load and Lateral Displacement

The lateral load applied to the models was measured by the load cell shown in Fig. 4.4. Prior to testing the load cell was calibrated, using an AVERY Universal Testing Machine, to an accuracy of ± 1%.

Lateral deflection and rotation of the concrete loading block relative to the pin connections with the lateral load reaction frame were measured using 300 mm travel Sakae 20 FLP 300 kohm linear potentiometers, as shown in Fig. 4.8.

4.5.2 Longitudinally Aligned Linear Potentiometers

For units 1-5, 8 and 9 linear potentiometers with up to 50 mm travel were used, as illustrated in Fig. 4.9(a), to enable the distribution of tube longitudinal strain and curvature in the vicinity of the critical sections to be determined. These potentiometers were mounted on stands that had been tack-welded onto the outside surface of the tube, although for potentiometers N5, S5, N6 and S6 one end of the potentiometer was bearing directly on the concrete loading block. Thus if the tube slipped through the concrete loading block due to poor bond, then the gauge length of potentiometers N5, N6, S5 and S6 would effectively be larger than the 100 mm indicated in Fig. 4.9(a).

For units 6 and 7 which had circumferential discontinuities in the tube, 100 mm travel potentiometers were used as shown in Fig. 4.9(b) to measure separation of the tube across the discontinuities.

The outstands, from the tube surface, and gauge lengths of the linear potentiometers given in Fig. 4.9 are the nominal values, the actual dimensions were obtained immediately prior to testing.

4.5.3 Strain Gauges

Electrical resistance strain gauges were placed on the outside surface of the tube and on the reinforcing cage at and in the vicinity of the expected critical sections. The preliminary investigation (4.24) in this study had indicated that for test units with continuous casing, the critical sections were within the zones of tube local buckling approximately 30 mm from the top and bottom faces of the loading block. For units 6 and 7 which had circumferential discontinuities in the tube 200 mm from the top and bottom faces of the loading block, it was anticipated that the critical sections would be at the positions of discontinuity.

4.5.3.1 Outside Surface of the Tube

Three arrays of strain gauges were used. Test units 1-5 used Array I, units 8 and 9 used Array II and units 6 and 7 used Array III. These arrays are illustrated in Fig. 4.10. The strain gauges used to measure uni-directional strain were SHOWA type KFC-5-C1-11, gauges arranged in rectangular rosettes were SHOWA type N34-FA-2-120-11. The rosettes occupied an area of approximately 10 mm x 10 mm, and the uni-directional gauges were approximately 5 mm long. Thus unless the gauges were located at a local buckle, strain gradient effects within the area of a rosette or a uni-directional gauge were anticipated to be small.

Strain gauges in Array I enabled the two-dimensional strain field on the outside surface of the tube over a distance of 100 mm from both the top and bottom faces of the loading block to be measured. Array II included the gauges from Array I plus additional uni-directional gauges to enable the longitudinal strains on the tube surface within the concrete loading block to be measured. In Array III 48 rosettes were clustered on the outside surface of the tube within 150 mm of either of the sections of casing discontinuity, 28 uni-directional gauges were also present to enable the longitudinal strain distribution along the length of the tube to be measured.

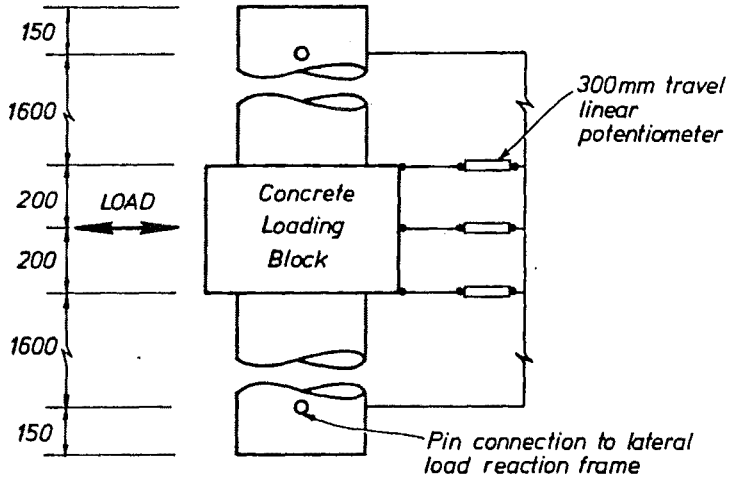

FIG. 4.8 : MEASUREMENT OF CONCRETE LOADING BLOCK ROTATION AND LATERAL DISPLACEMENT

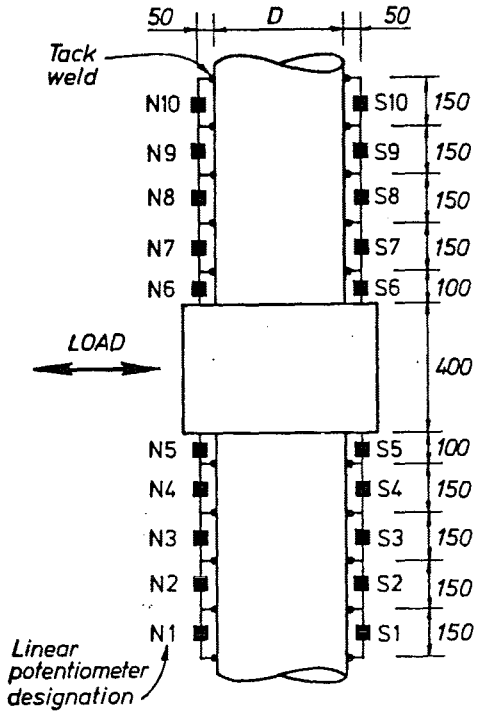

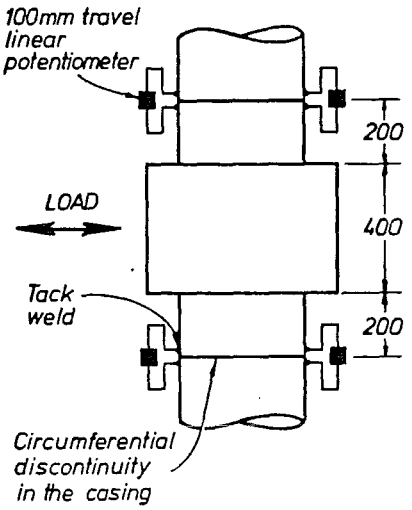

FIG. 4.9a : MEASUREMENT OF TUBE LONGITUDINAL STRAINS AND CURVATURES

FIG. 4.9b : MEASUREMENT OF TUBE GAP ACROSS THE CIRCUMFERENTIAL DISCONTINUITIES

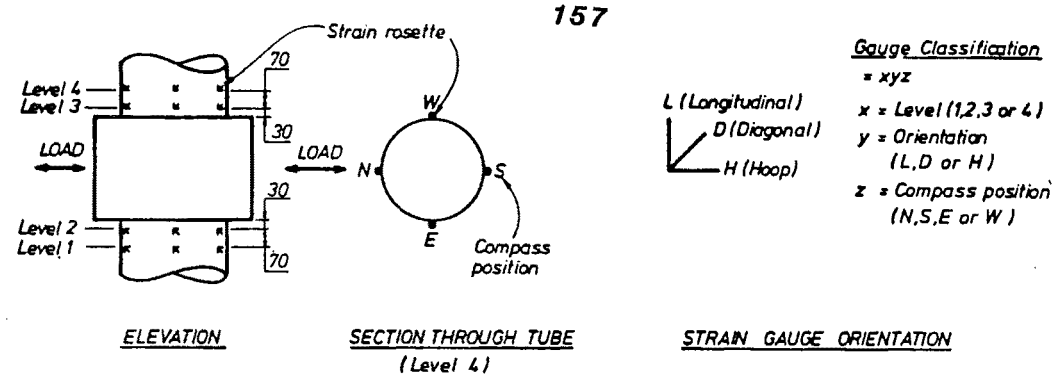

ARRAY I - UNITS 1-5

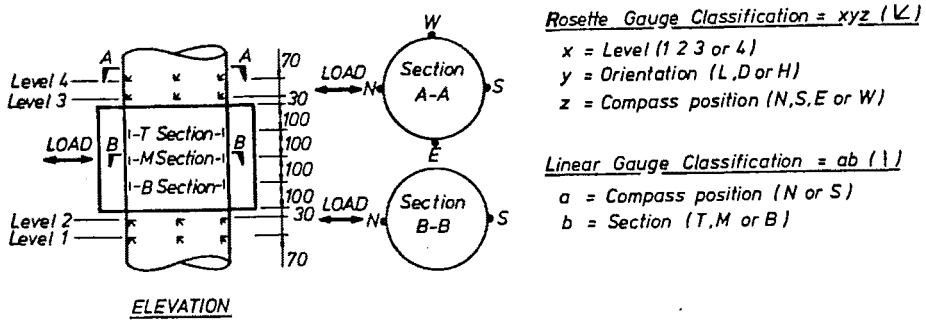

ARRAY II - UNITS 8 & 9

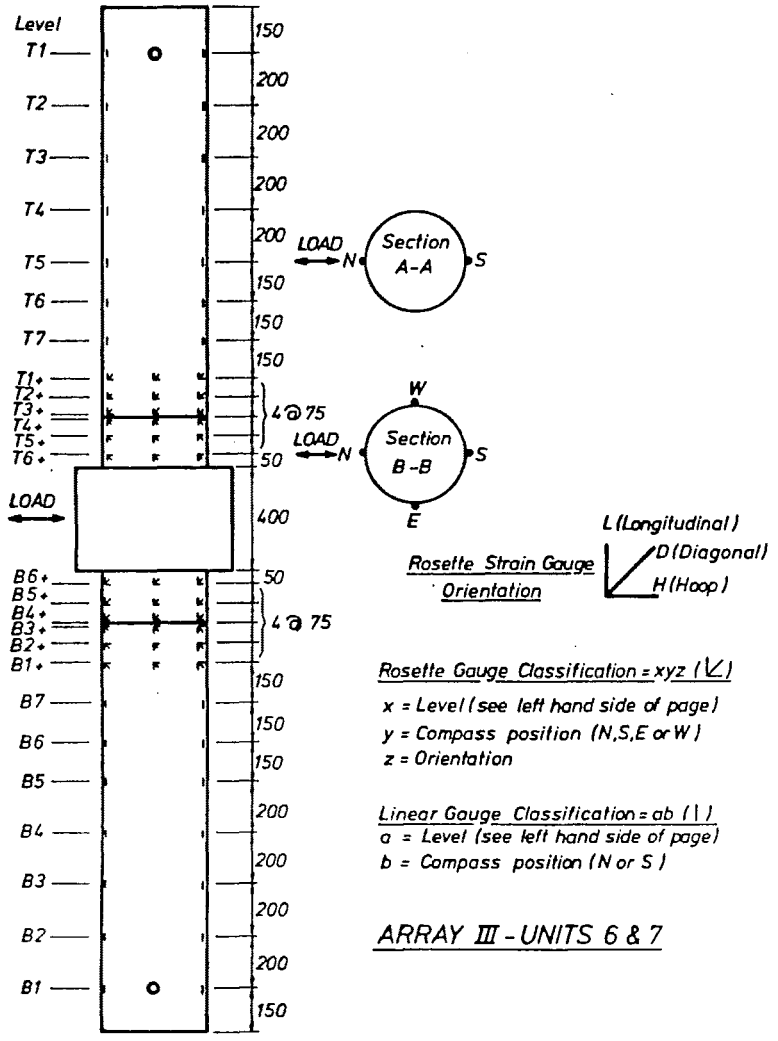

ARRAY III - UNITS 6 & 7

FIG. 4.10 : POSITIONS OF STRAIN GAUGES ON THE OUTSIDE SURFACE OF THE TUBE

4.5.3.2 Longitudinal Reinforcement

Figure 4.11 indicates the position of the strain gauges, SHOWA type N34-FA-2-120-11, that were mounted on the longitudinal reinforcing bars. These gauges were located at and in the vicinity of the anticipated critical sections, and for units 8 and 9 also at the midheight section. Typically four or five of the reinforcing bars at the chosen section were strain-gauged.

4.5.3.3 Spiral Reinforcement

The position of the strain gauges, SHOWA type N34-FA-2-120-11, mounted on the spiral reinforcement are indicated in Fig.4 .12. These gauges were expected to indicate the effectiveness of the spiral reinforcement in resisting shear force and confining the concrete.

4.5.4 Data Acquisition and Reduction

Voltage readings from the electrical resistance strain gauges and linear potentiometers were recorded on punch tape by a Solartron Data Transfer Unit, and reduced by a special purpose computer program. To provide a visual indication of progress during testing, Hewlett-Packard X-Y plotters were used to monitor the lateral load-lateral deflection and lateral load-plastic hinge rotation responses. So that lateral deflection could be accurately monitored during testing, a Hewlett-Packard digital voltmeter was wired to the 300 mm travel potentiometer (see Fig. 4.8) at the midheight of the concrete loading block.

4.6 MATERIAL PROPERTIES

The materials used for the steel-encased reinforced concrete model bridge piles were specified to be representative of the materials used currently in the construction of prototype bridge piles in New Zealand.

Samples of reinforcement contained in the concrete loading blocks were not tested, as the exact stress-strain characteristics of this steel which was designed to remain elastic during testing were not considered to be of importance.

4.6.1 Concrete

Strengths of the concrete contained in the loading blocks and inside the tubes are shown in Table 4.4. The concrete was obtained from a local ready-mix contractor. Ordinary Portland Cement was used and the aggregate was a graded greywacke with a maximum aggregate size of 13.2 mm. A target strength (at an age of 28 days) of 28 MPa and a slump of 120 mm were specified for the concrete inside the tubes. High strength concrete ($f'_c \geq 40$ MPa) with a slump of 100 mm was specified for the concrete inside the loading blocks.

Cylinder compression (f'_c) and modulus of rupture (f_t) tests were performed on concrete samples 28 days after pouring and at the time of testing the model piles. These tests were performed in accordance with New Zealand Standard specifications (4.28). The cylinders had a height of 200 mm and a diameter of 100 mm and the blocks used in the modulus of rupture tests had a square 150 mm x 150 mm cross-section.

At the time of testing, the concrete inside the tubes had an unconfined compression strength (f'_c) of 29-31 MPa. The modulus of rupture tests gave an average tensile strength of $f_t = 0.82\sqrt{f'_c}$.

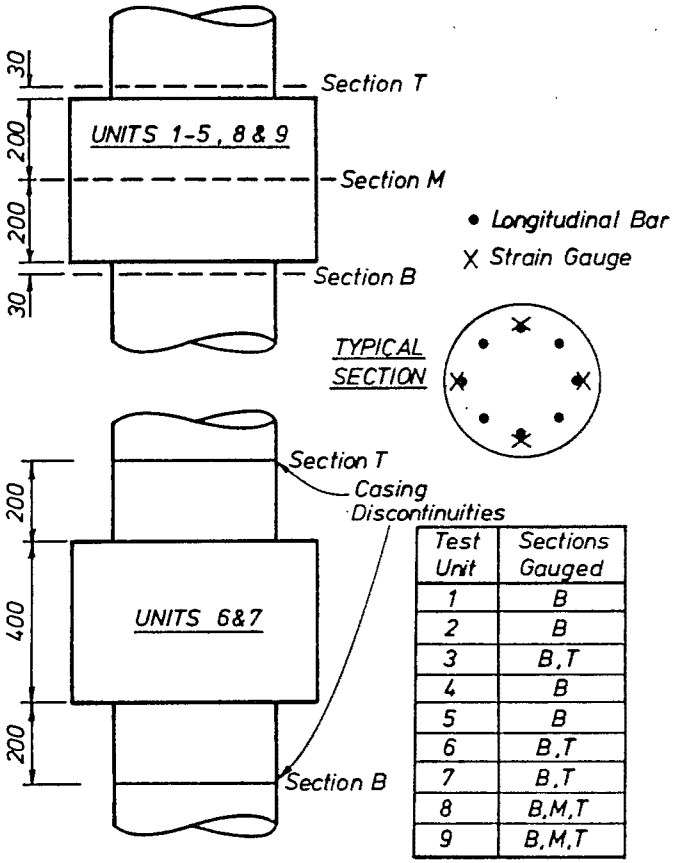

Test Unit	Sections Gauged
1	B
2	B
3	B,T
4	B
5	B
6	B,T
7	B,T
8	B,M,T
9	B,M,T

FIG. 4.11 : POSITIONS OF STRAIN GAUGES ON LONGITUDINAL REINFORCEMENT

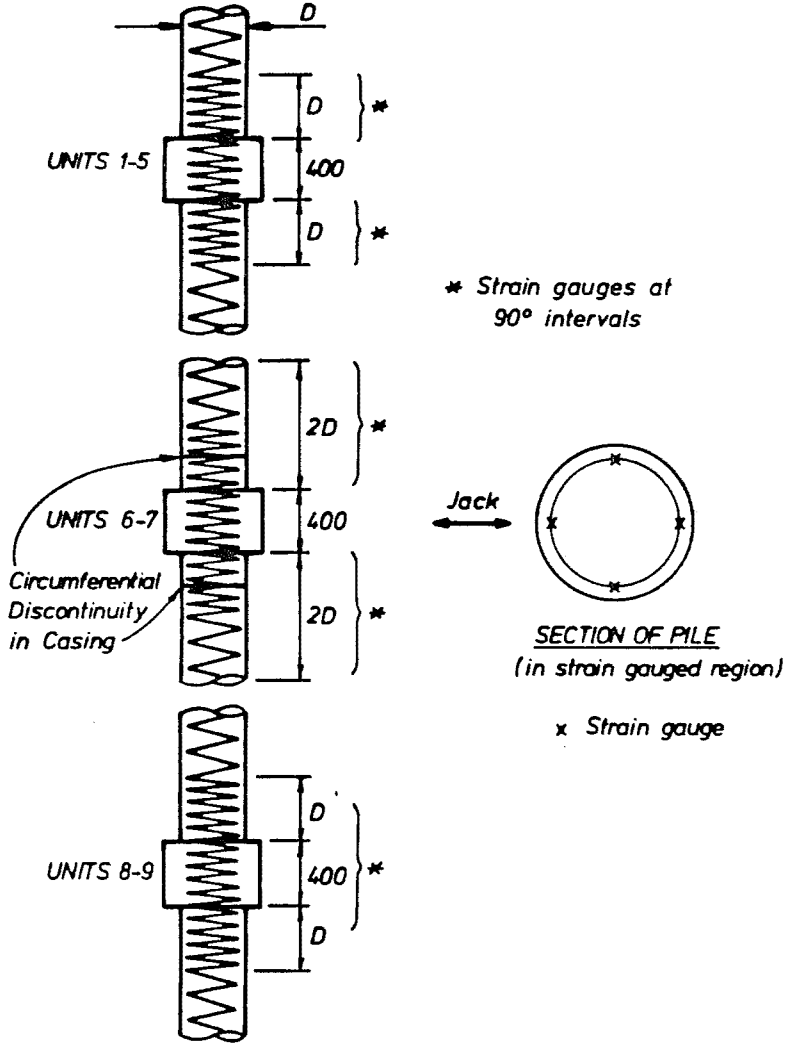

FIG. 4.12 : POSITIONS OF STRAIN GAUGES ON SPIRAL REINFORCEMENT

4.6.2 Steel Tubes

Figures 4.13 to 4.16 show plots of stress vs strain obtained from coupon tests of tube samples. Each of the plotted stress vs strain curves represents the average result from three samples tested in accordance with NZS 3404-1977 (4.29). Results from three types of test are indicated:

(i) flat plate, before it was bent into a tube (Flat Plate Sample);
(ii) restraightened tube, loaded in the longitudinal direction of the rolled tube (Longitudinal Sample); and
(iii) restraightened tube, loaded in the hoop direction of the rolled tube (Hoop Sample).

4.6.2.1 Unit 1 (see Fig. 4.13)

Since unit 1 (t = 9.53 mm) was constructed using a hot-formed tube, no flat plate samples were available and it is likely that the actual stress-strain characteristics in the longitudinal and hoop directions were similar. The cold-working which was necessary to restraighten the hoop samples, prior to coupon testing, is the main reason for the apparent difference between the responses of the longitudinal and hoop samples shown in Fig. 4.13. This cold-working produces very significant hoop strains which are in the range of 3.0% compression to 3.0% tension (from Fig. 3.2, $-t/(D-t) \leq \varepsilon_H \leq t/(D-t)$).

The longitudinal samples had ultimate and yield strengths of 421 MPa and 295 MPa respectively which are reasonably typical of mild steel, although strain-hardening commenced at 1.5% strain, which is lower than the 2% to 3% strain obtained typically for mild steel. This apparent low strain at commencement of strain-hardening could have been due to the inevitable small amount of cold working which would have occurred in preparing these samples for testing.

4.6.2.2 Units 2-7 (see Figs. 4.14 and 4.15)

The flat plate samples of steel from units 2-7 (t = 3 mm or 5 mm) show characteristics typical of mild steel with yield and ultimate strengths of approximately 345 MPa and 455 MPa respectively, and a strain at commencement of strain-hardening of 3%.

Samples of the tube which were restraightened, prior to coupon testing, in the longitudinal direction of the tube show a lower strain at the commencement of strain-hardening than do the flat plate samples, due to the inevitable small amount of cold-working which would have occurred in preparing these samples for testing.

Restraightened samples tested in the hoop direction of the tube do not exhibit a pronounced yield stress, as a result of cold-working from both the original shaping of the tube and the subsequent restraightening for sample testing. Hoop strains of up to 1.7% (unit 2, D/t = 60), 1.1% (unit 3, D/t = 90), 0.8% (unit 4, D/t = 120), 0.7% (unit 5, D/t = 150), and 1.3% (units 6 and 7, D/t = 80) would have been induced by the original shaping of the tube. Thus the work-hardening effects should be more evident in the test units with small casing D/t ratios. Due to the additional work-hardening associated with the restraightening of samples tested in the hoop direction of the tube, it is probable that the actual stress-strain characteristics of the tube in the hoop direction were intermediate between those of the flat plate and the restraightened hoop samples.

4.6.2.3 Units 8 and 9 (see Fig. 4.16)

Units 8 and 9 (t = 1.96 mm) were fabricated from tubes that were much weaker than conventional mild steel, as the tensile strength was only approximately 327 MPa. There was also no evidence of a sharply defined yield point in the stress-strain curves, even for the flat plate samples. However the steel used in

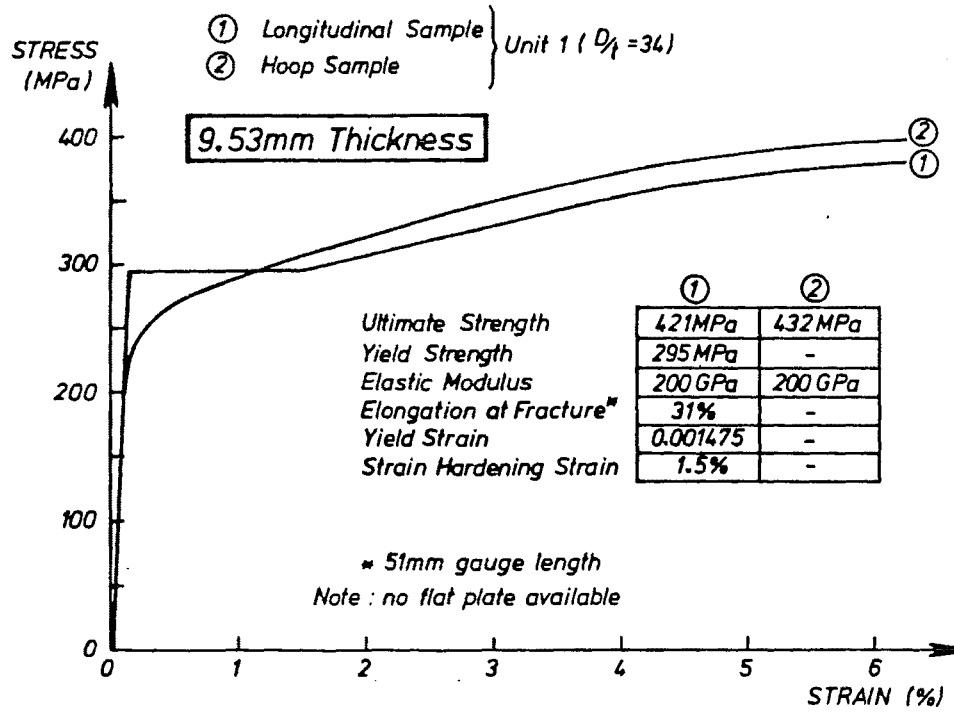

FIG. 4.13 : TUBE STRESS-STRAIN CHARACTERISTICS (t = 9.53 MM)

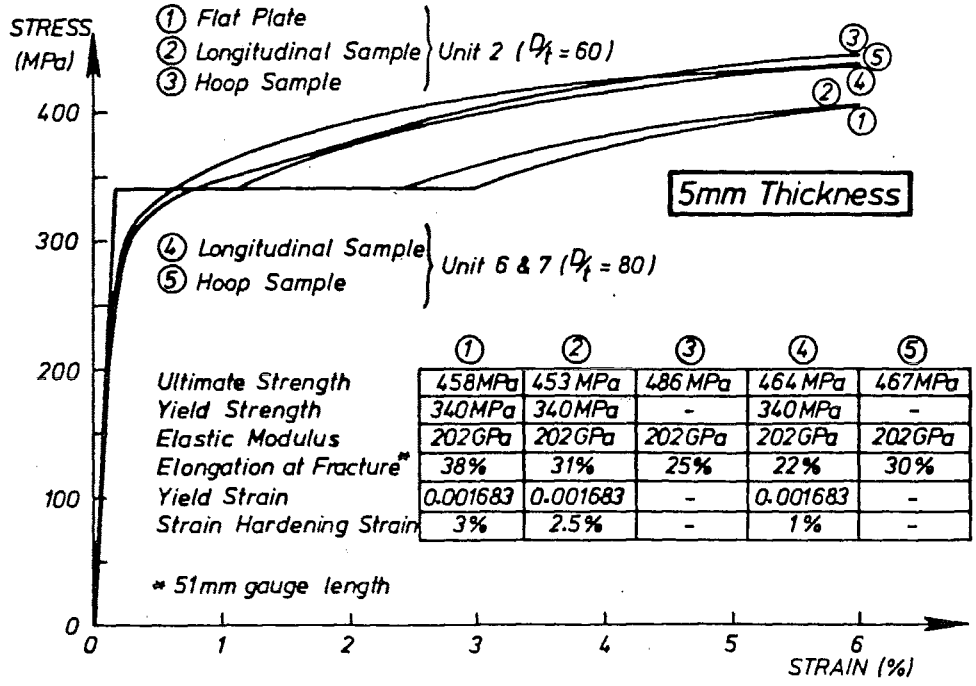

FIG. 4.14 : TUBE STRESS-STRAIN CHARACTERISTICS (t = 5 MM)

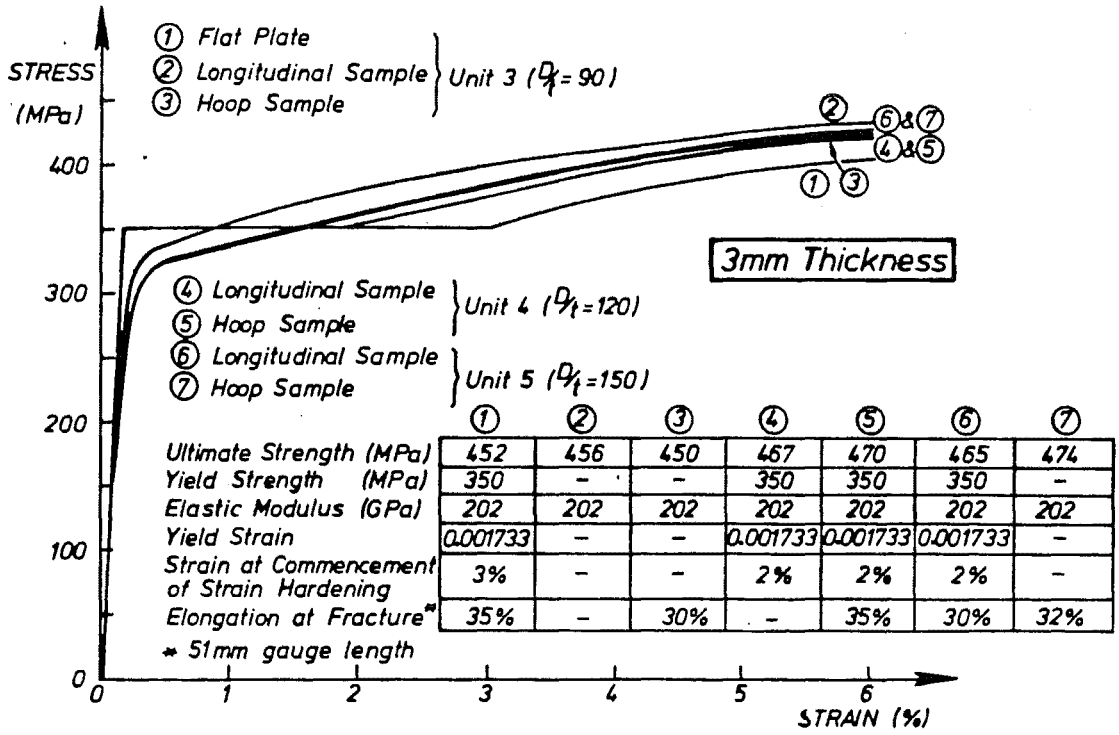

	①	②	③	④	⑤	⑥	⑦
Ultimate Strength (MPa)	452	456	450	467	470	465	474
Yield Strength (MPa)	350	–	–	350	350	350	–
Elastic Modulus (GPa)	202	202	202	202	202	202	202
Yield Strain	0.001733	–	–	0.001733	0.001733	0.001733	–
Strain at Commencement of Strain Hardening	3%	–	–	2%	2%	2%	–
Elongation at Fracture*	35%	–	30%	–	35%	30%	32%

FIG. 4.15 : TUBE STRESS-STRAIN CHARACTERISTICS (t = 3 MM)

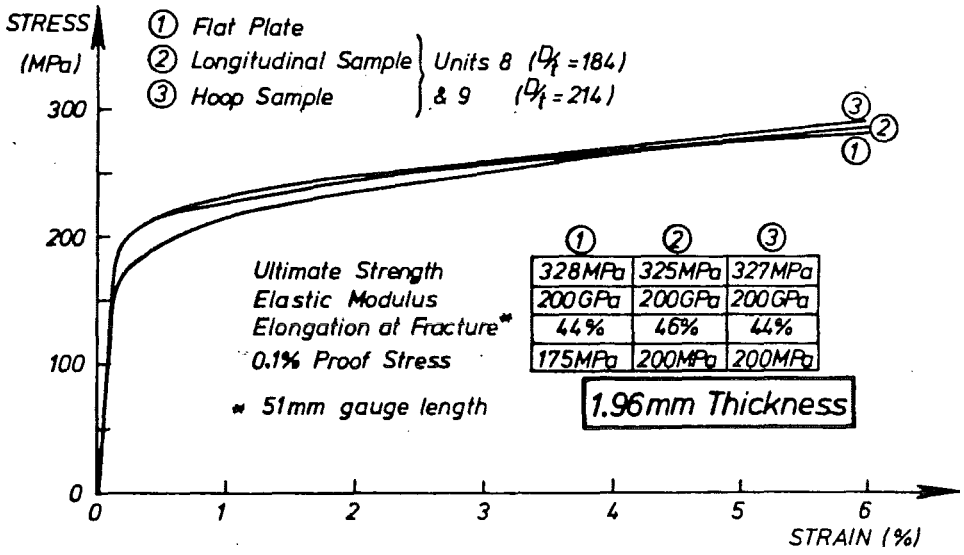

	①	②	③
Ultimate Strength	328MPa	325MPa	327MPa
Elastic Modulus	200GPa	200GPa	200GPa
Elongation at Fracture*	44%	46%	44%
0.1% Proof Stress	175MPa	200MPa	200MPa

FIG. 4.16 : TUBE STRESS-STRAIN CHARACTERISTICS (t = 1.96 MM)

units 8 and 9 was more ductile than the steel used in units 1-7, as is shown by a comparison of the elongations at fracture.

4.6.3 Longitudinal Reinforcing Steel

Figure 4.17 shows the stress-strain response obtained during uniaxial-tension-load testing of samples of the D16 longitudinal reinforcing steel. Each curve plotted represent average result from four tests. Negligible scatter occurred between the samples in a given batch. Typical mild steel characteristics are exhibited.

4.6.4 Spiral Reinforcing Steel

Figure 4.18 shows plots of stress vs strain which were obtained from the uniaxial-tension-load testing of samples of the R10 spiral reinforcement. Each of the indicated curves represents the average of three tests.

Samples of the R10 steel which were taken before the spiral was formed show typical mild steel behaviour with low yield and ultimate strengths and a strain at commencement of strain-hardening of approximately 3%. Samples of R10 steel that were taken from a restraightened section of a previously formed spiral show evidence of extensive work-hardening. It is probable that the actual stress-strain characteristics of the in-place spiral reinforcement were intermediate between those indicated for the straight bar samples and the restraightened bar samples.

4.7 SUMMARY OF TEST UNIT DETAILS

A summary of the actual test unit details is given in Table 4.5. The values of the longitudinal-compression load ($P \cong 0.1 f'_c(A_c + A_t)$) used in the tests are also given.

4.8 TEST PREPARATION AND PROCEDURE

4.8.1 Test Unit Preparation

The test rig has already been illustrated in Fig. 4.4. Full structural details of the test frame and a description of the procedure for installing the test unit in the rig are contained in the report of Ang et al (4.12).

4.8.2 Experimental Procedure

Before testing of the units was commenced, tensile testing of steel samples and compressive testing of concrete samples had been performed. This enabled the theoretical ultimate flexural strength (H_i) of the units to be calculated in accordance with the procedure given in Section 4.2.3. These rules are similar to those used in calculating the theoretical ultimate flexural strength of reinforced concrete (4.17).

The basic pattern of cyclic loading on the test units is shown in Fig. 4.19. This pattern consisted of successively one cycle to a displacement ductility factor ($= \Delta/\Delta_y$, where Δ = lateral displacement, and Δ_y = yield displacement) of $\mu = \pm 3/4$, followed by two cycles to each of $\mu = \pm 2, \pm 4, \pm 6$ and ± 8. Subsequently, if the condition of the test unit permitted dynamic cycling at a frequency of 0.12 Hertz and a lateral displacement of ± 60 mm was performed. Finally if the test unit was still in sound condition, a large displacement pulse ($\Delta \cong 140$ mm) was applied. However it was not always convenient or appropriate to follow the above lateral displacement pattern in full, and variations were adopted depending on the circumstances.

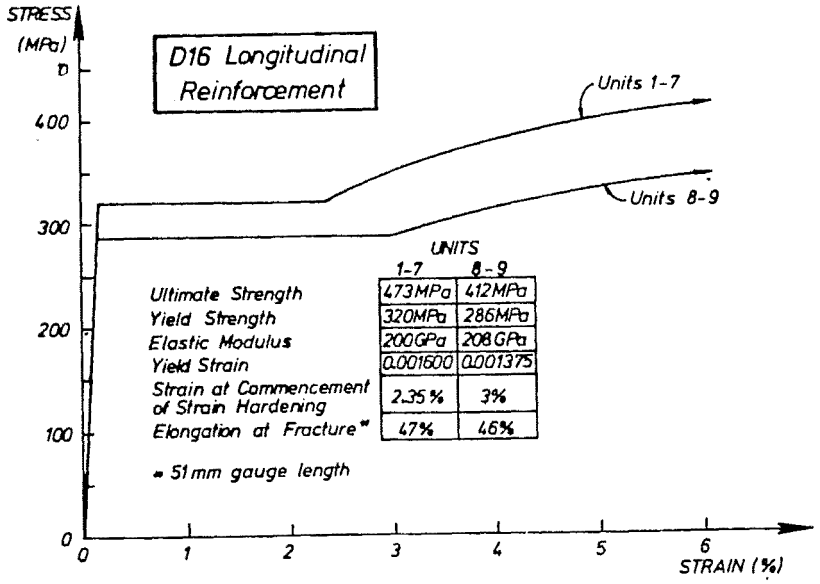

FIG. 4.17 : LONGITUDINAL REINFORCEMENT STRESS-STRAIN CHARACTERISTICS

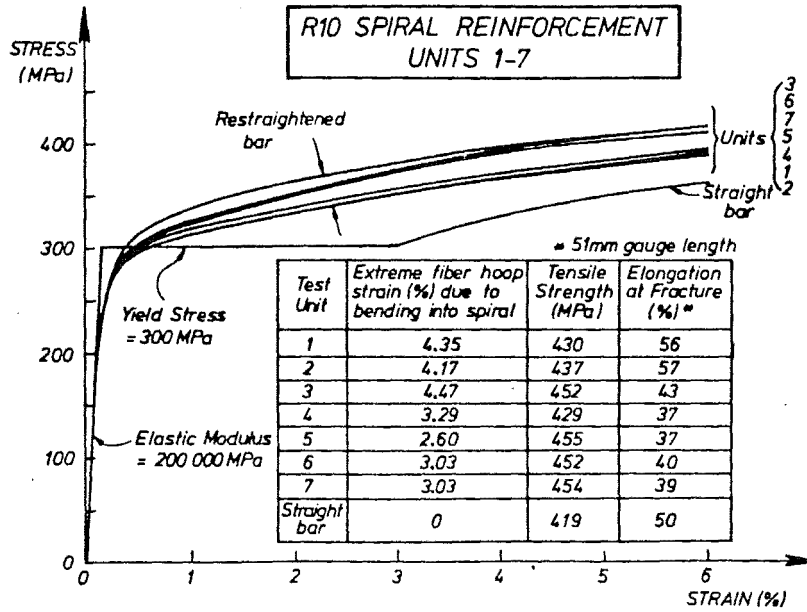

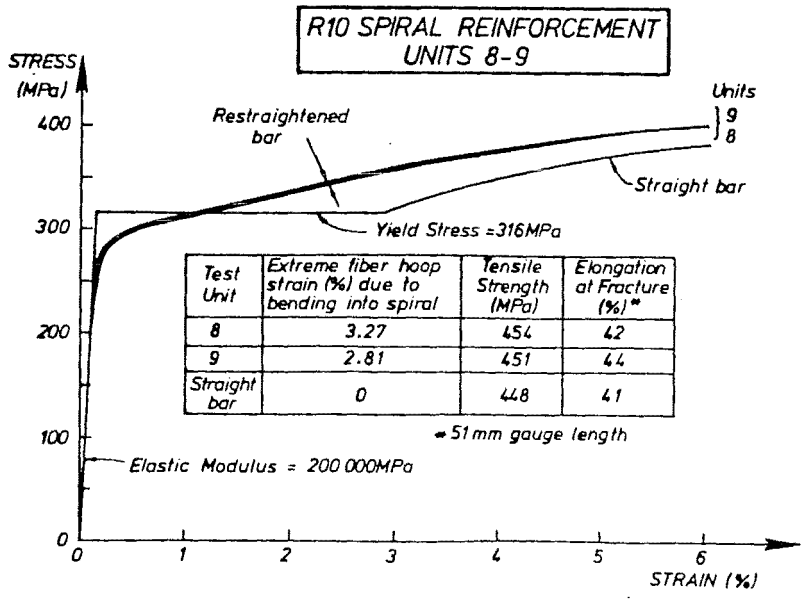

FIG. 4.18 : SPIRAL REINFORCEMENT STRESS-STRAIN CHARACTERISTICS

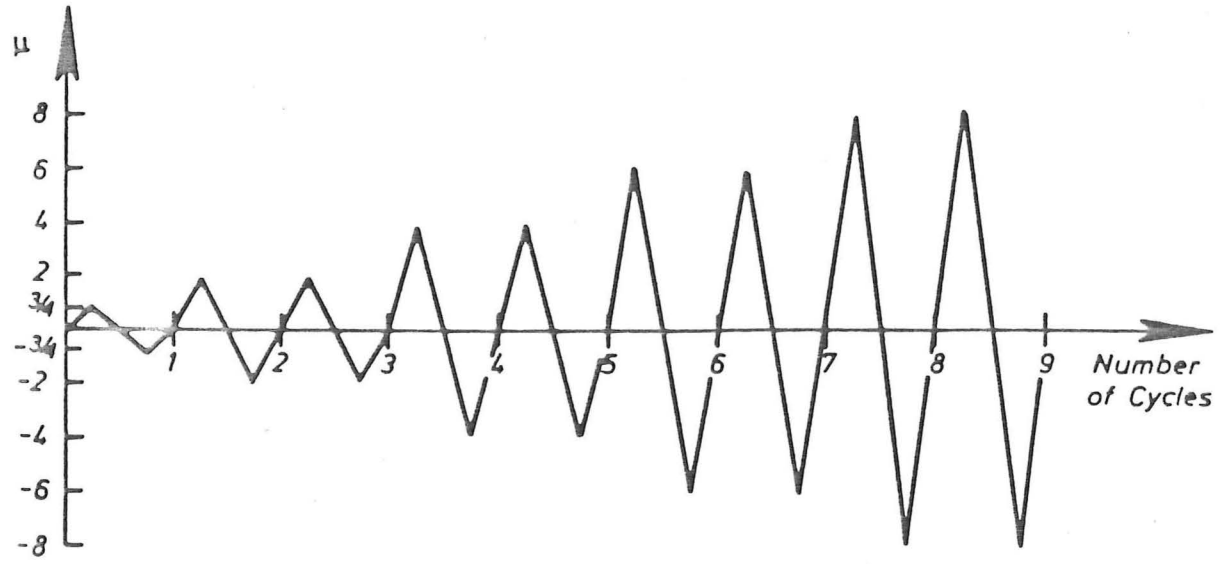

FIG. 4.19 : ENVISAGED STATIC LOADING SEQUENCE

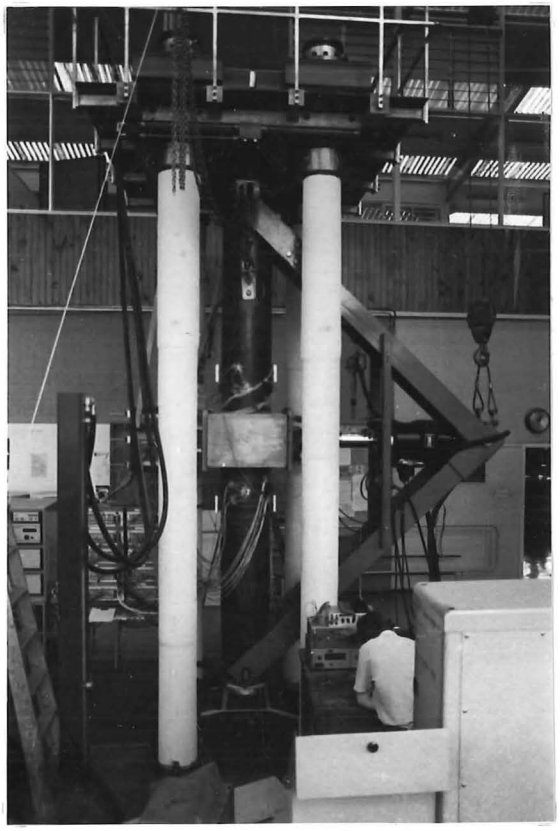

FIG.4.20a : OVERALL VIEW OF TEST SET-UP

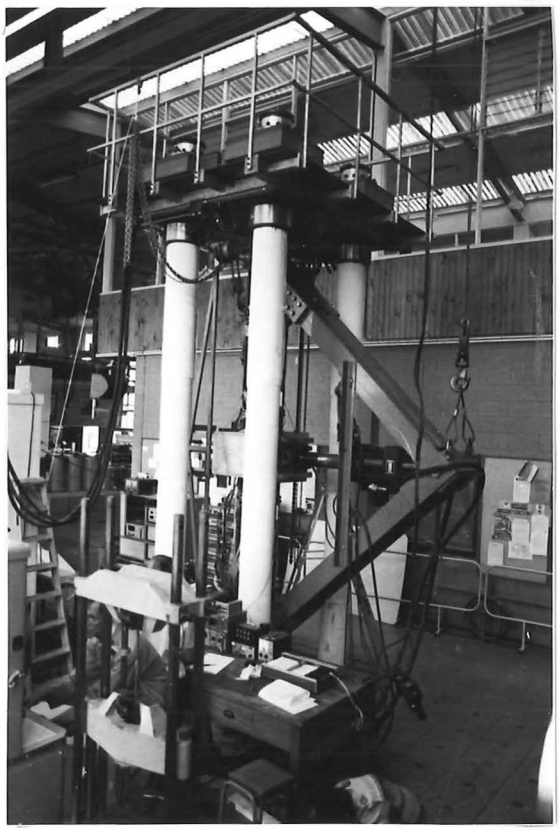

FIG. 4.20b : OBLIQUE VIEW OF TEST SET-UP

In determining the deflection Δ corresponding to a given ductility factor μ , it was necessary to know the value of the yield deflection Δ_y. This was determined from the first cycle of loading ($\mu = \pm 3/4$) which involved loading to firstly $0.75H_i$ (75% of the theoretical ultimate load) and then to $-0.75H_i$. The yield deflection was then calculated from:

$$\Delta_y = 2/3 \ (|\Delta^+| + |\Delta^-|) \qquad (4.5)$$

where Δ^+ = deflection at lateral load $H = 0.75H_i$
and Δ^- = deflection at lateral load $H = -0.75H_i$

It should be noted that the yield deflection calculated in this fashion is larger than the deflection at first yield of the steel, and corresponds to the deflection at yield for idealised perfectly elastic-plastic response. In this idealised response, the elastic stiffness corresponds to the average of the secant stiffnesses at experimental lateral loads of $H = 3/4H_i$ and $H = -3/4H_i$.

During static testing, the nett longitudinal load (i.e. the sum of the DARTEC load plus the load induced by the inclined arms of the MTS reaction frame,(see Fig.4.4) on the test unit was kept constant by adjusting the DARTEC longitudinal load after every increment of MTS lateral load.Unfortunately, from the point of view of consistency with the static testing, it was not possible to adjust the DARTEC-induced longitudinal load during dynamic testing. Thus the nett longitudinal load on the test unit during dynamic testing varied with the level of load in the MTS actuator. However the dynamic testing did simulate piles in a twin pile bent under horizontal earthquake attack in the direction perpendicular to the axis of the bridge, since in this case the longitudinal loads in the piles also vary as the horizontal inertia load varies.

During static testing, testing was load-controlled by increments of $0.25H_i$ for loads of up to $\pm 0.75H_i$. At loads of larger magnitude, testing was displacement controlled with increments of μ typically equal to 0.5, up to the level of μ appropriate for that cycle.

Complete sets of strain gauge and linear potentiometer readings were taken at every increment of lateral load for the initial cycle ($\mu = \pm 3/4$), and then subsequently at every new level of lateral displacement as well as at the peaks of the subsequent cycles.

Figure 4.20 shows overall views of the experiment in action.

4.9 EXPERIMENTAL RESULTS - CONTINUOUS CASINGS

4.9.1 General Observations

Figures 4.21-4.27 contain photographs of test units 1-5, 8 and 9 after various stages of testing. The performance of these test units was strongly influenced by the development of local buckles in the tube at sections just outside the concrete loading block (see Figs. 4.21-4.28).

For unit 1 ($D/t = 34$) the local buckling was first perceptible at the first excursion to $\mu = 4$. For the other units ($D/t \geq 60$), local buckling was first observed at the peak of the first excursion to $\mu = 2$. Under cyclic loading, the local buckles formed and then were partially restraightened as the longitudinal strain reversed from compression to tension. At the end of static testing when the test unit was restraightened to give zero lateral displacement, bulging was apparent right around the perimeter of the sections just outside the concrete loading block.

(a) CONDITION AFTER STATIC TESTING
(μ = -4(v))

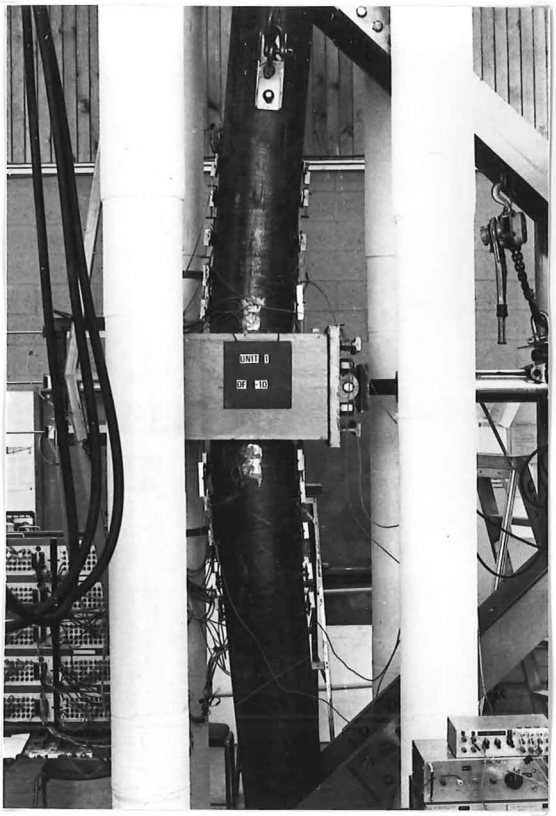

(b) TEST UNIT UNDER LARGE LATERAL DISPLACEMENT
(μ = -10)

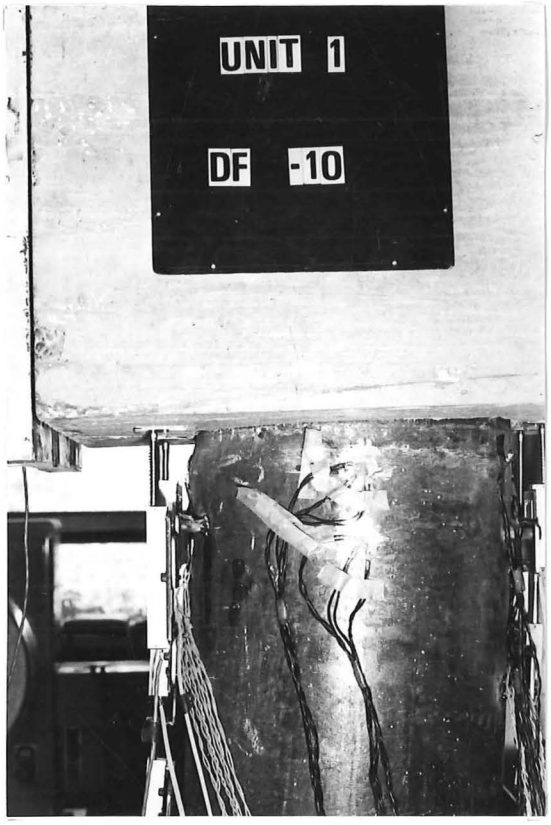

(c) LOCAL BUCKLING AT μ = -10

(d) POST-MORTEM TO TEST, CRUSHED CONCRETE UNDERLYING ZONES OF TUBE LOCAL BUCKLING

FIG. 4.21 : UNIT 1 (D/t = 34)

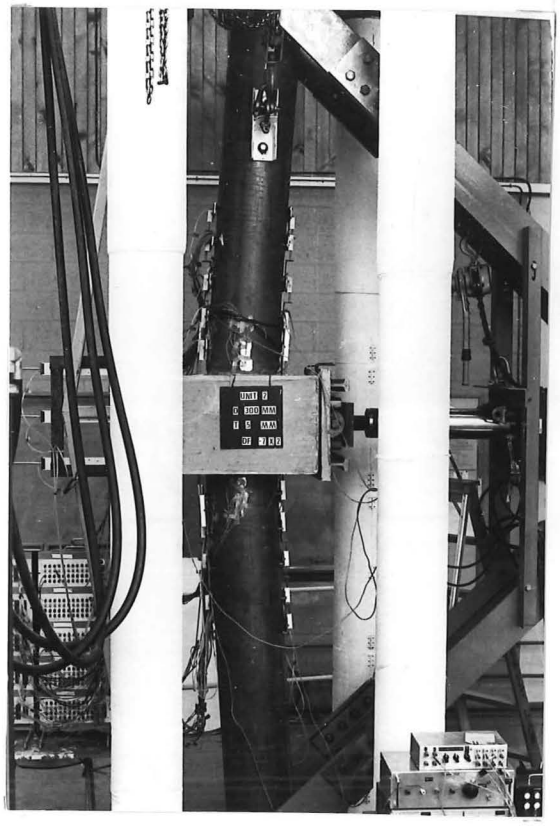

(a) TEST UNIT AT PEAK DISPLACEMENT (μ = -7(ii))

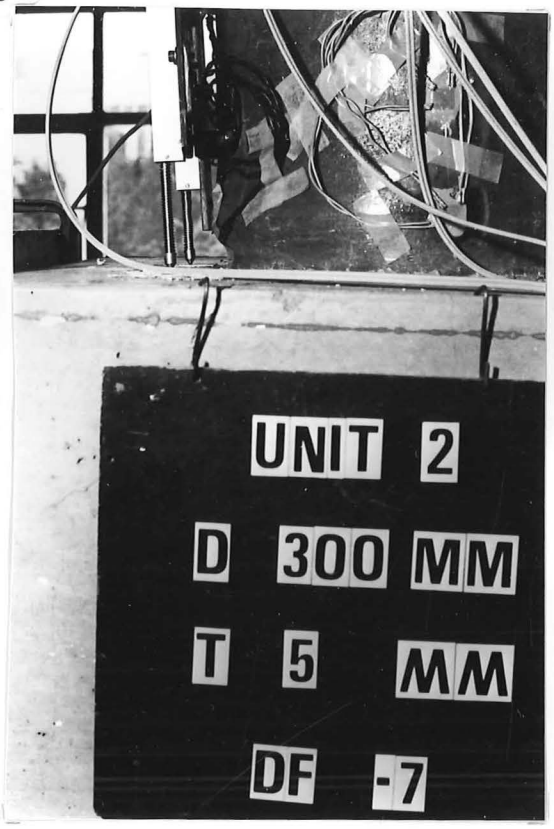

(b) CLOSE-UP VIEW OF LOCAL BUCKLING, AT PEAK DISPLACEMENT (μ = -7)

(c) CLOSE-UP VIEW OF CRACKED CONCRETE LOADING BLOCK AND SEPARATION OF CONCRETE LOADING BLOCK FROM THE TUBE ON THE SIDE SUBJECTED TO LONGITUDINAL-TENSION STRAINS, AT PEAK DISPLACEMENT (μ = -7)

(d) POST-MORTEM TO TEST, CRUSHED CONCRETE UNDERLYING ZONES OF TUBE LOCAL BUCKLING

FIG. 4.22 : UNIT 2 (D/t = 60)

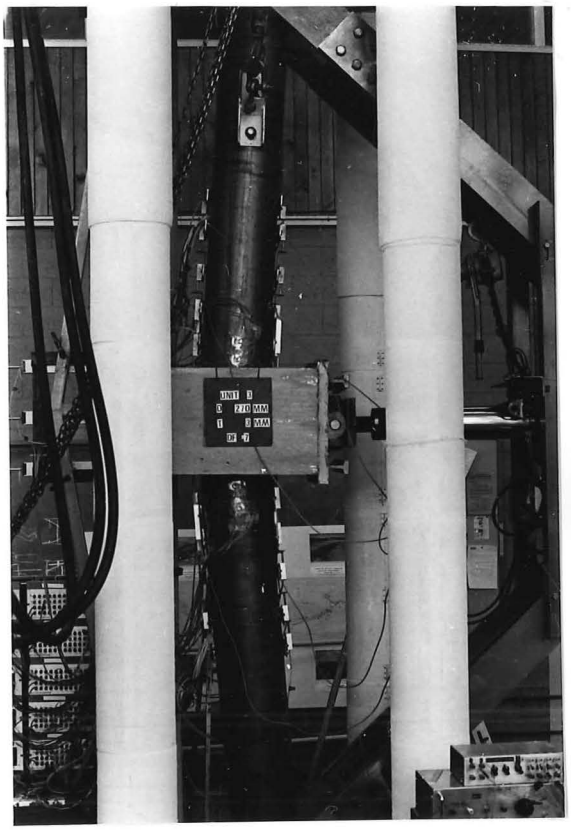

(a) TEST UNIT AT PEAK DISPLACEMENT (μ = -7)

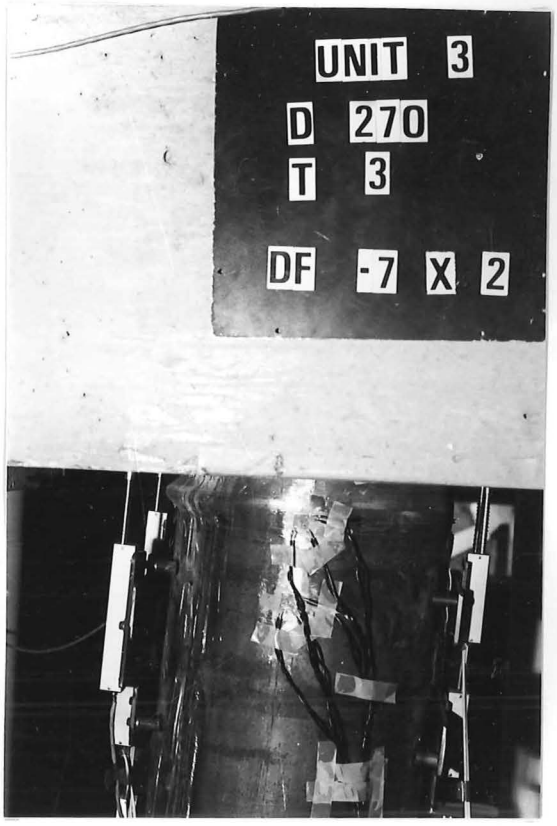

(b) CLOSE-UP VIEW OF LOCAL BUCKLING AT PEAK DISPLACEMENT (μ = -7(ii))

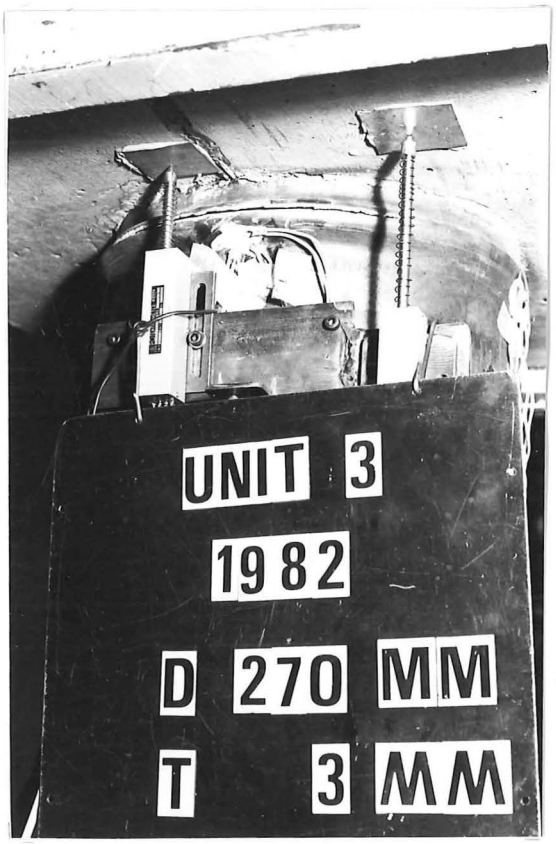

(c) HORIZONTALLY EXTENDING FRACTURING OF THE TUBE WHICH OCCURRED DURING DYNAMIC TESTING

(d) POST-MORTEM TO TEST, CRUSHED CONCRETE UNDERLYING ZONES OF TUBE LOCAL BUCKLING

FIG. 4.23 : UNIT 3 (D/t = 90)

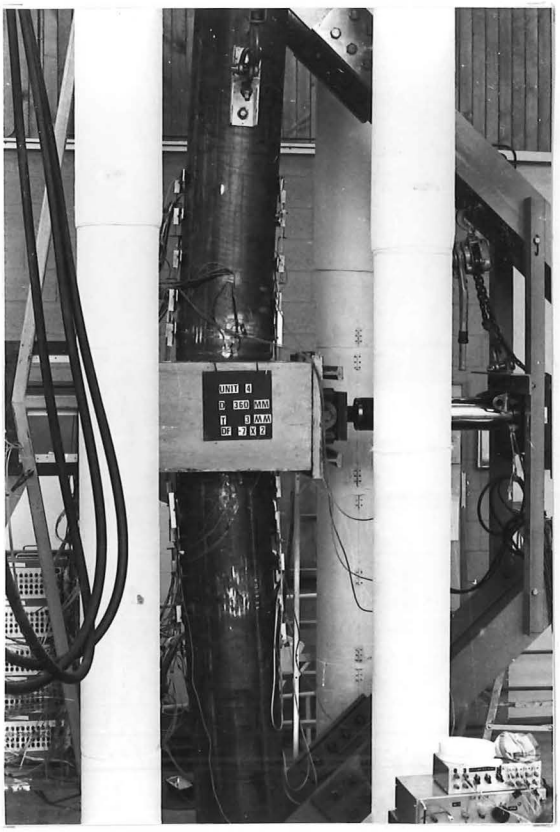

(a) TEST UNIT AT PEAK DISPLACEMENT (μ = -7(ii))

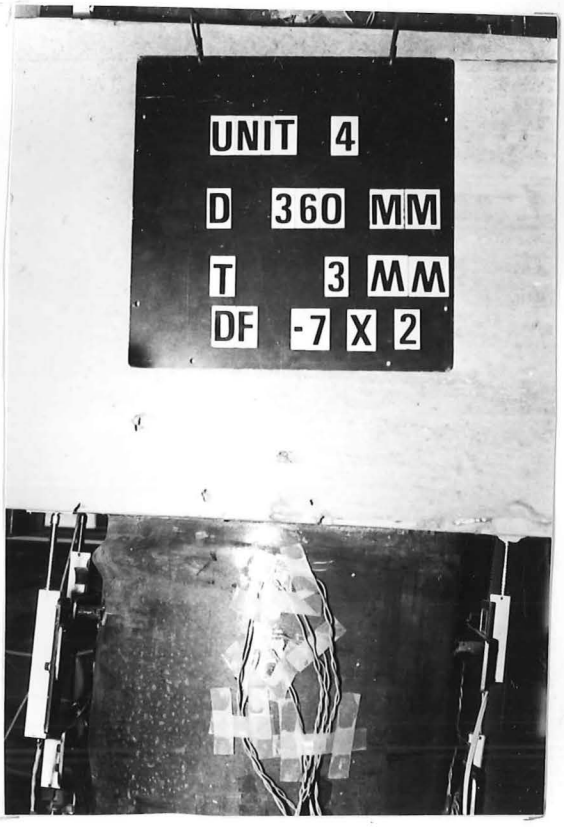

(b) CLOSE-UP VIEW OF LOCAL BUCKLING AT PEAK DISPLACEMENT (μ = -7(ii))

(c) VIEW OF PLASTIC HINGE AREA AFTER DYNAMIC TESTING

(d) POST-MORTEM TO TEST, CRUSHED CONCRETE UNDERLYING ZONES OF TUBE LOCAL BUCKLING

FIG. 4.24 : UNIT 4 (D/t = 120)

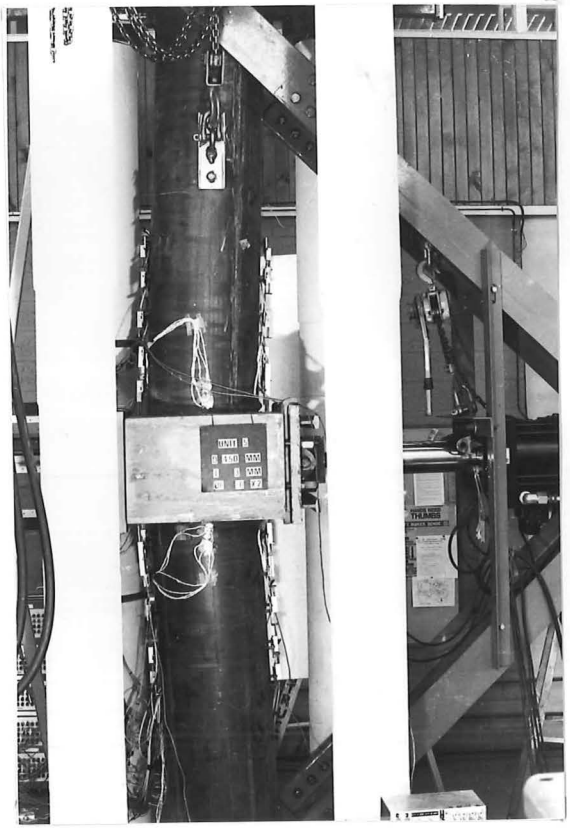

(a) TEST UNIT AT PEAK DISPLACEMENT (μ = -6(ii))

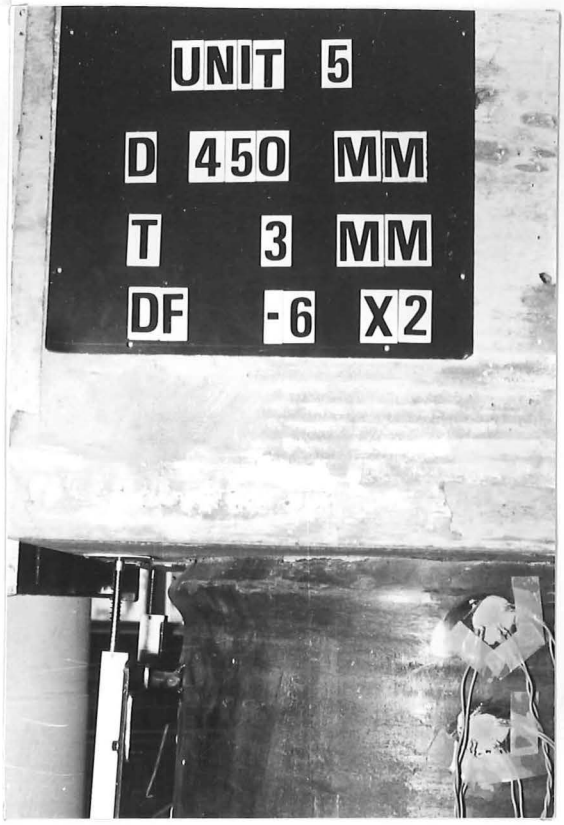

(b) CLOSE-UP VIEW OF LOCAL BUCKLING AT PEAK DISPLACEMENT (μ = -6(ii))

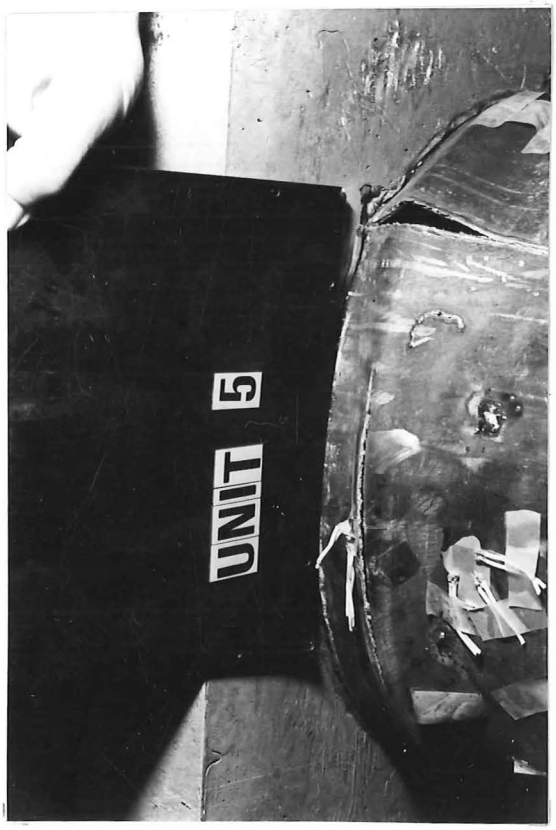

(c) VIEW OF PLASTIC HINGE AREA AFTER DYNAMIC TESTING

(d) POST-MORTEM TO TEST, CONCRETE UNDERLYING ZONES OF TUBE LOCAL BUCKLING

FIG. 4.25 : UNIT 5 (D/t = 150)

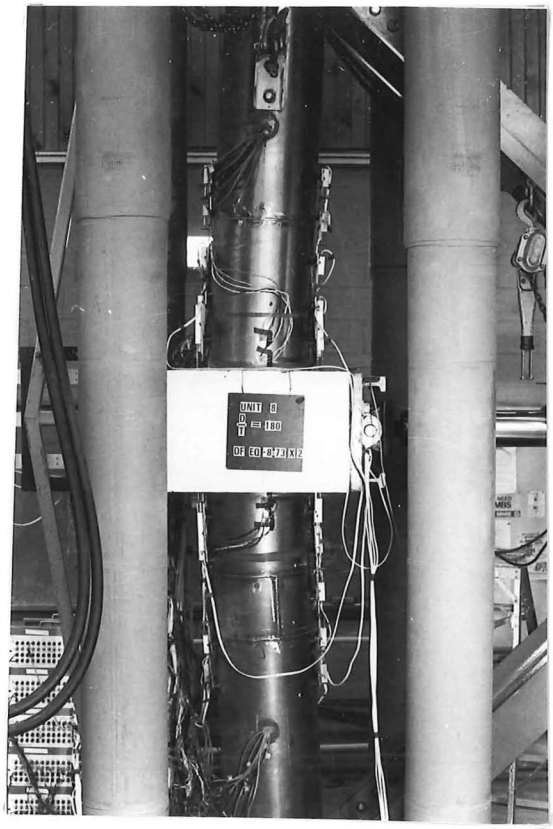

(a) TEST UNIT AT PEAK DISPLACEMENT (μ = -8.7(ii))

(b) CLOSE-UP VIEW OF LOCAL BUCKLING AT PEAK DISPLACEMENT (μ = -8.7(ii))

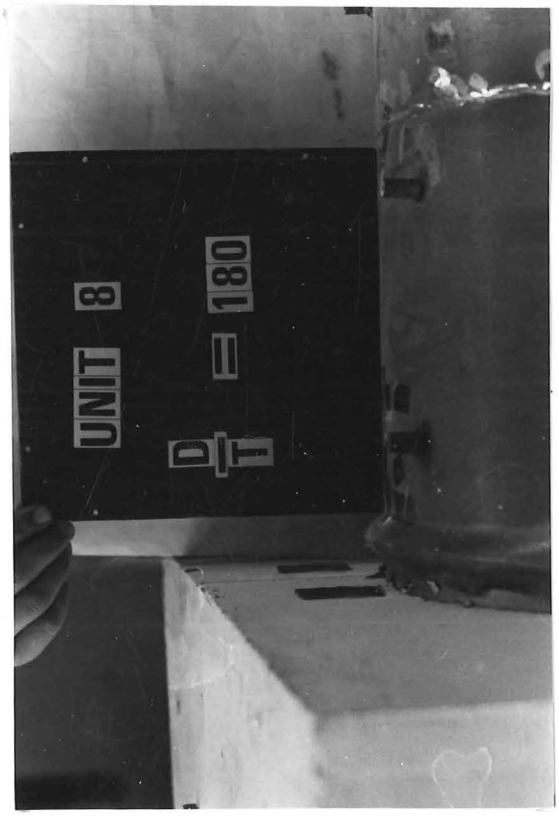

(c) VIEW OF PLASTIC HINGE AREA AFTER DYNAMIC TESTING

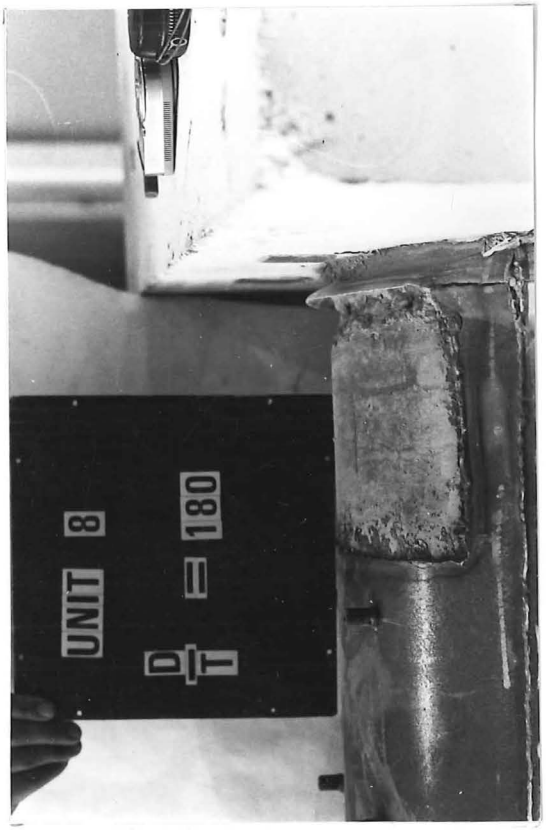

(d) POST-MORTEM TO TEST, CRUSHED CONCRETE UNDERLYING ZONES OF TUBE LOCAL BUCKLING

FIG. 4.26 : UNIT 8 (D/t = 184)

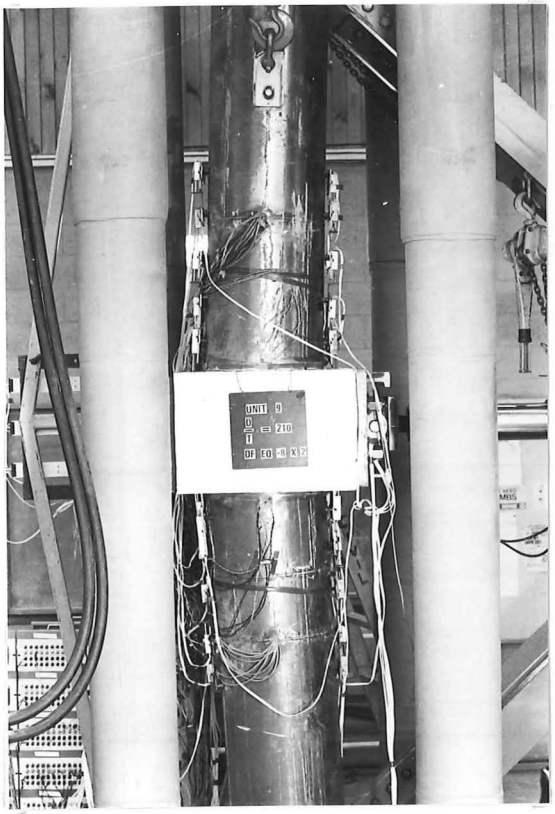

(a) TEST UNIT AT PEAK DISPLACEMENT (μ = -8(ii))

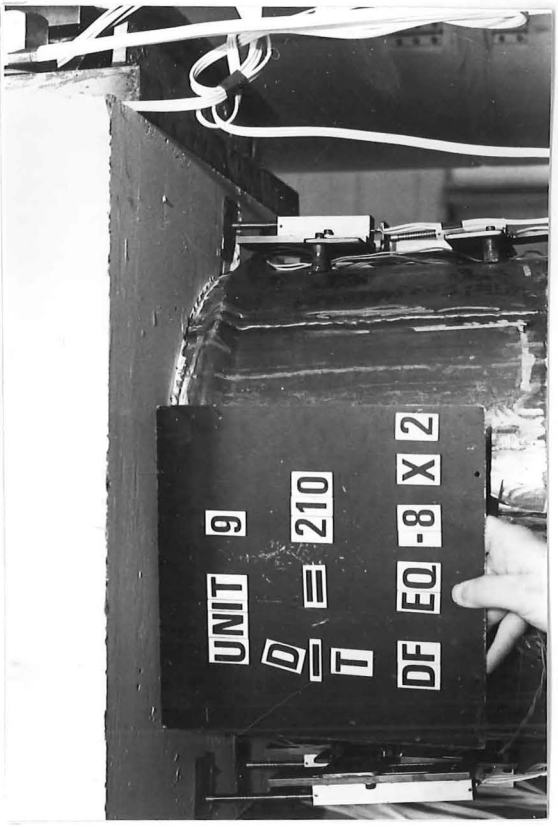

(b) CLOSE-UP VIEW OF LOCAL BUCKLING AT PEAK DISPLACEMENT (μ = -8(ii))

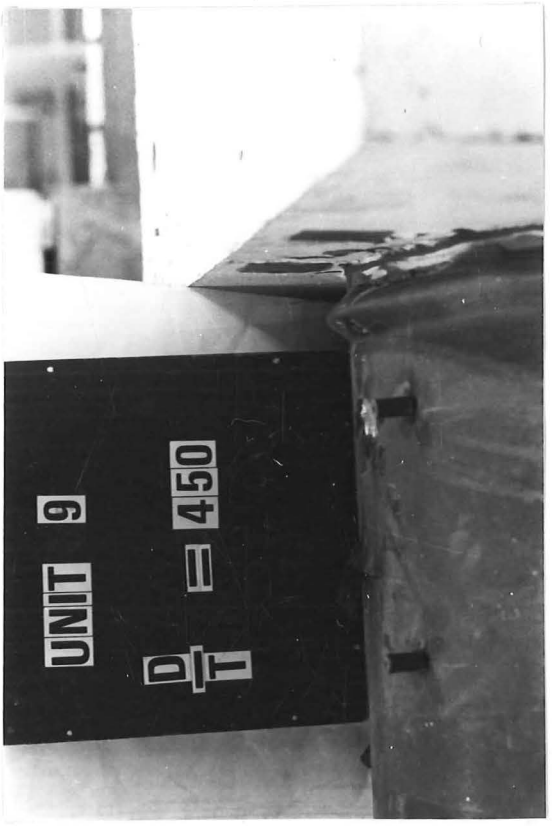

(c) VIEW OF PLASTIC HINGE ZONE AREA AFTER DYNAMIC TESTING

(d) POST-MORTEM TO TEST, CONCRETE UNDERLYING ZONES OF TUBE LOCAL BUCKLING

FIG. 4.27 : UNIT 9 (D/t = 214)

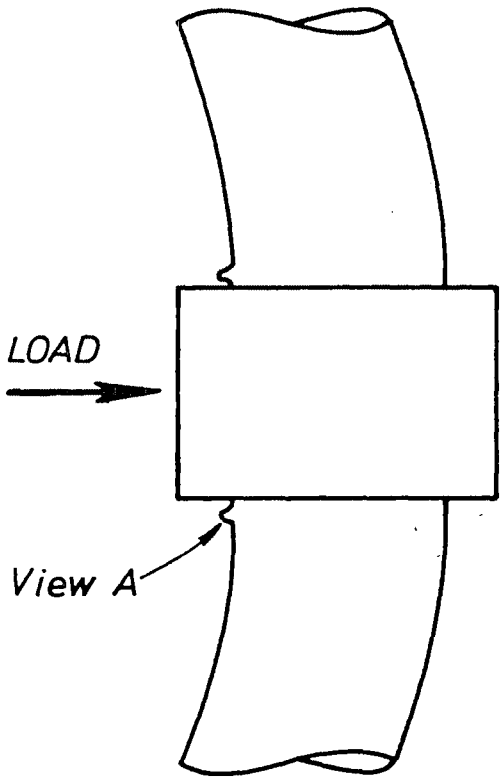

NOTE :-

1. $2L_e$ corresponds to the average of the upper and lower local buckles
2. Outstand corresponds to the maximum of the upper and lower bulges

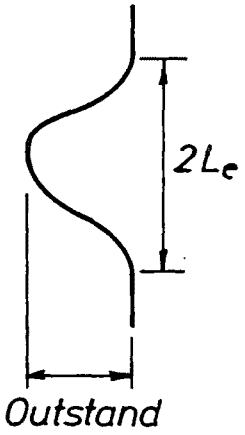

ELEVATION OF TEST UNIT

VIEW A OF LOCAL BUCKLE

FIG. 4.28 : DEFINING LOCAL BUCKLE GEOMETRY

Table 4.6 summarises the local buckling details as at the end of static testing of the test units. The longitudinal extent of local buckling $2L_e$ and the "Outstand" of the peak of the local buckle from its position in an undeformed configuration are shown in Fig. 4.28. The experimental results show that the outstand of the local buckles tended to increase with decreasing wall thickness (or increasing casing D/t ratio). Thus as expected the severity of local buckling increases with increasing casing D/t ratio. It is also shown that the longitudinal extent of local buckling $2L_e$ varied from 35 to 70 mm. Test units with thick tube walls tended to have a larger longitudinal extent of local buckling than did those with thin walls.

Table 4.6 also contains predictions to the longitudinal extent of local buckling $2L_e$ based on the tube wall behaving locally as a column with tangent modulus (E_t) being that appropriate at the commencement of steel strain-hardening (see equation 3.12). In Section 3.4.5 this approach was shown to give good agreement with the experimental results from longitudinal-compression-load tests of thick-walled (D/t = 25.6) concrete-filled tubes. However for test units 1-5, 8 and 9 which were dominated by flexural behaviour, the use of equation 3.12 resulted in a substantial underestimate of the experimentally determined values of $2L_e$. Thus the presence of a gradient in the distribution of longitudinal strain across the section, due to flexure, resulted in an increase in the length of local buckling from that predicted under uniform longitudinal-compression strain conditions.

Units 1-4, 8 and 9 showed no evidence of tube fracturing during static testing. However in unit 5 (D/t = 150) towards the end of static testing a longitudinally extending crack in the casing appeared at the position of a weld defect, indicating local failure of the tube under hoop-tension stress. The crack eventually extended for 70 mm and was located half-way between the N (loading face of test unit) and E (90° around from loading face) faces of this test unit.

During dynamic testing due to low cycle fatigue, fracturing which ran horizontally through the peaks of the local buckles occurred in test units 3,4,5, 8 and 9 ($D/t \geq 90$). Longitudinal splits also developed in units 8 and 9 at this stage of testing along longitudinally running welds.

It was visually obvious at all stages of testing that the plastic rotation was concentrating at the regions of local buckling, with the rest of the test unit remaining relatively straight and hence relatively elastic. This implied the effective plastic hinge lengths (i.e. the zone of concentrated plasticity) in the test units was relatively short, and hence the curvature ductility demands in the regions of local buckling were very large, as shown later in Section 4.10.1.

Design of the reinforced concrete loading blocks had been performed with the intention of making the blocks perform unobtrusively as they transferred lateral load from the MTS actuator to the model pile. In most of the tests, the blocks sustained only minor cracking as intended. However for unit 2, the block developed a wide crack (see Fig. 4.22c) and eventually lost its stiffness with the result that the performance of this unit degraded severely. It is emphasised that this apparent bad performance was not due to the quality of the steel-encased reinforced concrete model pile itself.

During testing of the units, it was observed that slip was occurring between the tube and the concrete loading block as a result of low bond strength between the smooth steel tube and the surrounding concrete. This was particularly apparent on the side of the tube subjected to longitudinal tension strain (see Fig. 4.22c), since Poisson's ratio contraction of the tube would cause the tube

and the loading block to separate. This slip, as discussed later in the chapter, meant that it was difficult to ascertain the effective gauge length of the longitudinally aligned linear potentiometers (N5, N6, S5 and S6; see Fig. 4.9a) bearing on the concrete loading block.

After testing had been completed, casing at the N or S faces (positions of maximum longitudinal strain under bending) adjacent to the concrete loading blocks was removed. This exposed the concrete underlying the regions of local buckling which was found to be crushed to a depth of approximately the same length as the longitudinal extent of the local buckle (see Figs. 4.21-4.27). Concrete outside the regions of the buckled casing had retained its cohesion. However Schmidt hammer tests of the exposed concrete within 150 mm of the buckled casing indicated concrete compressive strengths of less than 10 MPa compared with the original strengths of 29-31 MPa.

4.9.2 Hysteretic Performance

Hysteresis loops which show the overall response of test units 1-5, 8 and 9 to lateral load are given in Figs. 4.29-4.44. Three types of loops are shown:

(i) Lateral Load vs Lateral Deflection;

(ii) Lateral Load vs Rotation at top plastic hinge;
- This rotation corresponds to that measured by the pair of linear potentiometers N6 and S6 which were mounted just above the concrete loading block (see Fig. 4.9a), and

(iii) Lateral Load vs Rotation at bottom plastic hinge;
- This rotation corresponds to that measured by the pair of linear potentiometers N5 and S5 which were mounted just beneath the concrete loading block.

Although the bulk of the plastic rotation will concentrate at the zones covered by potentiometers N5, S5, N6 and S6, it should be noted that as shown later in Section 4.9.3, some plastic rotation occurred outside these zones.

The hysteresis loops obtained during static testing were actually quite irregular. This was due to relaxation (i.e. reduction in lateral load at a given lateral displacement) of the test unit at the end of each increment of testing and the longitudinal load adjustment which was also made at the end of each increment. For test units left unloaded over a period of time (e.g. overnight) creep recovery also caused minor irregularities in the hysteresis loops. These irregularities are insignificant as far as the simulation of seismic performance is concerned. Consequently the indicated hysteresis loops represent the envelope of response for each cycle.

4.9.2.1 Strength Characteristics

In the following chapter, a comparison of the experimentally obtained moment-curvature and lateral load-lateral deflection responses of these test units is made with predictions based on moment-curvature analyses. However as mentioned previously in Section 4.2.3, theoretical ultimate flexural capacities of steel-encased reinforced concrete members can be predicted, albeit less exactly, by assuming the casing acts as an equivalent array of reinforcing bars and analysing in accordance with American Concrete Institute (4.30) or New Zealand (4.17) Concrete Code requirements, where for the purpose of direct comparison with experiment actual and not nominal material strengths were used. For units 8 and 9, which as shown in Fig. 4.16 possessed casing which lacked a yield plateau in its stress-strain response, the actual stress-strain response as determined from the coupon tests were used in making these predictions. In Figs. 4.29-4.44, the lateral load-lateral deflection hysteresis loops are compared with these theoretical ultimate flexural capacities for both positive (H_i^+) and negative (H_i^-) lateral loads.

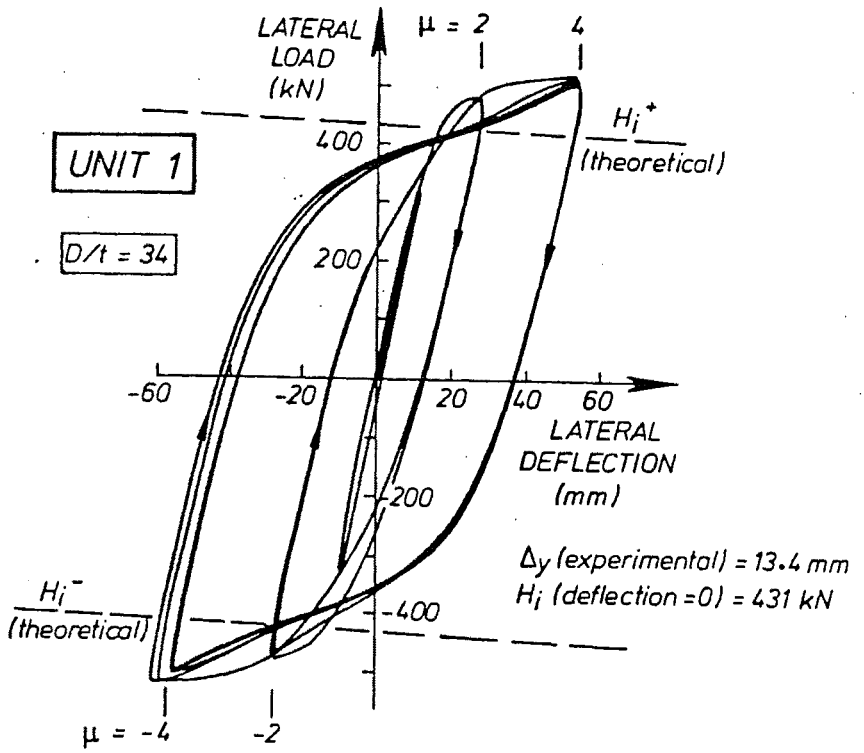

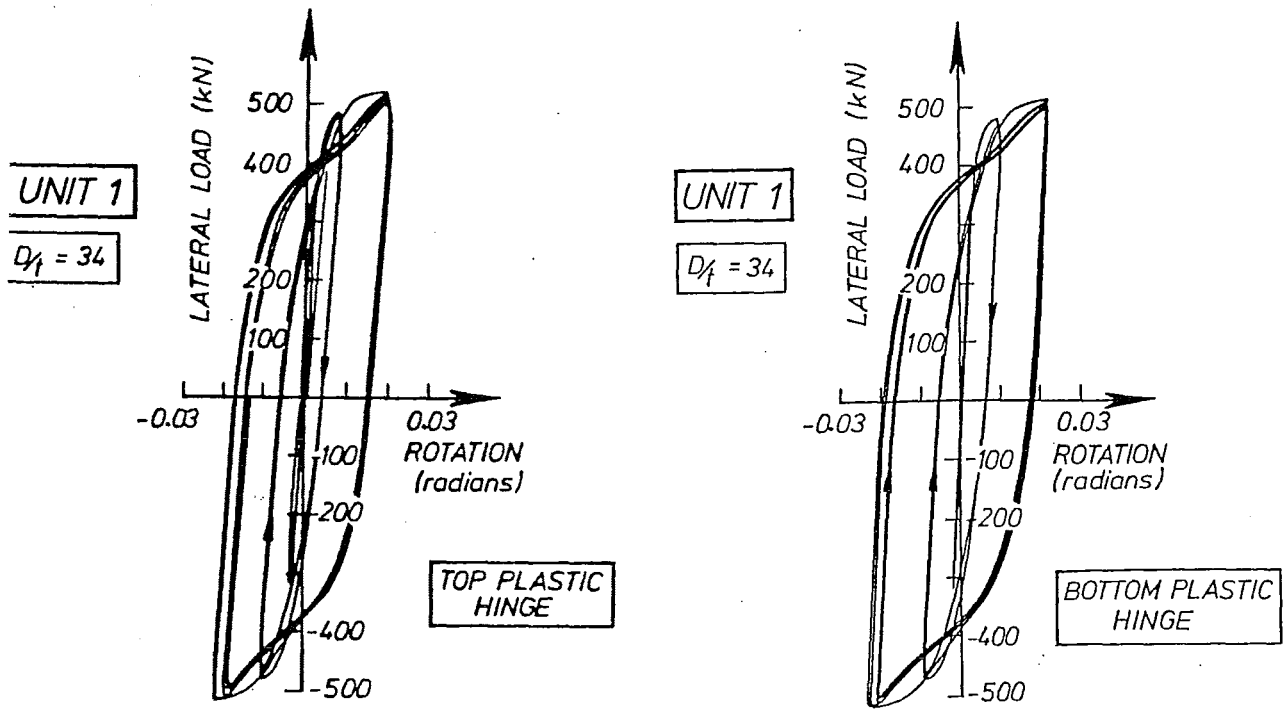

FIG. 4.29 : HYSTERESIS LOOPS FOR INITIAL STATIC LOADING OF UNIT 1

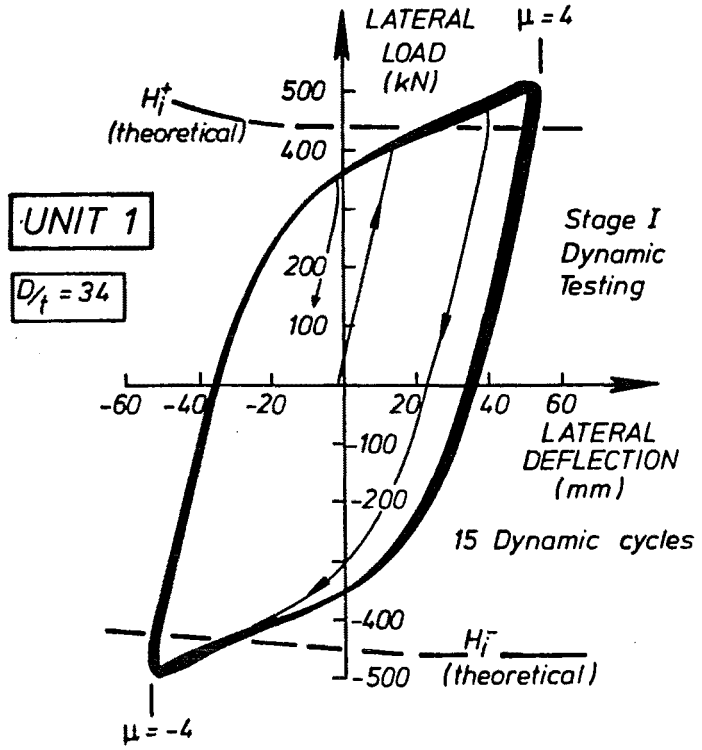

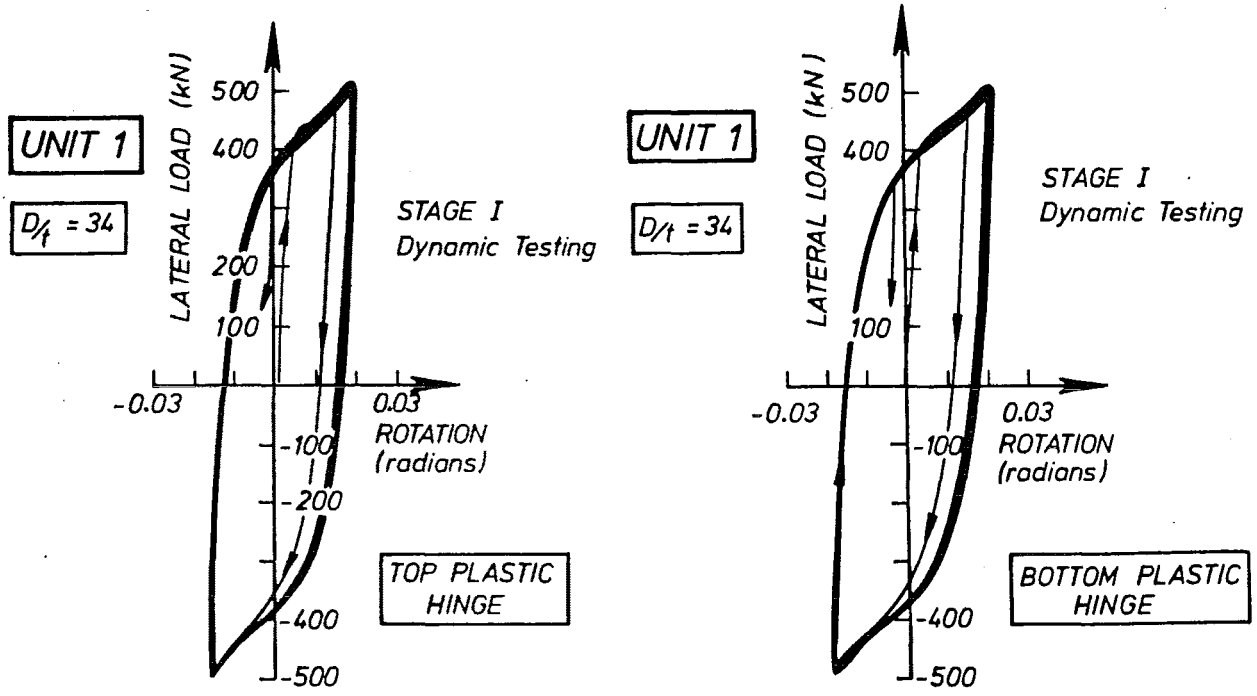

FIG. 4.30 : HYSTERESIS LOOPS FOR STAGE I DYNAMIC LOADING OF UNIT 1

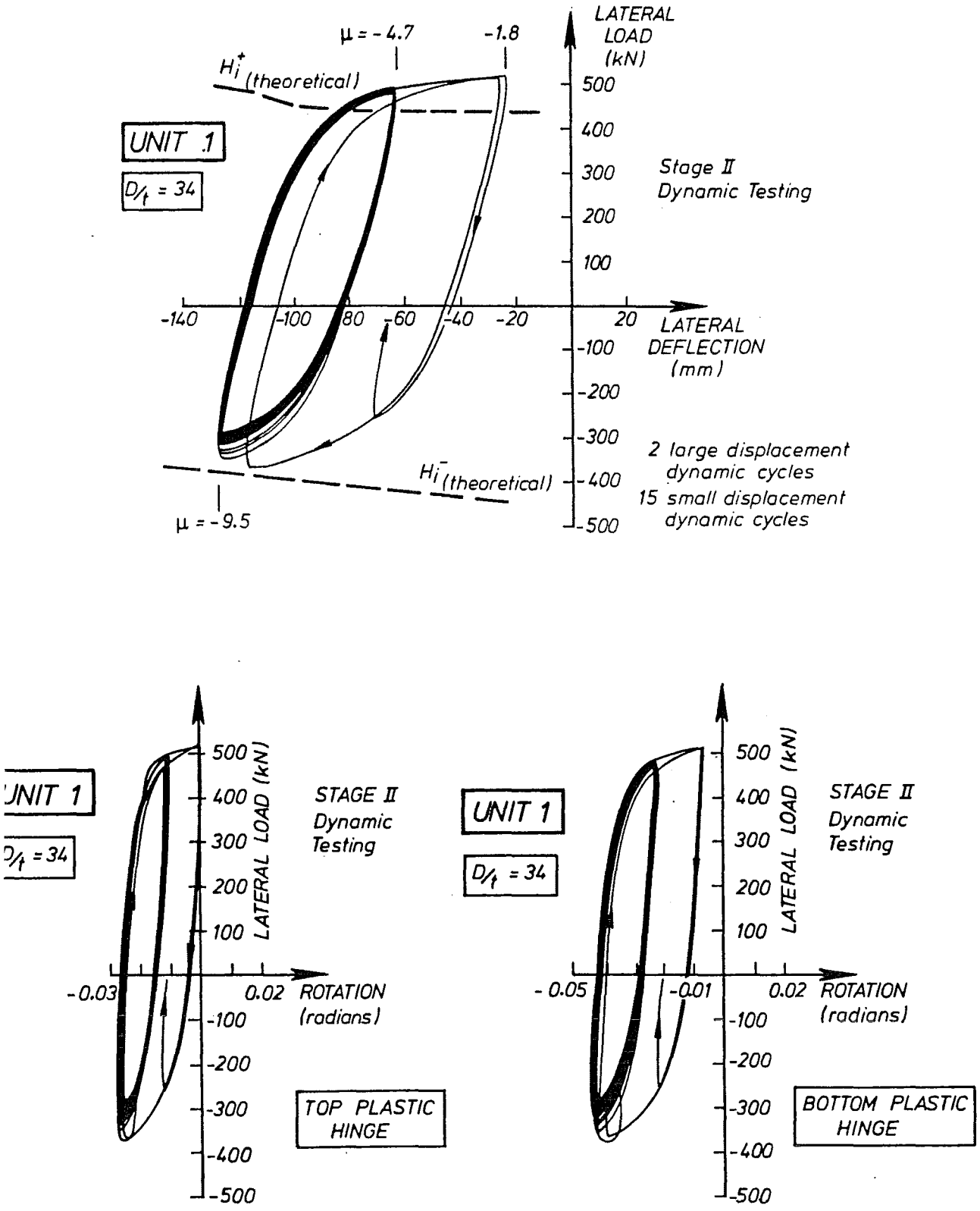

FIG. 4.31 : HYSTERESIS LOOPS FOR STAGE II DYNAMIC LOADING OF UNIT 1

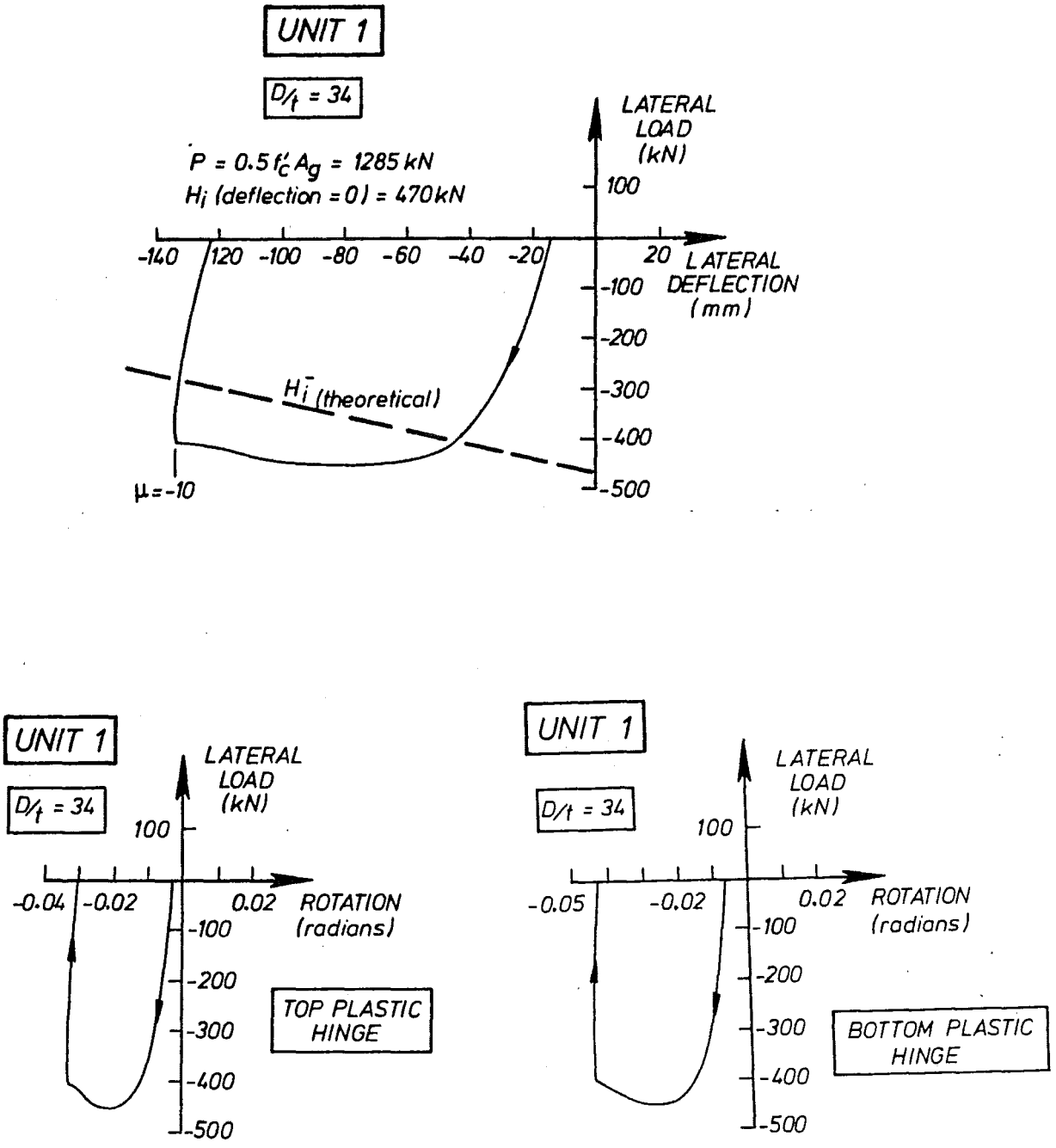

FIG. 4.32 : HYSTERESIS LOOPS FOR FINAL STATIC LOADING OF UNIT 1

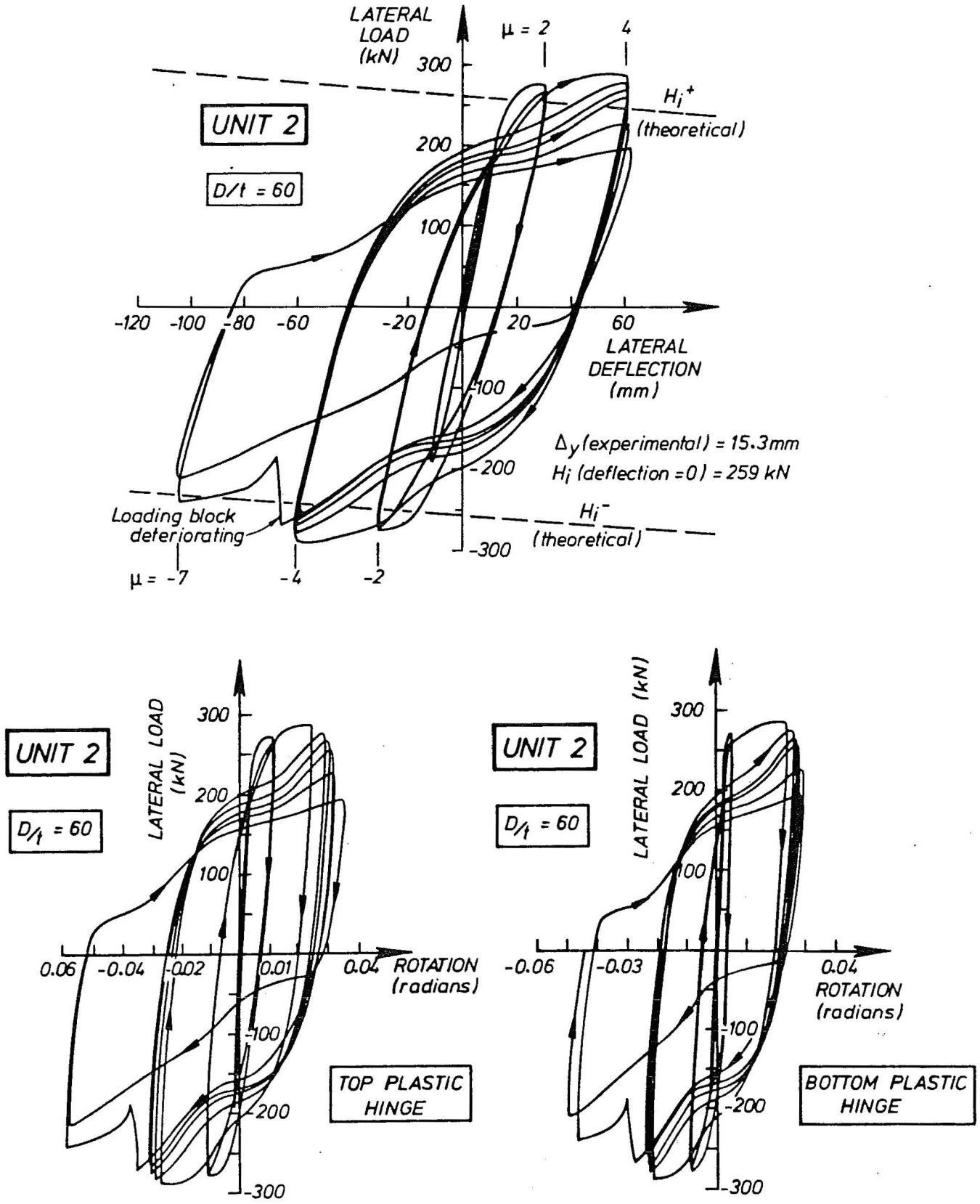

FIG. 4.33 : HYSTERESIS LOOPS FOR STATIC LOADING OF UNIT 2

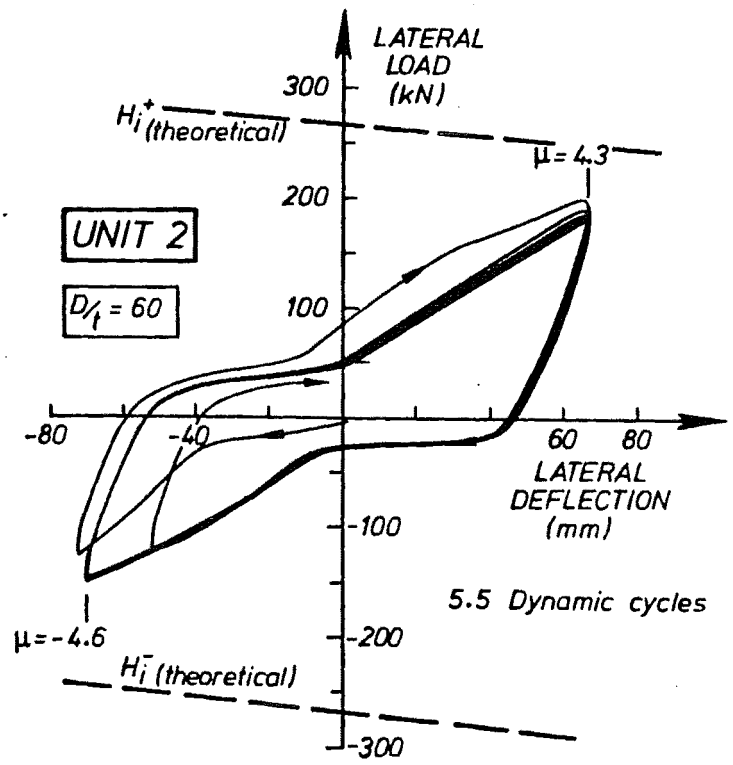

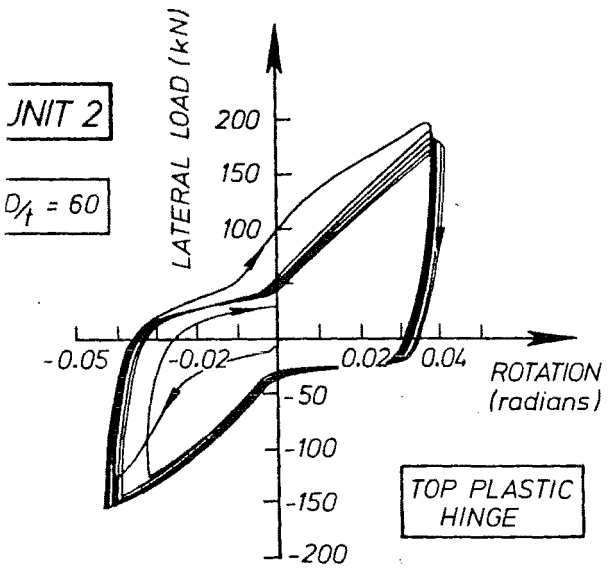

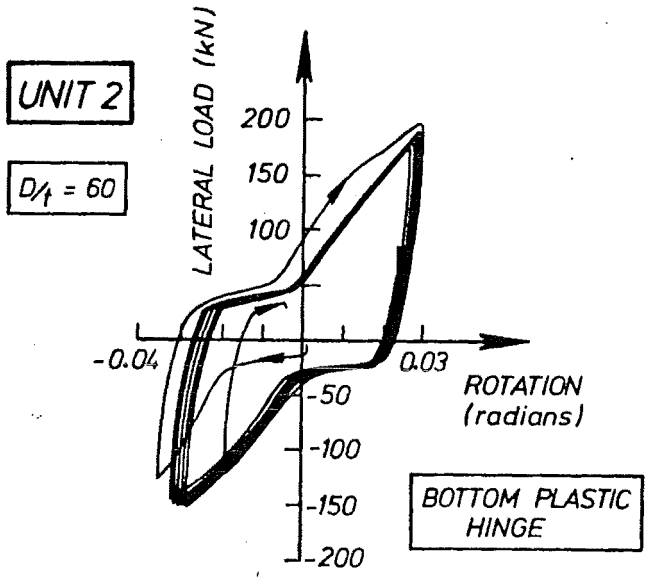

FIG. 4.34 : HYSTERESIS LOOPS FOR DYNAMIC LOADING OF UNIT 2

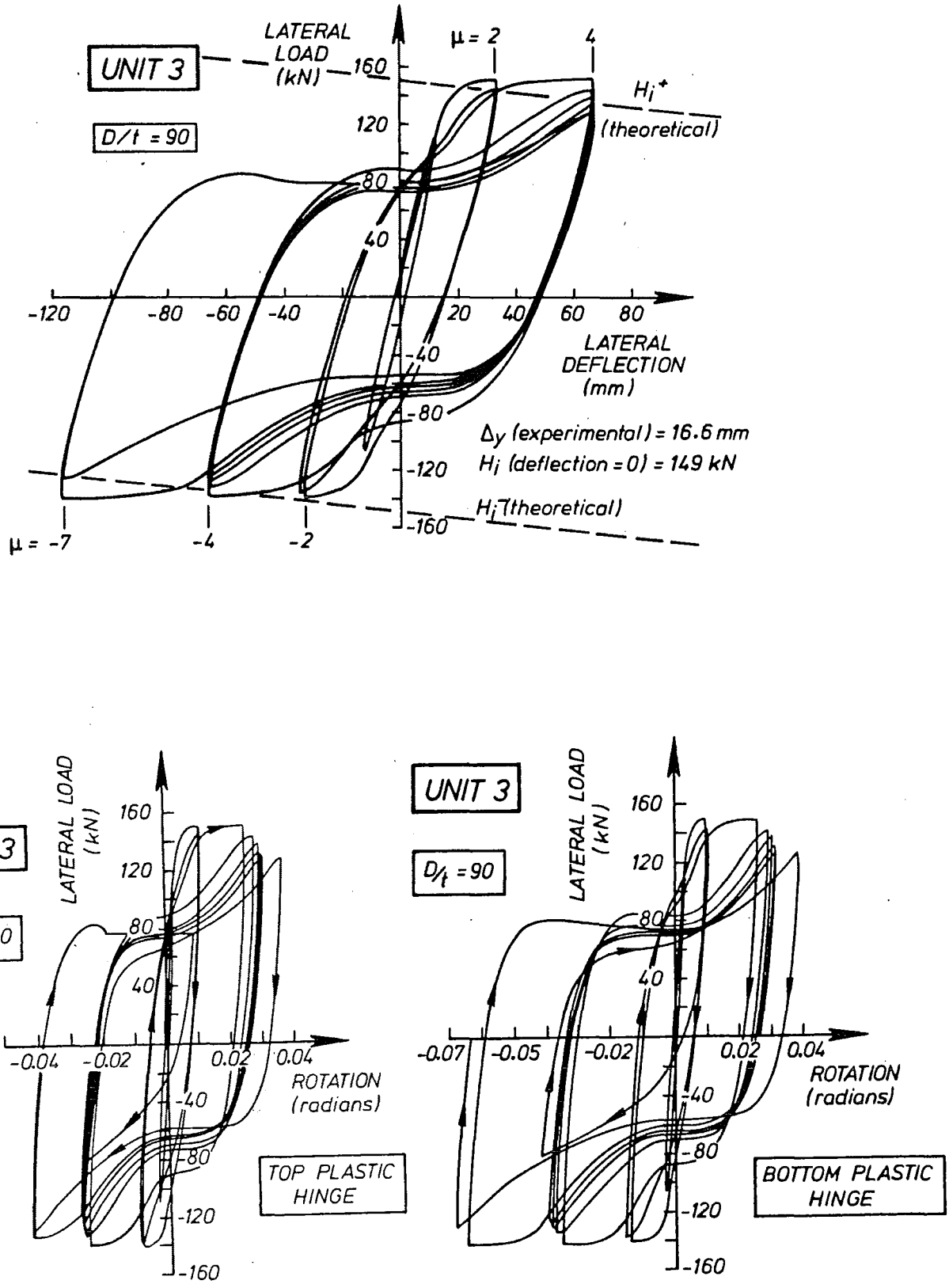

FIG. 4.35 : HYSTERESIS LOOPS FOR STATIC LOADING OF UNIT 3

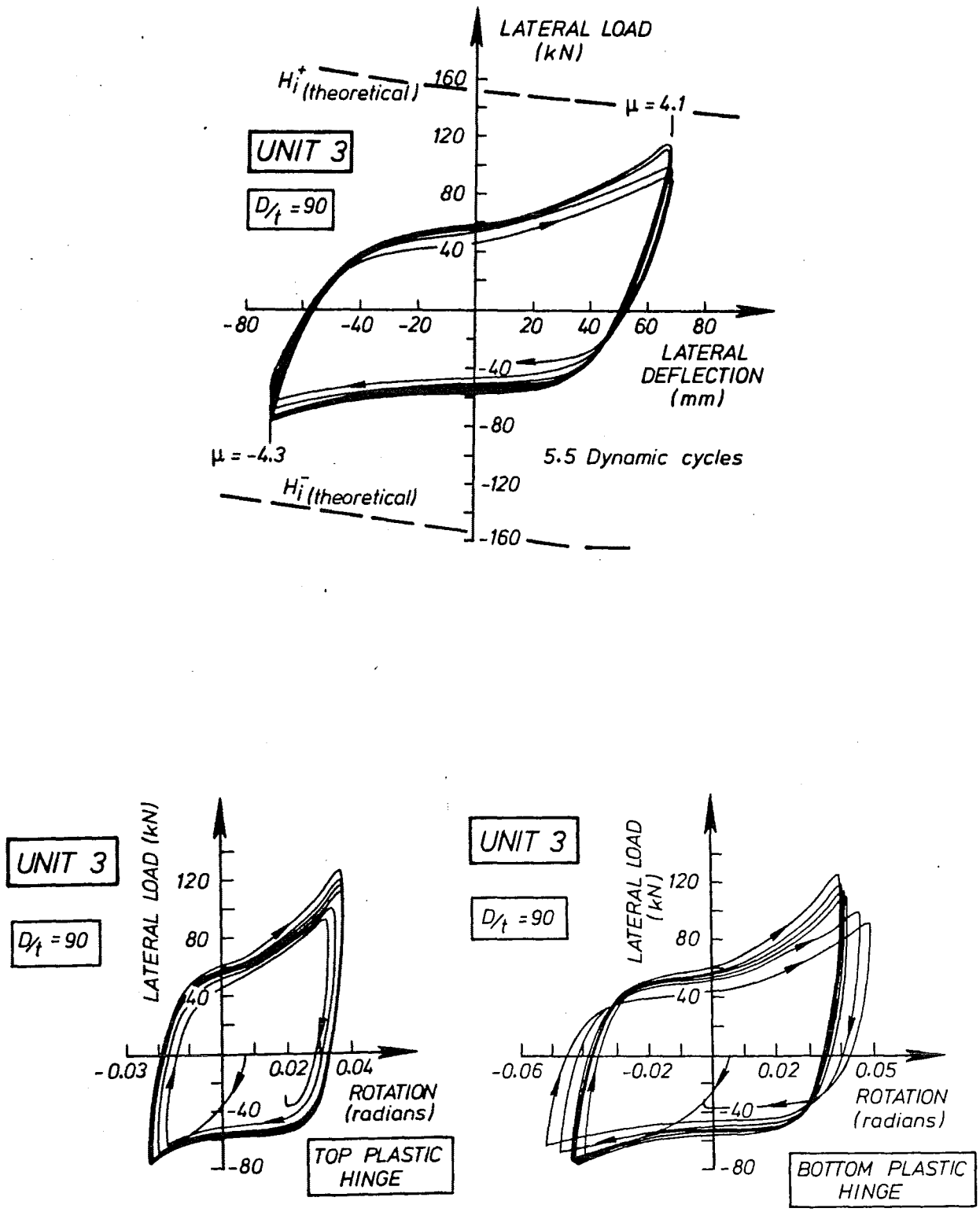

FIG. 4.36 : HYSTERESIS LOOPS FOR DYNAMIC LOADING OF UNIT 3

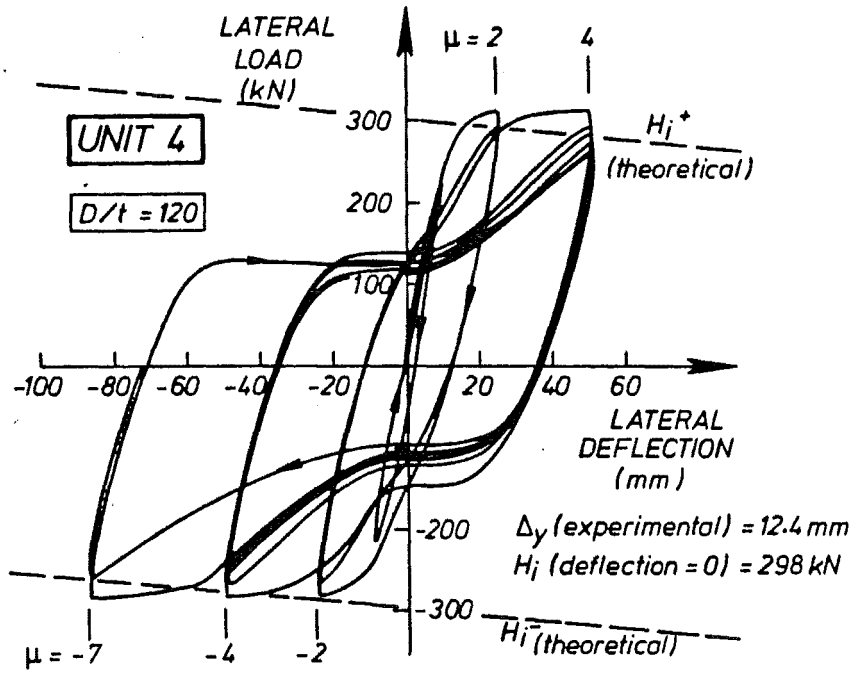

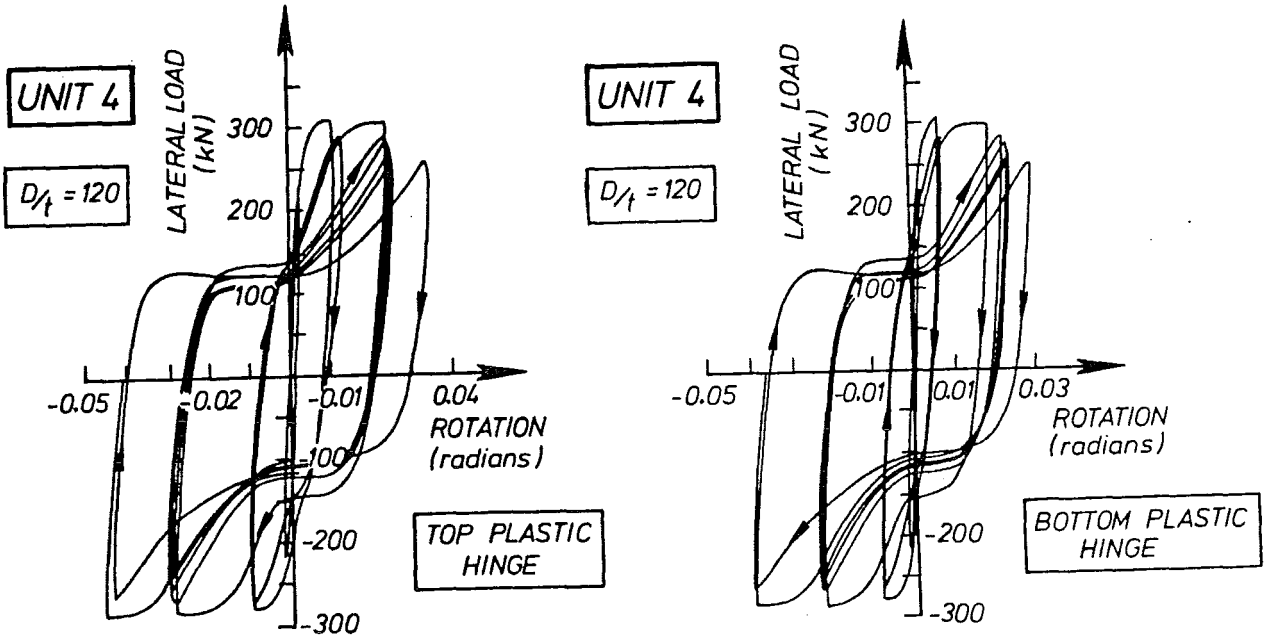

FIG. 4.37 : HYSTERESIS LOOPS FOR STATIC LOADING OF UNIT 4

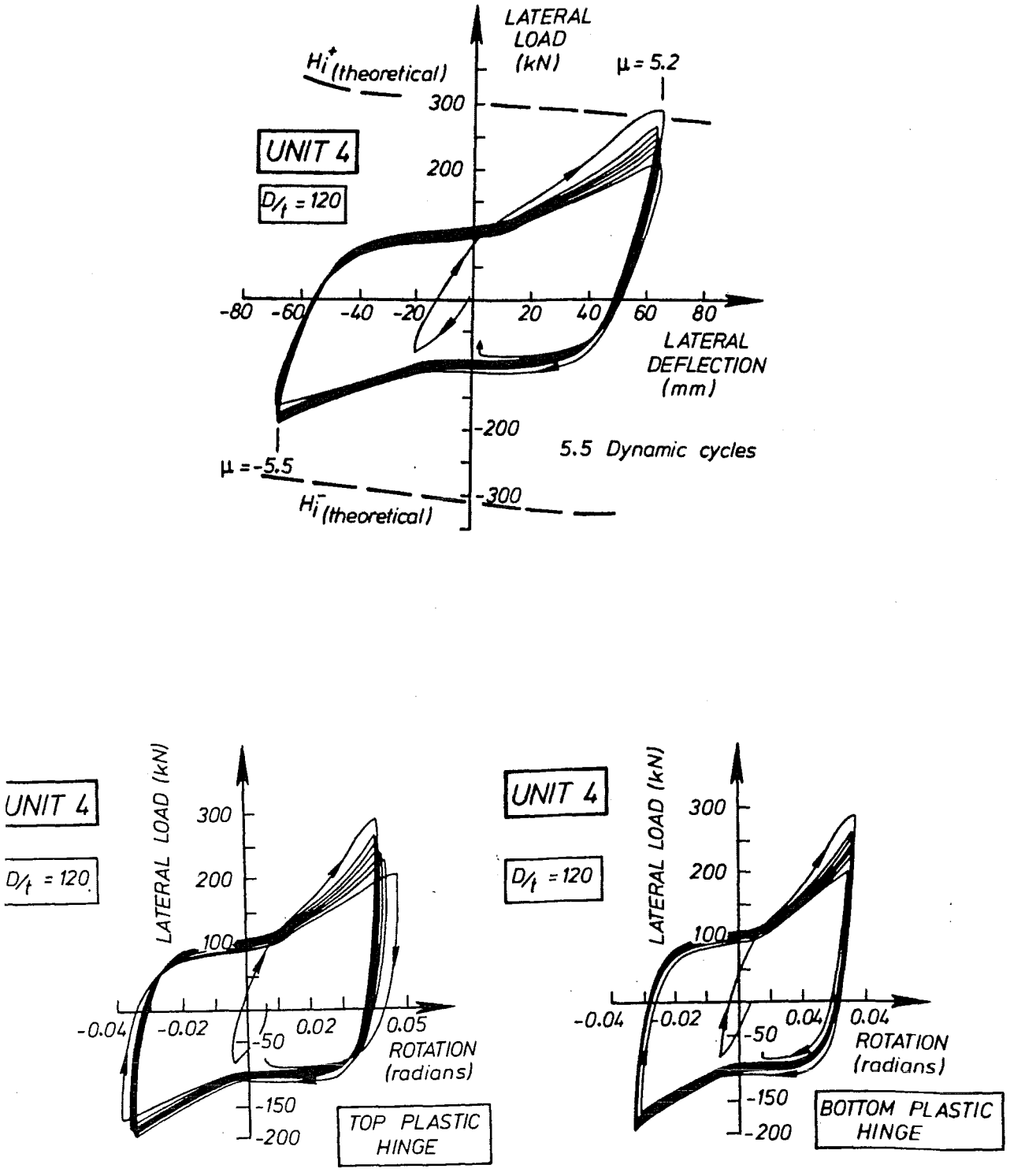

FIG. 4.38 : HYSTERESIS LOOPS FOR DYNAMIC LOADING OF UNIT 4

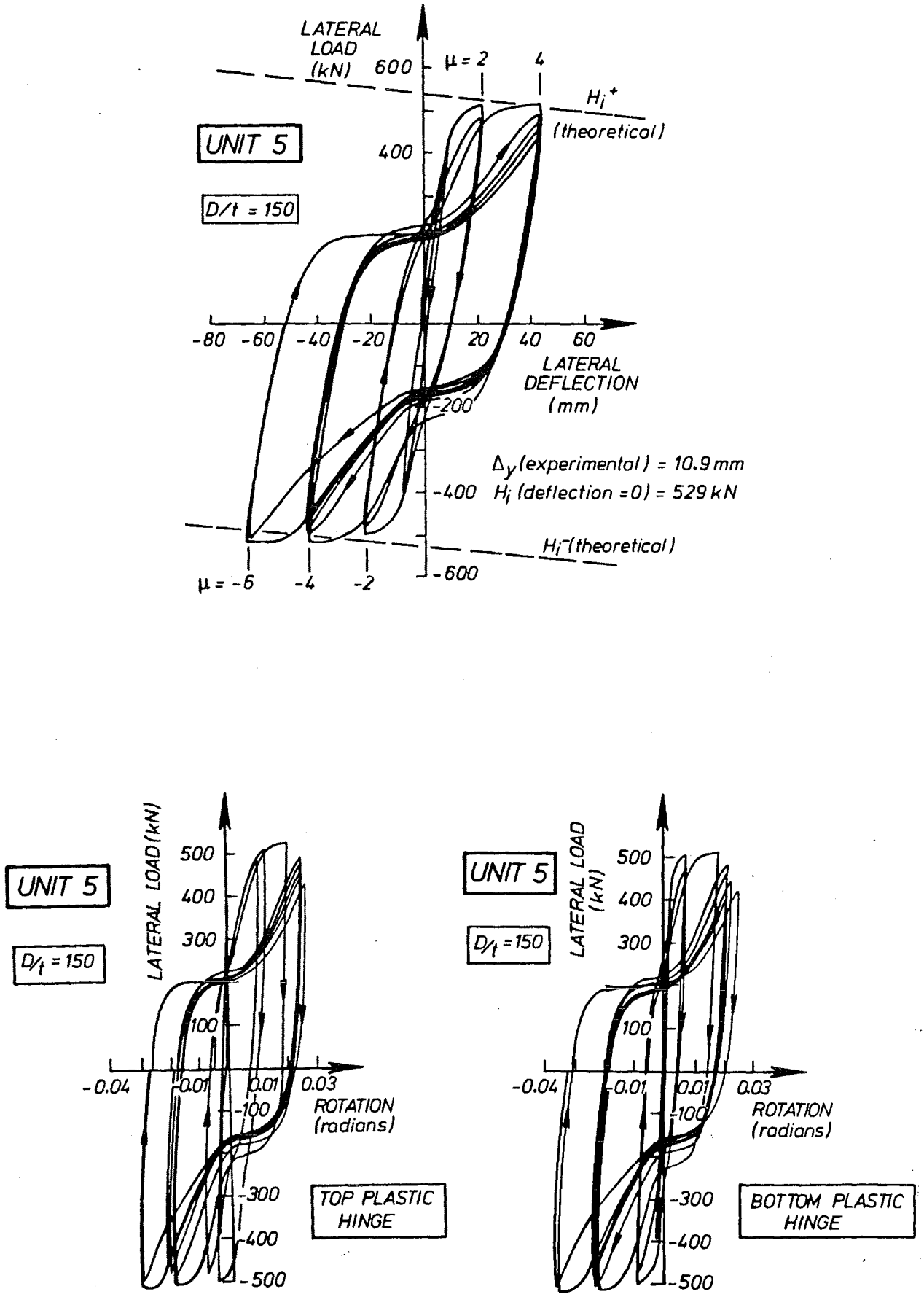

FIG. 4.39 : HYSTERESIS LOOPS FOR STATIC LOADING OF UNIT 5

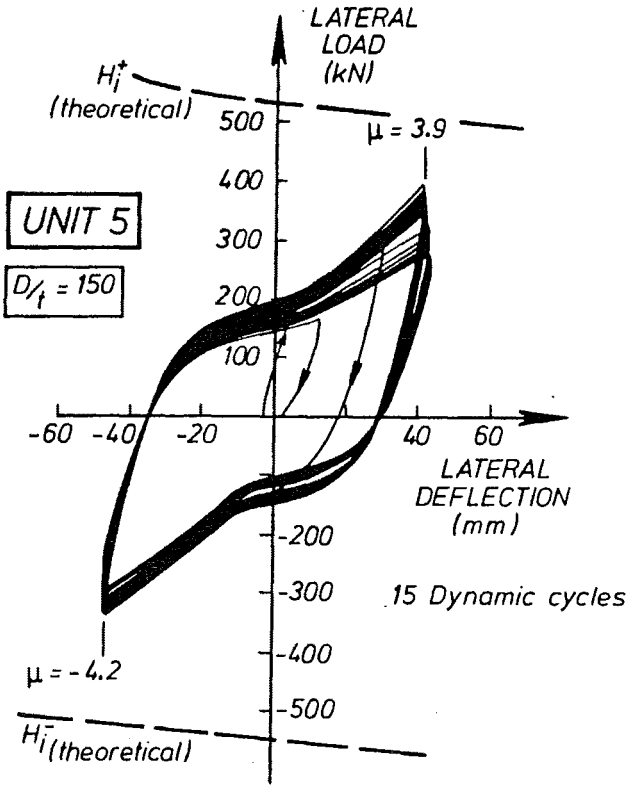

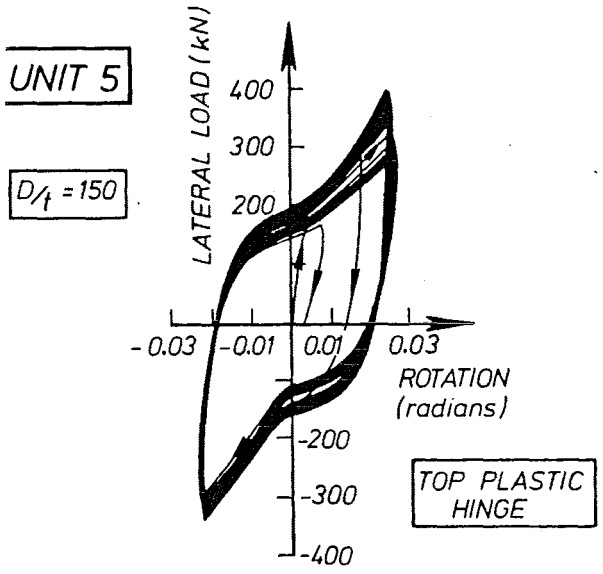

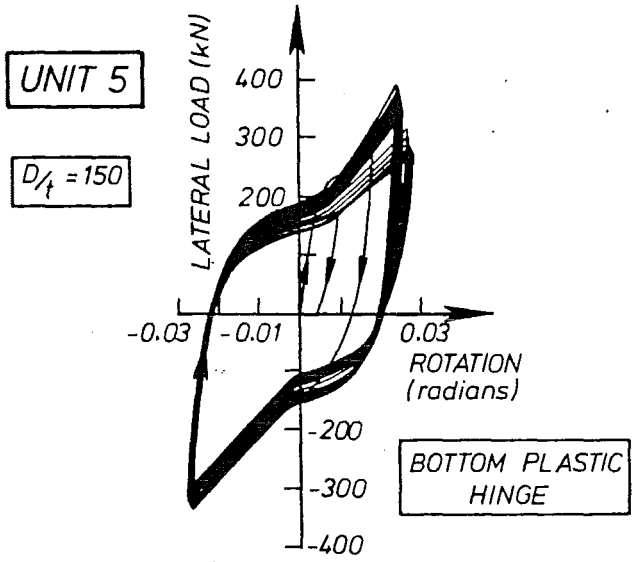

FIG. 4.40 : HYSTERESIS LOOPS FOR DYNAMIC LOADING OF UNIT 5

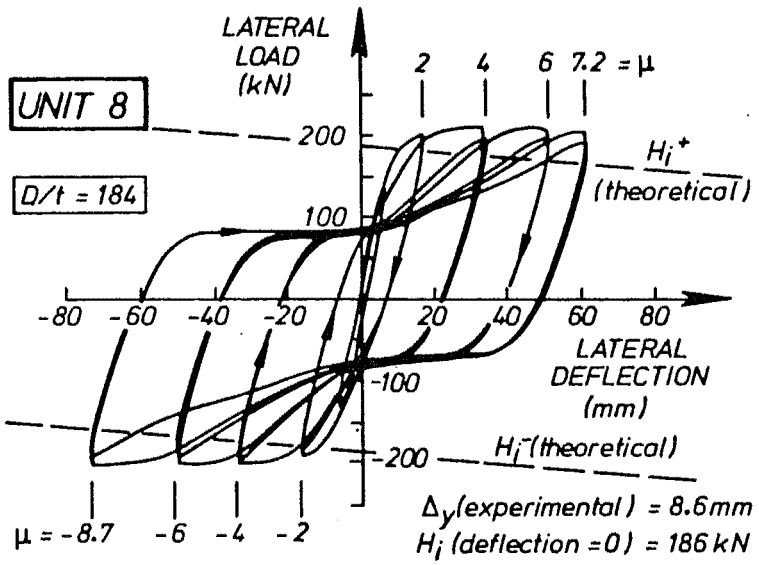

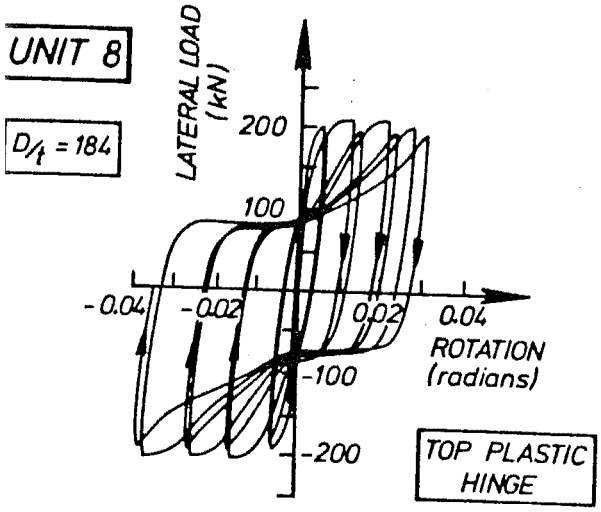

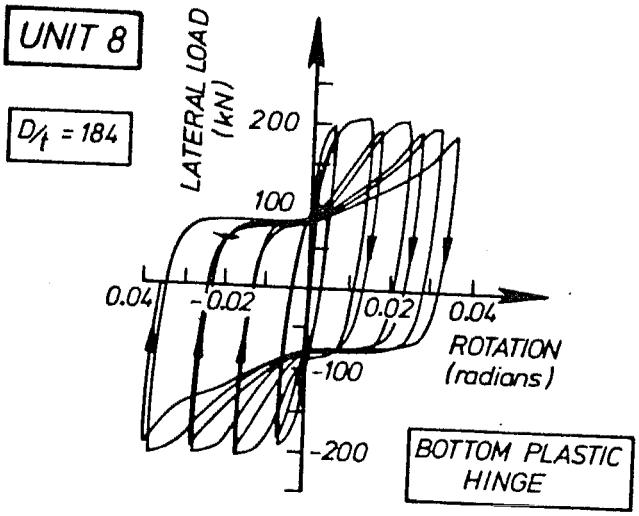

FIG. 4.41 : HYSTERESIS LOOPS FOR STATIC LOADING OF UNIT 8

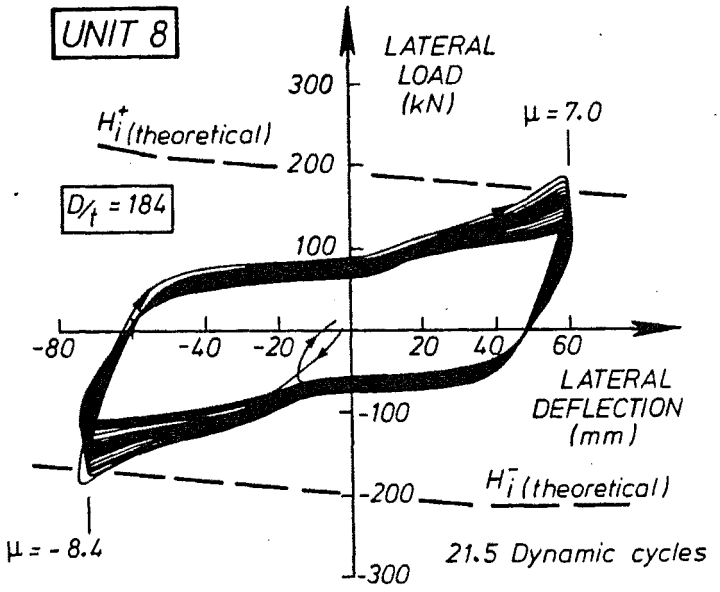

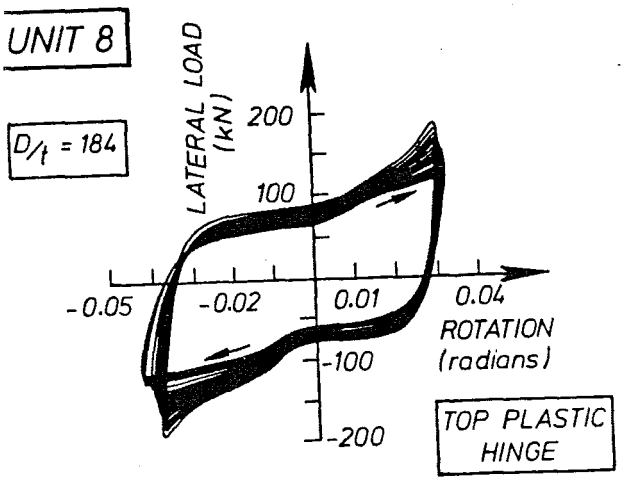

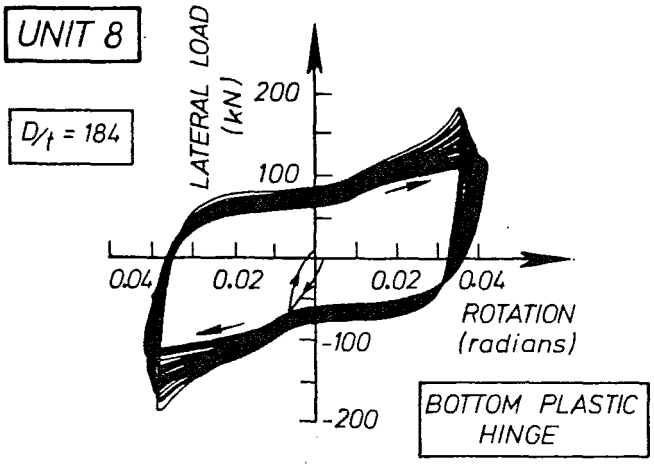

FIG. 4.42 : HYSTERESIS LOOPS FOR DYNAMIC LOADING OF UNIT 8

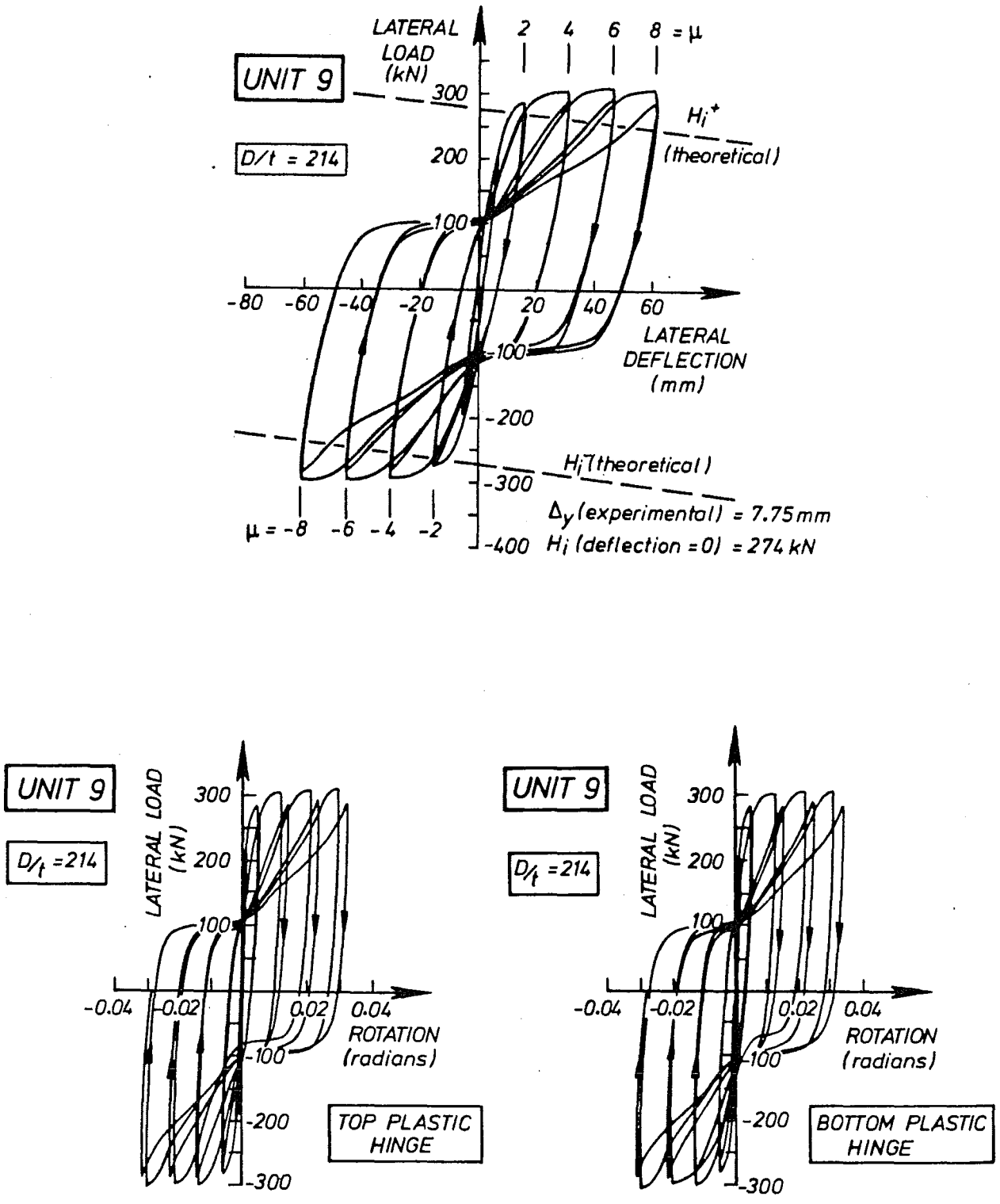

FIG. 4.43 : HYSTERESIS LOOPS FOR STATIC LOADING OF UNIT 9

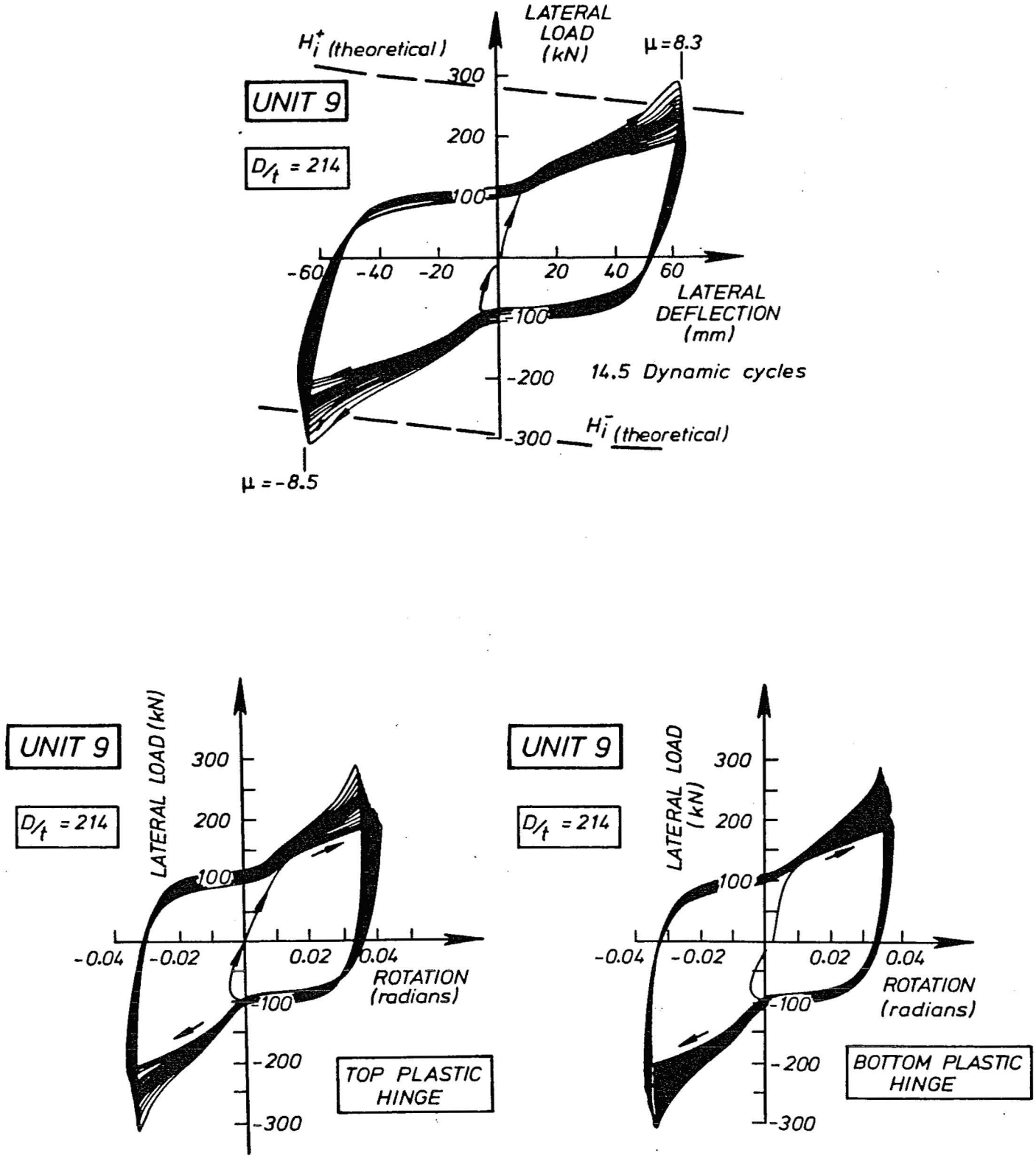

FIG. 4.44 : HYSTERESIS LOOPS FOR DYNAMIC LOADING OF UNIT 9

The theoretical predictions H_i^+ and H_i^- are functions of lateral displacement due to the P-Δ effect. Figure 4.45 shows in indealised form a test unit under longitudinal load P, lateral load H and lateral displacement Δ. As shown in the diagram there are two contributions to the moment at the plastic hinges. The primary contribution (= 0.8H) is due to the lateral load, and the secondary contribution (= 1.09P.Δ) is due to the longitudinal load. Under lateral load and deflection of the same sign, the P-Δ effect reduces the resistance of the test unit to lateral load, while for lateral load and deflection of opposite signs, the P-Δ effect enhances the resistance of the test unit to lateral load. During static loading, the longitudinal load P was kept constant and thus H_i^+ and H_i^- were linear functions of Δ. However under dynamic loading, P was varying as a function of the MTS actuator load and thus H_i^+ and H_i^- were at this stage non-linear functions of Δ.

In general the hysteretic loops show that these model piles performed very well at large displacement ductility factors. However there is a trend towards degradation of performance as testing proceeds, or between units as the casing D/t ratio increases.

The maximum strength reached in each of the experiments was in excess of the theoretical ultimate flexural strength. Figure 4.46 shows the variation of test unit overstrength, which is the margin by which the actual strength exceeded the theoretical strength, versus the casing D/t ratio. For units 1-5 the percentage overstrength decreases from 28% at a casing D/t ratio of 34 to 5% at a casing D/t ratio of 150. This trend could be expected because as the casing D/t ratio increases, strength enhancement due to steel strain-hardening and concrete confinement would decrease. In view of this, it is initially surprising that units 8 and 9 (casing D/t ratio of 184 and 214 respectively) have overstrengths in excess of the overstrengths for units 2-5 ($60 \leq D/t \leq 150$).

The reason for these larger overstrength values in units 8 and 9 is the low strain at commencement of strain-hardening which occurs in the 1.96 mm thick casing of these units as shown in Fig. 4.16. Figure 4.13 shows that the 9.53 mm thick casing used in unit 1 also strain-hardens at a lower strain (1.5%) than is normal (2% to 3%) in typical New Zealand mild steel. Thus as shown in Fig. 4.46 for prototype piles constructed out of typical New Zealand mild steel, the trend of overstrength versus casing D/t ratio given by units 2-5 ($60 \leq D/t \leq 150$) is appropriate.

Ang et al (4.32) have developed an empirical relationship for the overstrength of New Zealand designed ductile reinforced concrete members above that predicted by using the New Zealand Concrete Code (4.17) method for assessing the theoretical ultimate flexural strength, where the actual steel and concrete properties were used in calculating this theoretical strength. The relationship predicts that overstrength varies with the level of longitudinal load. However for a longitudinal load of $P = 0.1f'_cA_g$ (A_g = gross area of reinforced concrete section) which is the same as that used in testing units 1-5, 8 and 9, the overstrength is predicted to be 13%. Thus as shown in Fig. 4.46 for casing D/t ratio > 75, typical steel-encased reinforced concrete bridge piles have less overstrength than do New Zealand designed ductile reinforced concrete members, while the reverse applies for D/t < 75.

In calculating the theoretical ultimate flexural strengths of the test units, the influence of tube local buckling was ignored. However despite the severe cyclic loading conditions, all of the test units exceeded their theoretical strength based on the steel tube acting as an equivalent array of reinforcing bars, even at high ductility levels where tube local buckling was extensive. Since test units had casing D/t ratios in the range of 34-214 and the New Zealand (4.17) and American Concrete Institute (4.30) Concrete Codes restrict structural use of the casing to members with D/t approximately < 80 (see equation 4.1), it appears this restriction is unnecessary.

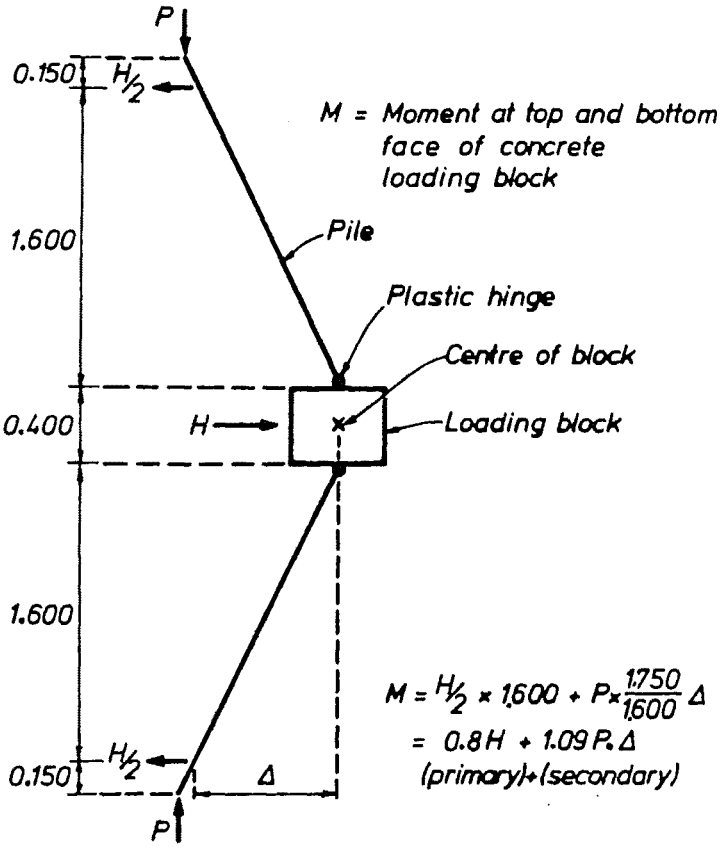

FIG. 4.45 : MOMENT AT FACES OF CONCRETE LOADING BLOCK

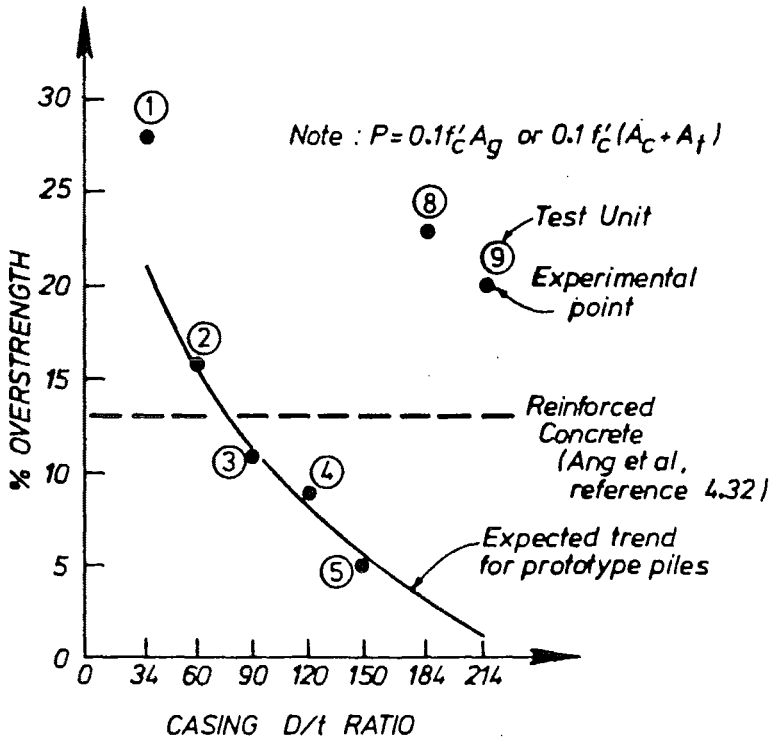

FIG. 4.46 : OVERSTRENGTH OF MODEL PILES

4.9.2.2 Seismic Performance Criteria

Table 4.7 summarises details of the cyclic loading of the test units with continuous casing. In this table, the variable μ represents the displacement ductility demand based on the midheight displacement of the concrete loading block. Variables μ_{TOP} and μ_{BOT} represent the displacement ductilities for the length of the test unit above and beneath respectively the test unit midheight. Figure 4.47 illustrates the method of calculating μ_{TOP} and μ_{BOT} by allowing for the rotation θ which in practice occurs at the test unit midheight. Variables $|\mu|_{max}$, $|\mu_{TOP}|_{max}$ and $|\mu_{BOT}|_{max}$ represent the maximum absolute values of μ, μ_{TOP} and μ_{BOT} respectively; while $\Sigma|\mu|$, $\Sigma|\mu_{TOP}|$ and $\Sigma|\mu_{BOT}|$ represent the cumulative displacement ductility factors based on μ, μ_{TOP} and μ_{BOT} respectively. As shown in Table 4.7 values of μ_{TOP} and μ_{BOT} were not obtained during dynamic testing.

Small variations in geometry and material strengths throughout the length of the test units results in the two plastic hinges developing in unsymmetrical fashion, as shown in exaggerated form in Fig. 4.47, and the hysteresis loops (Figs. 4.29-4.44). Hence in general $\mu \neq \mu_{TOP} \neq \mu_{BOT}$. This is reflected in Table 4.7. where the cumulative displacement ductility factors after static testing in the top half of the test units $\Sigma|\mu_{TOP}|$ and the bottom half of the test units $\Sigma|\mu_{BOT}|$ are shown. In four of the test units $\Sigma|\mu_{TOP}| > \Sigma|\mu_{BOT}|$ while in three of the test units $\Sigma|\mu_{BOT}| > \Sigma|\mu_{TOP}|$. The average ratio of the larger of $\Sigma|\mu_{TOP}|$ and $\Sigma|\mu_{BOT}|$ to the smaller of $\Sigma|\mu_{TOP}|$ and $\Sigma|\mu_{BOT}|$ is 1.11. Thus in steel-encased reinforced concrete model piles the extent of unsymmetrical behaviour is relatively small when compared with the grossly unsymmetrical behaviour which has been reported (4.12, 4.14-4.16) in similar model tests of reinforced or pretensioned concrete members.

All of the test units were subjected to severe levels of simulated seismic lateral displacement. The two performance criteria used in New Zealand (see Section 4.2.3) for the simulated seismic testing of ductile structures require structural behaviour to be ductile at $|\mu| = 6$ and $\Sigma|\mu| = 32$ (4 cycles at $\mu = \pm 4$). All units were subjected to cyclic loading which exceeded these values of $|\mu|$ and $\Sigma|\mu|$. For example even after the first stage of static testing, a minimum $\Sigma|\mu|$ of 50.1 had been imposed on each of the seven test units, while at the completion of all stages of testing a minimum $\Sigma|\mu|$ of 110.3 and $|\mu|$ of 6.07 had been imposed. Reference to Figs. 4.29-4.44 shows that ductile behaviour was occurring at the end of static testing. Thus these two seismic performance criteria were easily satisfied.

4.9.2.3 Shape of Hystersis Loops

Figures 4.29-4.32 show the hysteretic performance of unit 1. This unit was stronger than had originally been anticipated. Thus in the initial static testing cycling could only be performed up to $\mu = \pm 4$, as at that stage the load capacity of the MTS actuator was equalled. The subsequent dynamic cycling did not appreciably degrade the strength of this unit. Thus to achieve a larger μ, the longitudinal load P was increased from $0.1f'_c(A_c + A_t)$ to $0.5f'_c(A_c + A_t)$. Although this increase in P had the effect of increasing the theoretical ultimate flexural strength of the test unit from 345 kNm to 376 kNm, it also meant that the P-Δ moment was magnified by a factor of 5. Thus it proved possible to displace this test unit to $\mu = -10$ (defined in terms of the yield displacement found with the original longitudinal load of $P = 0.1f'_c(A_c + A_t)$). Even at this stage, as shown in Fig. 4.32, unit 1 was gaining strength in excess of that predicted by $\bar{H}_i$ (allowing for $P = 0.5f'_c(A_c + A_t)$).

The hysteresis loops for unit 1 show the characteristics of a compact steel member, as might be expected with the casing occupying 11.4% of the gross section

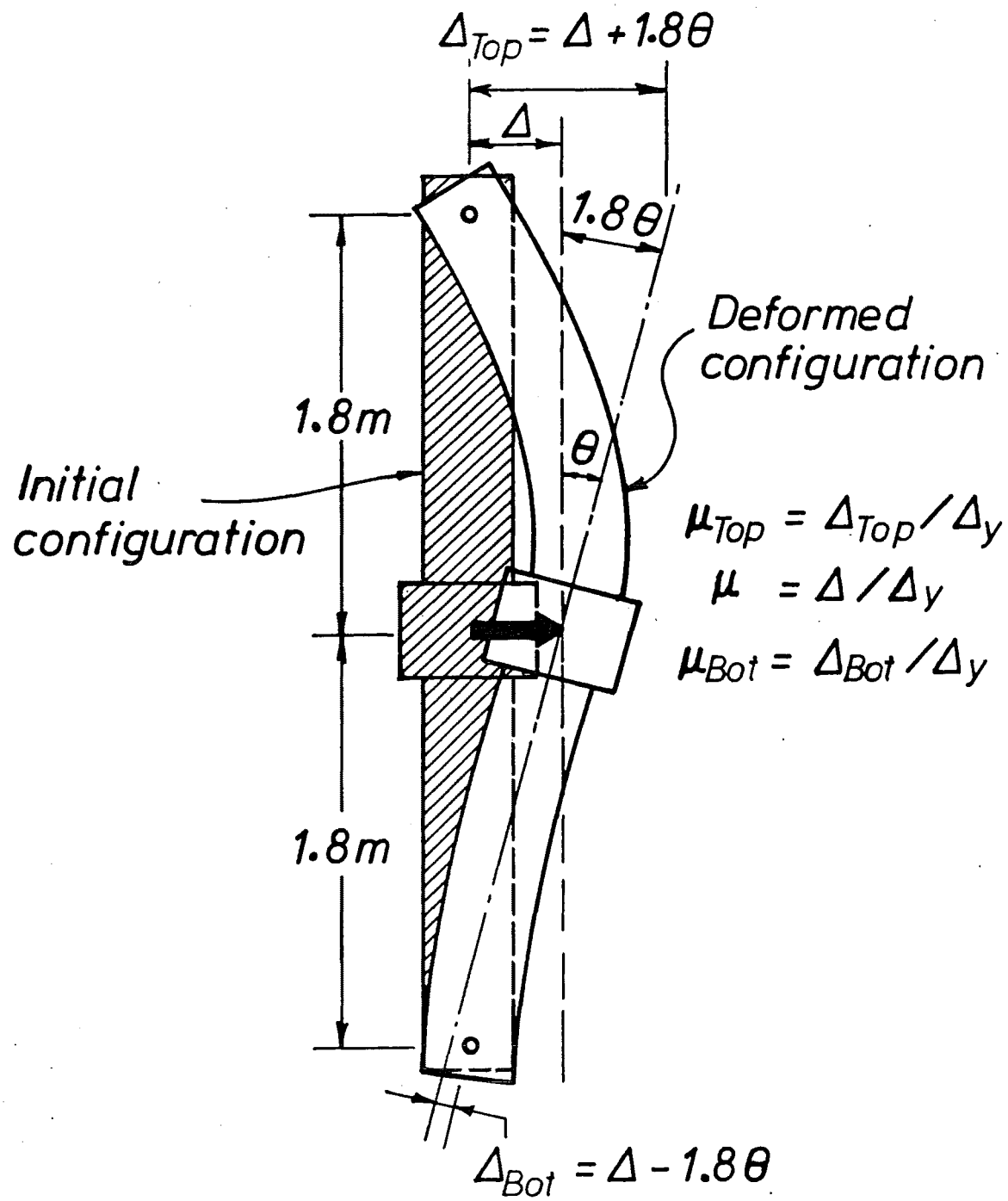

FIG. 4.47 : UNSYMMETRICAL PLASTIC HINGING

area. Although local buckling occurred during the first cycle to $\mu = \pm 4$, strength and stiffness degradation of the hysteresis loops for unit 1 was minimal. The loops also show the characteristics of the Bauschinger effect which results in the response becoming non-linear at a comparatively early stage as the lateral load reverses.

In Section 4.9.1, it was commented that large cracks in the concrete loading block resulted in the apparent bad performance of unit 2. This is clearly shown in Figs. 4.33 and 4.34 where a large loss of strength and stiffness is shown to have occurred with each succeeding cycle to magnitudes of μ equal to or greater than 4. It is emphasised again that this apparent bad performance of the test unit, due to failure of the loading block, should not be attributed to the model pile itself.

It was also mentioned in Section 4.9.1 that cracking of the tube extending longitudinally along a weld defect occurred during static testing of unit 5. This cracking did not appear to significantly influence the static loading hysteretic performance of this unit, as can be seen by comparing Figs. 4.37 (unit 4, D/t = 120) and 4.39 (unit 5, D/t = 150). The crack was located at the NE position on the section (i.e. 45° around the perimeter from the position (N) where the maximum longitudinal strains occur). This is the probable reason for the crack having little apparent effect on test unit performance during static testing, since even before cracking at the NE position occurred, values of longitudinal-compression strain and hence hoop-tension stress would have been relatively low when compared with the peak values which occurred at the N position of the section.

In general the hystersis loops show stable test unit behaviour. However as was mentioned in Section 4.9.1, damage tended to concentrate at the two positions of local buckling. This is reflected in the lateral load-rotation diagrams obtained using potentiometers mounted just above and beneath the concrete loading block. In these diagrams, at each succeeding level of μ the rotation increases markedly, and at the second cycle to a given μ the rotations are often larger than at the first cycle, which indicates a redistribution of plasticity into the zones of local buckling. The load-rotation graphs also show that damage tended to concentrate at one of the local buckles in preference to the other, which is in agreement with the trend shown in Table 4.7 where it was shown that in general $\mu_{TOP} \neq \mu_{BOT}$.

Units with large casing D/t ratios (e.g. unit 9, D/t = 214) exhibit pronounced pinching of the hysteresis loops through the middle range of deflections for the cycles to high ductility levels. This pinching is not as pronounced for units with small casing D/t ratios (e.g. unit 1, D/t = 34).

The pinching is clearly caused by the concrete behaviour, as test units with large casing D/t ratios are more dominated by concrete behaviour than are test units with small casing D/t ratios. Further, the cyclic longitudinal-load testing of concrete-filled and empty tubes with thick walls (see Figs. 3.11 and 3.12) showed pinching of the hysteresis loops occurred only in the concrete-filled tube tests. It is also apparent from Figs. 4.29 - 4.44 that for cycles to large ductility levels, the stiffness of the test units increases markedly as the zero deflection line is passed, since at that stage the concrete cracks which opened previously under longitudinal-tension stress will be closing and hence longitudinal-compression stress can then be transferred through the previously cracked concrete.

It was reported in Section 4.9.1 that fracturing of the casing extending in the longitudinal (units 8 and 9) and hoop (units 3,4,5,8 and 9) directions of the tube occurred during dynamic testing. However as shown in Figs. 4.36, 4.38, 4.40, 4.42 and 4.44, although this resulted in some loss of load-carrying capacity, failure of these five units did not occur at this stage. This was because of the sound performance of the well-confined reinforced concrete which was underlying the fractured casing.

For a given test unit little difference was observed when the last cycle of static loading was compared with the first cycle of dynamic loading. This was because the damage done as testing proceeded offset any possible strength increase due to loading going from static to dynamic strain rates.

4.9.2.4 Energy Dissipation Characteristics

It is of interest to compare the energy dissipation characteristics of steel-encased reinforced concrete test units, similar reinforced concrete test units and idealised members with elastic-plastic response. Energy dissipation characteristics are important for stiff structures which have fundamental periods of vibration less than about 0.5 seconds. For such structures the "equal energy" principle governs response rather than the "equal displacement" principle (4.25). Thus a stiff structure with thin hysteresis loops (low energy dissipating characteristics) will be subjected by an earthquake to a larger displacement ductility factor than will an otherwise identical structure with thick hysteresis loops. This is of significance to steel-encased reinforced concrete members, since from Figs. 4.29 to 4.44 test units with large casing D/t ratios were shown to have relatively thin hysteresis loops when compared with units which had small casing D/t ratios.

In Fig. 4.48, the lateral load-lateral displacement response of an idealised elastic-plastic system which has been cycled successively to $\mu = \pm 3/4, \pm 2, \pm 4, \pm 6$ and ± 8 is shown. The yield strength of this idealised system was taken to be equal to the theoretical ultimate flexural strength at zero displacement H_i of the test unit (i.e. overstrength was ignored). The loading, unloading and reloading stiffnesses were taken as being equal to the theoretical ultimate strength of the test unit divided by the experimentally obtained yield deflection H_i/Δ_y. Although it appears that the P-Δ effect is ignored by this approach, it should be noted that the P-Δ effect increases the lateral load capacity for half of each cycle and decreases capacity for the other half of each cycle. Thus the P-Δ effect has no influence on the overall energy dissipated in each cycle.

For a complete cycle to displacement ductility levels of $\pm\mu$, the energy absorbed by the elastic-plastic system E_{EP} is:

$$E_{EP} = 4 H_i \Delta_y (\mu - 1) \qquad (4.6)$$

A dimensionless energy dissipation ratio E_R which compares the actual energy dissipated E, in a given test unit, with that dissipated by the elastic-plastic system E_{EP} can be defined as:

$$E_R = E/E_{EP} \qquad (4.7)$$

Values of E were obtained using a planimeter to measure the area (proportional to E) within each load-displacement loop.

A plot of the energy dissipation ratio E_R versus casing D/t ratio for the steel-encased reinforced concrete test units at a $\Sigma|\mu|$ of 32 (corresponding to 4 cycles at $\mu = \pm 4$) is given in Fig. 4.49. Also indicated are the results for conventionally designed ductile (4.17) reinforced concrete octagonally sectioned test units as tested by Ang et al (4.12) and Zahn et al (4.14) which both had longitudinal-compression loads of $0.1 f'_c A_g$. From Fig. 4.49 as the casing D/t ratio $\to 0$: $E_R \to 1$. This occurs because in a very thick-walled steel-encased reinforced concrete member, reduction of dissipated energy due to the Bauschinger effect is roughly compensated for by an increase in dissipated energy due to test unit overstrength. For casing D/t ratio > 100 : $E_R \cong 0.6$, which is similar to the value of E_R shown for the two reinforced concrete test units.

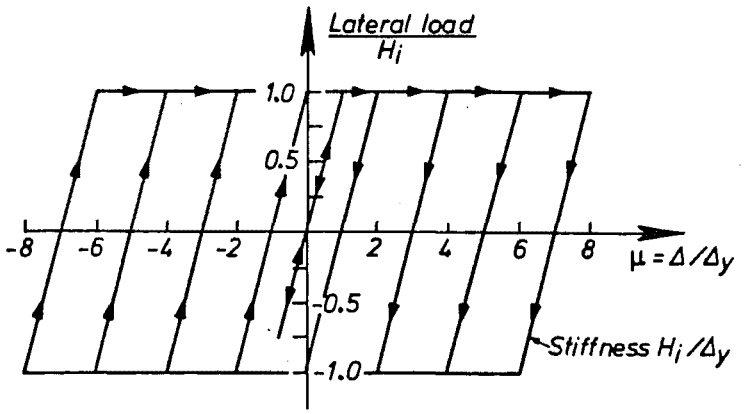

FIG. 4.48 : CYCLING OF AN IDEALISED ELASTIC-PLASTIC MEMBER

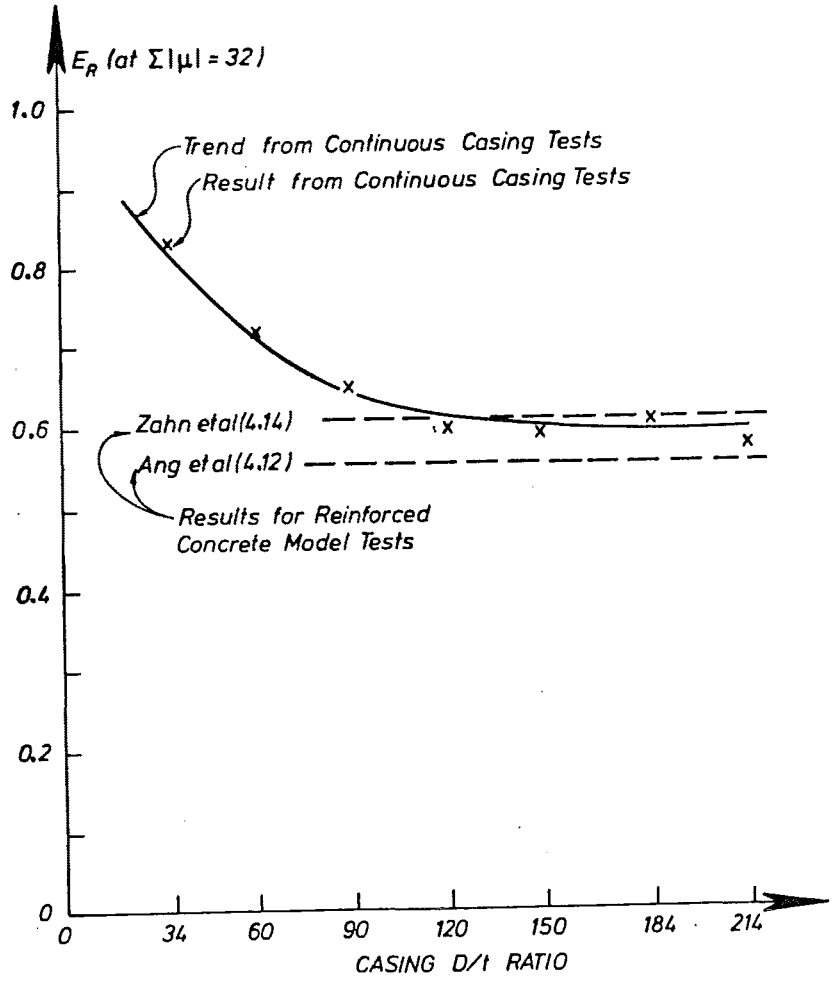

FIG. 4.49 : ENERGY DISSIPATION RATIO E_R vs CASING D/t RATIO AT A CUMULATIVE DISPLACEMENT DUCTILITY FACTOR OF 32

In Fig. 4.50 the energy dissipation ratio E_R is plotted against the cumulative displacement ductility factor $\Sigma|\mu|$ for the steel-encased reinforced concrete and the reinforced concrete test units. In general E_R is shown to reduce as $\Sigma|\mu|$ and the casing D/t ratio increase. From both Figs. 4.49 and 4.50 it appears that prototype steel-encased reinforced concrete piles ($60 \leq D/t \leq 180$) have similar energy-dissipating characteristics to conventionally designed ductile reinforced concrete columns.

4.9.3 Distribution of Curvature Along the Length of the Test Units

Determination of profiles of curvature distribution for the model piles was complicated by difficulty in assessing the effective gauge length over which linear potentiometers N5, N6, S5 and S6 operated. These four potentiometers were mounted on the casing via tack-welded stands at one end, and the concrete loading block at the other end as was previously shown in Fig. 4.9a where nominal gauge lengths of 100 mm were indicated for these instruments.

In Section 4.9.1 it was commented that the model piles were observed to be slipping through the concrete loading blocks. Referring to Fig. 4.51, consider the four points A, B, C and D which were initially on the surface of the tube adjacent to either the upper or lower face of the block. Due to slip between the concrete loading block and the tube, as bending of the pile occurs, these points move to A', B'. C' and D' respectively. Because potentiometers N5, N6, S5 and S6 were mounted on the block at one end, their effective gauge length was thus greater than the nominal gauge length of 100 mm. On the assumption of zero friction between tube and block, their effective gauge lengths were taken to be 300 mm, corresponding to the nominal gauge length (100 mm) plus half the depth of the concrete loading block (200 mm). Since all the other linear potentiometers were mounted at both ends on stands which were tack-welded to the casing, their effective gauge length corresponds to the nominal gauge length of 150 mm indicated in Fig. 4.9a.

The average longitudinal strain over the gauge length of each potentiometer was calculated as the deflection indicated by the potentiometer divided by the effective gauge length over which the potentiometer was operating. The average curvature over the length covered by each pair of potentiometers (e.g. N1 and S1, N2 and S2, etc.) was then calculated by dividing the difference between the longitudinal strains at opposite potentiometers by the distance (nominally equal to D + 100 mm, see Fig. 4.9a) between the potentiometers.

Figures 4.52-4.58 show profiles of curvature at the peaks of the first and last cycles to each value of displacement ductility μ which were obtained during the static testing of units 1-5, 8 and 9 respectively. In these figures the implied levels of curvature ductility ratio ψ/ψ_y are also indicated, where ψ = curvature and ψ_y = yield curvature. The values of yield curvature used were those obtained from the moment-curvature analyses described subsequently in Chapter 5. It should be noted that these yield curvatures are greater, by a factor of about 1.13, than the curvatures at first yield of the steel and correspond to the elastic curvature at the theoretical ultimate moment for an elastic-plastic idealisation of moment curvature behaviour.

Curvature ductility factors with magnitudes of up to 20 are indicated to have occurred during static testing. However, plastic rotation had been observed to concentrate in the regions of local buckling which had longitudinal extents in the range of 35-70 mm (see Table 4.6), while as mentioned earlier in this section the effective gauge length of the potentiometers (N5, N6, S5 and S6) in the zones of the local buckles was 300 mm. Thus the peak values of curvature ductility ratio ψ/ψ_y indicated in Figs. 4.52 - 4.58 are likely to grossly underestimate

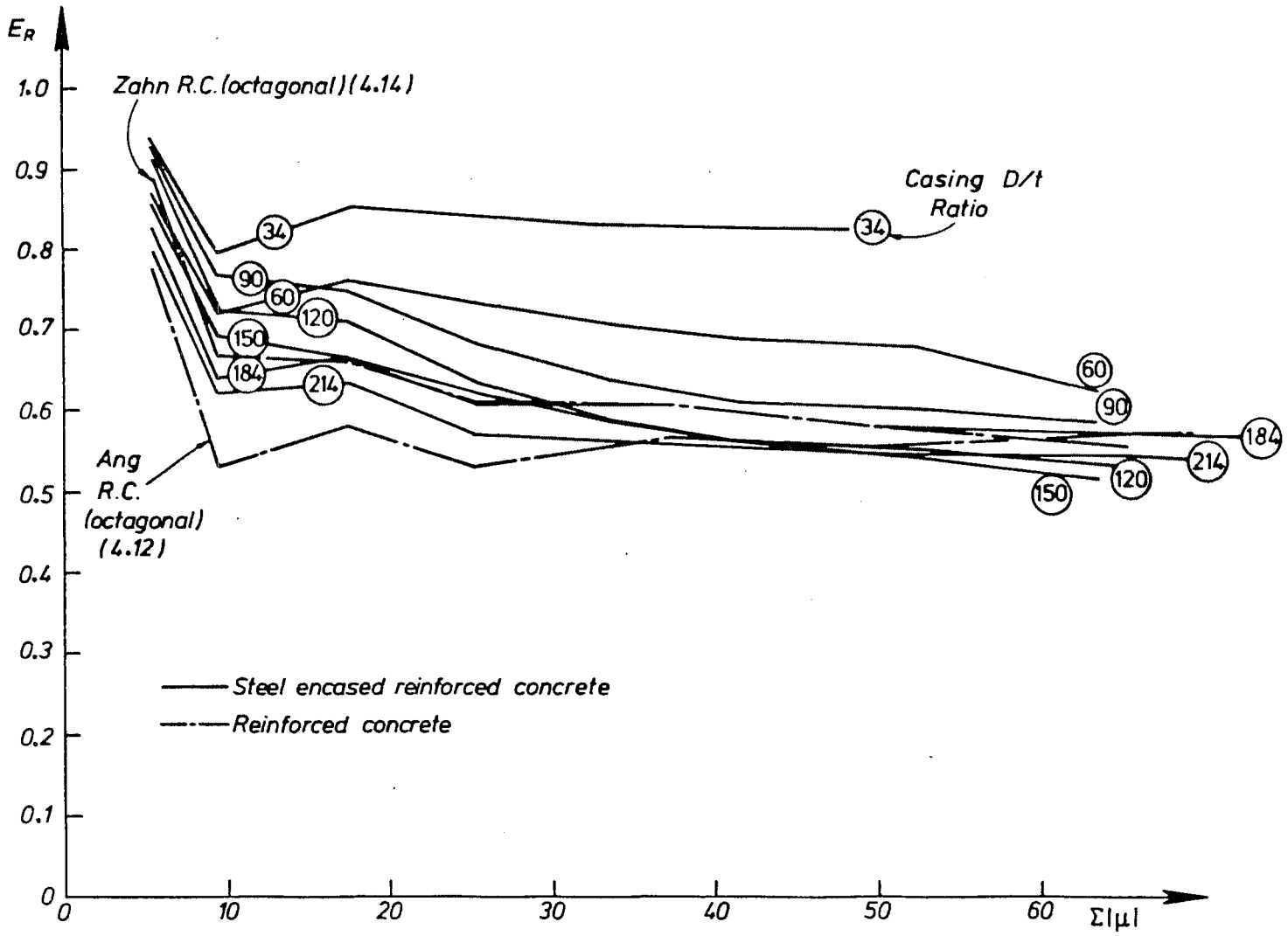

FIG. 4.50 : ENERGY DISSIPATION RATIO E_R VS CUMULATIVE DISPLACEMENT DUCTILITY FACTOR $\Sigma|\mu|$

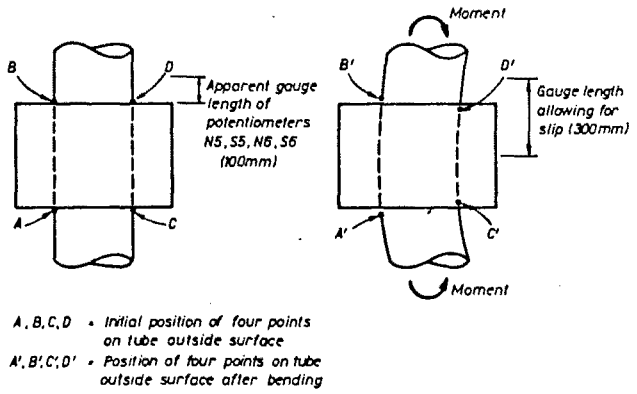

FIG. 4.51 : SLIP OF TUBE THROUGH THE CONCRETE LOADING BLOCK

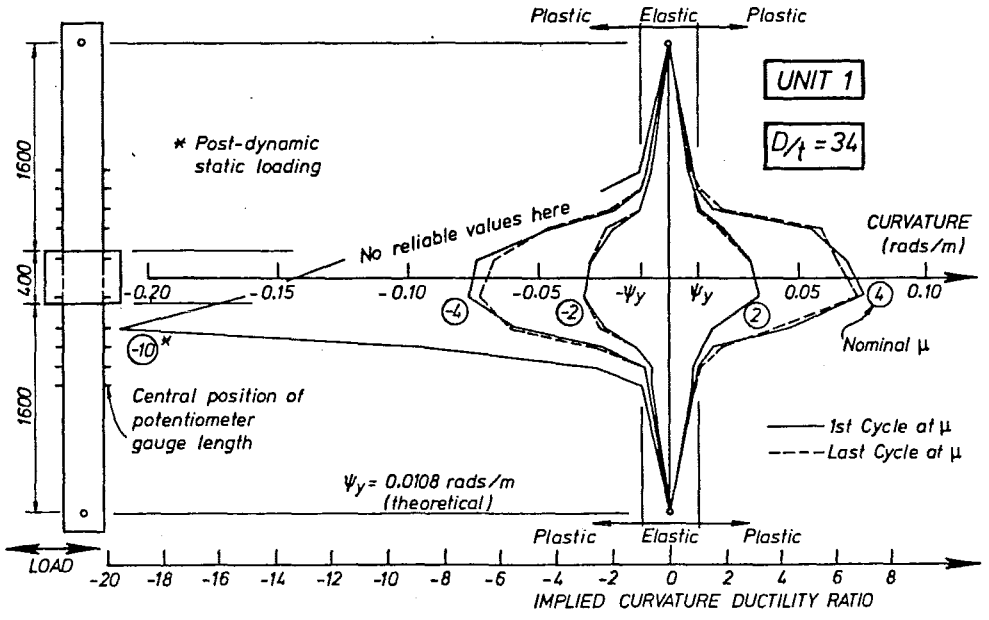

FIG. 4.52 : CURVATURE PROFILES FOR UNIT 1

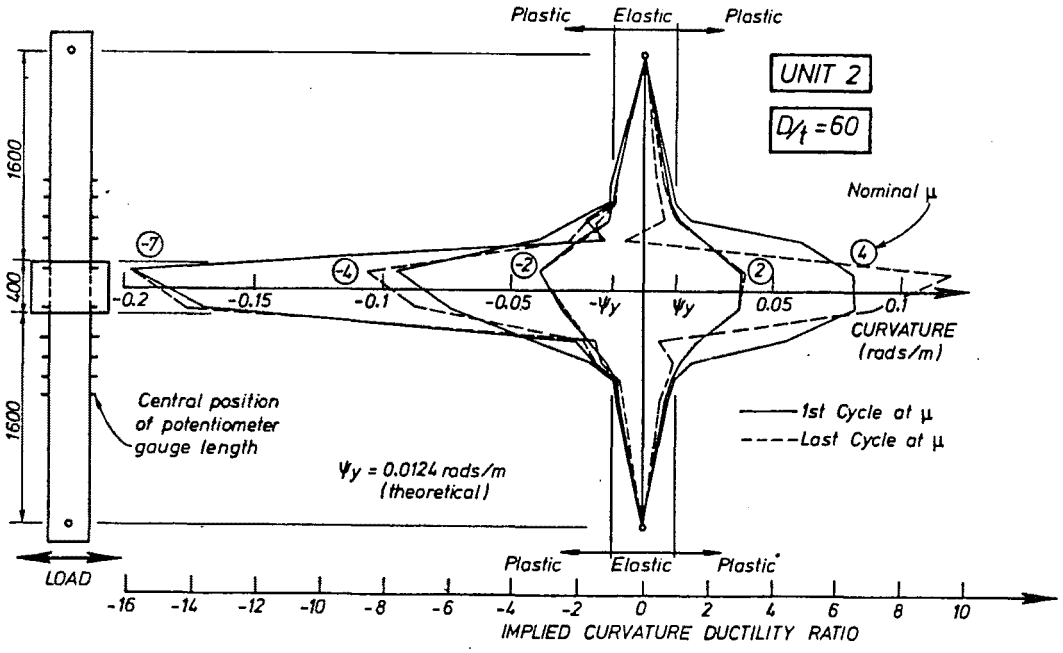

FIG. 4.53 : CURVATURE PROFILES FOR UNIT 2

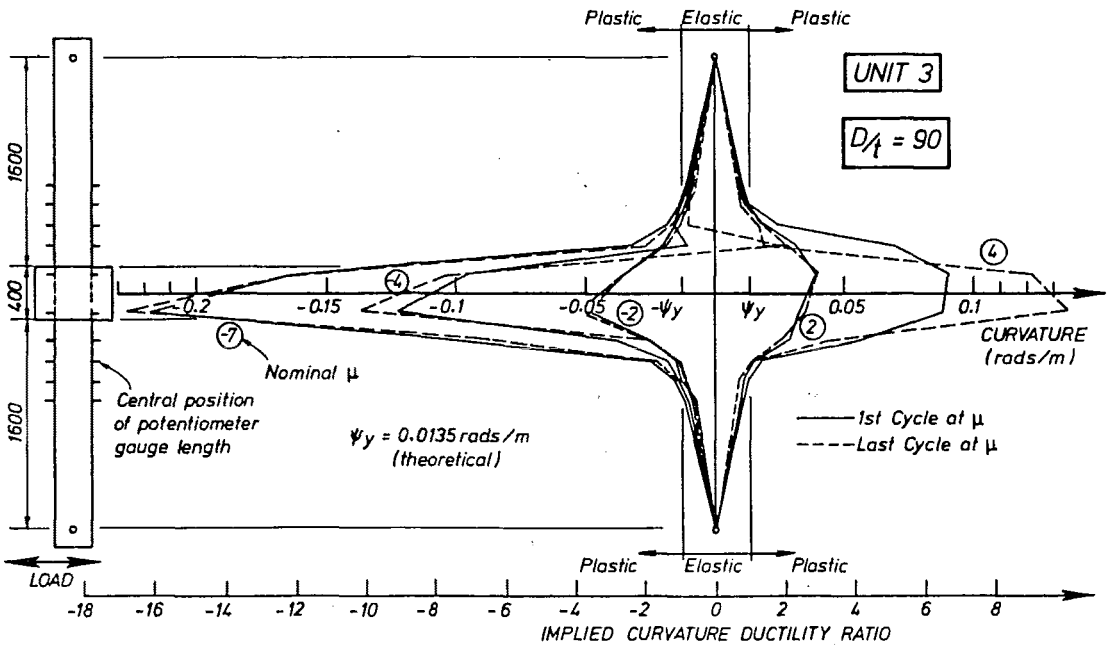

FIG. 4.54 : CURVATURE PROFILES FOR UNIT 3

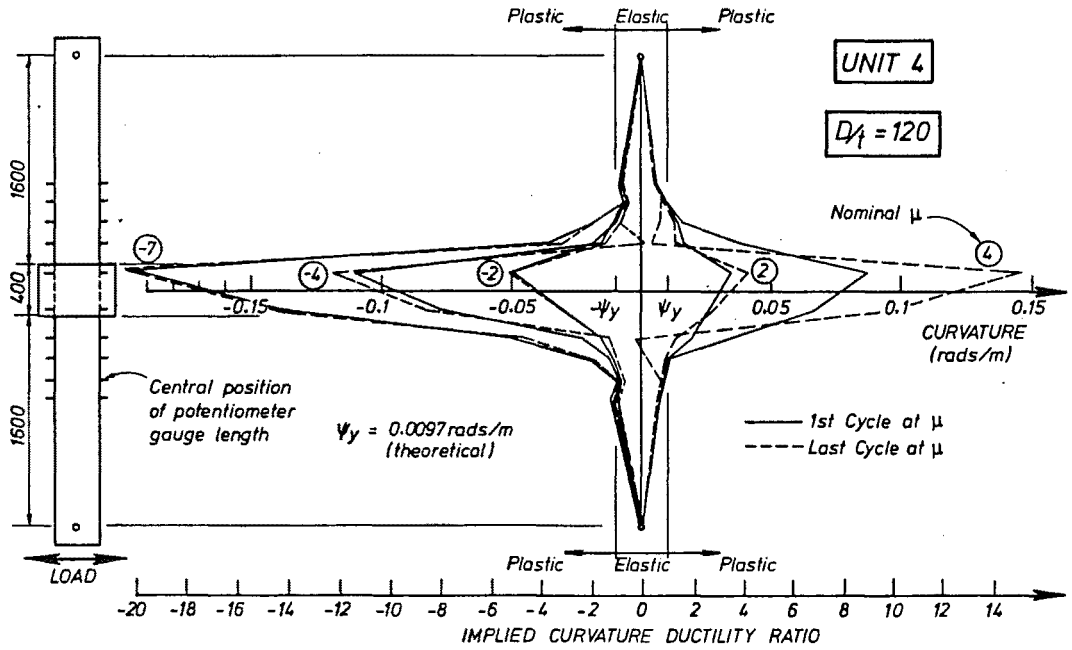

FIG. 4.55 : CURVATURE PROFILES FOR UNIT 4

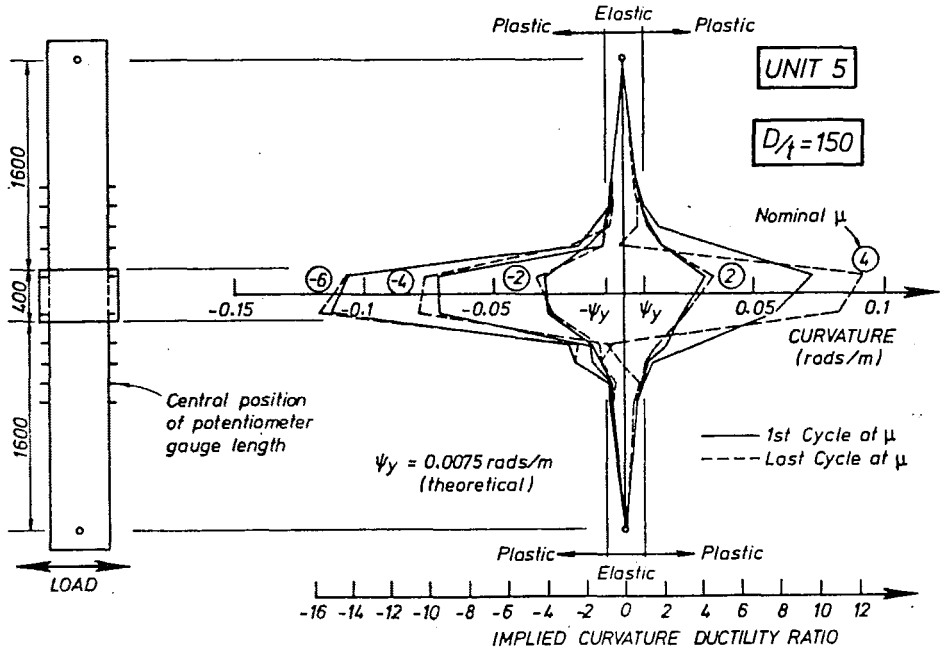

FIG. 4.56 : CURVATURE PROFILES FOR UNIT 5

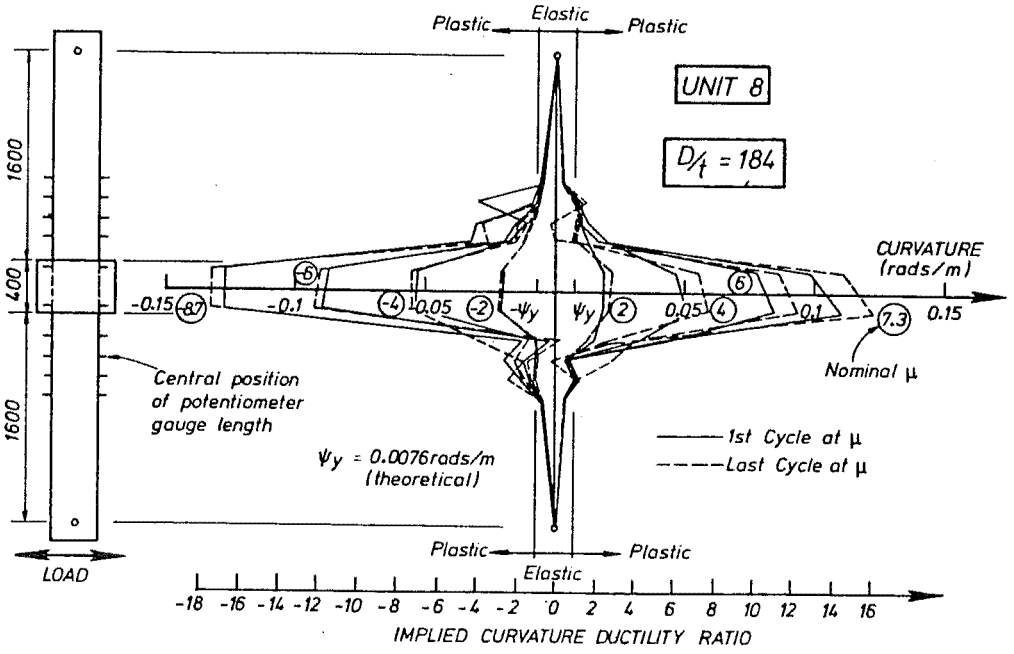

FIG. 4.57 : CURVATURE PROFILES FOR UNIT 8

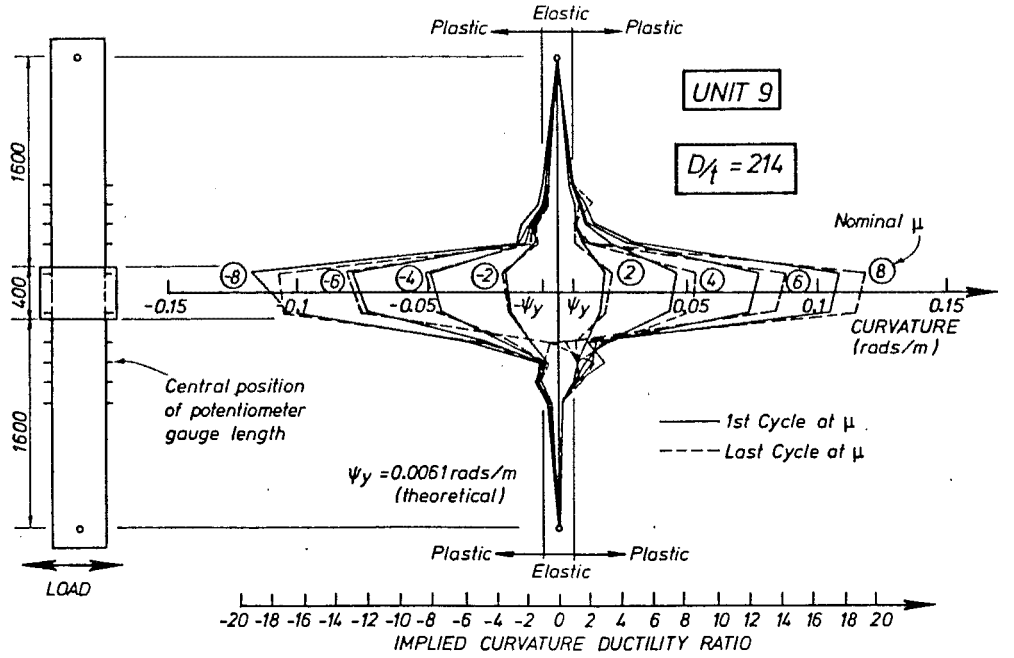

FIG. 4.58 : CURVATURE PROFILES FOR UNIT 9

the actual peak values. However the figures do indicate that on average significant plasticity ($\psi/\psi_y \geq 1$) occurred over the central 44% (a length of 1700 mm) of the test units. The unsymmetrical nature of plastic hinging is also indicated in these figures. Redistribution of curvature, between the first and last cycles at a given level of μ, into the zones where local buckling occurs is apparent particularly for units 2-5, 8 and 9 at the higher ductility levels. This indicates some degradation of performance as cyclic loading proceeded.

4.9.4 Distribution of Longitudinal-Compression Strains Along the Length of the Test Units

In Figs. 4.59-4.61 representative distributions of longitudinal-compression strain on the casing surface in the vicinity of the regions of local buckling are shown for units 1, 4 and 9 respectively. Two methods of strain measurement are shown. The first method used electrical resistance strain gauges located on the outside surface of the tube on the principal loading diameter, at the positions shown in Fig. 4.10. The second method interpolated the longitudinal strain between opposing linear potentiometers back to the surface of the tube.

At low displacement ductility factors ($\mu \leq 2$ for units 2-5, 8 and 9; and $\mu \leq 4$ for unit 1) before local buckling became significant, the strain gauges should give a good indication of local strain. However at high μ, local buckling often resulted in erratic gauge readings since large strain gradients occur in the vicinity of the bulging. At all values of μ linear potentiometers mounted away from the block (N1-N4, S1-S4, N7-N10 and S7-S10) gave reliable indications of strain. However the difficulties mentioned previously in assessing the effective gauge length (assumed to be 300 mm compared with the nominal 100 mm) over which the four potentiometers (N5, S5, N6 and S6) mounted against the loading block operated meant that strains calculated from these four potentiometers were of dubious quality.

The longitudinal strain distributions present a sometimes confused and contradictory indication of the value and position of the maximum longitudinal-compression strain. However in general at $\mu = \pm 2$, the strain gauges indicated a peak strain of roughly twice that given by the linear potentiometers which were adjacent to the block. For unit 1 this observation is roughly correct throughout static testing. Thus for unit 1 a maximum longitudinal-compression strain, assessed by the strain gauges, of approximately 3.5% was present at $\mu = -10$.

For units 2-5, 8 and 9 at $|\mu| > 2$ the longitudinal-compression strains indicated by strain gauges were in general substantially lower than those indicated by potentiometers. In some cases the strain gauges indicated tensile strains, probably due to local buckling effects. Thus for these six units at high levels of μ, the potentiometers give the more reliable measure of longitudinal strain. However as local buckling occurred over a length considerably shorter than the gauge length of the four potentiometers adjacent to the block, it is likely that the actual maximum longitudinal-compression strains were at least twice as large (cf. unit 1) as the 2-3% indicated by the potentiometers.

Figure 4.61 indicates that although longitudinal-compression strains inside the block were often in excess of yield strain, these strains were usually lower than those outside the block. Thus penetration of tube longitudinal-compression strain inside the block was at least partially restrained by friction between the block and the tube.

4.9.5 Distribution of Longitudinal-Tension Strain Along the Length of the Test Units

In Fig. 4.62 representative distributions of longitudinal-tension strain on the casing surface in the vicinity of the two regions of local buckling are shown for unit 8. Despite the large amount of scatter which is shown, it is

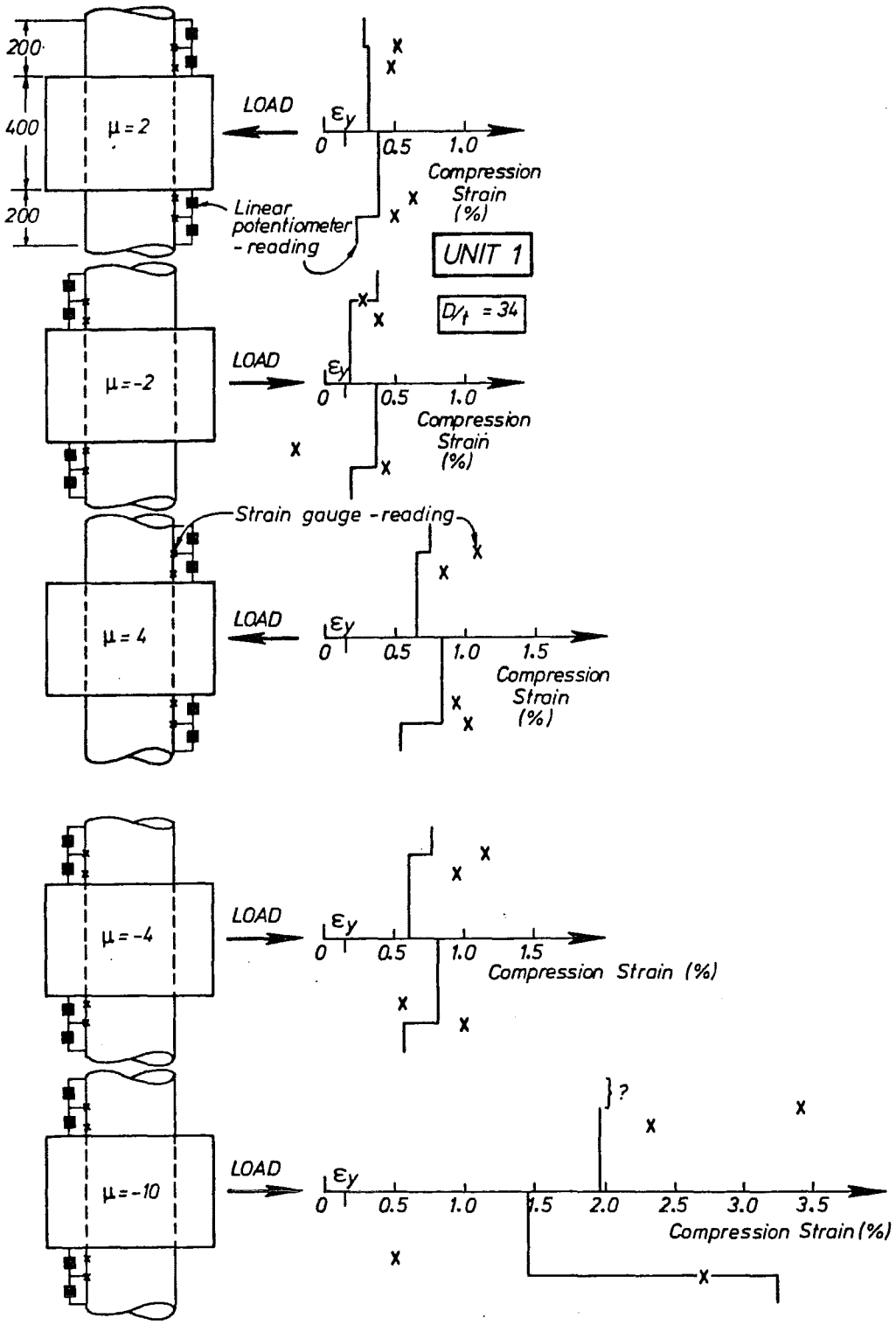

FIG. 4.59 : DISTRIBUTIONS OF LONGITUDINAL-COMPRESSION STRAIN FOR UNIT 1

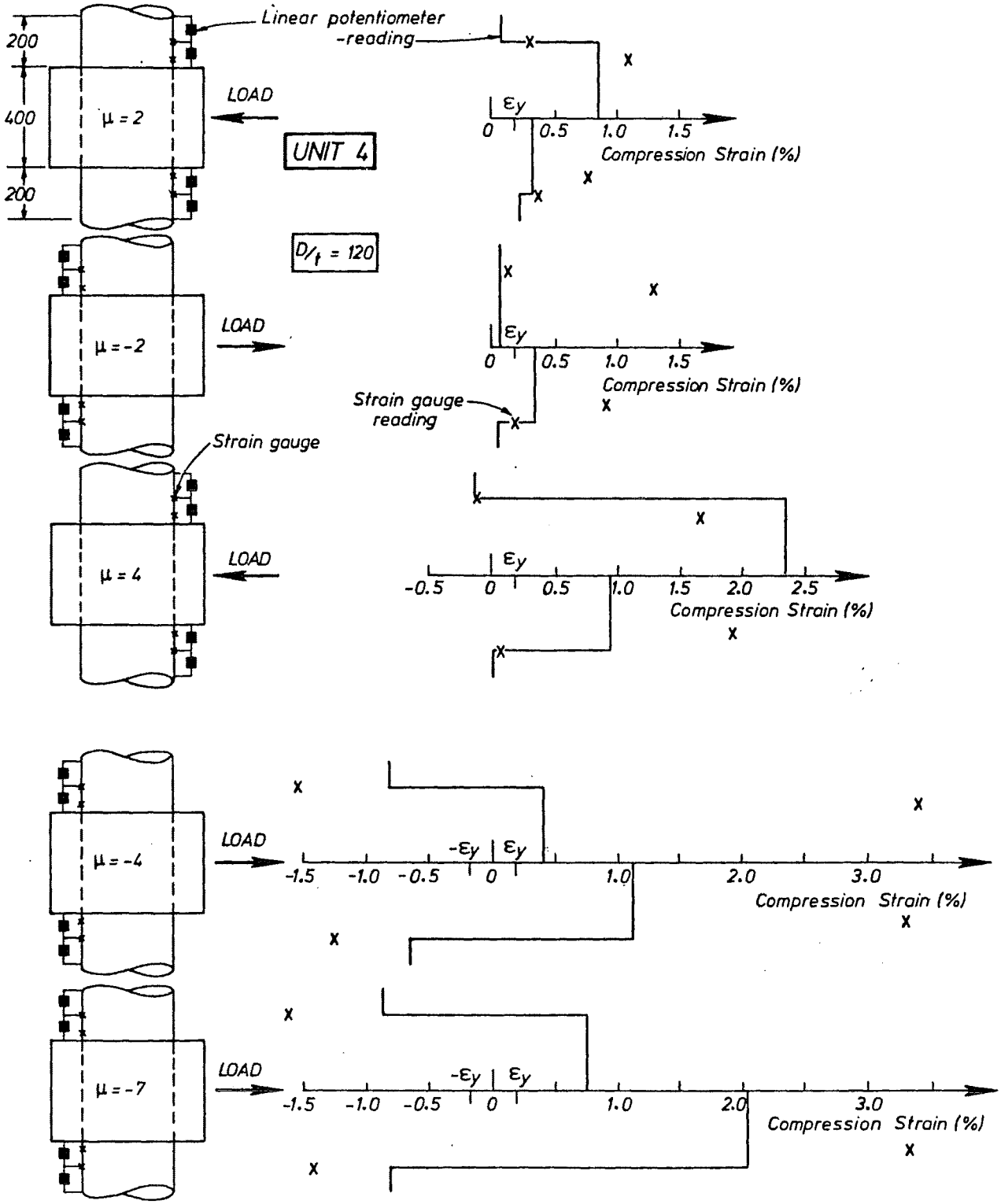

FIG. 4.60 : DISTRIBUTIONS OF LONGITUDINAL-COMPRESSION STRAIN FOR UNIT 4

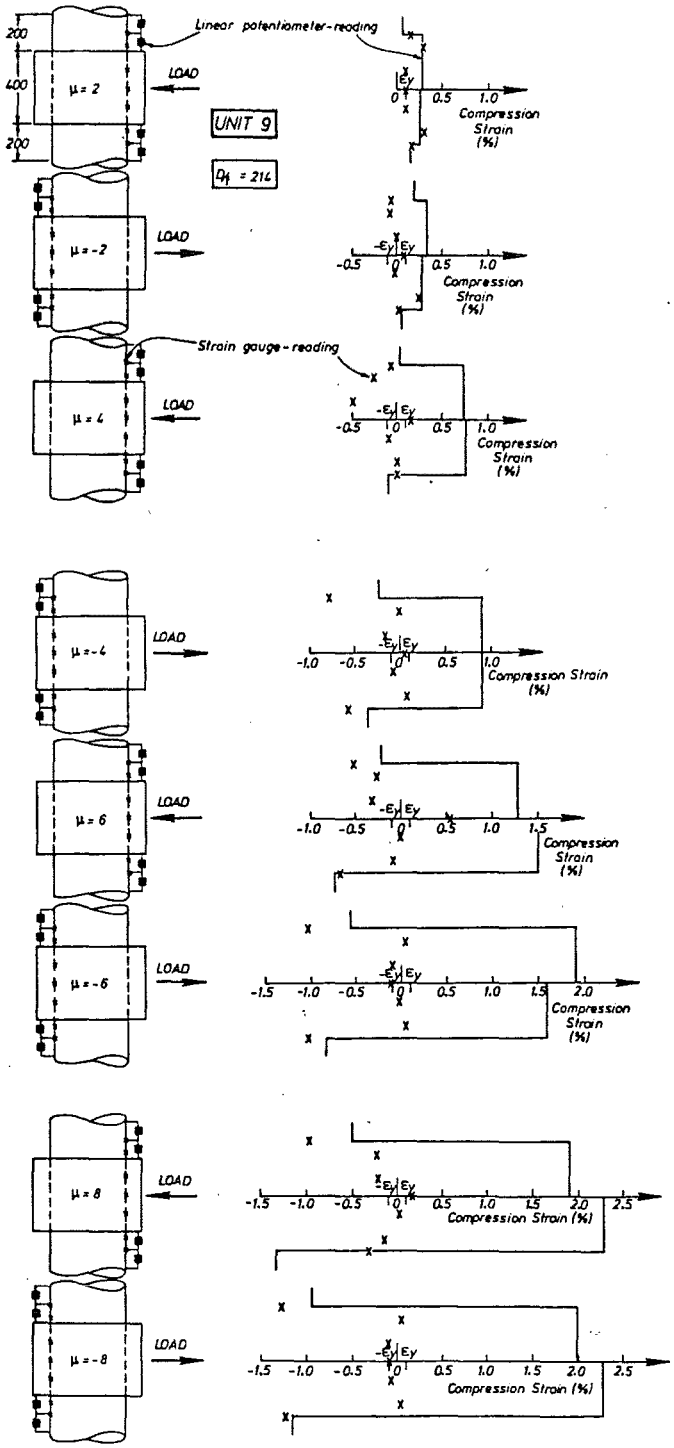

FIG. 4.61 : DISTRIBUTIONS OF LONGITUDINAL-COMPRESSION STRAIN FOR UNIT 9

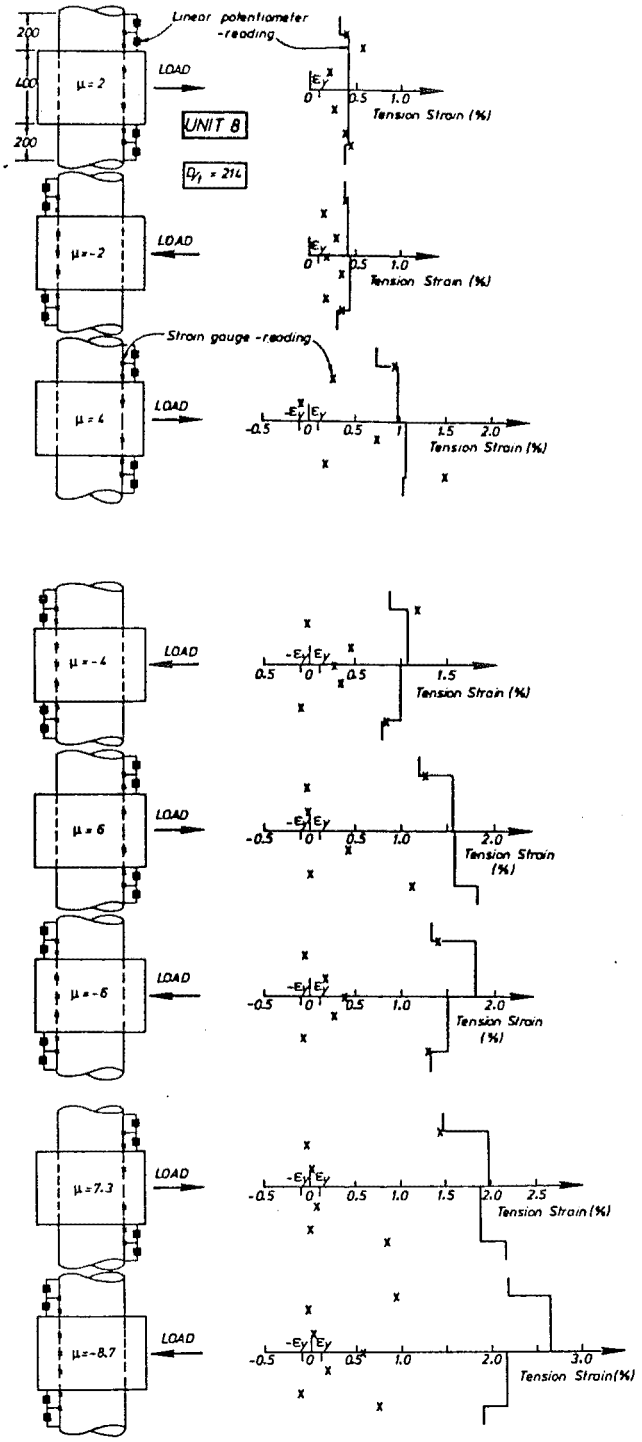

FIG. 4.62 : DISTRIBUTIONS OF LONGITUDINAL-TENSION STRAIN FOR UNIT 8

evident from the strain gauge results that a substantial penetration of longitudinal-tension strain into the block occurs, with strains of up to four times the yield strain being measured in this region.

At displacement ductilities μ of ±2 peak strains obtained from linear potentiometers were similar in magnitude to those indicated by strain gauges which shows that the assumed gauge length of 300 mm for potentiometers N5, S5, N6 and S6 is reasonable. At higher levels of $|\mu|$, strains indicated by potentiometers were usually larger than those measured by strain gauges. At this stage the local buckles were affecting the strain gauge results, since the local buckles were not completely straightening-out under strain reversal. Thus the potentiometers give a more realistic, although probably low, estimate of the peak longitudinal-tension strain. In units 1-5, 8 and 9 a maximum longitudinal-tension strain of approximately 2.5%, as indicated by potentiometers, was reached by the end of static testing.

4.9.6 Confining Strains on the Casing Outer Surface

Representative distributions of confining strain $(\varepsilon_H + 0.3\varepsilon_L)$ on the casing outer surface are given in Figs. 4.63 and 4.64 for units 1 and 9 respectively. In the elastic range, hoop stress σ_H can be calculated from the hoop strain ε_H, longitudinal strain ε_L, Young's Modulus E_s and Poisson's ratio ν_s ($\cong 0.3$) as was given in equation 2.12. Thus σ_H is proportional to $(\varepsilon_H + 0.3\varepsilon_L)$. In the plastic range and under cyclic loading conditions, the simple constitutive equation 2.12 does not apply. Nevertheless in Figs. 4.63 and 4.64 distributions of confining strain $(\varepsilon_H + 0.3\varepsilon_L)$ are given as an index to describe the growth of hoop stresses in the casing. For comparative purposes, yield strain ε_y $(= \sigma_y/E_s)$ is also indicated on these figures.

Strain rosettes located at the N and S extremities of the diameter of the section parallel to the loading direction indicated very large values of confining strain when compared with rosettes located at the E and W extremities of the perpendicular diameter. This could be expected as concrete dilatancy and tube local buckling which result in large hoop stresses increase as the level of longitudinal-compression strain increases.

Strain rosettes located only 30 mm from the upper or lower faces of the concrete loading block were, as can be seen from Table 4.6, either on or adjacent to the crest of the local buckles. At these two sections, the confining strains were as large as 6%. However rosettes located 100 mm from the block showed considerably smaller strains. This is further evidence that the plastic deformation was concentrating at the local buckles.

4.9.7 Strains in the Spiral Reinforcement

Representative distributions of strain in the spiral reinforcement for units 1, 4 and 9 during static loading are shown in Figs. 4.65-4.67 respectively. In these units the spiral reinforcement has two main roles. The first role was that of helping to confine the concrete in the regions where longitudinal and lateral loads combine to result in large values of longitudinal-compression strain. The second role was that of helping to increase the shear capacity of the section. Shear force is predominantly resisted close to the neutral axis of the section. Thus the confining and shear roles were assumed to be uncoupled as shown in Figs. 4.65-4.67.

In general the results show that the spiral reinforcement was more highly stressed in its confinement role than in its shear role. For all units, yield strain ε_y was attained and exceeded at the confinement positions. However the largest recorded strain at the shear positions was $0.75\varepsilon_y$.

The distributions of strain along the confinement positions show that the hoop strains in the spiral reinforcement were large in the vicinity of the local

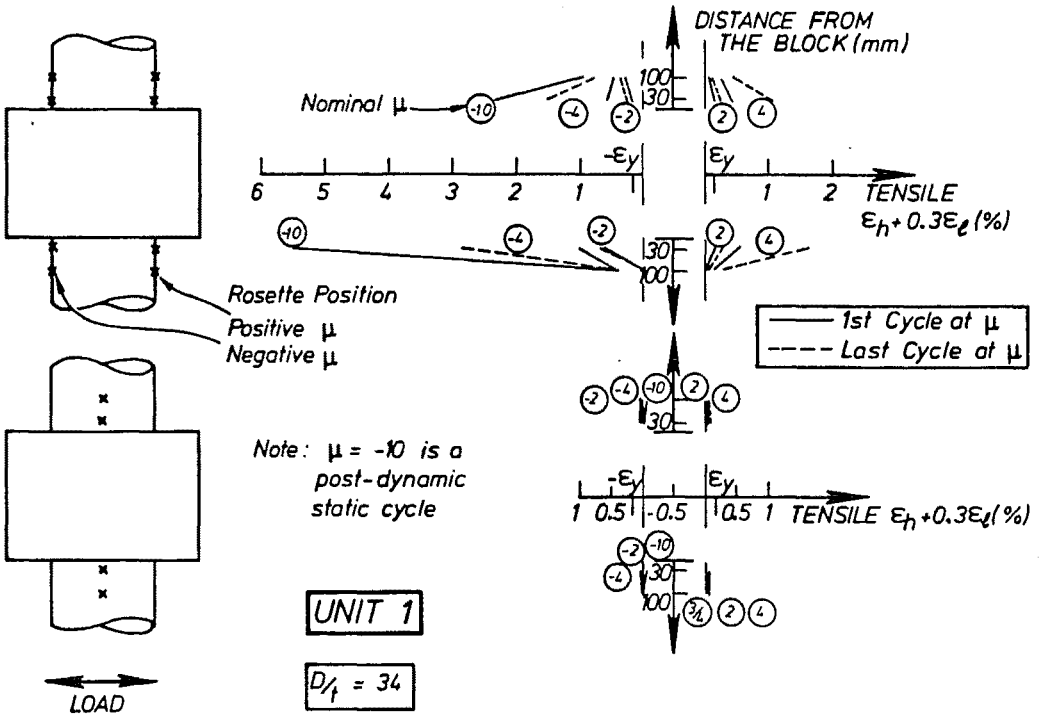

FIG. 4.63 : CONFINING STRAINS ($\varepsilon_H + 0.3\varepsilon_L$) ON THE TUBE OUTER SURFACE FOR UNIT 1

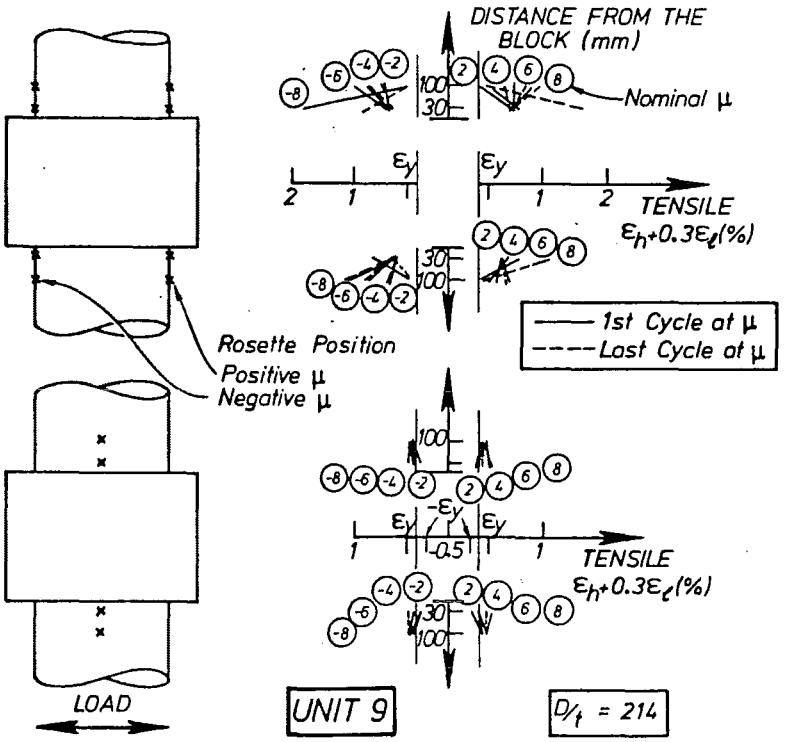

FIG. 4.64 : CONFINING STRAINS ($\varepsilon_H + 0.3\varepsilon_L$) ON THE TUBE OUTER SURFACE FOR UNIT 9

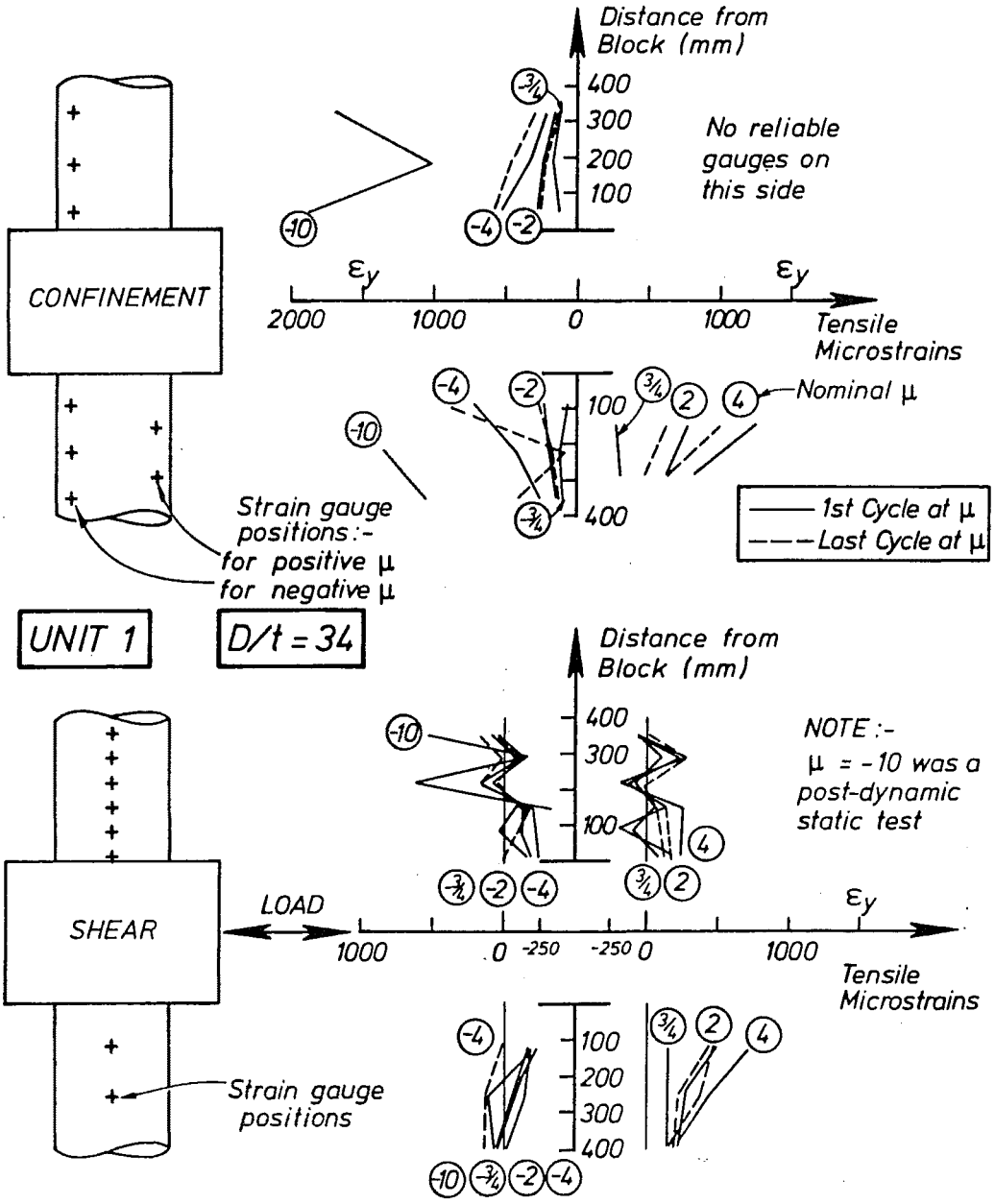

FIG. 4.65 : STRAINS IN THE SPIRAL REINFORCEMENT FOR UNIT 1

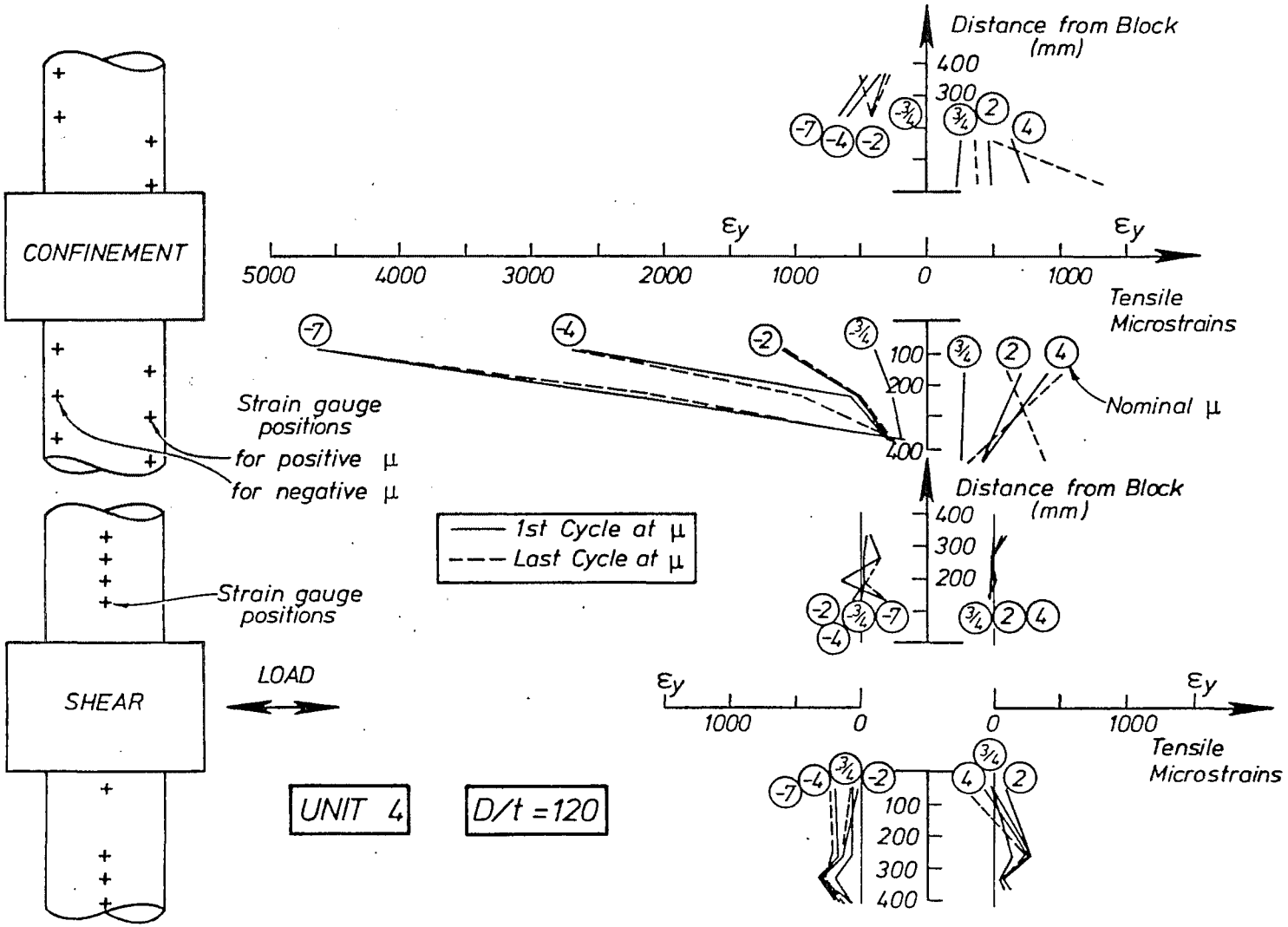

FIG. 4.66 : STRAINS IN THE SPIRAL REINFORCEMENT FOR UNIT 4

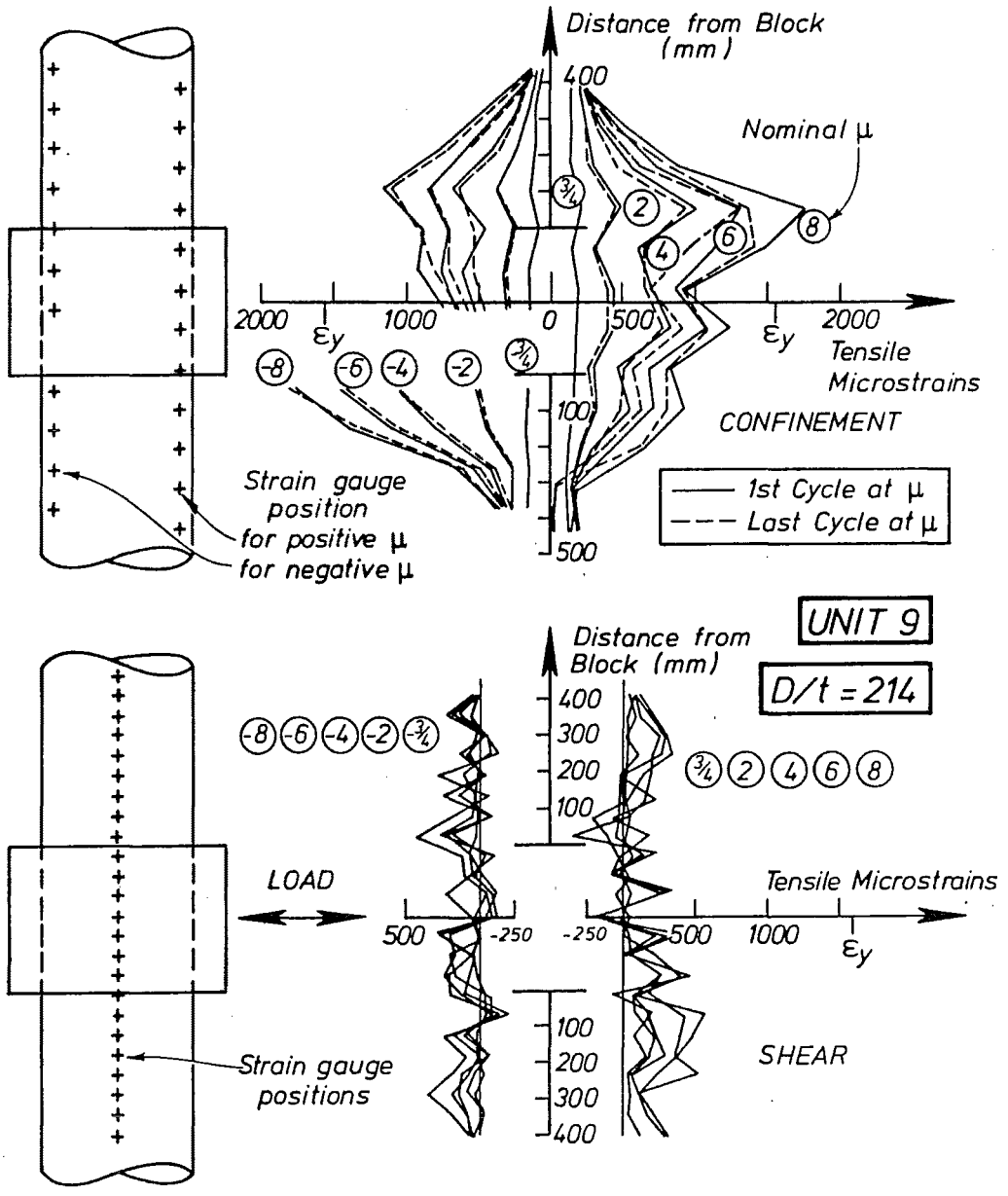

FIG. 4.67 : STRAINS IN THE SPIRAL REINFORCEMENT FOR UNIT 9

buckles (Table 4.6 indicates that the local buckles were all located within 70 mm of the concrete loading block). Strain outside the local buckles along the confinement positions reduces abruptly as distance from the local buckle increases. This again emphasises that plasticity concentrates over a very short region in the vicinity of the local buckles.

The strain distributions along the shear positions show a zig-zag pattern which does not build to a peak, and is relatively random over the strain-gauged region. Since the spiral reinforcement was not yielding in its shear role, it is clear that the concrete and the casing were more than capable of resisting the applied shear force.

4.10 ANALYSIS OF RESULTS - CONTINUOUS CASINGS

4.10.1 Estimating Maximum Curvature and Longitudinal Strains

In the preceding sections comments have been made on the difficulties in accurately assessing the maximum values of curvature and longitudinal strain in the test units. However there was shown to be strong experimental evidence that the plastic rotations were to a large degree concentrated at the regions of local buckling.

In this section for displacement ductility levels up to those at which local buckling was first observed ($\mu = 4$ for unit 1, $\mu = 2$ for units 2-5, 8 and 9), it is assumed that deformations measured by linear potentiometers N5, N6, S5 and S6 were occurring uniformly over the effective (300 mm) gauge length of these instruments. At higher ductility levels, these assumptions are also followed in assessing longitudinal-tension strain, but in assessing the peak values of longitudinal-compression strain it is assumed that all of the deformation indicated by the potentiometers occurred uniformly over a gauge length which was equal to the longitudinal extent $2L_e$ of local buckling (see Table 4.6). At very large values of displacement ductility factor this approach should give good estimates to the values of peak longitudinal-compression strain ε_c and curvature ductility factor ψ/ψ_y, since local buckling was well developed at this stage. However at values of displacement ductility factor just above those at which local buckling was first observed ψ/ψ_y and ε_c will be overestimated.

Figures 4.68 and 4.69 show plots of estimated curvature ductility factor ψ/ψ_y against displacement ductility factor μ before and after local buckling had occurred respectively. Results shown represent ψ/ψ_y at the negative peaks of the first cycle to given levels of μ; if the last cycles had been used then even larger values of ψ/ψ_y would have resulted (see Figs. 4.52-4.58). Also shown is a typical result for similar reinforced concrete models (4.10-4.14) which were tested at the University of Canterbury.

In assessing the ψ/ψ_y vs μ response for reinforced concrete models at $|\mu| > 1$, the following procedure was used. The curvature distribution for a cantilever under lateral tip load was idealised as shown in Fig. 4.70. Park and Paulay (4.27) have shown that the resulting value of ψ/ψ_y can be expressed in terms of the cantilever length L, the displacement ductility factor μ and the idealised plastic hinge length ℓ_p as

$$\left|\frac{\psi}{\psi_y}\right| = \frac{L^2\,(|\mu| - 1)}{3\ell_p\,(L - \ell_p/2)} + 1 \qquad (4.8)$$

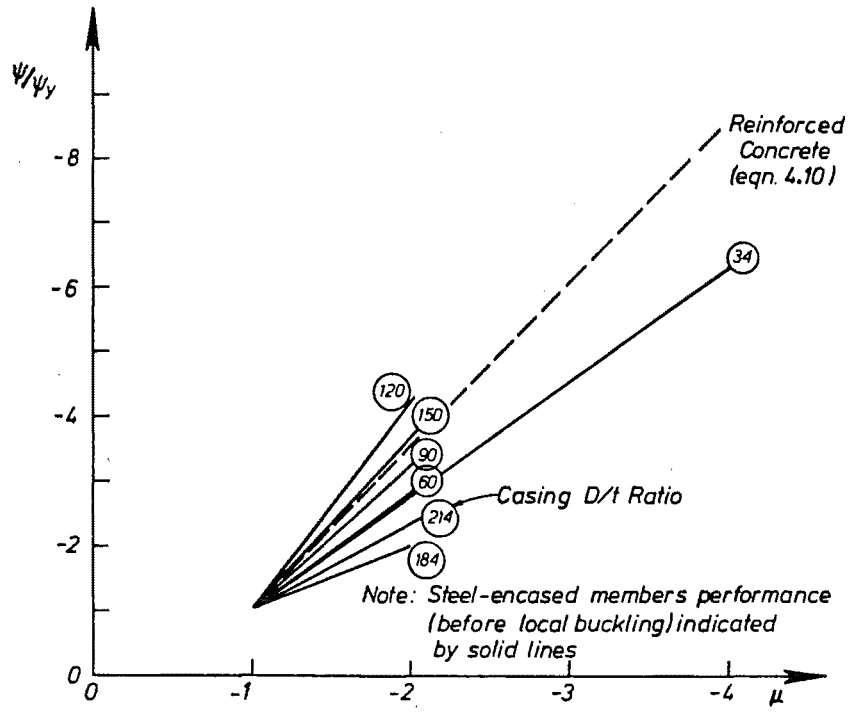

FIG. 4.68 : VARIATIONS OF CURVATURE DUCTILITY FACTOR ψ/ψ_y WITH DISPLACEMENT DUCTILITY RATIO μ, BEFORE TUBE LOCAL BUCKLING

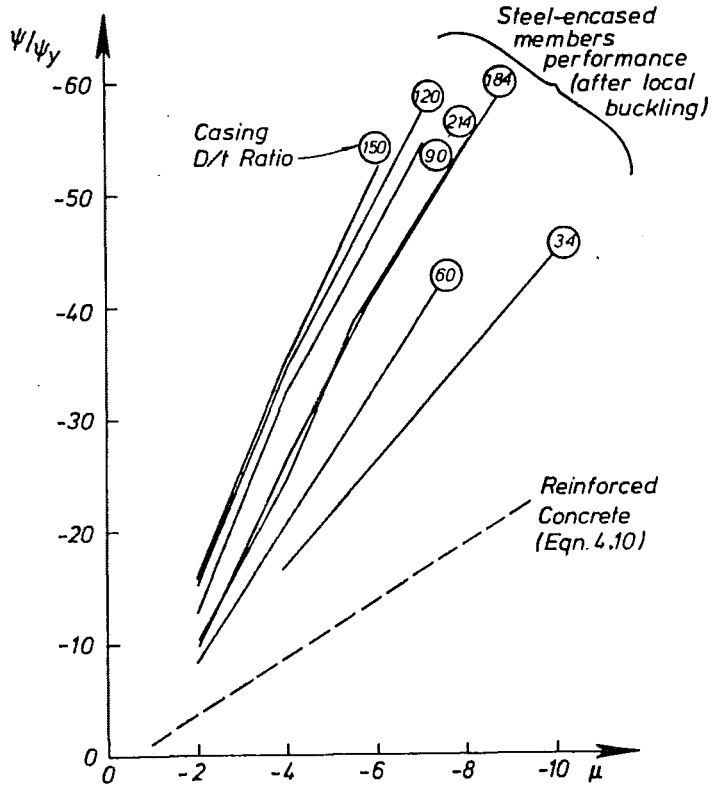

FIG. 4.69 : ESTIMATED VARIATION OF CURVATURE DUCTILITY RATIO ψ/ψ_y WITH DISPLACEMENT DUCTILITY RATIO μ, AFTER TUBE LOCAL BUCKLING

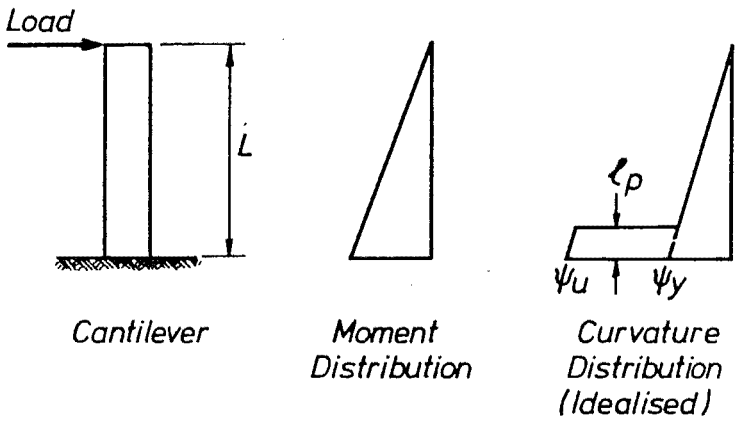

FIG. 4.70 : IDEALISED CURVATURE DISTRIBUTION FOR A CANTILEVER WHICH IS LOADED INTO THE PLASTIC RANGE

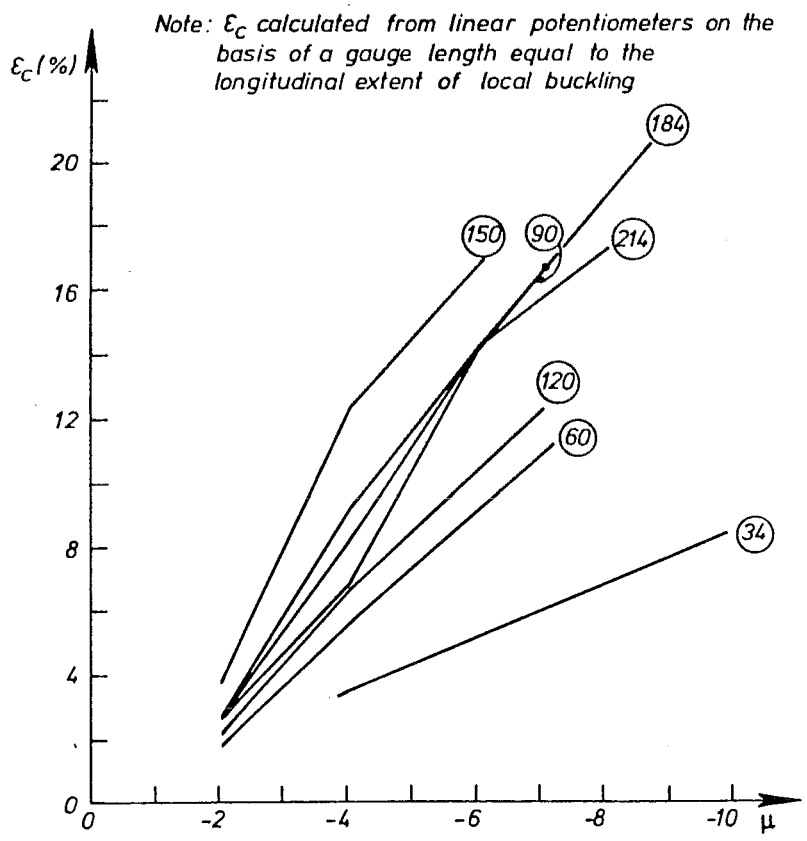

FIG. 4.71 : ESTIMATED VARIATIONS OF MAXIMUM LONGITUDINAL-COMPRESSION STRAIN ε_c WITH DISPLACEMENT DUCTILITY LEVEL μ, AFTER TUBE LOCAL BUCKLING

From tests of reinforced concrete members under similar geometric and loading conditions to those of the steel-encased reinforced concrete models, Priestley and Park (4.33) have shown that

$$\ell_p = 0.08\,L + 6\,d_b \qquad (4.9)$$

where d_b = diameter of longitudinal reinforcing bar. The first term in equation 4.9 represents the spread of plasticity which occurs due to moment gradient and member overstrength effects, while the second term represents spread of plasticity due to bond slip between the flexural reinforcement and concrete. In approximately half-scale model tests of reinforced concrete members d_b was typically equal to 16 mm, and as for the steel-encased members the cantilever length L was equal to 1600 mm. Thus the plastic hinge length ℓ_p can be taken as 224 mm. Substituting these values of L and ℓ_p into equation 4.9 gives:

$$|\psi/\psi_y| = 2.56(|\mu| - 1) + 1 \qquad (4.10)$$

which is plotted as a dashed line in Figs. 4.68 and 4.69.

In Fig. 4.68 it is shown that before local buckling occurs and at a given value of $|\mu|$, the $|\psi/\psi_y|$ values in steel-encased reinforced concrete members are typically slightly less than those for reinforced concrete members. However in Fig. 4.69 it is shown that after local buckling had occurred $|\psi/\psi_y|$ values tend to increase as the casing D/t ratio increases. This occurs because, as shown in Table 4.6, as the casing D/t ratio increases the longitudinal extent $2L_e$ of local buckling decreases and hence the plastic rotation concentrates over a shorter length, which is to the detriment of structural performance. At large ductility levels (e.g. $|\mu| > 6$), curvature ductility demands in steel-encased reinforced concrete members with large casing D/t ratios are of the order of three times those of reinforced concrete members.

Steel-encased reinforced concrete members are however inherently more ductile than conventionally designed reinforced concrete members due to the better confined concrete in the steel-encased member. This offsets the difference in $|\psi/\psi_y|$ at high levels of $|\mu|$ between the two types of members.

In Fig. 4.71, the variations of estimated peak longitudinal-compression strain ε_c against $|\mu|$ (for $|\mu|$ greater than that necessary to cause local buckling) are shown. Extremely large values of ε_c were estimated to have been reached during testing. For example a maximum compression strain of 20.6% was estimated to have been reached during testing of unit 8 (D/t = 184). It is also shown in Fig. 4.71 that for a given $|\mu|$, in general ε_c increases with casing D/t ratio, due to the relatively short length of the local buckles which occur for test units with large casing D/t ratio.

4.10.2 Shear Resistance

Test units 1-5, 8 and 9 all sustained lateral loads in excess of the flexural strengths predicted by an approach similar to that used in reinforced concrete design (see Section 4.9.2.1), while visual observations and the low values of strain (close to the neutral axis position) on the spiral reinforcement indicated that shear strength was adequate to sustain flexural strength at high ductility levels. In the rest of this section the above observation is justified theoretically. It is assumed that shear force in steel-encased reinforced concrete members is carried in the same fashion as it is in reinforced concrete members (4.27). That is, an assessment is made of the concrete shear carrying capacity, with the shortfall between shear demand and

concrete capacity being carried by a truss mechanism involving hoop-tension stresses in casing and spiral reinforcement across concrete cracks orientated at 45° to the longitudinal axis of the member.

Shear Force Carried by Concrete

The test units were subjected to a longitudinal-compression load P of $0.1f'_c(A_c + A_t)$. For this condition the New Zealand Concrete Code (4.17) states that no reliance should be placed on concrete reisting shear force in the plastic hinge zone. Priestley and Park (4.33) and Ang et al (4.32) have demonstrated that the Code is too conservative for reinforced concrete columns with spiral reinforcement having a volumetric ratio ρ_s of greater than 1%. Ang et al (4.32) found that in plastic hinge zones concrete shear capacity is independent of the level of longitudinal-compression load and may be calculated from

$$v_c = 0.185\sqrt{f'_c} \qquad (4.11)$$

where v_c = concrete shear stress capacity (MPa)
f'_c = concrete cylinder compressive strength (MPa).

To obtain the shear force carried by the concrete V_c, v_c is multiplied by the nominal area of concrete which is effective in resisting shear. For circular reinforced concrete members, Ang et al (4.32) recommended that only 80% of the gross concrete area was assumed to resist shear, as the other 20% would spall. For steel-encased reinforced concrete members spalling is prevented and thus it is appropriate to assume that 100% of the concrete area provides shear resistance. Hence $V_c = 0.185\sqrt{f'_c}.\pi(D - 2t)^2/4$. Ang et al (4.32) also commented that concrete shear capacity tended to increase as the volume of longitudinal and lateral steel increased. Thus it is possible that for steel-encased reinforced concrete members which have a larger proportion of steel than do ordinary reinforced concrete members, strength in excess of that predicted by equation 4.11 will be present.

Shear Force Carried by Spiral Reinforcement

The shear force carried by spiral reinforcement V_{sp} can be calculated (4.32) from:

$$V_{sp} = \frac{\pi}{4}\,(2A_{sp}.\,\sigma_{sp})\,\frac{D_{sp}}{s} \qquad (4.12)$$

where A_{sp} = area of spiral reinforcement
σ_{sp} = stress in spiral reinforcement
D_{sp} = centre to centre diameter across the spiral reinforcement
s = centre to centre pitch of spiral reinforcement.

The value of σ_{sp} was assessed from the strain distributions (e.g. Figs. 4.65-4.67) by multiplying the strain by the elastic modulus. The strain used was the maximum strain obtained from the average of any two adjacent strain gauges located on the diameter perpendicular to the loading axis.

Shear Force Carried by Tube

The shear force carried by the tube V_t can then be calculated from

$$V_t = V - V_c - V_{sp} \qquad (4.13)$$

where V is the externally applied shear force.
Similarly to equation 4.12, V_t can be expressed as

$$V_t = \pi(D - t).t.\sigma_{HV} \qquad (4.14)$$

where σ_{HV} = average hoop-tension stress in the tube due to shear force.

Table 4.8 shows the resulting values of hoop-tension stress σ_{HV} in the tube. These values of σ_{HV} are typically less than 5% of σ_y. Thus it is clear that the tube has a more than adequate reserve of shear strength. It is recalled that under longitudinal-compression stress, hoop-tension stresses will reduce the longitudinal strength of the tube, while the converse applies under longitudinal-tension stress. Thus the nett effect of tube hoop-tension stresses σ_{HV} on overall flexural strength is negligible as demonstrated experimentally.

4.10.3 Possibility of Strain-Age Embrittlement

Priestley and Park (4.33) have expressed concern about the possibility of local buckling of steel casing in an earthquake initiating strain-age embrittlement of the casing which could result in brittle fracture of the casing under a later earthquake. They conservatively recommended "that for design purposes, curvatures be limited to those likely to induce incipient local buckling". As local buckling was first observed at $\mu \doteq 2$ for test units with casing D/t ratios of 60-214, and $\mu = 4$ for the test unit with a casing D/t ratio of 34, this is a very restricting recommendation.

Strain-age embrittlement results when structural steel is strained plastically and then allowed to age at an ambient or elevated temperature. The ageing results in increased ultimate and yield strengths, but markedly reduced ductility. Erasmus and Pussegoda (4.34 and 4.35) have identified four contributing causes to the brittle failure of the steel used in New Zealand reinforcing bars:

(i) bends with low radii of curvature;

(ii) stress concentrations at the base of deformations for reinforcing bars which have been bent;

(iii) high strain rates, such as occur in earthquakes or under a hammer blow; and

(iv) low temperature at the time of failure.

Pussegoda (4.35) has commented that strain-age embrittlement is unlikely to be a problem in plain bars because of the absence of the above condition (ii). Clearly then, tubes will also not be as susceptible to strain-ageing as are deformed bars.

Pussegoda (4.35) tested deformed reinforcing bars at laboratory temperatures of between 0°C and 4°C under shock loading at strain rates typical of those

occurring in earthquakes. Brittle failures were produced for bends with inside radii of $3.0d_b$, and ductile failures for bends with inside radii of $3.5d_b$ or greater. On the basis of these tests Pussegoda recommended that bends, in deformed reinforcing bars, should have inside radii of $3.5d_b$ or larger.

For units 1-5, 8 and 9 at the time of testing, radii of curvature R_ψ of the casing in the regions of local buckling were not directly measured. However the radii were subsequently estimated from the outstand and longitudinal extent of local buckling which were measured at the end of static testing (see Table 4.6). The method used in estimating R_ψ is shown in Fig. 4.72. Between points "a" and "c" on the diagram a parabolic distribution of the deflected shape is assumed. From small deflection theory and using a finite difference approach then:

$$R_\psi \cong -(d^2y/dx^2)^{-1}$$

$$\cong \left[-(y_c - 2y_b + y_a)/(x_b - x_c)^2\right]^{-1}$$

$$\cong 0.25L_e^2/\text{Outstand} \qquad (4.15)$$

In Fig. 4.73 ratio of local buckle radii to tube thickness R_ψ/t at the end of static testing are plotted against casing D/t ratio. The recommendation of Pussegoda for the minimum value of R_ψ/d_b (= 3.5) is also indicated on this figure. The results show that for a casing D/t ratio of 34, there is definitely no danger of brittle failure due to strain-age embrittlement. Results for other casing D/t ratios (60 - 214) indicate that the casing would be in danger of brittle failure if it behaved as a deformed reinforcing bar. However because of the absence of deformations on the casing, strain-age embrittlement is unlikely to be a problem at any casing D/t ratio. It should also be noted that even if brittle failure of the casing occurred, there is still a well-confined reinforced concrete member underneath. In Section 4.11 it is shown that such members,where circumferential discontinuities in the casing are present, behave in a very ductile fashion.

4.11 EXPERIMENTAL RESULTS - DISCONTINUOUS CASINGS

4.11.1 General Observations

Figures 4.74 and 4.75 contain photographs of test units 6 and 7 after various stages of testing. The performance of these two units was dominated by the plastic hinges which formed at the two positions of casing discontinuity.

At an early stage of testing during the first cycle to $\mu = \pm 3/4$, the tack welds which had been holding the separate lengths of casing together broke and subsequently gaps developed between the separate lengths of casing in the regions of flexurally induced longitudinal tension. Figure 4.76 shows how the gaps increased with $|\mu|$. The gaps were first evident on the first cycle to $\mu = \pm 2$ and eventually increased to 50 mm by the end of static testing (see Figs. 4.74b and 4.75b). Unsymmetrical behaviour was exhibited as the gaps at the top and bottom discontinuities increased at different rates. Under cyclic loading, the gaps formed and closed alternately on the N and S faces of the section as the displacement reversed. In the reinforced concrete that was just beneath the positions of casing discontinuity, a large horizontal flexural crack formed. Thus, as is also indicated in Figs. 4.74a and 4.75a, it was visually obvious that plastic rotation was concentrating in the reinforced concrete core in the vicinity of the casing discontinuities. On the side of the section subjected

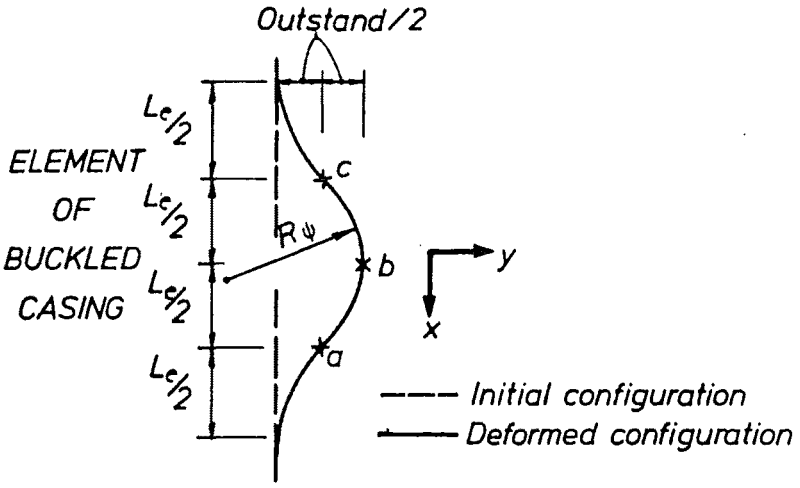

R_ψ = Radius of Curvature (Average for length a-c)

$2L_e$ = Length of visible local buckling

Outstand = Maximum distance local buckle stands out from initial configuration

$$R_\psi \approx 1/(d^2y/dx^2)$$

$$\approx [(y_c - 2y_b - y_a)/(x_b - x_c)^2]^{-1}$$

$$= 0.25 L_e^2/\text{Outstand}$$

FIG. 4.72 : ESTIMATING RADII OF CURVATURE R_ψ OF LOCAL BUCKLES

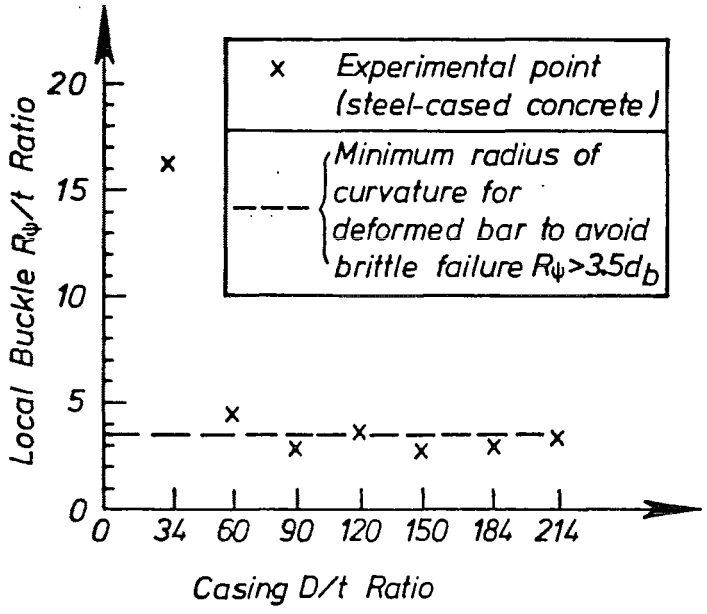

FIG. 4.73 : LOCAL BUCKLE R_ψ/t RATIO VS CASING D/t RATIO

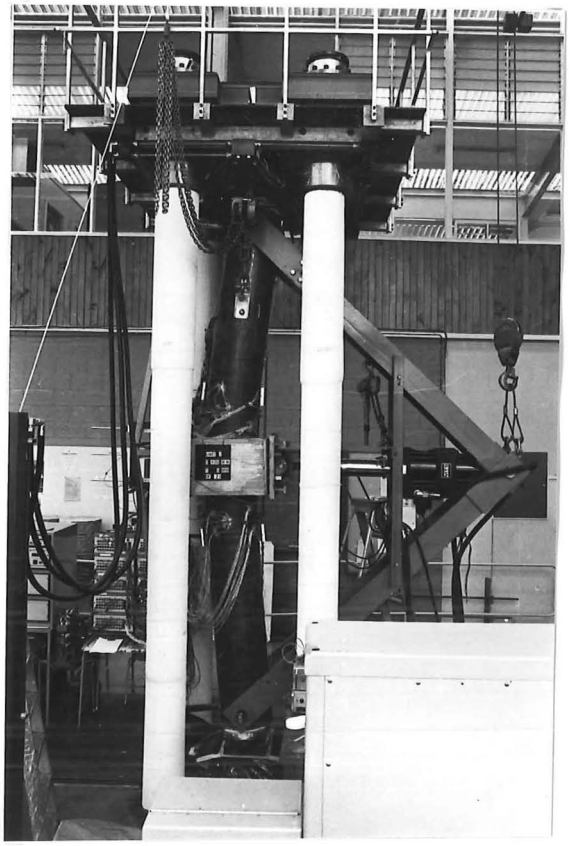

(a) TEST UNIT UNDER LARGE DISPLACEMENT

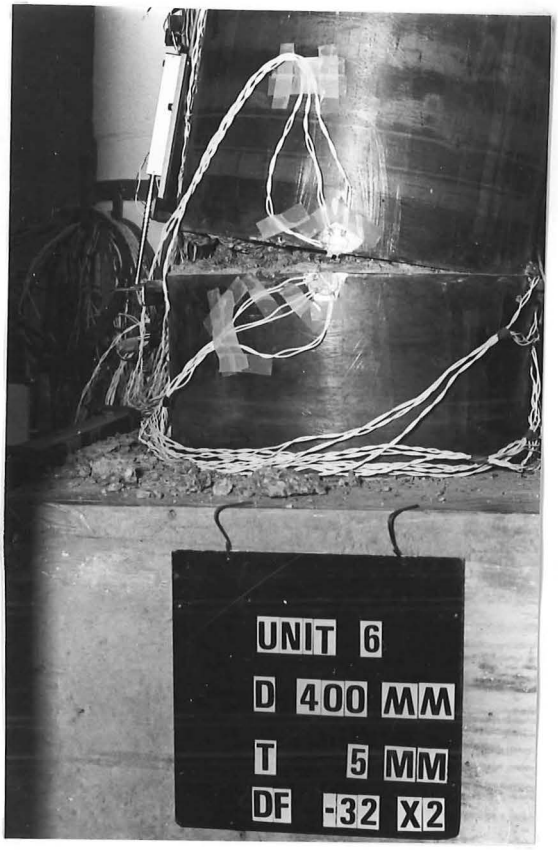

(b) VIEW OF PLASTIC HINGE AREA AT LARGE DISPLACEMENT

(c) POST-MORTEM TO TEST, CRUSHED CONCRETE UNDERLYING CASING DISCONTINUITY

FIG. 4.74 : UNIT 6 (SPIRAL REINFORCEMENT R10-200)

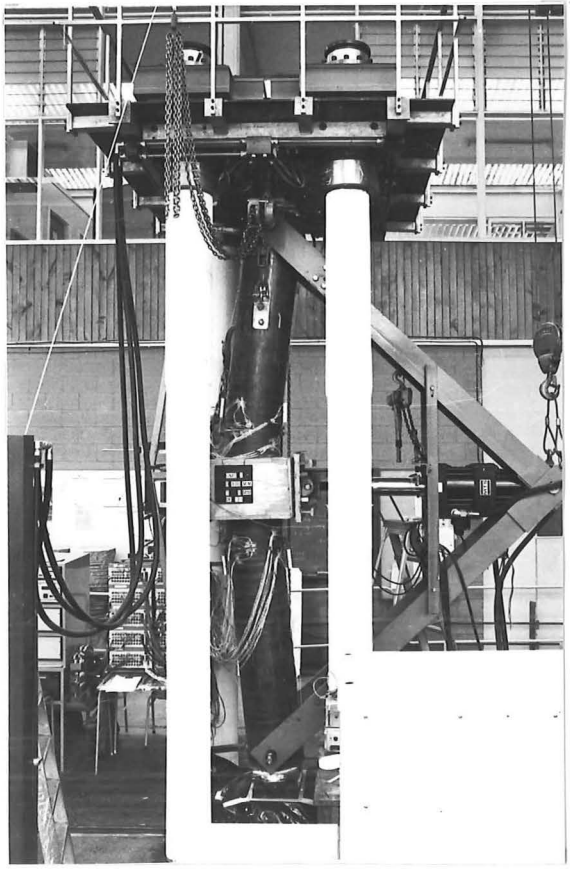

(a) TEST UNIT UNDER LARGE DISPLACEMENT

(b) VIEW OF PLASTIC HINGE AREA AT LARGE DISPLACEMENT

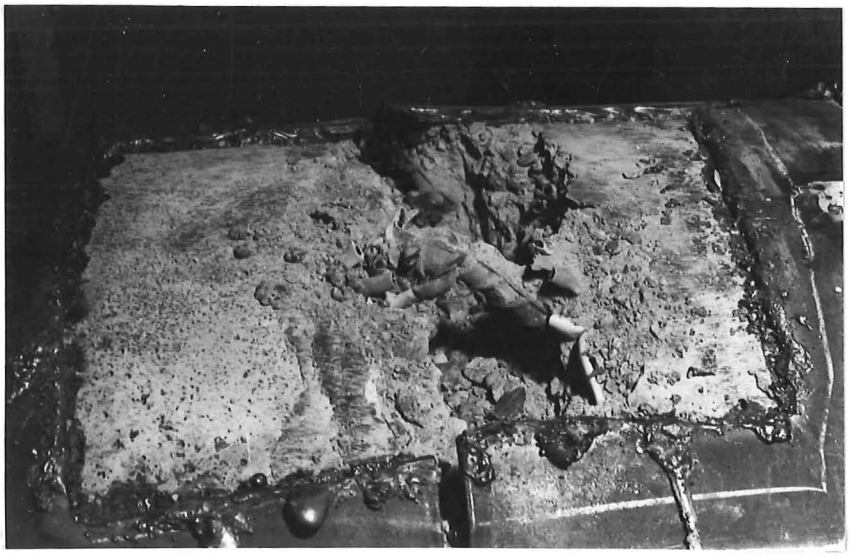

(c) POST-MORTEM TO TEST, CRUSHED CONCRETE AND FRACTURED LONGITUDINAL REINFORCEMENT UNDERLYING CASING DISCONTINUITY

FIG. 4.75 : UNIT 7 (SPIRAL REINFORCEMENT R10-110)

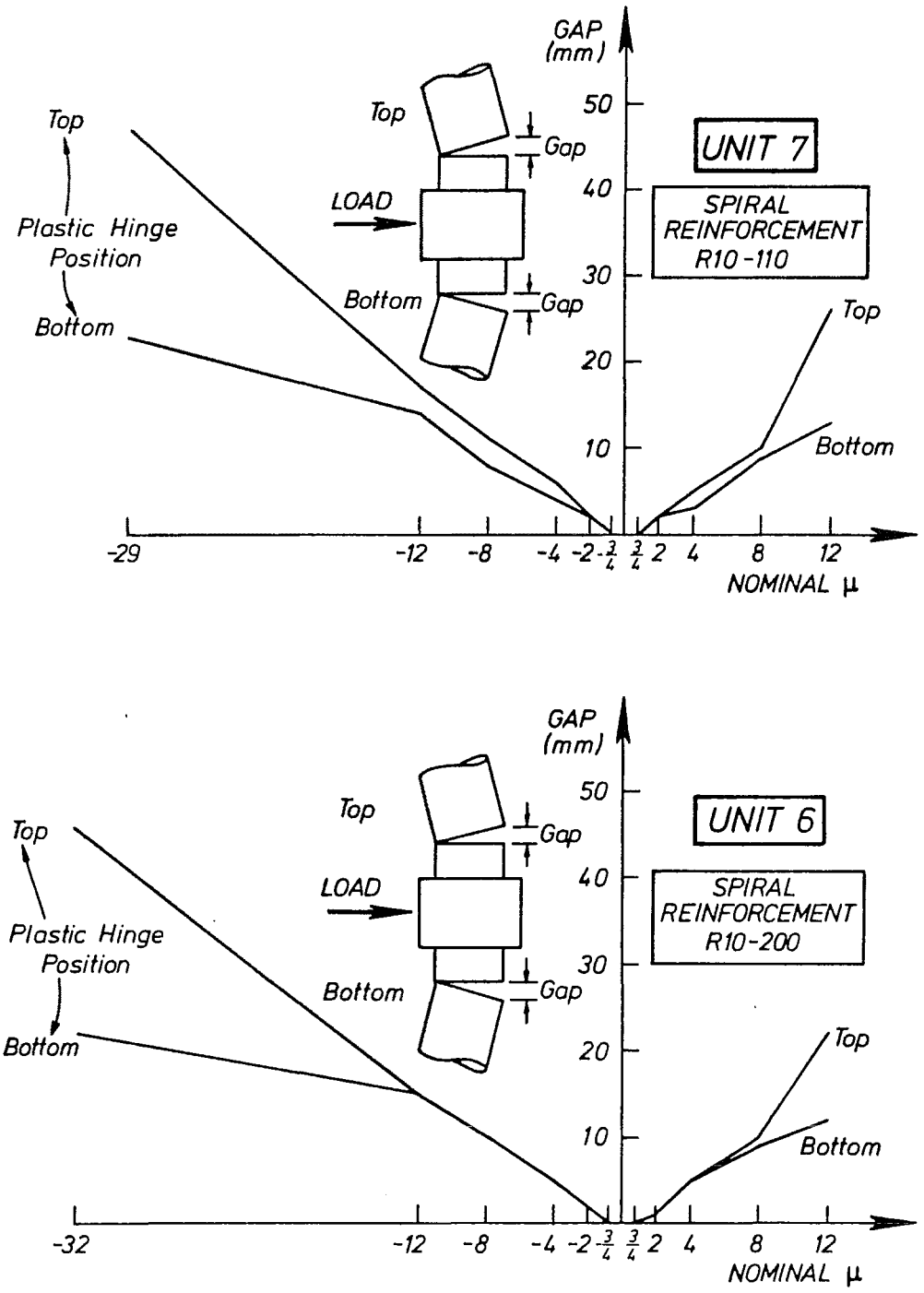

FIG. 4.76 : GROWTH OF GAPS BETWEEN ADJACENT LENGTHS OF TUBE

to longitudinal tension, separation and slip of the tube relative to the concrete loading block was visible. Towards the end of static testing as shown in Figs. 4.74b and 4.75b one of the lengths of tube had a tendency to push inside the other length of tube at the positions of discontinuity. This had the effect of locally bulging the outermost tube. During subsequent dynamic testing, fracturing of the longitudinal reinforcing bars occurred. In unit 6 (spiral reinforcement R10-200 in the plastic hinge zone) one of the nine D16 longitudinal bars fractured, while in unit 7 (R10-110) four of the nine D16 bars fractured. As a post-mortem to the test, casing was removed from the test unit at either the N or S faces (see Figs. 4.74c and 4.75c) in the vicinity of the sections of casing discontinuity. This revealed zones of crushed concrete of approximately 70 mm maximum depth and 60 mm longitudinal extent underneath the positions of casing discontinuity and also showed that some of the longitudinal bars had first buckled under compressive stress and then fractured under tensile stress. Schmidt hammer tests within 100 mm of the discontinuities showed the concrete had an unconfined compression strength of less than half the original capacity.

If it is assumed that the length of concentrated plasticity (i.e. the equivalent plastic hinge length ℓ_p) was equal to the 60 mm longitudinal extent of crushed concrete, then a value of $\ell_p/D = 0.15$ can be calculated for these two units. This value of $\ell_p/D = 0.15$ is considerably smaller than the value of 0.5 which has been typically obtained from similar tests of reinforced concrete models with continuous longitudinal reinforcement (4.10-4.14). Thus the presence of casing discontinuities causes a concentration of plastic rotation in the underlying reinforced concrete core, which implies extremely large curvature ductility ratios at the critical sections. Zanza (4.36) observed a similar concentration of plastic rotation when testing reinforced concrete columns which had lapped splices of longitudinal reinforcement in the plastic hinge zones, since such splices are also a source of strength discontinuity. However it is recalled that a similar concentration of rotation occurred in the units with continuous casings, since in those units plastic rotation concentrated at the local buckles which had longitudinal extents in the range of 35-70 mm.

4.11.2 Hysteretic Performance

Hysteresis loops which show the overall lateral load-lateral deflection responses of test units 6 and 7 during static and dynamic testing are given in Figs. 4.77 and 4.78.

4.11.2.1 Strength Characteristics

Theoretical load capacities H_i^+ and H_i^- of the test units under positive and negative lateral loads respectively are also given in Figs. 4.77 and 4.78. The calculation of these theoretical load capacities was based on measured material strength parameters (concrete f'_c and longitudinal reinforcement σ_y), the ACI stress block for concrete in compression, compatibility of longitudinal strain and an ultimate compression strain ε_c of 0.003. The effect of P-Δ moments was also taken into account as discussed previously in Section 4.9.2.1. Because the casing was not continuous in the plastic hinge zones, it was ignored in the calculation of theoretical strength. Clearly this approach is conservative because it ignores longitudinal-compression stress which is carried in the casing due to end-bearing, and it also ignores the confining effect of the casing on the concrete. These effects are considered later in this and succeeding chapters.

Units 6 and 7 exhibited very good strength characteristics when compared with the theoretical ultimate strength of the reinforced concrete core. Despite the difference in the pitch of spiral reinforcement between units 6 and 7, the same overstrength of 42% above H_i^+ and H_i^- was available in both units.

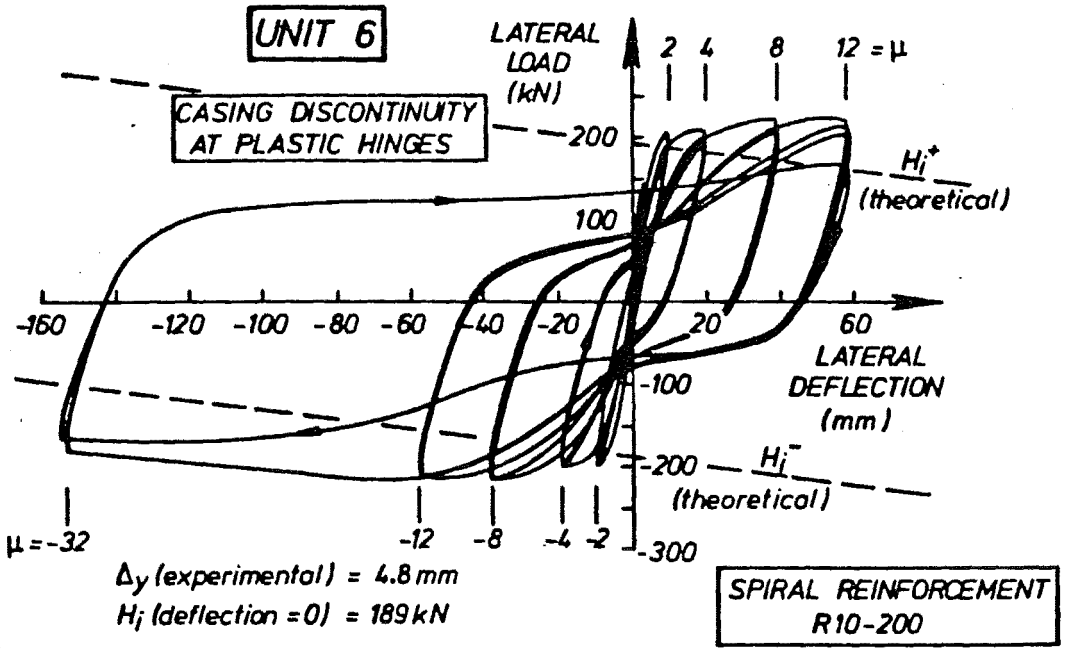

(a) STATIC LOADING

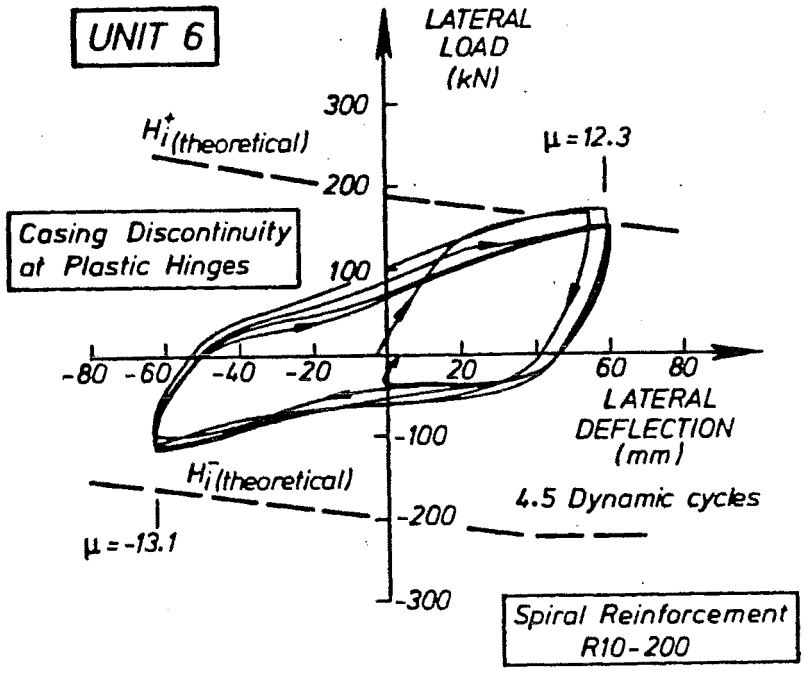

(b) DYNAMIC LOADING

FIG. 4.77 : UNIT 6 HYSTERESIS LOOPS

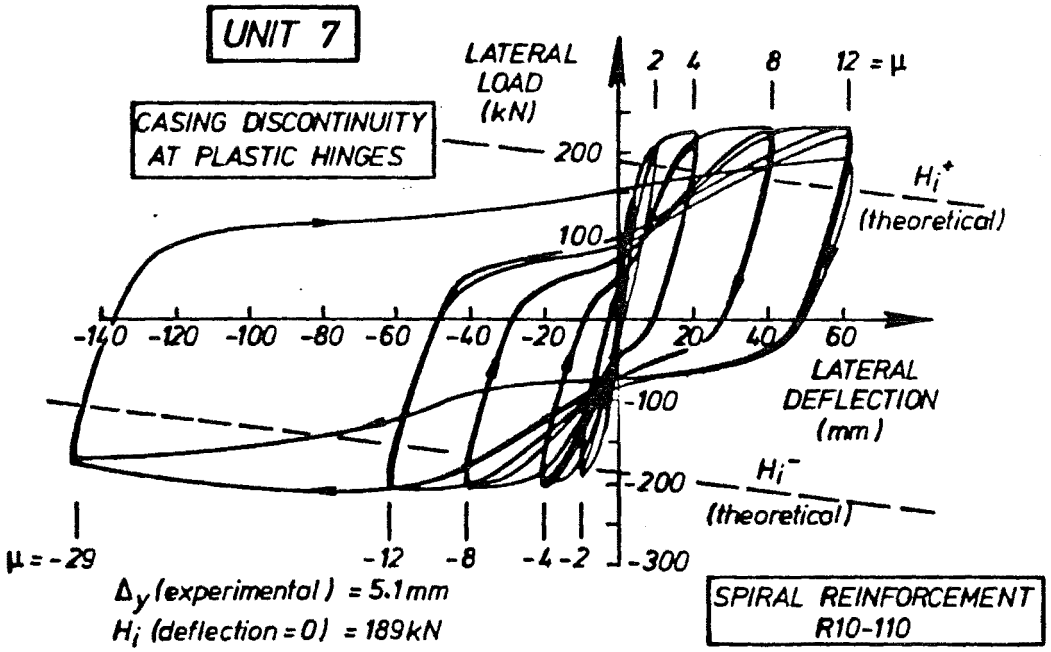

(a) STATIC LOADING

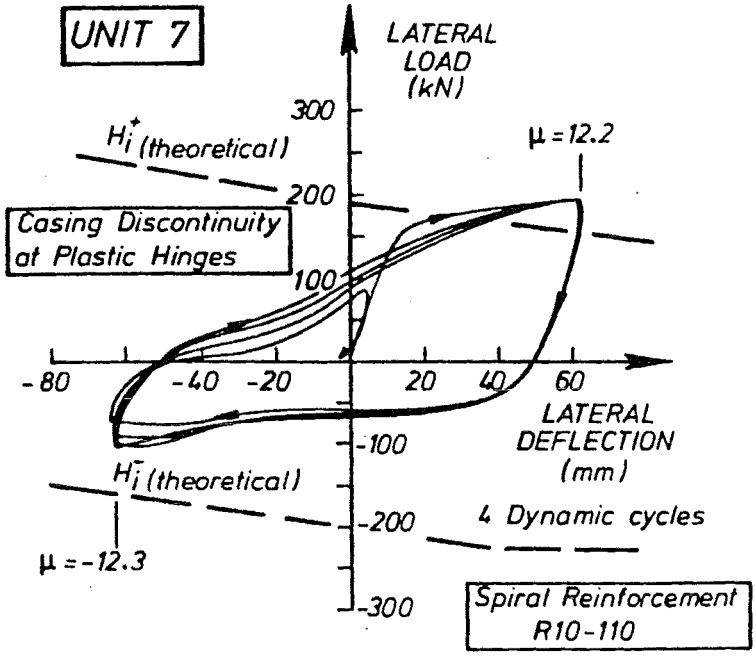

(b) DYNAMIC LOADING

FIG. 4.78 : UNIT 7 HYSTERESIS LOOPS

This compares with the average 13% overstrength found by Ang et al (4.32) to apply to similarly tested reinforced concrete test units also with a longitdunal-compression load of $P = 0.1f'_cA_g$. Thus the casing was significantly contributing to the flexural strength of these two test units.

4.11.2.2 Seismic Performance Criteria

Table 4.9 summarises details of the cyclic loading of the test units which possessed casing circumferential discontinuities in the plastic hinge zones. Unit 6 had R10 spiral reinforcement at 200 mm spacing in the zone of the casing discontinuities, while unit 7 had R10 spiral reinforcement at 110 mm spacing.

Unsymmetrical rotation at the two plastic hinges developed to a large degree in these two test units as the average ratio of the larger of $\Sigma|\mu_{TOP}|$ and $\Sigma|\mu_{BOT}|$ to the smaller of $\Sigma|\mu_{TOP}|$ and $\Sigma|\mu_{BOT}|$ was 1.23 (cf. 1.11 for the average of the tests with continuous casings).

Extremely large ductility levels were achieved in these two test units. At the end of static testing $|\mu|_{max}$ and $\Sigma|\mu|$ values of approximately 30 and 205 respectively were reached. These compare with values of $|\mu|_{max}$ and $\Sigma|\mu|$ of 6 and 32 respectively which have been recommended for seismic performance testing of structures (see Section 4.2.3). At the end of static testing, ductile performance was still occurring in units 6 and 7. Thus the seismic performance criteria were easily satisfied.

4.11.2.3 Shape of Hysteresis Loops

During static testing, stable hysteretic performance was exhibited with the second cycle to each ductility level showing only a small amount of strength and stiffness degradation relative to the first cycle. However for cycles to large levels of $|\mu|$, the hysteresis loops were significantly pinched through the middle range of deflections. Pinching was more severe for units 6 and 7 (see Fig. 4.77 and 4.78) which had casing circumferential discontinuities, than it was for units 1-5, 8 and 9 (see Figs. 4.29-4.44) which had continuous casing throughout their length.

In units 6 and 7, casing in the vicinity of the circumferential discontinuities may be considered to act similarly to concrete, since on the side of the section subjected to longitudinal-tension strain the casing does not contribute to strength but on the side subjected to longitudinal-compression strain the casing does contribute to flexural strength. Thus the gaps which open up between adjacent lengths of casing are analogous to concrete cracks. Initially when loading reverses at the critical sections, units 6 and 7 only possess flexural stiffness due to the reinforcing bars. However when a lateral deflection of zero is reached, the previously open concrete cracks and the casing gap close, and thus from this stage the compressive strength and stiffness of casing and concrete are utilised. Hence as shown in Figs. 4.77 and 4.78, after the zero deflection line is passed the flexural stiffness of units 6 and 7 markedly increase.

Under dynamic loading units 6 and 7 show deteriorating hysteretic performance due to fracturing of the longitudinal reinforcing bars. However it is emphasised that the dynamic testing was performed after the test units had already survived the equivalent of many earthquakes (i.e. at end of static loading: for unit 6 $\Sigma|\mu| = 208$ and for unit 7 $\Sigma|\mu| = 206$, compared with the seismic performance criterion of cyclic loading to $\Sigma|\mu| = 32$). There was also no significant difference in the performance of units 6 and 7, indicating that the role of spiral reinforcing in confining the concrete was masked by the more dominating presence of the casing.

4.11.2.4 Energy Dissipation Characteristics

Figure 4.79 shows a comparison of the energy dissipation characteristics of units 6 and 7 which contained discontinuous casings, unit 1 (D/t = 34) and 9 (D/t = 214) which contained continuous casings, and a reinforced concrete test unit which was tested by Ang et al (4.12). The figure is plotted in terms of energy dissipation ratio E_R versus cumulative displacement ductility factor $\Sigma|\mu|$, where as outlined in Section 4.9.2.4 E_R represented the ratio of actual energy dissipated to the energy dissipated by an idealised elastic-plastic member with the same theoretical ultimate strength H_i (i.e. overstrength ignored) and elastic stiffness H_i/Δ_y.

At $\Sigma|\mu| = 32$ (equivalent to 4 cycles at $\mu = \pm 4$), E_R for units 6 and 7 are clearly inferior to those of the units with continuous casings and conventionally designed ductile reinforced concrete members. However for units 6 and 7 substantial overstrength occurs and thus for $\Sigma|\mu|$ approximately greater than 40, E_R increases with $\Sigma|\mu|$ to a level similar to that of test units with continuous casings and large casing D/t ratios.

From Fig. 4.79 it appears that the provision of spiral reinforcement does marginally improve the energy-dissipation characteristics, since for $\Sigma|\mu| > 20$ unit 7 (R10-110 spiral reinforcement in the plastic hinge zone) dissipates more energy than does unit 6 (R10-200). For example at $\Sigma|\mu| = 100$, unit 7 had dissipated 4% more energy than had unit 6.

4.11.3 Distribution of Longitudinal-Compression Strain Along the Length of the Test Units

Distributions of longitudinal-compression strain along the length of unit 6 at the extremities (N and S) of the diameter parallel to the direction of lateral load at various levels of displacement ductility μ are given in Fig. 4.80. Distributions were similar for unit 7.

The distributions show that longitudinal-compression strains increased with μ. Yield strain ε_y was achieved as early as $\mu = \pm 2$. By the end of static testing, longitudinal-compression strains in excess of 5% had been measured. Thus appreciable additional flexural strength was developed at the sections of discontinuity due to longitudinal-compression stress in the tube which is developed in end-bearing.

Longitudinal-compression strain generally peaked at the sections of casing discontinuity and then reduced rapidly away from these sections. Thus the local weakness in the casing continuity clearly concentrated plastic damage over a very short length of the test units. This is in agreement with the observation of a short length of crushed concrete (longitudinal extent = 60 mm) in the vicinity of the casing discontinuities (see Figs. 4.74c and 4.75c).

4.11.4 Distribution of Longitudinal-Tension Strain Along the Length of the Test Units

Distributions of longitudinal-tension strain along the length of unit 6 at the N and S positions and various levels of displacement ductility are given in Fig. 4.81. Distributions were similar for unit 7.

The strain distributions generally indicated that zero or compressive strain and hence zero longitudinal-tension stress existed on the casing surface adjacent to the discontinuities. The presence of compressive strain was due to compressive yielding which was achieved before load reversed, subsequently when load reversed only elastic recovery of compressive strain would have been achieved and thus residual levels of plastic compressive strain remained.

Initially as distance away from the discontinuities is increased, the longitudinal-tension strains also increase. At 150 mm from the discontinuity

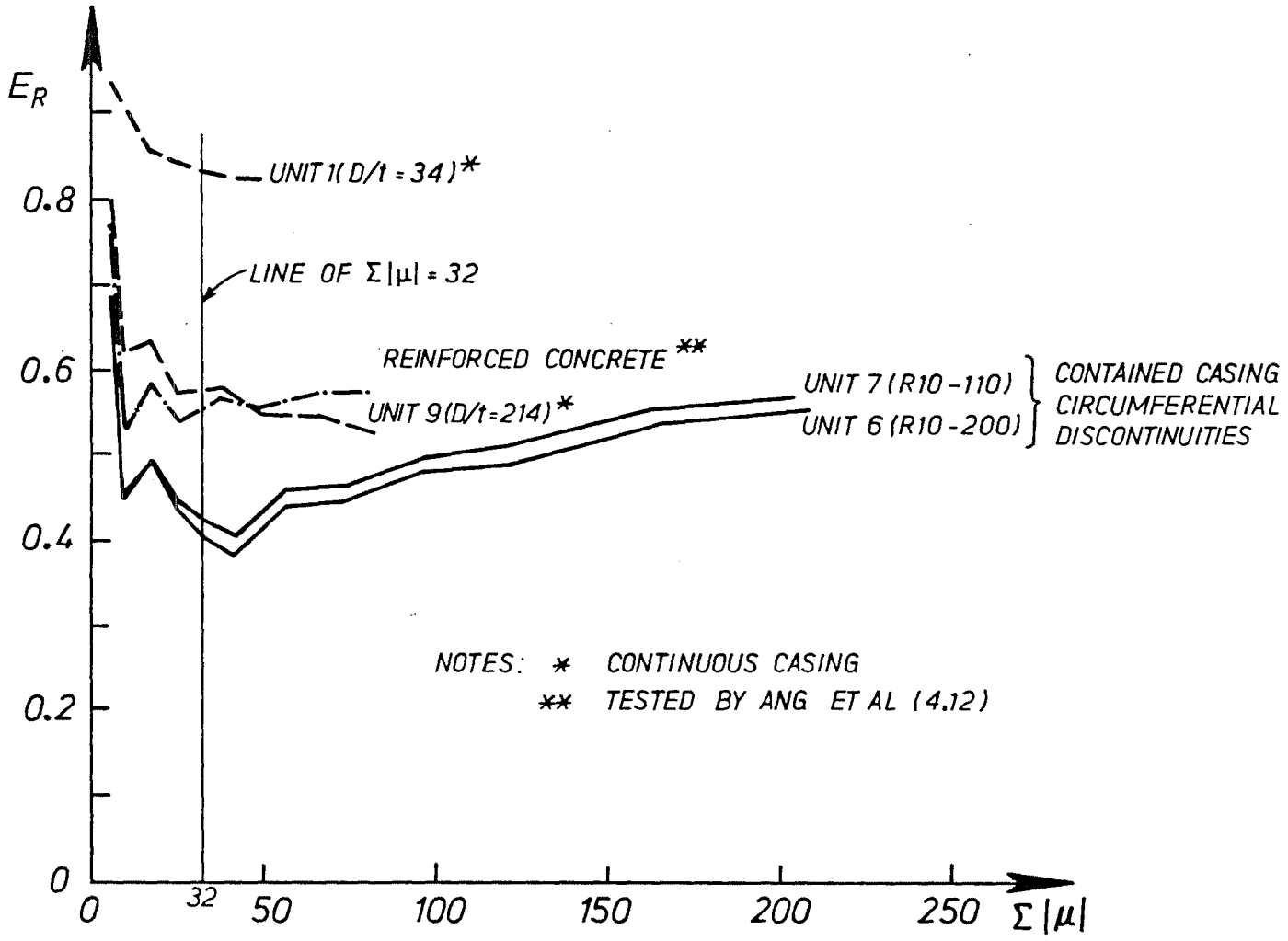

FIG. 4.79 : ENERGY DISSIPATION RATIO E_R VS CUMULATIVE DISPLACEMENT DUCTILITY FACTOR $\Sigma|\mu|$

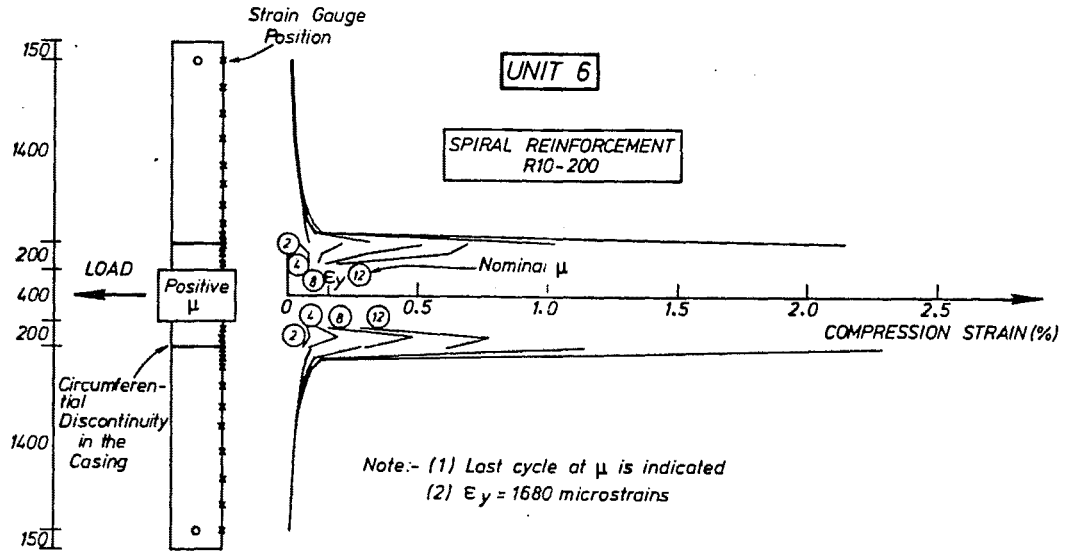

(a) POSITIVE μ

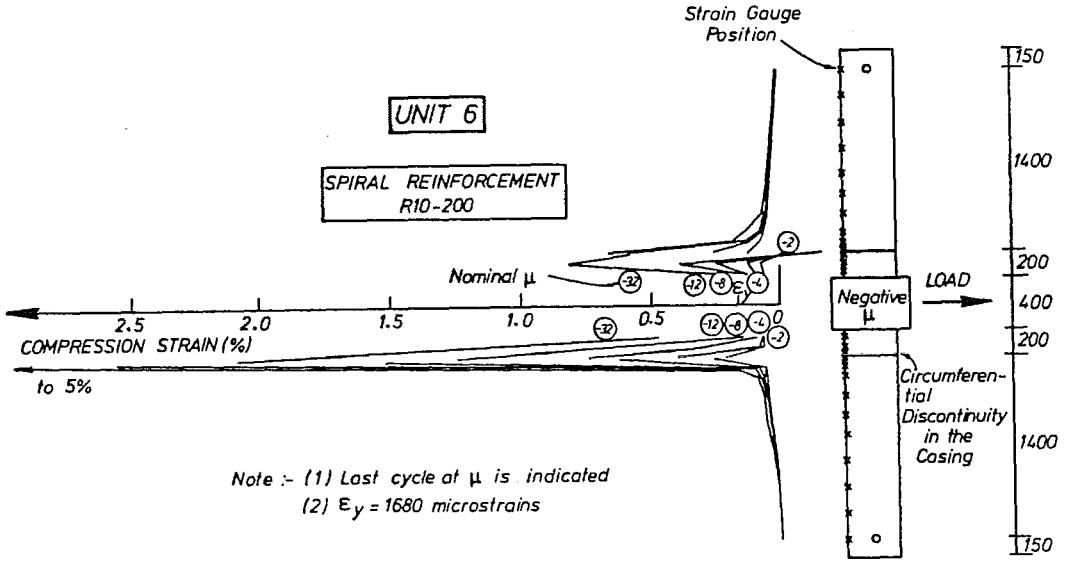

(b) NEGATIVE μ

FIG. 4.80 : LONGITUDINAL-COMPRESSION STRAIN DISTRIBUTION FOR UNIT 6

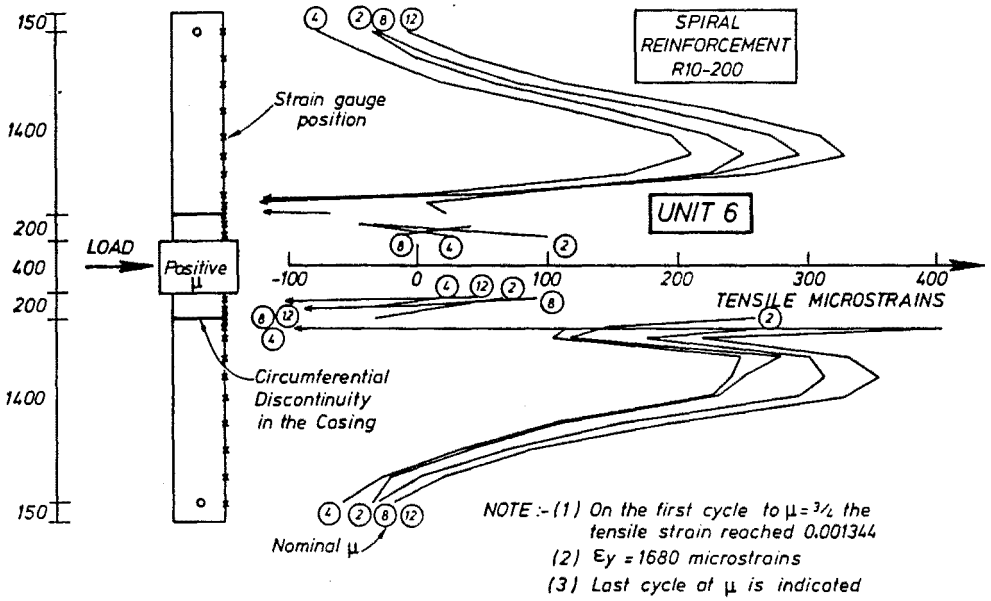

(a) POSITIVE μ

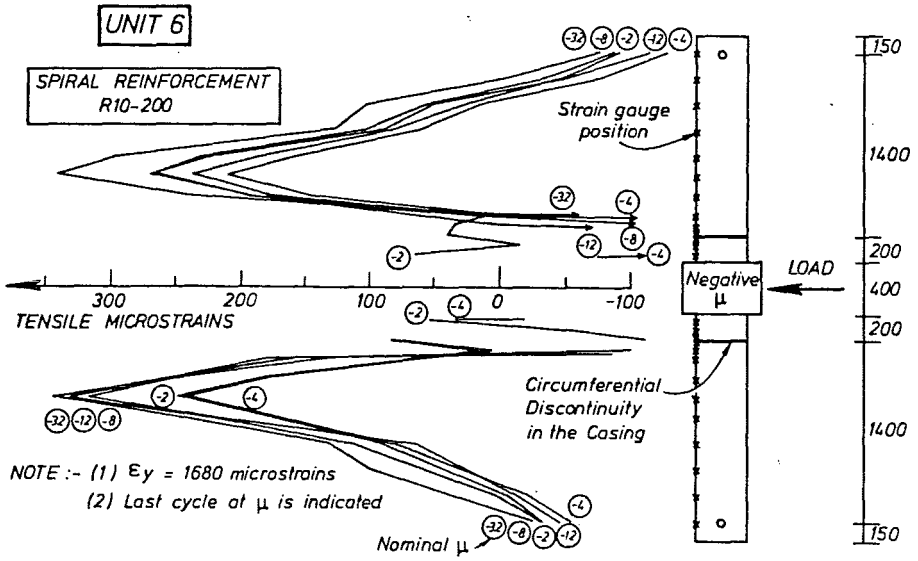

(b) NEGATIVE μ

FIG. 4.81 : LONGITUDINAL-TENSION STRAIN DISTRIBUTION FOR UNIT 6

in the direction of the concrete loading block the longitudinal-tension strains approach 100 microstrain ($0.06\varepsilon_y$). As distance from the casing discontinuities towards the ends of the test units is increased, longitudinal-tension strains increase to a peak at about 450 mm from the discontinuities. The longitudinal-tension strains at the peaks vary between 250 and 400 microstrain ($0.15\varepsilon_y$ to $0.24\varepsilon_y$). Strains then decrease from these peaks as distance towards the ends of the units is covered. At the ends of the test units small values of longitudinal-compression strain were present due to the presence of longitudinal-compression load and the absence of bending moment. Clearly all of the above values of longitudinal-tension strain were small when compared with the casing yield strain ε_y (1683 microstrain). However they do indicate that units 6 and 7 derive additional stiffness from tensile stressing of the casing away from the positions of casing discontinuity.

It should also be mentioned that for unit 6 on the first cycle which was to $\mu = \pm 3/4$, a longitudinal-tension strain of 1344 microstrain was reached. This large tensile strain occurred in the vicinity of a stronger than anticipated tack weld which allowed tensile force to be carried between the adjacent lengths of tube before the weld broke.

It is also significant that generally as μ increased, the values of longitudinal-tension strain also tended to increase. This implies that as testing proceeded, the bond (or friction) conditions between tube and concrete improved. As cyclic loading proceeds the concrete tends to expand laterally, while under longitudinal-tension stress the tube tends to contract laterally due to Poisson's ratio effect. The resulting friction that occurs when concrete and tube laterally interact is the reason for increased bond strength between tube and concrete. In Section 4.12.2 the value of this bond strength is quantified.

4.11.5 Distribution of Longitudinal Strain at the Sections of Casing Circumferential Discontinuity

Distributions of longitudinal strain across the section of the lower casing discontinuity (i.e. plastic hinge beneath the block) are shown for unit 7 in Fig. 4.82. Similar distributions were found to exist at the other plastic hinge of unit 7, and in both plastic hinges of unit 6. Strains in either three or four of the nine bars which act as longitudinal reinforcement are indicated, and tube longitudinal strains on both sides of the discontinuities at the N, S, E and W positions are also shown.

Strain distributions were relatively linear at $\mu = \pm 3/4$ and ± 2, but at larger $|\mu|$ pronounced non-linearities in the longitudinal strain distributions of both the reinforcing bars and the casing were evident. The reinforcing bar distributions became non-linear due to the increasing effects of concrete cracking and hence bond slip. In the casing large longitudinal-compression strains developed at the N and S positions where end-bearing of adjacent lengths of casing occurred, at the E and W positions where only a negligible amount of end-bearing occurred only small longitudinal-compression strains developed. This showed that the Bernoulli-Navier hypothesis of plane sections remaining plane on bending is invalid for the tube at these sections.

Since the casing provides longitudinal-compression strength (and not longitudinal-tension strength) at the sections of discontinuity, it would be expected that the neutral axis position would be close to the position of maximum longitudinal-compression strain. This is verified by Fig. 4.82 where it is shown that reinforcing bar strains are predominantly tensile. Tensile strains of up to 4% were measured in the reinforcing bars, and compressive strains of up to 5% were measured on the casing, which indicate that

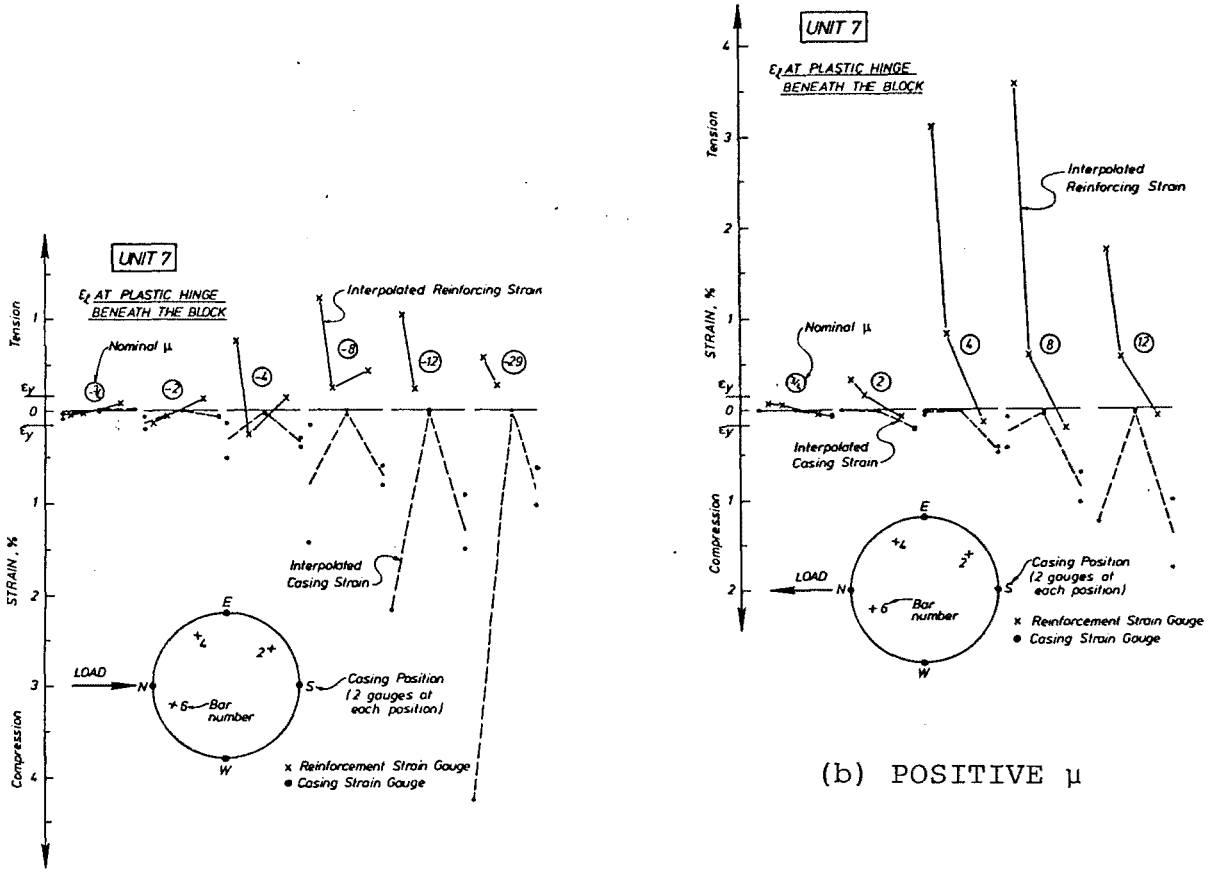

FIG. 4.82 : DISTRIBUTION OF LONGITUDINAL STRAIN AT PLASTIC HINGE BENEATH THE BLOCK FOR UNIT 7

significant strain-hardening of the steel was occurring at the sections of casing discontinuity.

4.11.6 Confining Strains on the Casing Outer Surface

An indication of the distribution of hoop stresses on the casing outer surface in the vicinity of the casing circumferential discontinuities is given in Figs. 4.83 and 4.84, which plot values of confining strain $(\varepsilon_H + 0.3\varepsilon_L)$ at different ductility levels. Caution should be exercised in interpreting results from these diagrams, since as stated in Section 4.9.6, hoop stress is only proportional to $\varepsilon_H + 0.3\varepsilon_L$ in the elastic range of tube behaviour.

The maximum hoop-tension stresses in the tube are expected at the N and S positions, as this is where the longitudinal-compression strains in the concrete are largest. Clearly this does occur, as at the N and S positions (see Fig. 4.83), typically the values of $\varepsilon_H + 0.3\varepsilon_L$ reach ε_Y by $\mu = \pm 4$, while at the E and W positions (see Fig. 4.84) ε_Y is not reached during the static testing of unit 7 and only just reached in testing unit 6.

The strain distributions at the N and S positions are sharply peaked in the vicinity of the casing circumferential discontinuities, with $\varepsilon_H + 0.3\varepsilon_L$ of up to 2.5% being reached. It has previously been shown that the casing also had large values of longitudinal-compression strain. Thus on the side of the section subjected to longitudinal-compression strain, in the vicinity of the casing discontinuities, the tube will have significant hoop-tension and longitudinal-compression stress. Values of $\varepsilon_H + 0.3\varepsilon_L$ decrease sharply, generally to zero, at a distance of 150 mm from the casing discontinuities. Thus again it is indicated that significant plasticity in these test units was occurring over very concentrated zones. It was also noticeable from Fig. 4.83 that of the three lengths of casing, the middle length tended to have the largest strains. This can be attributed to the larger bending moments that occur in the middle length of the casing compared with the two outer lengths.

4.11.7 Strains in the Spiral Reinforcement

Distribution of strain in the spiral reinforcement in the vicinity of the casing discontinuities are shown in Figs. 4.85 and 4.86 for units 6 and 7 respectively. The strain gauges have been separated into indicators of the shear (E and W positions) and confinement (N and S positions) roles of the spiral reinforcement in the same fashion as was described previously in Section 4.9.7.

For both units 6 (spiral reinforcement R10-200 mm centres in the plastic hinge zone) and 7 (R10-110 mm), yielding of the spiral reinforcement at either the shear or confinement positions did not occur until the peak of the cycle to $\mu = \pm 12$. The strain distributions peak in the vicinity of the discontinuities and then decrease to practically zero at a distance of 200 mm from the discontinuities. At the shear positions unit 7 had larger strains than did unit 6, while at the confinement positions the converse applied. There was a negligible difference in hysteretic performance between these two units, and since yielding of the spiral reinforcement did not occur until very large levels of ductility were attained ($\mu = \pm 12$), it is probable that nominal spacing (e.g. R10-400) of spiral reinforcing would have been adequate for these test units. Clearly the casing adequately confines the concrete, while adequate shear resistance was also available (see Section 4.12.1) without reliance being placed on the spiral reinforcement.

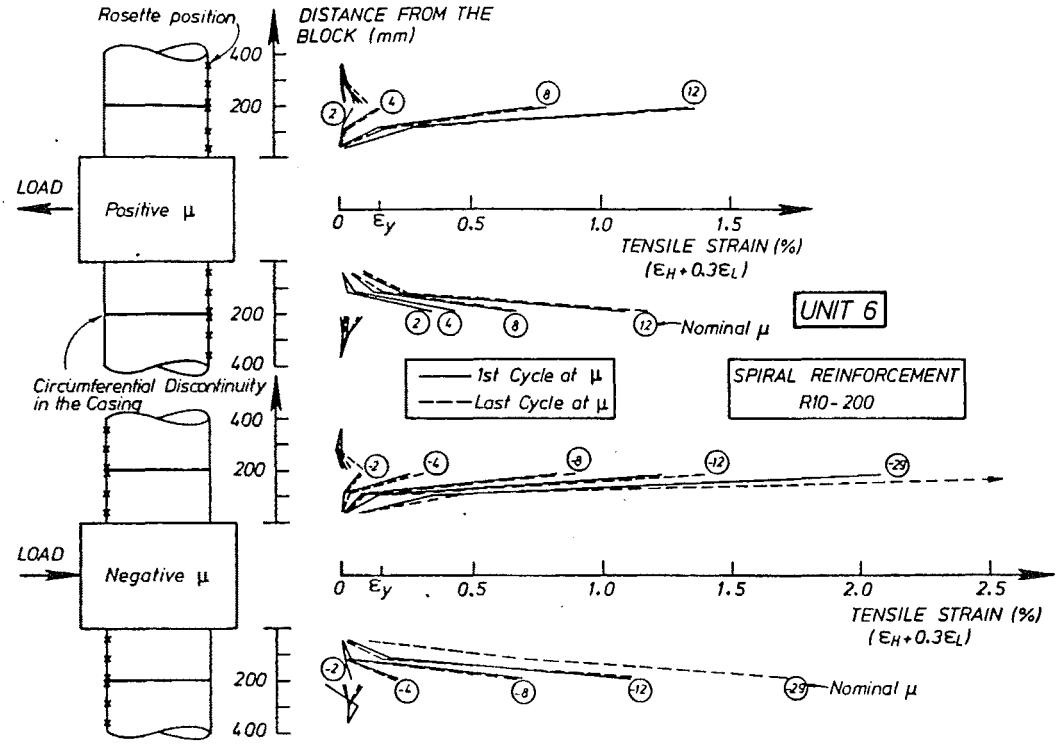

FIG. 4.83 : CONFINING STRAINS ($\varepsilon_H + 0.3\varepsilon_L$) ON THE CASING AT THE N AND S POSITIONS FOR UNIT 6

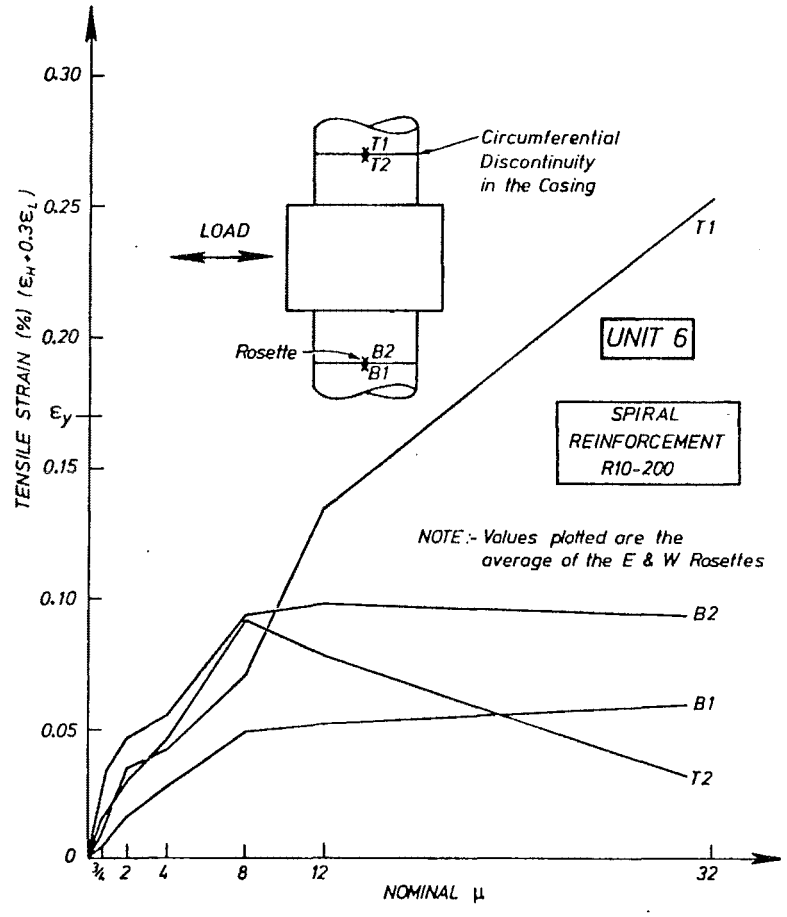

FIG. 4.84 : CONFINING STRAINS ($\varepsilon_H + 0.3\varepsilon_L$) ON THE CASING AT THE E AND W POSITIONS FOR UNIT 6

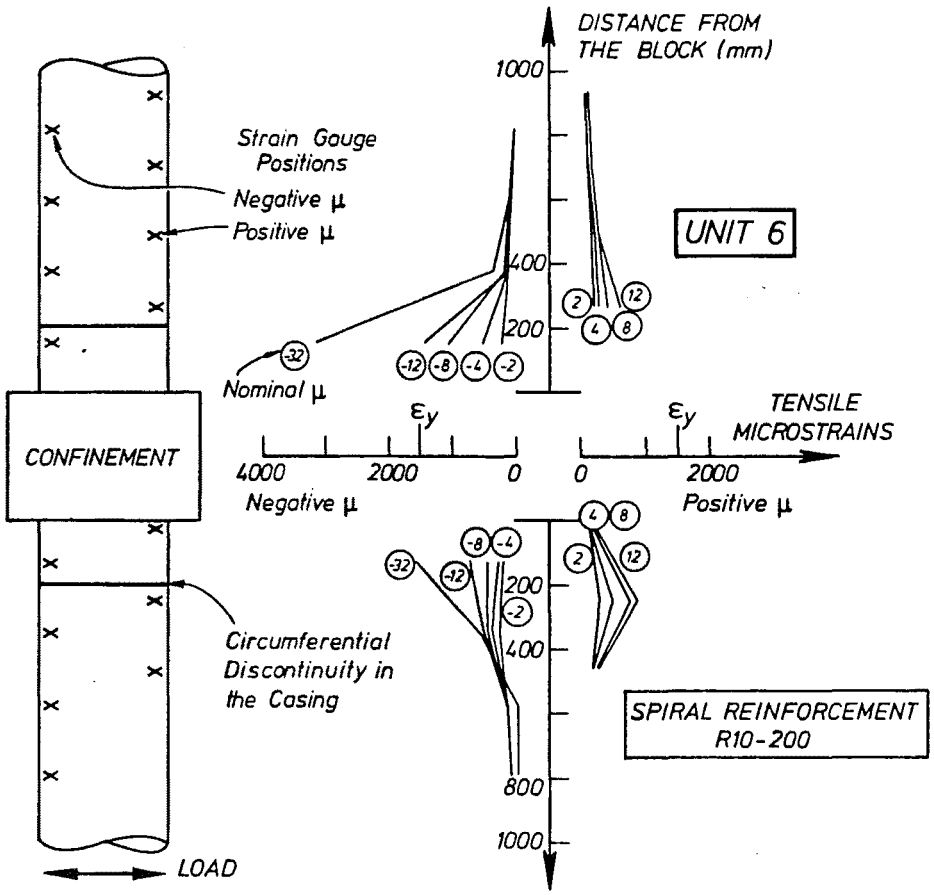

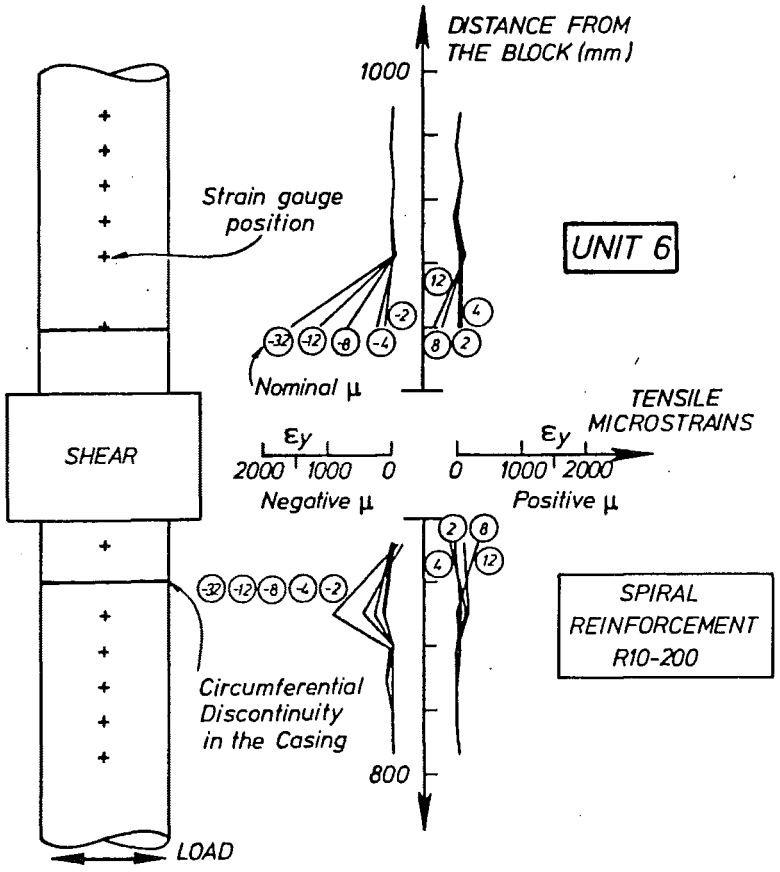

FIG. 4.85 : STRAINS IN THE SPIRAL REINFORCEMENT FOR UNIT 6

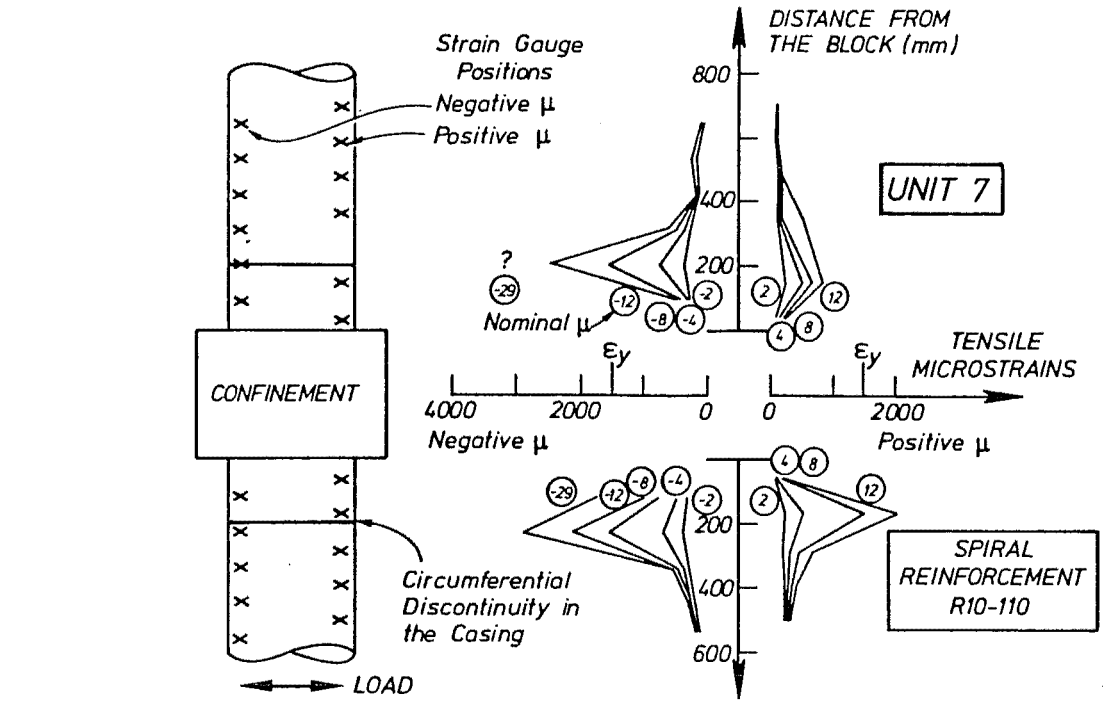

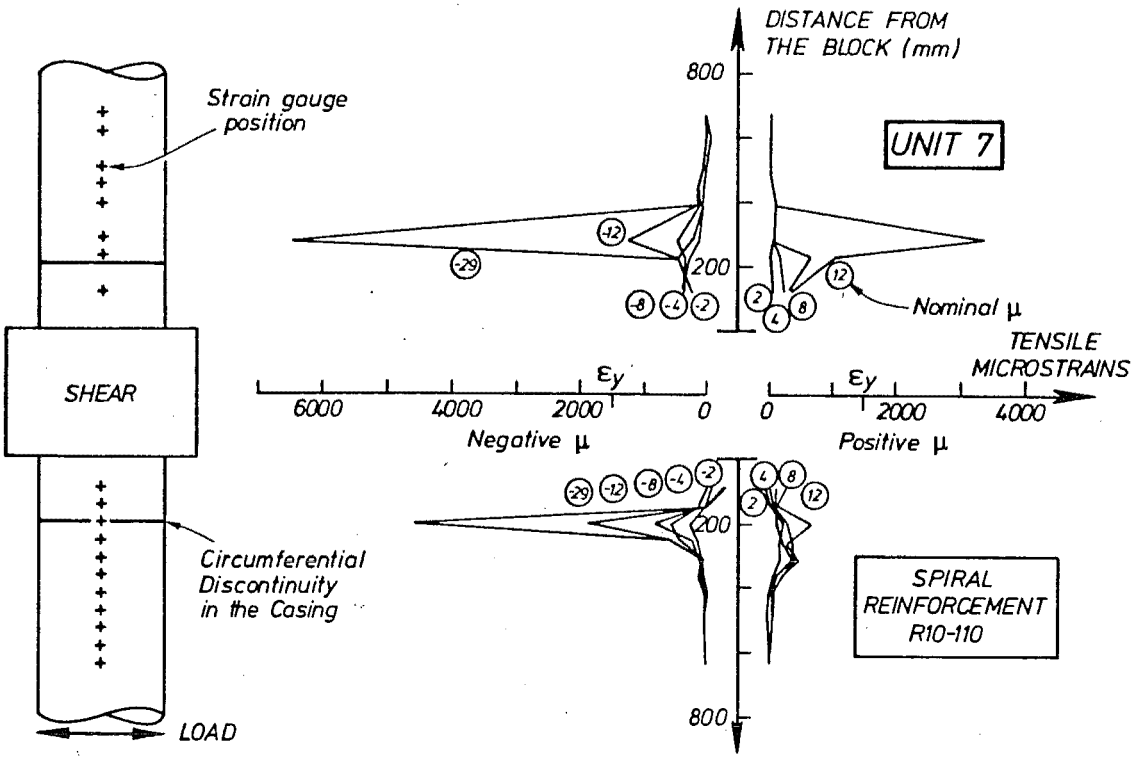

FIG. 4.86 : STRAINS IN THE SPIRAL REINFORCEMENT FOR UNIT 7

4.12 ANALYSIS OF RESULTS - DISCONTINUOUS CASINGS

4.12.1 Shear Resistance

For units 6 and 7 which had circumferential discontinuities in the casing at the critical flexural section, the most obvious form of potential shear failure is that due to sliding along horizontal concrete cracks at the discontinuities.

The New Zealand Concrete Code (4.17) requires that the area A_{vf} of shear friction reinforcement perpendicular to such a crack should be computed as

$$A_{vf} = \left[\frac{V_u}{\mu_f \phi} - P \right] / \sigma_y \qquad (4.16)$$

where V_u = ultimate shear force
P = longitudinal load (compression positive)
ϕ = capacity reduction factor (= 0.85 for shear)
μ_f = coefficient of friction (= 1.4 for monolithic concrete)
σ_y = yield stress of reinforcement across the crack

The Code allows any well-anchored longitudinal reinforcement within the section to be included in determining A_{vf} which for units 6 and 7 is equivalent to the area of the 9 D16 bars used as longitudinal reinforcement.

Equation 4.16 can be rearranged to give shear demand (V_u) on the left hand side and shear capacity on the right hand side:

$$V_u = \phi . \mu_f . \sigma_y . A_{vf} + \mu_f . \phi . P \qquad (4.17)$$

In units 6 and 7 the maximum shear force (V_u) was 115 kN. The first term on the right hnd side of equation 4.19 had a value of 689 kN and the second term had a value of 456 kN. Hence shear force capacity was equal to 1145 kN compared with the demand of 115 kN. Thus units 6 and 7 possessed a large reserve of strength against sliding shear failure.

4.12.2 Bond Strength Between Casing and Core Concrete

The effective bond strength between concrete and the smooth inside surface of the tube is important where only a short length of casing anchorage is present at the critical flexural sections. If for example plastic hinging in the piles occurs at a comparatively shallow depth, low bond strength may limit the flexural capacity of the piles shown in view B-B of Fig. 1.1.

Experimental research by Virdi and Dowling (4.37) has indicated that bond strength between the inside of plain circular tubes and internal concrete depends on interlocking of the steel surface with the concrete. The interlocking occurs due to steel surface roughness and variations in the shape of the cross-section of the tube. Variations in the length of the concrete-tube interface, casing D/t ratio and concrete compressive strength f'_c had little influence on the bond strength (stress). The reason for f'_c not influencing bond strength was because any increase in concrete strength was offset by an increase in the contraction of the concrete as it cools down after the initial rise in temperature associated with heat of hydration. This will tend to reduce the frictional force between tube and concrete. The tests of Virdi and Dowling involved pushing core concrete through the tube. Their results showed a marked degree of scatter. An average bond strength of 1.9 MPa, with a standard deviation of 0.5 MPa, was obtained. A design bond strength of 1 MPa was recommended on the basis of 95% of data being equal to or stronger than this stress. Their tests also showed that bond stress-slip behaviour is ductile, as a bond stress of close to the maximum value could be maintained almost indefinitely as slip occurred.

Morishita et al (4.38) also investigated the bond strength between the inside of plain circular tubes and internal concrete. However their tests involved longitudinally compressing the steel and investigating the rate at which concrete longitudinal stresses increased. These tests were quite different from the concrete "push-out" tests of Virdi and Dowling (4.37). In the tests of Morishita et al (4.38) when the steel is compressed longitudinally it expands laterally and hence tends to lose contact with the concrete. Conversely in the tests of Virdi and Dowling (4.37), the concrete is compressed longitudinally and thus expands laterally on to the tube. Hence the frictional strengths at the tube-concrete interface are quite different in the two types of tests. The tests of Morishita et al (4.37) indicated a bond strength of between 0.2 and 0.4 MPa which, as could be anticipated, is considerably smaller than the average bond strength of 1.9 MPa which was obtained by Virdi and Dowling (4.37).

However neither Virdi and Dowling (4.37) nor Morishita et al (4.38) conducted tests under the more severe conditions for bond strength of longitudinal-tension strain or cyclic longitudinal strain which are appropriate to steel-encased concrete piles under seismic attack.

Japanese investigators (4.39 and 4.40) have also tried to improve bond conditions between tube and concrete by two methods:

(i) They have used expansive instead of ordinary cement in order to counteract the gap that develops between tube and concrete as the concrete cures. Tests have shown that the use of expansive cement results in larger values of ultimate bond strength. However at large levels of tube-concrete slip, the bond stresses obtained for ordinary and expansive cements were approximately equal.

(ii) They have also used checkered patterns of small 1.5 mm or 3 mm high projections on the casing inside surface. The mechanical keying of concrete and tube achieved by this method was shown to enhance bond strength by a factor of 13 when compared with that achieved using plain tube.

In units 6 and 7 the build-up of longitudinal-tension stress in the tube in the vicinity of the sections of casing discontinuity is due to:

(i) flexural bond stress between tube and concrete; and

(ii) lateral load transferred into the tube due to the bending of the reinforced concrete core.

From the experimental data which were collected it was impossible to separate the above two causes. In the rest of this section it is assumed that the build-up of longitudinal-tension stress in the tube was due solely to (i) and thus equivalent effective values of bond stress were calculated.

Consider the freebody of an element of the tube which is shown in Fig. 4.87. Equilibrium of the freebody gives:

$$F_L + u \cdot b \cdot \Delta L = F_L + \Delta F_L \qquad (4.18)$$

where F_L = longitudinal force

ΔF_L = increment of longitudinal force over length ΔL

u = equivalent effective bond stress between tube and concrete.

ΔL = length of element

b = width of element.

Equation 4.20 can be rearranged to give:

$$u = \Delta F_L / (\Delta L \cdot b) \qquad (4.19)$$

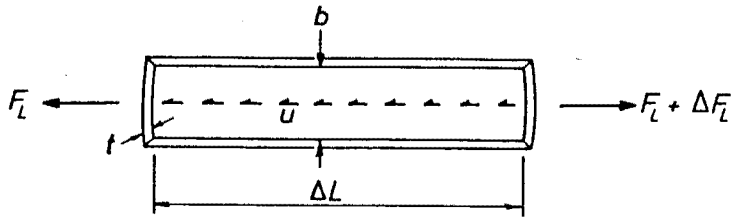

FIG. 4.87 : FREEBODY OF ELEMENT OF TUBE

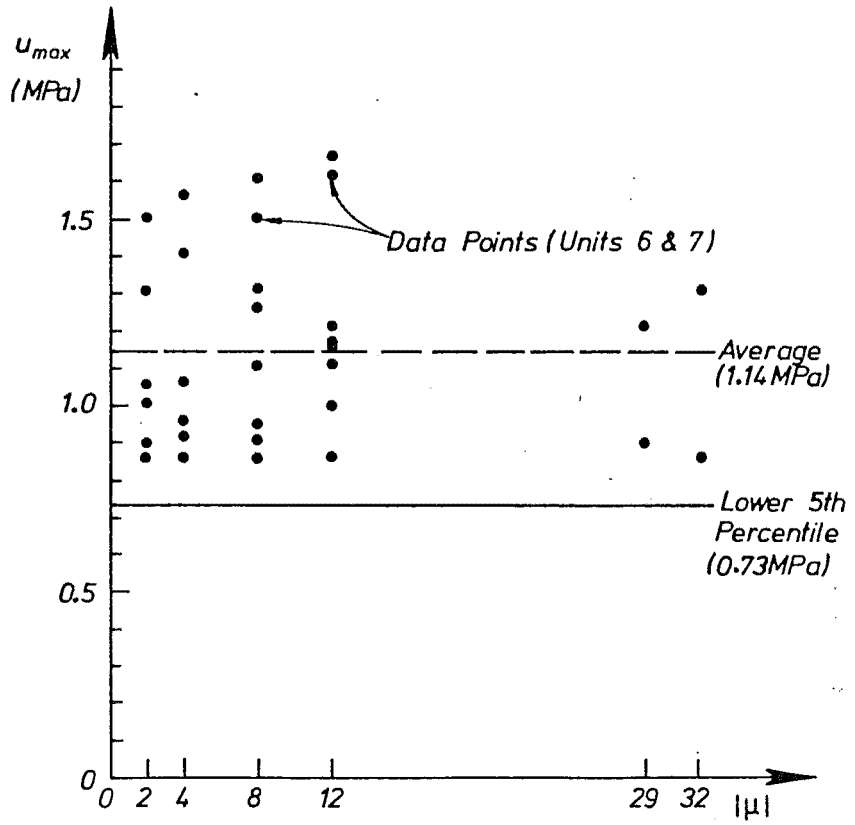

FIG. 4.88 : VARIATION OF EQUIVALENT BOND STRENGTH U_{MAX} WITH DUCTILITY LEVEL $|\mu|$

Now $\Delta F_L = \Delta\sigma_L \cdot b \cdot t$ (4.20)

where $\Delta\sigma_L$ = increment of longitudinal stress over length ΔL

Substituting equation 4.20 into equation 4.19 and simplifying gives:

$$u = (\Delta\sigma_L \cdot t)/\Delta L \quad (4.21)$$

In the elastic range and assuming uniaxial-stress conditions:

$$\Delta\sigma_L = E_s \cdot \Delta\varepsilon_L \quad (4.22)$$

where $\Delta\varepsilon_L$ = increment of longitudinal strain over length ΔL

Substituting equation 4.22 into equation 4.21 gives

$$u = E_s \cdot t \cdot \Delta\varepsilon_L/\Delta L \quad (4.23)$$

In units 6 and 7, E_s was 202 000 MPa and t was 5 mm. Thus

$$u\ (\text{MPa}) = 1010\ \Delta\varepsilon_L/(\Delta L\ (\text{metres})) \quad (4.24)$$

Hence for elastic behaviour and uniaxial-longitudinal stress conditions, the maximum value of u (u_{max}) occurs at the positions where the gradient in longitudinal strain is steepest. These positions were found to be about 200 mm from the casing discontinuities in the direction away from the concrete loading block (see Fig. 4.81).

Figure 4.88 shows the result of applying equation 4.24 to the experimental data provided by units 6 and 7 at the positions of steepest gradient in longitudinal strain. Despite the considerable degree of scatter that was shown in the data, the bond strength does not appear to degrade under the imposed cyclic loading conditions. It is probable that the tendency of the concrete to dilate under cyclic loading, and the steel to laterally contract under longitudinal-tension stress, is the main reason for this bond strength being sustained at high ductility levels. An average bond strength u_{max} of 1.14 MPa was calculated and a design recommendation for u_{max} of 0.73 MPa is made on the basis of the lower 5th percentile of an assumed normal distribution to the experimental data. These values of bond strength are intermediate between those found by Virdi and Dowling (4.37) and Morishita et al (4.38).

The implication of a bond strength of 0.73 MPa is that it would take a 10 mm thick tube, with a yield stress of 300 MPa, 4110 mm (= 10 x 300/0.73) to develop its yield strength.

4.13 CONCLUSIONS

The main results from the tests of steel-encased reinforced concrete members, which were subjected to a longitudinal-compression load of $0.1f'_c(A_c + A_t)$ and a cyclically varying central lateral load, can be summarised as follows:

4.13.1 Continuous Casings

For test units 1-5, 8 and 9 which had continuous casings and tube D/t ratios in the range of 34-214, sound performance was displayed under the simulated earthquake attack.

Theoretical ultimate flexural strengths were calculated using a strain compatibility approach, an A.C.I. stress block for the concrete in compression, a maximum concrete compression strain of 0.003, and the measured material strengths (concrete f'_c and steel σ_y). The actual strengths of the model piles were in the

range of 5% - 28% larger than the theoretical strengths calculated using the method described above. Although these values of overstrength tended to decrease with increasing tube D/t ratio, this implied that current Concrete Code (e.g. 4.17 and 4.30) requirements for a minimum thickness of tube (typically t > D/80) before structural use can be made of the tube are unnecessary. The presence of shear force was also shown to have a negligible effect on flexural strength.

Plastic damage to the units concentrated over very short lengths at the positions of local buckling which resulted in estimated values of longitudinal-compression strain of up to 21% and curvature ductility demands that were 1.9 (small tube D/t ratios) to 3.7 (large tube D/t ratios) times as large as those found in similar reinforced concrete test units at the same level of displacement ductility. However, strength, ductility and energy-dissipating characteristics of units with tube D/t ratios $\geq$ 60 were found to be similar to those of conventionally designed ductile reinforced concrete members, while these characteristics for the test unit with D/t = 34 were superior to those of reinforced concrete members.

Results showed that the casing provided adequate shear resistance, concrete confinement and also prevented the longitudinal reinforcement from buckling by keeping the cover concrete in position. Thus only nominal spiral reinforcement is required within the concrete core.

Previously expressed concern about the possibility of strain-age embrittlement of the tubes at the positions of local buckling was shown to be unwarranted, since the radii of curvature of the tubes at the local buckles were sufficiently large to avoid this effect.

4.13.2 Discontinuous Casings

For units 6 and 7 which had circumferential discontinuities in the tube in the plastic hinge zones, satisfactory performance under the simulated earthquake attack was displayed.

Theoretical ultimate flexural strengths were calculated using the procedure outlined in the previous section except that the presence of the casing was ignored (i.e.-strength based on reinforced concrete core). However since the tube did develop longitudinal-compression stress due to end-bearing of adjacent lengths of tube and the tube also confined the concrete, strengths of 42% in excess of the theoretical ultimate flexural strength were obtained. Significant levels of longitudinal tensile and compressive strain in the tube were also measured at sections away from the sections of casing discontinuity. Thus the overall stiffness of these units was also appreciably increased by the presence of the tube.

Plastic damage concentrated over very short lengths in the vicinity of the sections of casing discontinuity. Unit 6 had R10 spiral reinforcement at D/2 spacing, while unit 7 had spiral reinforcement at approximately D/4 spacing. However little apparent difference was noted between the performance of these two test units, since the tube more than adequately confined the concrete and a large reserve of shear strength was available. Thus nominal spiral reinforcement spacing (e.g. D) would have been sufficient.

On the basis of the rate at which longitudinal-tension stress increased with distance from the casing discontinuities, a design recommendation of 0.73 MPa for the equivalent ultimate bond strength between the tube and the concrete was made.

TABLE 4.1 : DETAILS OF TEST UNITS USED IN THE PRELIMINARY (4.24) INVESTIGATION

Unit	$\frac{P}{f'_c A_c + \sigma_y A_t}$	Lonitudinal D16 (1) Bars		5 mm Thick Casing		Spiral Reinforcing R10 (2) Bars		Concrete
		Number	σ_y (MPa)	Well anchored at critical flexural sections.	σ_y (MPa)	Spacing (3) (mm)	σ_y (MPa)	f'_c (MPa)
1	0.1	-	-	Yes	370	-	-	28
2	0.3	-	-	Yes	370	-	-	28
3	0.1	9	315	Yes	370	70	295	28
4	0.3	9	315	Yes	370	35	295	28
5	0.1	9	315	No	370	70	295	29
6	0.3	9	315	No	370	35	295	29

(1) Deformed bars of 16 mm diameter
(2) Plain bars of 10 mm diameter
(3) Applies to plastic hinge zone

TABLE 4.2 : TEST UNIT D,t AND SCALE FACTOR DETAILS

Test Unit	Nominal D/t	Actual D (mm)	Actual t (mm)	Actual D/t	Scale* Factor	Comment
1	30	325	9.53	34	0.95	Continuous Casing
2	60	300	5.00	60	0.50	
3	90	270	3.00	90	0.30	
4	120	360	3.00	120	0.30	
5	150	450	3.00	150	0.30	
6	80	400	5.00	80	0.50	Casing with Circumferential Discontinuities**
7	80	400	5.00	80	0.50	
8	180	360	1.96	184	0.20	Continuous Casing
9	210	420	1.96	214	0.20	

* Based on a prototype t of 10 mm
** Located 200 mm above and beneath the top and bottom faces respectively of the concrete loading block.

TABLE 4.3 : REINFORCING STEEL DETAILS

Test Unit	Number of D16 Bars	ρ_ℓ (2) %	Spacing of R10 Bars (mm)		Length of Potential Plastic Hinge (mm)	Cover (from inside of tube to outside of spiral) (mm)	ρ_s		Casing Continuity
			Potential Plastic Hinge	Outside Plastic Hinge			Tube (1)	Spiral (plastic hinge zone)	
1	5	1.0	135	150	1050	32	0.2085	0.0096	Continuous
2	5	1.1	135	150	1000	20	0.0944	0.0092	
3	4	1.1	185	185	940	15	0.0585	0.0073	
4	7	1.1	140	180	1120	20	0.0435	0.0072	
5	12	1.2	110	225	1300	25	0.0346	0.0072	
6	9	1.1	200	200	1200	25	0.0683	0.0042	Discontinuities Present
7	9	1.1	110	200	1200	25	0.0683	0.0084	
8	8	1.2	140	180	1120	20	0.0287	0.0072	Continuous
9	10	1.1	110	210	1240	25	0.0250	0.0078	

(1) Based on concrete core area to outside of spiral (to provide comparison with spiral ρ_s)
(2) ρ_ℓ = ratio of area of longitudinal reinforcement to gross area

TABLE 4.4 : CONCRETE STRENGTHS

Test Unit	Concrete Inside Tubes			Concrete Inside Loading Block		
	f'_c (MPa)		$\frac{f_t}{\sqrt{f'_c}}$	f'_c (MPa)		$\frac{f_t}{\sqrt{f'_c}}$
	28 day	at test		28 day	at test	
1	25	31	0.83	43	49	0.79
2	25	31	0.83	43	49	0.79
3	25	31	0.83	43	49	0.79
4	25	31	0.83	43	49	0.79
5	25	31	0.83	55	64	0.79
6	25	31	0.83	55	64	0.79
7	25	31	0.83	55	64	0.79
8	25	29	0.80	57	64	0.79
9	25	29	0.80	57	64	0.79

Note: f_t is the extreme fibre stress found in modulus of rupture tests.

TABLE 4.5 : SUMMARY OF ACTUAL TEST UNIT DETAILS

Test Unit	P (kN)	Casing					Concrete		Longitudinal Reinforcement		Spiral Reinforcement	
		D (mm)	t (mm)	D/t	σ_y (MPa)	Continuous	f'_c (MPa)	Cover (spiral to tube) (mm)	Number of D16 Bars	σ_y (MPa)	Pitch of R10 bars in hinge zone (mm)	σ_y (1) (MPa)
1	251	325	9.53	34	295 (1)	Yes	31	32	5	320	135	300
2	214	300	5	60	340 (1)	Yes	31	20	5	320	135	300
3	173	270	3	90	350 (1)	Yes	31	15	4	320	185	300
4	310	360	3	120	350 (1)	Yes	31	20	7	320	140	300
5	484	450	3	150	350 (1)	Yes	31	25	12	320	110	300
6	383	400	5	80	340 (1)	No	31	25	9	320	200	300
7	383	400	5	80	340 (1)	No	31	25	9	320	110	300
8	295	360	1.96	184	200 (2)	Yes	29	20	8	286	140	316
9	402	420	1.96	214	200 (2)	Yes	29	25	10	286	110	316

(1) Based on straight bar or flat plate value

(2) Indicates 0.1 percent proof stress (round-house stress-strain curve).

TABLE 4.6 : LOCAL BUCKLING CHARACTERISTICS AT END OF STATIC TESTING

Unit	D/t	t(mm)	EXPERIMENT			THEORY (see Section 3.4.5)				$\frac{(2L_e) \text{ experiment}}{(2L_e) \text{ theory}}$
			Outstand (mm)	$2L_e$ (mm)	$2L_e/t$	E_t (GPa)	σ_{cr} (MPa)	$2L_e$ (mm)	$2L_e/t$	
1	34	9.53	2	70	7.3	2	295	45	4.7	1.6
2	60	5	10	60	12.0	3	340	27	5.4	2.2
3	90	3	15	45	15.0	3	350	16	5.3	2.8
4	120	3	14	50	16.7	3	350	16	5.3	3.1
5	150	3	12	40	13.3	3	350	16	5.3	2.5
8	184	1.96	14	35	18.2	2 (2)	214 (2)	11	5.6	3.2
9	214	1.96	16	40	20.8	2 (2)	214 (2)	11	5.6	3.6

Notes: (1) Figure 4.28 defines the dimensions of "outstand" and "$2L_e$"

(2) For units 8 and 9 which lacked a definite yield point, values of E_t and σ_{cr} were arbitrarily taken as those appropriate at a longitudinal strain of 1%.

TABLE 4.7 : IMPOSED DUCTILITY DEMANDS - CONTINUOUS CASINGS

Unit	Casing D/t Ratio	At Conclusion of Initial Static Testing						At Conclusion of All Testing	
		$\lvert\mu\rvert_{max}$	$\lvert\mu_{TOP}\rvert_{max}$	$\lvert\mu_{BOT}\rvert_{max}$	$\Sigma\lvert\mu\rvert$	$\Sigma\lvert\mu_{TOP}\rvert$	$\Sigma\lvert\mu_{BOT}\rvert$	$\lvert\mu\rvert_{max}$	$\Sigma\lvert\mu\rvert$
1	34	4.39	4.36	4.41	50.07	50.25	49.90	9.92	267.4
2	60	7.35	7.92	6.95	64.16	68.26	60.00	7.35	113.3
3	90	7.07	5.65	8.58	63.97	58.76	69.31	7.07	110.3
4	120	7.03	6.93	7.23	63.90	65.40	62.33	7.03	122.9
5	150	6.07	6.55	5.68	61.78	68.10	56.38	6.07	183.3
8	184	8.68	7.95	9.51	81.32	79.28	83.61	8.68	413.1
9	214	8.06	7.72	8.55	82.04	77.72	86.70	8.06	325.7

TABLE 4.8 : TUBE HOOP-TENSION STRESSES DUE TO SHEAR FORCE

Unit	SHEAR FORCE (kN)				Tube σ_{HV} (MPa)
	Total (V)	Concrete (V_c)	Spiral (V_{sp})	Tube (V_t)	
1	259	76	11	172	18
2	143	68	9	66	14
3	75	56	21	< 0	0
4	152	101	11	40	12
5	260	159	43	58	14
8	103	100	16	< 0	0
9	153	136	24	< 0	0

TABLE 4.9 : IMPOSED DUCTILITY DEMANDS - DISCONTINUOUS CASINGS

Unit	Spacing of R10 Spirals in Plastic Hinge Zone (mm)	At Conclusion of Initial Static Testing						At Conclusion of All Testing	
		$\lvert\mu\rvert_{max}$	$\lvert\mu_{TOP}\rvert_{max}$	$\lvert\mu_{BOT}\rvert_{max}$	$\Sigma\lvert\mu\rvert$	$\Sigma\lvert\mu_{TOP}\rvert$	$\Sigma\lvert\mu_{BOT}\rvert$	$\lvert\mu\rvert_{max}$	$\Sigma\lvert\mu\rvert$
6	200	31.6	24.2	40.8	208.0	201.8	213.0	31.6	324.2
7	110	29.3	19.5	42.9	205.9	171.7	241.3	29.3	301.5

Chapter Five

MOMENT-CURVATURE AND LOAD-DEFORMATION ANALYSES OF STEEL-ENCASED CONCRETE MEMBERS

5.1 INTRODUCTION

Previous investigators have conducted monotonic loading moment-curvature analyses to predict the response of prestressed concrete (5.1, 5.2, 5.3, 5.4), reinforced concrete (5.5 and 5.6) and steel-encased reinforced concrete (5.7) members to combined longitudinal and lateral load. Their results have shown that moment-curvature analyses for monotonic loading give a good approximation to the envelope of the experimental cyclic loading response. However in some cases of cyclic loading, the monotonic curve is not reached at large deformations because of a reduction in flexural strength and stiffness caused by low-cycle material fatigue.

In this chapter, an analytical method for determining the monotonic loading moment-curvature response of steel-encased reinforced concrete members is described. The "lateral interaction" and "uniaxial" models (see Chapter 2) were used in determining longitudinal stress-longitudinal strain response of tube and concrete. The resulting theoretical moment-curvature responses are compared with those obtained experimentally (see previous chapter). From the theoretical moment-curvature responses and linear distributions of bending moment on the member, theoretical lateral load-deflection responses were derived and these are also compared with those obtained experimentally.

5.2 ANALYSIS METHOD

A computer program MONOMC (available on request) was developed to obtain the theoretical moment-curvature and lateral load-lateral deflection responses of steel-encased reinforced concrete members to monotonic loading. The method used in solving the moment-curvature response, as described subsequently, is similar to that used for reinforced concrete members by Aoyama (5.8), Al-Noury and Chen (5.9)and Mander et al (5.10)

5.2.1 Analysis Assumptions

The following assumptions were made in the moment-curvature and lateral load-lateral deflection analyses:

(i) The continuously distributed material across a section can be discretised to a number of points which represent the lumped geometric properties of the longitudinal reinforcement, concrete and casing.

(ii) Plane sections remain plane on bending. This implies that a linear distribution of longitudinal strain exists across the section.

(iii) Longitudinal stress-strain curves for concrete, casing and longitudinal reinforcement were defined by a series of stress-strain coordinates, with response assumed to be piecewise-linear between adjacent coordinates.

(iv) The effects of strain gradient and shear force on the longitudinal stress-strain properties of the concrete were ignored.

(v) Shear deformations were ignored.

(vi) Time-dependent effects such as creep, shrinkage and impact loading were ignored.

(vii) Perfect bond between casing, longitudinal reinforcement and concrete was assumed. For poorly anchored casing at the critical flexural sections (e.g. units 6 and 7 from Chapter 4), this could be over-ridden by giving zero compressive and/or tensile strength to the casing.

(viii) Local buckling of steel (casing or longitudinal reinforcement) was assumed not to alter the stress-strain characteristics of this material.

Clearly assumptions (i) to (viii) are simplifications to actual behaviour, but previously (5.1-5.7) they have been found to result in good predictions of experimental behaviour.

5.2.2 Moment-Curvature Analysis

Response of an Elastic Continuous System

A simplified description of the analysis method is given by considering an elastically behaving section which is subjected to a gradient in its longitudinal strain distribution as shown in Fig. 5.1. Also shown in this figure are the sign conventions used for strain, stress, curvature, longitudinal load and moment.

Longitudinal strain at a distance x from the centroid can be defined as:

$$\varepsilon(x) = \varepsilon_o + \psi . x \tag{5.1}$$

where ε_o = longitudinal strain at the centroid
ψ = curvature (= gradient in longitudinal strain)

The corresponding longitudinal stress at a distance x from the centroid is:

$$\begin{aligned} f(x) &= E . \varepsilon(x) \\ &= E . \varepsilon_o + E . \psi . x \end{aligned} \tag{5.2}$$

where E = modulus of elasticity.

Longitudinal load can be calculated from:

$$\begin{aligned} P &= \int f(x) . dA \\ &= \int (E . \varepsilon_o + E . \psi . x)\, dA \\ &= \varepsilon_o \int E . dA + \psi \int E . x . dA \end{aligned} \tag{5.3}$$

Moment about the line $x = 0$ can be calculated from:

$$\begin{aligned} M &= \int f(x) . x . dA \\ &= \int (E . \varepsilon_o + E . \psi . x) . x . dA \\ &= \varepsilon_o \int E . x . dA + \psi \int E . x^2 . dA \end{aligned} \tag{5.4}$$

Equations 5.3 and 5.4 can be expressed in matrix notation as:

$$\begin{bmatrix} P \\ M \end{bmatrix} = \begin{bmatrix} EA & EB \\ EB & EI \end{bmatrix} \begin{bmatrix} \varepsilon_o \\ \psi \end{bmatrix} \tag{5.5}$$

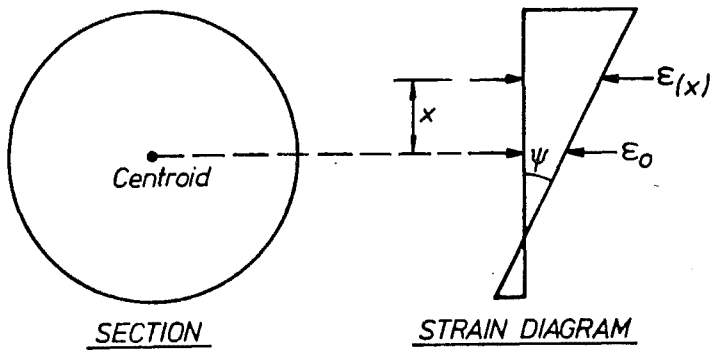

Sign conventions :

(1) x - positive upwards

(2) Strain, stress, force - compression positive

(3) Moment, curvature - positive when largest compression strain is at the top of the section

FIG. 5.1 : SECTION UNDER LONGITUDINAL AND FLEXURAL LOADS

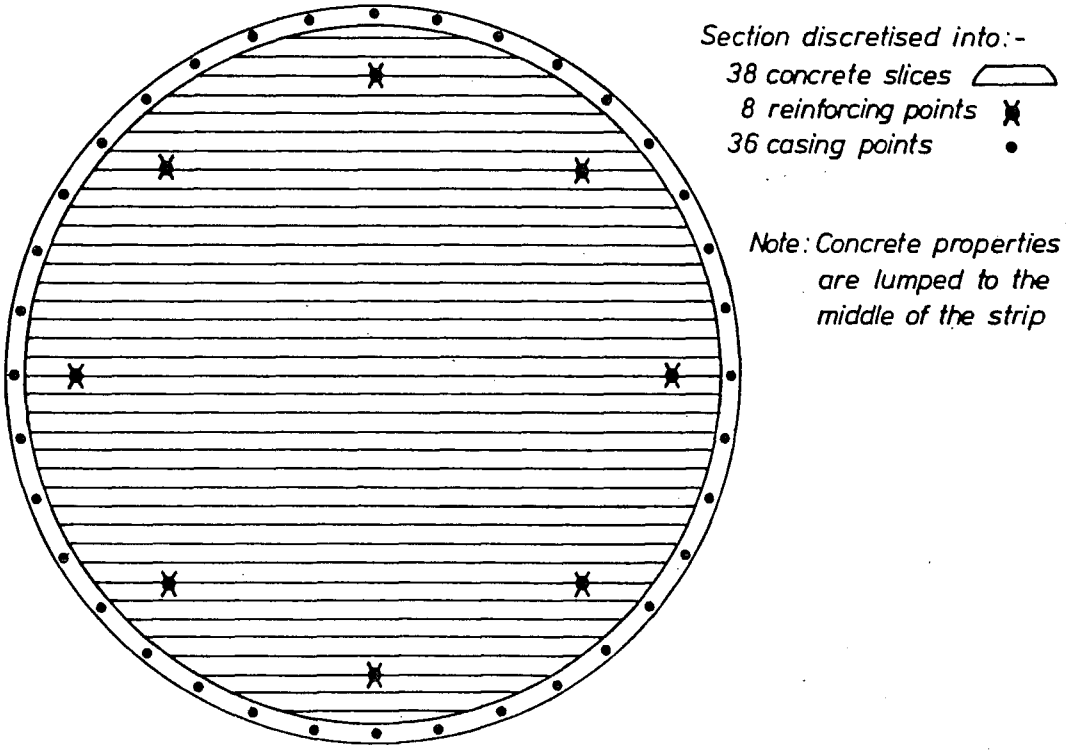

FIG. 5.2 : DISCRETISATION OF STEEL-ENCASED REINFORCED CONCRETE SECTION

where A = area of section
B = first moment of area of section about x = 0
I = second moment of area of section about x = 0

. Response of Discretised Non-Linear System

For a discretised (see Fig. 5.2) rather than continuous system, and for nonlinear rather than linear stress-strain relations, then equation 5.5 can be expressed in incremental form as:

$$\begin{bmatrix} \Delta P \\ \Delta M \end{bmatrix} = \begin{bmatrix} Q_{11} & Q_{12} \\ Q_{21} & Q_{22} \end{bmatrix} \begin{bmatrix} \Delta\varepsilon_o \\ \Delta\psi \end{bmatrix} \tag{5.6}$$

where $$Q_{11} = \sum_{i=1}^{n} \left[(E_t)_i . (\Delta A)_i \right] \tag{5.7}$$

$$Q_{12} = Q_{21} = \sum_{i=1}^{n} \left[(E_t)_i . (\Delta A)_i . (x)_i \right] \tag{5.8}$$

$$Q_{22} = \sum_{i=1}^{n} \left[(E_t)_i . \{ (\Delta A)_i . (x_i)^2 + (\Delta I)_i \} \right] \tag{5.9}$$

where $(\Delta A)_i$ = area lumped to the ith discretisation

$(x)_i$ = distance from the centroid of the section to the ith discretisation

$(\Delta I)_i$ = local second moment of area of the material represented by the ith discretisation

$(E_t)_i$ = tangent slope of the stress-strain curve for the material represented at the ith discretisation (based on strain reached at the end of the previous increment).

The above summations are performed over the n discretisations that represent the concrete slices, casing points and reinforcing points shown in Fig. 5.2. It should be noted that in calculating Q_{22}, local bending of the material represented at each discretisation is allowed for by the term $(E_t)_i.(\Delta I)_i$. This local bending has commonly been ignored in moment-curvature analyses with the result that for the same quantity of discretisations an analysis including $(E_t)_i.(\Delta I)_i$ will give better accuracy than will an analysis excluding $(E_t)_i.(\Delta I)_i$.

By solving equation 5.6 for a large number of deformation increments ($\Delta\varepsilon_o$ or $\Delta\psi$), the moment-curvature response can be determined in piecewise fashion. However consider the stress-strain path followed by the material lumped at the ith discretisation, as shown in Fig. 5.3a. It can be seen that the calculated stress-strain response diverges from the true response due to the error of using the tangent stiffness at the start of an increment as the stiffness over the whole increment.

This divergence can be corrected, in the following increment, by adding the resulting out-of-balance forces and moments from one increment on to the values of ΔP and ΔM used in the next increment, with the result shown in Fig. 5.3(b). The out-of-balance force (Q_{13}) and moment (Q_{23}) at the end of an increment can be calculated from:

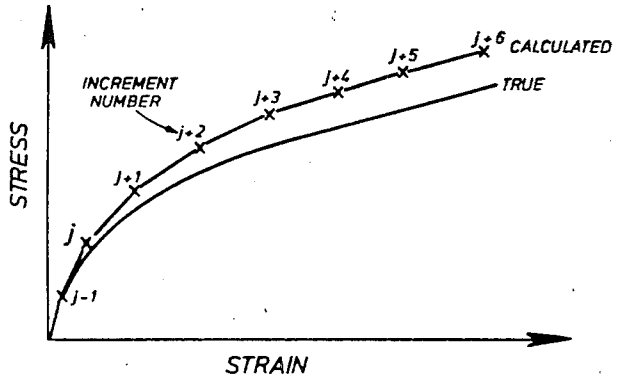

FIG. 5.3(a) DIVERGENCE OF TRUE AND CALCULATED STRESS-STRAIN PATHS

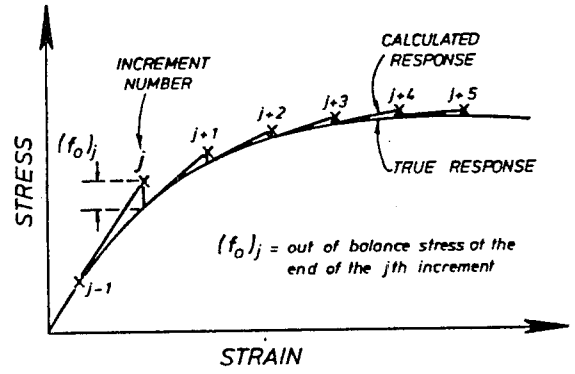

FIG. 5.3(b) CORRECTION OF CALCULATED STRESS-STRAIN PATH

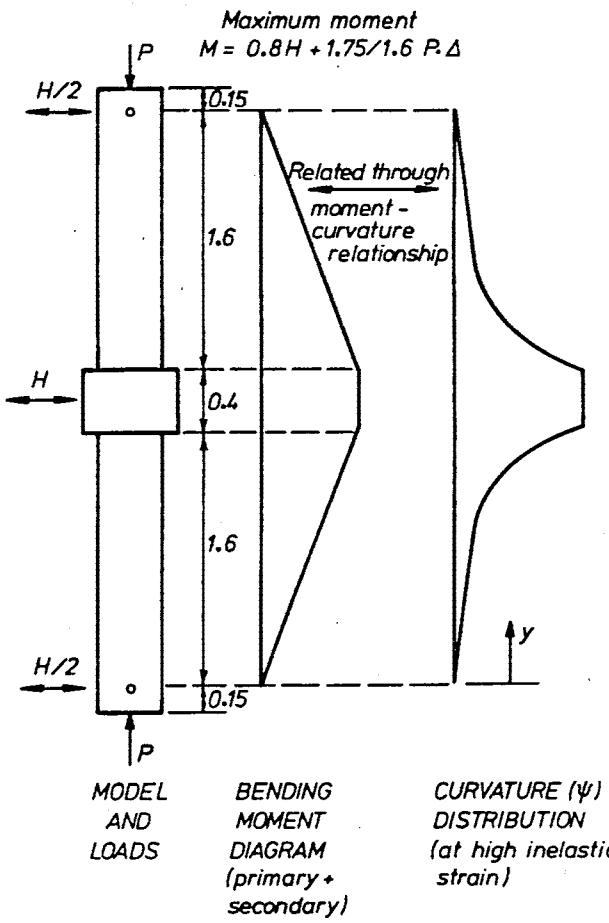

FIG. 5.4 : MOMENT AND CURVATURE DISTRIBUTIONS ON MODELS

$$Q_{13} = \sum_{i=1}^{n} \left[(f_o)_i \cdot (\Delta A)_i \right] \tag{5.10}$$

$$Q_{23} = \sum_{i=1}^{n} \left[(f_o)_i \cdot (x)_i \cdot (\Delta A)_i \right] \tag{5.11}$$

where $(f_o)_i$ = out-of-balance stress at the ith discretisation at the end of the previous increment.

Thus finally the solution method can be represented as:

$$\begin{bmatrix} \Delta P \\ \Delta M \end{bmatrix} + \begin{bmatrix} Q_{13} \\ Q_{23} \end{bmatrix} = \begin{bmatrix} Q_{11} & Q_{12} \\ Q_{21} & Q_{22} \end{bmatrix} \begin{bmatrix} \Delta \varepsilon_o \\ \Delta \psi \end{bmatrix} \tag{5.12}$$

In the initial stages of the analysis, the longitudinal load is placed on the section in increments. At this stage $\Delta\psi = \Delta M = 0$ and $\Delta\varepsilon_o$ can be solved from ΔP by rearranging the top row of equation 5.12:

$$\Delta\varepsilon_o = (\Delta P + Q_{13})/Q_{11} \tag{5.13}$$

After the required level of longitudinal load (P) has been incrementally placed on the section, the next stage involves successively increasing the curvature on the section. At this stage $\Delta P = 0$ and $\Delta\varepsilon_o$ can be solved by rearranging the top row of equation 5.12:

$$\Delta\varepsilon_o = (Q_{13} - Q_{12} \cdot \Delta\psi)/Q_{11} \tag{5.14}$$

Substituting equation 5.14 into the bottom row of equation 5.12 gives:

$$\Delta M = \frac{Q_{21}}{Q_{11}} (Q_{13} - Q_{12} \cdot \Delta\psi) + Q_{22} \cdot \Delta\psi - Q_{23} \tag{5.15}$$

Thus by progressively applying first equation 5.13 and later equation 5.15, the complete moment-curvature response of a given section at a given longitudinal load can be developed. It should be noted that both equations 5.13 and 5.15 use Q_{11}, which represents the longitudinal stiffness of the section (see equation 5.7) in their denominators. Numerical problems can develop when the magnitude of Q_{11} is very small when compared with the magnitude of the numerators shown in equations 5.13 and 5.15. Thus in the computer program (MONOMC) Q_{11} was stipulated to have a minimum magnitude of 1% of its initial magnitude.

5.2.3 Lateral Load-Deflection Analysis

Theoretical lateral load-lateral deflection responses were calculated for the test units (1-5, 8 and 9) with continuous casings which were described in the previous chapter. In that chapter it was noted that bond between the concrete loading block and the casing was poor, resulting in a large penetration of casing longitudinal strain into the region of the block. In the theoretical analyses described subsequently, it was assumed that strain penetration was complete and the moment carried by the steel-encased reinforced concrete member inside the block was the same as that carried at the face of the block. The resulting bending moment distribution on the member is shown in Fig. 5.4.

From the previously calculated moment-curvature relationship, it is then possible to also determine the curvature distribution of the member, as is also shown in Fig. 5.4.

For a given curvature distribution, the lateral deflection of the mid-height of the test unit relative to the position of pin connection with the lateral load reaction frame (150 mm from top and bottom of test units, as shown in Fig. 5.4) is given by:

$$\Delta = \int_{o}^{1.8} \psi \cdot y \cdot dy \qquad (5.16)$$

In practice the integration was accomplished by dividing the curvature diagram into a number of slices and numerically evaluating the integral using Simpson's rule.

The maximum moment on the member including both primary and secondary effects is as shown in Fig. 5.4:

$$M = 0.8H + 1.09\ P \cdot \Delta \qquad (5.17)$$

Thus the lateral load H which is present at a given value of moment M and deflection Δ can be calculated as:

$$H = 1.25\ (M - 1.09\ P \cdot \Delta) \qquad (5.18)$$

To determine the lateral load-lateral deflection $(H - \Delta)$ response, the curvature at the face of the concrete loading block was successively incremented. At a given value of this curvature, the corresponding value of moment (M) at the face of the block was obtained from the previously calculated moment-curvature relationship. The bending moment distribution follows from this value of M (see Fig. 5.4), and hence from the moment-curvature relationship the curvature distribution also follows. Thus from equation 5.16 lateral deflection (Δ) can be calculated. Then from equation 5.18, the given value of longitudinal load P and the above determined values of M and Δ, the lateral load H can be calculated.

5.2.4 Practical Application of Analyses

In the practical application of the previously mentioned moment-curvature analysis techniques, it is necessary to select the number of casing points, reinforcing bar points and concrete slices to which the section is discretised. Clearly the number of reinforcing bar points should be equal to the number of reinforcing bars, but intuitively the numbers of casing points and concrete slices are not obvious. Typical analyses were performed for unit 9 of the tests described in Chapter 4 (number of reinforcing bars = 10). It was assumed that the concrete slices were of equal width and all of the casing points had identical areas, and it was further assumed that the number of casing points equalled the number of concrete slices. It was found that at a curvature of 0.1 rads/m, the moments obtained using the number of casing points = 20, 30, 40 and 50 were only 1.2%, 0.5%, 0.3% and 0.2% respectively different from the moment obtained using 100 casing points. Thus on the basis of an error of less than 1% being satisfactory, a choice of 30 concrete slices and 30 casing points was made for the subsequent analyses.

A similar study was performed to indicate the number of longitudinal slices the model pile should be subdivided into to numerically evaluate the integral given in equation 5.16. The results showed that typically there was less than 0.1% difference in the values of lateral deflection Δ

calculated using 100 slices and 20 slices. Thus in the subsequent analyses a choice of 20 slices was adopted.

5.3 . ANALYSIS OF TEST UNITS WITH CONTINUOUS CASINGS

In the previous chapter, the experimental response of steel-encased reinforced concrete members (units 1-5, 8 and 9) with continuous casings was described. .In the following sections, the theoretical responses of these units are described and compared with the experimental results. Four types of analyses were performed:

(i) Response assessed on the basis of an empty tube.

(ii) The response of the composite member assessed on the basis of the "Uniaxial Models" (see Chapter 2).

(iii) The response of the composite member assessed on the basis of the "Lateral Interaction Models" (see Chapter 2).

(iv) Response assessed on the basis of the "Lateral Interaction Models" with an approximate allowance for the additional confinement offered to the concrete by the spiral reinforcement. (This is ignored in the "Lateral Interaction Models" which are described in Chapter 2).

5.3.1 Material Longitudinal Stress-Strain Relations

The longitudinal stress-strain response of the D16 reinforcement in both compression and tension was assumed to be in accordance with the behaviour defined by the tensile test results shown previously in Fig. 4.17 (i.e. uniaxial-stress behaviour).

Figures 5.5 - 5.8 show the longitudinal stress-strain behaviour of the casings (t = 9.53 mm, 5 mm, 3 mm and 1.96 mm respectively) obtained using the "lateral interaction" and "uniaxial" models. "Uniaxial" model behaviour was assumed to be identical to that indicated by the coupon tests (see Figs. 4.13-4.16). From Figs. 5.5-5.8 it is apparent that lateral interaction significantly enhances the tensile capacity of the tube, but markedly reduces the compressive capacity.

Figures 5.9-5.10 show the longitudinal stress-strain behaviour of the concrete (f'_c = 31 MPa and 29 MPa respectively) obtained using the "uniaxial" and "lateral interaction" models. Also indicated are results from a modified form of the "lateral interaction" model which makes an approximate allowance for the presence of spiral reinforcement.

It is difficult to rationally allow for the combined confinement offered by tube and spiral reinforcement to concrete. The spiral reinforcement is located within the section away from the positions of peak longitudinal-compression strain, and as mentioned in Chapter 2, equivalent volumes of tube and spiral reinforcement do not have the same confining effect on the concrete. However in an approximate attempt to rationally allow for the increased confinement offered to the concrete, it was assumed that the spiral reinforcement was acting as a notional continuous tube around the outside of the gross concrete area. This notional tube was assumed to have the same volume as the spiral reinforcement, and for longitudinal strains $\varepsilon_L < 0.002$ was assumed to be unstressed while for $\varepsilon_L \geq 0.002$ was assumed to be at yield in a state of uniaxial-hoop-tension stress. For the purpose of calculating concrete response, this hoop stress was then added to the hoop-tension stress that develops in the casing.

A comparison of the "lateral interaction" and "uniaxial" model results from Figs.5.9 and 5.10 shows the enhancement to concrete strength and marked

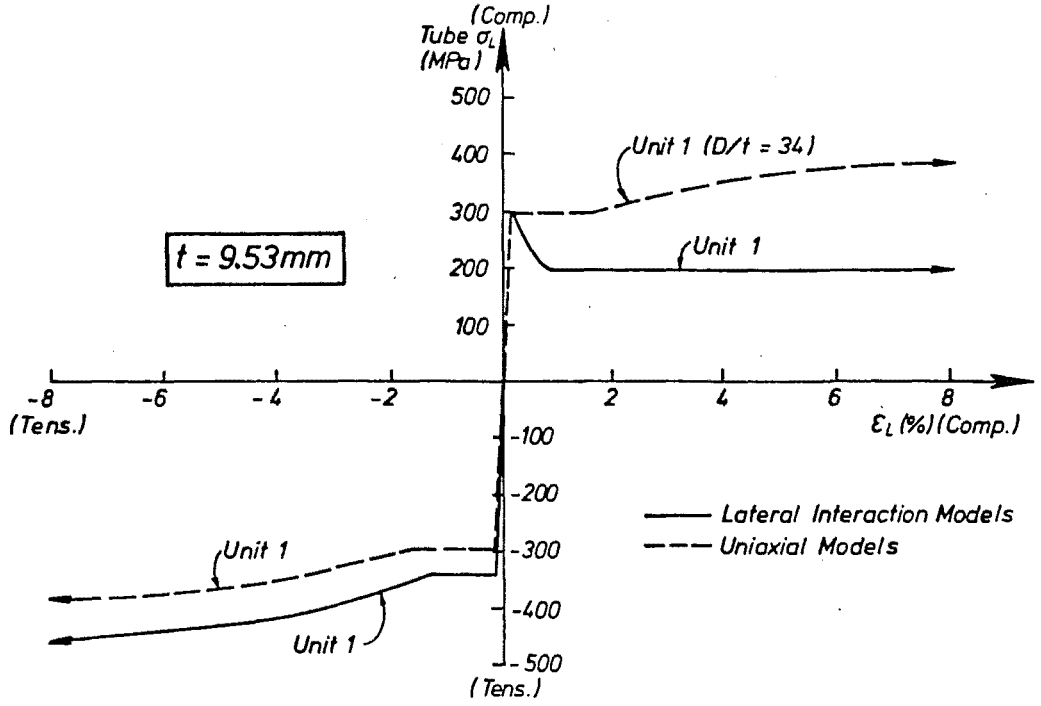

FIG. 5.5 : ASSUMED LONGITUDINAL STRESS-STRAIN BEHAVIOUR OF 9.53 MM THICK TUBE

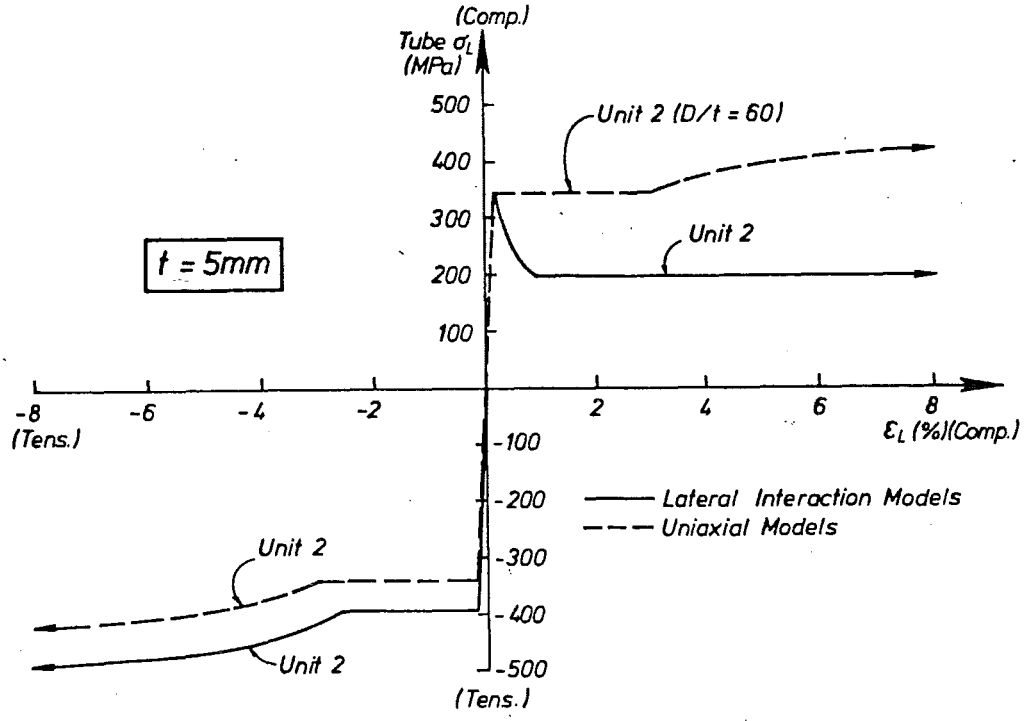

FIG. 5.6 : ASSUMED LONGITUDINAL STRESS-STRAIN BEHAVIOUR OF 5 MM THICK TUBE

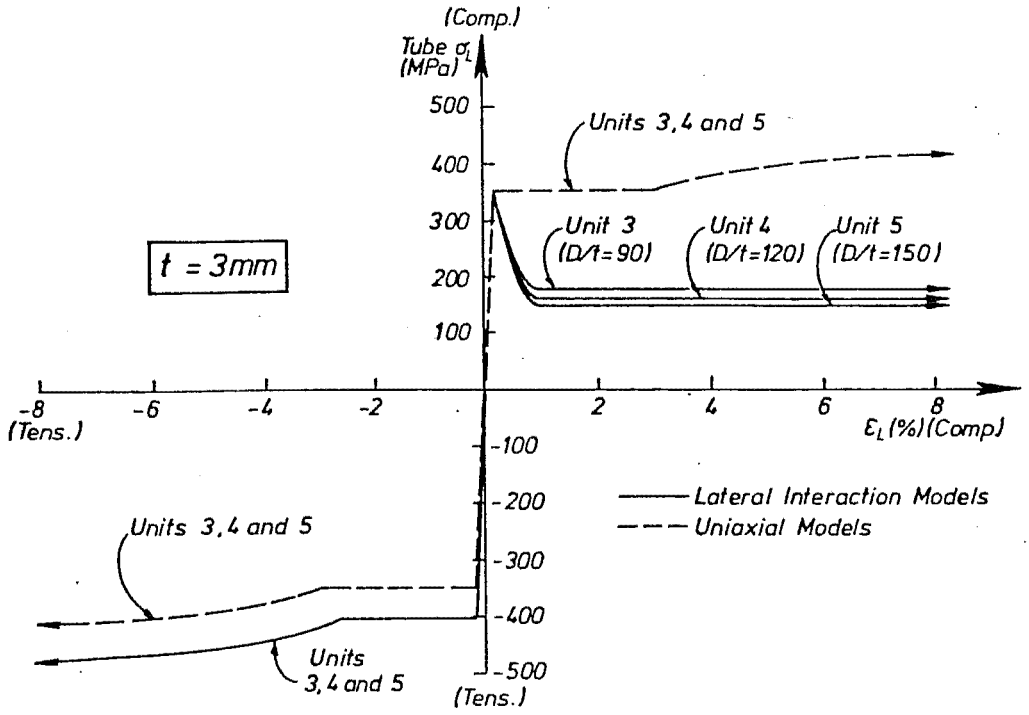

FIG. 5.7 : ASSUMED LONGITUDINAL STRESS-STRAIN BEHAVIOUR OF 3 MM THICK TUBE

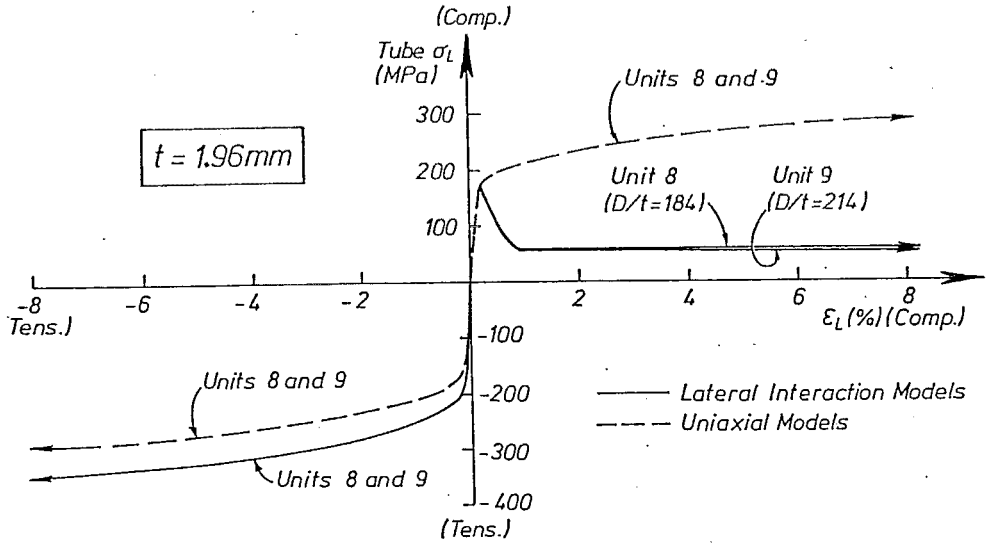

FIG. 5.8 : ASSUMED LONGITUDINAL STRESS-STRAIN BEHAVIOUR OF 1.96 MM THICK TUBE

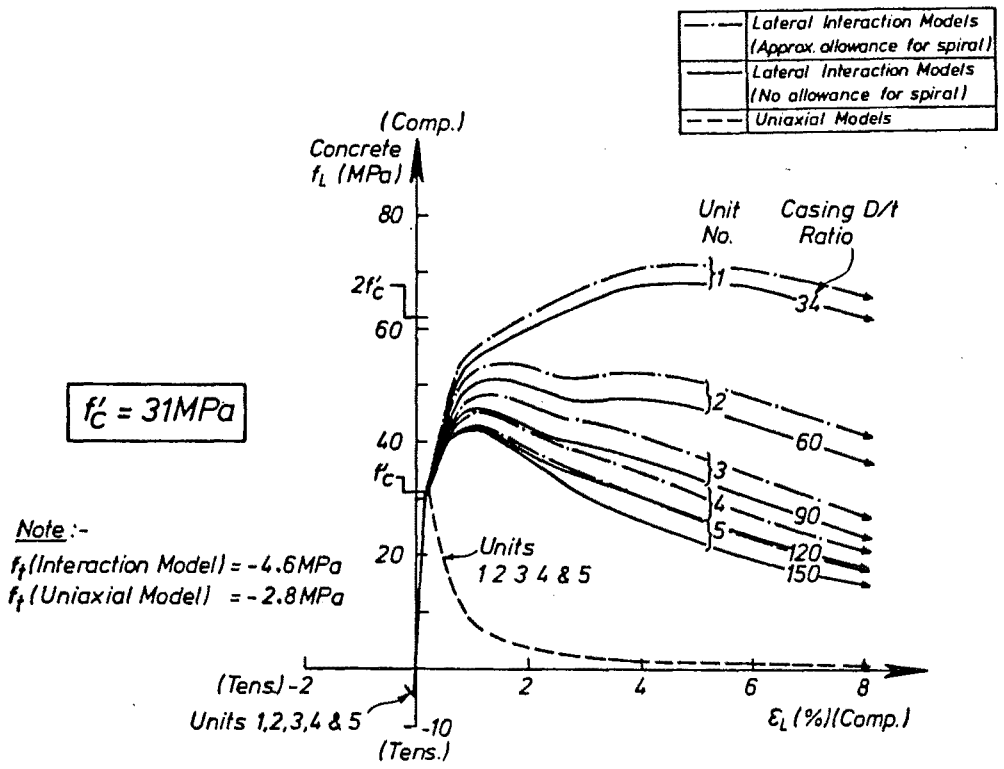

FIG. 5.9 : ASSUMED LONGITUDINAL STRESS-STRAIN BEHAVIOUR OF THE CONCRETE (f'_c = 31 MPa)

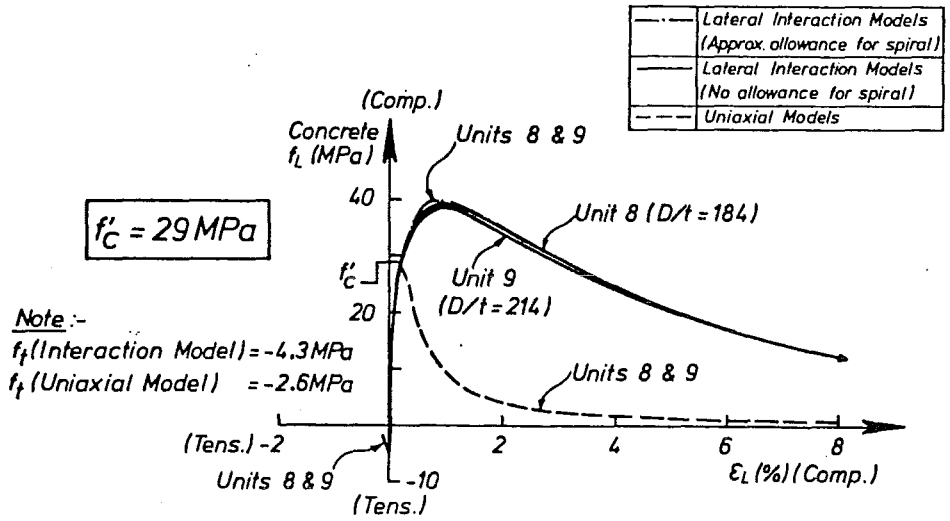

FIG. 5.10 : ASSUMED LONGITUDINAL STRESS-STRAIN BEHAVIOUR OF THE CONCRETE (f'_c = 29 MPa)

enhancement to concrete ductility that result from the presence of the tube. It is also clear that the spiral reinforcement results in only a small improvement to the stress-strain performance of the concrete, for example allowance for the spiral reinforcement makes only a difference of 1 - 3 MPa to the peak concrete compressive strength.

5.3.2 Moment-Curvature Responses

Figures 5.11-5.17 show the theoretical moment-curvature responses for units 1-5, 8 and 9 respectively. Also indicated are theoretical moment-curvature coordinates at a peak concrete compression strain of $\varepsilon_c = 0.003$, theoretical cracking moments M_{cr} (based on peak tensile stresses in the concrete which were equal to 60% of the measured modulii of rupture), theoretical moments at first yield of steel M_y, and theoretical ultimate flexural strengths M_i. Moments M_i were calculated as described in Section 4.2.3 using actual material strength parameters, $\varepsilon_c = 0.003$ and a strain compatibility approach. Finally the diagrams also show the experimentally determined moment-curvature coordinates during the first cycle of loading (at $\mu = 1/4, 1/2, 3/4$), and at the positive displacement peaks at higher ductility levels, where it should be noted that two or more cycles were performed at given values of displacement for cycles to $|\mu| \geq 2$. Before local buckling occurred, these coordinates were assessed on the basis of complete penetration of casing longitudinal strain into the concrete loading block (i.e. 300 mm gauge length for linear potentiometers N5, N6, S5 and S6 instead of the nominal 100 mm gauge length, see Fig. 4.51). After local buckling occurred, to allow for the more concentrated distribution of plasticity, smaller values of gauge length were chosen as described previously in Section 4.10.1. The major conclusions that can be drawn from these figures are:

(i) In general the envelope of the experimental responses is in good agreement with theoretical responses predicted using the "lateral interaction" models.

(ii) The spiral reinforcement has a negligible influence on the moment-curvature characteristics of the test units.

(iii) Tube-concrete lateral interaction significantly enhances the flexural strength and ductility of steel-encased reinforced concrete members.

(iv) The assumption of complete penetration of the casing longitudinal strain into the block is valid, since experimental and theoretical responses are in close agreement.

5.3.3 Lateral Load-Deflection Responses

Figures 5.18-5.24 show the theoretical lateral load-lateral deflection responses of units 1-5, 8 and 9 respectively. Also indicated are experimentally obtained load-deflection coordinates at displacement ductilities of $\mu = 1/4$, 1/2 and 3/4, and at the peaks of subsequent cycles where it should be noted that two or more cycles were performed at given values of displacement for cycles to $|\mu| \geq 2$.

In general the theoretical monotonic responses obtained by using the "lateral interaction" models show good agreement with the envelope of experimental cyclic responses, as represented by experimental values of load-deflection coordinates at the peaks of cycles. However, particularly in unit 1, theoretical predictions sometimes underestimated experimental response, since under cyclic loading strain-hardening of steel will occur at lower magnitudes of strain than occurs under monotonic loading (5.10). During static testing for $|\mu| \geq 2$, the envelopes to the experimental responses generally indicated that the lateral load-carrying capacity was maintained at a roughly constant level. Thus the reduction in lateral load-carrying capacity caused by P-Δ

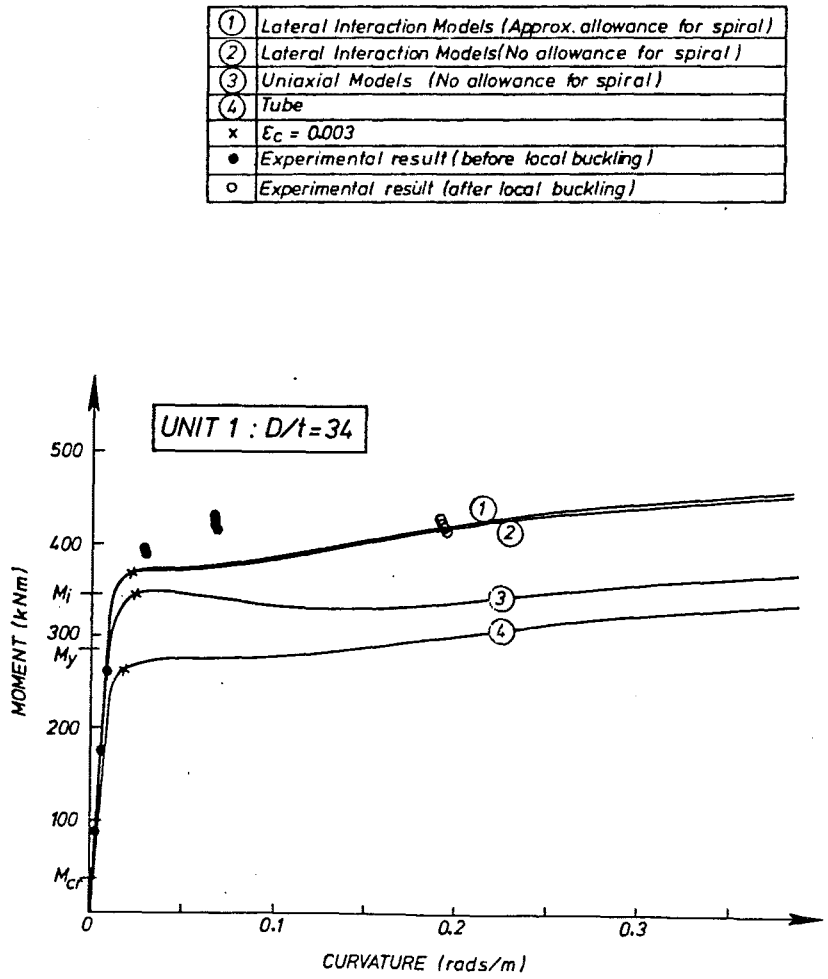

FIG. 5.11 : MOMENT-CURVATURE RESPONSES FOR UNIT 1

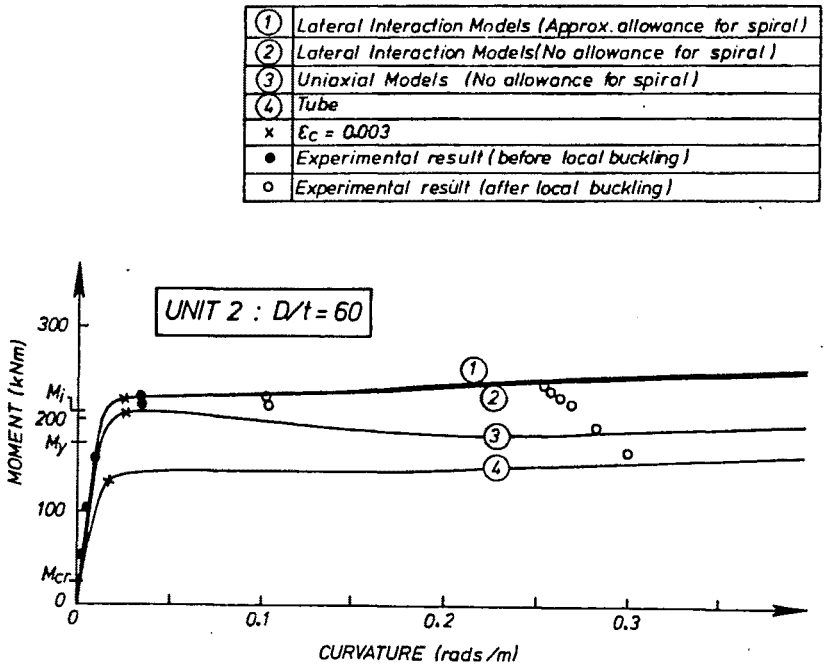

FIG. 5.12 : MOMENT-CURVATURE RESPONSES FOR UNIT 2

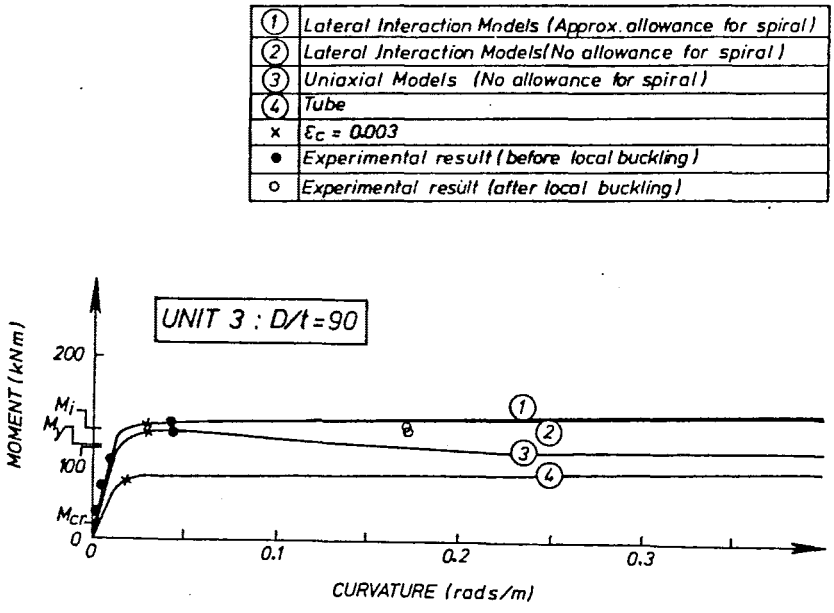

FIG. 5.13 : MOMENT-CURVATURE RESPONSES FOR UNIT 3

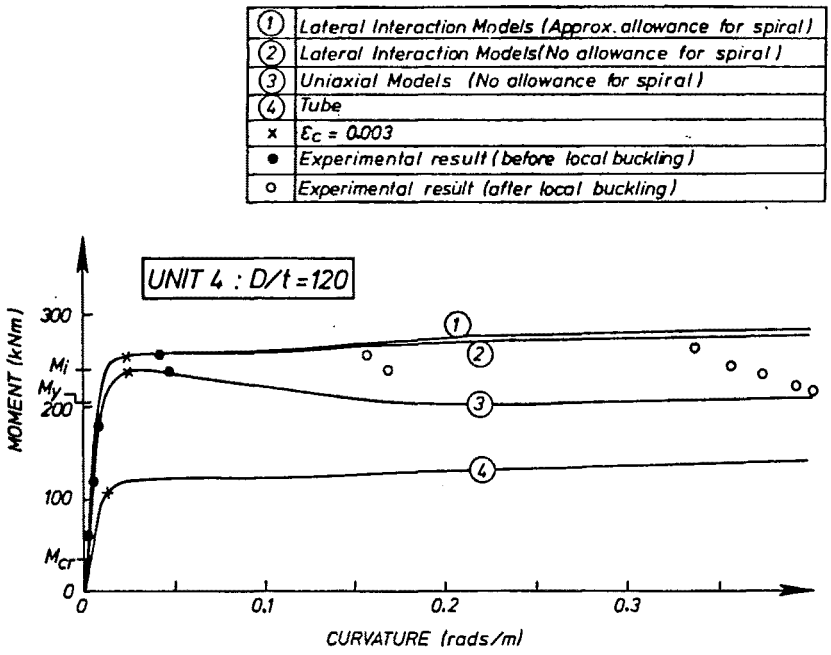

FIG. 5.14 : MOMENT-CURVATURE RESPONSES FOR UNIT 4

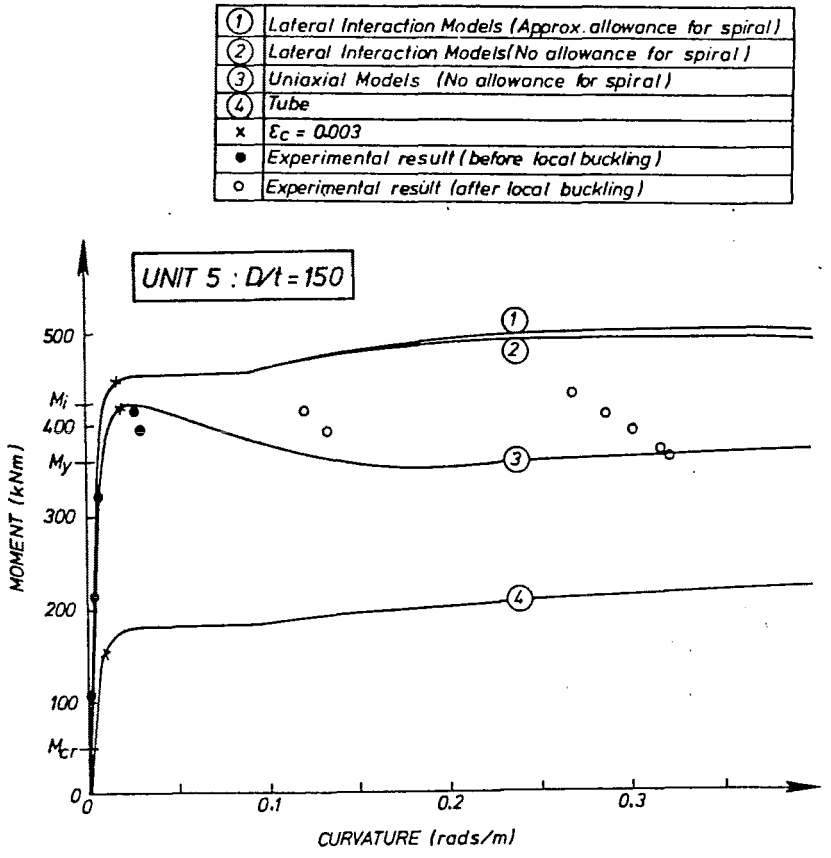

FIG. 5.15 : MOMENT-CURVATURE RESPONSES FOR UNIT 5

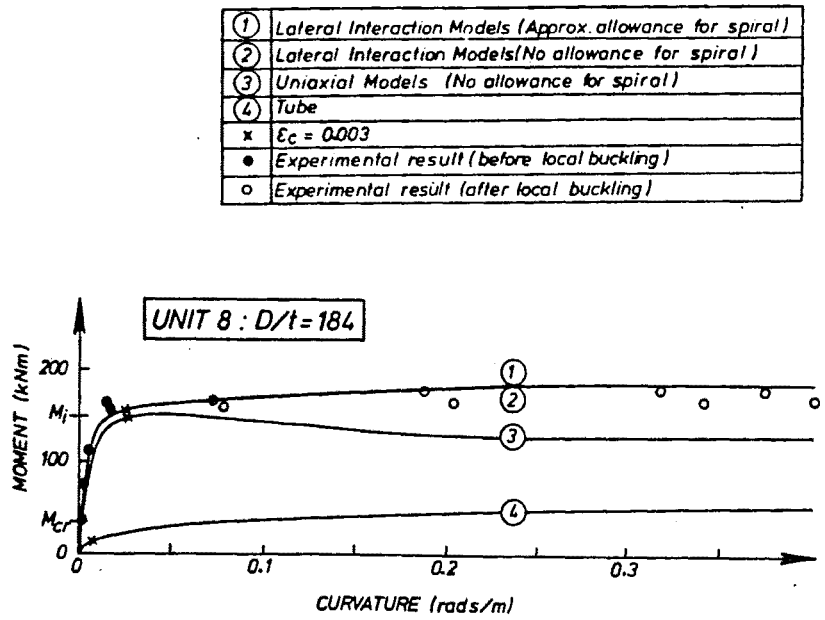

FIG. 5.16 : MOMENT-CURVATURE RESPONSES FOR UNIT 8

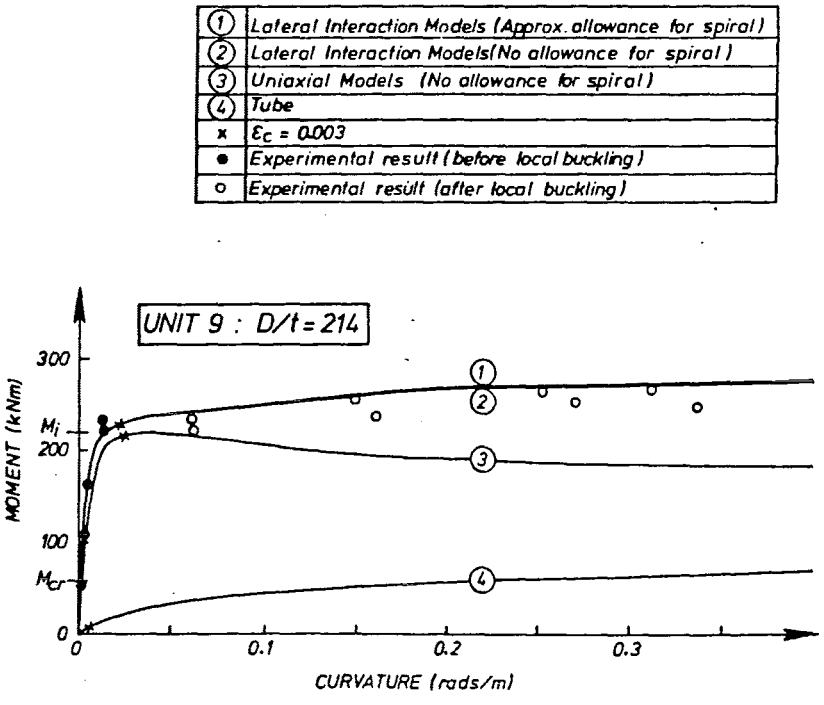

FIG. 5.17 : MOMENT-CURVATURE RESPONSES FOR UNIT 9

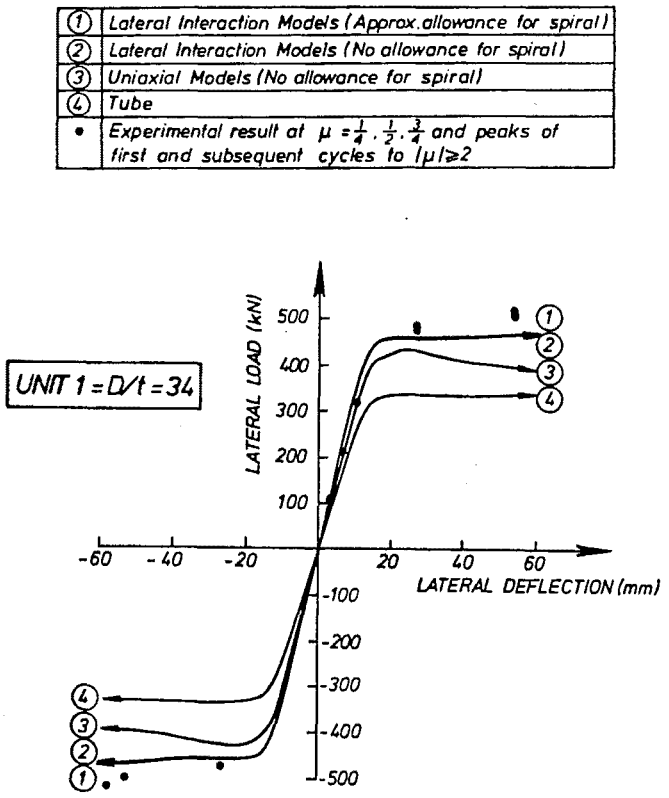

FIG. 5.18 : LOAD-DEFLECTION RESPONSES FOR UNIT 1

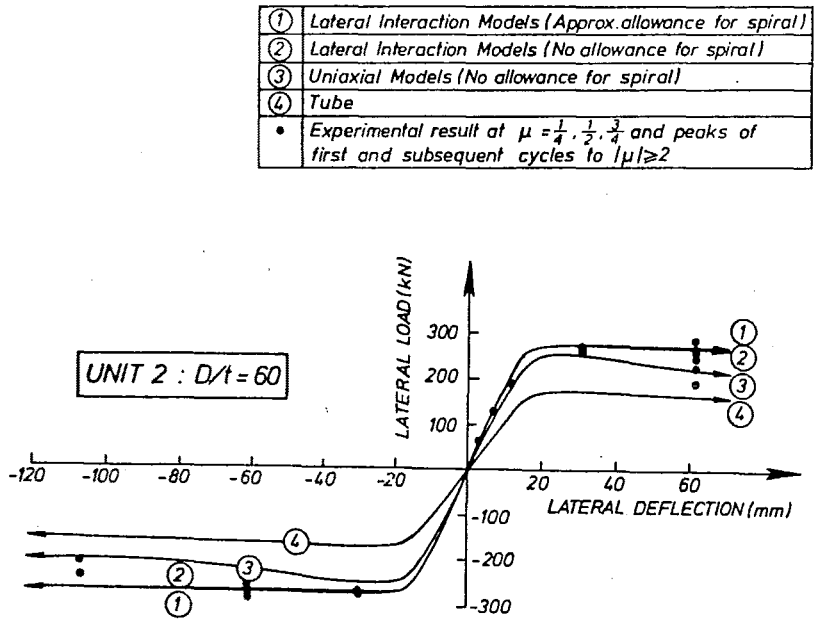

FIG. 5.19 : LOAD-DEFLECTION RESPONSES FOR UNIT 2

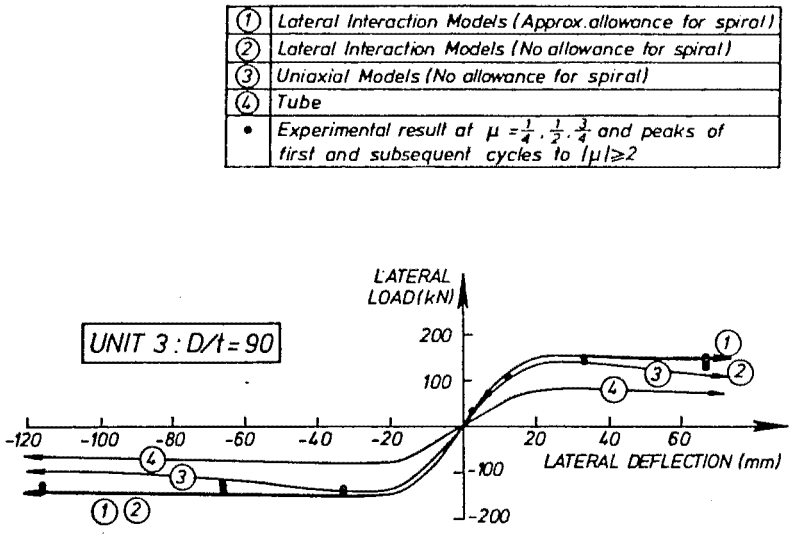

FIG. 5.20 : LOAD-DEFLECTION RESPONSES FOR UNIT 3

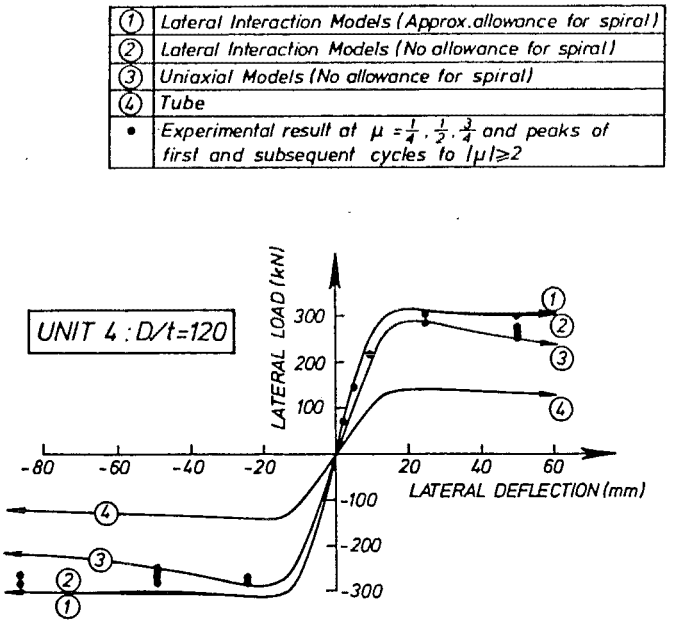

FIG. 5.21 : LOAD-DEFLECTION RESPONSES FOR UNIT 4

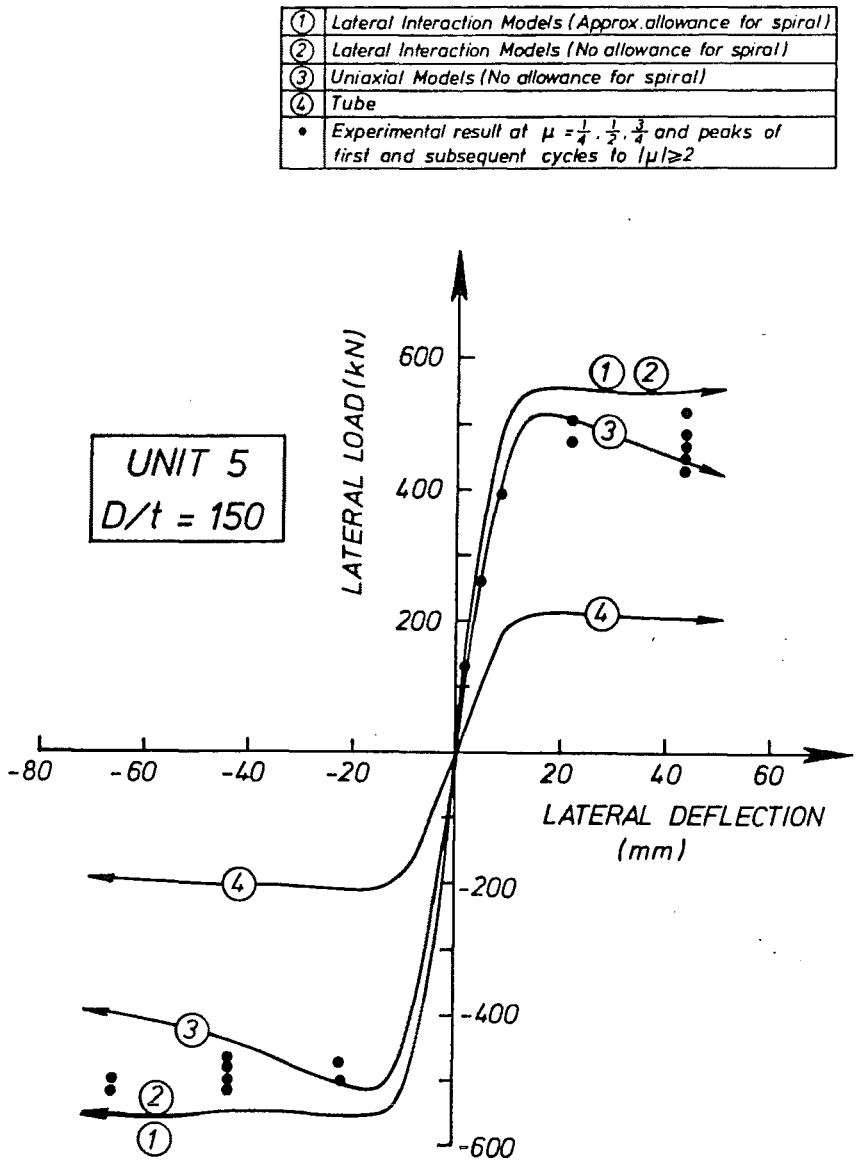

FIG. 5.22 : LOAD-DEFLECTION RESPONSES FOR UNIT 5

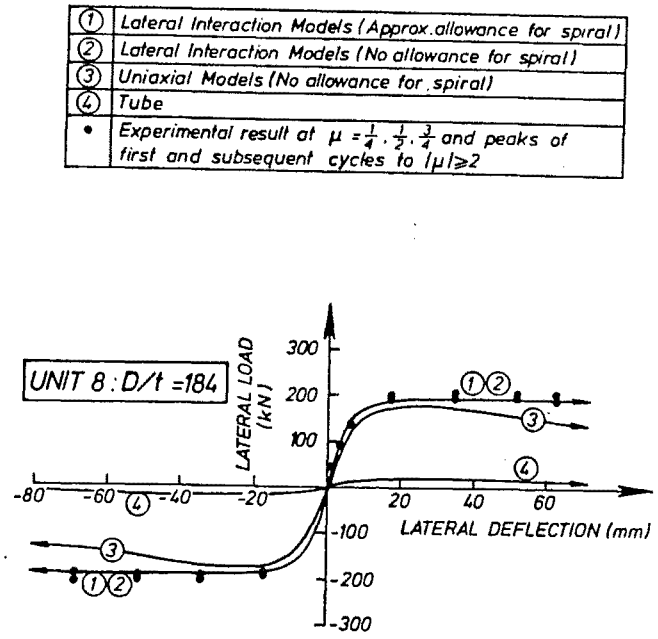

FIG. 5.23 : LOAD-DEFLECTION RESPONSES FOR UNIT 8

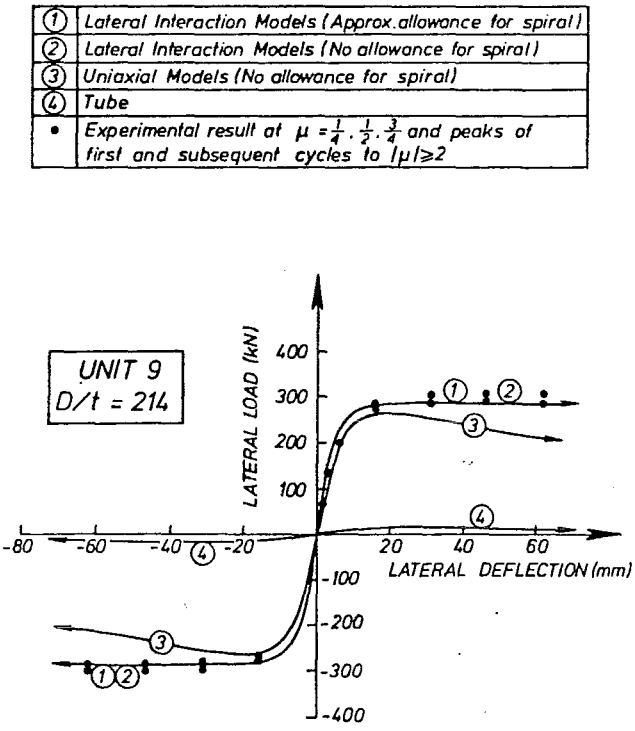

FIG. 5.24 : LOAD-DEFLECTION RESPONSES FOR UNIT 9

effect was offset by increases in capacity due to steel strain-hardening and concrete confinement. It is also shown that the composite member is appreciably stronger than predictions based on the "uniaxial" models and empty tube response. The load-deflection responses also confirm that confinement offered to the concrete by the spiral reinforcement is insignificant.

Figure 5.25 shows an overall comparison of the theoretically and experimentally obtained flexural strengths of the test units. For this purpose the maximum experimentally obtained moment M_{exp} (considering both primary and secondary moments) was compared with the maximum theoretically obtained moment at deflections of less than or equal to the maximum deflection imposed during testing.

From Fig. 5.25, for the average of the 7 tests, the "lateral interaction" models with and without allowance for spiral reinforcement predict 99% and 98% respectively of the maximum experimentally obtained moment, while on average the "uniaxial" models and the theoretical ultimate flexural strength (M_i) predict 87% and 86% respectively of the maximum experimental moment. It is also shown that the moment at first yield of the steel (M_y) is approximately equal to 75% of the maximum experimental moment. The maximum moment carried by the empty tube (M_t) and the moment at which concrete cracks (M_{cr}), as expected, decrease and increase respectively with increasing casing D/t ratio.

A comparison of the maximum moments predicted by use of the "uniaxial" and "lateral interaction" models shows that tube-concrete lateral interaction enhances the flexural strength of the composite member to approximately 13% above the strength predicted assuming uniaxial material behaviour.

5.3.4 Comparison of Yield Curvatures and Deflections

Theoretical values of yield curvature ψ_y corresponding to an elasto-plastic idealisation of behaviour were calculated from the moment-curvature response predicted using the "lateral interaction" models. To obtain these theoretical values of ψ_y, as shown in Fig. 5.26, the curvatures corresponding to 3/4 of the theoretical ultimate flexural strength (3/4 M_i) were multiplied by 4/3. From the ratio of M_i/M_y shown in Fig. 5.25, it can be inferred that the yield curvature calculated in the above fashion will be approximately 15% larger than the curvature at first yield of the steel. Experimental values of ψ_y were assessed in a similar fashion from potentiometers N5, N6, S5 and S6 by multiplying the average curvature indicated at $\mu = \pm 3/4$ by 4/3.

In Fig. 5.27, the theoretical values of ψ_y were compared with experimentally obtained values. From the figure, the theoretical predictions for ψ_y are closely matched by the experimental results obtained on the basis of full penetration of casing longitudinal strain into the block (i.e. 300 mm effective gauge length for potentiometers N5, S5, N6 and S6, see Fig. 4.51). Experimental results obtained on the basis of zero strain penetration (i.e. 100 mm gauge length) obviously overestimate the theoretical results. On average the experimental ψ_y (with full strain penetration) was equal to 107% of the theoretical ψ_y.

Theoretical and experimental yield deflections Δ_y were derived in a similar fashion to that used in deriving yield curvatures ψ_y.
In Fig. 5.28, the experimental results are compared with theoretical results predicted on the basis of either full strain penetration into the loading block or zero strain penetration. Clearly, theoretical predictions based on full strain penetration gave the best comparison with experiment, since on average these predictions were approximately equal to 89% of the experimental values, while predictions based on zero strain penetration gave approximately 63% of the experimental values.

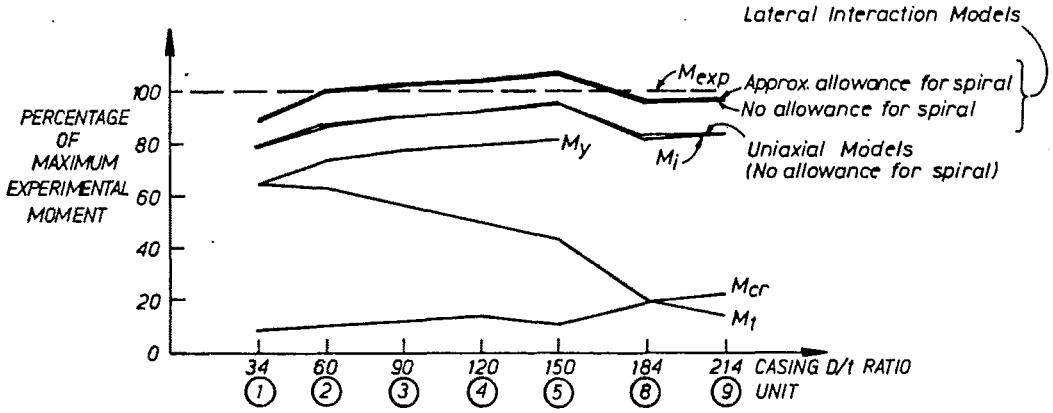

FIG. 5.25 : COMPARISON OF MAXIMUM THEORETICAL AND EXPERIMENTAL MOMENTS

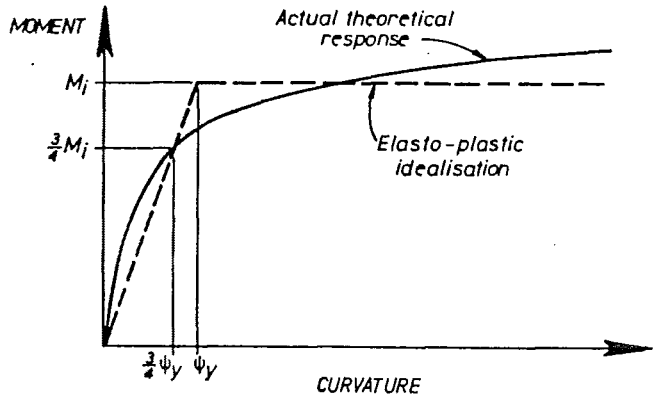

FIG. 5.26 : CALCULATING THEORETICAL YIELD CURVATURE ψ_y

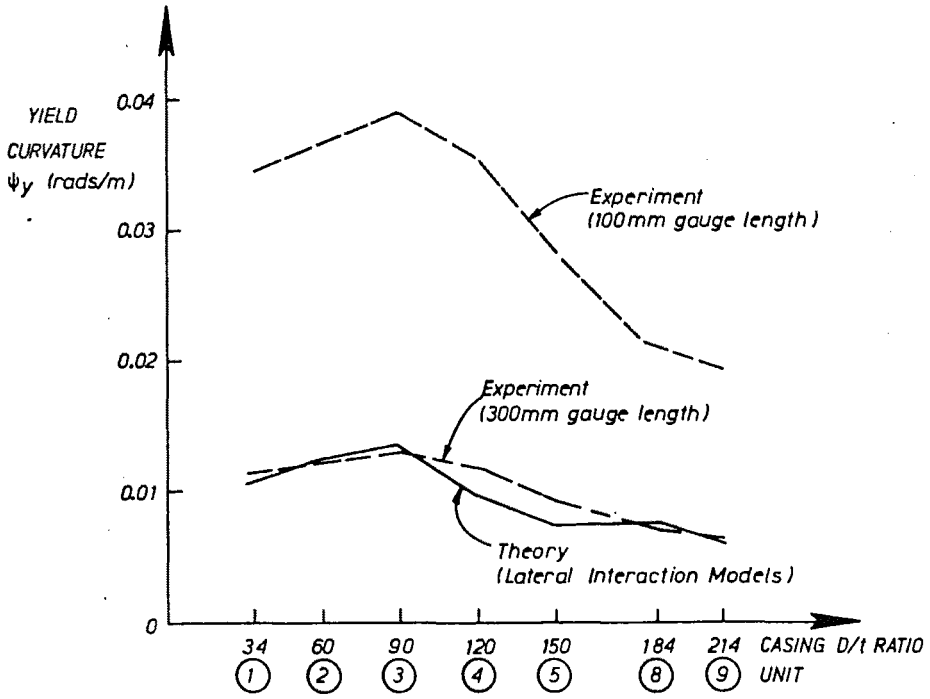

FIG. 5.27 : COMPARISON OF YIELD CURVATURES ψ_y

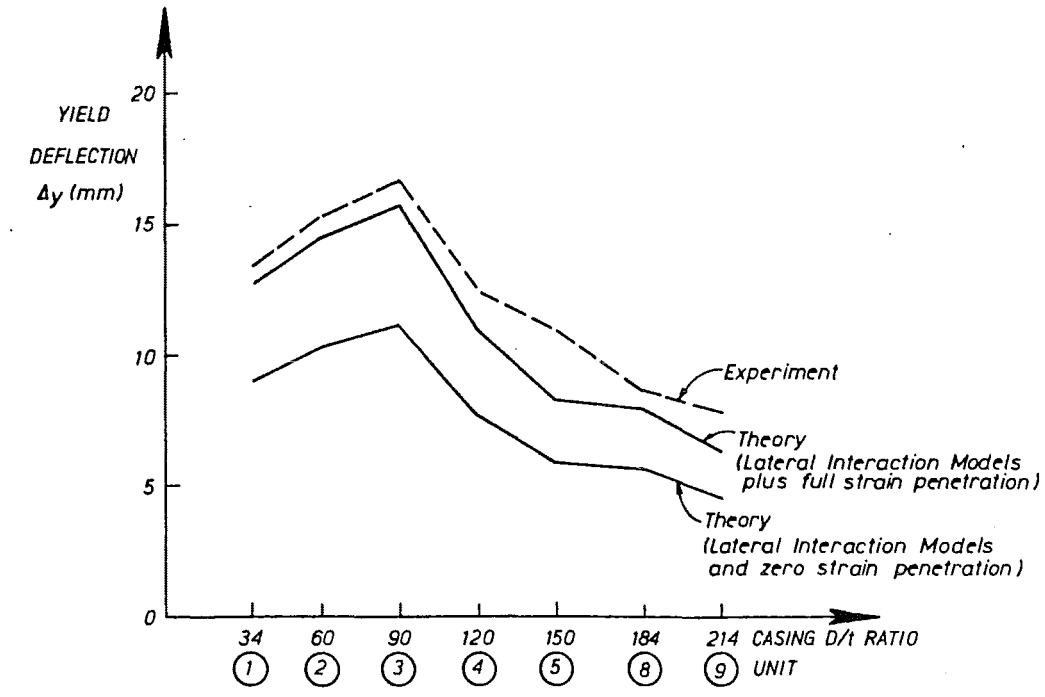

FIG. 5.28 : COMPARISON OF YIELD DEFLECTIONS Δ_y

5.4 ANALYSIS OF TEST UNITS WITH DISCONTINUOUS CASINGS

In the previous chapter, the experimental responses of steel-encased reinforced concrete members (units 6 and 7), with circumferential discontinuities in their casings were described. In the following sections theoretical responses of these units are described and compared with the experimental results.

In Chapter 4 it was shown that although at the critical flexural sections of units 6 and 7 the casing was incapable of developing longitudinal-tension stress. At these sections, the casing was developing longitudinal-compression stress in end-bearing and through hoop-tension stress was also providing effective confinement to the concrete. Further, at sections away from the critical sections, significant levels of both tensile and compressive longitudinal strain in the tube were measured. This meant that the casing was also contributing to the overall load-deflection stiffness of units 6 and 7. In order to quantify these effects, three different analyses were conducted as shown in Table 5.1 (see end of chapter).

The "upper estimate" is based on continuous tube behaviour with concrete and casing response being in accordance with the "lateral interaction" models. "Likely behaviour" assumes the tube is unstressed under longitudinal-tension strain but under longitudinal-compression strain the tube behaves in accordance with the "lateral interaction model", and hence both confines the concrete and develops longitudinal-compression stress. The "lower estimate" is based on an unstressed tube and uniaxial-stress behaviour in the reinforced concrete core.

5.4.1 Material Longitudinal Stress-Strain Relations

The longitudinal stress-strain response of the D16 longitudinal reinforcement was taken to be identical to that shown previously in Fig. 4.17. Figures 5.29 and 5.30 show the longitudinal stress-strain behaviour of concrete and casing respectively, obtained using both the "lateral interaction" and "uniaxial" models. Since as shown in Sections 4.11.2 and 5.3, the presence of internal spiral reinforcement made little difference to moment-curvature and load-deflection behaviour, its effect was ignored.

5.4.2 Moment-Curvature Responses

Figure 5.31 shows the three possible theoretical moment-curvature responses of units 6 and 7. Also shown are the theoretical moments at peak concrete longitudinal-compression strains ε_c of 0.003; the maximum experimentally obtained moment M_{exp}; and the theoretical ultimate flexural strength M_i of the test units based on the reinforced concrete section (tube assumed to be unstressed), $\varepsilon_c = 0.003$, measured f'_c and σ_y and a strain compatibility approach. The experimental moment-curvature responses at the critical flexural sections are not plotted, since during testing it was not possible to measure curvatures in the reinforced concrete core underlying the casing discontinuities.

From Fig. 5.31, at large curvatures the maximum experimental moment M_{exp} is best approximated by a theoretical response based on "likely behaviour" (e.g. at a curvature of 0.4 rads/m this theoretical moment is equal to $0.98M_{exp}$). Thus under longitudinal-compression strain the casing is appreciably contributing to flexural strength. The theoretical estimates based on continuous casings ("upper estimate") and stress-free casings ("lower estimate") grossly overestimate and underestimate respectively the value of M_{exp}.

5.4.3 Lateral Load-Deflection Responses

Along the length of test units with casing discontinuities, varying degrees of slip between the casing and the reinforced concrete core will occur. Thus the moment-curvature relationship at one section may not be appropriate at another section. For example, at a great distance from the discontinuities, moment-curvature response will be close to that assessed on the basis of perfect

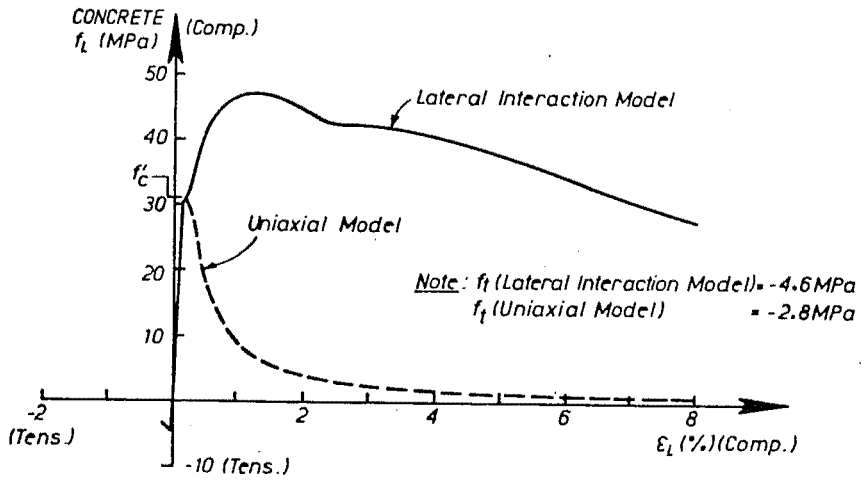

FIG. 5.29 : ASSUMED LONGITUDINAL STRESS-STRAIN RESPONSE OF THE CONCRETE FOR UNITS 6 AND 7 (f'_c = 31 MPa)

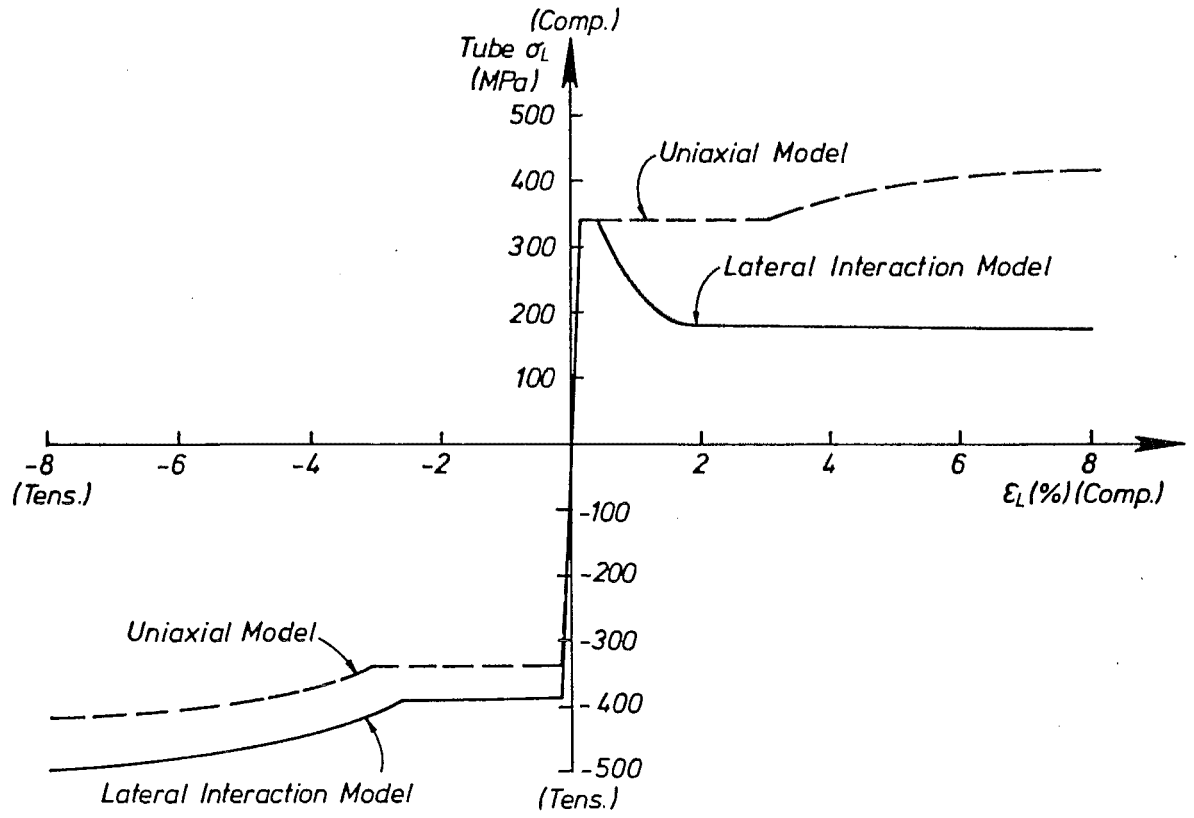

FIG. 5.30 : ASSUMED LONGITUDINAL STRESS-STRAIN RESPONSE OF THE CASING FOR UNITS 6 AND 7

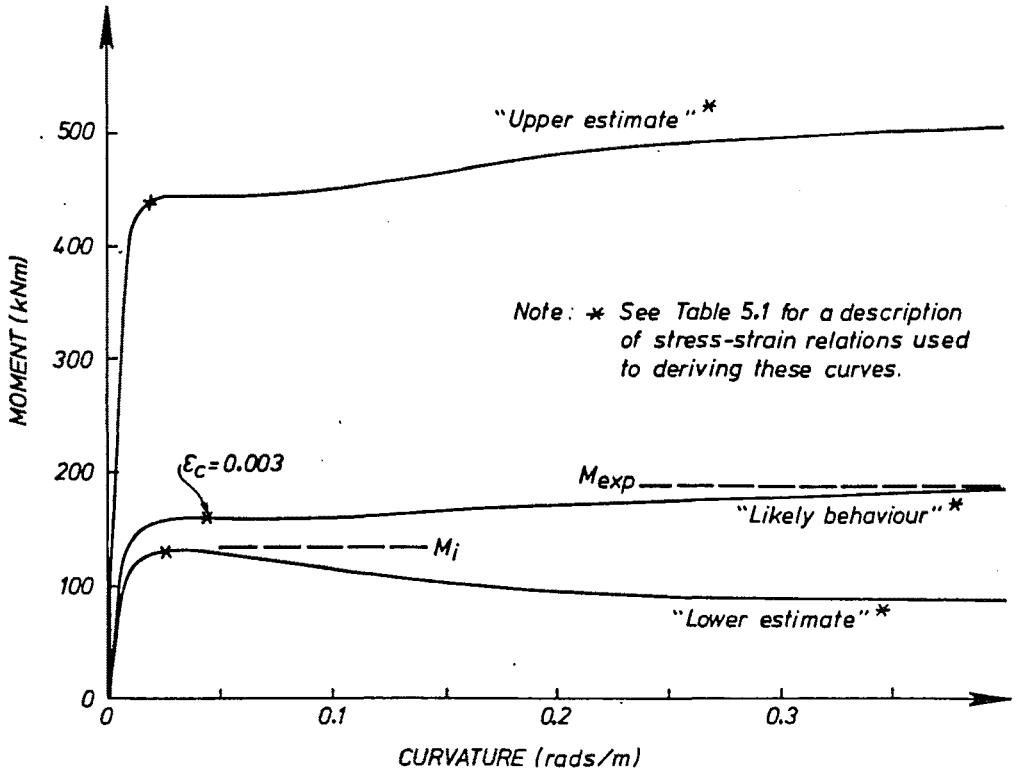

FIG. 5.31 : MOMENT-CURVATURE RESPONSES FOR UNITS 6 AND 7

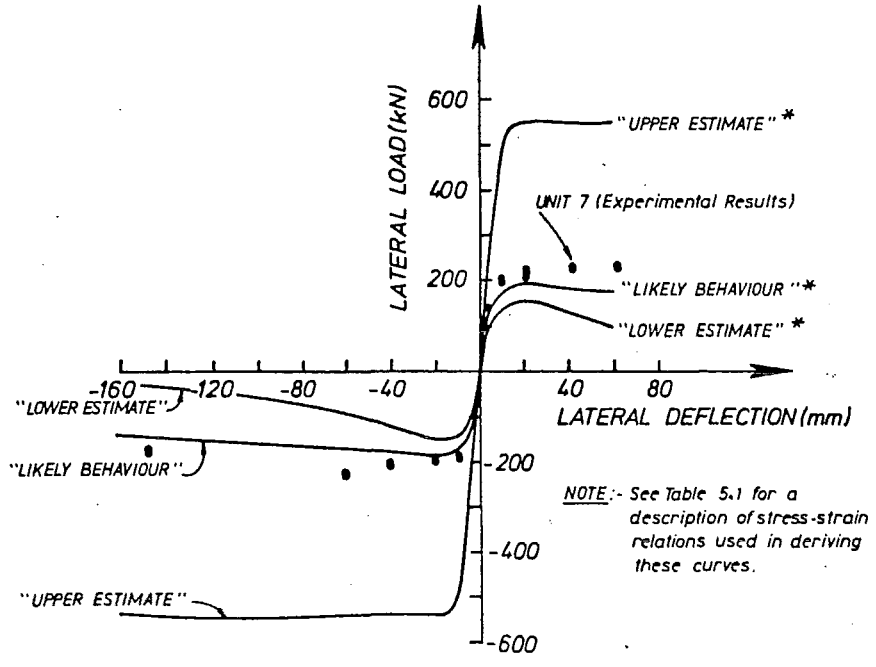

FIG. 5.32 : LATERAL LOAD-DEFLECTION RESPONSES FOR UNITS 6 AND 7

bond between tube and concrete. However close to the discontinuities, slip between casing and the reinforced concrete core will result in a weaker moment-curvature response. Because of uncertainty in assessing the effect of slip on the moment-curvature relationships, it was not possible to accurately define the curvature distribution for a given bending moment distribution. Since a good estimate of the curvature distribution is required before lateral deflection Δ can be calculated (see equation 5.16), it was thus not possible to accurately calculate the theoretical lateral load-deflection (H-Δ) relationship for the test units with casing discontinuties.

In determining the response of structures to earthquake attack, a good estimate of the elastic stiffness of the structure is required to enable the subsequent calculation of the structure's fundamental period of vibration. In this section, the lateral load-deflection response of the test units with discontinuous casings were roughly assessed assuming the moment-curvature response based on either of the "lower estimate", "likely behaviour" or the "upper estimate" were appropriate right along the length of the unit. Figure 5.32 shows responses predicted from these analyses and experimental results at μ = 1/4, 1/2 and 3/4 and at peaks of the cycles to $|\mu| \geq 2$. Although as could be inferred from the discussion contained earlier in this section, the above assumption of one moment-curvature response applying to the whole member is crude, it appears that a good estimate of lateral stiffness is obtained by assuming an elastic stiffness intermediate between that shown by the "upper estimate" and "likely behaviour". Thus the presence of longitudinal-tension strain in the casing, which was noted in Chapter 4, does increase the overall stiffness of these units to a level marginally above that provided by the reinforced concrete core and the tube under longitudinal-compression stress. It is also shown that post-elastic behaviour is reasonably (and slightly conservatively) predicted by response based on the tube being ineffective under longitudinal-tension strain ("likely behaviour" analysis).

5.5 CONCLUSIONS

In this chapter methods for theoretically determining the monotonic loading moment-curvature and lateral load-deflection responses of steel-encased reinforced concrete members were described and compared with experimental results.

5.5.1 Comparison of Results for Test Units with Continuous Casings

Very good agreement between the envelope of the cyclic loading experimental response of test units with continuous casings (see Chapter 4) and theoretical predictions which used the "lateral interaction" models (see Chapter 2) were obtained. For the seven test units on average, maximum experimental strength was predicted to within 2%, yield curvature to within 7%, yield deflection to within 11%, and post-elastic behaviour was also closely predicted. Theoretical predictions based on uniaxial-stress behaviour significantly underestimated the experimental response.

It was demonstrated that spiral reinforcement had negligible influence on the moment-curvature characteristics of steel-encased reinforced concrete members (with $34 \leq D/t \leq 214$). This results because the concrete is already well confined by the tube.

5.5.2 Comparison of Results for Test Units with Discontinuous Casings

Flexural strength of test units (see Chapter 4) with circumferential discontinuities in the casings was satisfactorily predicted by assuming that under longitudinal-compression strain the casing contributed to flexural strength,

while under longitudinal-tension strain the casing was unstressed. On the basis of a crude assumption that the moment-curvature relationship was independent of position along the length of the test units, the experimental load-deflection response was shown to be intermediate between that assessed on the basis of continuous casing and the casing being totally ineffective under longitudinal-tension strain.

TABLE 5.1 : MODELS ADOPTED FOR ANALYSIS OF PILES WITH DISCONTINUOUS CASINGS

ANALYSIS	CASING		CONCRETE		LONGITUDINAL BARS
	Compressive ε_L	Tensile ε_L	Compressive ε_L	Tensile ε_L	
"Upper Estimate"	LATERAL INTERACTION	LATERAL INTERACTION	LATERAL INTERACTION	LATERAL INTERACTION	UNIAXIAL
"Likely Behaviour"	LATERAL INTERACTION	UNSTRESSED	LATERAL INTERACTION	UNIAXIAL	UNIAXIAL
"Lower Estimate"	UNSTRESSED	UNSTRESSED	UNIAXIAL	UNIAXIAL	UNIAXIAL

Chapter Six

MODEL TESTS OF STEEL-ENCASED CONCRETE PILES IN A DRY SAND FOUNDATION

6.1 INTRODUCTION

In Chapter 4 it was shown that steel-encased reinforced concrete members responded in a ductile fashion when tested essentially as vertical beams with low longitudinal-compression load and a cyclically varying central lateral load. However as discussed in Section 4.2.3 and shown in Fig. 4.2, it was considered that this loading scheme was more severe than that present on prototype piles subjected to seismic attack. Further, although, as discussed in Section 1.4.2, a substantial number of model and full-scale tests have been conducted of pile-soil systems subjected to lateral load, these tests have almost exclusively been restricted to the elastic range of the pile member's behaviour. Thus to more realistically evaluate the effect of large seismic-induced lateral displacements on pile members, it was decided to conduct 11 tests on small-scale (D = 115 mm) model piles in a dry sand foundation. As a suitable centrifuge device was not available these tests were performed under normal gravity conditions. Although the response of the soil will be grossly affected by this absence of a properly scaled gravity field, it was felt that the lateral structural response of the pile member which is not directly related to the gravity field would be satisfactorily modelled.

The model piles were typically embedded to a depth of 20D in the dry sand foundation. Factors investigated in the tests included:

(i) the method of application of lateral load (monotonic, large amplitude cyclic, or successively from small to large amplitude cyclic);
(ii) the soil density (medium or loose); and
(iii) head condition (free or capped).

Experimental results are presented in the form of lateral load-deflection hysteresis loops, and pile strain and curvature distributions. These results are analysed to obtain pile lateral deflection, bending moment, shear force and soil lateral pressure distributions. The resulting soil lateral pressure-lateral deflection-depth responses are compared with predictions based on the Reese et al. semi-empirical model [6.1). Finally, and of most significance, the relationship between curvature and displacement ductility ratios which was deduced from the experimental results is compared with a prediction based on "equivalent cantilever" response.

6.2 DESIGN OF THE TEST SERIES

The choice of a suitable diameter for the model piles and the overall dimensions of the tank in which the pile and its foundation were contained was based on a compromise. Clearly to avoid severely distorting results between model and prototype, particularly with regard to soil behaviour, it is desirable to conduct tests on as large a scale as possible. However practical considerations

relating to the size of the testing facilities imply that a small scale is desirable. As a compromise, piles with a diameter of 115 mm and a steel tank with inside dimensions of 2.54 m (length-parallel to the line of lateral load application) x 1.3 m (width-perpendicular to the line of lateral load application) x 2.6 m (depth) were chosen. Thus although quite a large quantity of sand was used (approximately 14 tonnes), the tests can be considered to have been conducted at a scale of 1/10 (for typical prototype pile diameter = 1150 mm). For simplicity of testing, and since vertical loads on piles are generally small when compared with the capacity of the pile member itself, the tests were conducted without an externally applied vertical load.

6.2.1 Free-Head Pile Series

The first series of tests involved continuous concrete-filled tubes, without internal reinforcement. These model piles were embedded 20 pile diameters (2300 mm) in the sand foundation and subjected to lateral load at a height of 1.5 pile diameters (173 mm) above sand level (see Fig. 6.1). Model piles were constructed from the same batches of tube and concrete used in the AVERY series of longitudinal-load tests previously described in Chapter 3 (tube diameter D = 115 mm, tube wall thickness t = 4.5 mm, tube yield strength σ_y = 308 MPa and concrete unconfined-compression strength f'_c = 34 MPa - at time of pile tests).

As described later in Section 6.8, a moment-curvature analysis of the model piles was conducted in which it was assumed that concrete and tube behaved in accordance with the "lateral interaction" models (see Chapter 2). At a maximum concrete longitudinal strain of ε_c = 0.003, this analysis indicated that the model piles had a theoretical flexural strength of M_i = 20.0 kNm, and based on an elastic-plastic idealisation of moment-curvature behaviour a yield curvature of ψ_y = 0.0337 rads/m. This implied an idealised elastic flexural stiffness (M_i/ψ_y) of EI = 593 kNm^2.

Originally it had been intended to conduct tests using three densities of sand - dense, medium and loose. However due to subsequent difficulties in densifying such a large volume of sand, only medium (units 2, 3, 4 and 12) and loose (units 1, 5, 6, 7 and 13) densities were achieved. To study the inelastic response of the piles it had also been intended to force the piles to respond in a flexible rather than rigid fashion, since flexible piles are subjected to larger curvatures than are rigid piles.

From Woodward et al (6.2) to obtain flexible pile response (base of pile subjected to insignificant rotation):

$$L_{emb} \cdot \sqrt[5]{\frac{n_h}{EI}} \geq 4.0 \qquad (6.1)$$

while for rigid pile response (base of pile subjected to significant rotation):

$$L_{emb} \cdot \sqrt[5]{\frac{n_h}{EI}} \leq 2 \qquad (6.2)$$

where n_h = coefficient of horizontal subgrade reaction [F/L^3 units]

L_{emb} = embedded length of pile (= 2.3m in pile tests).

For dry cohesionless dense and loose soils Edmonds et al (6.3) recommend n_h = 15000 kN/m^3 and 2000 kN/m^3 respectively, implying $n_h \cong$ 9000 kN/m^3 for a medium density.

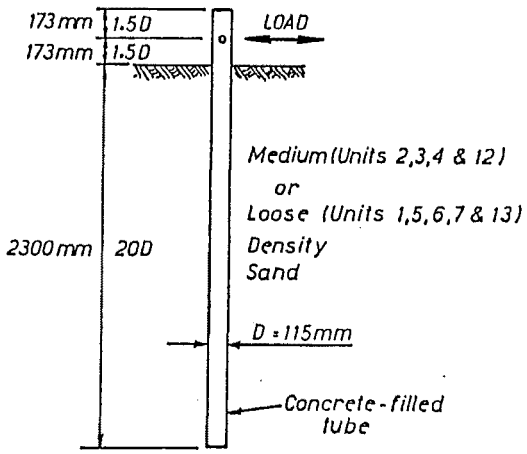

FIG. 6.1 : FREE-HEAD PILE TESTS

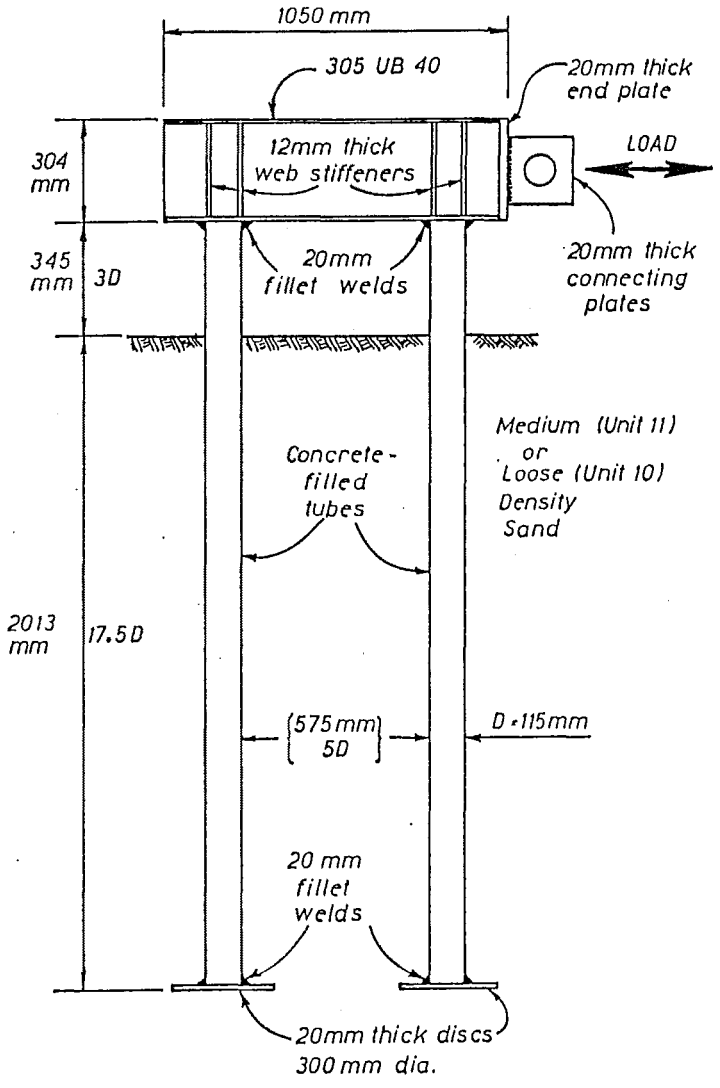

FIG. 6.2 : CAPPED-HEAD PILE TESTS

Thus $L_{emb} \sqrt[5]{\frac{n_h}{EI}} = \begin{cases} 4.4 \text{ dense sand} \\ 4.0 \text{ medium sand} \\ 2.9 \text{ loose sand} \end{cases}$

Hence the tests with a medium density sand were expected to exhibit flexible pile behaviour, while tests with loose sand were expected to exhibit pile behaviour intermediate between that of a flexible and a rigid pile. The dense sand case (not tested) is included above for comparative purposes.

The "equivalent cantilever" method as outlined by Edmonds et al (6.3) was used to estimate the lateral load H_i at the theoretical flexural strength of the pile, and the load-level lateral deflection Δ_y at the yield point (based on idealised elastic-plastic behaviour) of the pile-soil system. The depth-to-fixity (beneath ground level) for the equivalent cantilevers for the purpose of calculating moments (L_m) and deflection (L_D) are calculated as:

$$L_m = 0.78 \left(\frac{EI}{n_h}\right)^{0.2} \tag{6.3}$$

$$L_D = 1.8 \left(\frac{EI}{n_h}\right)^{0.2} \tag{6.4}$$

Thus $L_m = \begin{cases} 0.409 \text{ m} & \text{dense sand} \\ 0.453 \text{ m} & \text{medium sand} \\ 0.612 \text{ m} & \text{loose sand} \end{cases}$

and $L_D = \begin{cases} 0.943 \text{ m} & \text{dense sand} \\ 1.045 \text{ m} & \text{medium sand} \\ 1.411 \text{ m} & \text{loose sand} \end{cases}$

The lateral load H_i at theoretical ultimate flexural strength can then be calculated from:

$$H_i = \frac{M_i}{L_m + 0.173} \tag{6.5}$$

where 0.173 m is the height of load application above the sand surface.

Hence $H_i = \begin{cases} 34.4 \text{ kN} & \text{dense sand} \\ 31.9 \text{ kN} & \text{medium sand} \\ 25.5 \text{ kN} & \text{loose sand} \end{cases}$

Similarly the idealised yield deflection can be calculated from:

$$\Delta_y = \frac{H_i \, (L_D + 0.173)^3}{3EI} \tag{6.6}$$

Hence $\Delta_y = \begin{cases} 26.9 \text{ mm} & \text{dense sand} \\ 32.4 \text{ mm} & \text{medium sand} \\ 57.0 \text{ mm} & \text{loose sand} \end{cases}$

Thus as is commonly recognised, the pile-soil deflection characteristics are more sensitive to the sand density than are the pile-soil strength characteristics.

6.2.2 Capped Head Pile Series

The second series of tests involved twin concrete-filled tubes (no internal reinforcement) which were connected together by a universal beam, as shown in Fig. 6.2. Unit 11 was tested in a medium density sand and unit 10 in a loose sand. The model piles which had the same section and material strengths as those used in the free-head tests were embedded 17.5 D (2013 mm) in the sand foundation, and the pile cap soffit was located 3D (345 mm) above sand level. Lateral load was applied through the midheight of the pile cap. The pile cap (305UB40) had a flexural stiffness of EI = 17000 kNm^2, which was 29 times the value of EI for each pile. Since lateral load will introduce tensile load on one pile and compressive load on the other 20 mm thick 300 mm diameter steel discs were welded on to the base of the piles to restrict vertical movement of the piles.

The "equivalent cantilever" method (6.3) was also used to estimate: (i) the lateral load (H_i) at flexural strength (ε_c = 0.003) of the piles, (ii) the load-level lateral deflection (Δ_y) at the idealised yield point of the pile-soil system, and (iii) the longitudinal loads induced in the piles (P). For this purpose the same values of M_i, L_m and L_D as given in the previous section were used. Allowance was made for the 0.345 m (3D) vertical distance between sand level and the pile cap soffit, the 0.152 m vertical distance between the soffit and the midheight of the pile cap, and the 0.690 m horizontal distance between pile centres.

Hence ignoring the second order effect of vertically induced pile loads, from consideration of Fig. 6.3a, H_i can be calculated as:

$$H_i = \frac{4M_i}{L_m + 0.345} \qquad (6.7)$$

Thus , again including the dense sand case (not tested) for comparative purposes, H_i has values of:

$$H_i = \begin{cases} 106 \text{ kN} & \text{dense sand} \\ 100 \text{ kN} & \text{medium sand} \\ 84 \text{ kN} & \text{loose sand} \end{cases}$$

Similarly, ignoring the effect of longitudinal load, from consideration of Fig. 6.3b, Δ_y can be calculated from:

$$\Delta_y = \frac{H_i (L_D + 0.345)^3}{24EI} \qquad (6.8)$$

Hence $$\Delta_y = \begin{cases} 15.9 \text{ mm} & \text{dense sand} \\ 18.9 \text{ mm} & \text{medium sand} \\ 32.0 \text{ mm} & \text{loose sand} \end{cases}$$

Finally the longitudinal loads induced on the piles can be calculated from consideration of Fig. 6.3a, as:

$$P = \pm \frac{H_i}{0.690} \left(\frac{L_m + 0.345}{2} + 0.152 \right) \qquad (6.9)$$

Thus $$P = \begin{cases} \pm 81 \text{ kN} & \text{dense sand} \\ \pm 80 \text{ kN} & \text{medium sand} \\ \pm 77 \text{ kN} & \text{loose sand} \end{cases}$$

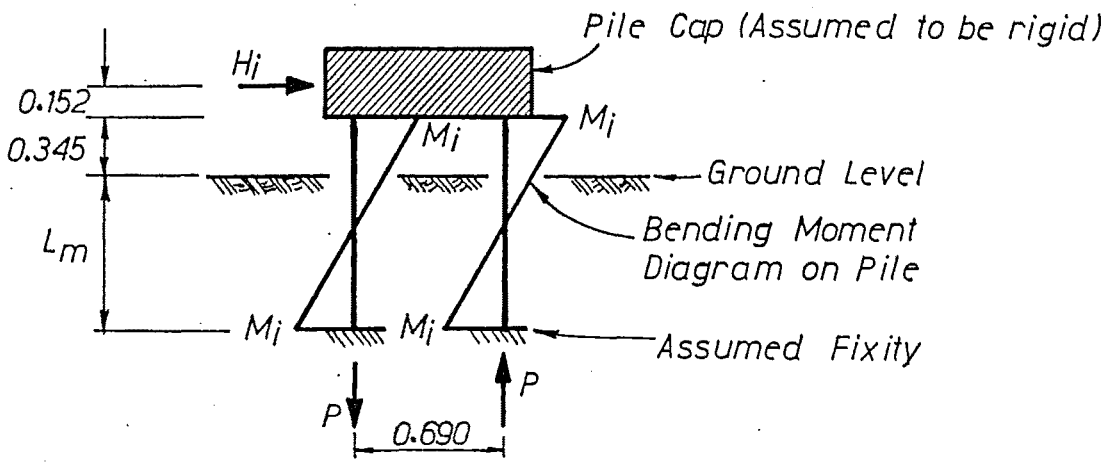

FIG. 6.3(a) CALCULATING THEORETICAL LATERAL LOAD CAPACITY H_i (AND LONGITUDINAL LOAD P).

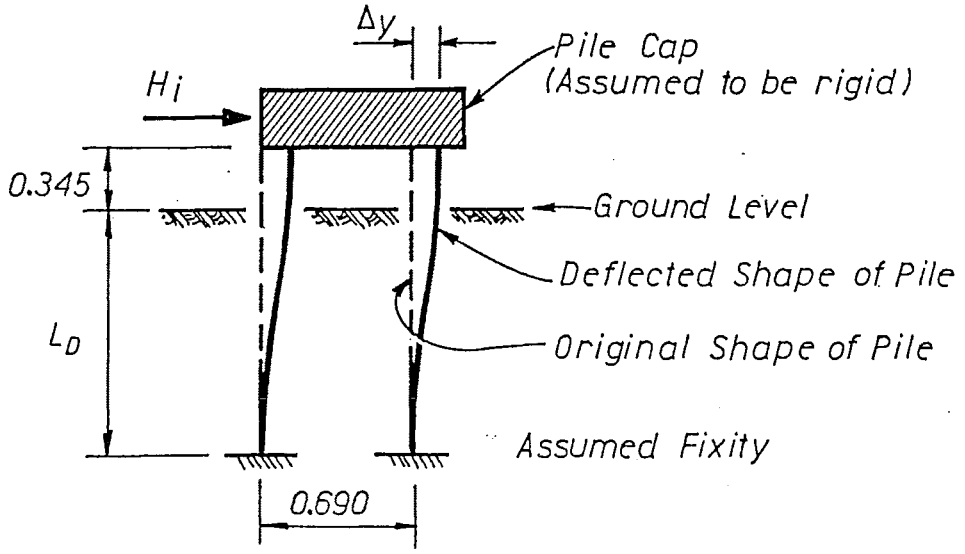

FIG. 6.3(b) CALCULATING THEORETICAL YIELD DEFLECTION Δ_y

6.2.3 Test Rig

The steel tank in which the sand foundation was retained was designed with the intention that the tank boundaries would have a negligible effect on the response of the pile-soil system to lateral load. To fulfill this criterion a tank 2.540 m (length) x 1.3 m (width) x 2.6 m (depth) was designed.

This tank depth gave a vertical distance between the pile and tank bases of:

(i) 587 mm (5.1D) - units 10 and 11 (twin piles connected by a pile cap)

(ii) 185 mm (1.6D) - unit 8

(iii) 300 mm (2.6D) - all other units

} free-head condition

The larger distance was present for units 10 and 11 since piles in these tests were expected to be subjected to substantial vertical loads, whereas all other units were expected to have negligible levels of vertical loads. Figure 6.4 shows the distribution of vertical stress under an infinitely long strip footing derived from elastic half-space solutions as taken from Poulos and Davis (6.4). At a depth of 5.1 times the foundation width the vertical stress will be only approximately 12% of the average pressure present immediately underneath the footing. Thus the tank base should have only a small effect on the performance of units 10 and 11.

Goldsmith (6.5) has conducted model tests on flexible piles with small diameter (4.26 mm $\leq$ D $\leq$ 10.0 mm) embedded in either dense or loose sand and subjected to lateral displacements of up to 0.82D at sand level. Figure 6.5 shows the limits of observable sand displacement which were determined by a stereo-photogrammetric technique. On the basis of results from these tests it would appear that minimum distances from the tank wall to the outside of the pile should be 8D parallel to the line of lateral load and 5D perpendicular to the line of lateral load. To satisfy this criterion for the tests conducted under free-head conditions, edge distances of 1213 mm (10.5D) parallel to the line of lateral load and 593 mm (5.2D) perpendicular to this line were adopted. For the twin pile tests (units 10 and 11) parallel to the direction of load an edge distance of 868 mm (7.5D) was present which is close to the minimum edge distance criterion mentioned above.

Structural details of the steel tank are shown in Fig. 6.6. The tank walls and associated supporting beams were conservatively designed to resist "at-rest-sand pressures" at working stress levels.

Lateral load was transferred to the test units through a double acting hydraulic jack of 500 kN capacity and 300 mm stroke. The frame which was used to react against the hydraulic jack is shown in Fig. 6.7. The beam which protrudes horizontally from the top of the reaction frame over the top of the steel retaining tank was present to facilitate positioning of the test units and the hydraulic jack prior to the commencement of testing.

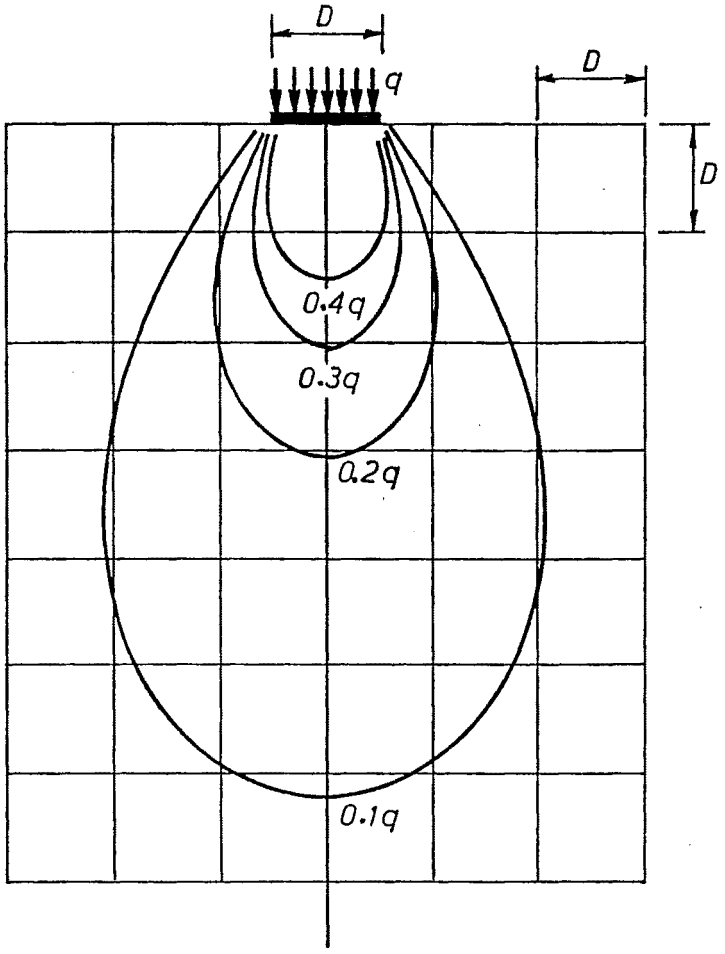

FIG. 6.4 : VERTICAL STRESSES (q) UNDER INFINITELY LONG STRIP FOOTING - AFTER POULOS AND DAVIS (6.4)

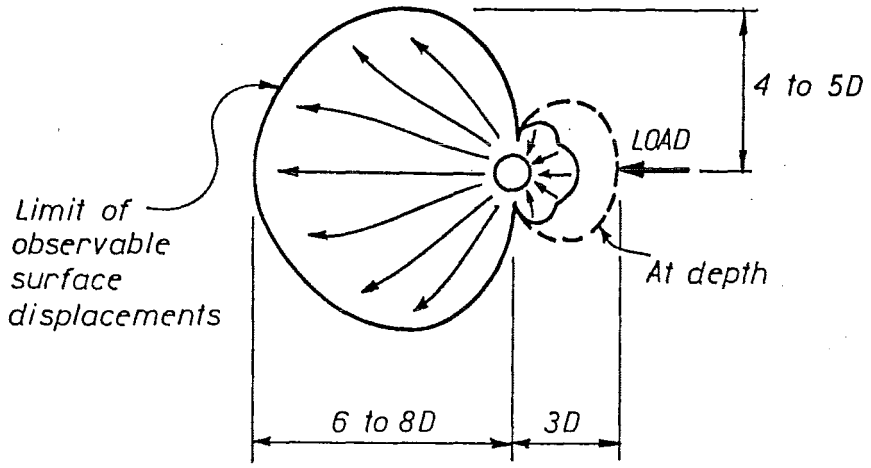

FIG. 6.5 : VECTOR DISPLACEMENT FIELD SHOWING DIRECTION OF SURFACE SAND MOVEMENTS CAUSED BY A LATERALLY LOADED PILE - AFTER GOLDSMITH (6.5)

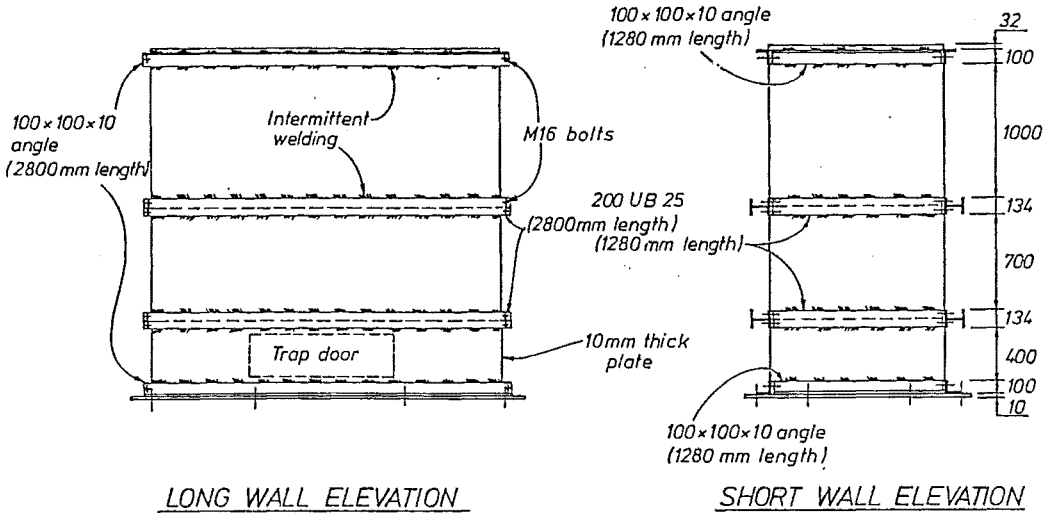

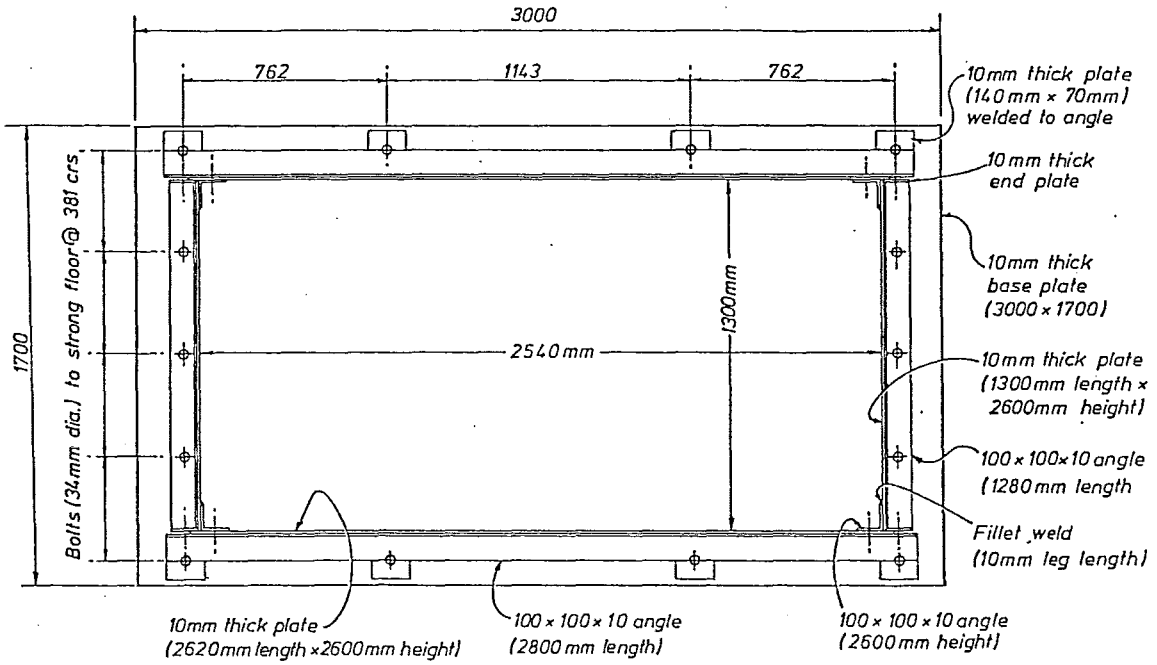

FIG. 6.6 : STRUCTURAL DETAILS OF STEEL RETAINING TANK

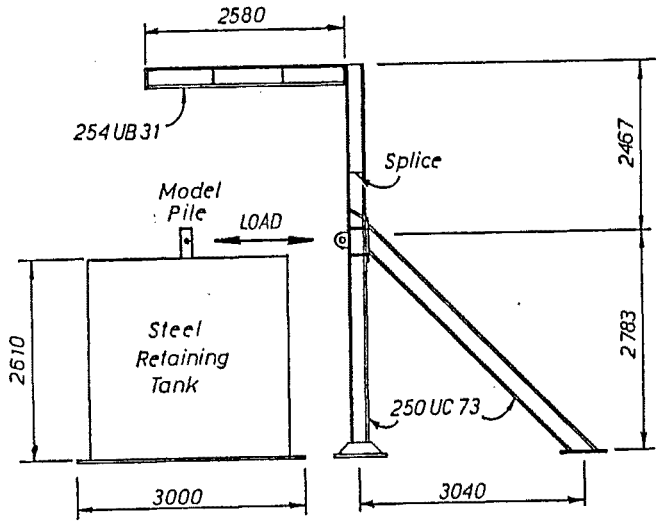

FIG. 6.7 : REACTION FRAME

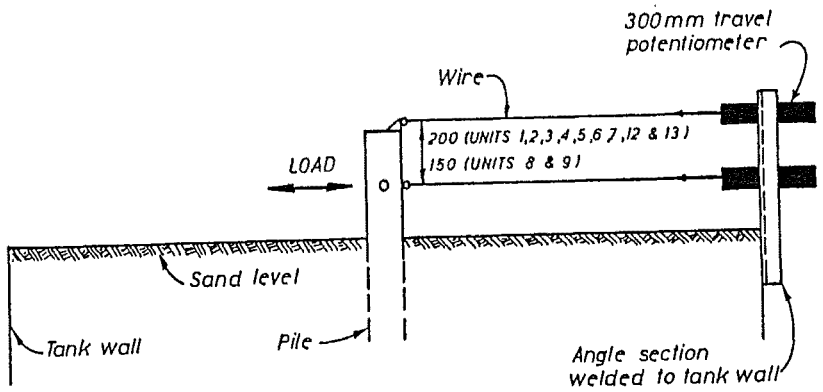

FIG. 6.8 : LOAD-LEVEL DISPLACEMENT AND ROTATION MEASUREMENTS (PILES UNDER FREE-HEAD CONDITION)

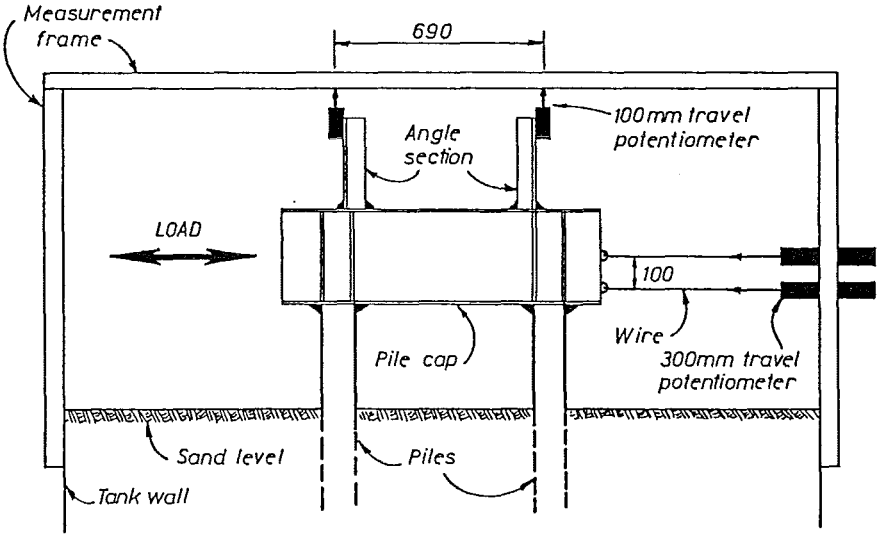

FIG. 6.9 : LOAD-LEVEL DISPLACEMENT AND ROTATION MEASUREMENTS (PILES UNDER CAPPED-HEAD CONDITION)

6.3 CONSTRUCTION OF THE MODEL PILES

The construction sequence for the test units was as follows:

(i) The steel tubes (D = 115 mm and t = 4.5 mm) were received in 3 metre lengths from the manufacturer. These lengths of tube were cut to the lengths indicated in Figs.6.1 and 6.2 with care being taken to ensure that the ends of the tubes were square with the longitudinal direction of the tube.

(ii) For tubes which were to be subsequently tested under free-head conditions, end plates of 10 mm thickness and 115 mm diameter were welded on to the bottom end of the tubes. For tubes which were tested under capped-head conditions, discs of 20 mm thickness and 300 mm diameter were welded on to the bottom end of the tubes.

(iii) For the steel-encased piles which were to be tested under free-head conditions; tubes of 115 mm length, 25.4 mm inside diameter and 6.4 mm wall thickness were inserted and welded to the model piles. These 115 mm length tubes were present to facilitate the transfer of lateral load to the model piles.

(iv) The model piles were then erected into a vertical position and braced against surrounding scaffolding. Concrete, which was provided by a local ready-mix contractor, was poured through the middle of each pile in three lifts per test unit. Following each lift, the concrete was rodded by a 6 mm diameter bar.

(v) The concrete was then left to cure for a week with damp hessian placed over any exposed concrete.

(vi) For the steel-encased piles which were to be tested under free-head conditions, end plates were welded on to the top of the models.

(vii) The steel-encased piles which were subsequently to be tested under capped-head conditions were then located in position and welded on to the pile cap (305UB40).

6.4 INSTRUMENTATION

6.4.1 Lateral Load

Lateral load was monitored through load cells. For tests conducted under free-head conditions, loads of the order of ± 35 kN had been anticipated (see Section 6.2.1). For these tests a load cell of ± 50 kN capacity was utilised which allowed loads to be obtained to a resolution of 0.02 kN and an accuracy of ± 1%. For tests conducted under capped-head conditions, loads of the order of ± 110 kN (see Section 6.2.2) had been anticipated. In these tests a ± 500 kN capacity load cell was used to read loads to a resolution of 0.2 kN and an accuracy of ± 1%.

6.4.2 Load-Level Displacements and Rotation

For the model piles tested under free-head condition, lateral displacement at load-level and either 150 mm or 200 mm above load-level were monitored by the use of 300 mm travel linear potentiometers mounted between the model pile and the end of the tank as shown in Fig. 6.8. The use of two potentiometers mounted in this fashion allowed the subsequent calculation of load-level rotation, as the difference in deflection indicated by these potentiometers divided by the distance between these instruments.

The arrangement of displacement-measuring devices used in the twin-pile tests is shown in Fig. 6.9. Pile cap lateral displacements at load-level and 100 mm beneath load-level were measured by 300 mm travel linear potentiometers. Vertical movements of the piles were monitored by 100 mm travel linear potentiometers mounted coaxially with each of the piles between the top of the pile cap and an overhead measuring frame. Rotation of the pile cap was obtained by two methods:

(i) the difference in deflection between the 100 mm travel potentiometers divided by the distance (690 mm) between these instruments; and

(ii) the difference in deflection between the 300 mm travel potentiometers divided by the distance (100 mm) between these instruments.

Rotations derived from method (i) were expected to be approximately 20 times as accurate as those derived from method (ii). Thus method (ii) was only used as a check on method (i).

The linear potentiometers were Sakae brand. At small ($\leq$ 2% of travel) and large ($\geq$ 10% of travel) values of deflection, the manufacturers claim these instruments have an accuracy of $\pm$ 3% and $\pm$ 1% respectively.

6.4.3 Strain Gauges

Free-Head Pile Series

Nine model piles were tested in the free-head pile series. Three of these models (units 1, 4 and 7) were not strain-gauged, while the other six models (units 2, 3, 5, 6, 12 and 13) were tested with longitudinally orientated strain gauges mounted on the outside of the tube at the extremities of the loading diameter. These strain gauges (SHOWA N34-FA-2-120-11) enabled distributions of pile curvature to be determined, and hence by subsequent analyses (see Section 6.10.1) also distributions of pile lateral deflection, bending moment, shear force and soil lateral pressure.

Originally it had been intended to test model piles in three densities (dense, medium and loose) of sand. Thus as shown in Fig. 6.10, three different arrays of strain gauges were used. In the next chapter, a method for analysing pile-soil systems under lateral load is described. Preliminary analyses using this method were conducted to predict curvature distributions in the model piles. For regions of the piles anticipated to be subjected to large curvatures, strain gauges were placed at small spacing (28 mm = 0.25D); while in regions expected to be subjected to small curvatures, gauges were placed at larger spacing (58 mm = 0.5D or 115 mm = D). From Fig. 6.10, it can be seen that the depth at which peak curvature occurred was expected to increase, as the density of sand decreased.

Since when the tests were actually conducted only medium and loose density sands were achieved, the six units were rearranged to be tested with the three different strain gauge patterns as follows:

(i) Medium Density Sand Tests - Unit 2 (Array I)
Unit 3 (Array I)
Unit 12 (Array II)

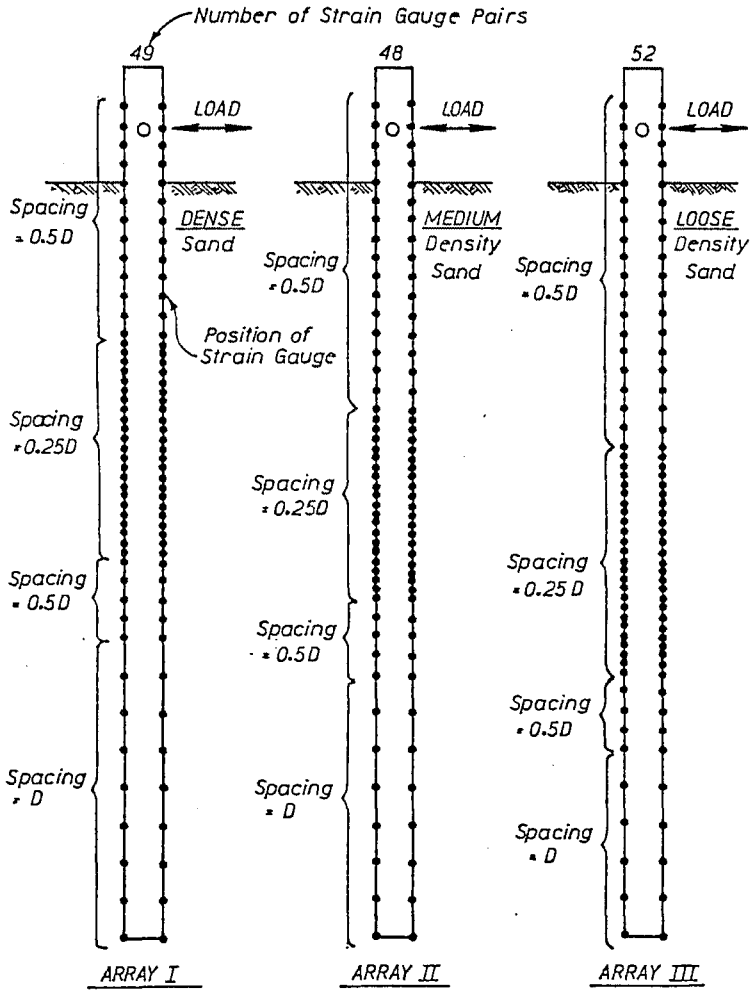

FIG. 6.10 : LONGITUDINALLY ORIENTATED STRAIN GAUGES FOR FREE-HEAD PILE SERIES

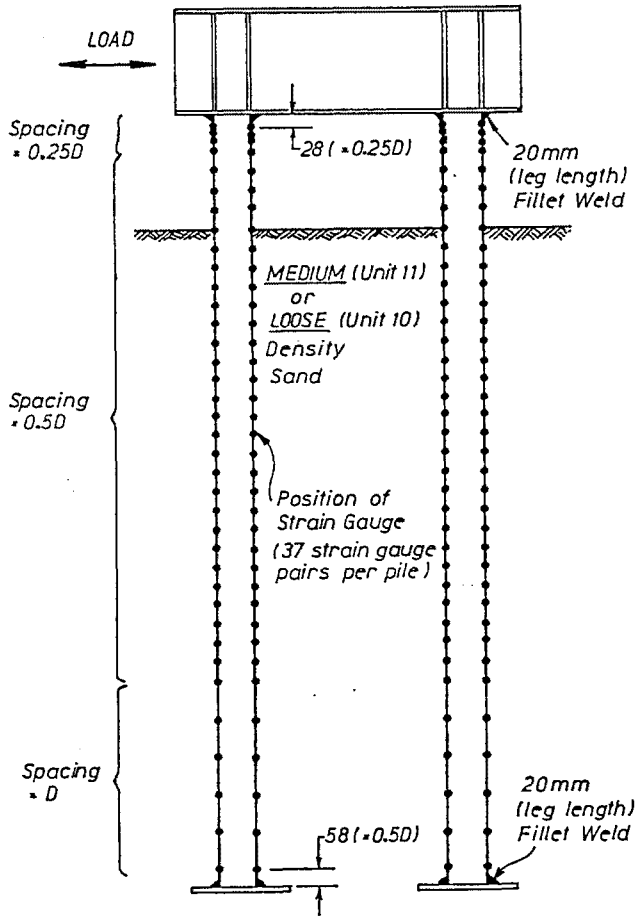

FIG. 6.11 : LONGITUDINALLY ORIENTATED STRAIN GAUGES FOR CAPPED-HEAD PILE SERIES

(ii) Loose Density Sand Tests - Unit 5 (Array II)
Unit 6 (Array III)
Unit 13 (Array III)

As approximately 100 strain gauges were used for each test unit, a substantial volume of strain gauge wiring was also associated with each unit. This wiring was tightly taped to the outside of the tube, with approximately half of the wires proceeding upwards along the pile and the other half downwards along the pile. Because of concern about the effect of these wires modifying the soil-structure interaction of these models, three further tests (units 1, 4 and 7) were conducted without strain gauges.

Capped-Head Pile Series

For the tests (units 10 and 11) involving twin piles connected by a pile cap, a total of 37 strain gauge pairs were mounted on each pile as indicated in Fig. 6.11. Preliminary analyses, in which it was assumed that the pile cap was constrained against rotation and vertical movement, indicated that peak curvatures would occur in the regions of the pile adjacent to the cap. Thus strain gauge spacings were smaller in these regions.

6.5 MATERIAL PROPERTIES

6.5.1 Sand

It was decided to use a dry cohesionless material for the soil medium since:

(i) Relative to most soils, this material is relatively clean and easy to handle.

(ii) It is relatively easy to place uniformly at a known density which means that test results are easily repeatable.

(iii) As the overburden pressure increases so too do the strength and stiffness of uniform sand. Thus sand models most naturally occurring soils which increase in strength and stiffness with depth.

(iv) The response of sand to load is essentially independent of time.

The grading curve for the silica sand which was used in the tests is shown in Fig. 6.12. This indicates that a fine-medium grained sand of uniform grading was used. The average particle size was approximately 0.2 mm (0.0017D). Thus localised effects from individual soil particles were expected to be negligible (cf. a prototype pile in contact with boulders).

Fendall (6.6) and Goldsmith (6.5) have tested model piles at a scale of about 1/100 under normal gravity conditions. They installed model piles in the sand by driving. By using both a stereo-photogrammetric technique and pressure transducers mounted flush with the pile surface, they determined that soil movement and lateral pressures induced by pile-driving were of a similar order to those induced by subsequent large-displacement lateral loading.

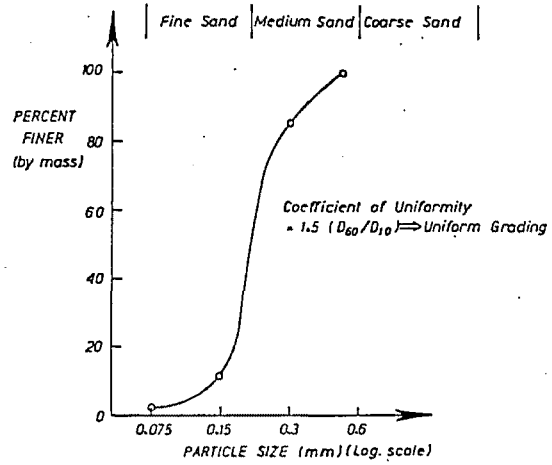

FIG. 6.12 : GRADING CURVE FOR THE SILICA SAND

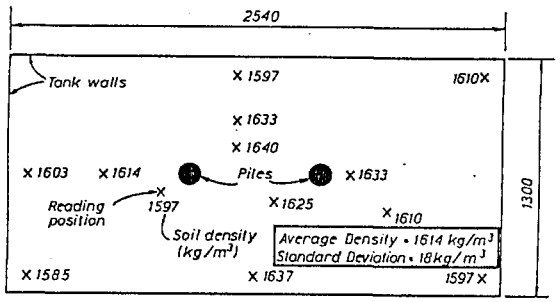

Soil Densities Obtained Prior to Testing Unit 11 (Medium density sand)

FIG. 6.13 : SOIL DENSITY READINGS

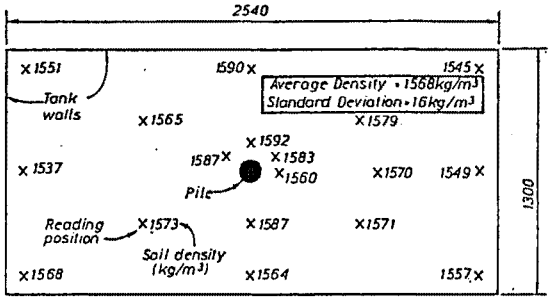

Soil Densities Obtained Prior to Testing Unit 12 (Medium density sand)

FIG. 6.13 (CONTINUED)

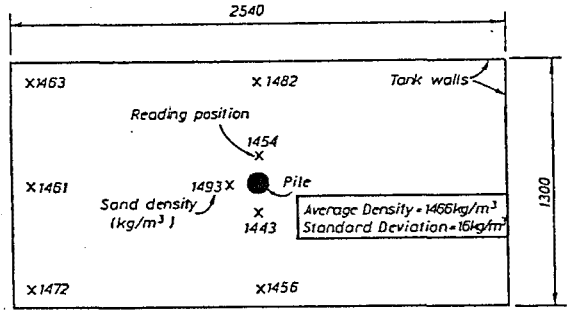

Soil Densities Obtained Prior to Testing Unit 13 (Loose density sand)

FIG. 6.13 (CONTINUED)

Fendall has also commented that sand placed in a box at the same density by different methods (e.g. (i) showering from a height of 500 mm; or (ii) showering from zero height and subsequently applying vibration) will have different strength and stiffness characteristics. Thus clearly the soil properties are very dependent on the method of installing both sand and pile.

In the tests described in this chapter, the model piles were hung in position from an overhead beam and soil was then deposited around the pile. This installment method simulates soil conditions better for bored piles than for driven piles. To achieve a loose density, sand was placed in the retaining tank by showering from a nozzle, the soil was then allowed to roll, thus ensuring a loose compaction. To achieve a medium density, the retaining tank was filled in approximately 300 mm layers with poker vibration being applied after each layer was placed. In addition to this intermittent poker vibration, a vibrating machine was operated continuously during the sand-filling operation which took approximately 2.5 hours and also for a further period of approximately 7.5 hours after the retaining tank had been filled. For the single pile tests, the machine was bolted to the top of the pile, while for the twin pile tests the machine was bolted to the top flange of the pile cap half-way between the piles.

Nuclear densometer readings of the average density of the sand over the top 200 mm of the retaining tank were obtained prior to testing units 11, 12 and 13, as shown in Fig. 6.13. Relatively uniform sand densities were obtained throughout this top layer of sand, since for a given test unit the standard deviation of the readings was approximately equal to 1% of the average of the readings. However for the medium density sands there was a small trend of decreasing sand density as distance from the piles is increased. This could be expected as the main source of vibration was the machine located on top of these piles. From the readings taken prior to testing units 12 and 13 (single pile tests), the loose density sand had an average density of ρ = 1466 kg/m^3, while the medium density sand had an average density of ρ = 1568 kg/m^3. However the readings taken prior to testing unit 11 (twin pile and medium density sand) indicated an average density of ρ = 1614 kg/m^3. Since density readings had not been taken prior to testing units 1-10, it was not known whether the difference in densities between the tests conducted in "medium density sand" for single and twin piles was due to inherent difficulties in exactly reproducing the same soil conditions or due to the different vibration characteristics of the single and the twin piles.

The relationship between soil density ρ and internal angle of friction ϕ was determined by conducting shear box tests on a sample of the sand. Values of ϕ were required to subsequently enable the Reese et al (6.1) semi-empirical model to be used to derive theoretical soil lateral stress-lateral deflection-depth responses. The shear box tests were conducted using a normal pressure of 104 kPa, and difference in density between tests was achieved by varying the amount of vibration applied to the shear box prior to applying shear stress. This is similar to the method used in varying the sand density for the model pile tests. Angles of internal friction ϕ were then calculated from:

$$\phi = \tan^{-1}\left(\frac{\tau}{104}\right) \qquad (6.10)$$

where τ = maximum shear stress applied to the sand sample [kPa units].

The resulting ϕ vs ρ relationship is shown in Fig. 6.14. For soil densities of ρ = 1466 kg/m^3 (unit 13 - loose density sand, single pile), 1568 kg/m^3 (unit 12 - medium density sand, single pile) and 1614 kg/m^3 (unit 11 - medium density sand, twin piles); a regression line through the ϕ - ρ data gives ϕ = 27.3°, 29.6° and 30.6° respectively. These three ϕ values compare favourably with the Peck

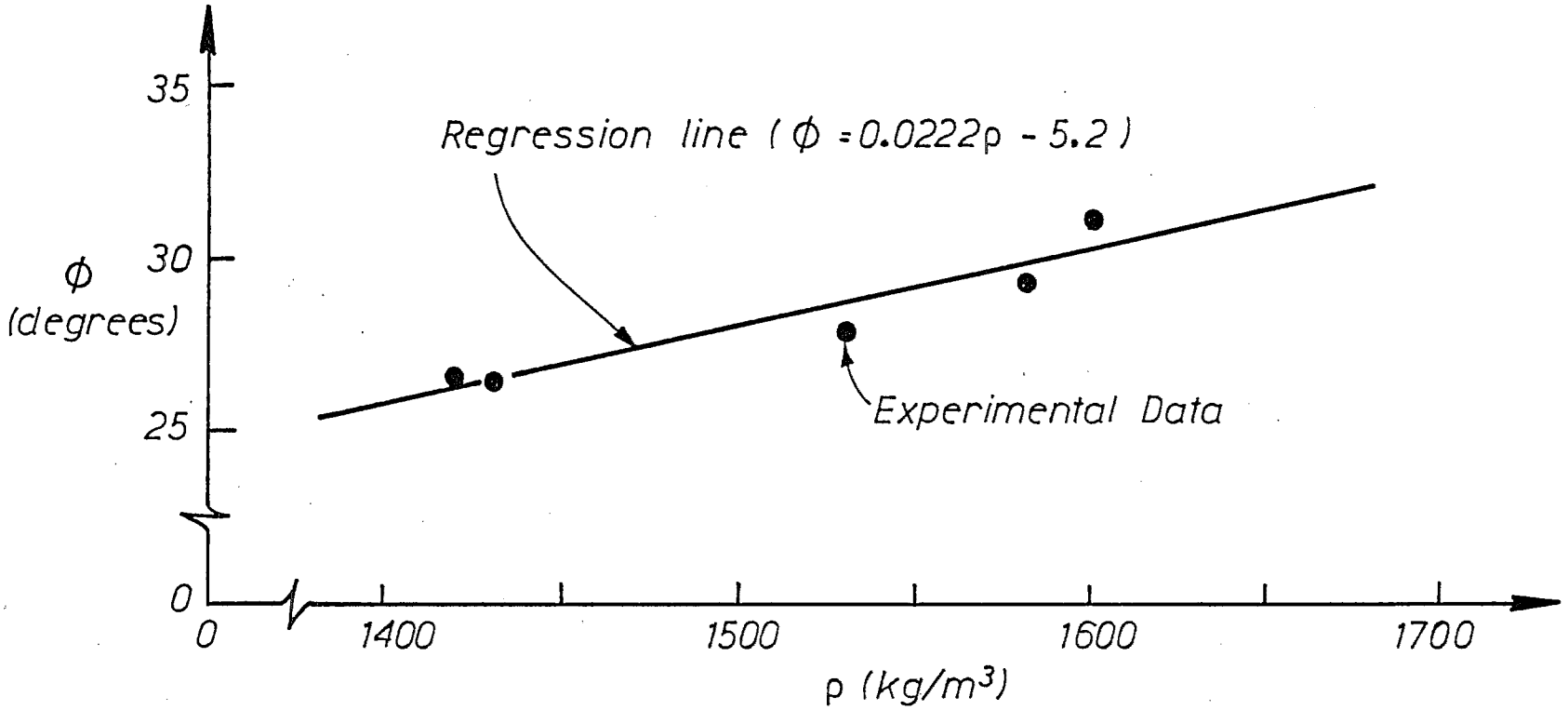

FIG. 6.14 ANGLE OF INTERNAL FRICTION ϕ VS DENSITY ρ .

et al (6.7) representative values for a uniform graded sand of 27.5° (loose) - 34° (dense).

For the purpose of conveying the sand a 5 metre long auger was used. This auger was driven by a 2.7 kilowatt motor and discharged sand through a flexible rubber hose. This enabled the retaining tank to be filled (or discharged) in a period of approximately 2.5 hours. The retaining tank was discharged through a trap door near the bottom of one of the long walls (see Fig. 6.6). In between tests, sand was temporarily stored in a wooden retaining bin.

Finally with the advantage of hindsight it is recommended that if similar tests to these are performed a coarser grained sand should be used, since the fine grained sand used in these tests created a severe dust nuisance.

6.5.2 Tubes

The tubes used in the model pile tests were from the same batch of steel as those used in the longitudinal load tests described previously in Chapter 3. Stress-strain responses of coupon samples of the tube were shown in Fig. 3.1.

The tubes had a diameter of D = 115 mm and a wall thickness of t = 4.5 mm giving a tube D/t ratio of 26. Although this casing D/t ratio is smaller than that typically used in prototype piles ($60 \leq D/t \leq 180$), it meant that reliable strain gauge readings could be obtained to high longitudinal strain levels. From the results of Chapter 4, if thinner walled tubes had been used local buckling at relatively low ductility levels could have resulted in erratic gauge readings which would have made the study of pile inelastic behaviour hard to quantify.

6.5.3 Concrete

Concrete used in the model pile tests was from the same batch as that used in the AVERY series of longitudinal load tests discussed previously in Chapter 3. Details of the concrete were given in Section 3.2.3. However it should be noted that the model pile tests were conducted at a later stage than the longitudinal load tests, by which time the concrete cylinder strength had increased from 32 to 34 MPa.

6.6 TEST PREPARATION

Figure 6.15 shows a photograph of test unit 10 (twin piles connected to a pile cap) immediately prior to this unit being positioned in the retaining tank, the large volume of strain gauge wiring and the steel discs welded to the base of the piles which were present to help restrain longitudinal movement of the piles are evident. Figure 6.16 shows a photograph of the sand-filling operation in action. Figures 6.17 and 6.18 show close-up and far-off views respectively of the test set-up immediately prior to the testing of unit 10.

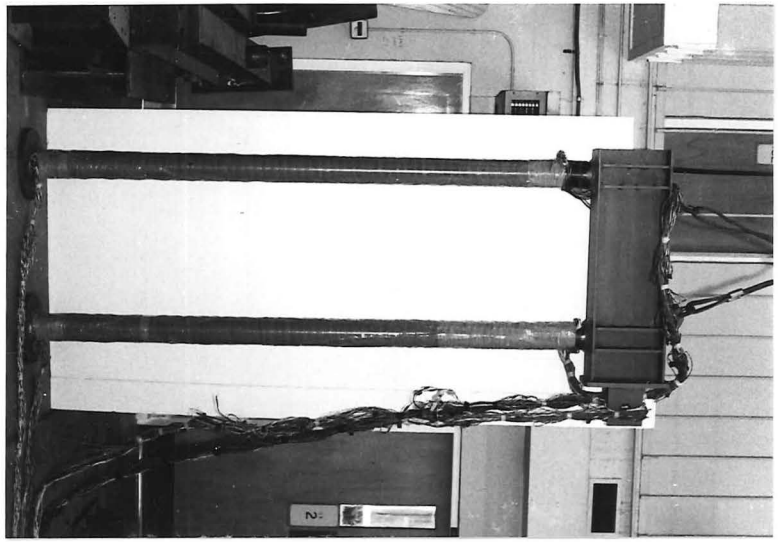

FIG. 6.15 : UNIT 10 IMMEDIATELY PRIOR TO BEING POSITIONED IN THE RETAINING TANK

FIG. 6.16 : SAND-FILLING OPERATION IN ACTION

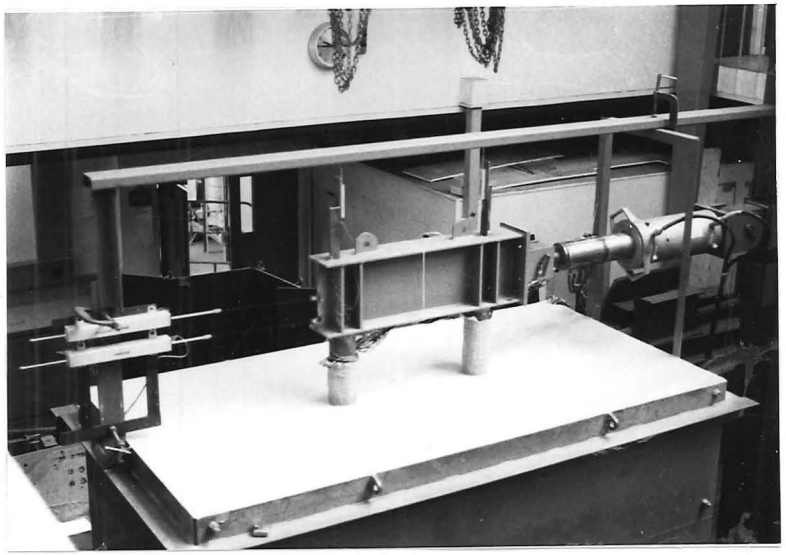

FIG. 6.17 : CLOSE-UP VIEW OF THE TEST SET-UP FOR UNIT 10

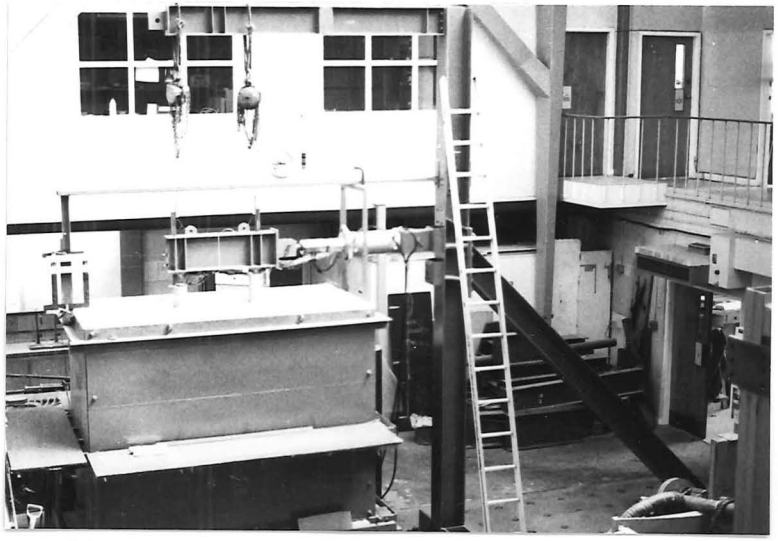

FIG. 6.18 : FAR-OFF VIEW OF TEST SET-UP FOR UNIT 10

6.7 TEST PROCEDURE

Testing involved the slow incremental application of lateral displacement to the model piles. Lengthy pauses were taken in between displacement increments so that data could be recorded and observations of pile and sand movements could be made.

Three types of lateral displacement patterns were planned for the tests as shown in Fig. 6.19 and described below:

(i) The first pattern involved monotonically loading the units out to a load-level lateral displacement of the order of 300 mm (2.6D).

(ii) The second pattern involved large amplitude cyclic lateral loading at a load-level displacement of either ± 0.5D or ± D.

(iii) The third pattern involved successively small to large amplitude lateral loading with 2 cycles to load-level displacements of ± 0.025D, ± 0.05D, ± 0.1D, ± 0.2D, ± 0.3D, ± 0.4D, ± 0.5D, ± 0.75D and ± D.

In addition, for some of the cyclic tests a large displacement pulse was applied as a finale to the tests. Test units 12 and 13 were tested with pattern (i), units 1, 2 and 6 with pattern (ii) and units 3, 4, 5, 7, 8, 9, 10 and 11 with pattern (iii).

It should be noted that the above displacement patterns are very severe in terms of modelling the effects of earthquakes on piles. Berrill et al (6.8) recommend that in New Zealand seismic displacements at the centre of mass of a single degree-of-freedom oscillator be calculated from:

$$\Delta_\mu = C_{\Delta\mu} \cdot Z_H \qquad (6.11)$$

where Z_H = return period coefficient (= 0.80 for 100 year return period earthquake , and 1.33 for a 250 year return period earthquake)

$C_{\Delta\mu}$ = basic displacement coefficient [mm units].

Figure 6.20 shows a plot of $C_{\Delta\mu}$ as a function of design displacement ductility level μ and fundamental period of vibration T of the oscillator for New Zealand seismic zone A.

Typical prototype bridge substructures will have $T \leq 1.5$ seconds, which implies that $C_{\Delta\mu} \leq 300$ mm. For structures which use large diameter piles, the values of T and hence $C_{\Delta\mu}$ will tend to be smaller than those obtained for structures using small diameter piles. However for typical prototype piles with diameters in the range of 600 mm-1800 mm and $C_{\Delta\mu} = 300$ mm, this implies that a severe earthquake (e.g. return period = 250 years) will impose lateral displacements in the range of 0.22D - 0.67D at the bridge centre of mass. These levels of displacement are considerably smaller than the displacements of up to 2.6D which were imposed on the model piles.

6.8 SUMMARY OF TEST UNIT DETAILS

Table 6.1 provides an overall summary of test unit details (e.g. head condition, soil density and displacement patterns).

Results from moment-curvature analyses of the steel-encased pile sections are given in Fig. 6.21. These analyses were performed using the "lateral interaction" models (see Chapter 2) and actual material properties of the tube

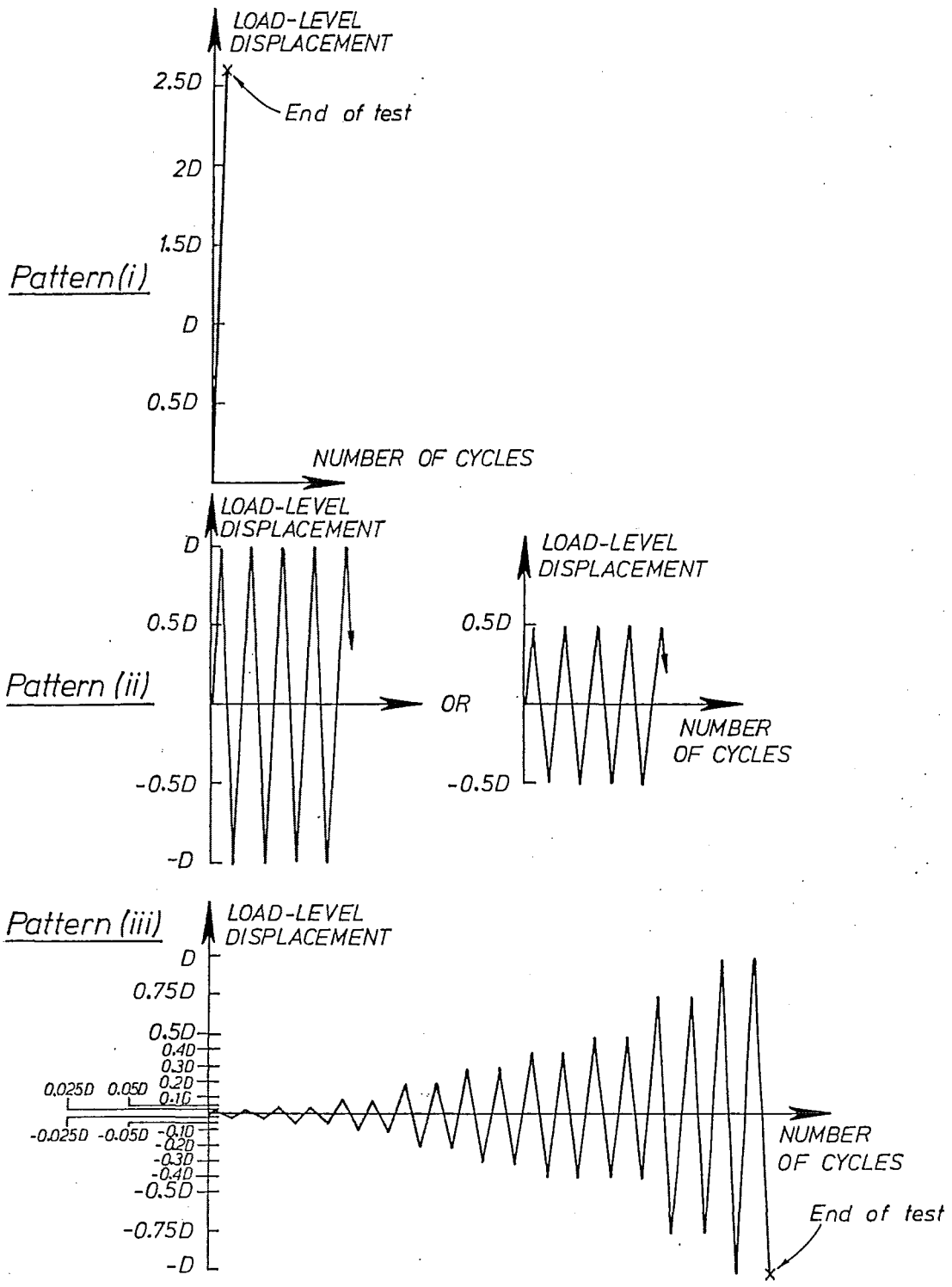

FIG. 6.19 PLANNED LATERAL DISPLACEMENT PATTERNS.

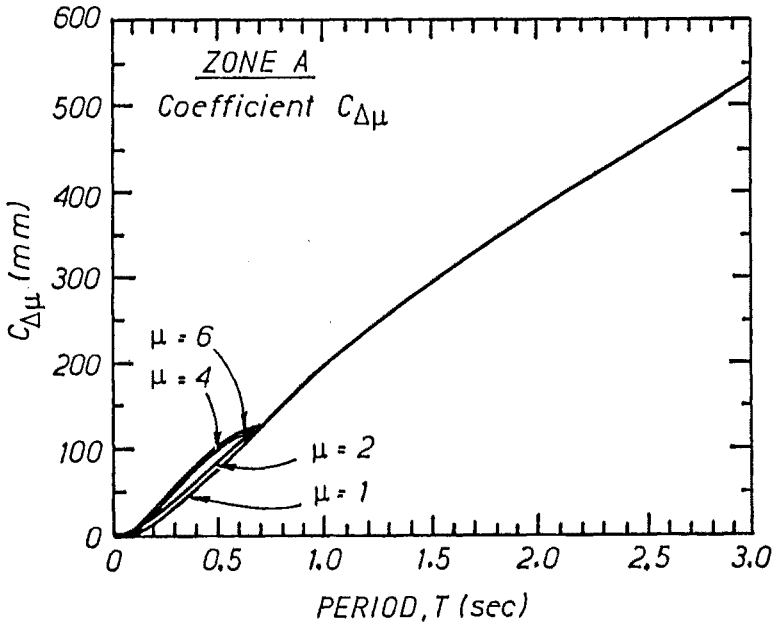

FIG. 6.20 : OBTAINING BASIC DISPLACEMENT COEFFICIENT $C_{\Delta\mu}$ FOR NEW ZEALAND SEISMIC ZONE A - AFTER BERRILL ET AL (6.8)

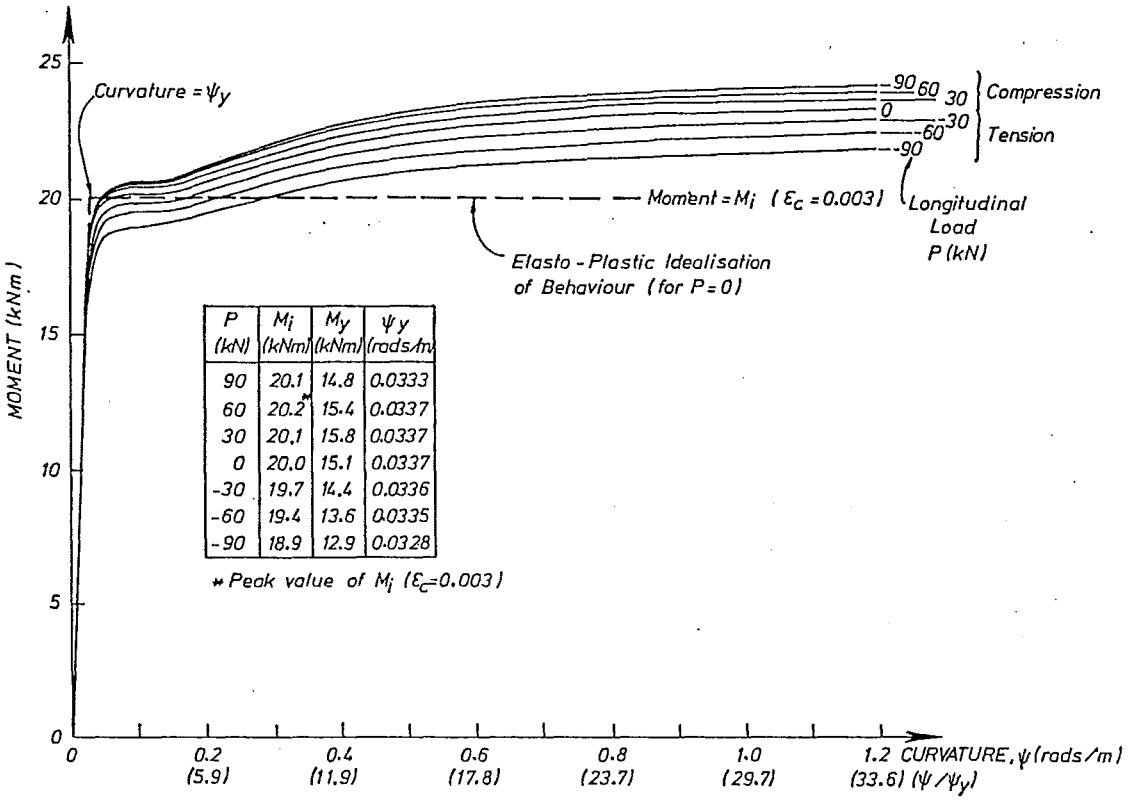

P (kN)	M_i (kNm)	M_y (kNm)	ψ_y (rads/m)
90	20.1	14.8	0.0333
60	20.2*	15.4	0.0337
30	20.1	15.8	0.0337
0	20.0	15.1	0.0337
-30	19.7	14.4	0.0336
-60	19.4	13.6	0.0335
-90	18.9	12.9	0.0328

* Peak value of M_i (ε_c=0.003)

FIG. 6.21 : MOMENT-CURVATURE RESPONSE OF MODEL PILES

and concrete. Since for the twin-pile tests the overturning effect of the lateral load induces longitudinal load in the piles, the moment-curvature analyses were conducted at a variety of levels of longitudinal load ($P = 0$, ± 30 kN $= \pm 0.08f'_c(A_c + A_t)$ ± 60 kN $= \pm 0.17f'_c(A_c + A_t)$, ± 90 kN $= \pm 0.25f'_c(A_c + A_t)$ to cover the anticipated range of longitudinal loads which were shown in Section 6.2.2. From these analyses, moments at $\varepsilon_c \doteq 0.003$ (M_i) and first yield of the steel (M_y), and the curvature at idealised yield (ψ_y) of the section based on an elastic-plastic idealisation of behaviour (see Section 5.3.4) were obtained. These values are listed in Fig. 6.21.

Within the range of longitudinal loads P which were analysed, Fig. 6.21 shows that the idealised yield curvature ψ_y is insensitive to P since the ratio of the maximum to the minimum value of ψ_y is 1.03. This occurs because as the level of longitudinal-compression load increases, flexural strength and stiffness increase at approximately the same rate. Thus a yield curvature of $\psi_y = 0.0337$ rads/m ($P = 0$ case) is taken as being approximately appropriate over the anticipated range of longitudinal loads (-90 kN $< P <$ 90 kN). The average ratio of M_y to M_i was 0.74, which indicates that the curvature at first yield of the tube was approximately equal to $0.74\psi_y$ (74% of the idealised yield curvature). The analyses also show that significant overstrength of the piles can occur. For example at a curvature of $\psi = 1.2$ rads/m (curvature ductility ratio of $\psi/\psi_y = 35.6$), flexural strength is approximately equal to $1.17M_i$ (117% of the moment at a maximum concrete strain of $\varepsilon_c = 0.003$).

TABLE 6.1 : SUMMARY OF TEST UNIT DETAILS

Unit Number	Strain-Gauges	Head Condition	Members	Initial Soil Density	Displacement Pattern
1	No	Free	Concrete-filled tube	Loose	Large Amplitude Cyclic
2	Yes	Free	Concrete-filled tube	Medium	Large Amplitude Cyclic
3	Yes	Free	Concrete-filled tube	Medium	Small to Large Amplitude Cyclic
4	No	Free	Concrete-filled tube	Medium	Small to Large Amplitude Cyclic
5	Yes	Free	Concrete-filled tube	Loose	Small to Large Amplitude Cyclic
6	Yes	Free	Concrete-filled tube	Loose	Large Amplitude Cyclic
7	No	Free	Concrete-filled tube	Loose	Small to Large Amplitude Cyclic
10	Yes	Capped	Concrete-filled tubes + Pile Cap	Loose	Small to Large Amplitude Cyclic
11	Yes	Capped	Concrete-filled tubes + Pile Cap	Medium	Small to Large Amplitude Cyclic
12	Yes	Free	Concrete-filled tube	Medium	Monotonic
13	Yes	Free	Concrete-filled tube	Loose	Monotonic

Note: No units 8 and 9.

6.9 EXPERIMENTAL RESULTS - FREE HEAD PILES

The following sections contain the experimental results from the steel-encased concrete model piles (units 1-7, 12 and 13) tested under free-head conditions.

6.9.1 General Observations

Sand movement first became visually obvious when the load-level lateral displacement of the pile was of the order of 0.025D (2.9 mm). At this stage, sand that was immediately in front of the pile had heaved, while sand immediately behind the pile had settled. As testing, either cyclic (units 1-7) or monotonic (units 12 and 13), proceeded the extent and magnitude of sand movement increased and indications of sand shear dislocation also became apparent on the top surface of the sand.

Figures 6.22 and 6.23 contain photographs which show the development of pile and sand movement as the monotonic lateral loading of unit 12 (medium density sand) and 13 (loose density sand) proceeded. From these figures at load-level lateral displacement of 0.2D and larger, the surfacing of roughly fan-shaped zones of soil shear failure is apparent. The surface dimensions of these zones at peak load-level displacement ($\cong$ 298 mm = 2.6D) and a method for calculating the depth D_w at which the passively formed wedge of sand intersects the pile are shown in Fig. 6.24. From Figs. 6.22-6.24 it can be seen that a larger volume of sand was subjected to shear failure in the medium density (unit 12) than in the loose density (unit 13) sand test. From the information given in Fig. 6.24 and the values of angle of internal friction ϕ given in Section 6.5.1 (ϕ = 27° for loose density and 30° for medium density), the depth of the soil wedges D_w can be estimated as 350 mm (3.0D) in the medium density sand and 250 mm (2.1D) for loose density sand.

Figure 6.25 shows a comparison of the sand profiles at longitudinal and lateral centreline sections of the tank at the peak load-level displacements ($\cong$ 298 mm = 2.6D) attained in units 12 and 13. For both units 12 (medium density sand) and 13 (loose density sand), significant densification of the sand occurred in the vicinity of the model pile, although this is more marked for the model pile tested in loose sand. At the centre of the roughly conical-shaped depression which formed in the wake of the pile, the surface level had settled by 185 mm (= 1.61D) in the medium density test and 200 mm (= 1.74D) in the loose density test. For both units 12 and 13, as shown in Figs. 6.22-6.24, the zones of soil shear failure were at least 100 mm clear of the walls, so major modification to the soil behaviour due to boundary effects from the tank wall should not have resulted.

Figure 6.26 shows a comparison between units 5(loose density sand, small to large amplitude cyclic loading), 6 (loose density sand, large amplitude cyclic loading) and 13 (loose density sand, monotonic loading) of sand profiles at a load-level pile lateral displacement of 0.5D (57.5 mm). Clearly a large decrease in soil volume, and hence increase in soil density, occurs due to the cyclic loading. Figure 6.27 shows a similar comparison for tests conducted in medium density sand where the reduction in volume which occurs with cyclic loading is significant but not as marked as for loose density sand.

Evidence of an increase in sand density, in the cyclic tests, was also gained by measuring the angle of repose of the sand slopes in the roughly conical-shaped depressions which trailed the pile. For the loose density sand tests, the angle of repose was observed to increase from 30° (at displacement $\cong$ 0.2D) to 36° (end of test), while for the medium density sand tests the angle increased from 38° to 41°. It should be noted that these angles of repose are in poor agreement with the angles of internal friction ϕ for the sand which from Section 6.5.1 were

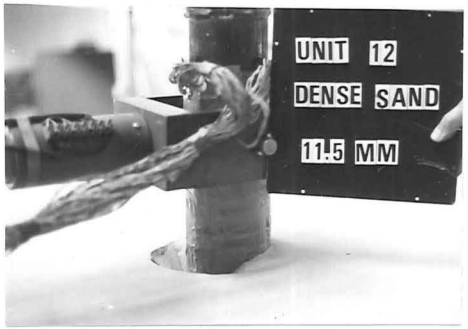

(a) DISPLACEMENT = 0.1D

(d) DISPLACEMENT = 0.5D

(g) DISPLACEMENT = 2D

(b) DISPLACEMENT = 0.2D

(e) DISPLACEMENT = 0.75D

(h) DISPLACEMENT = 2.59D

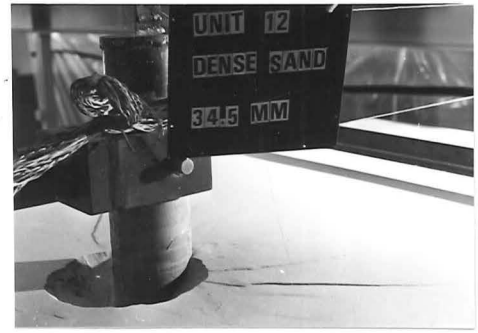

(c) DISPLACEMENT = 0.3D

(f) DISPLACEMENT = D

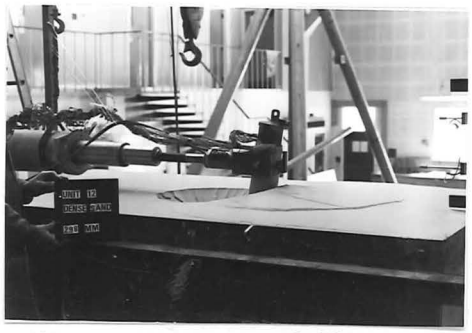

(i) DISPLACEMENT = 2.59D

FIG. 6.22: UNIT 12 (MONOTONIC TEST, MEDIUM DENSITY SAND)

(a) DISPLACEMENT = 0.5D

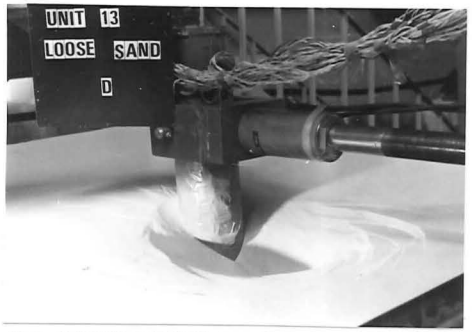

(b) DISPLACEMENT = D

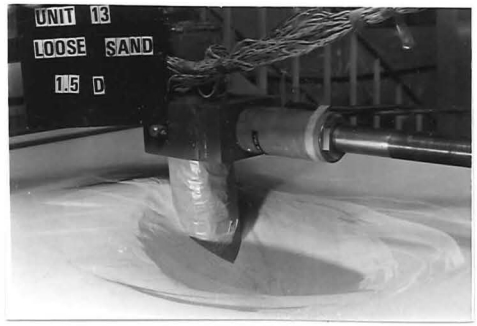

(c) DISPLACEMENT = 1.5D

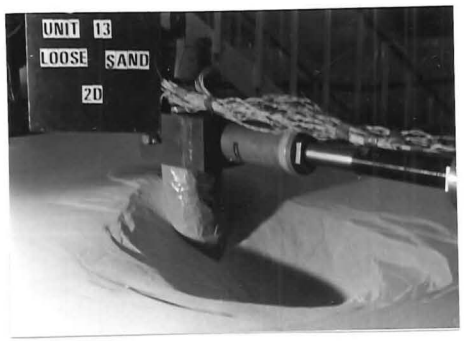

(d) DISPLACEMENT = 2D

(e) DISPLACEMENT = 2.5D

(f) DISPLACEMENT = 2.6D

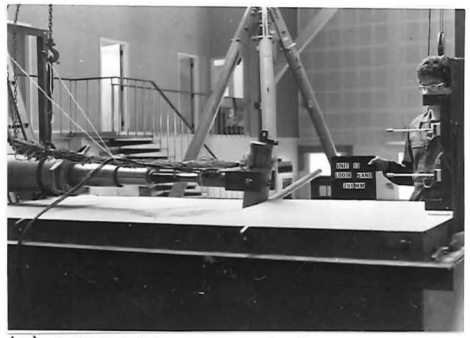

(g) DISPLACEMENT = 2.6D

FIG. 6.23 : UNIT 13 (MONOTONIC TEST, LOOSE DENSITY SAND)

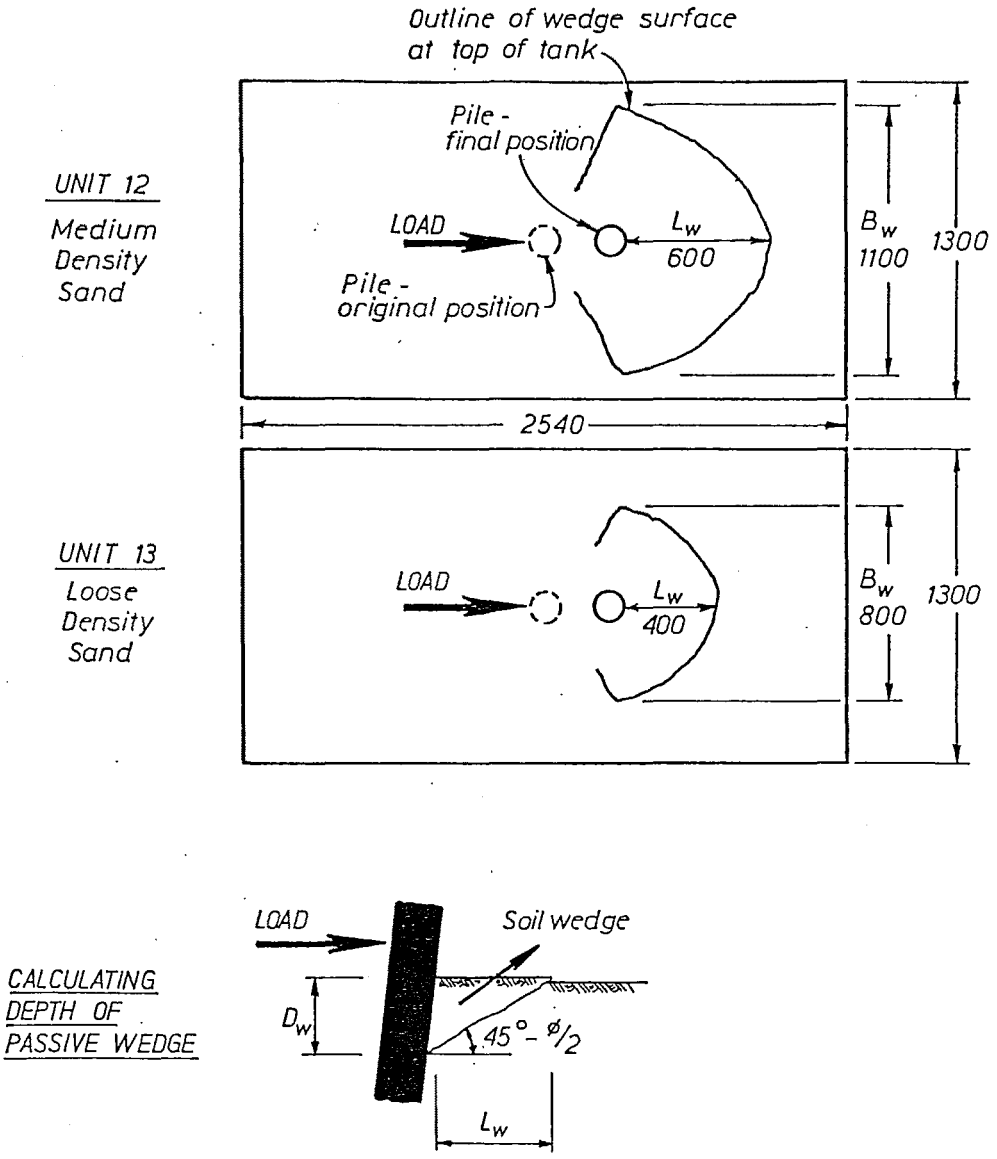

FIG. 6.24 EXTENT OF SOIL PASSIVE WEDGES AT LOAD-LEVEL LATERAL DISPLACEMENT ≅ 298 MM.

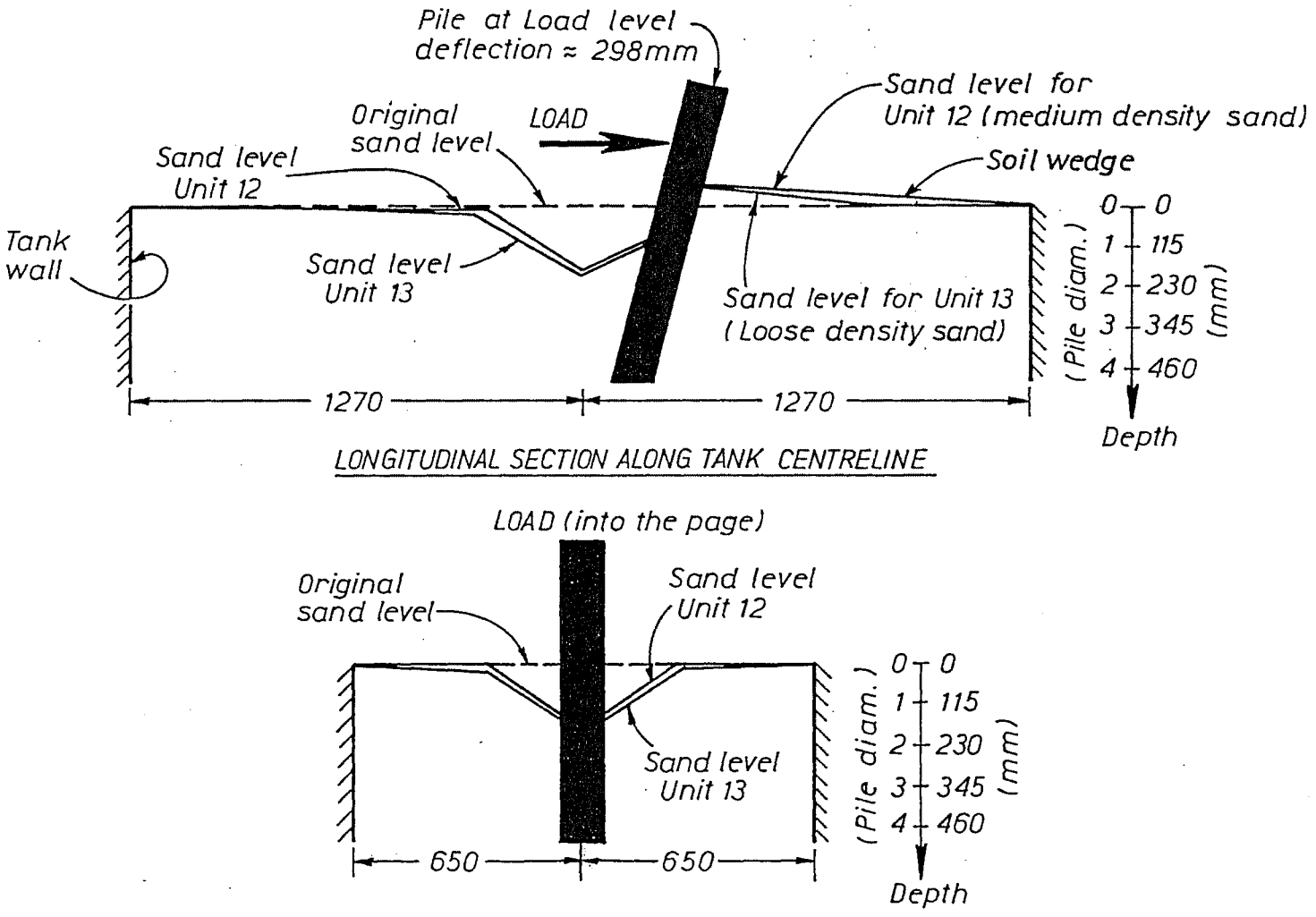

FIG. 6.25 COMPARISON BETWEEN MONOTONIC TESTS CONDUCTED IN MEDIUM AND LOOSE DENSITY SANDS (LOAD-LEVEL LATERAL DISPLACEMENT ≅ 298 MM).

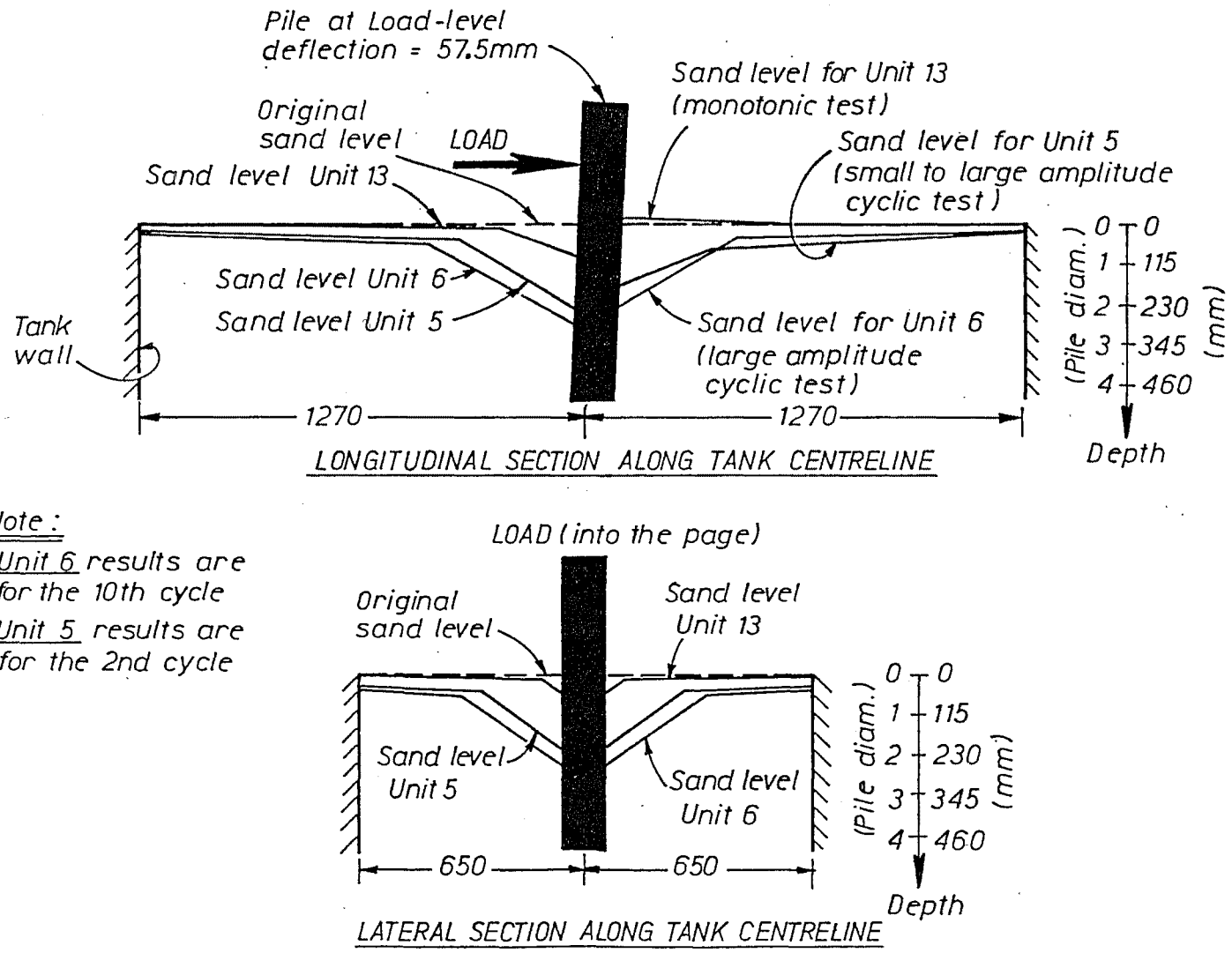

FIG. 6.26 COMPARISON BETWEEN CYCLIC AND MONOTONIC TESTS CONDUCTED IN A LOOSE DENSITY SAND (LOAD-LEVEL LATERAL DISPLACEMENT = 57.5 MM)

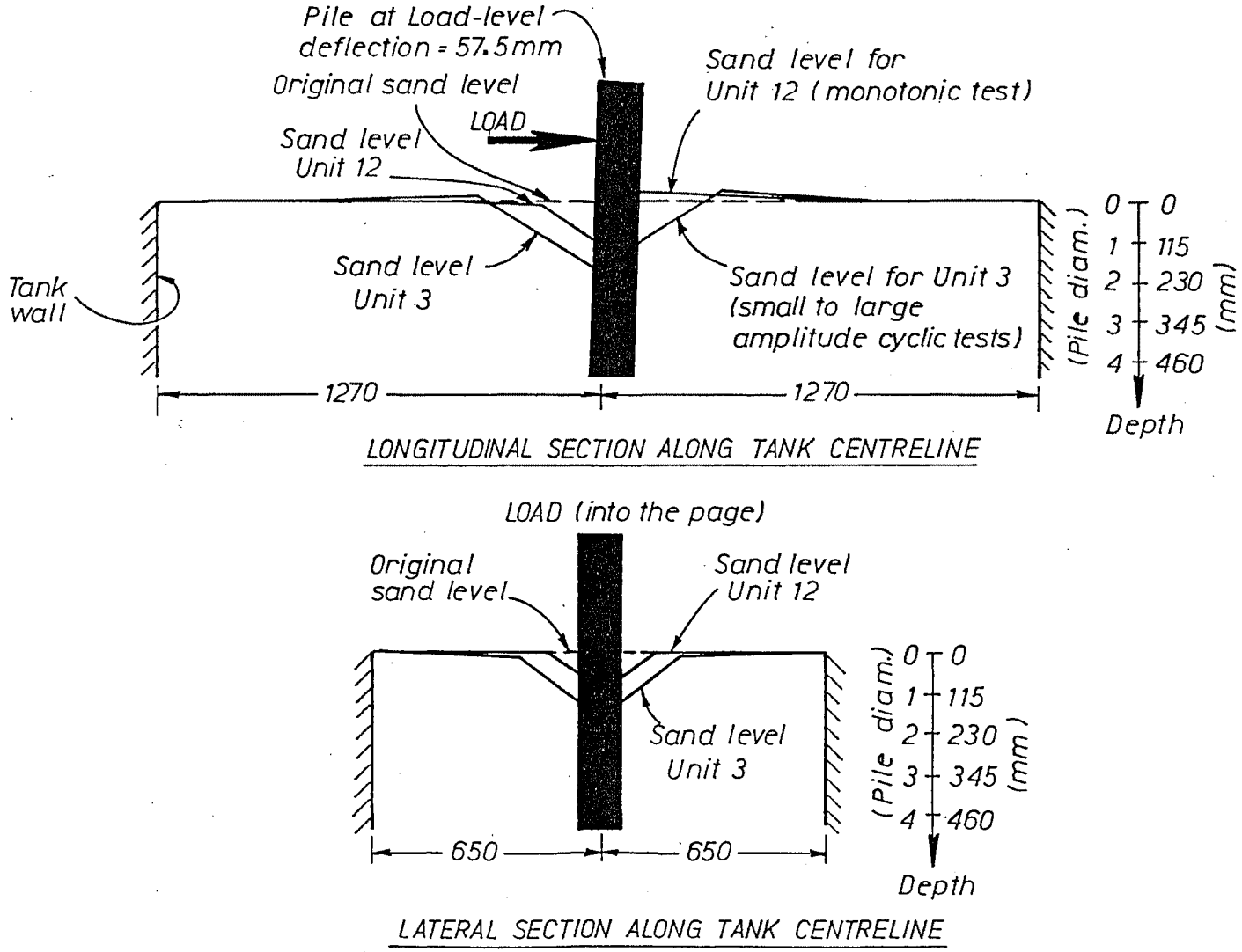

FIG. 6.27 COMPARISON BETWEEN CYCLIC AND MONOTONIC TESTS CONDUCTED IN A MEDIUM DENSITY SAND (LOAD-LEVEL LATERAL DISPLACEMENT = 57.5 MM)

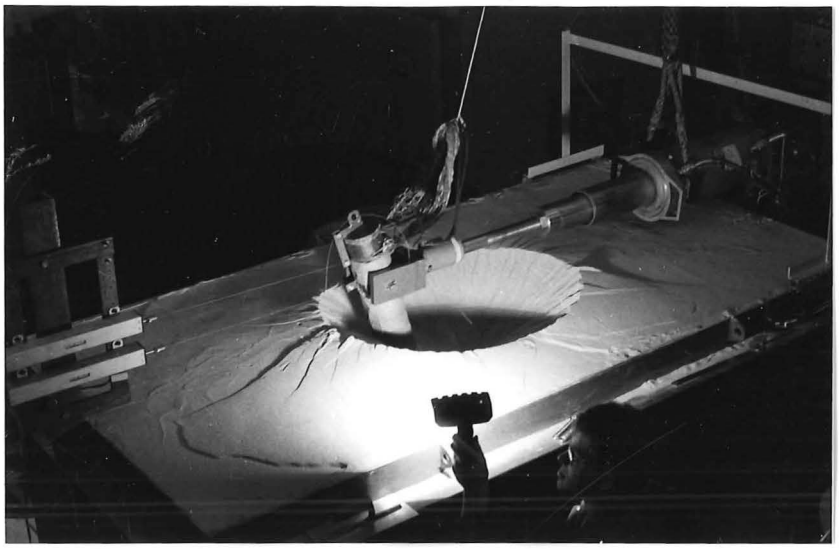

FIG. 6.28 : SOIL PASSIVE WEDGE INTERSECTING TANK WALL DURING FINAL STAGE OF TESTING UNIT 2

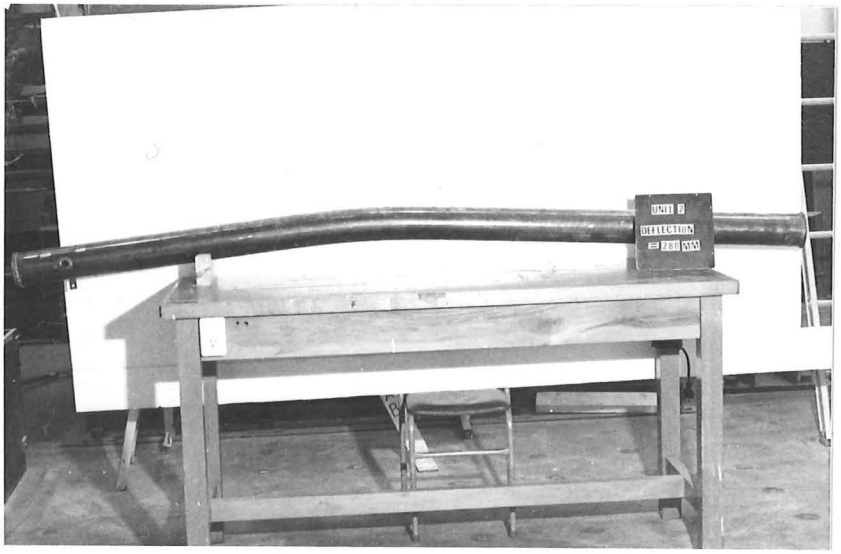

FIG. 6.29 : CONDITION OF UNIT 2 AFTER TESTING

expected to be in the range of 27° (loose) - 34° (dense). The reason for this discrepancy is that the angle of internal friction ϕ is not a constant as is commonly assumed, but is a function of the overburden pressure as has been verified by Fukushima and Tatsuoka (6.11) and Ponce and Bell (6.12). Thus the difference in these two sets of experimentally obtained angles can be explained by the lack of overburden pressure which applies to the angle of repose measurements and the effective overburden pressure of 104 kPa which applies to the angles of internal friction determined from the shear box tests (see Section 6.5.1).

As with the monotonic tests, shear dislocation on the top surface of the sand was observed in the cyclic tests. For the cyclic tests, shear dislocation first appeared at load-level displacements which were in the range of 0.1D-0.5D (cf. 0.2D for the monotonic tests). For units 3-7 and all except the final stages of testing of units 1 and 2, the soil wedges were clear of the tank walls. In the final stages of testing units 1 and 2 (at load-level displacements of 2D and greater), soil wedges were observed to intersect the tank walls as shown for unit 2 in Fig. 6.28. Thus at that stage significant modification to the behaviour of the sand could have resulted from the presence of the tank walls. However from the discussion contained in Section 6.7, results at displacements of less than 0.67D are of direct relevance to seismic induced behaviour, and displacements of 2D and greater are outside those expected to occur in bridge piles under earthquake conditions.

Following tests, the model piles were inspected for signs of damage. No fracturing or local buckling of the casing was observed in these post-mortems. Figure 6.33 shows a photograph of the final condition of unit 2, which was the most damaged of the test units described in this section. From the figure it can be seen that well-developed plasticity occurred over a considerable length of the pile, with peak curvature occurring at a depth of approximately six pile diameters. In Section 4.2.3, it was noted that pile-soil systems under lateral load have a flat bending moment distribution in the vicinity of the critical section. This was predicted to result in a longer plastic hinge length and hence smaller curvature ductility demand in the pile than in an "equivalent cantilever" (linear bending moment distribution) at the same level of displacement ductility. This prediction is qualitatively confirmed by Fig. 6.33, and discussed further in Section 6.10.8.

6.9.2 Lateral Load-Lateral Displacement Performance

Figures 6.30 and 6.31 shows the monotonic lateral load-load level lateral displacement responses of units 12 (medium density sand) and 13 (loose density sand) respectively. At a peak load-level lateral displacement of 2.6D (≅ 298 mm), loads reached in units 12 and 13 were 21.8 kN and 8.8 kN respectively, which indicates the soil density has a large influence on lateral load-carrying capacity. It is apparent that the ultimate load of the piles was not reached since load-displacement response is still rising at the peak displacement. The figures also show that load-displacement response is almost continuously non-linear, even at small levels of displacement. For example for unit 12, at a deflection of 2.3 mm (= 0.02D) the lateral load is equal to 1.26 times the load at a deflection of 1.15 mm (0.01D). This non-linear behaviour is very different from the elastic or elastic-plastic behaviour which is commonly assumed in design.

From Figs. 6.30 and 6.31, it is also apparent that only a small proportion of the imposed lateral displacement is recovered upon unloading of the pile. It is subsequently shown (see Section 6.9.3) that the pile members were behaving elastically. Thus this residual displacement is due to soil behaviour. During loading the cohesionless soil flows into the cavity created in the wake of the pile, and this soil flow is responsible for permitting only partial recovery of pile lateral displacement on unloading. In comparison, an elastically behaving pile in cohesive soil might be expected to fully recover its initial position on

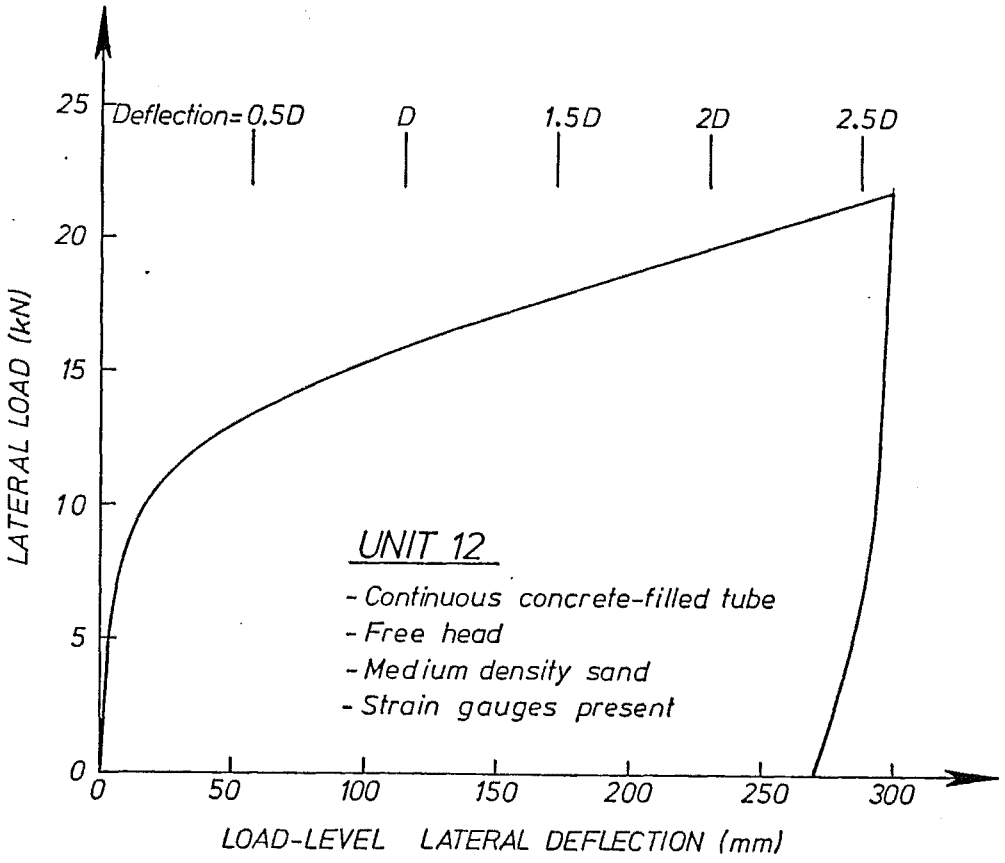

FIG. 6.30 : UNIT 12 (MONOTONIC TEST, MEDIUM DENSITY SAND) LATERAL LOAD-DEFLECTION RESPONSE

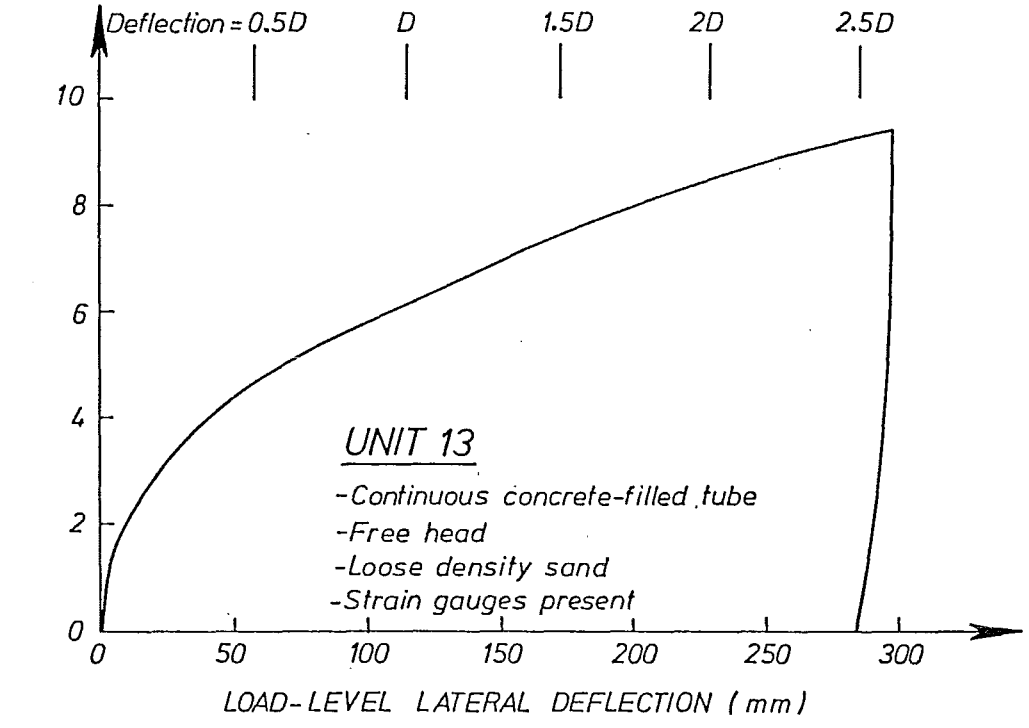

FIG. 6.31 : UNIT 13 (MONOTONIC TEST, LOOSE DENSITY SAND) LATERAL LOAD-DEFLECTION RESPONSE

unloading, since during loading the cohesive soil will not flow into the wake of the pile.

Figures 6.32-6.38 show the hysteresis loops of lateral load-lateral displacement response for units 1-7 respectively.

Lateral loading of unit 1 (no strain gauges present) was conducted as a pilot cyclic test. After the initial cycling (7 cycles at displacement = ± D) in loose sand, to obtain an estimate of medium density sand behaviour, the sand tank was topped up and relevelled and a further 6 cycles were performed prior to a large displacement pulse of -2.5D (- 288 mm) being applied. This topping up of the tank clearly enhanced the strength and stiffness of the model pile. The subsequent tests (units 2-7) were performed without topping up the sand level. From Fig. 6.32, excellent hysteretic behaviour was obtained for unit 1, since load-carrying capacity of the model pile increased with every cycle and even at the end of the large displacement pulse, load-carrying capacity was still increasing. However it is recalled from Section 6.9.1 that towards the end of testing at load-level lateral displacements of magnitude greater than 2D, soil wedges intersected the tank wall which could have increased the apparent soil shear strength.

For the model piles tested in medium density sand (units 2, 3 and 4, see Figs. 6.33-6.35 respectively), the hysteresis loops are stable with generally a small increase in load-carrying capacity occurring at succeeding cycles to the same peak load-level displacement. It is also shown that load-carrying capacity increased as load-level displacement increased.

For the model piles tested in loose sand (units 5, 6 and 7, see Figs. 6.36-6.38 respectively), significant expansion of the hysteresis loops occurs as cycling proceeds. For example for unit 6, at the peaks of the 2nd, 3rd.....9th and 10th cycles to a load-level lateral deflection of 57.5 mm (= 0.5D) the lateral loads were equal to 1.33, 1.55, 1.73, 1.88, 2.00, 2.10, 2.20, 2.27 and 2.35 times respectively the loads carried at the peak of the first cycle. Thus significant strength enhancement occurred with each succeeding cycle, although the rate of strength increase tended to reduce with each succeeding cycle. Furthermore, even at the end of the large displacement pulse of -2.5D (- 288 mm), the load-carrying capacity of unit 6 was still rising to a magnitude in excess of 15.2 kN.

In the previous section, it was noted that the sand level tended to drop as cyclic loading proceeded. This results in both the unsupported length of the pile and the sand density increasing. For medium density sand tests (see Figs. 6.33-6.35), it is apparent that the lateral load-carrying capacity lost due to an increase in the unsupported length of the pile is approximately offset by the increase in capacity due to the increasing soil density and hence strength, while for the loose density sand tests (see Figs. 6.36-6.38), the increase in load-carrying capacity due to the increase in soil strength more than offsets the loss of capacity due to an increase in the unsupported length of the pile.

Fendall (6.6) conducted lateral load tests on small-scale (≈ 1/100) piles which were driven into dry sand that was initially either loose or dense. Constant amplitude cyclic loading for model piles in dense sand produced degrading hysteretic behaviour, while in loose sand stable hysteretic behaviour was obtained. For model piles tested in loose sand, it is probable that the difference in hysteretic behaviour obtained in the tests of Fendall (6.6) and the tests described in this chapter which had expanding hysteresis loops, is due to the different techniques used in installing the model piles. In the tests of Fendall, piles were driven into the foundation which would have partially densified the initially loose sand, while the model piles described in this chapter were positioned in the retaining tank and then loose sand was poured around the piles. Both results are of relevance to prototype piles, since driving and boring are both commonly used in installing prototype piles, and boring which does not

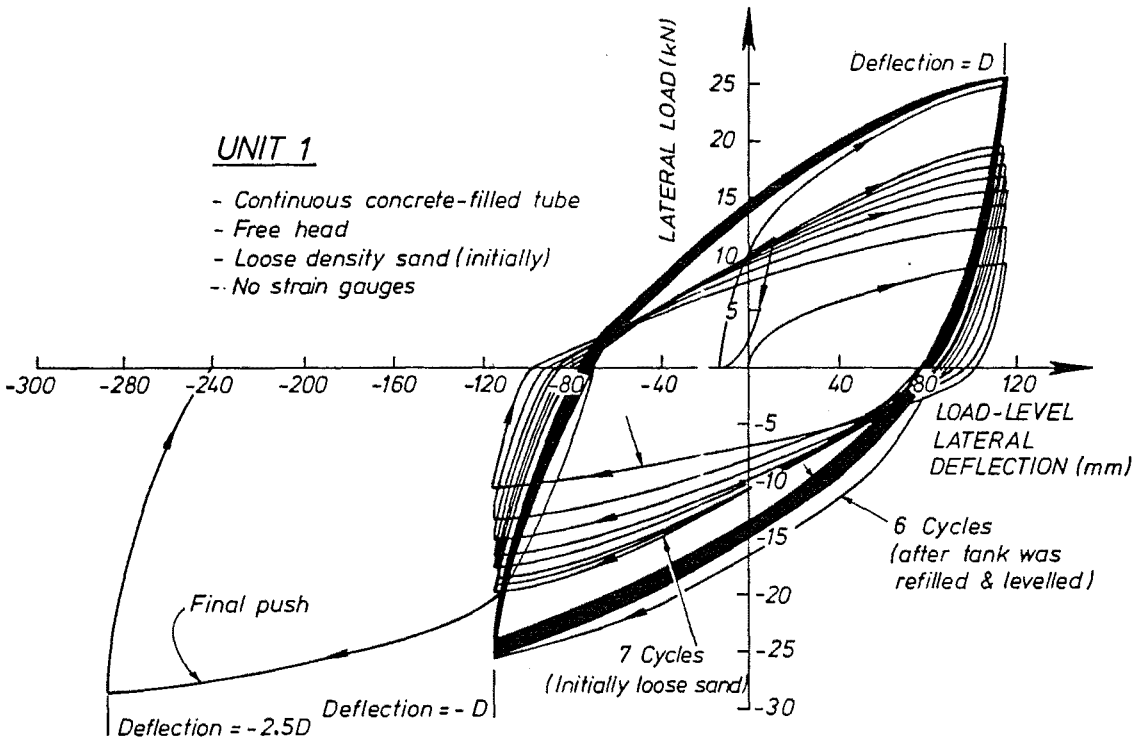

FIG. 6. 32 : UNIT 1 (CYCLIC TEST, INITIALLY LOOSE DENSITY SAND) HYSTERESIS LOOPS

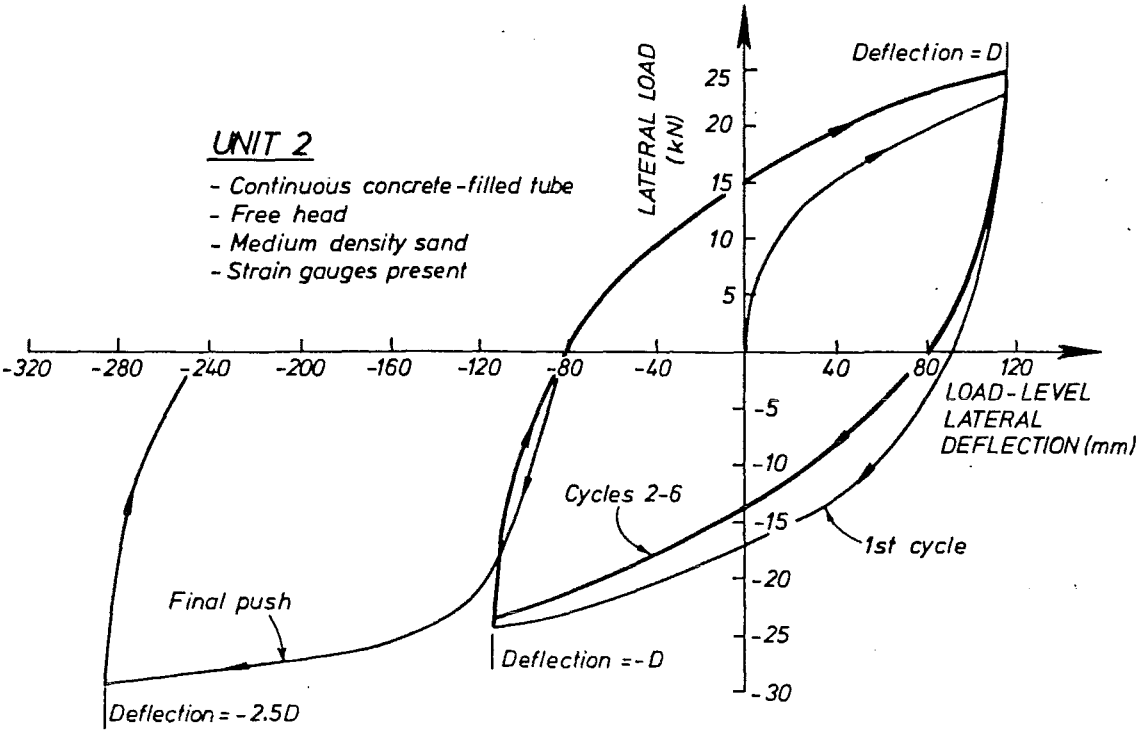

FIG. 6.33 : UNIT 2 (CYCLIC TEST, MEDIUM DENSITY SAND) HYSTERESIS LOOPS

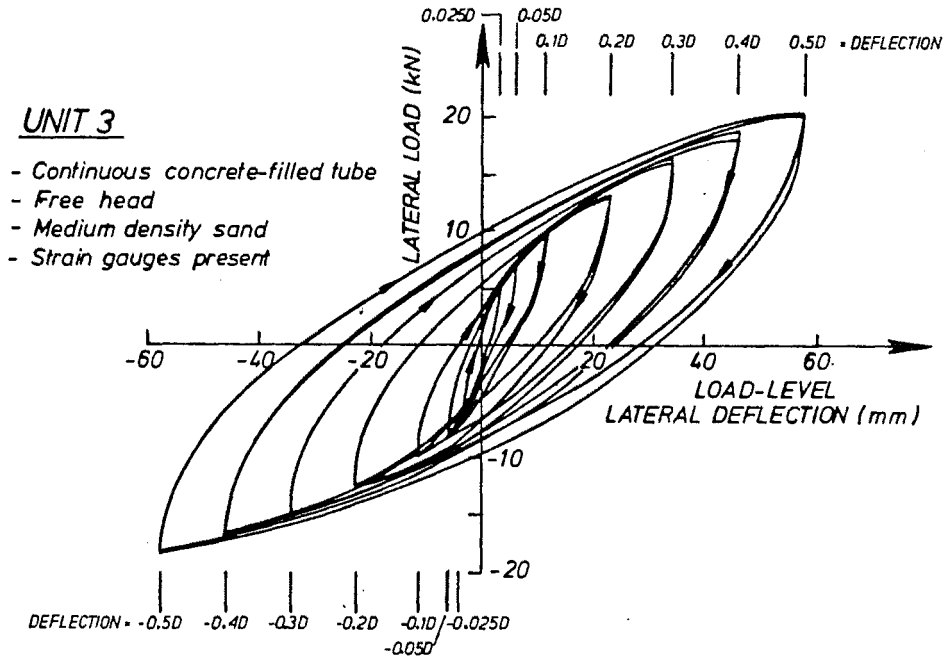

FIG. 6.34 : UNIT 3 (CYCLIC TEST, MEDIUM DENSITY SAND) HYSTERSIS LOOPS

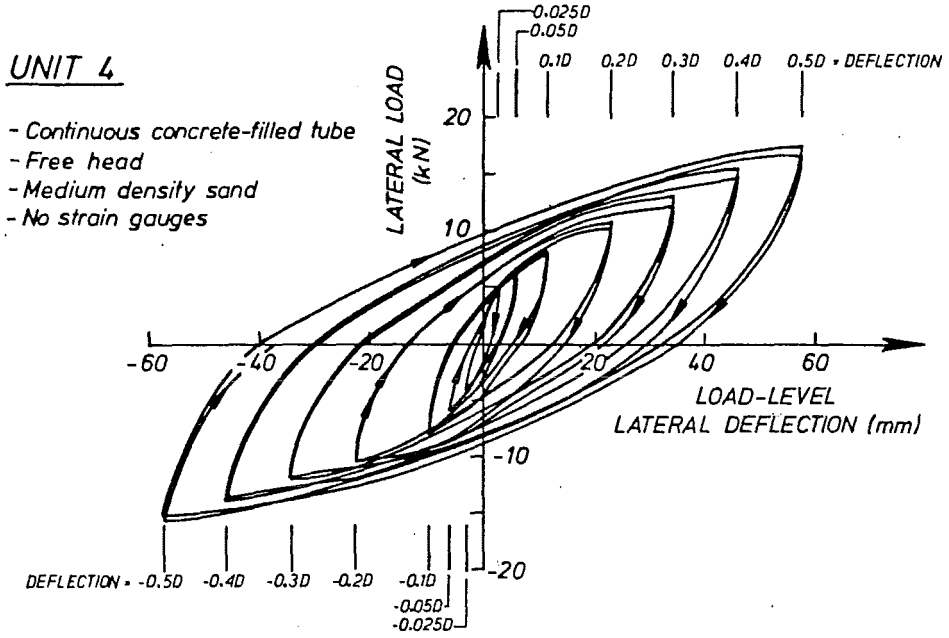

FIG. 6.35 : UNIT 4 (CYCLIC TEST, MEDIUM DENSITY SAND) HYSTERESIS LOOPS

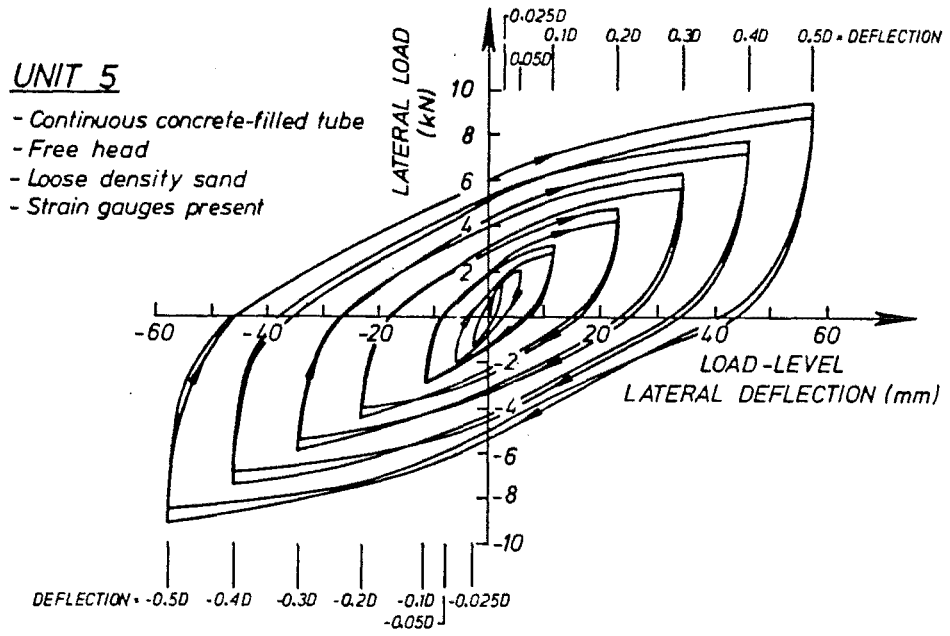

FIG. 6.36 : UNIT 5 (CYCLIC TEST, LOOSE DENSITY SAND) HYSTERESIS LOOPS

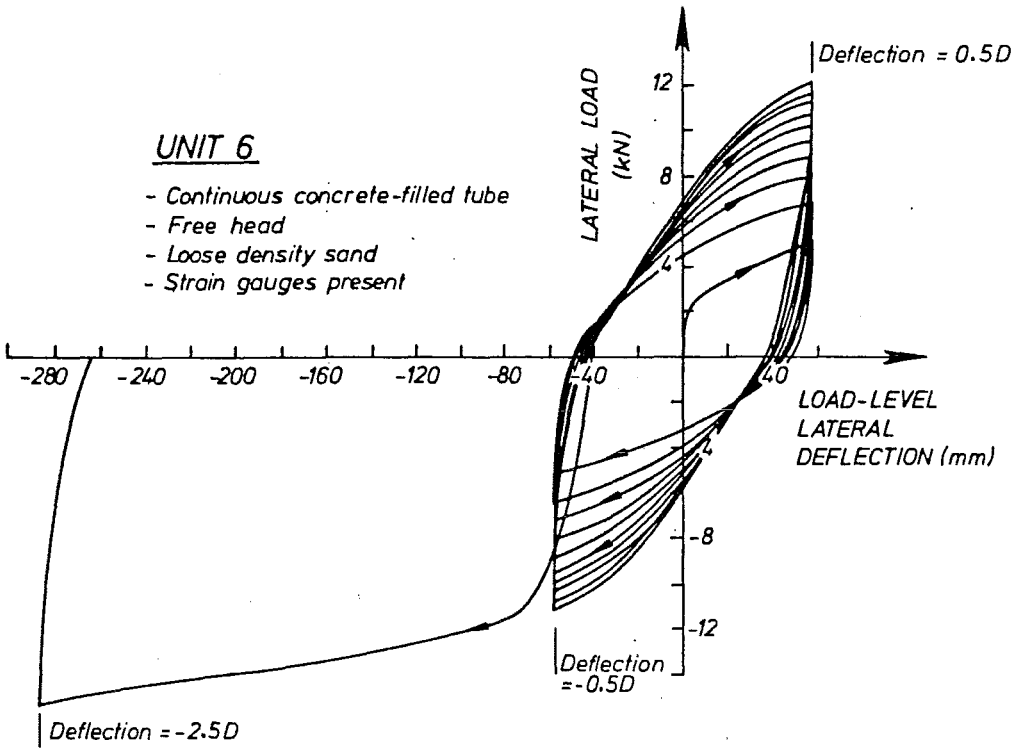

FIG. 6.37 : UNIT 6 (CYCLIC TEST, LOOSE DENSITY SAND) HYSTERSIS LOOPS

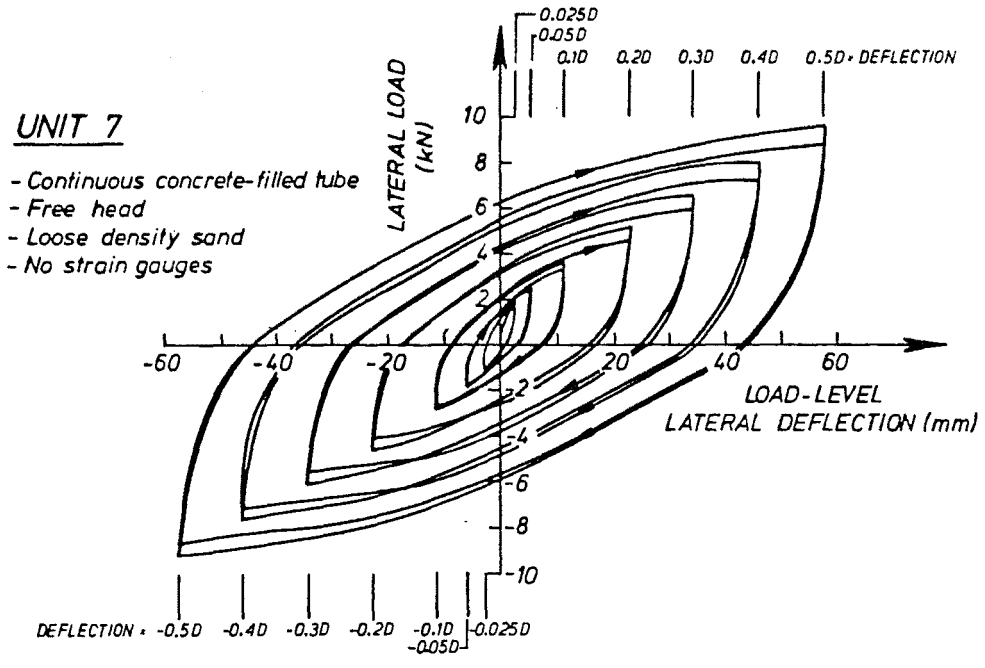

FIG. 6.38 : UNIT 7 (CYCLIC TEST, LOOSE DENSITY SAND) HYSTERESIS LOOPS

significantly densify the soil surrounding the pile will produce soil conditions similar to those obtained in the pile tests described in this chapter.

For the model tests described in this chapter, it is subsequently shown (Section 6.9.3) that the majority of the tests involved piles responding in an elastic manner. Thus the expanding hysteresis loops for the loose density sand tests, can be attributed to the significant level of soil flow into the wake of the pile which occurred as the pile was subjected to cyclic loading. This soil flow resulted in a marked increase in soil density and hence strength in the vicinity of the pile. A cohesive soil would not be expected to have this expanding hysteretic behaviour, since cohesive soil will not flow into the wake of the pile.

Expanding hysteresis loops will have a marked influence on the seismic behaviour of prototype piles. The implication is that the large reserve of hysteretic damping available from the soil will tend to reduce the pile response from that occurring with, for example, a soil behaving in an elastic-plastic or degrading fashion.

Figure 6.39 shows a comparison to both small ($\leq$ 7 mm) and large ($\leq$ 300 mm) deflection scales of the load-deflection responses obtained from the monotonic tests and the first half cycle of the cyclic tests. Theoretical elastic-plastic responses based on the values of H_i (theoretical ultimate load) and Δ_y (idealised yield deflection) predicted on the basis of equivalent cantilever behaviour as described previously in Section 6.2.1 are also given in these figures.

The experimental results at a given sand density show a significant amount of scatter. For example at a load-level displacement of 0.02D (= 2.3 mm), the five loose density sand tests had a load with an average value of 1.49 kN and a standard deviation of 0.28 kN; while the four medium density sand tests had a load with an average value of 4.52 kN and a standard deviation of 0.30 kN. The theoretical predictions are in poor agreement with the experimental responses. Experimentally obtained lateral loads were always less than the theoretical ultimate loads, implying that the equivalent depths-to-fixity were underestimated by use of the design procedure outlined in Section 6.2.1. It is also indicated that an elastic-plastic idealisation of response gives a poor representation of the experimentally obtained load-deflection responses which are significantly curved throughout the entire range of displacement. However, at load-level displacements of approximately 4 mm (0.035D) for the loose density sand and 8 mm (0.07D) for the medium density sand, the experimental and theoretical loads are in good agreement. Figure 6.39a also indicates that the presence of strain gauges and the associated wiring on the outside of the tube made little difference to pile load-deflection response.

Comparisons of monotonic response and envelopes to cyclic load-deflection responses for tests conducted in medium and loose density sand are shown in Figs. 6.40(a) and (b) respectively. These figures clearly show the enhancement to lateral load-carrying capacity which occurred as cyclic loading proceeded. This enhancement is more marked for tests conducted in loose sand than in medium sand. For example at a load-level displacement of 115 mm (D), in the medium density sand tests, unit 2 (cyclic test) supported a load 56% larger than the load carried by unit 12 (monotonic test), while in the loose density sand tests unit 1 (cyclic test) carried a load 218% larger than the load carried by unit 13 (monotonic test). This is a result of the extra soil densification which occurs under cyclic loading relative to monotonic loading.

6.9.3 Curvature Distribution

Figures 6.41-6.46 show profiles of pile curvature distribution at a variety of load-level lateral displacements which were obtained during the monotonic testing

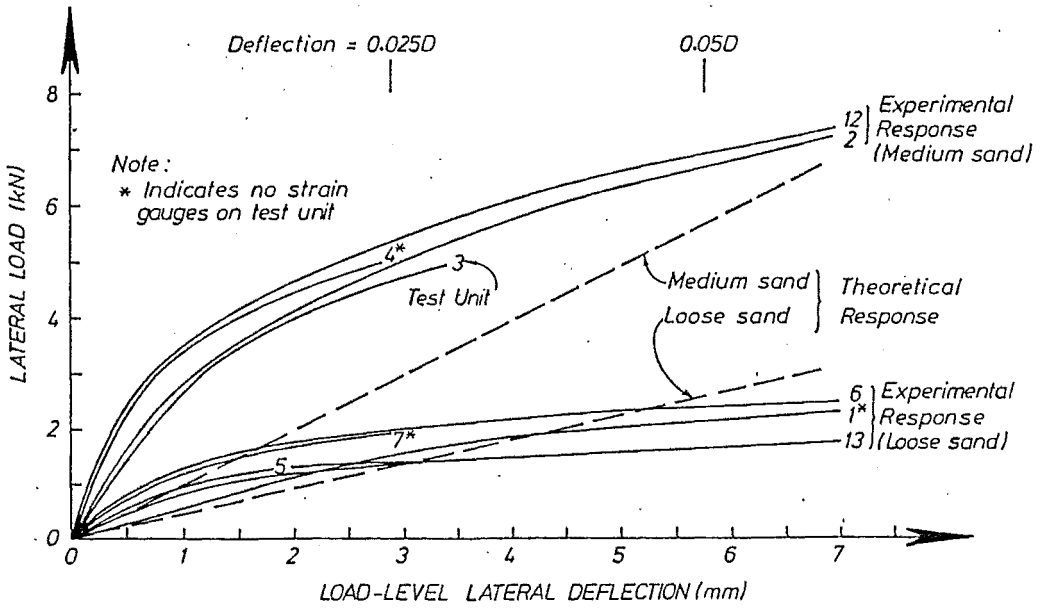

(a) SMALL DEFLECTION

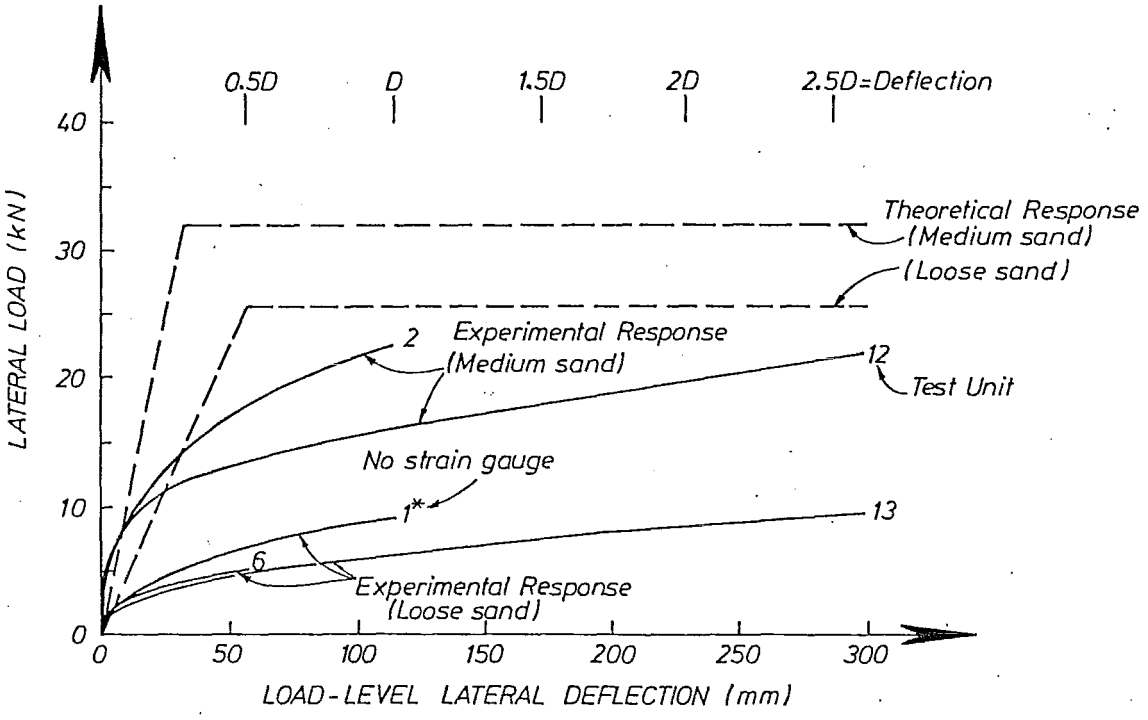

(b) LARGE DEFLECTION

FIG. 6.39 MONOTONIC LOAD-DEFLECTION COMPARISONS

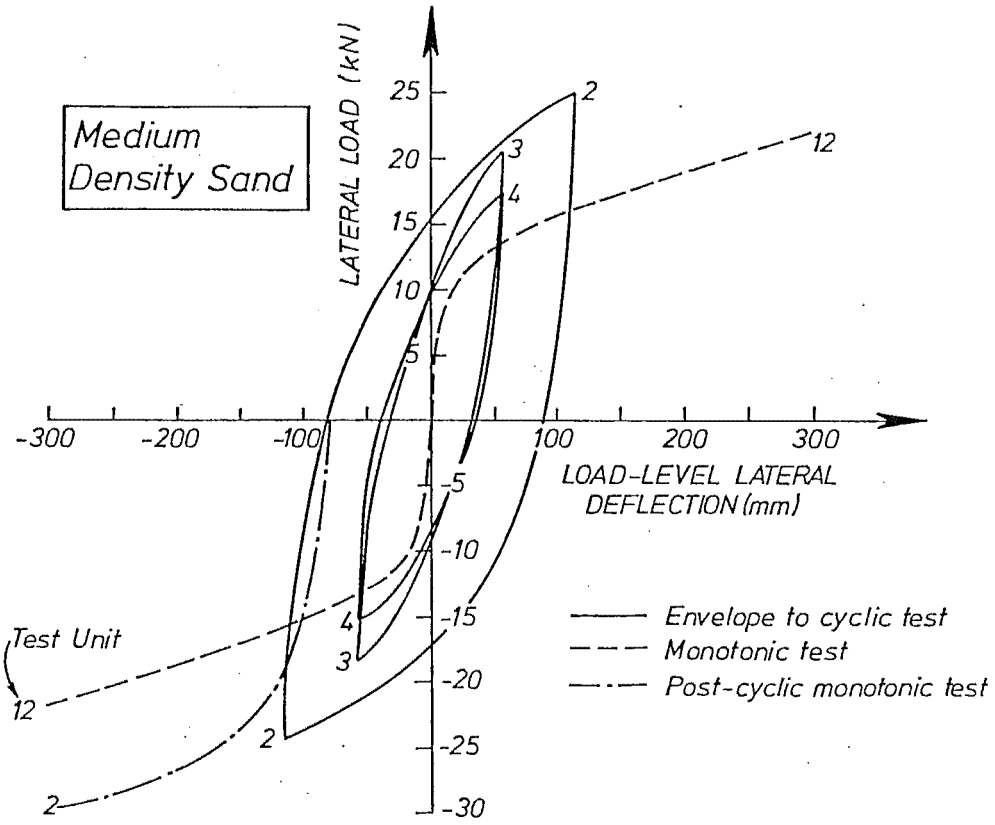

(a) MEDIUM DENSITY SAND

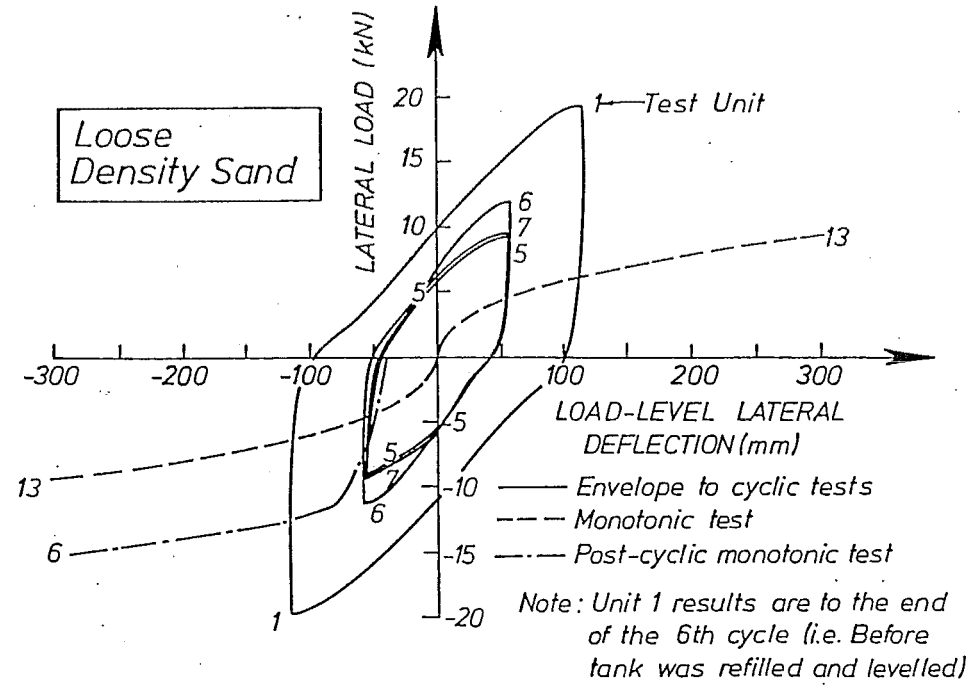

(b) LOOSE DENSITY SAND

FIG. 6.40 MONOTONIC AND CYCLIC LOAD-DEFLECTION COMPARISONS

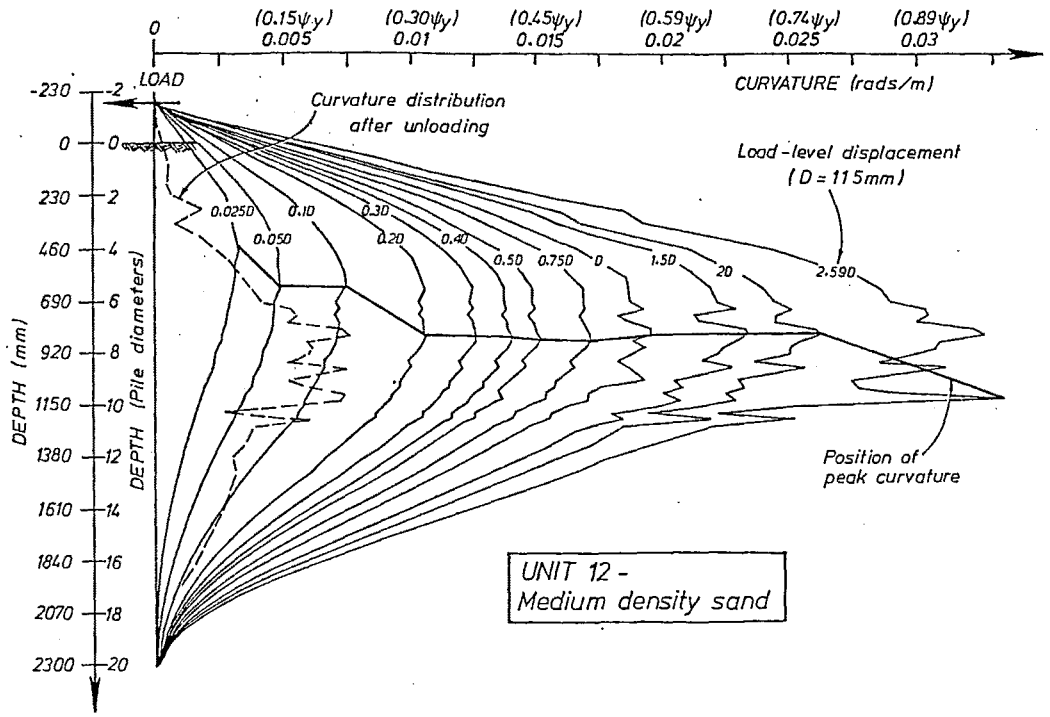

FIG. 6.41 : UNIT 12 (MONOTONIC TEST, MEDIUM DENSITY SAND) CURVATURE PROFILES

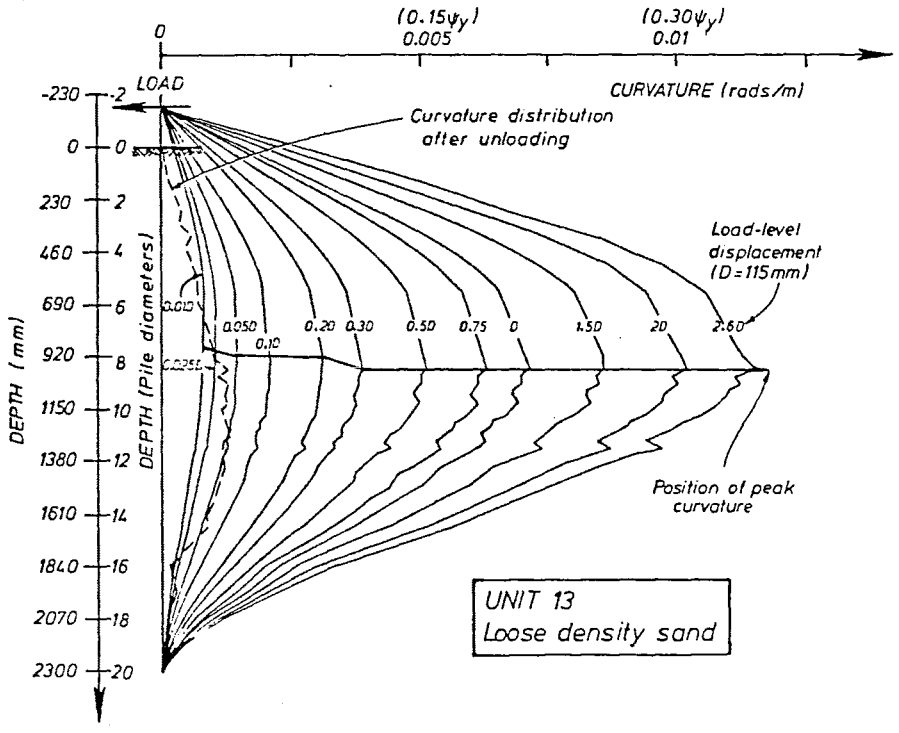

FIG. 6.42 : UNIT 13 (MONOTONIC TEST, LOOSE DENSITY SAND) CURVATURE PROFILES

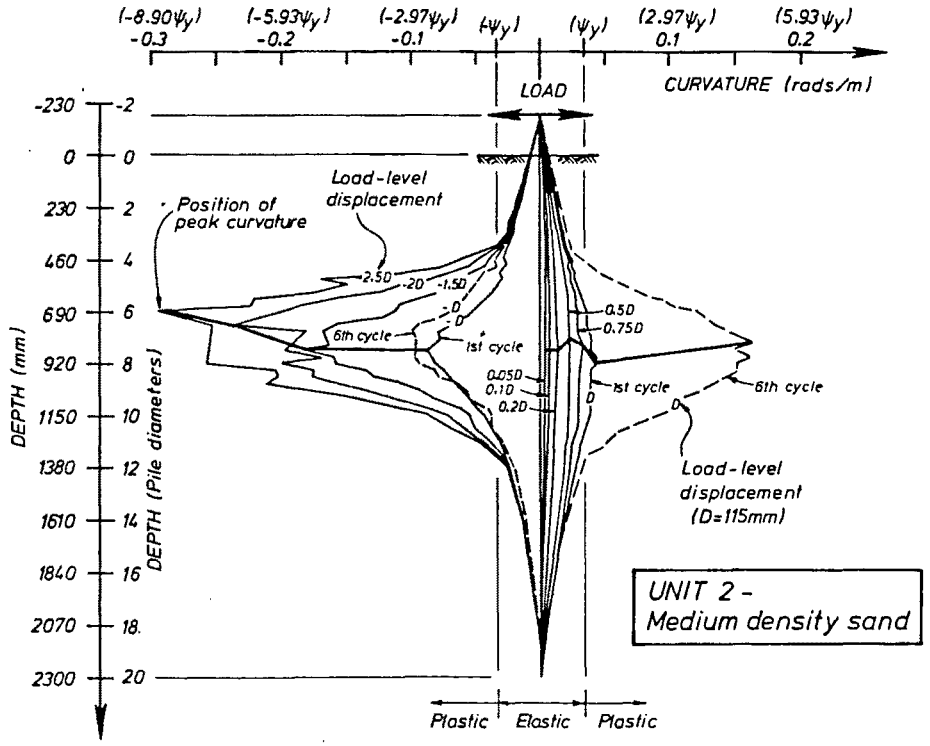

FIG. 6.43 : UNIT 2 (CYCLIC TEST, MEDIUM DENSITY SAND) CURVATURE PROFILES

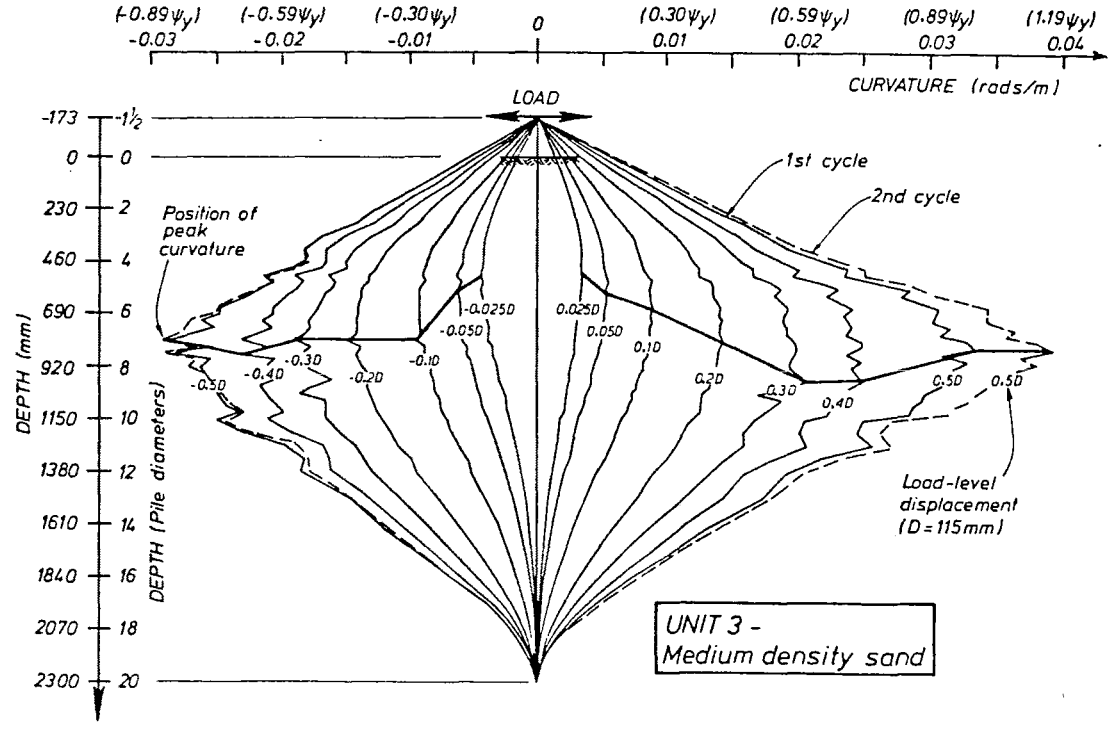

FIG. 6.44 : UNIT 3 (CYCLIC TEST, MEDIUM DENSITY SAND) CURVATURE PROFILES

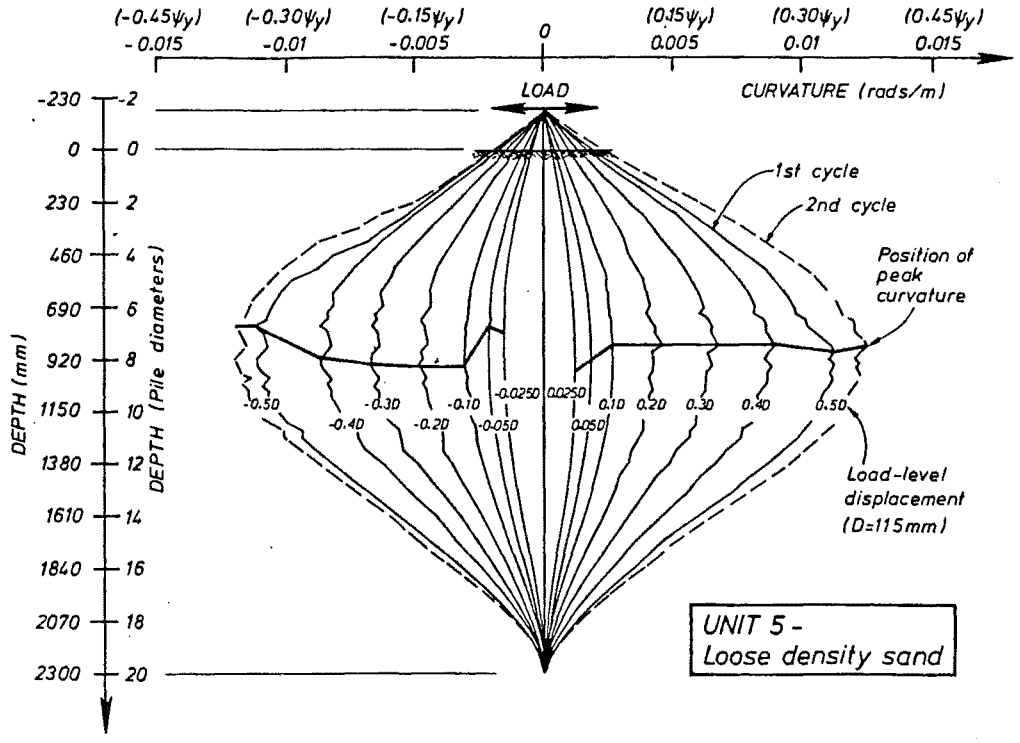

FIG. 6.45 : UNIT 5 (CYCLIC TEST, LOOSE DENSITY SAND) CURVATURE PROFILES

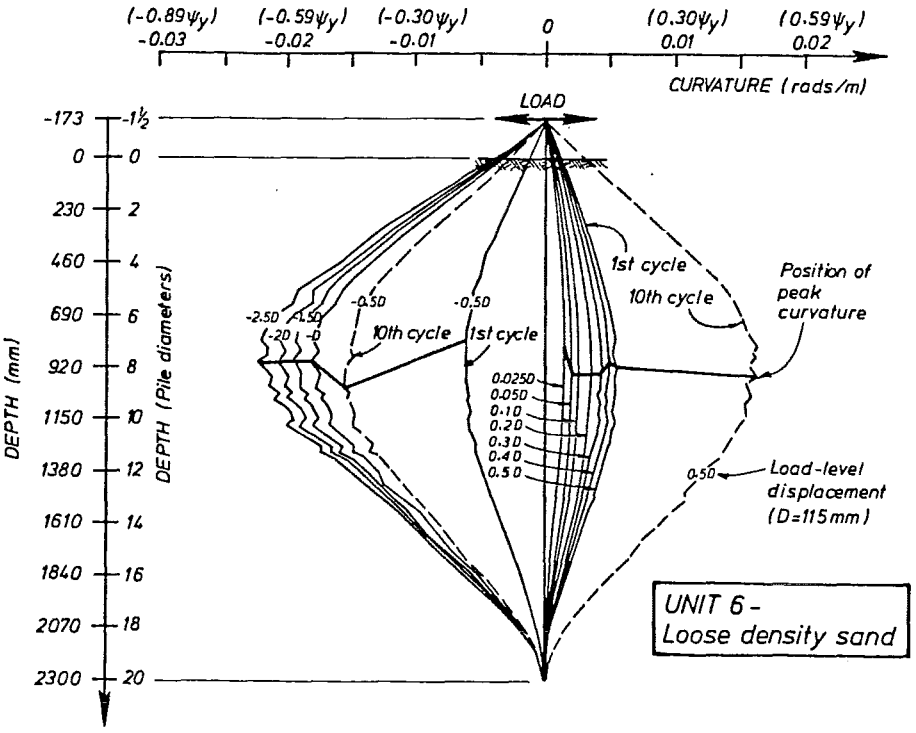

FIG. 6.46 : UNIT 6 (CYCLIC TEST, LOOSE DENSITY SAND) CURVATURE PROFILES

of units 12 and 13 and the cyclic testing of units 2, 3, 5 and 6 respectively. Values of curvature ductility ratio ψ/ψ_y based on the experimentally obtained curvature and the theoretical idealised yield curvature ψ_y (see Section 6.8), and the depth at which the peak curvature occurred for each of the profiles are also indicated on these figures.

Curvatures were obtained by dividing the difference in strain between opposite strain gauges of a pair (see Fig. 6.10) by the distance (equal to the diameter, D = 115 mm) between the gauges. The curvature profiles were then plotted by linearly interpolating the curvatures between the positions of strain gauge pairs.

The experimental results are a little erratic, especially during the later stages of testing in the vicinity of the positions of peak curvature. This occurs because the strain gauge pairs in this vicinity were located at very small spacing (0.25D = 28 mm). Thus small errors in the curvature data between strain gauge pairs result in the curvature profiles having a rather jagged appearance.

As the level of displacement or the number of cycles increased, curvatures tended to increase. However unit 2 was the only model pile subjected to significant plasticity with a maximum value of the curvature ductility ratio of $|\psi/\psi_y| = 8.75$ being obtained. In the other units the maximum value of $|\psi/\psi_y|$ was 1.17 (unit 3).

The following observations are made from the curvature profiles (see Figs. 6.41 and 6.42) obtained from the monotonic loading of units 12 (medium density sand) and 13 (loose density sand):

(i) At the same level of load-level lateral displacement, pile curvatures are larger in the medium density sand tests than in the loose density sand tests. This is to be expected, since soil pressures and hence pile bending moments will be larger at a given displacement for the medium density sand test than for the loose density sand test.

(ii) The experimentally determined position of peak curvature is very sensitive to the accuracy of the curvature data, since theoretically the gradient of the curvature will be very small in the vicinity of the peak curvature. However as load-level displacement increased from 0.025D (3 mm) to 2.6D (299 mm) the depth at which the peak curvature occurred dropped significantly from a level of 4D to 9.7D for the medium sand test and less significantly from 7.7D to 8.5D for the loose sand test. Since for these two tests the piles remained substantially elastic ($\psi/\psi_y < 1$), this change in position of peak curvature implied that the soil stiffness was reducing as the level of displacement increased.

(iii) Maximum values of $\psi/\psi_y = 0.99$ and 0.34 were obtained during loading of units 12 (medium density sand) and 13 (loose density sand) respectively. Thus these pile members behaved substantially in an elastic fashion during testing. However after unloading of these model piles, significant levels of residual curvature were present on the piles. For example unit 12 had a maximum residual curvature of $0.23\psi_y$, indicating that significant residual levels of bending moment, shear force and soil lateral pressure were also present in the piles. Thus the flow of granular soils around the pile which occurs during loading, upon unloading results in significant levels of both lateral displacement (see Section 6.9.2) and curvature of the pile.

The following observations are made from the curvature profiles (see Figs. 6.43-6.46) obtained from the cyclic testing of units 2 and 3 (medium density sand) and 5 and 6 (loose density sand):

(i) Cyclic loading, which as noted in the previous section densified the sand, also significantly increased the levels of curvature. For example from the first to the sixth cycles at a load-level displacement of D (115 mm), the peak curvature obtained in unit 2 (see Fig. 6.43) increased by a factor of 3.7.

(ii) In general the tests conducted in loose sand, during which the pile behaved elastically ($\psi/\psi_y < 0.66$), indicated a slight trend towards the depth at the position of peak curvature, increasing with displacement level. This is in agreement with the behaviour obtained during monotonic testing. For cyclic tests conducted in medium density sand, a significant trend towards an increase in depth for the position of peak curvature for increasing displacement and $\psi/\psi_y < 1$ was obtained. This is also in agreement with the behaviour obtained during monotonic testing. However for $\psi/\psi_y > 1$ (see Fig. 6.43, unit 2), the depth to the position of peak curvature tended to decrease as the level of displacement increased. This occurs because at this plastic stage of pile member behaviour, the pile flexural stiffness is reducing at a faster rate than the soil lateral stiffness.

(iii) From the results obtained from unit 2 (see Fig. 6.43) the considerable length of the pile subjected to significant plasticity is clearly shown. For example at the peak load-level displacement of -2.5D (-288 mm), $|\psi/\psi_y| > 1$ over a length of 8.2D and $|\psi/\psi_y| > 5$ over a length of 4.4D. This is in agreement with the qualitative observation (see Fig. 6.29) of a considerable length over which unit 2 was significantly bent.

6.10 ANALYSIS OF RESULTS - FREE-HEAD PILES

6.10.1 Determining Pile Lateral Deflection, Bending Moment, Shear Force and Soil Lateral Pressure Distributions

6.10.1.1 Background

It was shown in Section 1.4.2 that given the curvature distribution $\psi(x)$ (where x = distance along the pile axis) and flexural rigidity EI of an elastically behaving pile, then pile bending moment $M(x)$, shear force $V(x)$, slope $\theta(x)$, lateral deflection $y(x)$ and soil lateral pressure $p(x)$ distributions can be determined from:

$$M(x) = EI.\psi(x) \tag{6.12}$$

$$V(x) = EI.\frac{d\psi(x)}{dx} \tag{6.13}$$

$$p(x) = \frac{EI}{D}.\frac{d^2\psi(x)}{dx^2} \tag{6.14}$$

$$\theta(x) = \int \psi(x).dx \tag{6.15}$$

$$y(x) = \int\int \psi(x).dx.dx \tag{6.16}$$

It should, however, be noted that values of $p(x)$ which are calculated from equation 6.14 and referred to above as "soil lateral pressures" are not in fact equivalent to the actual soil lateral pressures on a pile. Before lateral loading has commenced at which stage $p(x) = 0$, significant but self-equilibrating soil lateral pressures will be present adjacent to the pile. Scott (6.13) notes that $p(x)$ represents the nett effect of three types of soil reaction on the pile, which occur subsequently to the "at-rest" (i.e. before lateral load is applied) condition of the pile:

(i) increase of soil pressure in front of the pile, as the pile pushes into that soil;

(ii) relief of soil pressure behind the pile, as the pile moves away from that soil;

and (iii) side friction on the pile as the pile shears through the soil.

However, for convenience in the rest of this thesis, p(x) will be referred to as soil lateral pressure.

Evaluation of pile slope $\theta(x)$ and lateral deflection $y(x)$ distributions using equations 6.15 and 6.16 is relatively straight-forward. Previous investigators (e.g. Scott (6.13) and Priestley (6.14)) have shown that any minor errors in the strain gauge and hence curvature distribution are smoothed out by the integration process. However obtaining pile shear force $V(x)$ and soil lateral pressure $p(x)$ distributions using equations 6.13 and 6.14 is more difficult since any errors in the strain gauge data will be magnified by the differentiation. Clearly, the somewhat irregular curvature distributions (see Figs. 6.41-6.46) deduced from strain gauge readings would result in extreme local variations of shear force and soil lateral pressure, unless some smoothing of the curvature distributions is done prior to differentiation.

Priestley (6.14) conducted a lateral load test on a 1.37 m diameter pile at the Mangere bridge construction site, Auckland, New Zealand. This test was restricted to the elastic range of pile behaviour. Curvature data at positions along the length of the pile were obtained. Subsequently, curves of best fit were graphically constructed through the raw curvature data and pile shear force distributions were determined from the gradients of these curves and the value of pile flexural rigidity EI. The shear force distributions were then graphically smoothed and the soil lateral pressure distributions were determined from the gradients of the smoothed shear force distributions and the value of pile diameter D. By this method, Priestley (6.14) obtained $p(x)$ distributions which were used to establish lateral subgrade coefficients $p(x)/y(x)$. These coefficients correlated well with log bore information. However judgement had been used in the curve-smoothing processes. Thus it is possible that if the same exercise had been conducted by another investigator somewhat different results could have been obtained.

Scott (6.13) performed 1/100 scale centrifuge tests on elastically behaving flexible piles. Prior to placing the model piles in the foundation, Scott accurately calibrated the strain gauges by placing a known bending moment distribution on the pile. During testing this enabled moments at the strain gauge positions to be determined to a high degree of accuracy. At a given stage of testing, the moment distribution along the pile was then determined by fitting quintic splines (a series of fifth order polynominals between adjacent strain gauge positions, with matching coordinates, first and second derivatives at the strain gauge positions) to the moment data at the strain gauge positions. The use of quintic splines for the moment distribution implies that between adjacent strain gauge positions, the pile shear force distribution will be quartic and the soil lateral pressure distribution will be cubic. The distributions obtained by this method also looked physically reasonable, although over a very short length near the top of the pile anomalous negative pressures were indicated where positive pressures were expected.

6.10.1.2 Method

(a) Determining Slope and Lateral Deflection Distributions

Figure 6.47 shows the notation used in numbering strain gauge pairs (1 = load-level pair) and also diagrams of pile curvature, slope and lateral deflection in the vicinity of the top 10 strain gauge pairs. Values of curvature ($\psi_1, \psi_2, \psi_3, \ldots$) for all strain gauge pairs and load-level slope (θ_1) and lateral deflection (y_1), were obtained directly from the experimental data. Assuming a linear distribution of curvature between data points, the value of slope at point $n+1$ could then be calculated from:

$$\theta_{n+1} = \theta_n + 0.5(x_{n+1} - x_n)(\psi_n + \psi_{n+1}) \qquad (6.17)$$

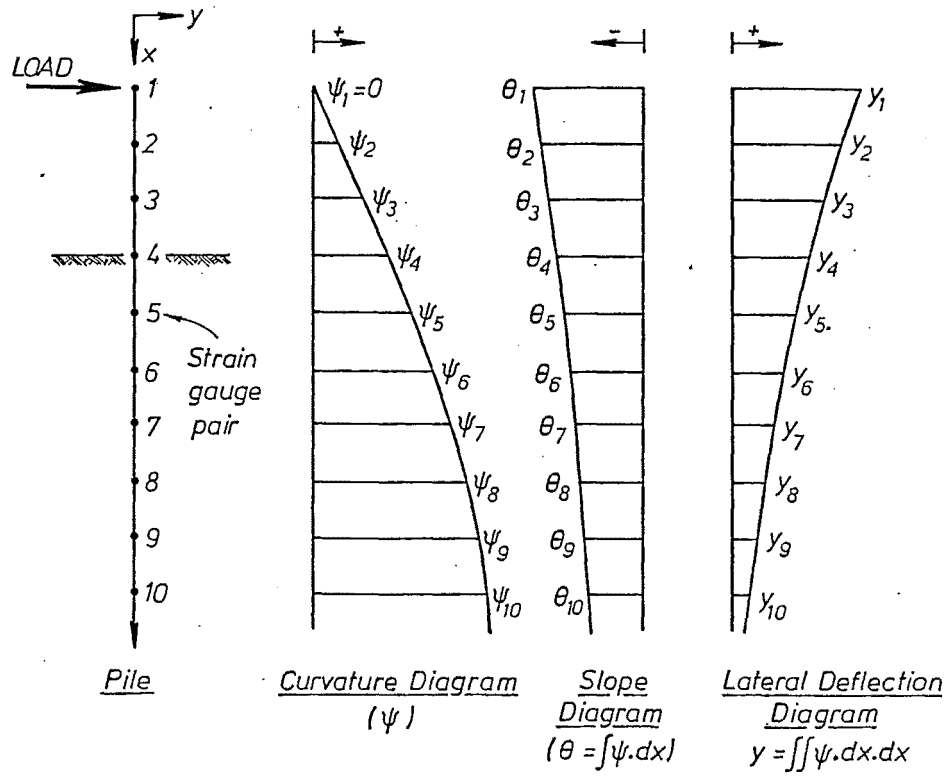

FIG. 6.47 OBTAINING SLOPE AND LATERAL DEFLECTION DISTRIBUTIONS

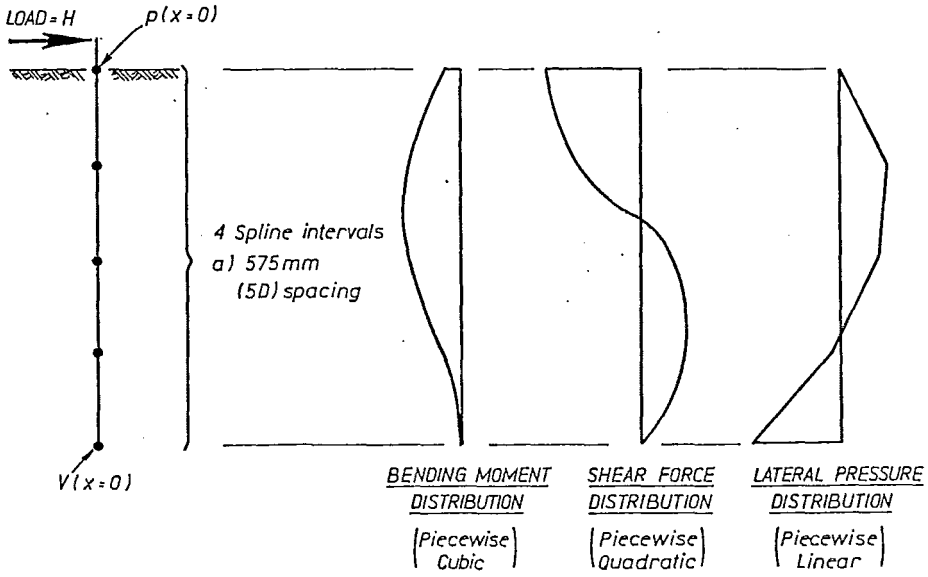

FIG. 6.48 RESULTS OF USING CUBIC SPLINES FOR MOMENT DISTRIBUTION.

Similarly, assuming a linear distribution of slope between data points, the value of lateral deflection at point n + 1 could then be calculated from:

$$y_{n+1} = y_n + 0.5(x_{n+1} - x_n)(\theta_n + \theta_{n+1}) \tag{6.18}$$

Thus the distributions of pile slope and lateral deflection could be determined by applying equations 6.17 and 6.18, step by step down the length of the pile.

(b) Determining Smoothed Curvature Distributions

The spline-fitting technique was not used to determine the curvature distribution since, as noted by Scott (6.13), this method is only appropriate when a very high degree of precision is present in the strain gauge data. Thus due to small errors in the strain gauge data, the curvature distributions shown in Figs. 6.41-6.46 are not suitable for the purpose of spline-fitting. Because of the large number of curvature distributions which required smoothing, it was also decided not to use the hand-smoothing technique used by Priestley (6.14).

For a given stage of testing, a computer analysis was performed to determine a polynomial curve which approximated the raw curvature data over the length of the pile from base to load-level. This "best fit" curve was determined using a "least squares" criterion (6.15).

In Fig. 6.10 it was shown that strain gauge pairs were located at smaller spacing near the middle of the piles than near the ends. To achieve a polynomial curve that fitted equally well over the whole length of the pile, the raw curvature data was weighted. Data from strain gauge pairs at load-level and at the base of the pile had a weighting of 8, while other strain gauge pairs located at spacings of D, 0.5D and 0.25D had weightings of 4, 2 and 1 respectively.

Preliminary analyses of the curvature data for unit 6 at the peak of the first cycle to a load-level lateral deflection of 0.5D (57.5 mm) indicated that polynomials of order 5-10 gave approximately equally good fits to the experimental data in terms of the least squares criterion. Thus a polynomial of order 5 was chosen for use in the subsequent analyses. Hence at a given stage of testing an expression for the smoothed curvature distribution could be obtained in the form of:

$$\psi(x) = C_o + C_1.x + C_2.x^2 + C_3.x^3 + C_4.x^4 + C_5.x^5 \tag{6.19}$$

where C_o, C_1, C_2, C_3, C_4 and C_5 = constants determined from the least squares criterion.

(c) Determining Pile Bending Moment and Shear Force and Soil Lateral Pressure Distributions

Initially analyses to determine distributions of pile bending moment, shear force and soil lateral pressure were performed using equations 6.12-6.14 and 6.19 to give:

$$M(x) = EI.\psi(x)$$
$$= EI(C_o + C_1.x + C_2.x^2 + C_3.x^3 + C_4.x^4 + C_5.x^5) \tag{6.20}$$

$$V(x) = EI \cdot \frac{d\psi(x)}{dx}$$
$$= EI(C_1 + 2C_2.x + 3C_3.x^2 + 4C_4.x^3 + 5C_5.x^4) \tag{6.21}$$

$$p(x) = \frac{EI}{D} \cdot \frac{d^2\psi(x)}{dx^2}$$
$$= \frac{EI}{D}(2C_2 + 6C_3x + 12C_4x^2 + 20C_5.x^3) \tag{6.22}$$

These equations were only applied in the linear range of pile member behaviour since they are inappropriate in the non-linear range. However, it was found that distributions of p(x), V(x) and M(x) obtained using this method gave a poor fit to the boundary conditions on the pile (e.g. at and above ground level p(x) should equal zero). Scott (6.16) had also come to the same conclusion when he attempted to obtain p(x) distributions using the same technique.

As mentioned in Section 6.10.1.1, Scott (6.13) had achieved some success by using quintic spline functions to obtain the distribution of bending moment between strain gauge pairs. To enable quintic splines to be obtained between a number of data points, the first and second derivatives (i.e. shear force and soil lateral pressure respectively) of the moment distribution have to be known at the top and bottom data points. At ground level (x = 0):

$$p(0) = 0 \tag{6.23}$$

$$V(0) = H \text{ (applied lateral load)} \tag{6.24}$$

$$M(0) = 0.173H \text{ (0.173 m is the distance from ground to load level)} \tag{6.25}$$

For the flexible piles tested by Scott (6.13) at the pile base ($x = x_b$):

$$p(x_b) = 0 \tag{6.26}$$

$$V(x_b) = 0 \tag{6.27}$$

$$M(x_b) = 0 \tag{6.28}$$

Similarly for the model pile tests described in Sections 6.9-6.10.8, at the pile base equations 6.27 and 6.28 are valid. However as shown later in Section 6.10.5, large values of $p(x_b)$ were obtained. Thus quintic splines could not be used and lower order cubic splines were used, for which only one of the derivatives (e.g. shear force or soil lateral pressure) at each of the pile base and ground level is required.

Using cubic splines for the moment distribution results in pile shear force and soil lateral pressure distributions that are composed of a series of quadratic and linear polynomials respectively. Preliminary analyses using either 10 or 20 spline intervals yielded somewhat erratic results. Thus the subsequent analyses were conducted using either 4 or 5 spline intervals.

Figure 6.48 shows the spacing (e.g. 5D for four spline intervals) of the spline endpoints and illustrative distributions of pile bending moment and shear force and soil lateral pressure. The figure also shows the boundary conditions which were used at ground level (soil lateral pressure = 0) and pile base (pile shear force = 0).

Theory for the use of cubic splines is given in the text of Gerald (6.17), and an outline of the analytical procedure is given below. For n spline intervals and hence n + 1 spline endpoints (endpoint 1 is at ground level and endpoint n + 1 is at the pile base), expressions for the second derivatives of the moments can be written as:

$$M''_{i+1} \cdot h_i + M''_i \cdot (2h_i + 2h_{i-1}) + M''_{i-1} \cdot h_{i-1} = 6\left(\frac{M_{i+1} - M_i}{h_i} - \frac{M_i - M_{i-1}}{h_{i-1}}\right) \tag{6.29}$$

where M''_{i+1}, M''_i, M''_{i-1} = second derivatives of the moment at spline endpoints i+1, i and i-1 respectively, h_i, h_{i-1} = spacing from spline endpoints i to i + 1 and i-1 to

to i respectively, M_{i+1}, M_i, M_{i-1} = moments at spline endpoints i+1, i and i-1 respectively. Equation 6.29 can be applied for values of i from 2 to n. The boundary condition of zero soil lateral pressure at ground level can be expressed as:

$$M_1'' = 0 \tag{6.30}$$

and the boundary condition of zero shear force at pile base can be expressed as:

$$M_n'' + 2M_{n+1}'' = \frac{6}{h_n^2} M_n \tag{6.31}$$

Thus for known values of h_i and M_i equations 6.29-6.31 can be solved to give values of M_i''.

In spline interval i where x will be in the range of x_i to x_{i+1}, expressions for pile bending moment and shear force and soil lateral pressure can be written as:

$$M(x) = a(x - x_i)^3 + b(x - x_i)^2 + c(x - x_i) + d \tag{6.32}$$

$$V(x) = 3a(x - x_i)^2 + 2b(x - x_i) + c \tag{6.33}$$

$$p(x) = [6a(x - x_i) + 2b]/D \tag{6.34}$$

where $$a = \frac{M_{i+1}'' - M_i''}{6h_i} \tag{6.35}$$

$$b = \frac{M_i''}{2} \tag{6.36}$$

$$c = \frac{M_{i+1} - M_i}{h_i} - \frac{2h_i M_i'' + h_i M_{i+1}''}{6} \tag{6.37}$$

$$d = M_i \tag{6.38}$$

Thus application of equations 6.32-6.38 for each spline interval will yield the complete distributions of pile bending moment and shear force and soil lateral pressure down the embedded length of the pile.

Moments M_i at the spline endpoints for use in the above described procedure were obtained from the smoothed curvature distributions (described previously in Section 6.10.1.2(b)) and the moment-curvature relationship (see Fig. 6.21). Since a cyclic moment-curvature relationship had not been developed, analyses to obtain pile bending moment and shear force and soil lateral pressure were only performed for the monotonic lateral load tests (units 12 and 13).

In Chapter 5 it was shown that experimental and theoretical moment-curvature responses were in good but not perfect agreement. For example from Section 5.3.4, on average experimental values of yield curvature were 7% larger than theoretical values. Because of this small divergence between experimental and theoretical moment-curvature responses, the p(x) distributions obtained as described above were subsequently scaled to be in a state of horizontal force equilibrium with the applied lateral load. Thus in the final form of the soil lateral pressure distribution:

$$\int_0^{2.3} p(x) \cdot D \cdot dx = H \tag{6.39}$$

where at ground level x = 0 and at pile base x = 2.3 m. The corresponding distributions of M(x) and V(x) were also scaled by the same factor. Typically this scaling resulted in a 6% adjustment to the M(x), V(x) and p(x) distributions.

6.10.2 Pile Lateral Deflection Distributions

Figures 6.49-6.54 show profiles of pile lateral deflection for units 12, 13, 2, 3, 5 and 6 respectively, at different stages during testing. As shown in Fig. 6.55, the deflected profile of a pile can be considered to be the sum of deflected profiles due to rigid pole deformation (straight) and flexible pile deformation (bent).

Profiles for units 12 (medium density sand) and 13 (loose density sand) which were tested in a monotonic fashion, indicate that the dominant mode of pile deformation was rigid pole rotation. For example at peak load-level lateral deflection (≅ 2.6D ≅ 299 mm), in the medium and loose density sand tests only 14% and 6% respectively of the lateral deflection at load level was due to pile flexural deformation. This result is contrary to the behaviour that was predicted in Section 6.2.1 where, using conventional pile design theory, it was indicated that the pile tested in medium density sand would behave in a flexible fashion (i.e. zero rigid pole rotation). Results for unit 12 (medium density sand) show that the position of zero lateral deflection on the pile increases in depth from about 10D to 13.5D as the load-level lateral deflection increased from 0.1D to 2.59D. However results from unit 13 (loose density sand) show that the position of zero lateral deflection was relatively stable at a depth of about 15D throughout all stages of testing. It is also clear that units 12 and 13 were subjected to substantial base lateral deflections, since at peak load-level deflections (≅ 299 mm) units 12 and 13 had pile base lateral deflections of -112 mm and -85 mm respectively.

Results from the cyclic testing of units 2, 3, 5 and 6 (see Figs. 6.51-6.54) show larger proportions of pile flexural deformation to pile rigid pole deformations than did the monotonic tests (units 12 and 13). This occurs because at a given load-level lateral deflection and soil density, pile curvatures are larger in the cyclic than in the monotonic tests as previously shown in Figs. 6.41-6.46. Pile flexural deformation was particularly apparent in the cyclic tests conducted in medium density sand (units 2 and 3). For example for unit 2 at the peak of the sixth cycle to a load-level lateral deflection of D, practically 100% of the pile deflected shape was due to flexural deformation. The cyclic tests also showed unsymmetrical behaviour, as the magnitudes of pile base lateral deflection at the positive and negative peaks of a cycle were in general not equal.

6.10.3 Pile Bending Moment Distributions

Figures 6.56 and 6.57 show bending moment distributions, at different load-level lateral displacements for units 12 and 13 respectively. Bending moments above ground level were obtained from static considerations (i.e. moment = lateral load x vertical distance to load level). Moments beneath ground level were obtained using the spline-fitting and scaling procedure described previously in Section 6.10.1.2. At ground level a good match is obtained between the moments obtained from these two methods. This gives confidence in the procedure outlined in Section 6.10.1.2. From Figs. 6.56 and 6.57, it is also significant that reversal of bending moment at depth does not occur.

6.10.4 Pile Shear Force Distributions

Figures 6.58 and 6.59 show shear force distributions at different load-level lateral displacements for units 12 and 13 respectively. Shear forces above ground level were obtained from static considerations (i.e. shear force = applied lateral load), while beneath ground level the spline-fitting and scaling procedure was used. At ground level a good match is obtained between the independently obtained shear forces, although this match is better at large than at small load-level deflections. This again implies confidence in results obtained from the spline-fitting and scaling procedure outlined in Section 6.10.1.2. It is also interesting to note that at a depth of about 15D, negative shear forces are indicated on the pile which were of the order of 70% of the applied lateral load.

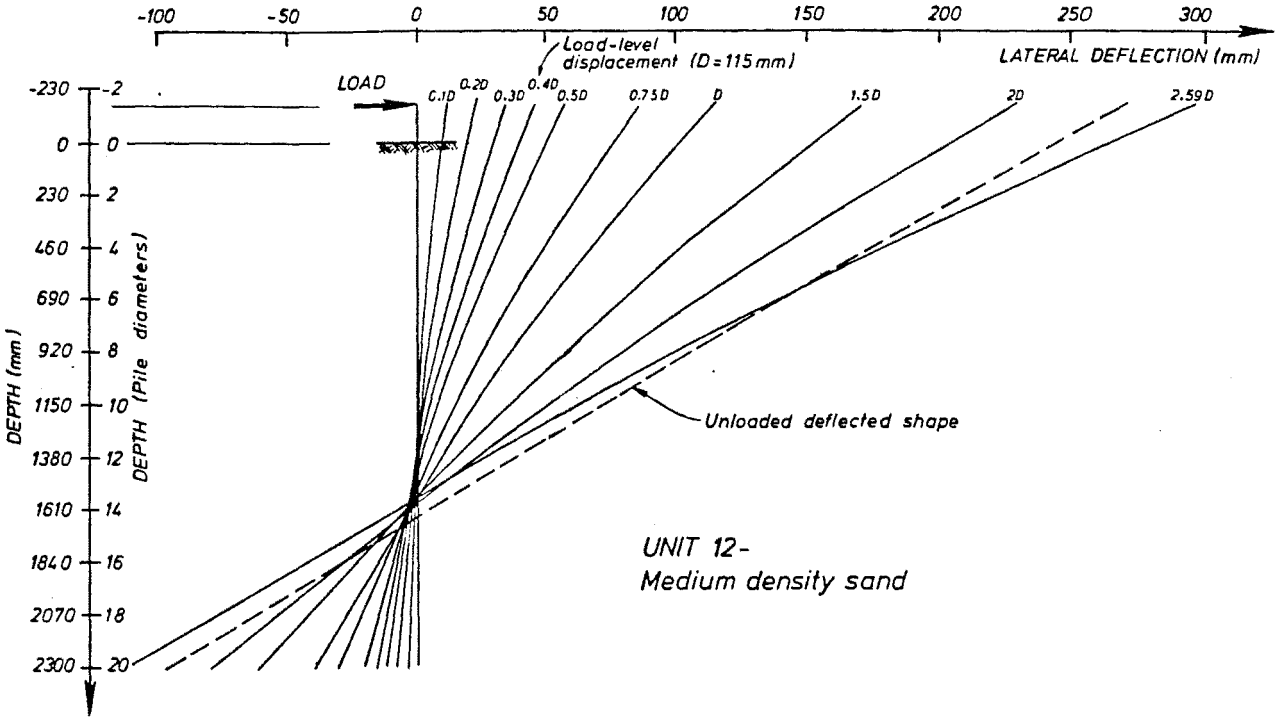

FIG. 6.49 : UNIT 12 (MONOTONIC TEST, MEDIUM DENSITY SAND) LATERAL DEFLECTION PROFILES

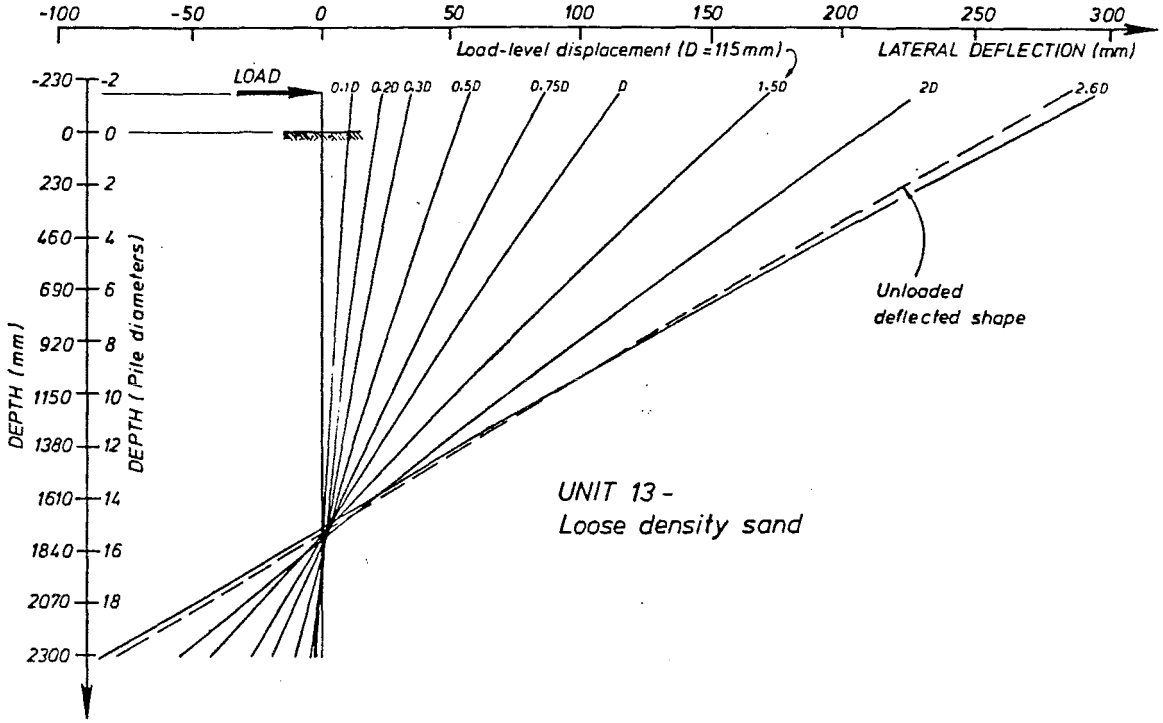

FIG. 6.50 : UNIT 13 (MONOTONIC TEST, LOOSE DENSITY SAND) LATERAL DEFLECTION PROFILES

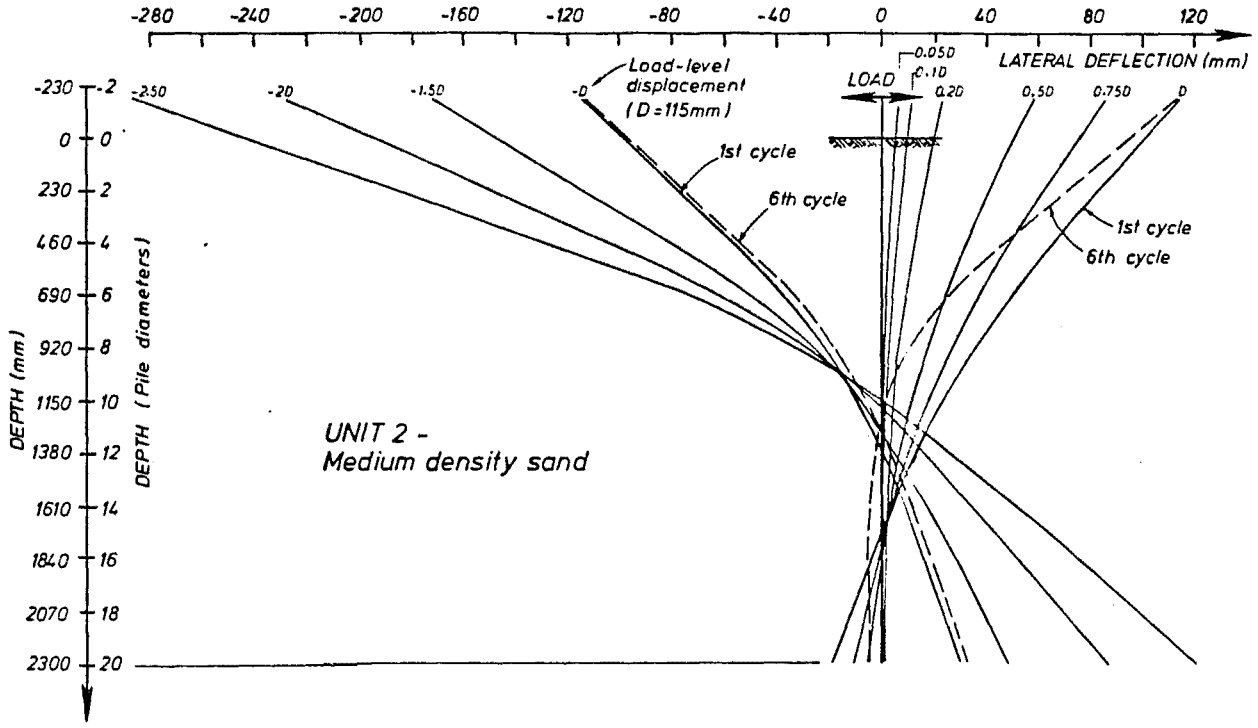

FIG. 6.51 : UNIT 2 (CYCLIC TEST, MEDIUM DENSITY SAND)
LATERAL DEFLECTION PROFILES

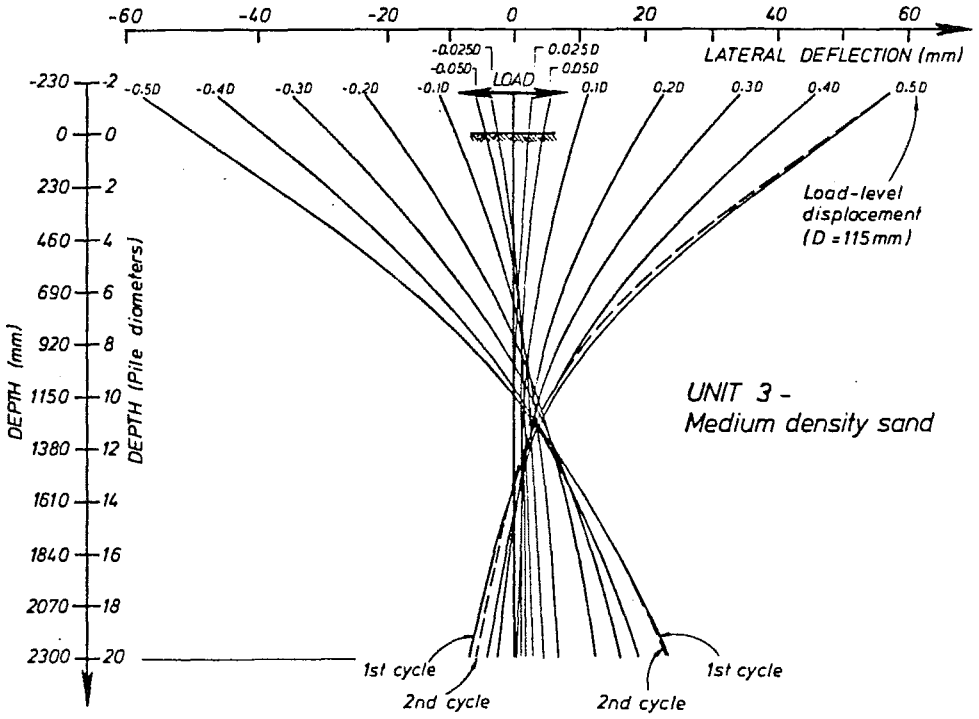

FIG. 6.52 : UNIT 3 (CYCLIC TEST, MEDIUM DENSITY SAND)
LATERAL DEFLECTION PROFILES

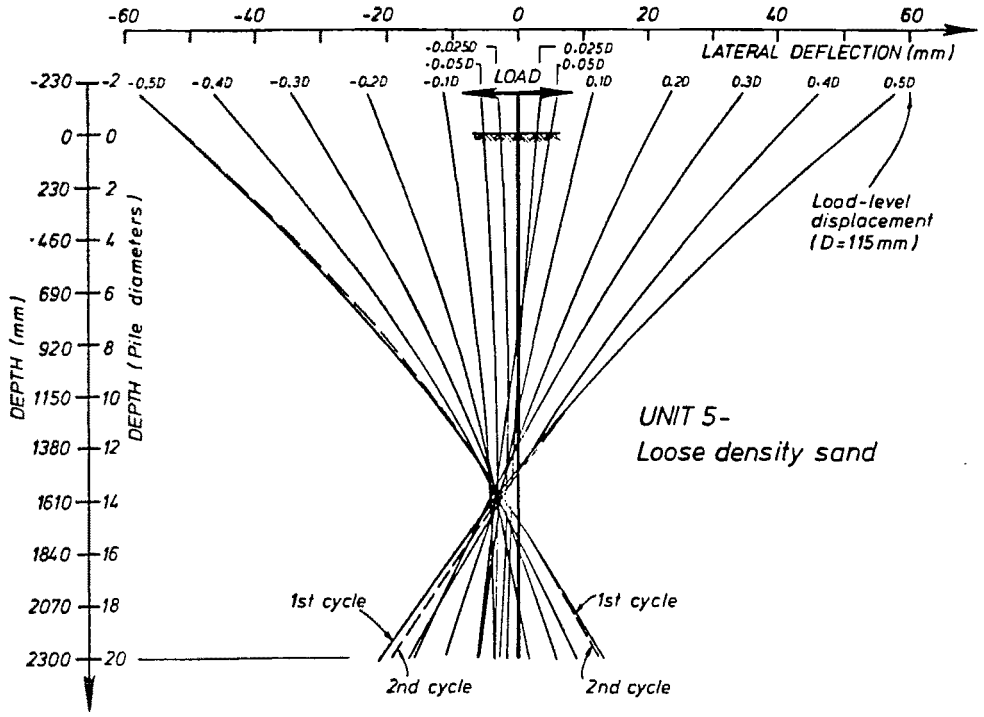

FIG. 6.53 : UNIT 5 (CYCLIC TEST, LOOSE DENSITY SAND)
LATERAL DEFLECTION PROFILES

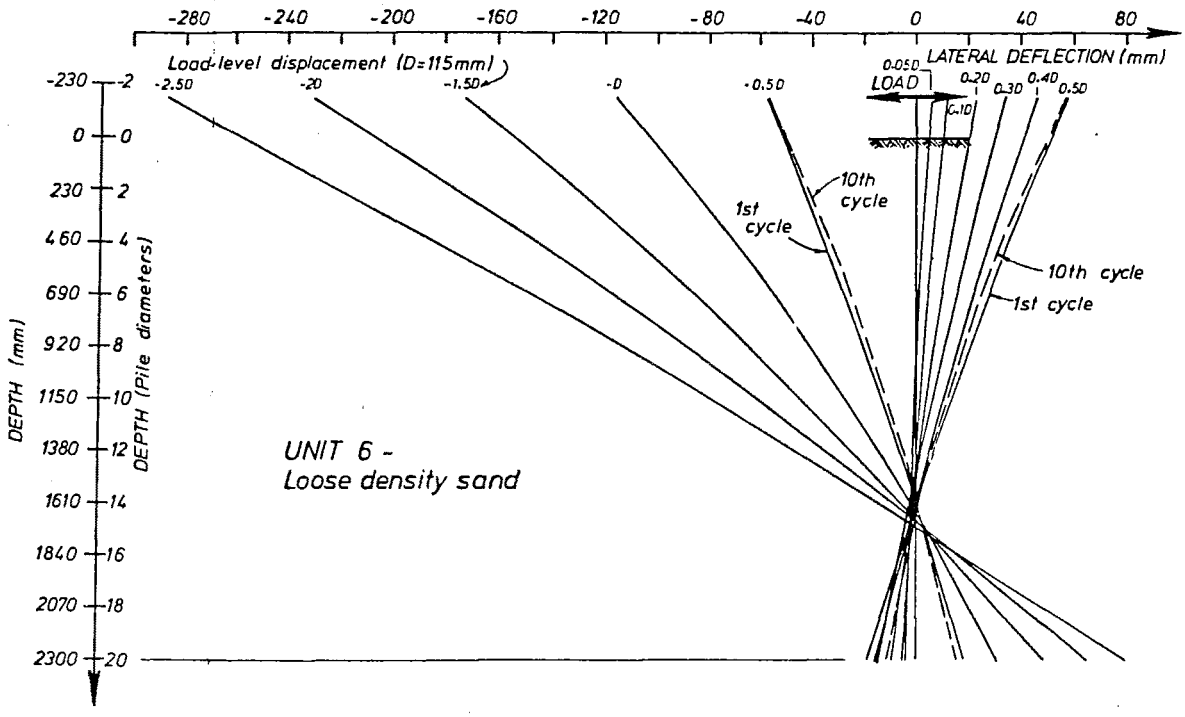

FIG. 6.54 : UNIT 6 (CYCLIC TEST, LOOSE DENSITY SAND)
LATERAL DEFLECTION PROFILES

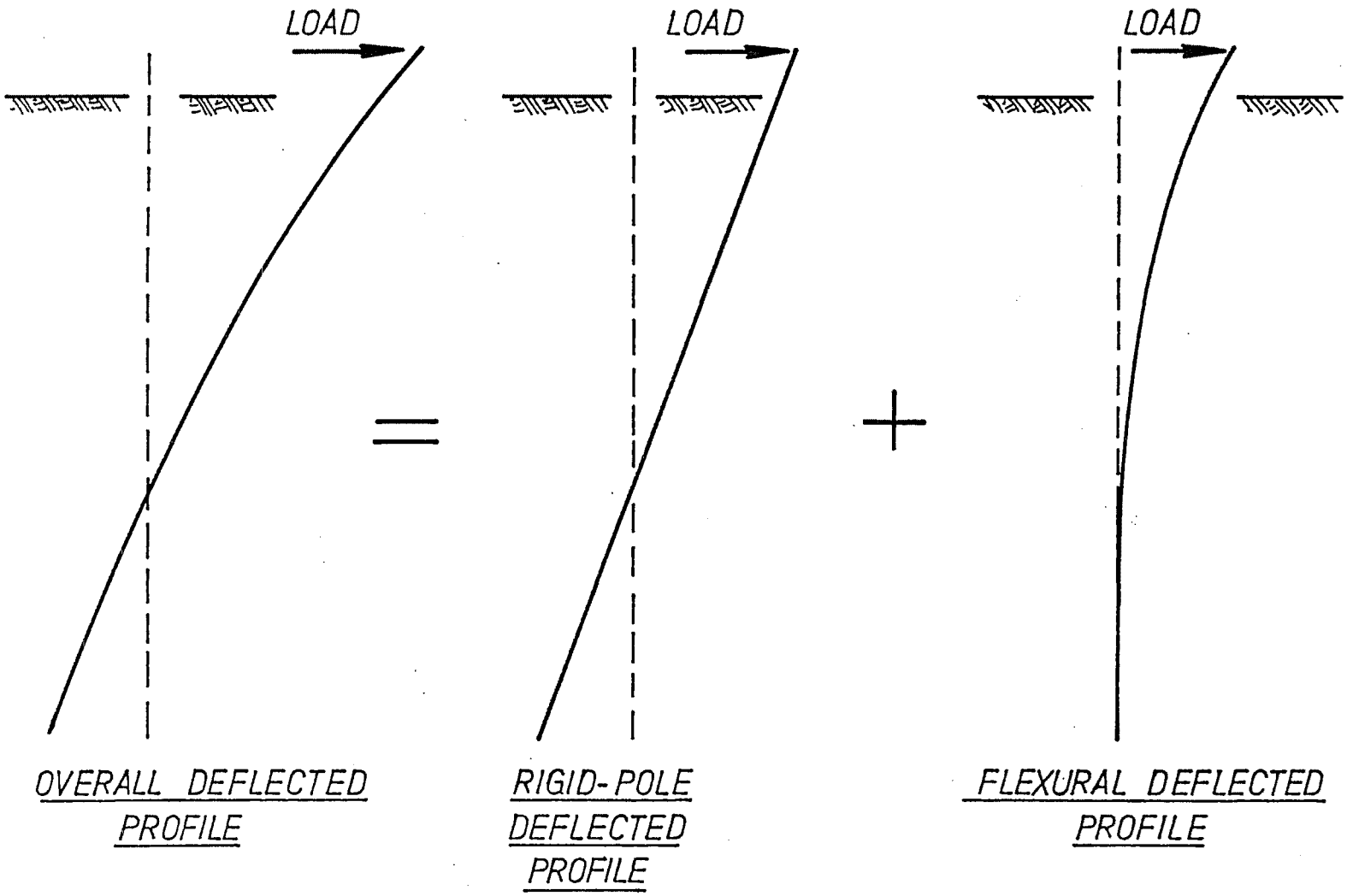

FIG. 6.55 COMPONENTS TO DEFLECTED SHAPE.

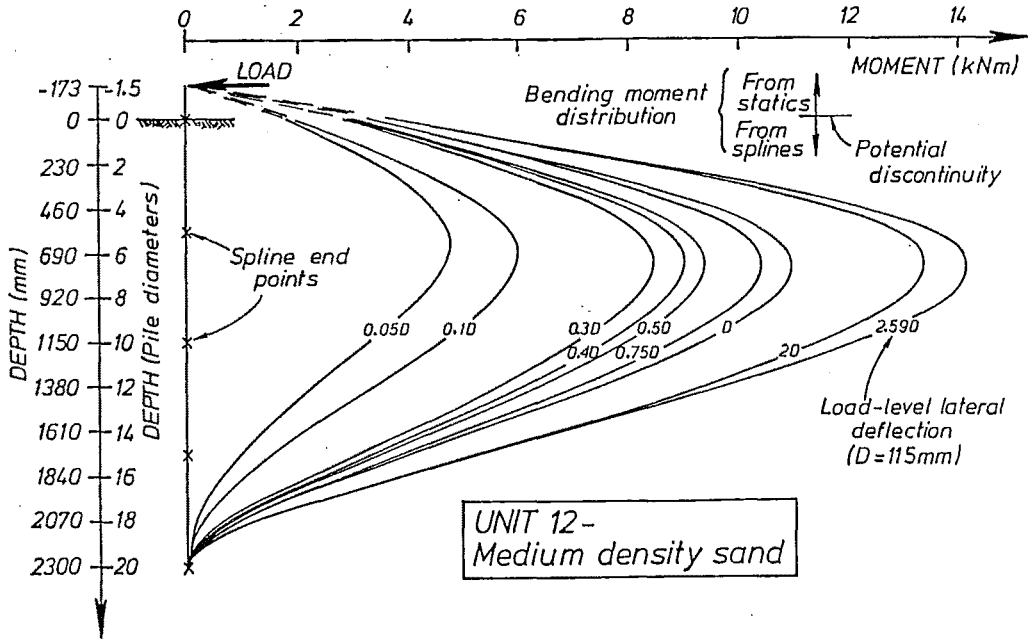

FIG. 6.56 UNIT 12 (MONOTONIC TEST, MEDIUM DENSITY SAND) BENDING MOMENT DISTRIBUTIONS

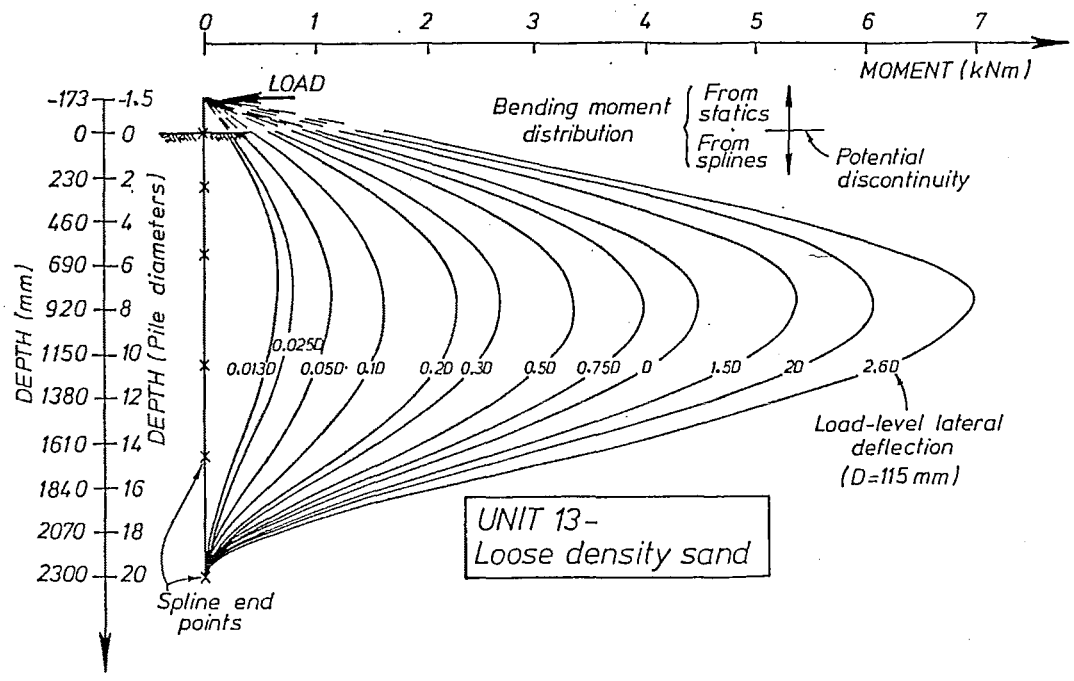

FIG. 6.57 UNIT 13 (MONOTONIC TEST, LOOSE DENSITY SAND) BENDING MOMENT DISTRIBUTIONS

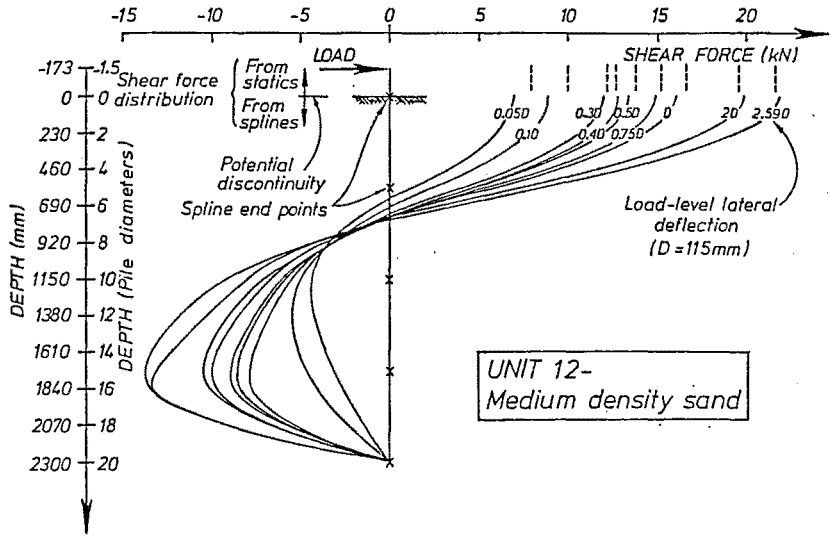

FIG. 6.58 UNIT 12 (MONOTONIC TEST, MEDIUM DENSITY SAND) SHEAR FORCE DISTRIBUTIONS

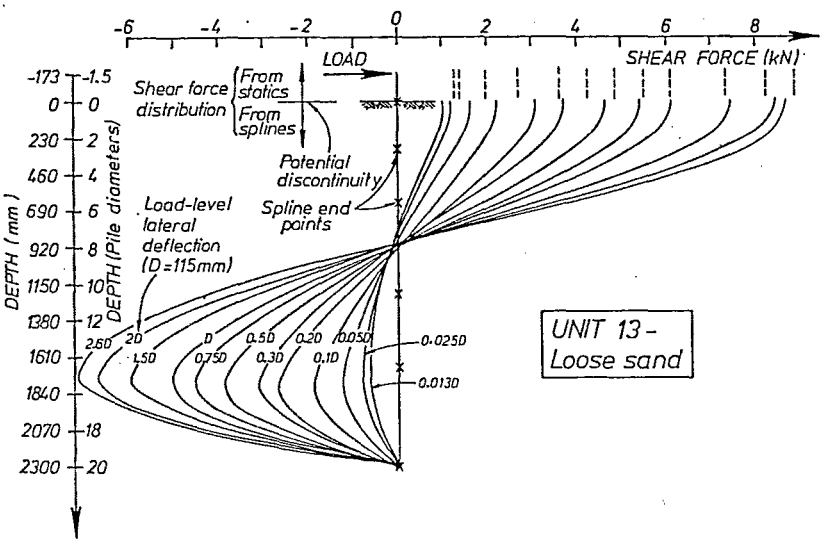

FIG. 6.59 UNIT 13 (MONOTONIC TEST, LOOSE DENSITY SAND) SHEAR FORCE DISTRIBUTIONS

6.10.5 Soil Lateral Pressure Distributions

Figures 6.60 and 6.61 show soil lateral pressure distributions, at different load-level lateral displacements, for units 12 and 13 respectively. Also indicated on these diagrams are lines showing multiples of passive pressure where passive pressure $p_p(x)$ is calculated from:

$$p_p(x) = \frac{1 + \sin\phi}{1 - \sin\phi} \cdot \rho g x \qquad (6.40)$$

where ϕ = angle of internal friction (given in Section 6.5.1)
ρ = soil density (also given in Section 6.5.1)
g = acceleration due to gravity (9.81 m/s^2)
x = depth beneath ground level.

The plotted soil lateral pressure distributions are relatively coarse, as they are comprised of either 4 or 5 piecewise linear segments. However the positions of zero lateral pressure (see Figs. 6.60 and 6.61) do approximately correspond to the positions of zero lateral deflection (see Figs. 6.49 and 6.50) which gives a further degree of confidence in the spline-fitting procedure. For unit 13 (loose density sand), the profiles of soil lateral pressure show a relatively gradual transition (within the limitations of a distribution represented in piecewise linear fashion) as depth down the pile is increased. This might be expected for the uniformly layered sand. However pressure distributions for unit 12 (medium density sand) are somewhat more irregular. Thus from Fig. 6.60, it is possible that soil lateral pressures may be overestimated and underestimated at depths of 5D and 10D respectively.

The large influence of soil density on the lateral pressures is shown, since the peak soil pressure in the medium density sand was at least twice that indicated for the loose density sand. In general from the results it also appears that peak soil lateral pressures had not been reached despite the large levels of imposed pile lateral displacement.

At the peaks of the positive lateral pressure zones of Figs. 6.60 and 6.61, soil pressures of the order of 7 (unit 13 - loose density sand) and 15 (unit 12 - medium density sand) times passive pressure are indicated. At the peaks of the negative lateral pressure zones (i.e. pile base), soil pressures of the order of 2.5 (unit 13 - loose density sand) and 4.5 (unit 12 - medium density sand) times passive pressure are indicated. These stresses may be compared with the value of 3 times passive pressure which has been recommended by Broms (6.18) for the design of piles in cohesionless soils. Broms obtained this soil pressure from back analysis of full-scale pile tests with an assumed pressure distribution. However he did not state the level of lateral displacement used in obtaining these soil pressures and it is quite possible that only low levels were used. It is also interesting to note that in the model tests (D = 10 mm) of Fendall (6.6), pressure transducers mounted in the pile indicated lateral stresses of the order of 25 times passive pressure at a load-level displacement of 0.6D. Thus a comparison of these three sets of test results (Broms, Fendall, and the tests described in this chapter) indicates that pile size (scale effect) and displacement level have a large influence on the level of soil lateral stress on the pile.

6.10.6 Soil Lateral Pressure - Lateral Deflection - Depth Responses

Figure 6.62 shows soil lateral pressure - lateral deflection - depth responses at the positions of spline endpoints for units 12 and 13 respectively. For both units a depth of 15D is close to the position on the pile where, under lateral load, zero lateral deflection occurs. Thus lateral deflections at spline endpoints in the vicinity of a depth of 15D are very sensitive to the accuracy of load-level rotation measurements. This is the probable reason for soil responses in this vicinity being weaker than might otherwise be expected.

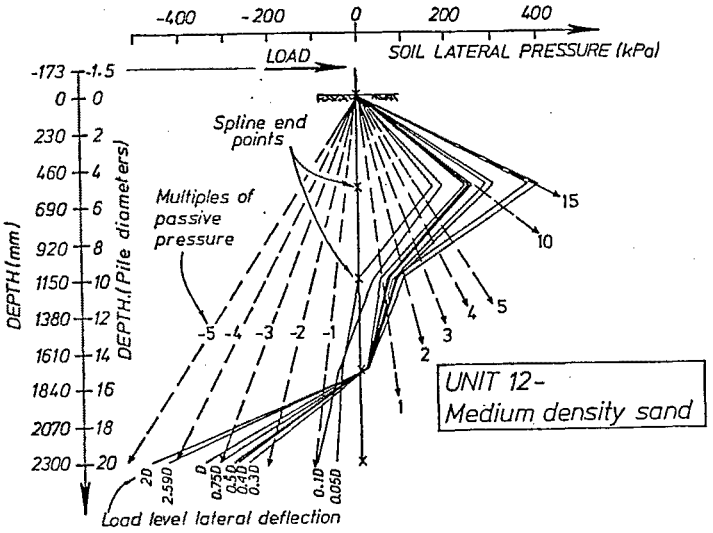

FIG. 6.60 UNIT 12 (MONOTONIC TEST, MEDIUM DENSITY SAND) SOIL LATERAL PRESSSURE DISTRIBUTIONS

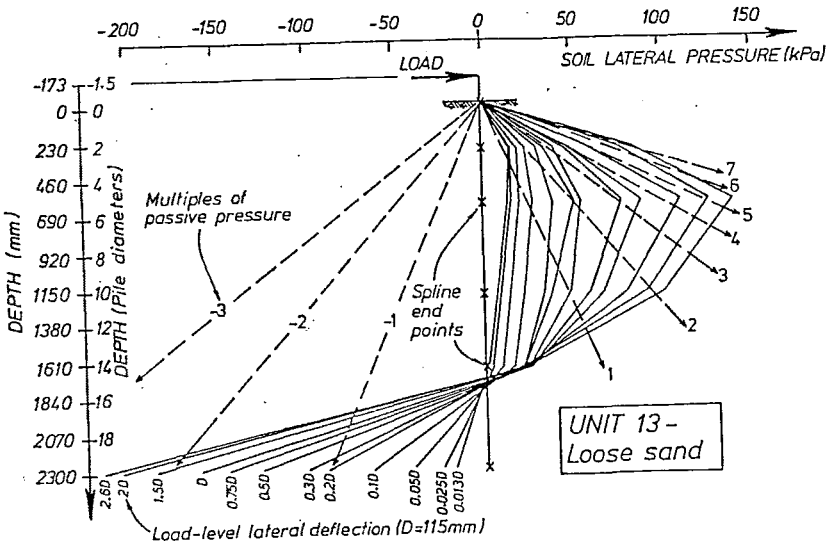

FIG. 6.61 UNIT 13 (MONOTONIC TEST, LOOSE DENSITY SAND) SOIL LATERAL PRESSURE DISTRIBUTIONS

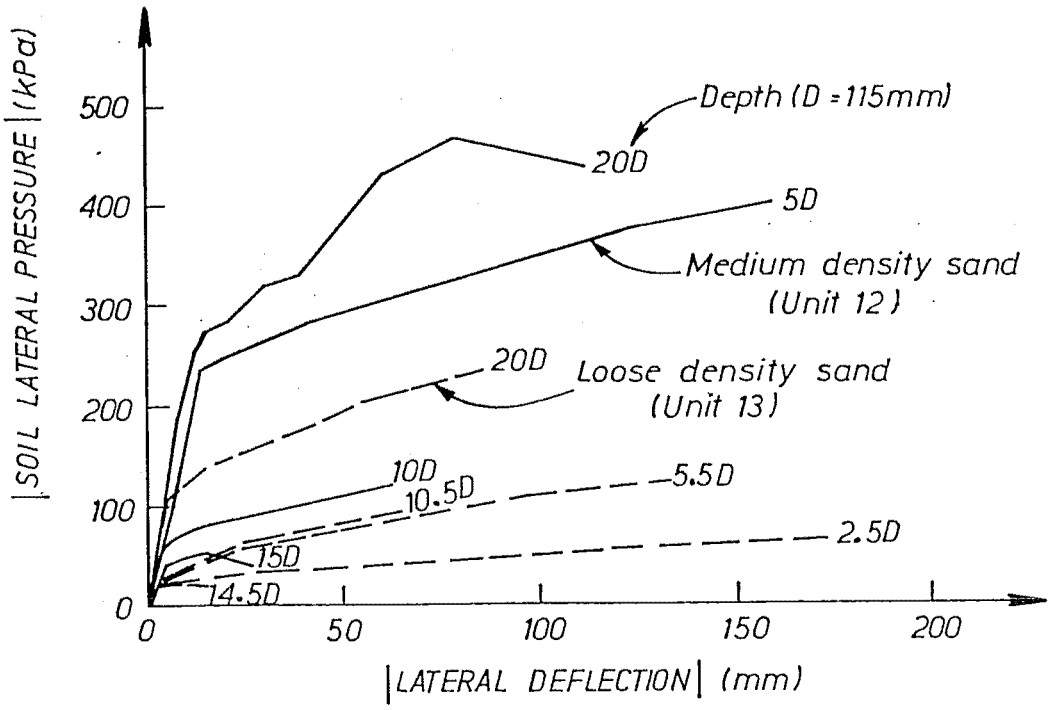

FIG. 6.62 EXPERIMENTAL SOIL LATERAL PRESSURE-DEFLECTION RESPONSES

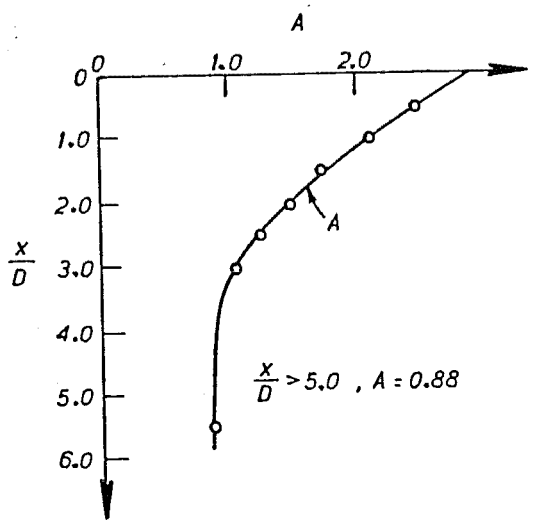

FIG. 6.63 EMPIRICAL COEFFICIENT "A" AS A FUNCTION OF DIMENSIONLESS DEPTH - AFTER REESE ET AL (6.1).

In general results from unit 13 (loose density sand) show that soil lateral pressure increases as depth or pile lateral deflection increases. Again, in general, from the significant upward slope at the ends of these curves, it is apparent that the ultimate soil lateral pressures were not reached.

Results from unit 12 (medium density sand) are not as consistent as those for unit 13, as might be expected from the somewhat irregular pressure distributions shown for unit 12 in Fig. 6.60. From Fig. 6.60 it appeared that soil pressures were overestimated and underestimated at depths of 5D and 10D respectively, which is in agreement with the result shown in Fig. 6.62 where at large deflections (> 4 mm) soil pressures at a depth of 5D are indicated to be larger than those at 10D. However in general results for unit 13 indicate that soil pressures increase with lateral deflection.

6.10.7 Comparison of Experimental Soil Responses with Predictions Based on Reese et al Model

As mentioned in Section 1.4.2, there are many semi-empirical models for determining soil response which use the concept of soil behaving as a series of horizontally orientated non-linear springs (i.e. continuous nature of soil ignored) located along the length of the pile. The most widely known of these is the Reese et al model (6.1). In this section the experimentally determined responses of the soil used in testing units 12 and 13 are compared with predictions based on the Reese et al model.

This model is based on a rational assessment of the ultimate value of lateral soil resistance which is obtained from the weaker of two possible failure modes:

(i) soil horizontal flow;

and (ii) soil passive wedge formation.

These two failure mechanisms were previously illustrated in Fig. 1.11. Mode (ii) tends to govern close to ground level and mode (i) at greater depth in the foundation. However despite this rational assessment, Reese et al still found it necessary to apply empirical calibration factors to these ultimate soil strengths to get good correlation with test data from the Mustang Island pile test (6.1). Soil response prior to ultimate stress being reached was obtained by calibration to give agreement with data from the Mustang Island pile test. Reese et al (6.1) also state that this model results in a good prediction of behaviour for results from other full-scale pile tests.

However it should be noted that the Mustang Island pile tests involved 610 mm diameter piles that were driven into a saturated foundation consisting of fine sand to silty fine sand of high relative density. No allowance is made in the model for the effect of pile installation which as observed in the model tests of Fendall (6.6) can result in as large an effect on the soil as the subsequent lateral loading. Furthermore, the Mustang Island tests were performed with relatively low ground-level lateral deflections in the range of 0 - 0.05D.

An outline of the model of Reese et al (6.1) is given below. The theoretical ultimate resistance in the soil at a given depth is given by the smaller of w_{ct} (passive wedge failure) or w_{cd} (horizontal flow failure), which are calculated as follows:

$$w_{ct} = \rho.g.x\left[\frac{K_o.x.\tan\phi.\sin\beta}{\tan(\beta-\phi).\cos\alpha} + \frac{\tan\beta}{\tan(\beta-\phi)}(D + x.\tan\beta.\tan\alpha) + K_o.x.\tan\beta.(\tan\phi.\sin\beta - \tan\alpha) - K_a.D\right] \quad (6.41)$$

$$w_{cd} = K_a.D.\rho.g.x\ (\tan^8\beta - 1) + K_o.D.\rho.g.x.\tan\phi.\tan^4\beta \qquad (6.42)$$

where ρ = soil density (beneath the water table use buoyant density)
g = acceleration due to gravity
x = depth
D = pile diameter
K_o = at-rest pressure coefficient (= 0.4)
ϕ = angle of internal friction of soil
$\beta = 45° + \phi/2$
$\alpha = \phi/2$
K_a = active pressure coefficient = $\tan^2(45° - \phi/2)$

It should be noted that in the above equations, w_{ct} and w_{cd} are given in terms of pile distributed load (= soil lateral stress x pile diameter) as described by Reese et al (6.1).

At a given depth the smaller of w_{ct} or w_{cd} is taken as the theoretical ultimate resistance of the soil w_c. The recommended value of ultimate resistance w_u is then calculated from:

$$w_u = A \cdot w_c \qquad (6.43)$$

where A is an empirical coefficient which for static loading can be determined from Fig. 6.63.

Shapes of the pile distributed load - lateral deflection ($w - y$, where $w = D \cdot p$) relationships which consist of 3 lines and a non-linear curve are shown in Fig. 6.64 for a number of depths. At a given depth w_m is defined by:

$$w_m = B \cdot w_c \qquad (6.44)$$

where B is an empirical coefficient which can be determined from Fig. 6.65. Deflections y_u and y_m which are shown in Fig. 6.64 are defined by:

$$y_u = 0.0375D \qquad (6.45)$$

and $$y_m = 0.0167D \qquad (6.46)$$

The initial elastic portion of the curve from $(y,w) = (0,0)$ to (y_k,w_k) at a given depth x is defined by:

$$w = n_h \cdot x \cdot y \qquad (6.47)$$

where n_h is the coefficient of horizontal subgrade reaction (to be taken as 5, 16 or 34 MPa/m for loose, medium or dense sand respectively). The non-linear curve between (y_k,w_k) and (y_m,w_m) is defined by:

$$w = C\,y^{1/n} \qquad (6.48)$$

where $$n = \frac{w_m}{y_m} \cdot \frac{y_u - y_m}{w_u - w_m} \qquad (6.49)$$

and $$C = \frac{w_m}{y_m^{1/n}} \qquad (6.50)$$

The deflection y_k is defined by:

$$y_k = \left(\frac{C}{n_h \cdot x}\right)^{n/n-1} \qquad (6.51)$$

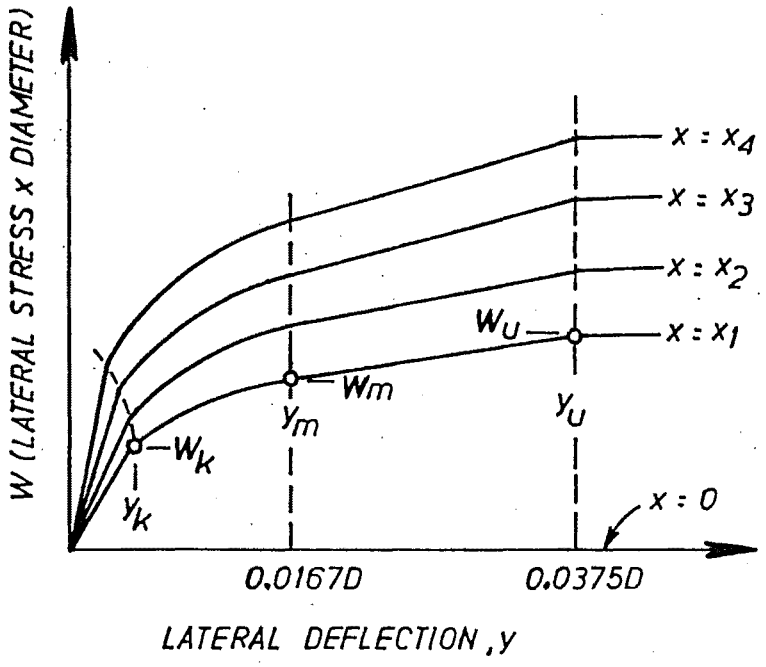

FIG. 6.64 TYPICAL FAMILY OF LATERAL STRESS-DEFLECTION CURVES

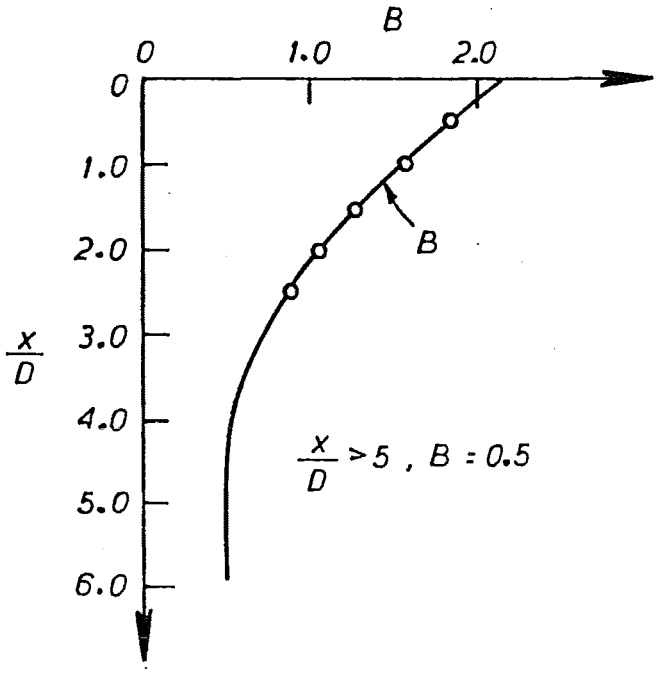

FIG. 6.65 EMPIRICAL COEFFICIENT "B" AS A FUNCTION OF DIMENSIONLESS DEPTH - AFTER REESE ET AL (6.1)

Figures 6.66 and 6.67 show soil lateral pressure (w.D)-lateral deflection (y) responses for units 12 and 13 respectively which were predicted using the Reese et al model (6.1). Also shown are the responses deduced from the experimental results of these units. Both experimental and predicted soil responses are plotted at depths corresponding to the spline endpoints.

Poor agreement is indicated between predictions and experiment in terms of the shape, stiffness and strength of the soil responses. For depths of 20D, the experimentally obtained soil responses are overestimated by predictions based on the Reese et al model (6.1), although in general at smaller values of depth closer agreement is obtained between the experimental results and the predictions. It is also apparent that the approximately elastic-plastic shape of the predicted soil responses is dissimilar to the non-linear gradually softening behaviour of the soil.

Thus it appears that the method of pile installation and the scale of the pile which differed markedly between the Mustang Island test (6.1), from which Reese et al (6.1) calibrated their soil model, and the model pile tests described in this chapter have a significant effect on the response of the foundation soil.

6.10.8 Variation of Curvature Ductility Ratio with Displacement Ductility Ratio

In this section the variation of curvature ductility ratio with displacement ductility ratio which was deduced from the flexural deformation of unit 2 is described and compared with a theoretical prediction based on an equivalent cantilever approach. Only unit 2 was examined since, as shown in Figs. 6.41-6.46, this was the only unit subjected to significant inelastic curvature.

From the measured values of load-level lateral displacement y_t, pile base lateral displacement y_b, and pile base rotation θ_b; the values of lateral displacement at load level due to rigid pole rotation (Δ_p) and flexure (Δ_f) can be calculated as shown in Fig. 6.68 and below:

$$\Delta_p = 2.473\theta_b \tag{6.52}$$

$$\Delta_f = y_t - y_b - \Delta_p \tag{6.53}$$

At a given load-level displacement, the maximum curvature on the pile is designated as ψ_{max}. Hence the curvature ductility ratio on the pile is equal to ψ_{max}/ψ_y where ψ_y, (the idealised yield curvature) was equal to 0.0337 rads/m, and as stated in Section 6.8 ψ_y corresponds to yield for an elastic-plastic idealisation of moment-curvature behaviour. The corresponding displacement ductility ratio μ, considering only pile flexural deformation is given by:

$$\mu = \Delta_f/\Delta_y \tag{6.54}$$

The idealised yield deflection Δ_y, also corresponding to an elastic-plastic idealisation of behaviour was obtained as shown in Fig. 6.69. This involved calculating a regression line through the $\psi_{max} - \Delta_f$ data obtained during the first half cycle of loading of unit 2 for the stage where $\psi_{max} < \psi_y$. Yield deflection Δ_y could then be obtained from the value of Δ_f corresponding to $\psi_{max} = \psi_y$. A value of $\Delta_y = 52.0$ mm was obtained in this fashion.

Equivalent cantilever behaviour was obtained by noting that an elastically behaving cantilever loaded laterally at its free end will have the following relationship between Δ_f, ψ_{max} and L (cantilever length):

$$\Delta_f = \frac{\psi_{max} \cdot L^2}{3} \tag{6.55}$$

At the idealised yield point of the cantilever, equation 6.55 can be expressed as:

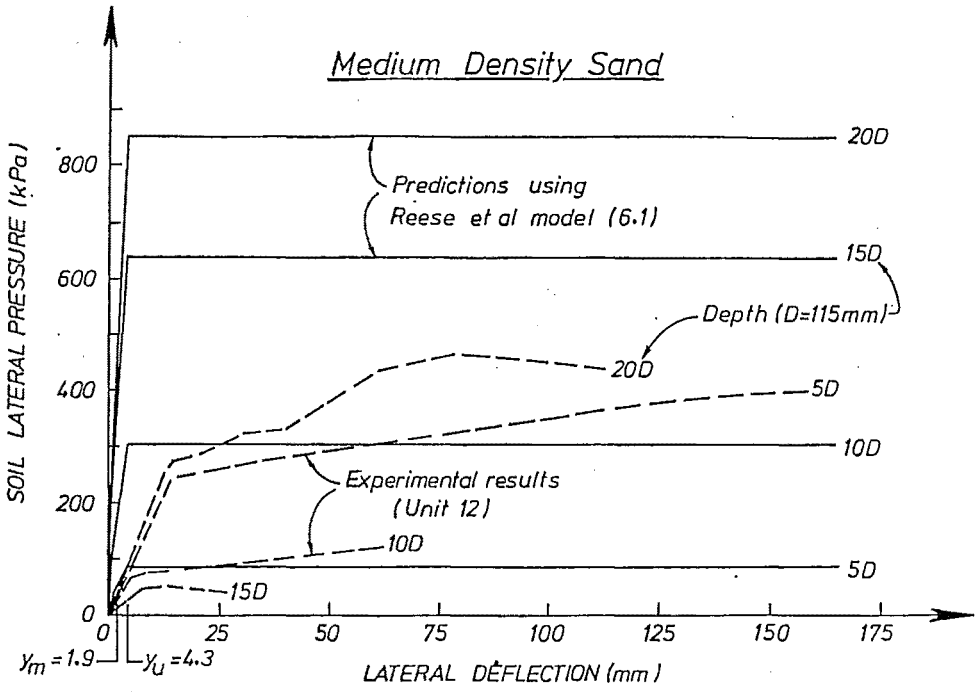

FIG. 6.66 COMPARISON OF EXPERIMENTAL AND THEORETICAL MEDIUM DENSITY SAND RESPONSES

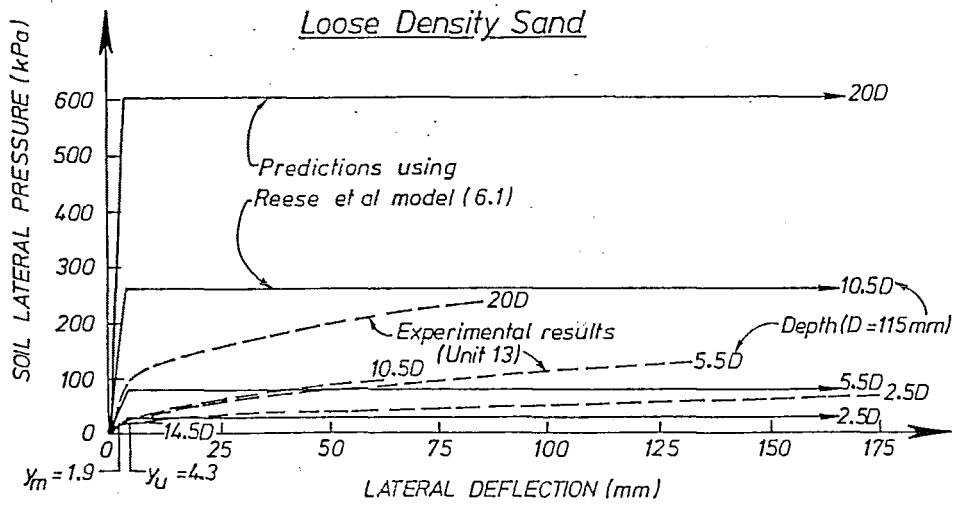

FIG. 6.67 COMPARISON OF EXPERIMENTAL AND THEORETICAL LOOSE DENSITY SAND RESPONSES

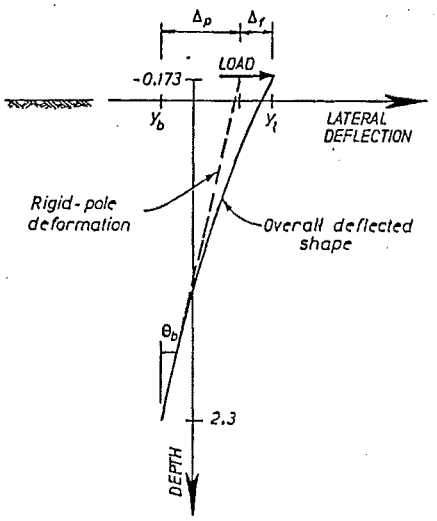

FIG. 6.68 CALCULATING RIGID-POLE AND FLEXURAL COMPONENTS OF DISPLACEMENT.

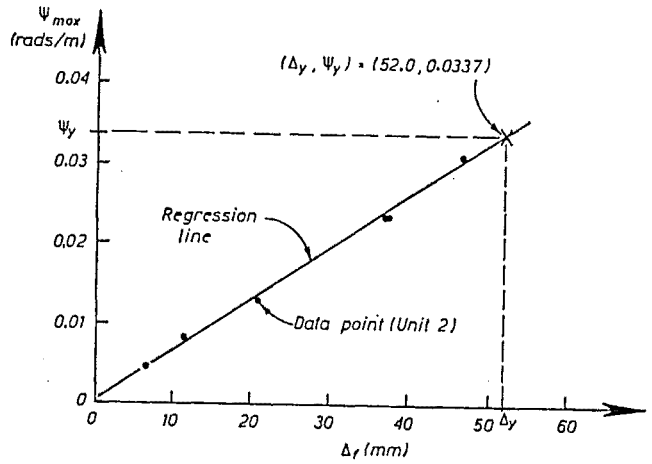

FIG. 6.69 DETERMINING YIELD CURVATURE Δ_y.

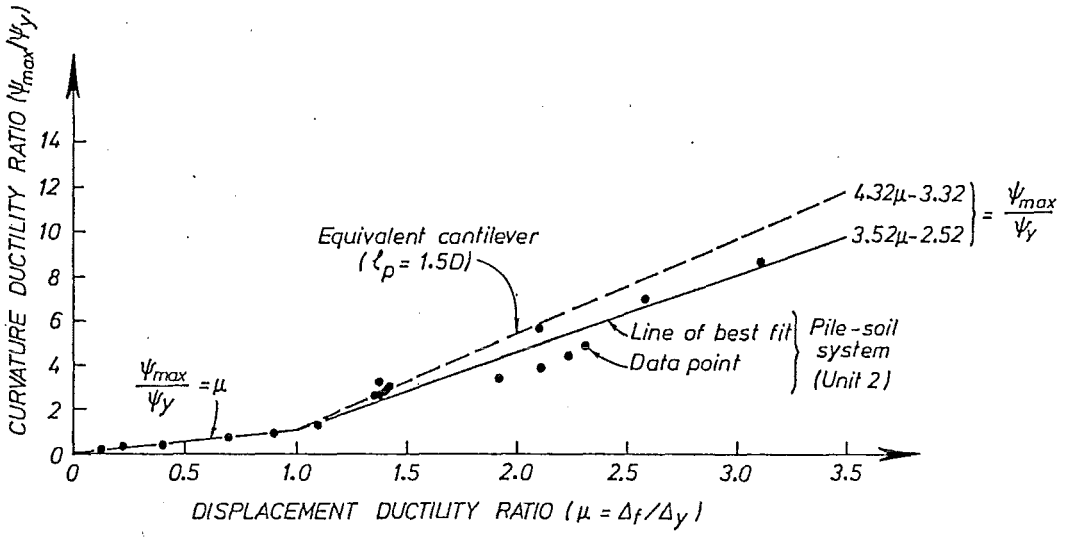

FIG. 6.70 CURVATURE DUCTILITY RATIO VS DISPLACEMENT DUCTILITY RATIO.

$$\Delta_y = \frac{\psi_y \cdot L^2}{3} \qquad (6.56)$$

To match the flexural behaviour of the real pile-soil system at yield, then Δ_y = 52.0 mm and ψ_y = 0.0337 rads/m which from equation 6.56 gives L = 2.15 m. In the plastic range of behaviour, the relationship between ψ_{max}/ψ_y, μ, L and ℓ_p (the equivalent plastic hinge length) is given (as described in Section 4.10.1) by:

$$\frac{\psi_{max}}{\psi_y} = \frac{L^2 (\mu - 1)}{3\ell_p (L - \ell_p/2)} + 1 \qquad (6.57)$$

It was also shown in Section 4.10.1 that before local buckling occurred (no local buckling was noticed in unit 2), the relationships between curvature and displacement ductility ratios for steel-encased reinforced concrete and reinforced concrete members were similar. From the results of a wide range of tests of reinforced concrete members, which were subjected to a linearly varying bending moment distribution, Priestley and Park (6.19) have shown that the equivalent plastic hinge length ℓ_p can be estimated from:

$$\ell_p = 0.08L + 6d_b \qquad (6.58)$$

However on the basis of tests of very squat members (small L/D ratios), they also recommend that ℓ_p not be taken as less than 0.3D, while for very slender members (large L/D ratios) they also recommend that ℓ_p not be taken as larger than 1.5D.

For an equivalent cantilever of length L = 2.15 m and diameter D = 0.115 m, then ℓ_p should be taken as 0.173 m (= 1.5D). Thus substituting L = 2.15 m and ℓ_p = 0.173 m into equation 6.57 gives:

$$\frac{\psi_{max}}{\psi_y} = 4.32\mu - 3.32 \qquad (6.59)$$

Figure 6.70 shows the $\psi_{max}/\psi_y - \mu$ data obtained by analysing unit 2 results from the first half-cycle to a load-level lateral displacement of D, the positive and negative peaks of subsequent cycles to displacements of ±D, and at displacements of -1.5D, -2D and -2.5D during the final stage of testing. Also shown on this figure are the $\psi_{max}/\psi_y - \Delta_f/\Delta_y$ relationships predicted (equation 6.59) assuming equivalent cantilever behaviour and ℓ_p = 1.5D and lines of best fit to the experimental data. In the elastic range of behaviour a best-fit line to the experimental data is

$$\frac{\psi_{max}}{\psi_y} = \mu \qquad (6.60)$$

while in the plastic range a best-fit line to the experimental data is

$$\frac{\psi_{max}}{\psi_y} = 3.52\mu - 2.52 \qquad (6.61)$$

For a given displacement ductility ratio $\mu > 1$, the real pile-soil system is shown to have a marginally lower curvature ductility demand than is predicted assuming equivalent cantilever behaviour and ℓ_p = 1.5D. For example at a μ of 3 the curvature ductility demands are 8.0 in the real pile-soil system and 9.6 in the equivalent cantilever. Thus the actual damage to a pile under large

displacement will be marginally lower than that predicted on the basis of equivalent cantilever behaviour and $\ell_p = 1.5D$.

This occurs because in the vicinity of the position of peak moment, in the real pile-soil system the moment gradient is low which results in a spread of plasticity or an enlargement to the effective plastic hinge length relative to the equivalent cantilever which is subjected to a significant constant level of moment gradient throughout its length.

It is also of interest to calculate the equivalent plastic hinge length ℓ_p for an equivalent cantilever to match the relationship between curvature and displacement ductility ratios which apply in the plastic range to the real pile-soil system. Thus for L = 2.15 m and equating the right hand sides of equations 6.57 and 6.61, it can be determined that ℓ_p = 215 mm or 1.87D. This value of ℓ_p is marginally larger than the 1.5D assumed previously for the equivalent cantilever.

Thus it appears that at a given displacement ductility ratio, pile curvature can be obtained (albeit slightly overestimated) by assuming equivalent cantilever behaviour with an equivalent plastic hinge in accordance with the recommendations of Priestley and Park (6.19) (see equation 6.58 and the associated text).

6.11 EXPERIMENTAL RESULTS - CAPPED HEAD PILES

Results from the twin pile tests (unit 10 - loose density sand and unit 11 - medium density sand) are described in the following sections. These piles were rigidly connected at their heads to a relatively stiff pile cap and subjected to cyclic lateral displacement of steadily increasing amplitude.

6.11.1 General Observations

Sand movement first became visually obvious when the load-level lateral displacement was of the order of 0.05D (5.8 mm). At this stage, sand in front of the piles had heaved, while sand behind the piles had settled. As the cyclic testing proceeded, the extent and magnitude of sand movement increased. For cycles to load-level lateral-displacements of magnitude 0.2D (23 mm) and greater, shear dislocation on the top surface of the sand was observed. Relative settlement of the leading pile and uplift of the trailing pile also occurred, resulting in rotation of the pile cap.

Figure 6.71 shows the above-surface displacement of unit 10 (loose density sand) and the top surface of the sand at the conclusion of testing. Figure 6.72 shows pile and sand movement at the peaks of a number of cycles during testing of unit 11 (medium density sand). Trends apparent in the single piles tested under free-head conditions (see Section 6.9.1), also occurred in the twin pile tests. The extent of sand subjected to shear failure was larger for the unit tested in medium than in loose density sand. Densification of the sand was also apparent as the cyclic loading proceeded, particularly in the vicinity of the piles of unit 10 which were embedded in an initially loose density sand. For all stages of the test conducted in loose density sand (unit 10), soil failure wedges were well clear of the tank walls. Thus it is inferred that tank boundary effects would have had a negligible influence on the response of the sand surrounding unit 10. However, for the test conducted in medium density sand (unit 11) at load-level lateral displacements greater than D, soil failure wedges did intersect the tank walls implying that significant modification to soil response due to boundary effects may have occurred at large pile displacements. However as mentioned earlier (see Section 6.7), displacements of magnitude greater than 0.67D are larger than those anticipated in prototype piles under seismic conditions. Thus in the range of primary interest, behaviour should not have been significantly influenced by boundary effects.

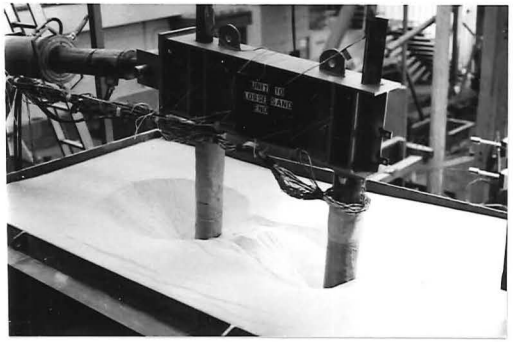

FIG. 6.71 UNIT 10 (CYCLIC TEST - TWIN PILES, LOOSE DENSITY SAND) AT END OF TEST

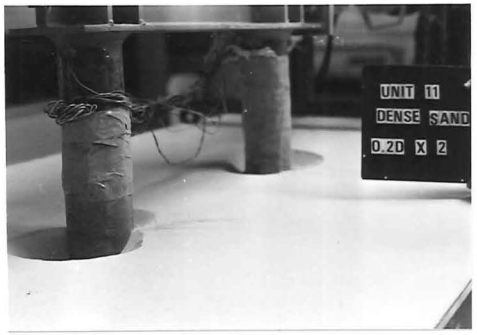

(a) DISPLACEMENT = 0.2D x 2

FIG. 6.72 UNIT 11 (CYCLIC TEST - TWIN PILES, MEDIUM DENSITY SAND

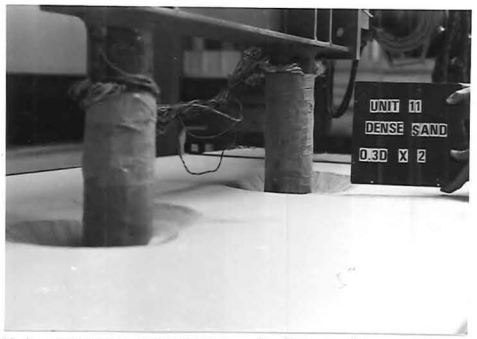

(b) DISPLACEMENT = 0.3D x 2

(c) DISPLACEMENT = 0.4D x 2

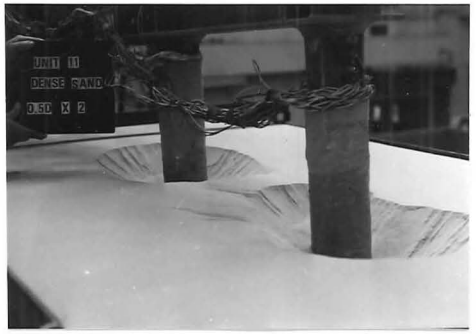

(d) DISPLACEMENT = 0.5D x 2

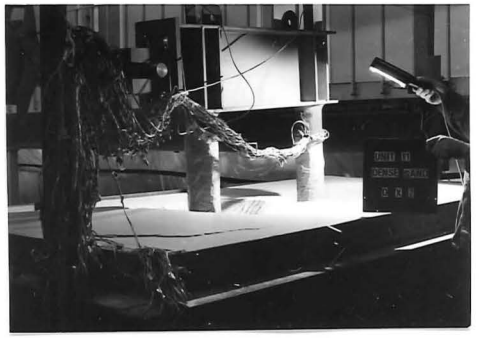

(e) DISPLACEMENT = D x 2

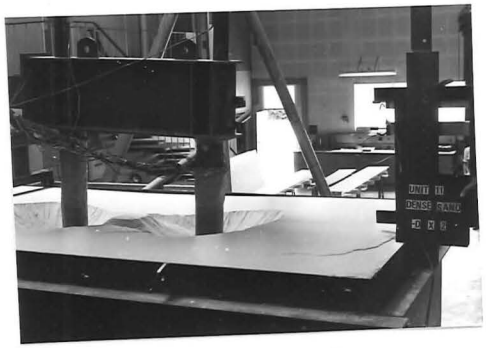

(f) DISPLACEMENT =-D x 2

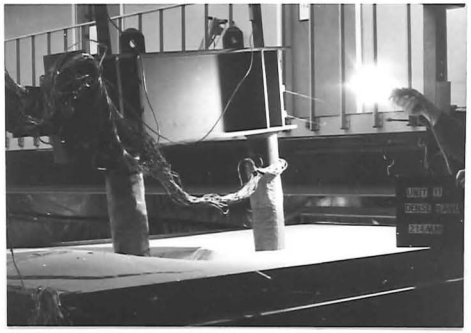

(g) DISPLACEMENT = 1.86D

Figure 6.73 shows a comparison of sand and pile profiles at longitudinal and lateral centreline sections of the tank at peak load-level lateral displacements (≅ 208 mm = 1.8D) attained in units 10 (loose density sand) and 11 (medium density sand). For both units, significant densification of the sand is indicated to have occurred in the vicinity of the piles, although as for the single piles tested under free head conditions (see Section 6.9.1) this densification is more marked in the loose than in the medium density sand tests. It is also apparent from figures 6.71-6.73 that under lateral load, the trailing pile in the bent underwent a loss of lateral support due to sand in front of this pile flowing into the wake of the leading pile.

Figures 6.74 and 6.75 show plots of the vertical (at top of the pile) and horizontal (at load-level) deflections of each pile. Rocking of the test units, which rotated the pile cap up to ±6°, did not result in equal magnitudes of settlement in the leading pile and uplift in the trailing pile. For unit 10 (loose density sand), during the early stages of testing (horizontal deflections of magnitude less than 0.3D), the average pile vertical movement was downwards, although at a later stage the piles tended to rise. At the end of testing unit 10, the average uplift of the two piles was 18 mm. For unit 11 (medium density sand), the average pile vertical movement was upwards throughout the cyclic loading. At the end of testing unit 11, the average uplift of the piles was 43 mm.

Since unit 10 was positioned in the tank and loose sand was then filled around the unit, it is probable that a very loose layer of sand was present immediately underneath the bottom of the piles. This would explain the initial trend of this unit towards settlement rather than uplift. For unit 11 and the later stages of testing of unit 10, the tendency for pile uplift to be larger in magnitude than pile settlement shows that, as expected, resistance to tensile load is generally smaller than resistance to compressive load. The greater average uplift in unit 11 (medium density sand) may also be partly explained by the larger pile head moments present on this unit (see Sections 6.11.3 and 6.12.4) which from equilibrium considerations implies larger longitudinal forces in the piles.

At this stage it is appropriate to re-emphasize that the effect of superstructure dead load on twin pile bent behaviour was not modelled. From figures 6.74 and 6.75 it is apparent that vertical movement of the pile occurs to a greater extent under tensile than under compressive longitudinal loading. Thus the effect of the superstructure dead weight, which was not modelled, would be to reduce the rocking tendency of the bent.

Following testing, the test units were taken out of the sand tank and inspected for signs of damage. No fracturing, local buckling or visible plastic curvature of the casing was observed in these post-mortems, implying that the piles had been substantially behaving in an elastic manner during testing. Welds connecting the piles to the pile cap and the 300 mm diameter discs (see figure 6.2) also showed no signs of damage.

6.11.2 Hysteretic Performance

Figures 6.76 and 6.77 show the hysteresis loops of lateral load-lateral displacement response for units 10 and 11 respectively. These loops show similar characteristics to those previously shown, in Section 6.9.2, for single piles tested under free-head conditions. Since, as postulated in the previous section and subsequently confirmed in Section 6.11.3, the piles behaved in a substantially elastic fashion throughout the testing of units 10 and 11, the following conclusions can be made from figures 6.76 and 6.77:

(i) Sand density had a considerable effect on the load-carrying capacity of the test units. At peak load-level lateral displacements (≅ ± 200 mm), the magnitudes of load carried by units 10 (loose density sand) and 11 (medium density sand) were approximately 20 kN and 33 kN respectively.

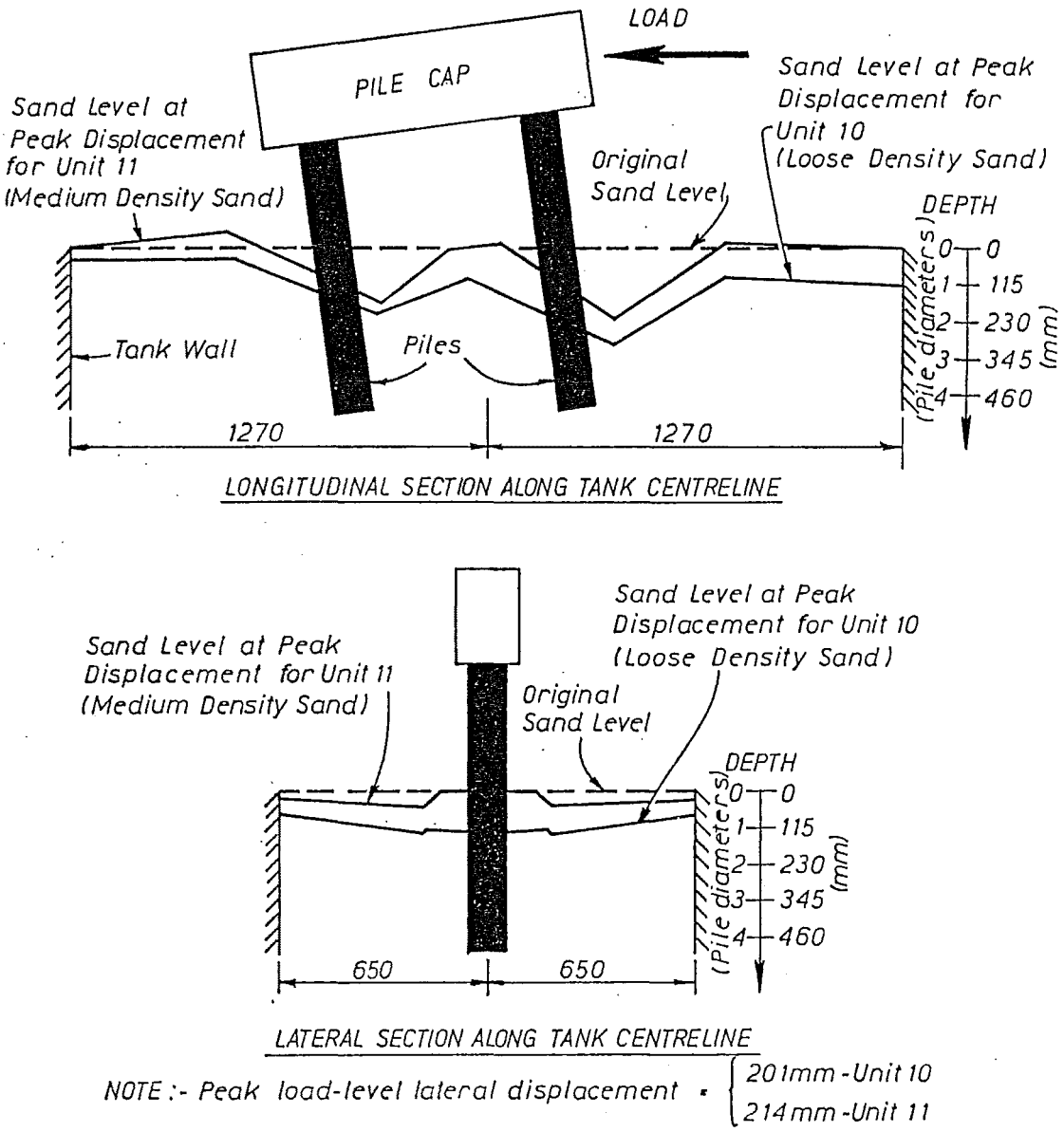

FIG. 6.73 SAND AND PILE MOVEMENT AT PEAK DISPLACEMENT IN TWIN PILE CYCLIC TESTS

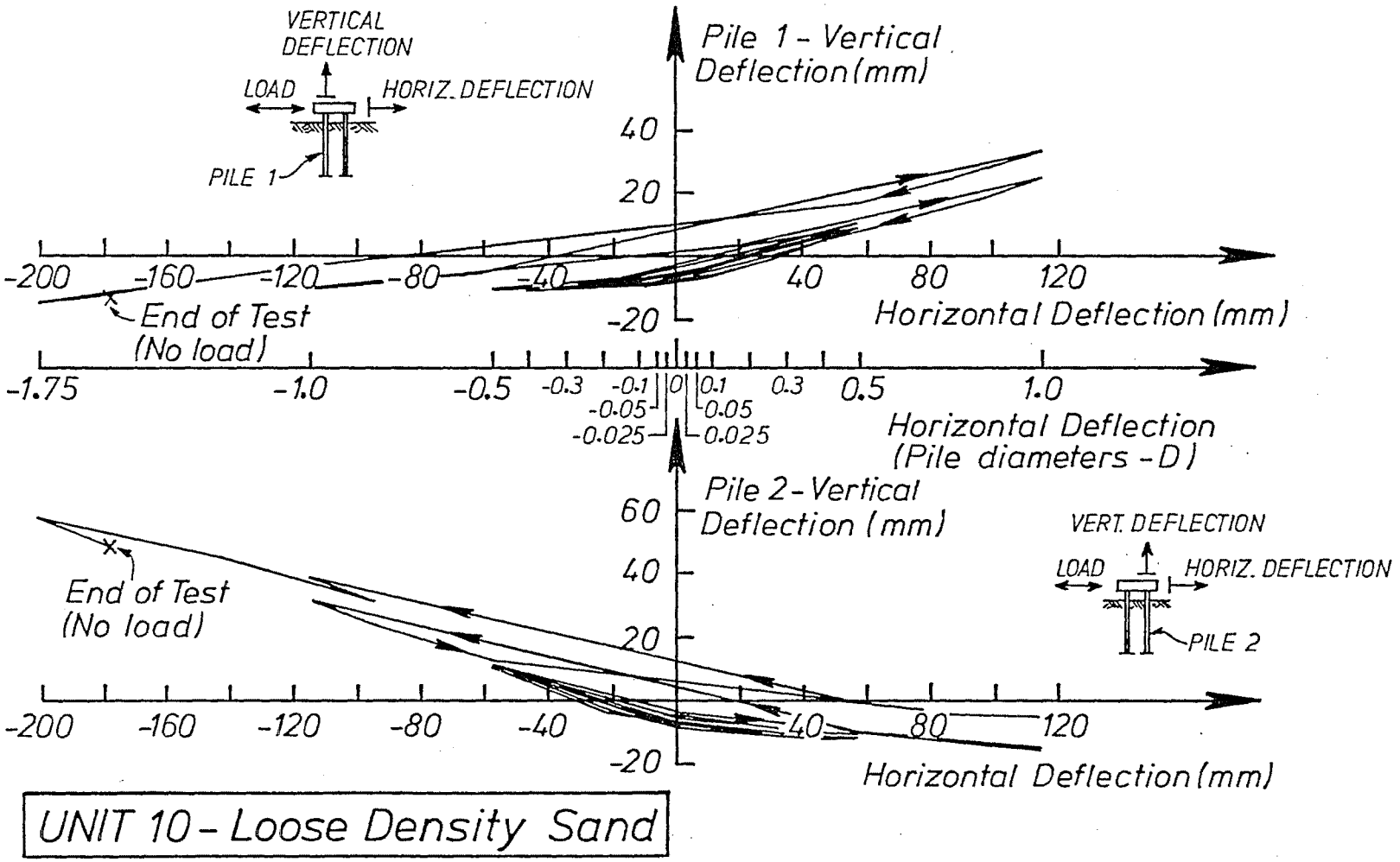

FIG. 6.74 UNIT 10 (LOOSE DENSITY SAND) PILES VERTICAL AND HORIZONTAL MOVEMENT

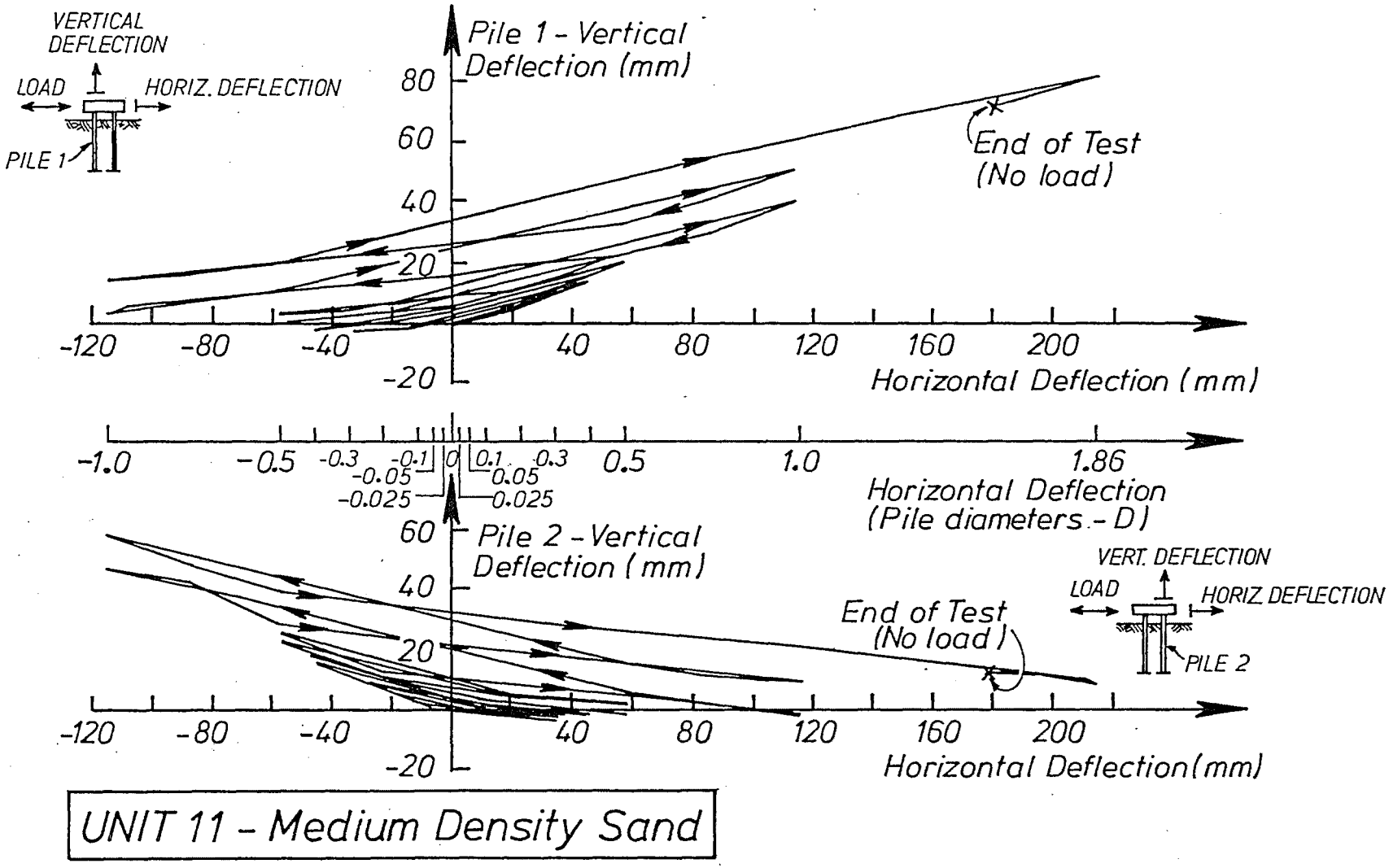

FIG. 6.75 UNIT 11 (MEDIUM DENSITY SAND) PILES VERTICAL AND HORIZONTAL MOVEMENT

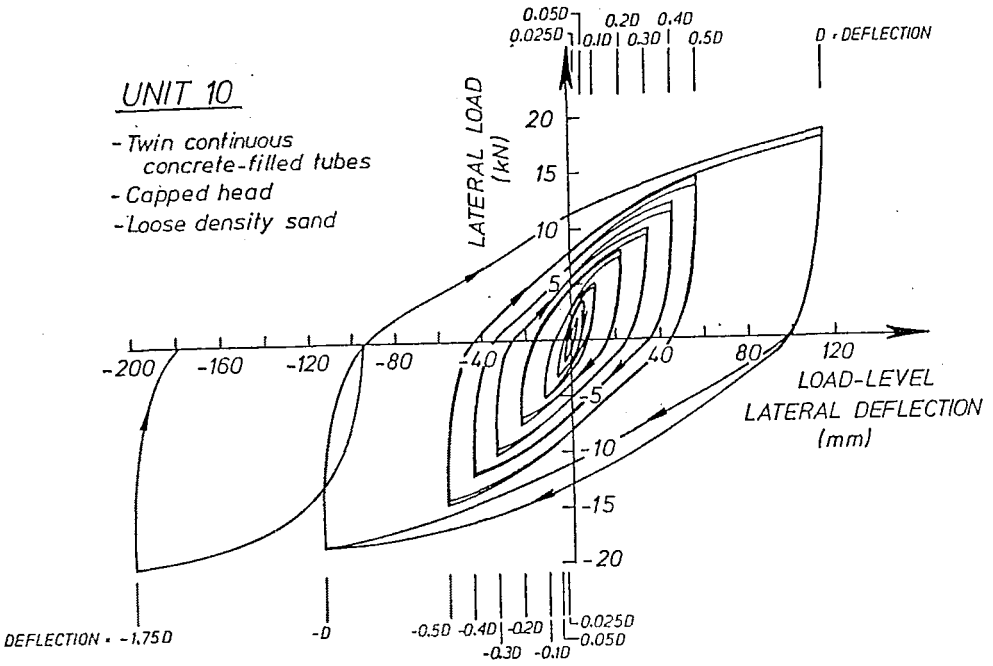

FIG. 6.76 UNIT 10 (CYCLIC TEST, LOOSE DENSITY SAND, TWIN PILES) HYSTERESIS LOOPS

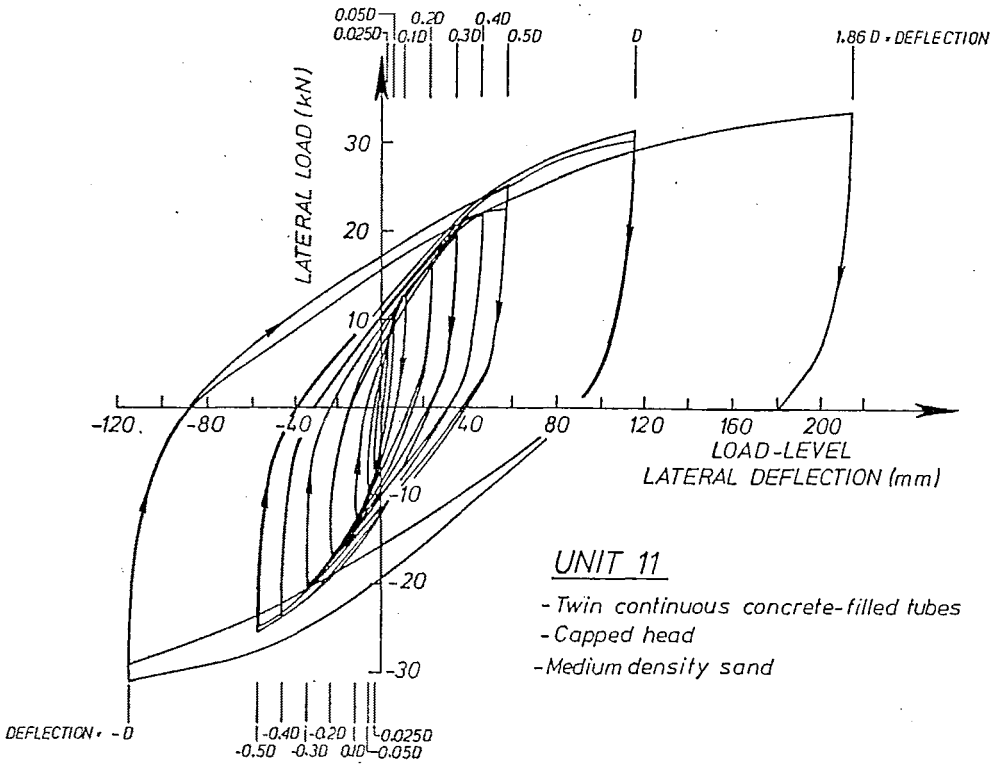

FIG. 6.77 UNIT 11 (CYCLIC TEST, MEDIUM DENSITY SAND, TWIN PILES) HYSTERESIS LOOPS

(ii) Good hysteretic behaviour was shown by unit 11 (medium sand), since stable well-rounded loops were obtained for this unit. Excellent hysteretic behaviour was shown by unit 10 (loose sand), since expanding hysteresis loops were obtained for this unit. This indicates that a large reserve of hysteretic damping would be available from the soil in an earthquake.

(iii) Load-carrying capacity increased with deflection in a non-linear fashion and ultimate loads were not reached despite the large level of imposed lateral displacement. It was also apparent that the common design assumption of elastic or elastic-plastic soil behaviour would be inappropriate to model the observed behaviour. This conclusion was also previously obtained from analysis of results from single free-head pile tests (see Section 6.10.6).

(iv) On unloading considerable residual displacements occurred in the piles. This was due to the flow of cohesionless soil around the pile which occurred during loading.

Figure 6.78(a) compares the experimental lateral load-lateral deflection responses obtained for units 10 and 11 during the first half-cycle of loading (deflection $\leq$ 2.9 mm). Figure 6.78(b) compares, for the full range of experimental deflections, the envelopes to the cyclic response of units 10 and 11. Also shown in Figs. 6.78(a) and (b) are theoretical elastic-plastic responses based on the values of H_i (theoretical ultimate lateral load, $\varepsilon_c = 0.003$), and Δ_y (idealised yield deflection) predicted assuming equivalent cantilever behaviour and zero rotation at the top of the piles as described previously in Section 6.2.2.

Figure 6.78(a) and (b) clearly contrast the difference in load-carrying capacity resulting from a change in soil density. It is also apparent that the predictions, which are based on assumptions used typically by bridge design engineers, give poor agreement with the experimental responses. In general the predictions overestimate load-carrying capacity and a wide margin exists between experimental and theoretical responses. This margin can be attributed to three causes:

(i) The difference in soil stiffness between that obtained in experiment and that assumed in theory;

(ii) The difference in pile top rotation between that observed in experiment (up to $\pm 6°$) and that assumed in theory (0°); and

(iii) Physical simplifications which are present in the equivalent cantilever model (see Section 6.2.2).

6.11.3 Curvature Distributions

Figures 6.79-6.82 show profiles of curvature distribution at the peaks of cycles, obtained for piles 1 and 2 of units 10 and 11 respectively. The proportions of yield curvature based on the experimentally obtained curvature ψ and the theoretical idealised yield curvature ψ_y (see Section 6.8), and the depth at which the peak curvature occurred for each of these profiles are also indicated on these figures.

Due to the small spacing between strain gauge pairs and small errors in curvature data, some of the profiles have a rather jagged appearance. However the following observations are made from these curvature profiles:

(i) Curvatures generally increased with deflection. The peak magnitudes of curvature ductility ratio reached were 0.58 in the loose density sand test (unit 10) and 1.50 in the medium density sand test (unit 11). Thus the piles behaved in essentially an elastic fashion throughout the testing. Curvatures were larger in the medium density sand test than in the loose density sand test because soil pressure and hence pile bending moments

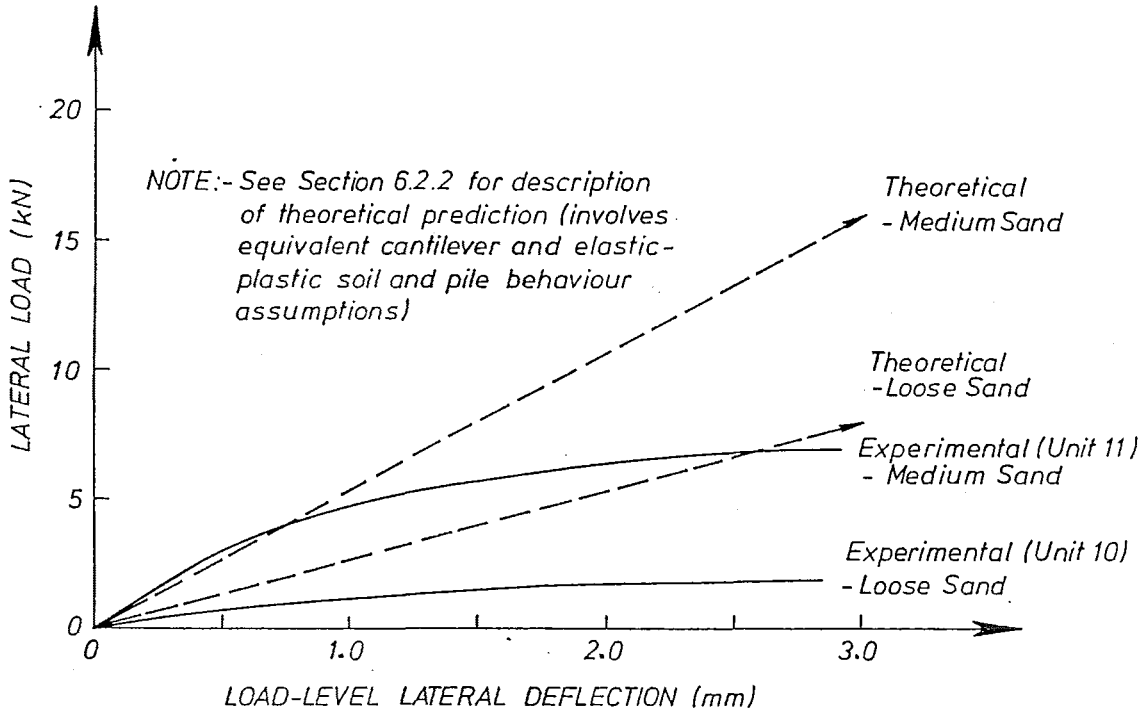

(a) MONOTONIC

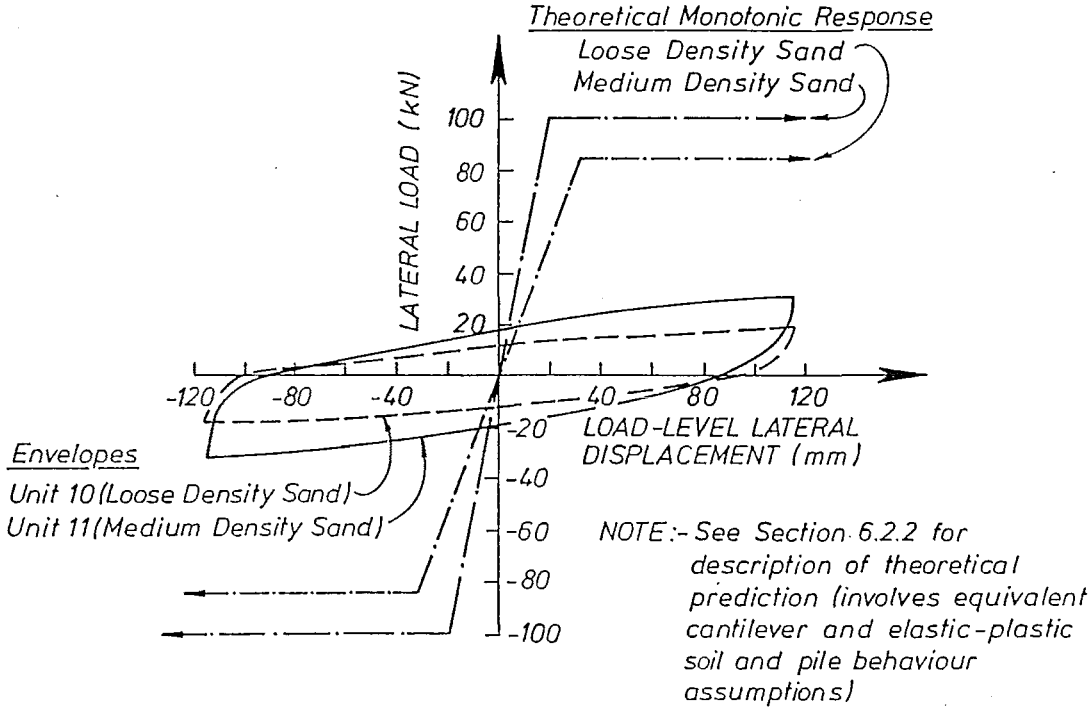

(b) CYCLIC

FIG. 6.78 COMPARISON OF PREDICTED (USING CONVENTIONAL THEORY) AND EXPERIMENTAL RESPONSES

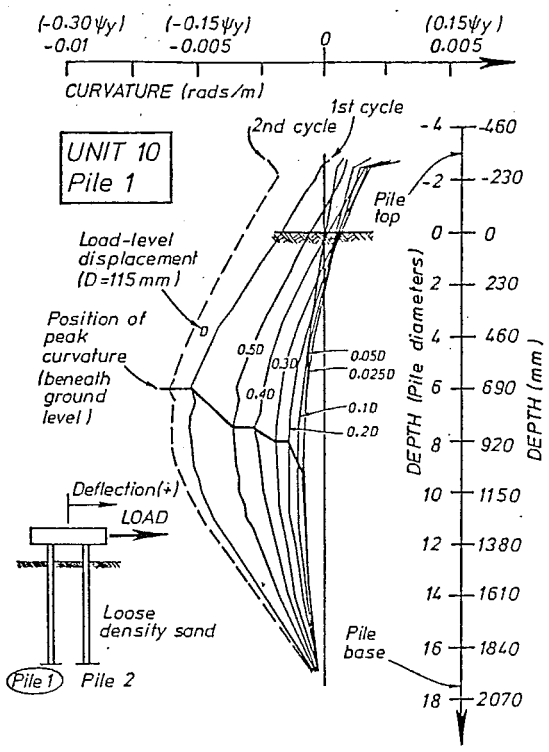

(a) POSITIVE DISPLACEMENTS

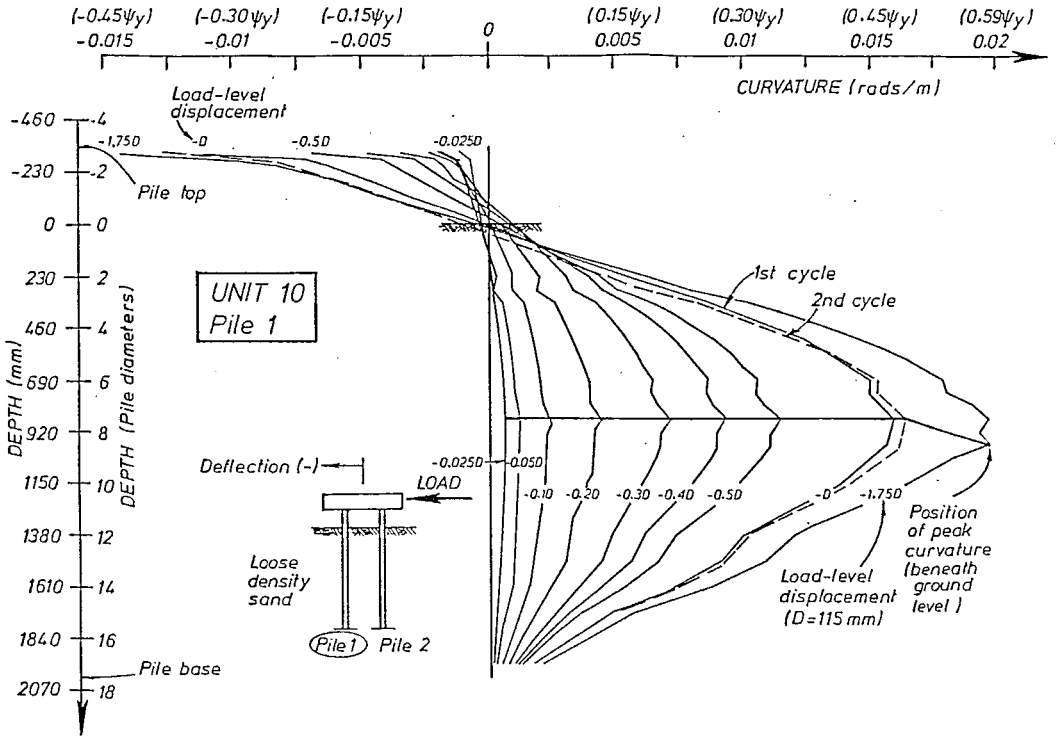

(b) NEGATIVE DISPLACEMENTS

FIG. 6.79 PILE 1 OF UNIT 10 (CYCLIC TEST, LOOSE DENSITY SAND, CAPPED-HEAD) CURVATURE PROFILES.

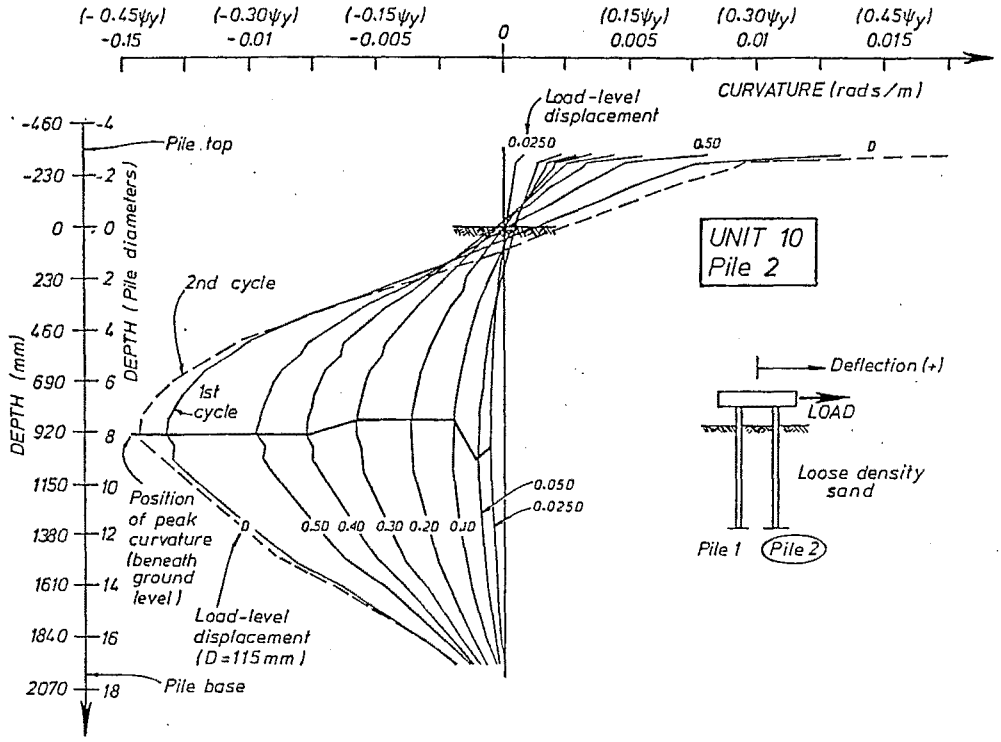

(a) POSITIVE DISPLACEMENTS

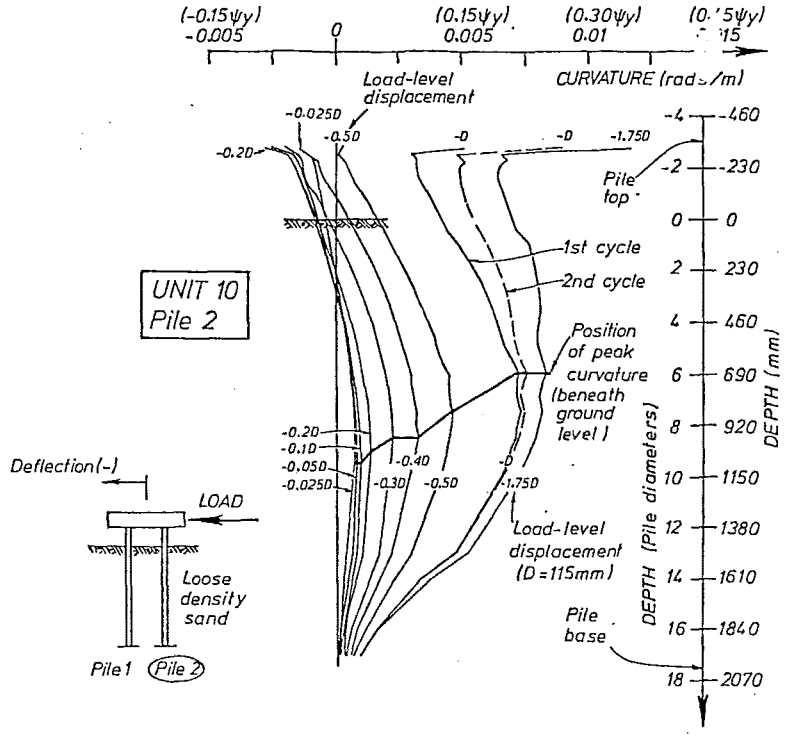

(b) NEGATIVE DISPLACEMENTS

FIG. 6.80 PILE 2 OF UNIT 10 (CYCLIC TEST, LOOSE DENSITY SAND, CAPPED-HEADS) CURVATURE PROFILES

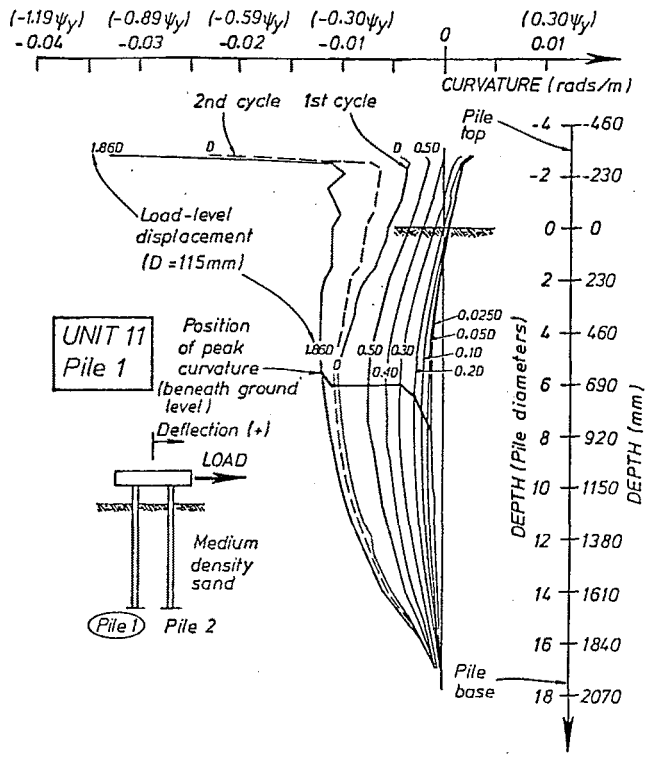

(a) POSITIVE DISPLACEMENTS

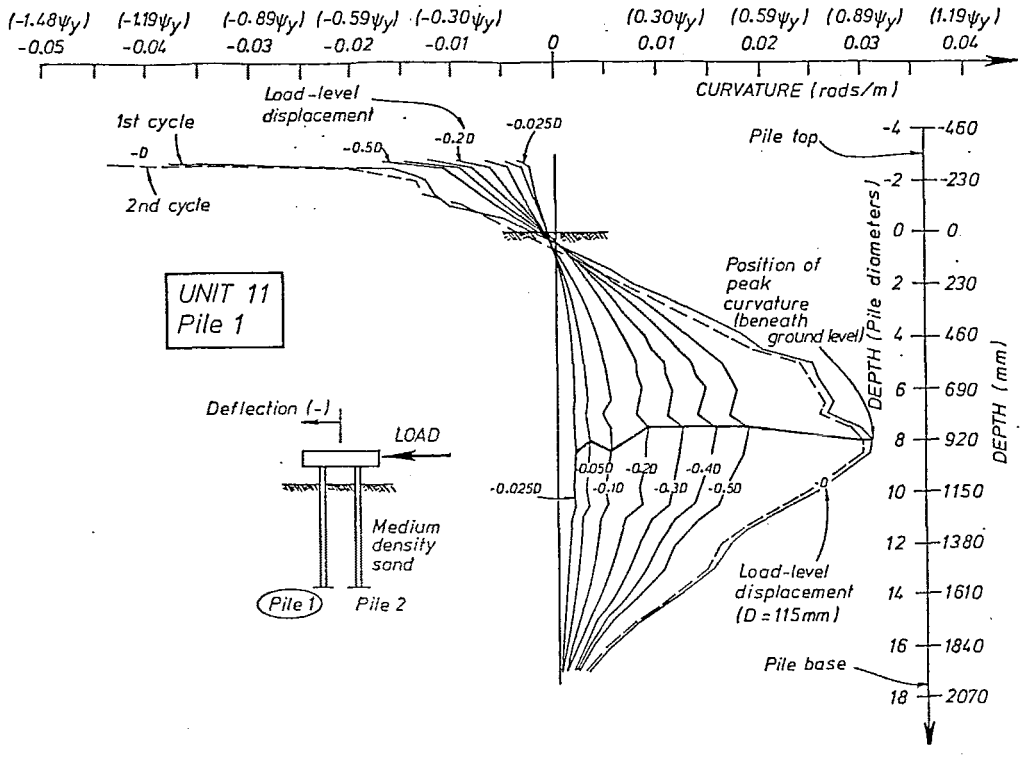

(b) NEGATIVE DISPLACEMENTS

FIG. 6.81 PILE 1 OF UNIT 11 (CYCLIC TEST, MEDIUM DENSITY SAND, CAPPED-HEADS) CURVATURE PROFILES

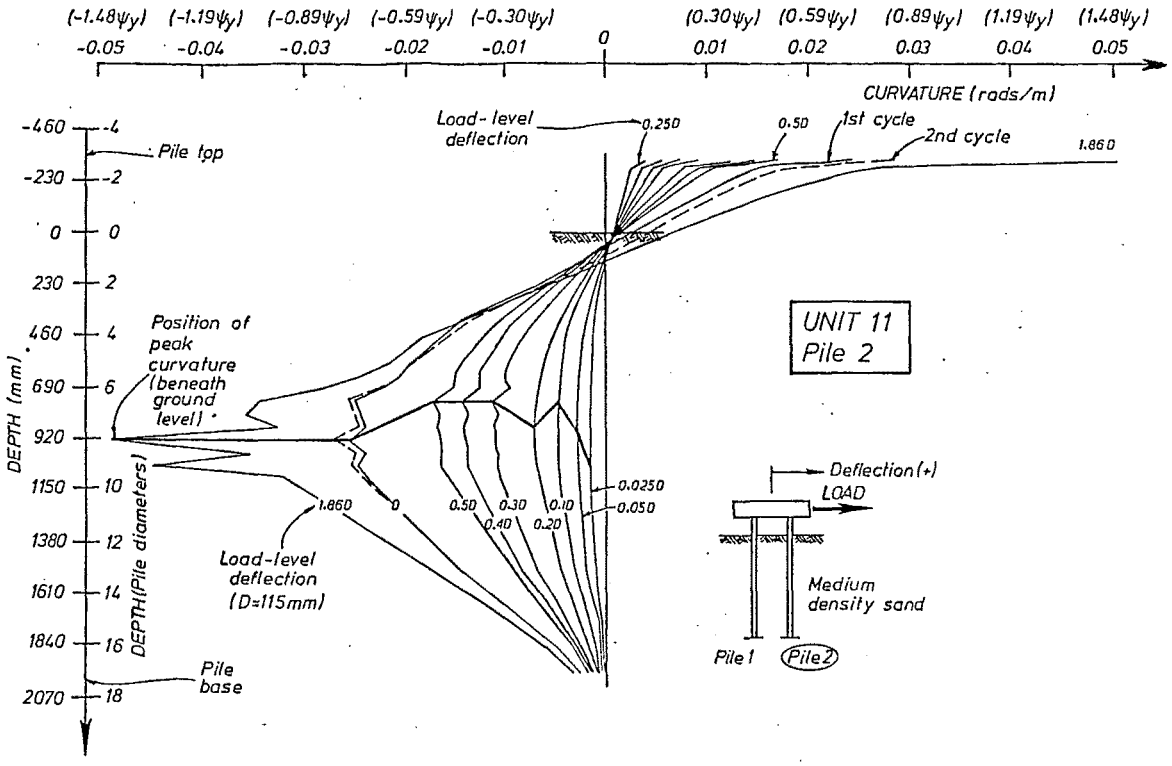

(a) POSITIVE DISPLACEMENTS

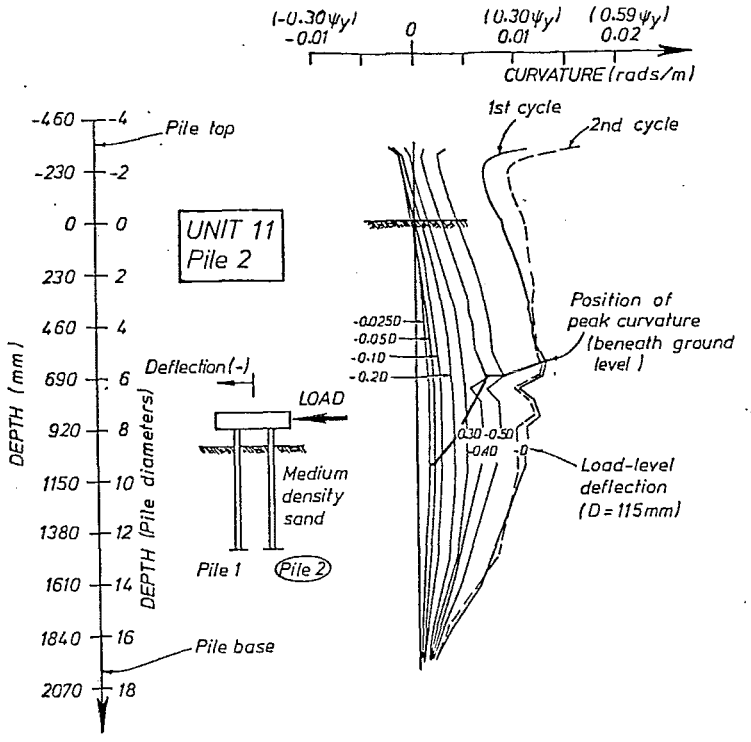

(b) NEGATIVE DISPLACEMENTS

FIG. 6.82 PILE 2 OF UNIT 11 (CYCLIC TEST, MEDIUM DENSITY SAND, CAPPED HEADS) CURVATURE PROFILES

will be larger for the medium density sand test. In general it is also shown that larger pile curvatures occurred in the second cycle to a displacement of ± D than in the first cycle to ± D, due to soil density increasing as testing proceeded.

(ii) For elastic pile behaviour, the slope of a curvature distribution should be constant above ground level, since shear force is constant above this level. In practice the curvature distributions (during elastic pile response) do have an approximately constant slope, with the exception of a small length adjacent to the pile cap soffit, where curvatures increase rapidly. It is felt that this is a result of shrinkage of the concrete away from the top of the pile which would locally prevent composite action developing in the member and hence result in the larger than anticipated curvature at this position.

(iii) At a given value of lateral displacement, the leading pile experienced significantly larger curvatures than the trailing pile, particularly at large levels of displacement. Thus pile bending moments and shear forces and soil lateral pressures will also be larger on the leading than on the trailing pile. This point is elaborated further in Section 6.12.1 where the distribution of lateral load between piles 1 and 2 is discussed.

(iv) The curvature distribution on a pile in the twin pile units may be considered to have resulted from three causes as shown in Fig. 6.83 and listed below:

(a) horizontal translation of the pile (with zero pile top rotation) under lateral load;

(b) rotation of the pile top due to rotation of the relatively stiff pile cap under the overturning effect of lateral load;

and (c) secondary moments due to P-Δ effects.

Curvature distributions from (a) and (b) generally act in an opposite sense. As the level of lateral displacement increases, curvatures due to P-Δ secondary effects, (c) will increase. For the trailing pile which will be under tensile longitudinal load the P-Δ effect will tend to reduce the overall level of curvature, while the reverse applies to the leading pile which will be under compressive longitudinal load. For both the leading and trailing piles, curvature distributions due to (b) would be expected to be similar. Curvature distributions due to (a) will be larger for the leading than for the trailing pile since, as shown in Section 6.11.1, the trailing pile suffers a relative loss of lateral support due to soil flowing into the wake of the leading pile which results in lower soil lateral pressure and hence pile bending moments on the trailing pile than on the leading pile. For the leading pile at all stages of testing, and the trailing pile during the early stages, the overall curvature profiles (see Figs. 6.79-6.82) are dominated by (a) - horizontal translation of the pile cap. However for the trailing pile during the later stages of testing, at the pile top curvatures due to pile cap rotation dominate and result in this pile being subjected to a curvature distribution of constant sign. Thus during an earthquake, damage will occur in an asymmetric fashion on the two piles in the bent.

(v) As the load-level lateral displacement increases, the position of peak curvature (beneath ground level) on the pile is relatively stable for the leading pile at a depth of about 8D, while for the trailing pile the position of peak curvature shows a tendency to rise.

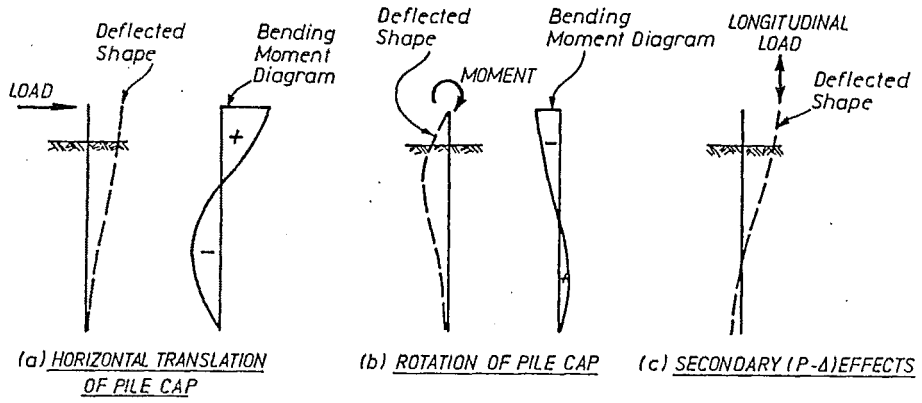

FIG. 6.83 CONTRIBUTIONS TO CURVATURE OF PILE

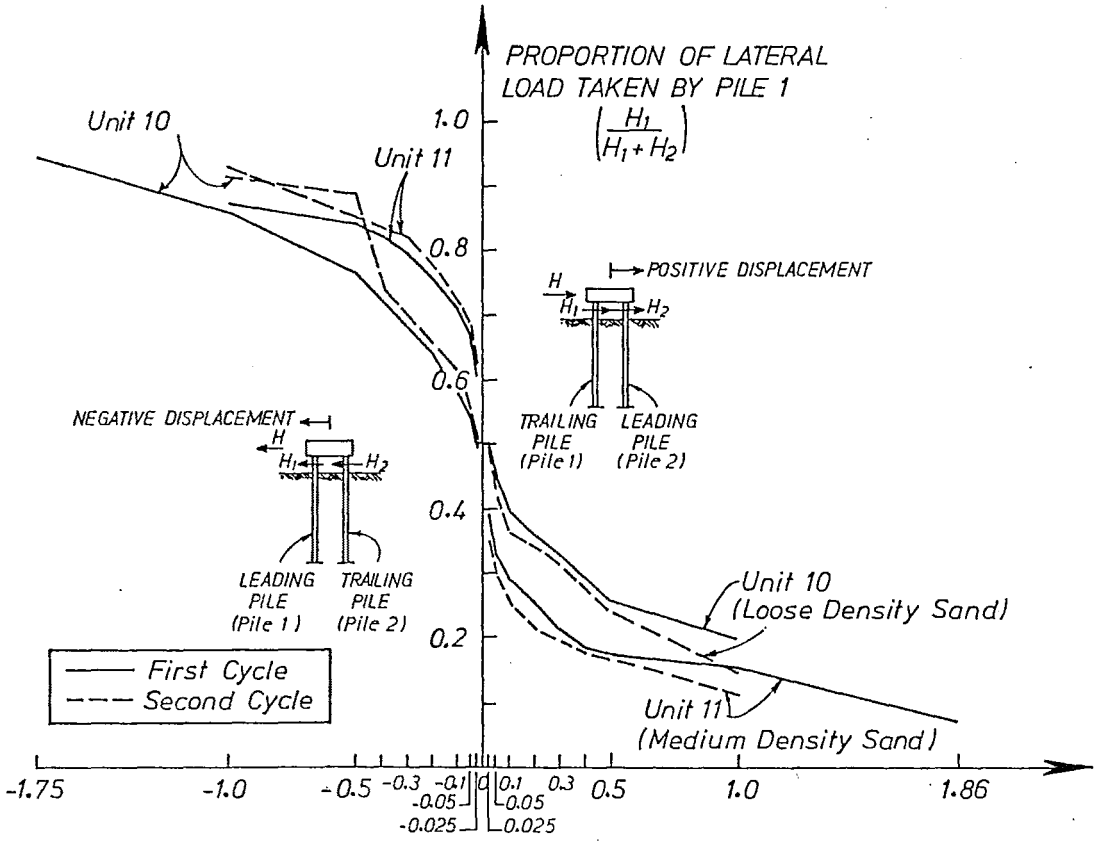

FIG. 6.84 DISTRIBUTION OF LATERAL LOAD BETWEEN PILES

6.12 ANALYSIS OF RESULTS - CAPPED-HEAD PILES

6.12.1 Lateral Load Distribution Between Piles

In Section 6.11.3 it was shown that the leading pile was subjected to a larger curvature than was the trailing pile. The share of lateral load between the piles at the peaks of cycles may be obtained from the curvature distribution by noting that:

(i) the lateral load carried by a pile is equal to the shear force V carried by that pile above ground level;

and (ii) $V = dM/dx = EI \cdot d\psi/dx$.

As was previously described in Section 6.11.3, due to local weakness of the concrete-filled tubes adjacent to the pile cap (approximately 3D above ground level), pile curvatures in this region were larger than anticipated from the trend shown below this region. Thus the lateral loads carried by the two piles were estimated from the change in pile curvature occurring between positions on the pile at ground level and 2 pile diameters above ground level:

$$H_1 = (EI)_{\text{pile 1}} \left[\psi(x = -2D) - \psi(x = 0)\right]_{\text{pile 1}} / 2D \qquad (6.62)$$

$$H_2 = (EI)_{\text{pile 2}} \left[\psi(x = -2D) - \psi(x = 0)\right]_{\text{pile 2}} / 2D \qquad (6.63)$$

where EI = pile flexural rigidity (function of curvature obtained from moment-curvature analysis, see Fig. 6.21)

H_1 = lateral load carried by pile 1

H_2 = lateral load carried by pile 2

$\psi(x)$ = curvature at depth x (negative values of x apply to above ground positions)

From Figs. 6.79-6.82, within the range of x = -2D to 0 the maximum magnitude of pile curvature was $0.62\psi_y$, indicating approximately linear moment-curvature behaviour (see Fig. 6.21, where tension-stiffening of concrete between cracks is taken into account) and hence approximately constant EI.

Values of H_1 and H_2 were calculated at the peaks of each cycle. Due to experimental scatter and the approximations inherent in the moment-curvature analysis (see Section 6.8), on average the sum of H_1 and H_2 differed from the applied lateral load H by approximately 0.12H.

Figure 6.84 shows a plot of the proportion of the total lateral load which is carried by pile 1 (i.e. $H_1/(H_1 + H_2)$). This plot was obtained by interpolating results from the first and second cycles to given (± 0.025D, ± 0.05D, ± 0.1D, etc) load-level lateral displacements. At the positive displacement peaks, pile 2 is the leading pile and pile 1 the trailing pile; while at the negative peaks, pile 1 is the leading pile and pile 2 the trailing pile.

As the sand density increased (loose to medium), the number of cycles increased (first to second) and the amplitude of lateral displacement increased, so too did the effects of lateral interaction between the piles resulting in the leading pile taking an increasing proportion of the lateral load. At a load-level displacement of 0.67D corresponding to the maximum displacement expected in a prototype pile during an earthquake (see Section 6.7), pile 1 (trailing pile) took 24%, 21%, 17% and 15% of the total lateral load for the first and second cycles of units 10 and 11 respectively. Fendall (6.6) has established from his tests of 10 mm and 20 mm diameter model piles that the lateral load carried by the leading pile is generally unaffected by soil movement caused by the trailing pile. Thus the above lateral load ratios imply a substantial reduction in pile group lateral load capacity from that calculated ignoring pile interaction effects. Pile lateral interaction effects occur because of the flow of soil from in front of the trailing pile into the wake of the leading

pile which results in a loss of lateral support for the trailing pile.

From Section 6.2.1, theoretical lateral load capacities of the single pile units were 31.9 kN (medium density sand foundation) and 25.5 kN (loose density sand foundation). From Section 6.2.2, theoretical capacities of the twin pile units were 100 kN (medium density sand foundation) and 84 kN (loose density sand foundation). Thus the twin pile units theoretically carried 3.13 (medium sand) and 3.29 (loose sand) times the lateral load carried by the single pile units. In calculating these theoretical strengths, the free-head condition of the single pile test units was taken into account. For the twin pile test units, zero pile head rotation and no lateral interaction between the piles had been assumed in the theoretical calculations.

Figure 6.85 shows the experimentally obtained ratio between lateral loads carried by the twin and single pile test units as a function of the load-level lateral displacement at the peak of cycles. The ratio is plotted for both medium and loose density sand and the first and second cycles of loading to displacements of ± 0.025D, ± 0.05D, ± 0.1D, ± 0.2D, ± 0.3D, ± 0.4D and ± 0.5D. Units 3 (medium density sand) and 7 (loose density sand) were taken as being representative of the single pile test units. At a given displacement typically the ratios of twin pile unit to single pile unit lateral load were 1.6 (cf. 3.29 theoretically) for loose density sand and 1.3 (cf. 3.13 theoretically) for medium density sand. Thus due to pile cap rotation and pile lateral interaction effects, the actual margin of lateral load-carrying capacity between the twin and the single pile test units was considerably smaller than was theoretically predicted.

It is also relevant to note that Fendall (6.6) has conducted tests of twin piles connected at their heads to a stiff capping beam by (i) rigid connection and (ii) pin connection. These tests have shown that lateral load-carrying capacities were similar in both cases. However, similarly with units 10 and 11, the tests conducted by Fendall did not model the effect of superstructure dead load which for the rigid connection case would reduce rocking of the substructure (no rocking occurs under pin connection conditions) and hence also result in a smaller amount of pile head rotation. Nevertheless from the above evidence, it does appear that designs allowing for additional load-carrying capacity on the assumption that the capping beam prevents pile head rotation may result in an unsafe structure. However it should be noted that fixed-head and free-head piles might equally well survive an earthquake, since the increased lateral load-carrying capacity of a fixed-head pile is generally accompanied by increased seismic inertia force due to the smaller fundamental period of vibration of the fixed-head pile (see Fig. 1.3).

From an extensive number of tests conducted on small-scale piles (diameter = 10 or 20 mm), Fendall (6.6) found that the most important parameter affecting lateral interaction of piles in a group was the pile spacing. Lateral interaction effects were found to increase as the pile spacing decreased. Fendall also observed that interaction effects were more significant in loose than in dense soils which is contrary to the trend shown by units 10 and 11 (see Fig. 6.84). For monotonic tests, pile lateral interaction effects were found by Fendall to increase as the ground-level lateral displacement increased from 0 to 0.15D. For larger displacements, interaction effects were similar to those at a displacement of 0.15D. Fendall also found that interaction effects increased as cyclic loading proceeded, even at displacements larger than 0.15D, which is confirmed by results from units 10 and 11.

Figure 6.86 gives the design recommendation of Fendall (6.6) for the ratio of trailing to leading pile lateral load as a function of pile spacing. The recommendation is based on a lower bound to his results and thus attempts to allow for other factors in an indirect but conservative fashion. Also shown in Fig. 6.86 are the ratios obtained for units 10 and 11 at peak displacement (≅ 1.8D).

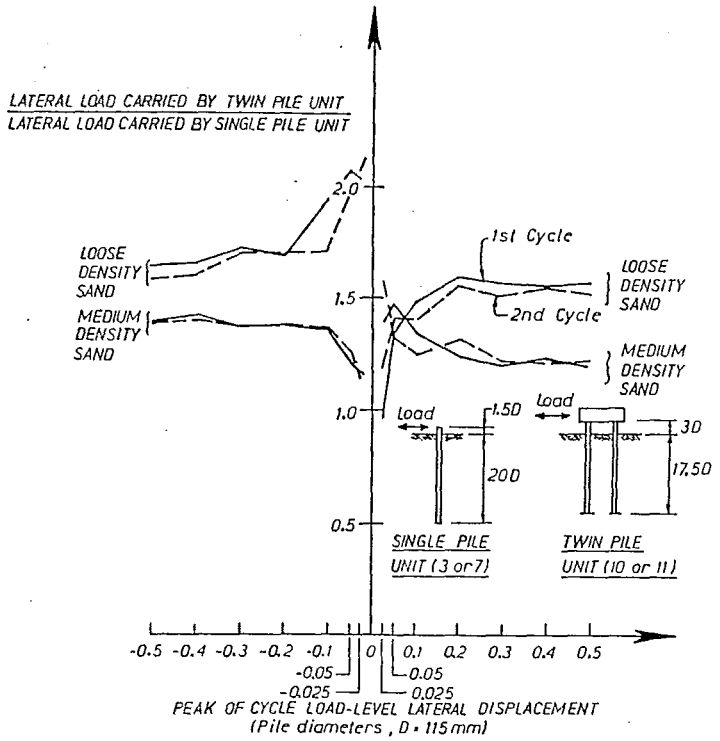

FIG. 6.85 COMPARISON BETWEEN LATERAL LOAD CAPACITIES OF SINGLE AND TWIN PILES.

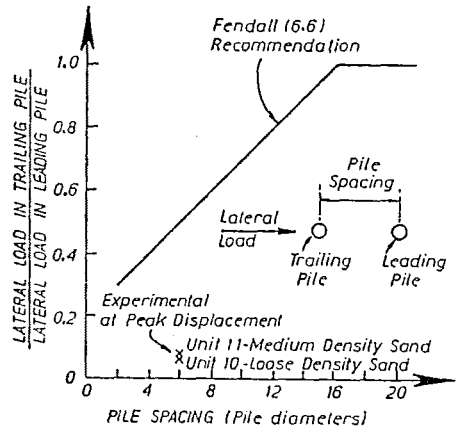

FIG. 6.86 COMPARISON OF LATERAL LOAD DISTRIBUTION FROM UNITS 10 AND 11 WITH FENDALL (6.6) RECOMMENDATION.

For a pile spacing of 6D which was appropriate for units 10 and 11, from the recommendation of Fendall (6.6), it can be predicted that the trailing pile takes only 50% of the lateral load taken by the leading pile. From the results obtained in testing units 10 and 11 (see Figs. 6.84 and 6.86) this prediction is unconservative at large magnitudes of lateral displacement. For example at maximum displacement (≅ 1.8D) for units 10 and 11 the trailing pile was found to take of the order of 7% of the lateral load taken by the leading pile, while at the expected peak seismic displacement = 0.67D (see Section 6.7), trailing piles from units 10 and 11 took 31% or less of the lateral load taken by the leading pile.

6.12.2 Determining Pile Lateral Deflection, Bending Moment, Shear Force and Soil Lateral Pressure Distributions

For the twin pile tests, distributions of pile lateral deflection, bending moment, shear force and soil lateral pressure were obtained in a similar fashion to that used in determining these distributions for the single pile tests (see Section 6.10.1.2). However there were two differences in the employed analytical procedures:

(i) In the single pile tests, moments at the pile base were approximately equal to zero. However in the twin pile tests, small but significant levels of moment were present at the pile base (see Figs. 6.79-6.82) due to the moment restraint offered to the base of these piles by the attached 10 mm thick, 300 mm diameter steel discs. In representing the conditon of zero shear force at the pile base for the single pile tests (see equation 6.31), it was assumed that M_{n+1} (moment at pile base) was zero. Thus for the twin pile tests, equation 6.31 was amended to give:

$$M''_n + 2M''_{n+1} = \frac{6}{h_n^2}(M_n - M_{n+1}) \qquad (6.64)$$

(ii) In the single pile tests, the distributions of soil lateral pressure which were obtained from the spline analysis were scaled to give a state of horizontal force equilibrium with the applied lateral load. For the twin pile tests, the combined distributions of soil lateral pressure for the two piles which were obtained from the spline analysis, were scaled to be in a state of horizontal force equilibrium with the applied lateral load. (For both sets of tests pile bending moment and shear force distributions from the spline analysis were subsequently scaled by the same factor as the soil lateral pressure distributions). For the twin pile test units, scaling typically resulted in a change to the distributions of 10%.

Since the moment-curvature analysis technique for steel-encased concrete piles had not been developed to the cyclic stage (see Chapter 5), as had the single pile tests, cubic spline analyses to determine pile bending moment and shear force and soil lateral pressure distributions were only performed for the monotonic stage of testing (i.e. first half-cycle of loading).

6.12.3 Pile Lateral Deflection Distributions

Figures 6.87(a) and (b) show distributions of pile lateral deflection during the first half-cycle of loading for units 10 (loose density sand) and 11 (medium density sand) respectively. It should be noted that, at this stage, the linear potentiometers used to obtain pile cap displacement and rotation (see Fig. 6.9) were operating over a range of less than 1% of their travel. Thus a high degree of accuracy is not expected from these distributions. Nevertheless the following observations are made from these figures:

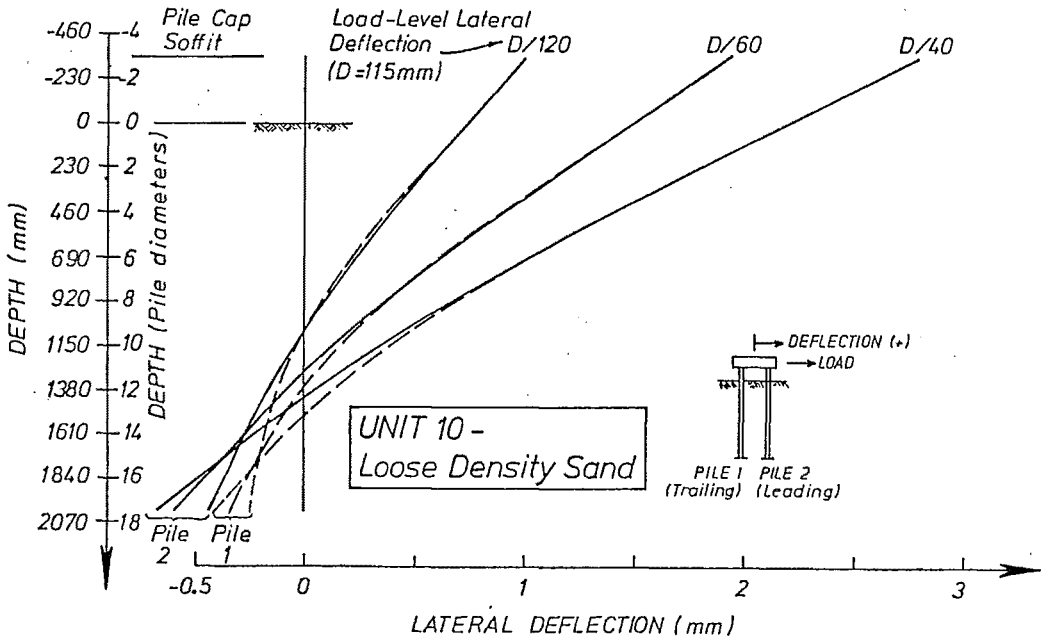

(a) UNIT 10 (LOOSE DENSITY SAND)

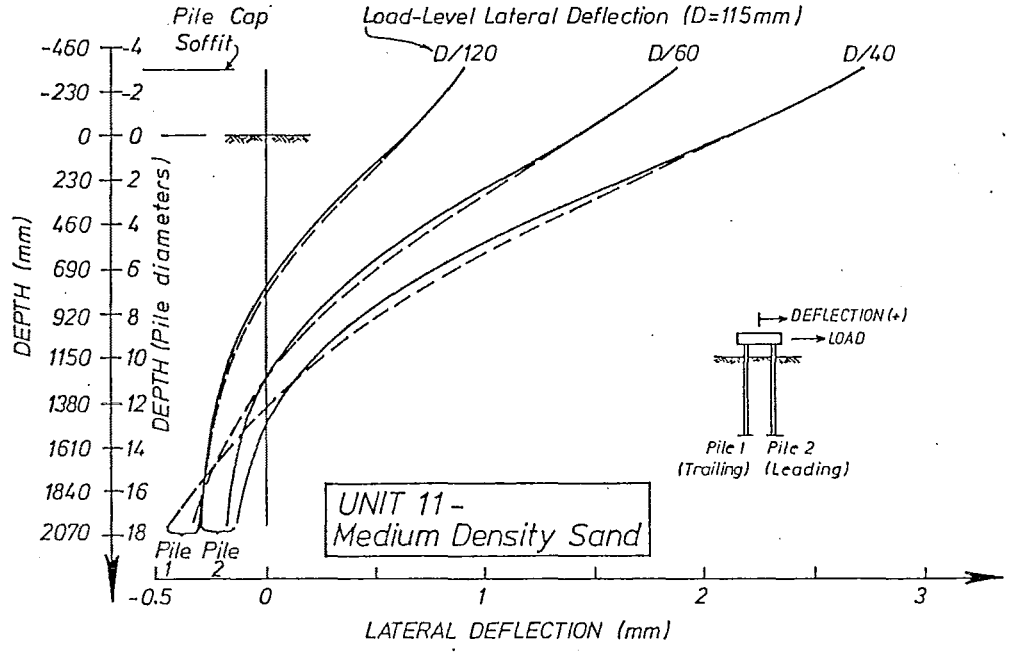

(b) UNIT 11 (MEDIUM DENSITY SAND)

FIG. 6.87 TWIN PILE TEST UNITS LATERAL DEFLECTION PROFILES FOR FIRST HALF-CYCLE.

(i) Significant rotation at the top of the piles is indicated, which confirms earlier observations (see Section 6.11.1). Overall the distributions of pile deflection indicate the piles behaved in a free-head fashion, although a small amount of reversed curvature is discernible at the pile heads.

(ii) The overall deflected shapes of the pile have significant contributions from both rigid pole and flexural deformation. As expected unit 11 (medium density sand) is more dominated by flexural deformation that is unit 10 (loose density sand) due to larger soil pressures occurring in the medium than in the loose density sand. Piles from unit 10 tended to have larger pile base lateral deflections than did piles from unit 11. This is also a consequence of the difference in soil density between the two tests.

(iii) In general at a given stage of testing, piles 1 and 2 were shown (see Figs. 6.79-6.82), to be subjected to different curvature distributions. This is reflected in Figs. 6.87(a) and (b) which show divergent deflected shapes for piles 1 and 2.

(iv) At a given stage of testing, for unit 10 (loose density sand) the leading pile (2) is shown to have a larger magnitude of pile base lateral deflection than is the trailing pile (1), while for unit 11 (medium density sand) the opposite trend is shown.

Deflected shapes at the peaks of cycles are shown in Figs. 6.88(a) and (b) and 6.89(a) and (b) for piles 1 and 2 of units 10 and 11 respectively. From these figures similar observations to those given earlier in this section, which applied to the first half cycle of loading, can be made. However it is also apparent that as the magnitude of cyclic displacement increased, so too did the proportion of the deflected shape which is due to rigid pole deformation. Since, apart from the final stage of testing unit 11, the pile members were shown (see Figs. 6.79-6.82) to behave in an elastic fashion. This implies a substantial reduction in the soil stiffness as the magnitude of pile movement increases.

6.12.4 Pile Bending Moment Distributions

Bending moment distributions obtained for the first half-cycle of loading for both piles of units 10 (loose density sand) and 11 (medium density sand) are shown in Figs. 6.90 and 6.91 respectively. The diagrams show large differences in bending moment distribution between the trailing (1) and the leading (2) piles. For unit 10 (loose density sand), the amplitude of the moment distribution tended to be larger for the trailing than for the leading pile, while the reverse trend was apparent for unit 11 (medium density sand). At this stage, the magntudes of lateral deflection were relatively small ($\leq$ D/40) which implies that the level of lateral interaction between the piles would also be small. Thus it is probable that the major cause of difference between the moment distribution in piles 1 and 2 is local variation in soil layering around each pile.

Despite the relatively large pile head rotations which occurred (see Fig. 6.87) some moment restraint was clearly offered to the piles by the pile cap. During the first half-cycle of loading, for unit 11 (medium density sand) this resulted in the peak positive moment (adjacent to pile cap) being larger in magnitude than the peak negative moment (in the ground). For unit 10 (loose density sand) peak positive moment was smaller than the magnitude of peak negative moment.

6.12.5 Pile Shear Force Distributions

Shear force distributions obtained for the first half-cycle of loading for both piles of units 10 (loose density sand) and 11 (medium density sand) are shown in Figs. 6.92 and 6.93 respectively. Significant levels of both positive and negative shear forces are indicated. For example for a given stage of testing and a given pile, the peak negative shear force has a magnitude of up to 80% of the magnitude of the peak positive shear force.

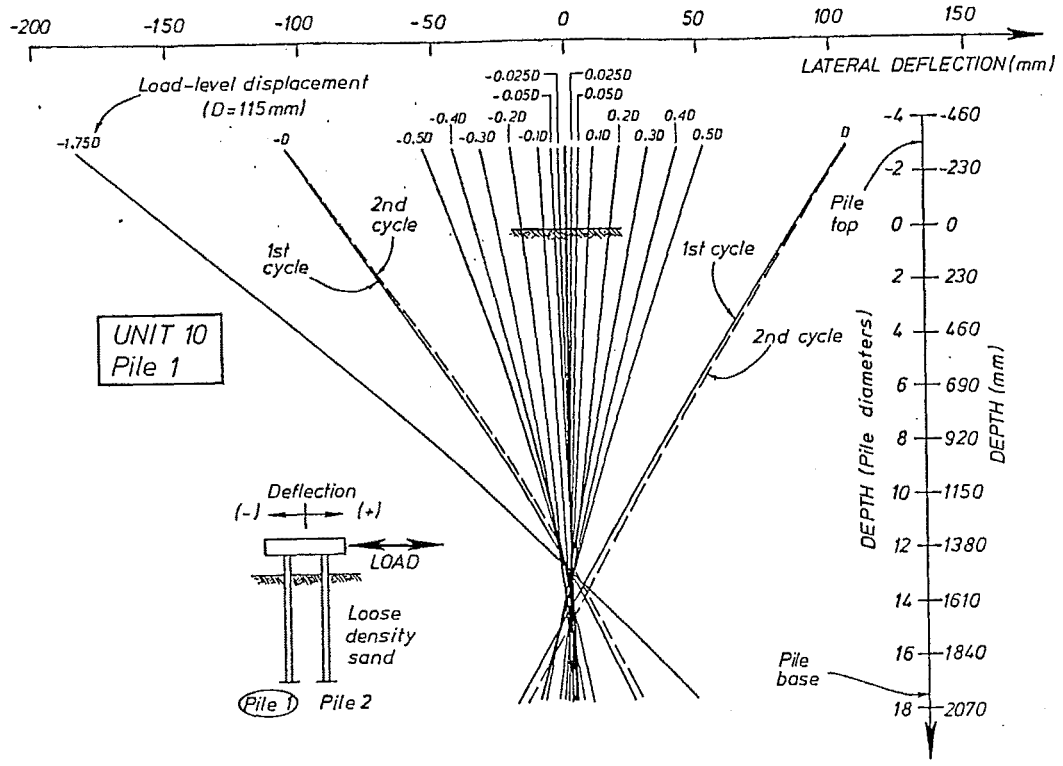

(a) PILE 1

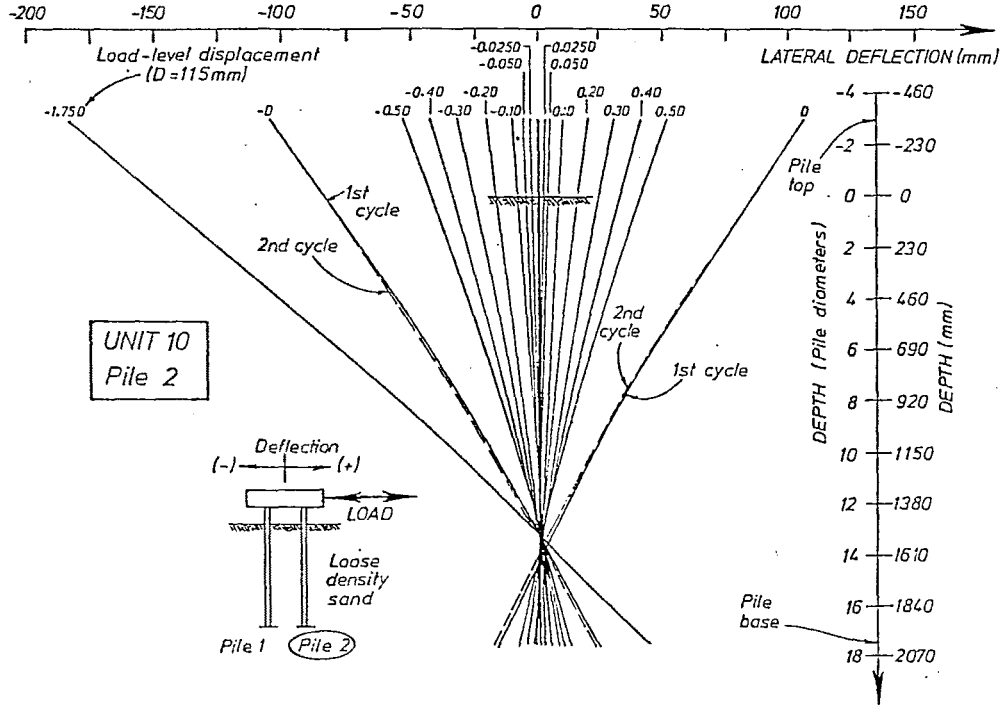

(b) PILE 2

FIG. 6.88 UNIT 10 (LOOSE DENSITY SAND) LATERAL DEFLECTION PROFILES AT PEAKS OF CYCLES.

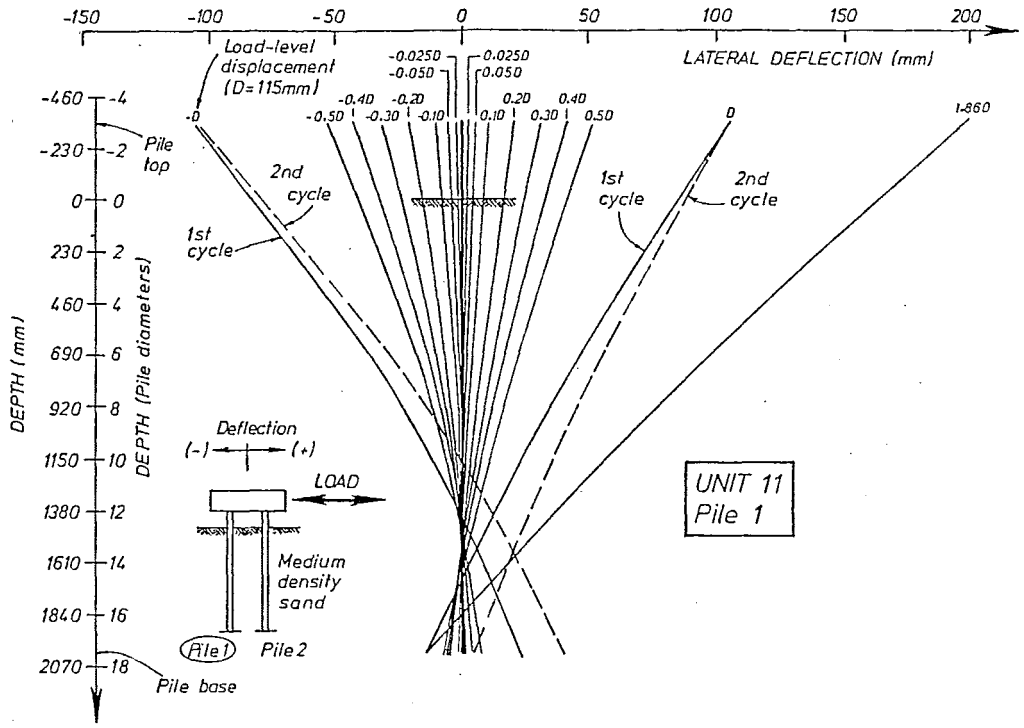

(a) PILE 1

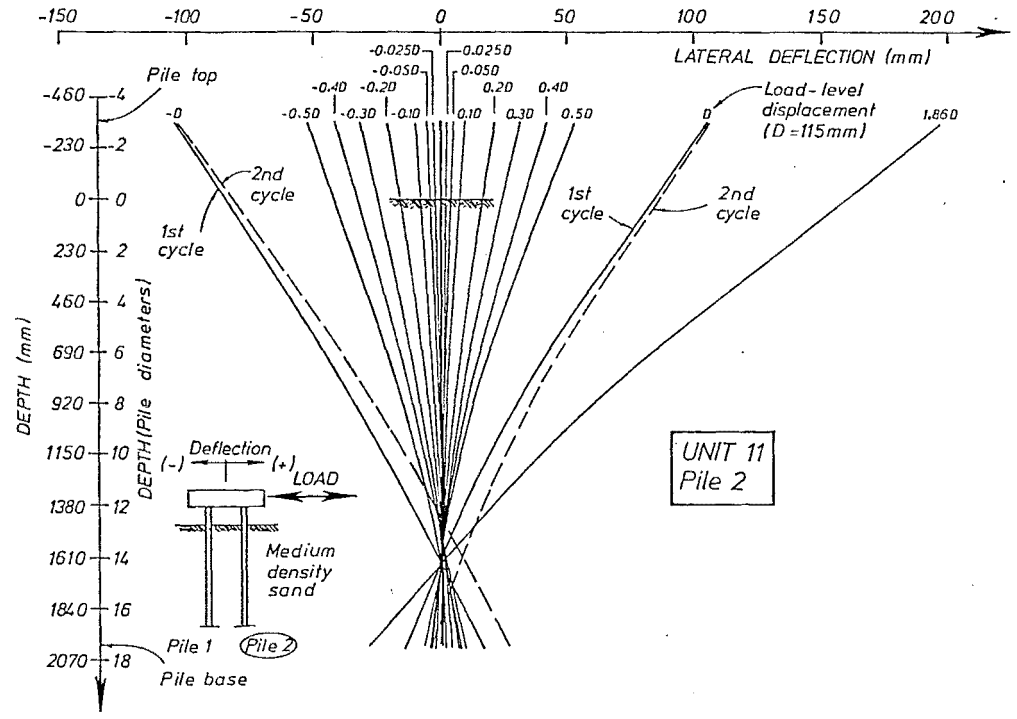

(b) PILE 2

FIG. 6.89 UNIT 11 (MEDIUM DENSITY SAND) LATERAL DEFLECTION PROFILES AT PEAKS OF CYCLES.

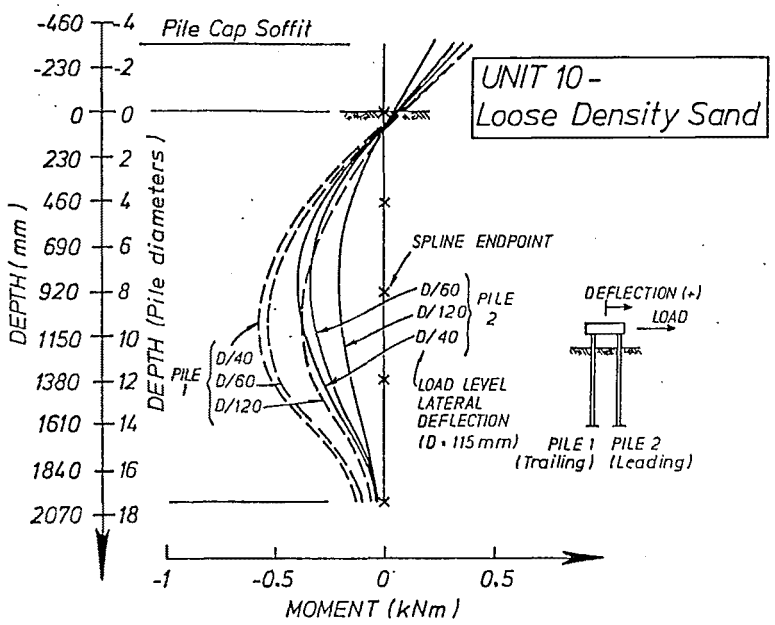

FIG. 6.90 UNIT 10 (LOOSE DENSITY SAND) BENDING MOMENT DISTRIBUTIONS.

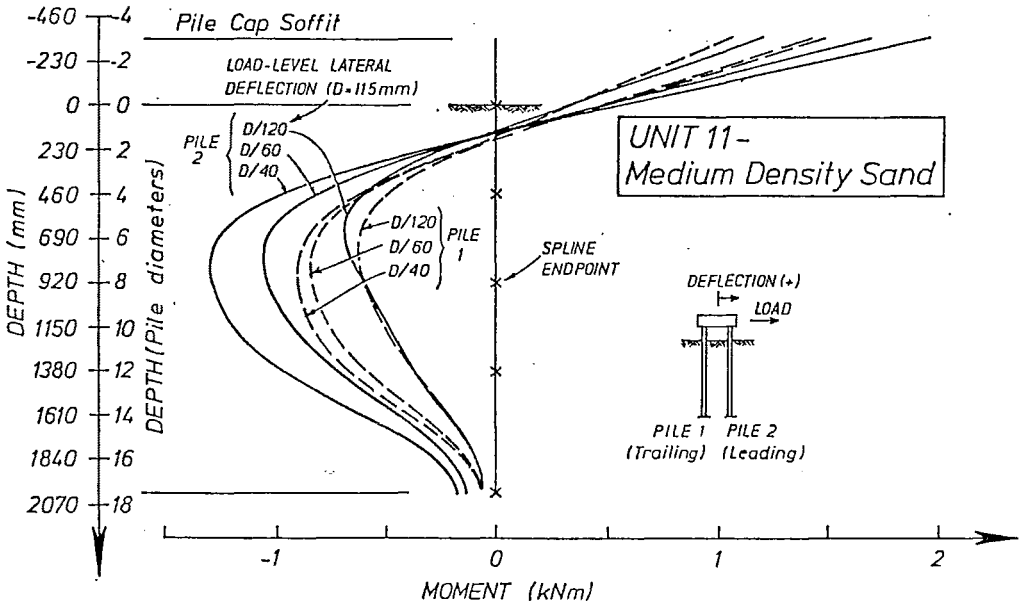

FIG. 6.91 UNIT 11 (MEDIUM DENSITY SAND) BENDING MOMENT DISTRIBUTIONS.

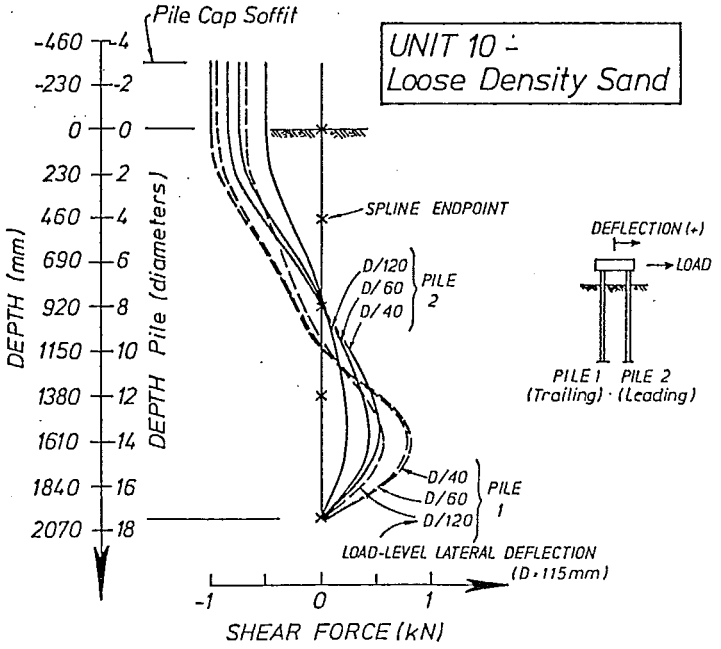

FIG. 6.92 UNIT 10 (LOOSE DENSITY SAND) SHEAR FORCE DISTRIBUTIONS.

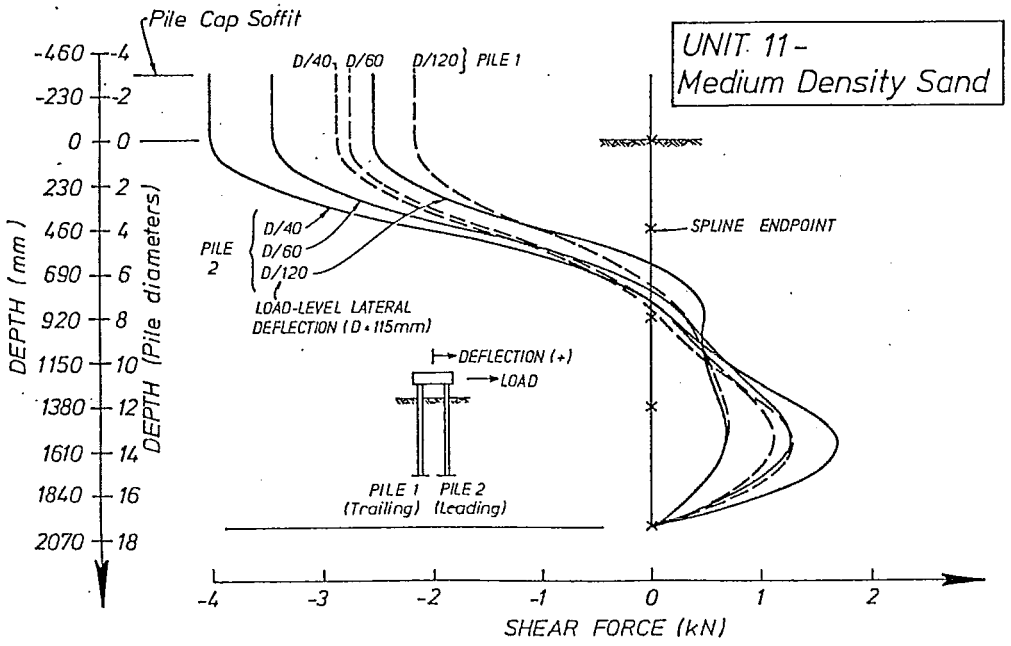

FIG. 6.93 UNIT 11 (MEDIUM DENSITY SAND) SHEAR FORCE DISTRIBUTIONS.

6.12.6 Soil Lateral Pressure Distributions

Soil lateral pressure distributions obtained for the first half-cycle of loading for both piles of units 10 (loose density sand) and 11 (medium density sand) are shown in Figs. 6.94 and 6.95 respectively. Also indicated on these figures are lines representing multiples of passive pressure which were calculated in a similar fashion to that previously given in Section 6.10.5.

Due to the limitation of using cubic spline functions over four intervals for the moment distribution, each lateral pressure distribution is relatively crudely represented by four piecewise linear equations. However, the results indicated that despite the relatively low level of lateral deflection (< D/40), lateral soil pressures of up to 70% (unit 10) and 330% (unit 11) of passive pressure were developed close to ground level. At the pile base, the magnitudes of pressure were up to 45% (unit 10) and 135% (unit 11) of passive pressure. The lower percentage magnitudes of passive pressure were developed near the pile base, since from Fig. 6.87 lateral deflections were smaller at the pile base than near ground level.

For a given test unit at a given stage of testing, the soil lateral pressure distributions on each pile are somewhat different. This is a direct consequence of the different pile bending moment distributions which in Section 6.12.4 were attributed to local variations in soil layering.

6.12.7 Soil Lateral Pressure-Lateral Deflection-Depth Responses

Figure 6.96 shows plots of soil lateral pressure against lateral deflection for both piles of units 10 and 11 at depths of 4D (460 mm) and 17.5D (2013 mm). These depths correspond to the positions of peak positive and negative pressures which were obtained from the spline analyses. The accuracy of the results plotted in Fig. 6.96 suffers from the limitations in the accuracy of the strain gauge and linear potentiometer data which have been previously discussed. However it is evident that significant softening of the soil response occurs from pile lateral deflections which are as low as 0.25 mm (≅ 0.002D). There is also a tendency for soil response to be stiffer at a depth of 17.5D than at 4D, although this trend is more apparent for unit 10 than for unit 11.

6.13 CONCLUSIONS

Eleven model tests of bridge substructures typically embedded 20 pile diameters (D = 115 mm) in a dry sand foundation and subjected to lateral load simulating seismic attack were conducted. Factors investigated included the method of lateral load application (monotonic, cyclic of large amplitude, or cyclic of successively increasing amplitude), the sand density (medium or loose) and the pile head condition (free or capped). The main results from these tests are summarised in the following sections.

6.13.1 Free-Head Piles

Sand Movement

From load-level lateral displacements of 0.025D (2.9 mm) and 0.2D (23 mm) soil movement and failure wedges respectively were observed. As testing proceeded, the extent and magnitude of soil displacement increased. For both the monotonic and cyclic tests, sand flowed from the front to the wake of the pile. In all tests, the sand density in the vicinity of the pile increased as testing proceeded. This was particularly evident for the cyclic tests conducted in loose density sand.

Lateral Load-Displacement Response

Throughout testing, lateral load-deflection responses were non-linear and were poorly matched by predictions based on conventional design theory. Ultimate loads were not reached even though load-level lateral displacements of up to 2.6D (298 mm)

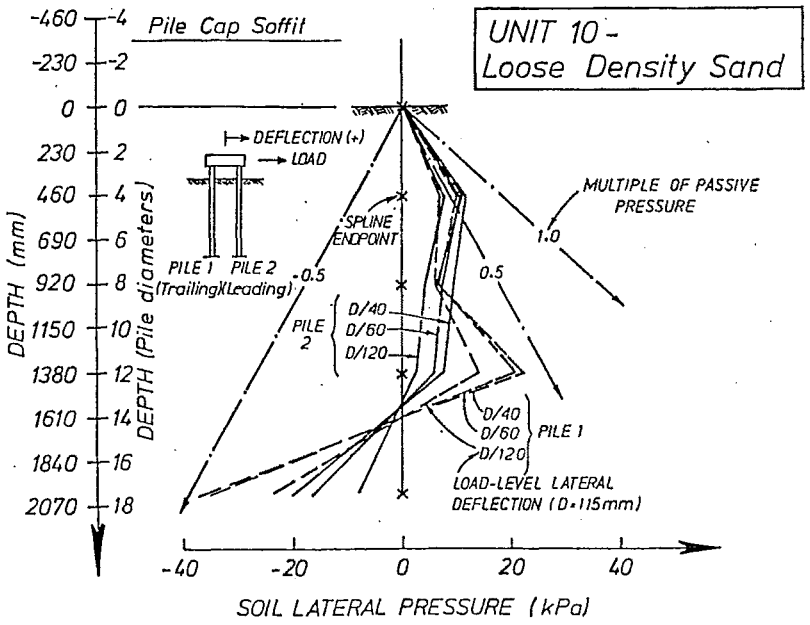

FIG. 6.94 UNIT 10 (LOOSE DENSITY SAND) SOIL LATERAL PRESSURE DISTRIBUTIONS.

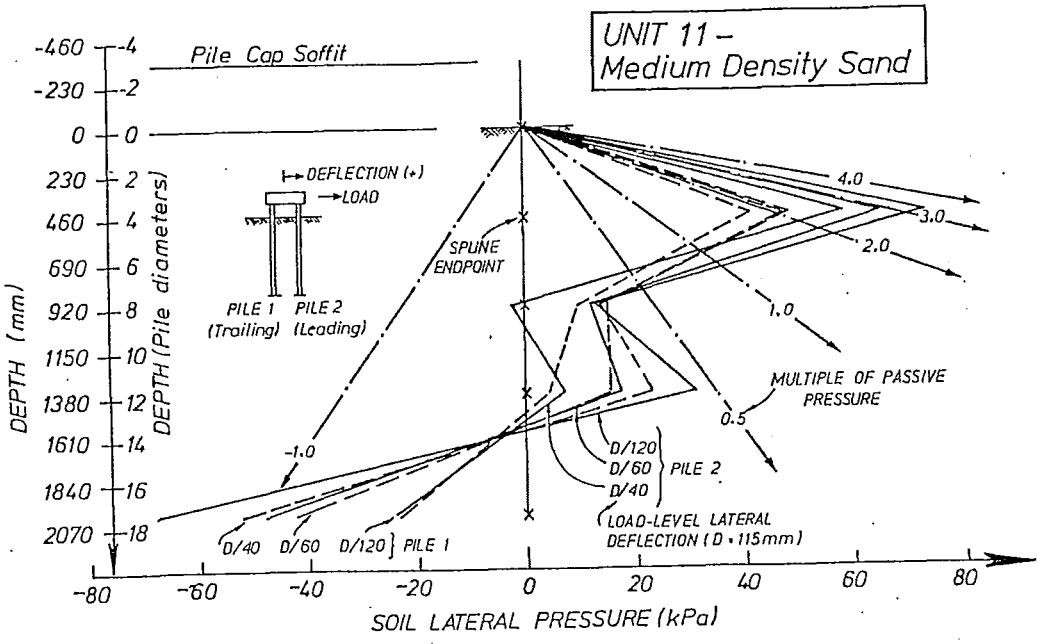

FIG. 6.95 UNIT 11 (MEDIUM DENSITY SAND) SOIL LATERAL PRESSURE DISTRIBUTIONS.

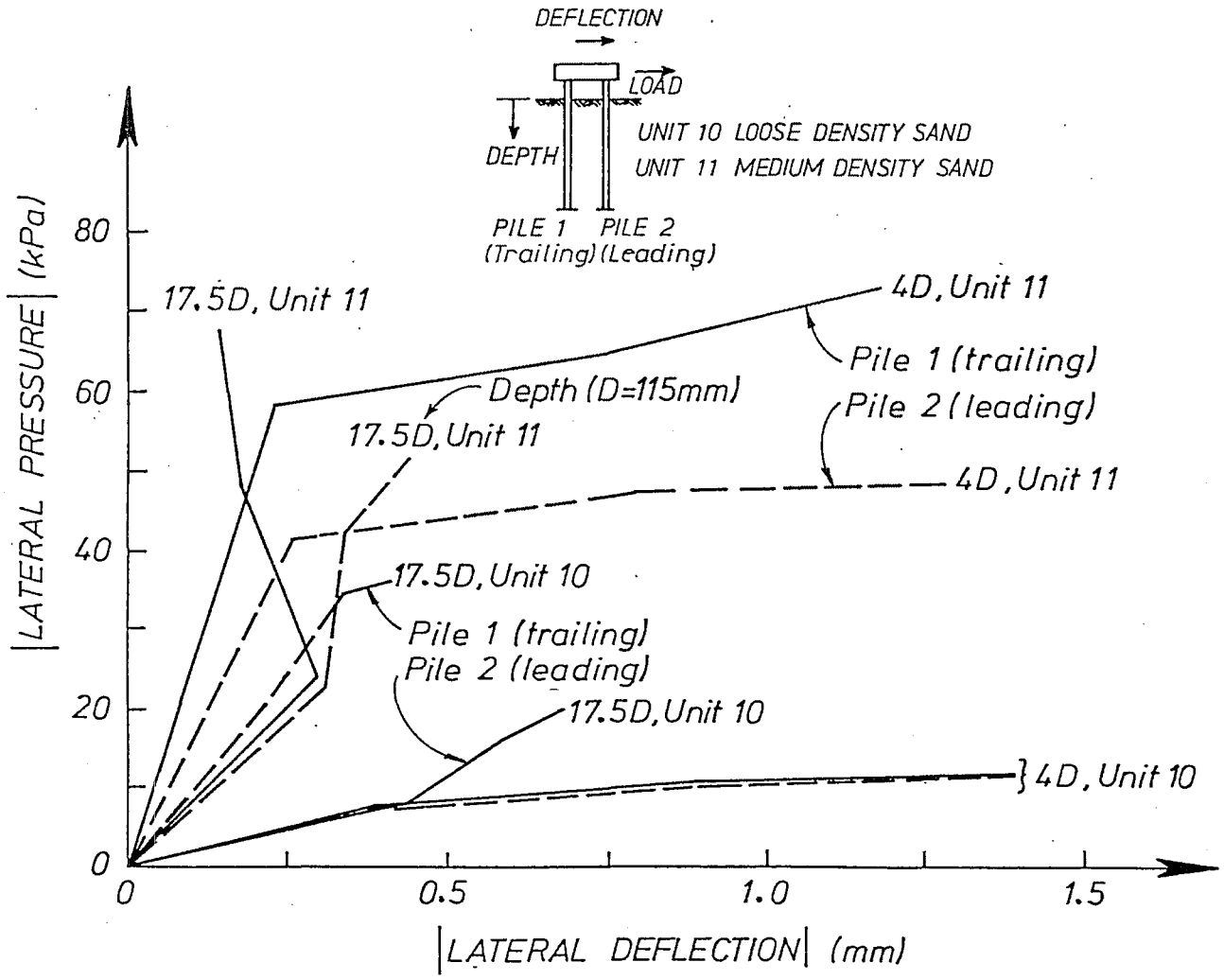

FIG. 6.96 SOIL LATERAL PRESSURE-LATERAL DEFLECTION RESPONSES FOR TWIN-PILE TEST UNITS.

were imposed. On unloading, substantial residual lateral displacements were present due to the flow of granular soil around the pile which had occurred during loading. For the cyclic tests, well-rounded hysteresis loops were obtained. In the medium density sand tests, these loops were stable, while in the loose density sand tests expanding loops were obtained, due to the substantial increase in soil density and hence strength which occurred under cyclic loading. Since the pile members generally behaved in an elastic fashion during testing, this implied a substantial reserve of hysteretic damping is available in the soil. Comparisons of load-deflection responses for tests prepared under similar conditions showed some divergence, while responses for tests prepared in medium density sand were of the order of twice as strong as those in loose density sand. Thus from the results of these and other researcher's tests, it can be concluded that the method of pile and sand instalment have a substantial influence on load-deflection response.

Pile Curvature Distributions

Distributions of pile curvature indicated that the position of peak pile bending moment fluctuates as the level of lateral displacement increases. This is due to relative changes in pile and soil stiffness which occur as the lateral displacement increases. For the typical case of an elastic pile and a soil which reduces in stiffness as the level of displacement increases, as the soil lateral displacement increases so does the depth at which the peak pile moment occurs. For the only model pile (unit 2) which was subjected to substantial inelastic strains, the relationship between curvature and displacement ductilities was determined. This relationship indicated that the pile-soil system could be modelled as an equivalent cantilever with an effective plastic hinge length of 1.87D. This relatively large length is a direct consequence of the low moment gradient which exists in the vicinity of the position of peak pile bending moment. The implication is that a pile forming a plastic hinge at depth in the ground will require an extremely large seismic displacement to induce structural failure.

Pile Deflected Shape

Generally pile deformed configurations were dominated by rigid pole rotation (perfectly straight pile), with a small amount of flexural deformation (bent pile) superimposed. In general, the deflected shape at the positive displacement peak of a cycle was not a mirror image of the shape at the negative peak. Thus unsymmetrical behaviour developed during testing.

Soil Lateral Pressures

At a given position on the pile, as the magnitude of lateral deflection increased so too did the soil lateral pressure. Pressures of up to 15 times passive pressure were developed. This may be compared with the ultimate soil lateral pressure of 3 times passive pressure recommended by Broms (6.18) on the basis of full scale pile tests (probably at relatively low levels of lateral deflection); and pressures of up to 25 times passive pressure obtained by Fendall (6.6) in model tests. Thus the level of pile lateral deflection and scale effects have a substantial influence on the soil lateral pressures which develop. It is probable that serviceability requirements (i.e. limiting deflection) would limit the soil lateral pressures assumed in design.

Design Recommendation

Current New Zealand design practice (6.20) for seismic design of bridge substructures was previously discussed in Section 1.2.1 and shown in Figs. 1.3 and 1.4. Substructures which are designed to form all their plastic hinges above ground level are permitted to be designed for full ductility (i.e. $\mu \leq 6$). However because of concerns with regard to inspection and repair of plastic hinges which form beneath ground level, substructures which are designed to form plastic hinges beneath ground level are currently designed for partial ductility (i.e. $\mu \leq 3$)

which implies (see Fig. 1.3) a larger seismic inertia load. However the tests described in this section have shown some benefits for substructures forming plastic hinges in the ground from:

(i) the large reserve of hysteretic damping available in the soil;

and (ii) the relatively long plastic hinge length which occurs in the vicinity of the position of peak moment on the pile.

Thus to account for these benefits, it is recommended that a design of full ductility ($\mu \leq 6$) is permitted for substructures which form plastic hinges in the ground.

6.13.2 Capped-Head Piles

Sand Movement

From load-level lateral displacements of 0.05D (5.8 mm) and 0.2D (23 mm) sand movement and failure wedges respectively were observed. As testing proceeded, rocking of the substructures which was due to relative settlement and uplift of the leading and trailing piles was also observed, although the average movement of the piles tended to be upwards. Under cyclic loading, the positions of leading and trailing piles alternated between the two piles. Between the two piles, sand tended to flow from in front of the trailing pile into the wake of the leading pile, resulting in a loss of lateral support for the trailing pile.

Lateral Load-Displacement Responses

Hysteretic loops were similar in shape to those described in the previous section for the free-head piles, and the density of the sand also had a marked influence on load-carrying capacity. In theoretical analyses it had been assumed that there was no pile cap rotation and no lateral interaction between the piles. These analyses predicted that the twin pile test units would have approximately 3.2 times the load-carrying capacity of the single pile test units. However as a result of pile cap and hence pile head rotation and lateral interaction of the piles due to soil flow, the actual margin between the twin and single pile test units was only approximately 1.5. Thus account should be taken of cap rotation and pile lateral interaction in the design of pile groups under lateral load. However in the model tests the effect of superstructure dead load was not modelled, and it was postulated that the presence of this load would reduce the level of pile cap and hence pile head rotation.

Pile Lateral Interaction

As the load-level lateral displacement increased, pile lateral interaction also increased, resulting in the trailing pile taking a decreasing proportion of the lateral load. For a maximum likely seismic load-level lateral displacement of 0.67D, on average the trailing pile took only 19% of the load taken by the leading pile. This resulted in asymmetric pile behaviour under lateral load. For example at peak displacements, the leading pile was subjected to double curvature of large magnitude, while the trailing pile was in a state of single curvature of small magnitude.

At very small load-level lateral deflections ($< D/40$) where lateral interaction effects would be expected to be negligible, large differences were obtained between the bending moment, shear force and lateral pressure distributions for piles 1 and 2. This implied that soil strength and stiffness is very sensitive to the soil layering around each pile.

Chapter Seven

FINITE DIFFERENCE ANALYSIS OF FREE-HEAD PILES UNDER LATERAL LOAD

7.1 INTRODUCTION

In sections 1.2.2-1.2.2.6 (also see figure 1.5), five methods (equivalent cantilever, elastic half-space, beam-on-elastic-foundation, beam and lumped spring, and finite element) which may be used to solve for the response of piles subjected to lateral load were briefly discussed. In Chapter 6, the equivalent cantilever method and coefficients of horizontal subgrade reaction (n_h) recommended by Edmonds et al (6.3) were found to result in poor predictions to the experimental response of small scale (D=115mm) piles under lateral load. In Chapter 7 from a finite difference approach, the beam and lumped spring method is used to solve the response of free-head piles to lateral load.

Previously the beam and lumped spring method has been utilised in two approaches to solve the response of pile-soil systems to lateral load.

(i) In the conventional stiffness approach, the unknowns to be solved are rotations and lateral deflections at the positions on the pile where the lateral springs are attached. This approach is commonly used in design offices, although elastic pile and soil behaviour is generally assumed. In solving for the response of single piles under lateral load, Carter (7.1) has utilised hyperbolic functions to represent the gradually softening lateral pressure-deflection characteristics of the soil, although he did not allow for non-linear pile behaviour. Toan and Pidgeon (7.2) have also used the conventional stiffness approach to analyse pile groups under lateral load, they allowed for non-linear pile and soil behaviour in a perfectly elastic-plastic fashion.

(ii) In the finite difference approach, the unknowns to be solved are the lateral deflections at the positions on the piles where the lateral springs are attached. Poulos and Davis (7.3) have described an algorithm which enables the response of single piles under lateral load to be solved using a finite difference approximation to the governing differential equation (equation 1.4). However, the description assumes elastic behaviour in both soil and pile. Reese (7.4) has extended this approach to allow for non-linear behaviour in the soil, although elastic pile behaviour was still assumed.

Since under seismic attack pile-soil systems may behave inelastically, it was decided to further extend the finite difference method to allow for the use of arbitrary non-linear functions in representing pile moment-curvature and soil lateral pressure-lateral deflection-depth characteristics. In the adopted solution technique, response is determined in an incremental fashion using tangent-stiffness properties of pile and soil.

In the beam and lumped spring method, the real continuum nature of the soil is effectively ignored, since the soil is assumed to act as a series of independently acting springs. However, this assumption which considerably simplifies the analytical method is generally regarded (7.5) as resulting in physically reasonable results.

The extended finite difference method was used to calibrate simple soil models which resulted in close predictions to the experimental response of model piles with free heads tested under monotonically increasing lateral load in medium (unit 12 from Chapter 6) and loose (unit 13) density sand foundations. Finally, using the soil model calibrated for medium sand, the response of a free-head prototype pile to large lateral displacement is described.

7.2 METHOD

7.2.1 Governing Differential Equation

Assuming that both pile and soil behave in a linearly elastic fashion, and including the second order effect of pile longitudinal load on behaviour, then the differential equation governing soil-pile interaction may be written as:

$$\frac{d^2M}{dx^2} + P.\frac{d^2y}{dx^2} + k.y = 0 \qquad (7.1)$$

where x = depth along pile member axis
y = lateral deflection of pile member (function of x)
P = longitudinal load
k = soil modulus of horizontal subgrade reaction [F/L^2 units] (function of x)
M = pile moment $= EI.\ d^2y/dx^2$

where EI = pile flexural rigidity
d^2y/dx^2 = pile curvature (function of x)

To allow for non-linear pile and soil behaviour equation 7.1 may be expressed in incremental form as:

$$\frac{d^2(\Delta M)}{dx^2} + P.\frac{d^2(\Delta y)}{dx^2} + k_t.(\Delta y) = 0 \qquad (7.2)$$

where Δy = increment of pile lateral deflection
k_t = tangent value of soil modulus of horizontal subgrade reaction [F/L^2 units]
ΔM = increment of pile moment

$$= (E_t I_t).\frac{d^2(\Delta y)}{dx^2} \qquad (7.3)$$

and $(E_t I_t)$ = tangent value of pile flexural rigidity

7.2.2 Finite Difference Formulation

To solve equation 7.2 in finite difference form, it is convenient to lump properties of the pile-soil system to a number of equally spaced nodes along the length of the pile, as shown in figure 7.1. Node m may be considered to be a general node on the pile, node 1 represents the pile base and node n represents the top of the pile (point of lateral load application). Nodes -1, 0, n+1 and n+2 are present to help represent the boundary conditions on either the base or the top of the pile. Node spacing is equal to h.

At node m, the first term of equation 7.2 can be approximated in finite difference form as

$$\left[\frac{d^2(\Delta M)}{dx^2}\right]_m \approx \frac{(\Delta M)_{m+1} - 2(\Delta M)_m + (\Delta M)_{m-1}}{h^2} \qquad (7.4)$$

Now at node m, $\Delta M = E_t I_t\ d^2(\Delta y)/dx^2$ may be approximated in finite difference form as:

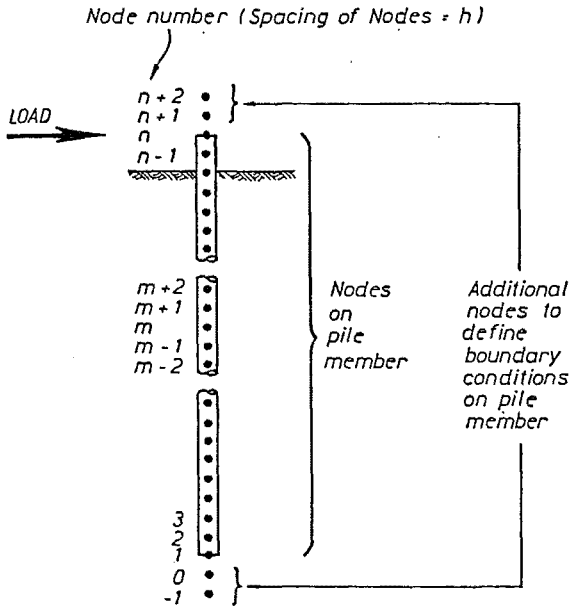

FIG. 7.1 - POSITION OF NODES ON PILE

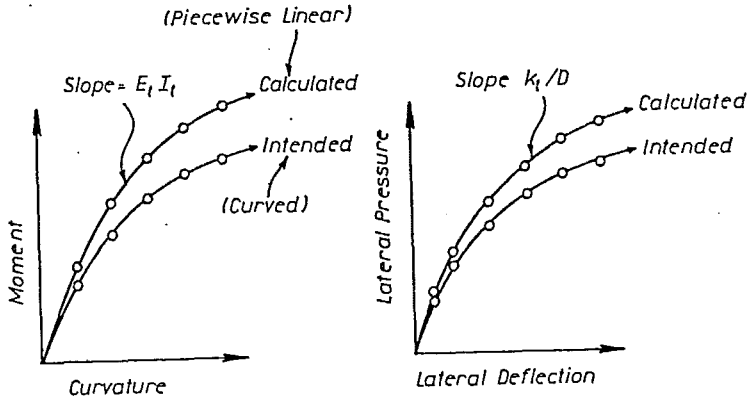

NOTE:- (1) o Represents end of one increment and start of the next.

(2) In a given increment, the slope of the calculated response corresponds to the slope at the start of that increment in the intended response.

FIG. 7.2 - DIVERGENCE OF INTENDED AND CALCULATED MOMENT-CURVATURE AND SOIL LATERAL PRESSURE-DEFLECTION RESPONSES

$$(\Delta M)_m \approx (E_t I_t)_m \frac{(\Delta y)_{m+1} - 2(\Delta y)_m + (\Delta y)_{m-1}}{h^2} \tag{7.5}$$

Substituting the result of equation 7.5 into equation 7.4, results in the first term of equation 7.2 being approximated as:

$$\begin{aligned}\left(\frac{d^2(\Delta M)}{dx^2}\right)_m \approx\ & (\Delta y)_{m+2}\left[\frac{(E_t . I_t)_{m+1}}{h^4}\right] \\ & + (\Delta y)_{m+1}\left[-2\frac{(E_t I_t)_{m+1}}{h^4} - 2\frac{(E_t I_t)_m}{h^4}\right] \\ & + (\Delta y)_m\left[\frac{(E_t I_t)_{m+1}}{h^4} + 4\frac{(E_t I_t)_m}{h^4} + \frac{(E_t I_t)_{m-1}}{h^4}\right] \\ & + (\Delta y)_{m-1}\left[-2\frac{(E_t I_t)_m}{h^4} - 2\frac{(E_t I_t)_{m-1}}{h^4}\right] \\ & + (\Delta y)_{m-2}\left[\frac{(E_t I_t)_{m-1}}{h^4}\right]\end{aligned} \tag{7.6}$$

At node m , the second term in equation 7.2 can be expressed in finite difference form as:

$$\left(P\frac{d^2(\Delta y)}{dx^2}\right)_m \approx P\frac{(\Delta y)_{m+1} - 2(\Delta y)_m + (\Delta y)_{m-1}}{h^2} \tag{7.7}$$

Finally at node m the third term in equation 7.2 can be expressed as

$$(k_t . (\Delta y))_m \approx (k_t)_m . (\Delta y)_m \tag{7.8}$$

Thus in finite difference form equation 7.2 can be approximated as:

$$\begin{aligned}& A_1(\Delta_y)_{m+2} + A_2(\Delta y)_{m+1} + A_3(\Delta y)_m + A_4(\Delta y)_{m-1} \\ & \quad + A_5(\Delta_y)_{m-2} \approx 0\end{aligned} \tag{7.9}$$

where

$$A_1 = \frac{(E_t I_t)_{m+1}}{h^4} \tag{7.10}$$

$$A_2 = \frac{P}{h^2} - 2\frac{(E_t I_t)_{m+1} + (E_t I_t)_m}{h^4} \tag{7.11}$$

$$A_3 = -2\frac{P}{h^2} + \frac{(E_t I_t)_{m+1} + 4(E_t I_t)_m + (E_t I_t)_{m-1}}{h^4} + (k_t)_m \tag{7.12}$$

$$A_4 = \frac{P}{h^2} - 2\frac{(E_t I_t)_m + (E_t I_t)_{m-1}}{h^4} \tag{7.13}$$

$$A_5 = \frac{(E_t I_t)_{m-1}}{h^4} \tag{7.14}$$

7.2.3 Boundary Conditions

Equation 7.9 can be applied for values of m from 1 (pile base) to n (load level). This results in n equations in n+4 unknowns ($(\Delta y)_{-1}$, $(\Delta y)_0$, ..., $(\Delta y)_{n+1}$, $(\Delta y)_{n+2}$), where nodes -1, 0, n+1 and n+2 are extra nodes beyond the top and bottom of the pile. Thus to solve for the unknowns, four further equations are required. These are obtained from the four boundary conditions on the pile:

(i) At the pile base (m=1), the pile bending moment is equal to zero. Hence from equation 7.5:

$$(\Delta y)_2 - 2(\Delta y)_1 + (\Delta y)_0 = 0 \tag{7.15}$$

(ii) Similarly at load level (m=n), for a pile with a free head pile bending moment is also equal to zero. Hence from equation 7.5:

$$(\Delta y)_{n+1} - 2(\Delta y)_n + (\Delta y)_{n-1} = 0 \tag{7.16}$$

(iii) At node m, the increment of pile shear force can be approximated as:

$$(\Delta V)_m = \frac{(\Delta M)_{m+1} - (\Delta M)_{m-1}}{2h}$$

$$= \left[(E_t I_t)_{m+1} \frac{(\Delta y)_{m+2} - 2(\Delta y)_{m+1} + (\Delta y)_m}{h^2} - (E_t I_t)_{m-1} \frac{(\Delta y)_m - 2(\Delta y)_{m-1} + (\Delta y)_{m-2}}{h^2} \right] /2h \tag{7.17}$$

At the pile base (m=1), the pile shear force is equal to zero. Hence from equation 7.17:

$$(\Delta y)_3 (E_t I_t)_2 + (\Delta y)_2 (-2E_t I_t)_2 + (\Delta y)_1 ((E_t I_t)_2 - (E_t I_t)_0)$$

$$+ (\Delta y)_0 (2E_t I_t)_0 + (\Delta y)_{-1} (-E_t I_t)_0 = 0 \tag{7.18}$$

(iv) At load level (m=n), the increment of pile shear force which is equal to the increment of applied lateral load ΔH may be treated as a known value. Hence from equation 7.17:

$$(\Delta y)_{n+2} \left(\frac{(E_t I_t)_{n+1}}{2h^3} \right) + (\Delta y)_{n+1} \left(\frac{-2(E_t I_t)_{n+1}}{2h^3} \right)$$

$$+ (\Delta y)_n \left(\frac{(E_t I_t)_{n+1} - (E_t I_t)_{n-1}}{2h^3} \right) + (\Delta y)_{n-1} \left(\frac{2(E_t I_t)_{n-1}}{2h^3} \right)$$

$$+ (\Delta y)_{n-2} \left(\frac{-(E_t I_t)_{n-1}}{2h^3} \right) = \Delta H \tag{7.19}$$

Thus from the simultaneous solution of equations 7.9, 7.15, 7.16, 7.18 and 7.19, the increments of lateral deflection $(\Delta y)_m$ may be solved.

7.2.4 Distributions of Pile and Soil Actions

From the solution for the increments of lateral deflection, corresponding increments of pile curvature $\Delta\psi$, moment ΔM, and shear force ΔV and soil lateral pressure Δp may be calculated in finite difference form from:

$$(\Delta\psi)_m = \frac{(\Delta y)_{m+1} - 2(\Delta y)_m + (\Delta y)_{m-1}}{h^2} \tag{7.20}$$

$$(\Delta M)_m = (E_t I_t)_m (\Delta\psi)_m \tag{7.21}$$

$$(\Delta V)_m = \frac{(\Delta M)_{m+1} - (\Delta M)_{m-1}}{2h} \tag{7.22}$$

$$(\Delta p)_m = \frac{(\Delta V)_{m+1} - (\Delta V)_{m-1}}{2h.D} \qquad (7.23)$$

where D = pile diameter

Thus as the results from the latest increment are added to the results of previous increments, it is possible to determine distributions of pile deflection, curvature, bending moment, and shear force and soil lateral pressure as well as the lateral load-deflection response.

7.2.5 Practical Implementation

To achieve accurate results with the above method, at the expense of additional computational effort, it is important that:

(i) a sufficient number of finite difference nodes are located along the length of the pile (e.g. spacing $\leq$ D/2); (This increases the accuracy of the finite difference approximations used in the governing differential equation.)

and (ii) the size of lateral load increment ΔH used in equation 7.19 is kept small. (This is because the values of pile and soil stiffness ($E_t I_t$ and k_t respectively) which are used in a given increment are those appropriate at the start of the increment. As shown in figure 7.2, if large increments are used the intended and calculated pile moment-curvature and soil lateral pressure-deflection responses will show a large degree of divergence.)

It should also be mentioned that the above outlined procedure is load-controlled and thus may be inappropriate for use when the gradient of the lateral load-deflection response is negative or has a relatively small positive value. In such cases a displacement-controlled incremental procedure is appropriate, and ΔH should be treated as an unknown and assumed values of $(\Delta y)_n$ (increment of load-level lateral displacement) used instead.

A computer program FD , which is available on request was developed to implement the algorithms described in the previous sections. Equations were solved directly using a matrix elimination technique.

7.3 PROPOSED TRI-LINEAR SOIL LATERAL PRESSURE-DEFLECTION RELATIONSHIPS

In section 6.10.7 the Reese et al (7.5) model for the soil lateral pressure-lateral deflection-depth relationship was described. This model was calibrated from test results of a large scale (D = 610mm) pile which was subjected to relatively small levels of lateral deflection ($\leq$ 0.05D). It was shown in section 6.10.7 that this model gave a poor estimate to the soil response deduced from tests of small-scale (D = 115mm) piles which were subjected to relatively large levels of lateral deflection ($\leq$ 2.6D). This poor estimate was attributed to the sensitivity of soil strength and stiffness to the methods of pile and sand installation as well as to the differences in scale and deflection level.

Because of this poor agreement, simple soil models which resulted in good predictions to the response of the small-scale piles (unit 12 - medium density sand and unit 13 - loose density sand) were calibrated. In the simple soil models, it is assumed that for a given level of lateral deflection y, soil lateral pressure p is linearly proportional to depth x . This linear assumption is in agreement with the Reese et al (7.5) model at depth in the foundation where soil horizontal flow governs behaviour, although close to ground surface where the formation of soil passive failure wedges governs behaviour, the Reese et al model predicts that soil lateral pressure p is approximately proportional to $x^{1.5}$. For a given depth x , the soil lateral pressure - lateral deflection (p-y)

relationship is assumed to be tri-linear:

For $|y| \leq 0.01D$: $p = n_{ht1} \cdot \frac{x}{D} \cdot y$ (7.24)

For $0.01D \leq |y| \leq 0.1D$: $p = [0.01 n_{ht1} \cdot x + n_{ht2} \cdot \frac{x}{D} (|y| - 0.01D)] \frac{y}{|y|}$ (7.25)

For $|y| \geq 0.1D$: $p = [0.01 n_{ht1} \cdot x + 0.09 n_{ht2} \cdot x + n_{ht3} \cdot \frac{x}{D} (|y| - 0.1D)] \frac{y}{|y|}$ (7.26)

where n_{ht1}, n_{ht2} and n_{ht3} = tangent value of coefficient of horizontal subgrade reaction (n_h) [F/L^3 units] for $|y| \leq 0.01D$; $0.01D \leq |y| \leq 0.1D$; and $|y| \geq 0.1D$ respectively.

Figure 7.3 shows the form of the tri-linear soil curves which were calibrated (by matching the experimental and theoretical lateral loads at load-level lateral displacements of 0.2D, 0.5D and 1.5D) from the tests conducted in medium (unit 12 - Chapter 6) and loose (unit 13) density sand foundations. The following comments are made from results shown in this figure.

(i) At small deflection levels (e.g. 0.01D), the ratio of soil lateral pressure in the medium density sand to that in the loose density sand is 8.15. At large deflection levels (e.g. D), this ratio is 2.22. Thus the sensitivity of sand lateral pressure to density decreases as the level of lateral deflection increases.

(ii) Significant positive soil stiffness is indicated throughout the range of lateral deflection. For loose and medium density sands at deflections greater than 0.1D, the tangent values of soil stiffness are equal to 0.041 and 0.008 times respectively the stiffnesses at deflections less than 0.01D. In comparison the Reese et al (7.5) model predicts that for deflections greater than 0.0375D the soil stiffness is zero.

and (iii) For medium and loose density dry cohesionless soils, Reese et al (7.5) recommend that values of coefficient of horizontal subgrade reaction (n_h) , which are appropriate at very low deflection levels, be taken as 16 and 5 MN/m^3 respectively. From figure 7.3, these values of n_h slightly underestimate and grossly overestimate the values of n_{ht1} found for medium and loose density sand respectively. Edmonds et al (7.6) recommend values of n_h equal to 9 MN/m^3 and 2 MN/m^3 for medium and loose density respectively dry cohesionless soils. These values are smaller than and equal to the values of n_{ht1} found for medium and loose density sand respectively. However, it should be noted that the values of Edmonds et al (7.6) are intended to apply as secant stiffnesses, and thus overestimate the stiffness of the soil at large deflection levels.

7.4 COMPARISON BETWEEN THEORETICAL AND EXPERIMENTAL RESPONSES

Theoretical analyses of the monotonic lateral load tests conducted in medium (unit 12 - Chapter 6) and loose (unit 13) density sands were performed using the extended finite difference method. In these analyses, moment-curvature response of these small diameter (D=115mm) piles was assumed to be in accordance with that previously given in figure 6.25 (for P = 0) which was developed taking into account lateral interaction of tube and concrete. Soil lateral pressure-lateral deflection-depth relationships according to both the tri-linear (see previous section) and the Reese et al (see section 6.10.7) soil models were also used in the analyses.

In the analyses finite difference nodes were located at a spacing of 0.5D (=57.5 mm) along the pile length. To limit the effect of stiffness overshoot (see figure 7.2), 2600 increments were used as the load-level lateral displacement was increased in a monotonic fashion to 2.6D (= 299mm).

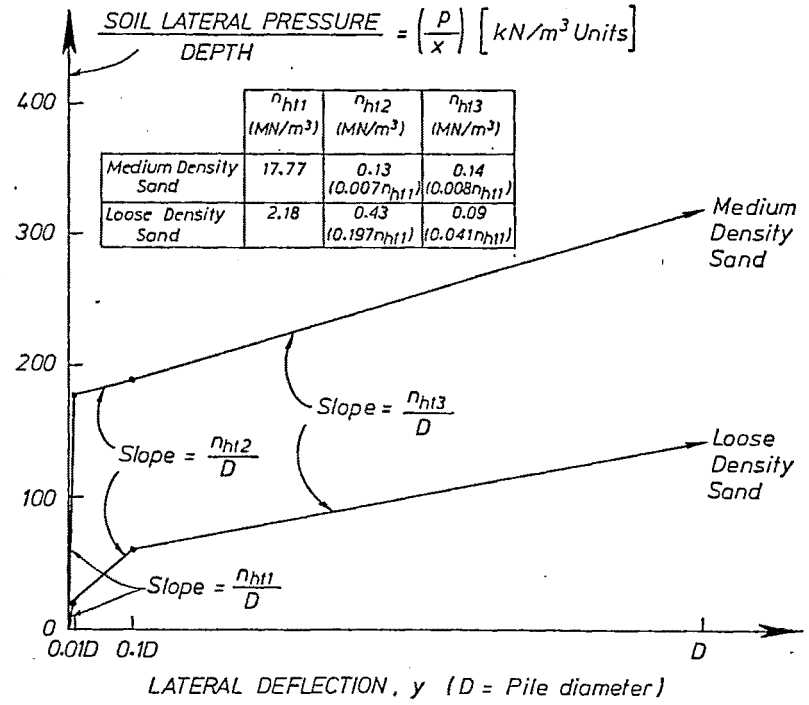

	n_{h11} (MN/m³)	n_{h12} (MN/m³)	n_{h13} (MN/m³)
Medium Density Sand	17.77	0.13 ($0.007n_{h11}$)	0.14 ($0.008n_{h11}$)
Loose Density Sand	2.18	0.43 ($0.197n_{h11}$)	0.09 ($0.041n_{h11}$)

FIG. 7.3 - PROPOSED TRI-LINEAR SOIL LATERAL PRESSURE-DEFLECTION RELATIONSHIPS

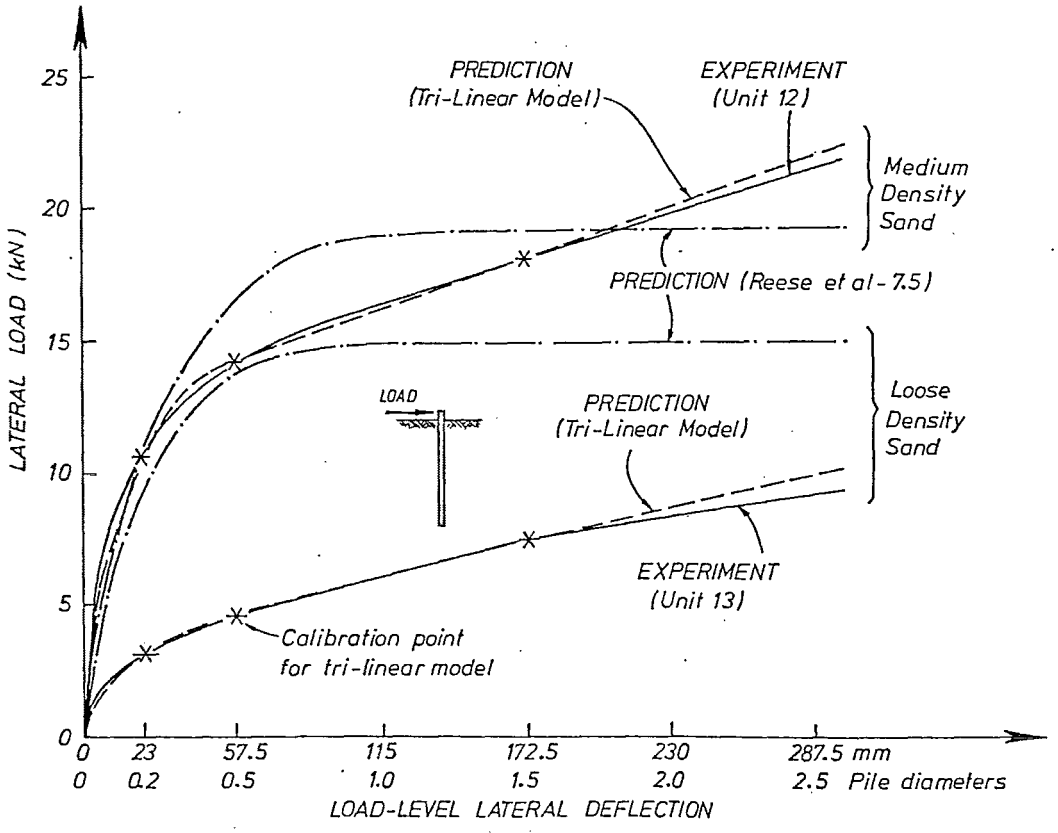

FIG. 7.4 - COMPARISON OF EXPERIMENTAL AND PREDICTED LATERAL LOAD-DEFLECTION RESPONSES

7.4.1 Lateral Load-Deflection Responses

Figure 7.4 compares for medium and loose density sand foundations, the lateral load - load level lateral displacement responses obtained from the experimental results, predictions using the Reese et al (7.5) soil model and predictions using the tri-linear soil model.

The tri-linear soil model was calibrated to match the experimental response at deflections of 0.2D, 0.5D and 1.5D. Thus in general agreement between experiment and the tri-linear model is very good, although for deflections less than 0.2D and greater than 1.5D small tendencies for the tri-linear model to underestimate and overestimate respectively the experimental response occur. As expected, the Reese et al model which was calibrated from different test results (D = 610mm, deflection $\leq$ 0.05D) gave poor agreement with the experimental responses of units 12 and 13 (D = 115mm, deflections $\leq$ 2.6D).

7.4.2 Curvature Profiles

In figure 7.5, results for peak curvature on the pile versus load-level lateral deflection obtained from the experimental results, predictions using the Reese et al (7.5) soil model and predictions using the tri-linear soil model are shown. Use of the Reese et al soil model results in a gross overestimate of the experimentally obtained peak curvature, while use of the tri-linear soil model results in a small (typically 10%) overestimate of the experimentally obtained peak curvature.

In Fig. 7.6(a), results for the depth at which peak curvature occurs versus load-level lateral displacement obtained from the experimental results, predictions using the Reese et al (7.5) soil model and predictions using the tri-linear soil model are shown. Since as previously discussed in Section 6.9.3, the moment gradient is small in the vicinity of the position of peak curvature on the pile, the experimental results for the position of peak curvature were very sensitive to small errors in the strain gauge data. Thus the maximum differences for the position of peak curvature (at a given displacement) between the experimental results and predictions based on the tri-linear model of 2D for medium density sand and 0.5D for loose density sand are quite good. Predictions based on the Reese et al model are up to 3.8D different from the experimental results. Figure 7.6(b) shows a comparison of predicted and experimental curvature profiles at peak displacement (= 2.6D at load level). At this stage the prediction based on the tri-linear soil model slightly overestimates the experimental curvature distribution, while the prediction based on the Reese et al (7.5) soil model grossly overestimates the experimental curvature distribution

7.5 ANALYSIS OF PROTOTYPE PILE BEHAVIOUR

In the following sections, the behaviour of a prototype flexible free-head pile under monotonic lateral load and superstructure-induced longitudinal load are examined using the finite difference method and the tri-linear soil model for medium density sand. It is assumed for convenience that the tri-linear model, calibrated from results of small-scale tests, is appropriate under full-scale conditions, though it must be recognised that scale effects would be expected to have significance.

7.5.1 Geometric and Material Details of Prototype Pile

The geometric details of the prototype steel-encased reinforced concrete pile are illustrated in figure 7.7(a). The chosen pile had a diameter of 1m, a tube wall thickness of 10mm, and was internally reinforced with 14D32 longitudinal bars. These bars occupied 1.4% of the gross area (= $0.014A_g$) of the pile. To simulate superstructure dead load, a longitudinal load of $P = 0.1f'_c(A_c + A_t)$ = 2356 kN (where f'_c = 30 MPa) was applied to the pile.

Uniaxial stress-strain characteristics of the tube and the reinforcing bars which were assumed are shown in figure 7.7(b). These characteristics are typical of those obtained from tests of samples of mild steel tube and bar as described earlier in this thesis. The moment-curvature response of the pile was obtained using the method decribed in Chapter 5 allowing for lateral interaction of tube and concrete and the longitudinal load on the pile. This response is shown in figure 7.7(c), together with an elasto-plastic idealisation of theoretical response

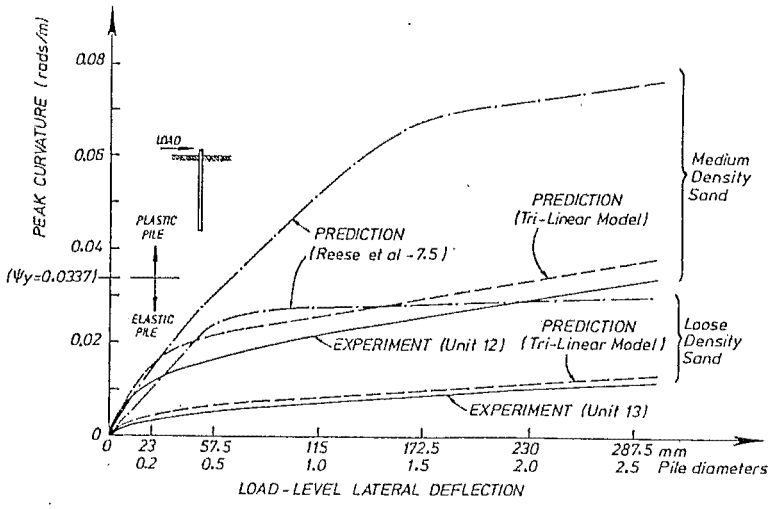

FIG. 7.5 : COMPARISON OF EXPERIMENTAL AND PREDICTED PEAK CURVATURE VS LOAD-LEVEL LATERAL DISPLACEMENT RESPONSES.

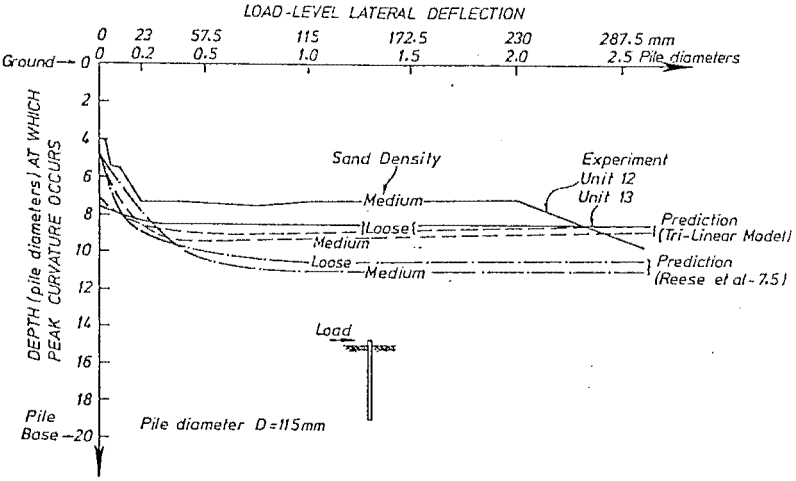

FIG. 7.6(a) : COMPARISON OF EXPERIMENTAL AND PREDICTED POSITIONS AT WHICH PEAK CURVATURE OCCURS.

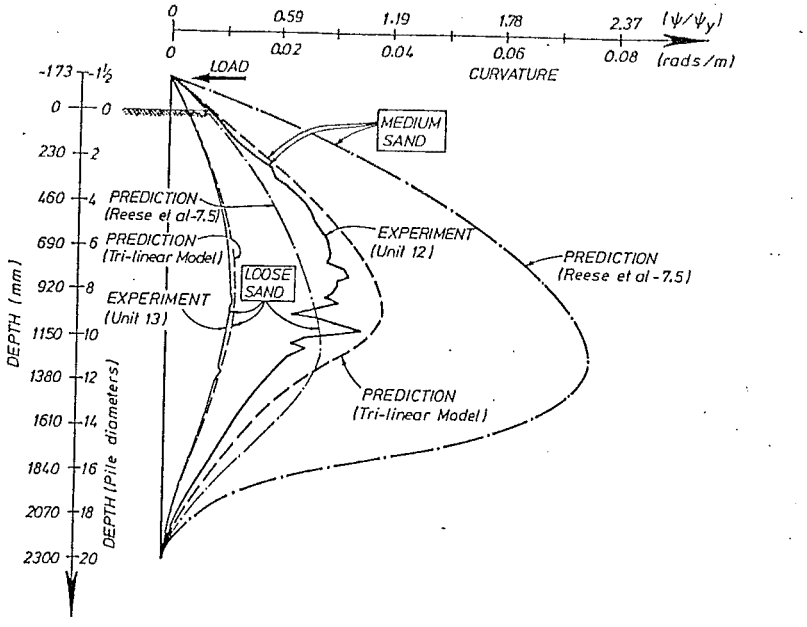

FIG. 7.6(b) : COMPARISON OF EXPERIMENTAL AND PREDICTED CURVATURE PROFILES AT PEAK DISPLACEMENT (2.6 PILE DIAMETERS).

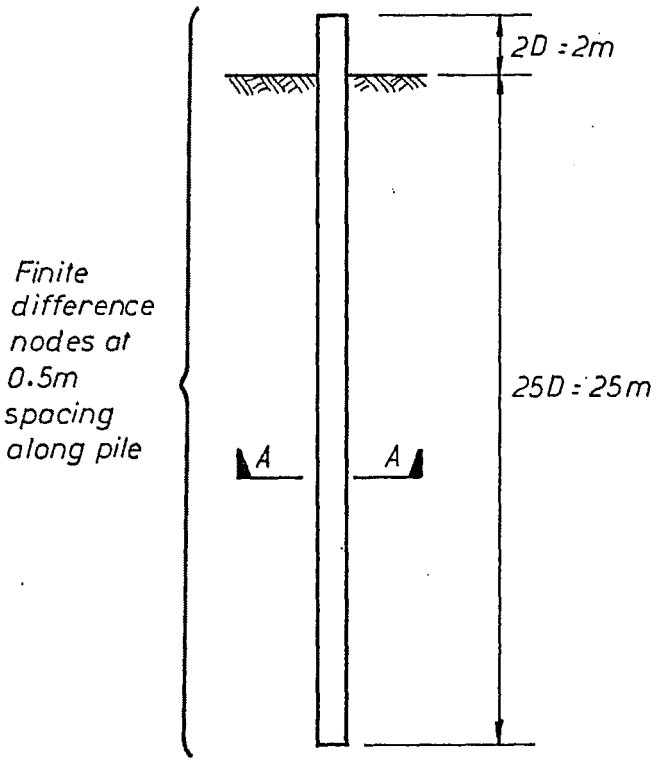

ELEVATION OF PROTOTYPE PILE

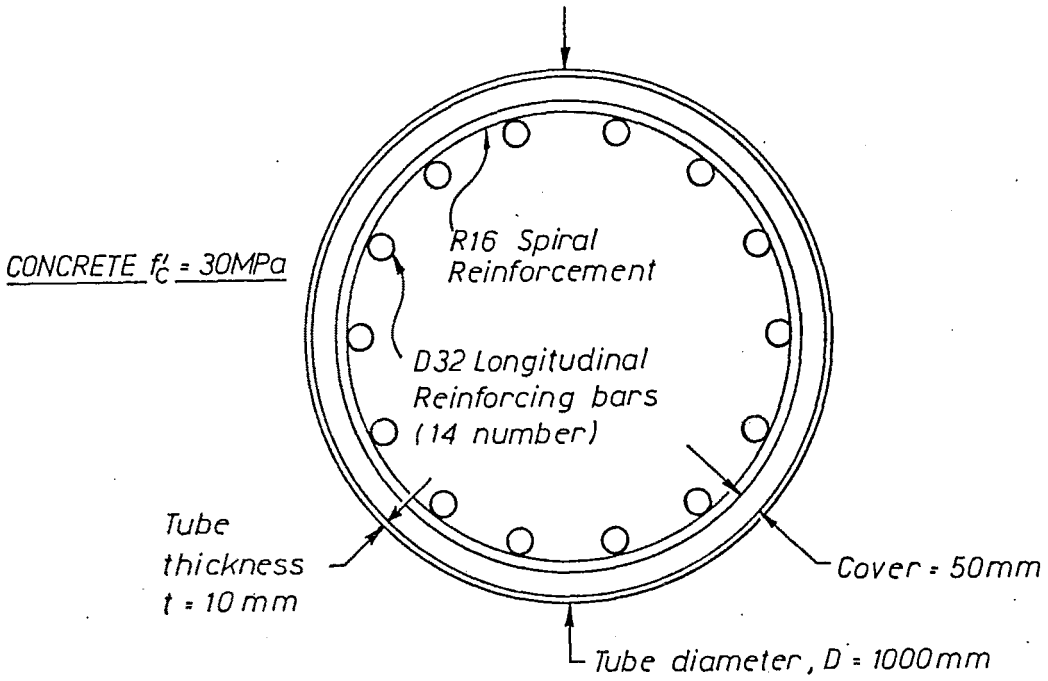

SECTION A-A

FIG. 7.7(a) - GEOMETRIC DETAILS FOR PROTOTYPE STEEL-ENCASED REINFORCED CONCRETE BRIDGE PILE

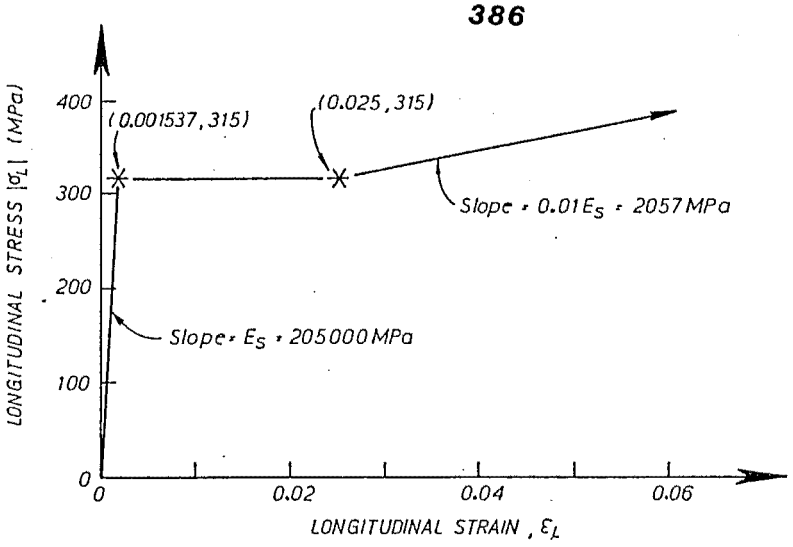

FIG. 7.7(b) - ASSUMED UNIAXIAL STRESS-STRAIN CHARACTERISTICS OF TUBE AND LONGITUDINAL REINFORCEMENT

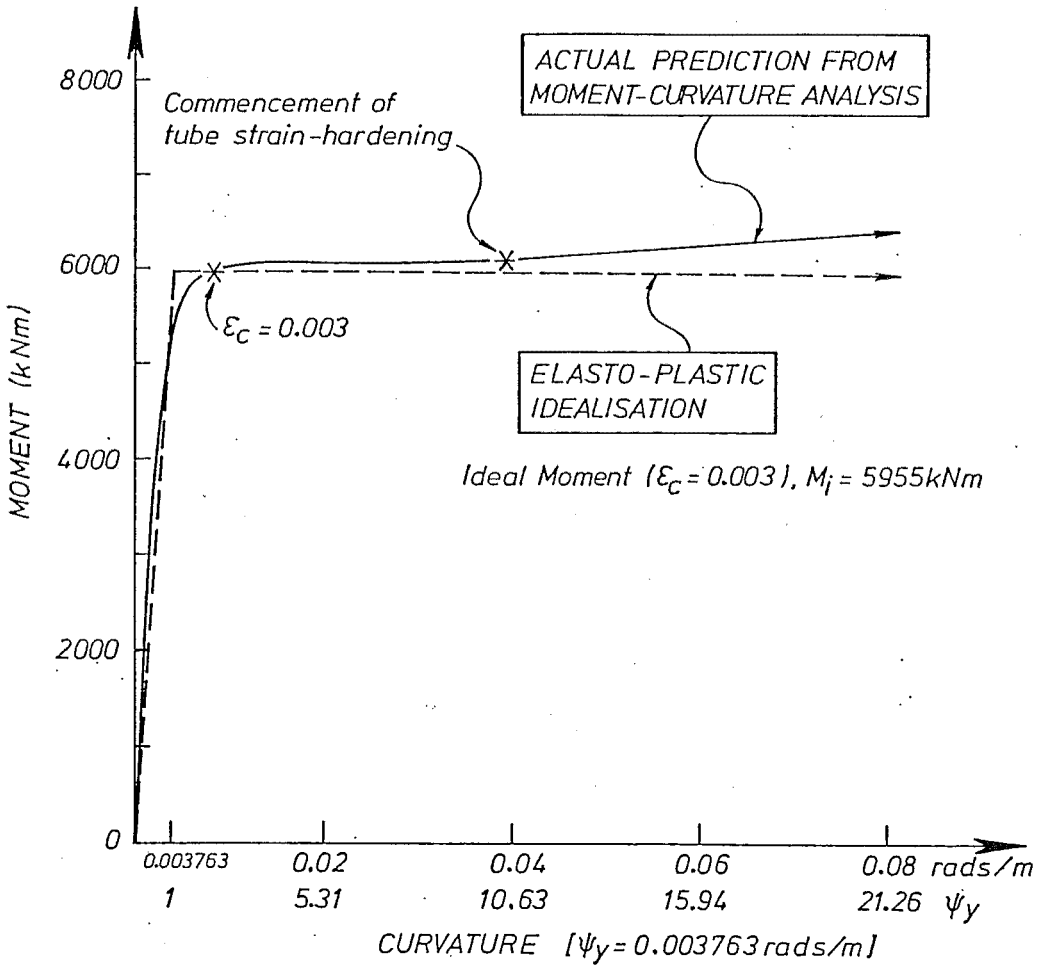

FIG. 7.7(c) - PREDICTED AND ELASTO-PLASTIC IDEALISATION OF PROTOTYPE PILE MOMENT-CURVATURE BEHAVIOUR

from which an idealised yield curvature of ψ_y = 0.003763 rads/m and an ideal moment (ε_c = 0.003) of M_i = 5955 kNm were obtained. From figure 7.7(c) a small level of flexural overstrength is shown. At a curvature of 0.08 rads/m (curvature ductility ratio = 21.3), overstrength of 7% above the ideal flexural strength is indicated.

The finite difference analysis was performed with nodes located at 0.5D (=0.5m) centres along the length of the pile. The load-level lateral displacement was increased from 0 to 1m in 1mm increments. Thus stiffness overshoot effects (see figure 7.2) should have been negligible.

7.5.2 Influence of P-Δ Effect on Behaviour

As discussed in section 7.2.2, P-Δ effect can be allowed for by the inclusion of an additional term in the governing differential equation (see equation 7.2). In this section, the response of the pile is described both including and ignoring P-Δ effect.

Figure 7.8 shows the lateral load-load level lateral displacement response of the pile. As expected, the influence of P-Δ effect increases as the level of lateral displacement increases. However for the prototype pile P-Δ effect made little practical difference to the lateral load-carrying capacity, since at peak displacement (= 1m) P-Δ effect only reduces the lateral load carried by 2%.

Figure 7.8 also shows significant positive stiffness occurs throughout the indicated range of load-level lateral displacement. At a deflection of 1m, stiffness is approximately equal to 1% of the initial stiffness.

Figure 7.9 shows the predicted deflected shapes of the prototype pile at peak load-level lateral displacement (= 1m) . As expected, P-Δ effect increases lateral deflection which occur beneath load-level.

Figure 7.10 shows the predicted curvature distributions of the prototype pile at peak load-level lateral displacement. It is interesting to note that for the given load-level lateral displacement, P-Δ effect reduces the peak curvature. This is because of the redistribution to the curvature distribution which occurs due to P-Δ effect. However, it is emphasised that at a given lateral load, P-Δ effect will increase the peak curvature on the pile. For a lateral load of 1400 kN, peak curvature predicted taking P-Δ effect into account was 9% larger than that predicted ignoring P-Δ effect.

Clearly from figures 7.9 and 7.10, the prototype pile exhibited flexible behaviour with the pile base being subjected to negligible levels of lateral deflection and curvature.

7.5.3 Distributions of Pile Lateral Deflection, Curvature, Bending Moment, Shear Force and Soil Lateral Pressure

Figures 7.11, 7.12, 7.13, 7.14 and 7.15 show distributions of pile lateral deflection, curvature, bending moment, shear force, and soil lateral pressure respectively at load-level lateral displacements of 0.01D, 0.1D, 0.2D, 0.3D, 0.4D, 0.6D, 0.8D and 1.0D (pile diameter, D = 1 metres). In these predictions P-Δ effect was taken into account.

From figure 7.11, lateral deflections are negligible (<< 1% of that at the pile head) for depths beneath 10m.

Figure 7.12 shows a large plastic hinge length occurs in the ground, since approximately 4 metres (= 4D) of the pile is subjected to curvatures larger than the idealised yield curvature (ψ_y) . Initially the position of peak curvature on the pile occurs at a depth of about 2.5m. Largely due to decreasing soil stiffness, the position occurs at a depth of about 4 m for load-level lateral displacements greater than 0.010m. A large degree of plasticity is predicted to develop

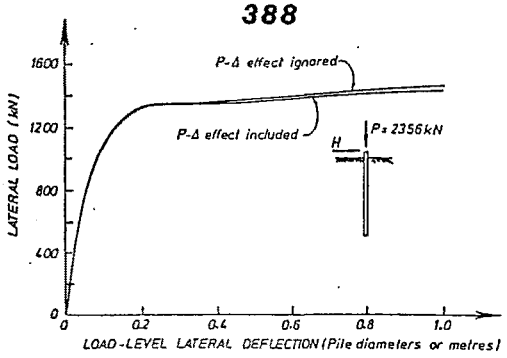

FIG. 7.8 - PREDICTED LATERAL LOAD-DEFLECTION RESPONSES (IGNORING AND INCLUDING P-Δ EFFECT)

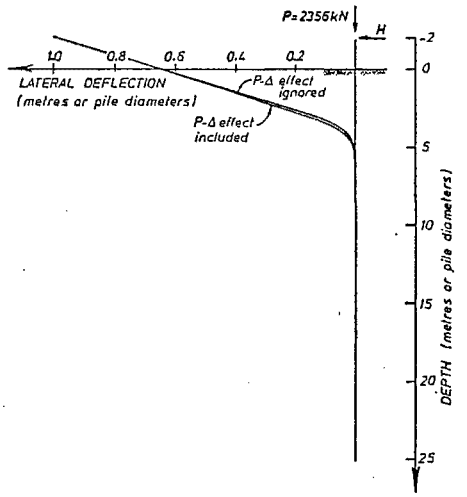

FIG. 7.9 - PREDICTED DEFLECTED SHAPES AT PEAK DISPLACEMENT (IGNORING AND INCLUDING P-Δ EFFECT)

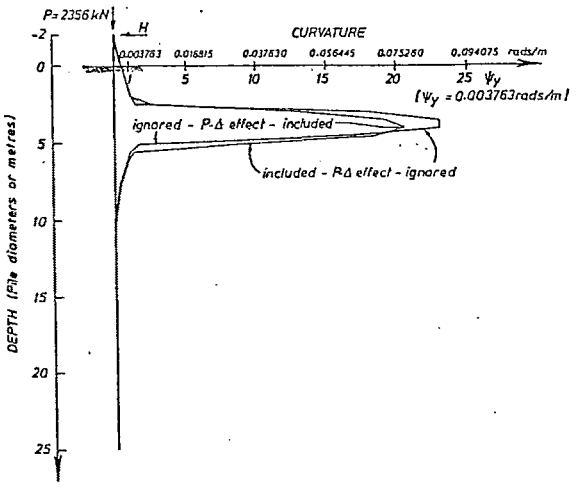

FIG. 7.10 - PREDICTED CURVATURE PROFILES AT PEAK DISPLACEMENT (IGNORING AND INCLUDING P-Δ EFFECT)

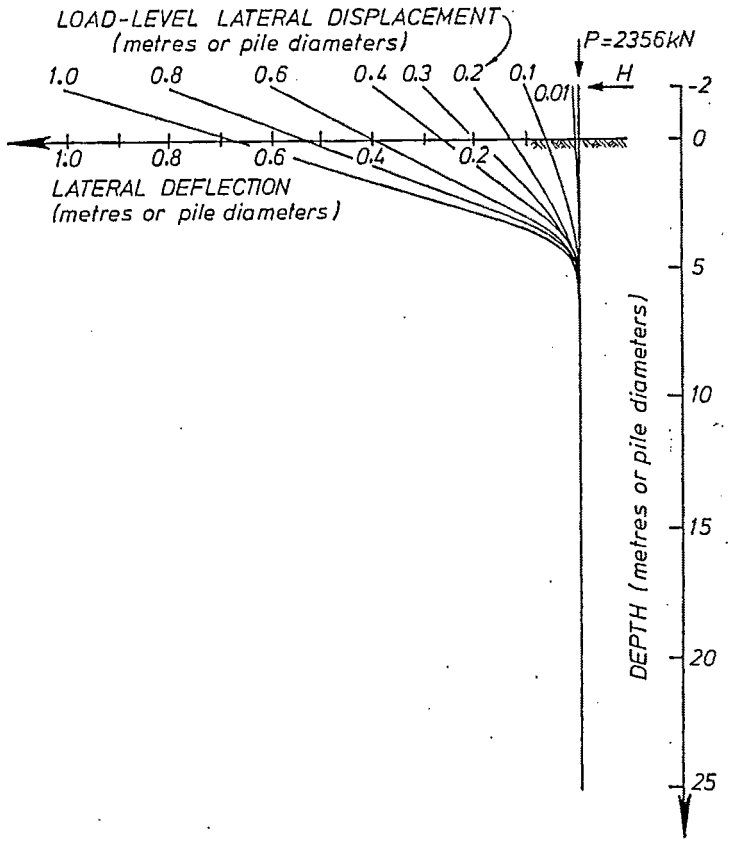

FIG. 7.11 - PREDICTED DEFLECTED SHAPES DURING MONOTONIC LOADING (P-Δ EFFECT INCLUDED)

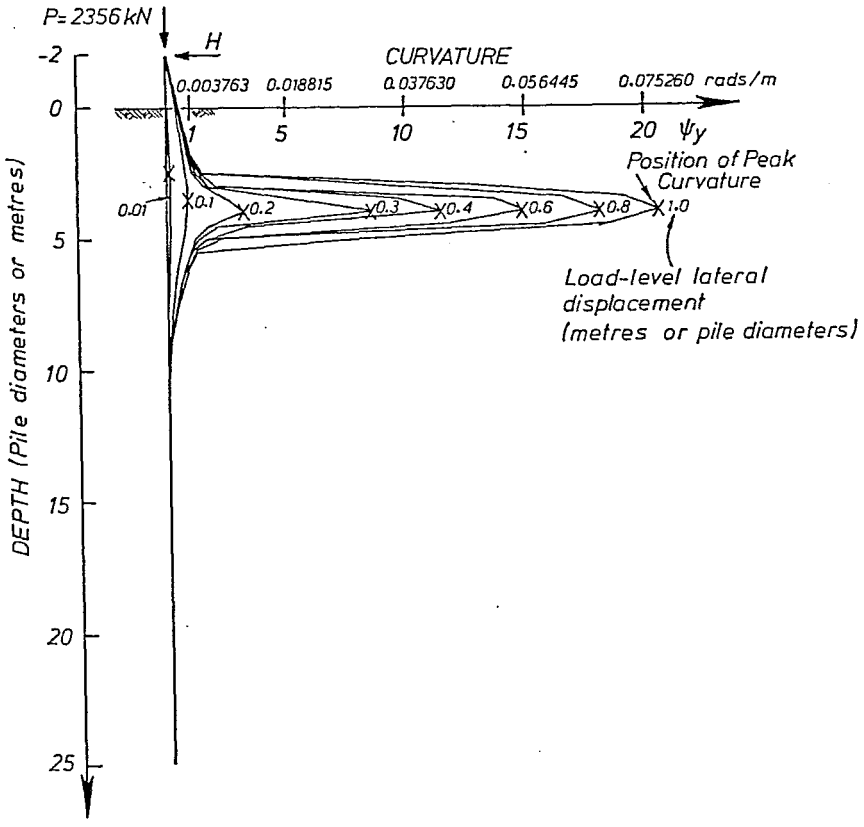

FIG. 7.12 - PREDICTED CURVATURE DISTRIBUTIONS DURING MONOTONIC LOADING (P-Δ EFFECT INCLUDED)

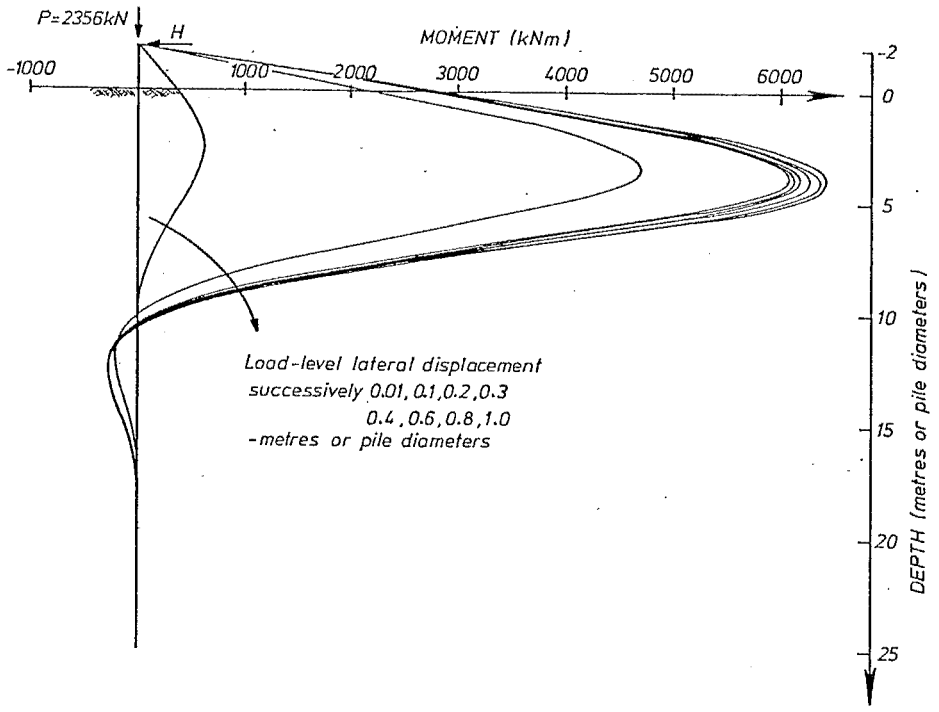

FIG. 7.13 - PREDICTED BENDING MOMENT DISTRIBUTIONS
(P-Δ EFFECT INCLUDED)

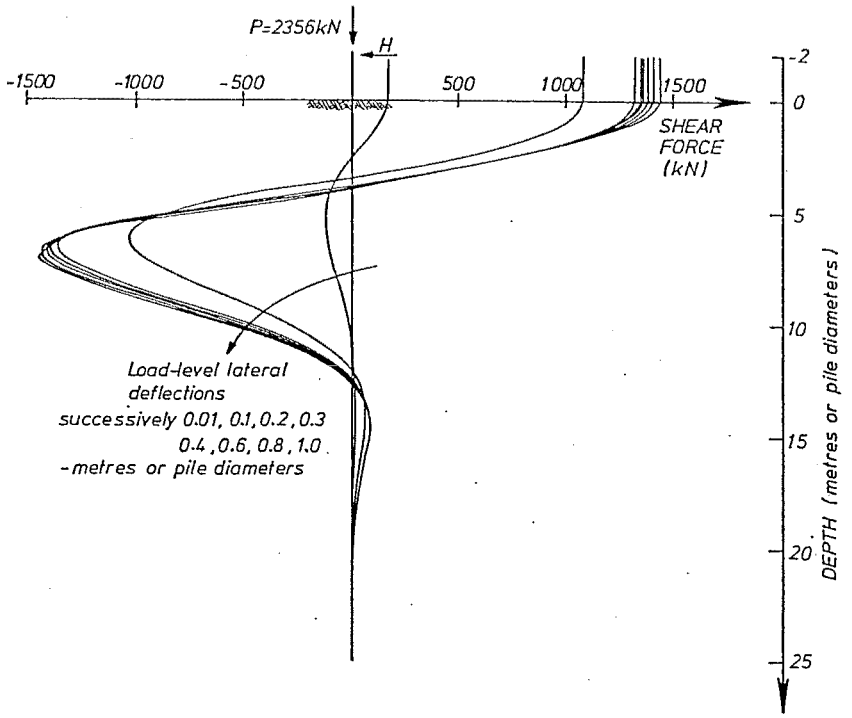

FIG. 7.14 - PREDICTED SHEAR FORCE DISTRIBUTIONS
(P-Δ EFFECT INCLUDED)

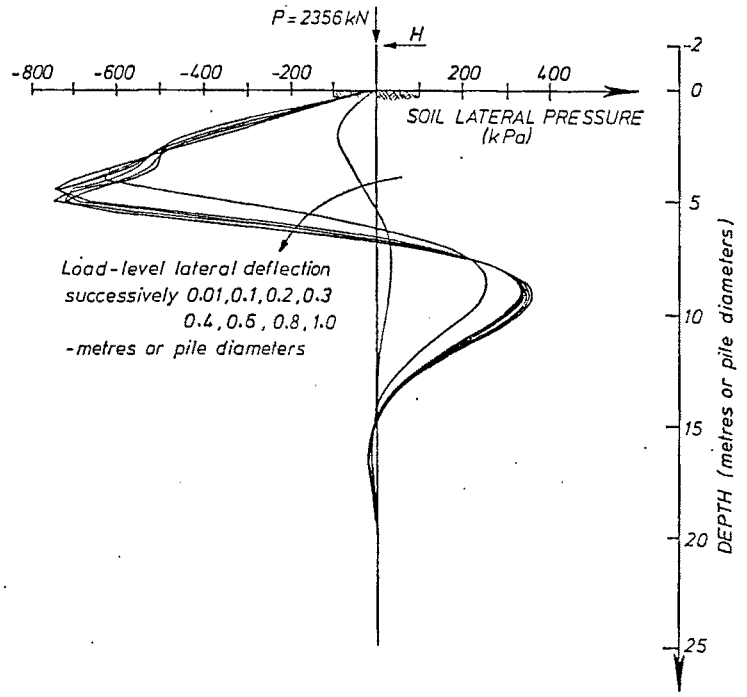

FIG. 7.15 - PREDICTED SOIL LATERAL PRESSURE DISTRIBUTIONS (P-Δ EFFECT INCLUDED)

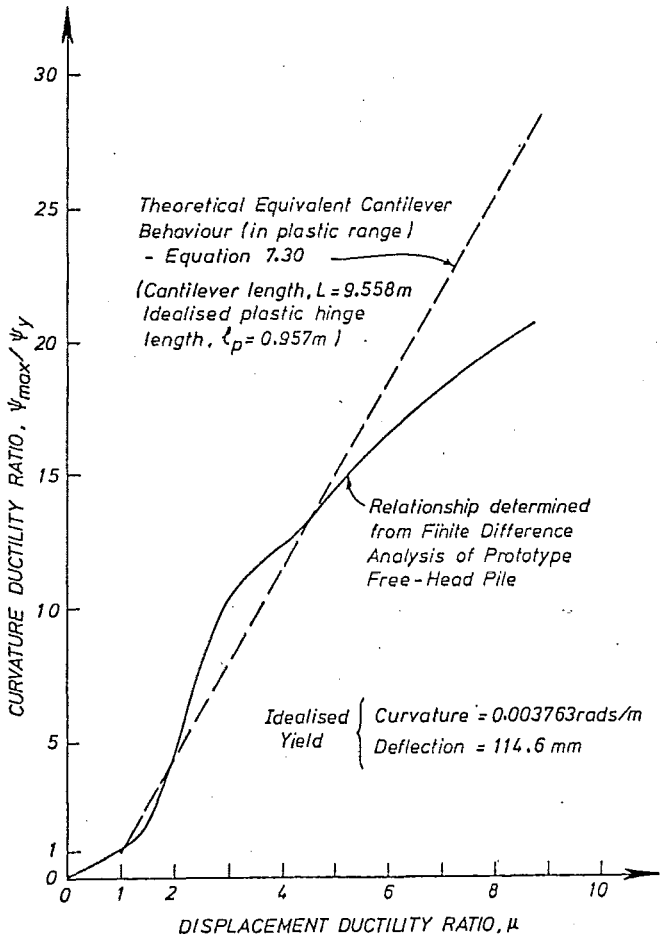

FIG. 7.16 - RELATIONSHIPS BETWEEN CURVATURE AND DISPLACEMENT DUCTILITY RATIOS

in the pile since the peak curvature ductility ratio reached was 20.6.

In solving the governing differential equation in finite difference form (equation 7.9), the unknowns are the increments of pile lateral deflection. As described in section 7.2.4, distributions of pile bending moment, shear force and soil lateral pressure are then obtained from the successive numerical differentiation of the distributions of pile of lateral deflection. This explains the minor irregularities which occur in the shear force and lateral pressure distributions, since numerical differentiation is very sensitive to any small errors which may develop in the lateral deflection distributions. From figures 7.13-7.15, significant levels of bending moment, shear force and lateral pressure occur over approximately 20m of the 25m embedded length of the prototype pile. These figures also show, that the distributions of moment, shear and pressure are relatively constant for load-level lateral displacements of 0.2D and greater. This is because as shown in figure 7.3, soil lateral pressure increases at a relatively small rate at large levels of lateral deflection.

7.5.4 Relationships Between Curvature and Displacement Ductility Ratios

In section 6.10.8, the relationship between curvature and displacement ductility ratio deduced from the lateral load testing (unit 2 - Chapter 6) of a small-scale (D = 115mm) pile was shown. In that section, it was shown that the pile had a relatively large effective plastic hinge length of 1.87D. In this section (7.5.4), a similar approach is used to deduce the relationship between curvature and displacement ductility ratios applying to the prototype pile.

The yield deflection Δ_y of the prototype pile was obtained using the method previously illustrated in figure 6.69. A regression line was drawn through the $\psi_{max} - y_t$ data (ψ_{max} = peak curvature and y_t = load-level lateral deflection = Δ_f for zero rigid pole deformation) for the stage where $\psi_{max} \leq \psi_y$ (ψ_y = idealised yield curvature = 0.003763 rads/m). Yield deflection was then taken from the regression line as the value of y_t corresponding to $\psi_{max} = \psi_y$. In this manner a value of yield deflection (Δ_y) of 114.6mm was obtained.

The resulting plot of curvature versus displacement ductility ratio is given in figure 7.16. Also shown in this figure is a relationship between curvature and displacement ductility ratios predicted assuming equivalent cantilever behaviour.

From equations 6.56, the length L of the equivalent cantilever may be calculated as:

$$L = \sqrt{\frac{3\Delta_y}{\psi_y}} \qquad (7.27)$$

Thus for Δ_y = 114.6mm and ψ_y = 0.003763 rads/m, the length of the equivalent cantilever may be calculated as equal to 9.558m (= 9.558D).

For the equivalent cantilever, the length ℓ_p of the equivalent plastic hinge may be calculated using the equation recommended by Priestley and Park (7.7):

$$\ell_p = 0.08L + 6d_b \qquad (7.28)$$

where d_b = diameter of longitudinal reinforcing bars.

Thus for 32mm diameter longitudinal reinforcing bars and a cantilever length L of 9.558m. The equivalent plastic hinge length is equal to 0.957m (= 0.957D).

In the plastic range, the relationship between curvature and displacement ductility ratios ($\psi_{max}/\psi_y - \mu$) for a cantilever is given by Park and Paulay (7.8) as:

$$\frac{\psi_{max}}{\psi_y} = \frac{L^2(\mu - 1)}{3\ell_p(L - \ell_p/2)} + 1 \qquad (7.29)$$

Substituting $L = 9.558\,m$ and $\ell_p = 0.957\,m$ into equation 7.29, results in the dashed line plotted in figure 7.16:

$$\psi_{max}/\psi_y = 3.505\mu - 2.505 \qquad (7.30)$$

From figure 7.16, this equation is in generally good agreement with the relationship between ψ_{max}/ψ_y and μ determined from the finite difference analysis. However at peak displacement ($\mu = 8.7$), from equation 7.30 it is predicted that the curvature ductility demand (ψ_{max}/ψ_y) is 28.1, while the finite difference analysis gave a value of 20.6. Thus at large displacements, the finite difference analysis implies the effective plastic hinge length is greater than 0.957m. From equation 7.29 and the finite difference analysis results at peak displacement ($\psi_{max}/\psi_y = 20.6$ and $\mu = 8.7$), it can be predicted that $\ell_p = 1.35m$ (or 1.35D).

However the conclusion reached in section 6.10.8 from the results of small-scale piles (D = 115mm) that:

> "..... at a given displacement, the pile curvature can be obtained (albeit slightly overestimated) by assuming equivalent cantilever behaviour with an equivalent plastic hinge length in accordance with the recommendation of Priestley and Park (7.7) (see equation 6.58 and associated text)....."

is substantiated by the results found in section 7.5.4.

7.5.5 Likely Effect of Severe Earthquake

It is also relevant to calculate the maximum seismic lateral displacement to which the prototype pile is likely to be exposed. From the initial stage of the lateral load-load level lateral displacement response of the prototype pile (figure 7.8), the elastic stiffness (k_e) of the pile-soil system under lateral load may be estimated as equal to 12.5 MN/m. The effective mass (M_e) at the pile head was taken as the longitudinal load (P = 2356 kN) on the pile divided by the acceleration due to gravity ($g = 9.81\,m/s^2$). The fundamental period of vibration T of the structure could then be obtained from:

$$T = 2\pi\sqrt{\frac{M_e}{k_e}} \qquad (7.31)$$

which gave T = 0.87 seconds.

For T = 0.87 seconds, a severe earthquake with a return period of 1000 years, and New Zealand seismic zone A then from the recommendations of Berrill et al (7.9), as given in section 6.7, the peak seismic displacement expected in the prototype pile is 300 mm (0.3D).

At a load-level lateral displacement of 0.3 m, from figure 7.16 the displacement ductility ratio is 2.6 and the curvature ductility ratio is 6.8. At this level of curvature from the results continued in Chapter 3, tube local buckling would be expected. However as shown in Chapter 3, steel-encased reinforced concrete members behaved in a stable fashion at curvature ductility ratios of the order of 50. Thus severe damage to the prototype pile would not be expected to occur under the action of seismic inertia loading.

7.6 CONCLUSIONS

In this chapter a method is decribed in which the monotonic response of a free-head pile to lateral load is solved using a finite difference approximation to the governing differential equation. In this method non-linear behaviour is allowed for by using an incremental analysis technique and tangent stiffness properties of pile and soil. The secondary ($P-\Delta$) effect of longitudinal load

on the pile was also taken into account.

The Reese et al (7.5) model for the soil lateral pressure-lateral deflection-depth response, which had been calibrated from test results of a large-scale (D = 610mm) pile subjected to relatively low deflection levels ($\leq$ 0.05D), was found to result in poor predictions of the experimental response of small-scale (D = 115mm) piles subjected to relatively large deflection levels ($\leq$ 2.6D). Thus simple tri-linear soil models were calibrated which gave good agreement with the experimental responses from the small-scale piles.

A prototype 1m diameter steel-encased reinforced concrete pile was then analysed using the finite difference method and the tri-linear soil model for medium density sand. It was shown that for a typical pile longitudinal load ($= 0.1(f'_c A_c + A_t)$), P-Δ effect had a negligible influence on the lateral load-deflection response for lateral deflections of up to 1m. From the finite difference analysis, the relationship between curvature and displacement ductility ratios was obtained. This relationship was found to be generally conservatively predicted (i.e. curvature ductility ratios overestimated) by a relationship derived on the basis of equivlent cantilever behaviour and the Priestley and Park (7.7) equation for the length of the effective plastic hinge. From the finite difference analysis, at a load-level lateral displacement of 1m (=D) a relatively large effective plastic hinge length of 1.35D was present due to the effect of low moment gradient in the plastic hinge zone. It was also shown that a severe earthquake (return period = 250 years) would initiate local buckling of the tube, but would not severely damage the prototype pile.

Chapter Eight

CONCLUSIONS AND RECOMMENDATIONS FOR FUTURE RESEARCH

8.1 CONCLUSIONS

The conclusion for each section of the work undertaken generally appear at the end of each of Chapters 2-7. Thus only a summary of the salient points reached during the course of this study are listed in the following sections.

8.1.1 Longitudinal Load Behaviour

Tensile and compressive longitudinal load tests were carried out on circular-sectioned concrete-filled tubes and showed that lateral interaction of tube and concrete occurs due to their different values of Poisson's ratio. This lateral interaction results in radial-compression stress in the concrete and hoop-tension stress in the tube with the composite response of concrete-filled tubes being stronger and generally stiffer than predicted from the sum of the independent responses of tube and concrete. For the longitudinal-compression load tests, the benefits of composite action were particularly apparent, since the concrete stabilised tube local buckling while the tube confined the concrete. Under longitudinal-tension load, it was apparent that the concrete considerably restricted Poisson's ratio lateral contraction of the tube.

Constitutive models which account for lateral interaction of tube and concrete, under monotonic longitudinal loading, were developed and calibrated to give good agreement with test data.

For tensile longitudinal load, tube response is predicted on the basis that the concrete is laterally rigid and hence zero hoop-tension strain occurs in the tube. This implies that the tube longitudinal strength is enhanced by 15.5% relative to its strength under uniaxial-stress conditions. Concrete response is predicted taking into account tensile stress carried by the concrete between cracks.

It was found that existing constitutive models do not adequately describe the behaviour of concrete and tube under longitudinal-compression load. Thus models were developed that allowed for the presence of hoop-tension stress in the tube which reduces the longitudinal-compression stress in the tube, and the presence of radial-compression stress in the concrete which enhances the longitudinal-compression stress in the concrete. Due to Poisson's ratio lateral expansion of the tube, it was shown that relative to spiral reinforcement the tube has a delayed confining effect on the concrete.

8.1.2 Strength and Ductility Characteristics of Steel-Encased Reinforced Concrete Members with Continuous Casings

Steel-encased reinforced concrete members, with continuous casings and diameter to thickness ratios in the range of 34 to 214, were tested essentially as vertical beams with a cyclically varying central lateral load and a low level of longitudinal-compression load. Sound performance was displayed under the simulated seismic attack.

Damage to the test units concentrated over very short lengths at positions of tube local buckling. This resulted in curvature ductility demands that were larger than those obtained in similar reinforced concrete test units at the same level of displacement ductility. However strength, ductility and energy-dissipating characteristics of units with casing diameter to thickness ratios of greater than 60 were found to be similar to those of conventionally designed ductile reinforced concrete members, while these characteristics for the unit with a casing diameter to thickness ratio of 34 were superior to those of reinforced

concrete members. Previously expressed concern about the possibility of strain-age embrittlement of the tubes at the positions of local buckling was found to be unwarranted, since the radii of curvature of the local buckles were sufficiently large to avoid this effect.

Analyses to determine the monotonic loading moment-curvature and lateral load-deflection responses of the test units were performed. Lateral interaction between tube and concrete was allowed for by using the constitutive models developed earlier in this study. Envelopes to the experimental cyclic loading responses were in good agreement with the theoretical monotonic loading predictions. For the average of the 7 test units, experimental strength, yield curvature and yield deflection were predicted to within 2%, 7% and 11% respectively. Theoretical predictions based on uniaxial-stress behaviour of tube and concrete significantly underestimated the experimental responses. It was also demonstrated that for steel-encased reinforced concrete members with casing diameter to thickness ratios in the range of 34 to 214, ductile behaviour results in the absence of spiral reinforcement. This occurs because the concrete is already well confined by the tube.

Theoretical ultimate flexural strengths were also calculated using a strain compatibility approach, uniaxial stress behaviour of steel and concrete, an A.C.I. stress block for the concrete in compression, a maximum concrete compression strain of 0.003, and the measured material strengths (concrete f'_c and steel σ_y). The experimentally obtained flexural strengths were in the range of 5% to 28% larger than the theoretical strengths calculated in the above manner. Thus it may be inferred that current Concrete Code (e.g. 4.17 and 4.30) requirements for a maximum ratio of tube diameter to thickness (typically $D/t \leq 80$) for structural use to be made of the tube are unnecessarily restrictive. The presence of typical levels of shear force was also shown to have a negligible influence on flexural strength.

8.1.3 Strength and Ductility Characteristics of Steel-Encased Reinforced Concrete Members with Casing Circumferential Discontinuities

Steel-encased reinforced concrete members with casing circumferential discontinuities in the plastic hinge zones performed well under combined longitudinal and cyclic lateral loading.

Damage concentrated over very short lengths in the vicinity of the sections of casing discontinuity. However, the presence of internal spiral reinforcement made little difference to performance, since the tube more than adequately confined the concrete and a large reserve of shear strength was available.

The flexural behaviour of these test units was slightly conservatively predicted by assuming the casing to be effective in compression but ineffective in tension at the discontinuity. Full contribution under longitudinal-compression strain allows for longitudinal-compression stress developing in end-bearing. Theoretical ultimate flexural strength based on the reinforced concrete core underestimated the experimental strength by 42%. The overall stiffness of these members was also enhanced by the presence of the tube, since significant levels of tensile and compressive longitudinal strain were measured away from the sections of casing discontinuity.

The bond stress-slip relationship between tube and concrete was found to be ductile. On the basis of the rate at which tube longitudinal-tension strain increased with distance from the discontinuities, a design recommendation of 0.73 MPa for the ultimate bond strength was made.

8.1.4 Free-Head Piles Under Lateral Load

Free-head steel-encased concrete model piles (diameter = 115mm) were embedded in either a medium or loose density dry sand and subjected to lateral load at a height of 1.5 pile diameters above sand level. Lateral load-deflection responses were non-linear and ultimate loads were not reached even for lateral displacements as large as 2.6 pile diameters. Lateral loads reached in the medium density sand tests were of the order of twice those reached in loose density sand tests. Under cyclic loading, well-rounded hysteresis loops were obtained. In the medium density sand tests the loops were stable, while for loose density sand tests the loops were expanding. Due to changes in the relative stiffness of pile and soil, the position of peak moment on the pile was found to be a function of displacement level. For the model pile subjected to large values of inelastic curvature, a relatively long effective plastic hinge length of 1.87 pile diameters was calculated from experimental data. This was due to the low moment gradient in the vicinity of the plastic hinge zone. The consequence of this is relative to a similar cantilever, low strains will occur in the pile at a given displacement ductility ratio. Soil lateral pressures were calculated from experimental data, and had values as large as 15 times passive pressure. Although these pressures were reached at extremely large values of lateral displacement, they were considerably larger than the value of three times passive pressure recommended for design by Broms (6.18).

Currently in New Zealand (6.20), substructures which are designed to form plastic hinge zones in the ground are designed for limited ductility ($\mu \leq 3$). This is because of concern with regard to inspection and repair of damage occurring in the plastic hinge zone as well as design uncertainties. However, because of the large reserve of hysteretic damping available in the soil and the relatively long plastic hinge zones which occur in the ground, it is recommended that such substructures be designed for full ductility ($\mu \leq 6$).

Experimental responses of the small-scale free-head piles were poorly matched by predictions based on conventional design theory. A method was developed in which the monotonic response of a free-head pile is solved using a finite difference approximation to the governing differential equation. In this method, non-linear behaviour is allowed for by using an incremental solution technique and tangent stiffness properties of pile and soil. The secondary ($P-\Delta$) effect of longitudinal load on the pile was also taken into account. Using the finite difference method, simple tri-linear soil lateral pressure-deflection relationships were calibrated to give good agreement with results from the small-scale pile tests. These models indicated significant ($\geq$ 0.8% of initial stiffness) positive stiffness was present in the soil at lateral displacements greater than 10% of a pile diameter. Using the finite difference method and the tri-linear soil model calibrated for medium density sand, a prototype 1m diameter steel-encased reinforced concrete pile was analysed. It was shown that under a severe earthquake (return period = 250 years), local buckling of the tube would have been initiated, but severe damage to the pile would not have occurred.

8.1.5 Capped-Head Piles Under Lateral Load

Twin steel-encased concrete model piles (diameter = 115mm) were spaced at a distance of 6 pile diameters and rigidly attached to a stiff capping beam. These piles were embedded 17.5 pile diameters in a dry sand foundation and subjected to cyclic lateral load. The twin piles tended to rise out of the foundation as cyclic loading proceeded, although relative settlement and uplift of the leading and trailing piles occurred which resulted in significant pile head rotation. It was felt that this relative movement of the piles would have been reduced if superstructure dead load had been modelled. Flow of soil from in front of the leading pile into the wake of the trailing pile was also observed. This resulted

in a relative loss of soil lateral support for the trailing pile which increased in magnitude as the level of lateral displacement increased. The overall result of soil flow between the piles and pile head rotation was that typically the twin piles with a capped head resisted only approximately 1.5 times the lateral load carried by a similar single pile with a free head.

8.2 RECOMMENDATIONS FOR FUTURE RESEARCH

The following sections contain lists of experimental and theoretical research topics which, if investigated, should lead to improved design and analysis techniques and provide a better understanding of the seismic behaviour of steel-encased reinforced concrete bridge piles.

8.2.1 Strength, Ductility and Stress-Strain Behaviour of Steel-Encased Reinforced Concrete Members

1. Tests of steel-encased reinforced concrete members with casing diameter to thickness ratios in the range of 34-214 have been conducted and prototype piles are typically constructed with casing diameter to thickness ratios in the range of 60-180. However, due to corrosion, late in the life of a bridge, the effective casing diameter to thickness ratio may be considerably larger than 214. Thus it would be useful to conduct a theoretical and experimental investigation into the seismic performance of such thin-walled members. In particular, it would be of interest to determine if the tube still provided adequate confinement to the concrete or whether the provision of internal spiral reinforcement was required to ensure ductile performance. For this problem the combined confining effect of tube and spiral reinforcement on the concrete would require careful consideration.

2. Constitutive models have been developed to allow for lateral interaction of tube and concrete under monotonic loading. To enable cyclic loading moment-curvature analyses to be conducted, it would be necessary to extend and calibrate these models from results of cyclic longitudinal loading tests.

3. It would also be useful to conduct a study of the seismic risk involved where the casing may be in good condition early in the life of the bridge, but due to corrosion in poor condition (i.e. reduced casing thickness) towards the end of the design life of the bridge.

8.2.2 Pile-Soil Systems Under Lateral Load

1. Poor agreement was obtained between the soil responses obtained from the model tests described in this thesis and the soil model of Reese et al (6.1). In-situ soil tests together with large deformation lateral load tests of piles at a variety of sites need to be conducted. Results from these and previous tests should then be correlated with theoretical work to enable improved soil models to be developed. These models would need to realistically allow for the effects of soil density, method of pile installation and scale on the lateral pressure-lateral deflection depth response of both cohesive and cohesionless soils which are adjacent to piles.

2. In Chapter 7, the theoretical behaviour of a 1m diameter steel-encased reinforced concrete pile embedded in a medium density sand and subjected to large lateral displacement was described. It would be useful to extend this study to more completely investigate the performance of prototype piles at large lateral displacements. The finite difference method described in Chapter 7 could be used in this study to allow for non-linear pile and soil behaviour. Factors investigated should include variations in the soil profile and the pile moment-curvature relationship. This study would enable general conclusions to be drawn on the lateral load-deflection response of piles and the behaviour of plastic hinges forming in the ground. Full scale large lateral displacement

tests should be undertaken to confirm results from the theoretical analyses.

3. The finite difference method described in Chapter 7 was developed for statically applied monotonic loading. This method could relatively easily be extended to the analysis of piles under dynamically applied cyclic lateral load. This could be achieved through the use of realistic hysteretic models for both pile and soil, and the addition of damping and inertia terms to the governing differential equation.

4. The study in this thesis has been directed at solving the pseudo-static response of piles to superstructure inertia loads which are generated during seismic events. Pile response close to ground level is governed by inertia loading. At great depth in the ground pile response is governed by free-field induced soil deformations. To quantify the effect of free-field induced deformations, analytical studies should be conducted where allowance is made for the effect of pile stiffness modifying the free-field induced deformation (see figure 1.7).

5. Earthquake loading is dynamic in nature. Thus shake table tests of small-scale piles embedded in a sand foundation could be used to enable the study of pile-soil response under earthquake conditions to be more properly investigated.

6. Twin-pile bent behaviour under lateral load was investigated in this thesis. However, the effect of superstructure dead load on the pile was not modelled. It would thus be useful to determine if superstructure dead load would reduce rocking of the piles to the extent that the piles behaved in substantially a fixed-head fashion.

REFERENCES

CHAPTER 1

1.1 STANFORD, P.R., CORMACK, L.G. and PARK, R., "Design Philosophy", Bulletin of the New Zealand National Society for Earthquake Engineering, Vol. 13, No. 3, September 1980, pp.229-231.

1.2 FISHER, R.W., LANIGAN, A.G. and STOCKWELL, M.J., "Small Bridges", Bulletin of the New Zealand National Society for Earthquake Engineering, Vol. 13, No. 3, September 1980, pp.269-273.

1.3 PARK, R.J.T., PRIESTLEY, M.J.N. and WALPOLE, W.R., "The Seismic Performance of Steel Encased Reinforced Concrete Bridge Piles", Bulletin of the New Zealand National Society for Earthquake Engineering, Vol. 16, No. 2, June 1983, pp.123-140.

1.4 BLAKELEY, R.W.G., CORMACK, L.G. and STOCKWELL, M.J., "Mechanical Energy Dissipating Devices", Bulletin of the New Zealand National Society for Earthquake Engineering, Vol. 13, No. 3, September 1980, pp.264-268.

1.5 BERRILL, J.B., PRIESTLEY, M.J.N. and PEEK, R., "Further Comments on Seismic Design Loads for Bridges", Bulletin of the New Zealand National Society for Earthquake Engineering, Vol. 14, No. 1, March 1981, pp.3-11.

1.6 BERRILL, J.B., PRIESTLEY, M.J.N. and CHAPMAN, H.E., "Design Earthquake Loading and Ductility Demand", Bulletin of the New Zealand National Society for Earthquake Engineering, Vol. 13, No. 3, September 1980, pp.232-241.

1.7 "Earthquake Resistant Design of Bridges", N.Z. Ministry of Works and Development Publication, C.D.P. 707/A, 1978.

1.8 EDMONDS, F.D., CARR, A.J., GOLDSMITH, P.R., NORTH, P.J., WOOD, J.H. and PRESTON, R.L., "Bridge Foundations", Bulletin of the New Zealand National Society for Earthquake Engineering, Vol. 13, No. 3, September 1980, pp.248-261.

1.9 POULOS, H.G. and DAVIS, E.H., "Elastic Solutions for Soil and Rock Mechanics", John Wiley, New York, 1974.

1.10 HETENYI, M., "Beams on Elastic Foundation", University of Michigan Press, Ann Arbor, 1946.

1.11 MARTIN, G.R., "Seismic Design Considerations for Bridge Foundations and Site Liquefaction Potential", Proceedings of Workshop on Earthquake Resistance of Highway Bridges, Applied Technology Council, California, January 1979, pp.206-227.

1.12 MARGASON, E. and HOLLOWAY, D.M., "Pile Bending During Earthquakes", Proceedings of the Sixth World Conference on Earthquake Engineering, New Delhi, India, 1977, pp.1690-1696.

1.13 "Code of Practice for the Design of Concrete Structures", NZS 3101, Standards Association of New Zealand, 1982, 127pp and Commentary.

1.14 "Building Code Requirements for Reinforced Concrete", ACI 318-83, American Concrete Institute, Detroit, 1983.

1.15 "Reinforced Concrete Structures, Design Code and Interpretation", Architectural Institute of Japan, 1982, 685pp.

1.16 SHEPPARD, D.A., "Seismic Design of Prestressed Concrete Piling", Prestressed Concrete Institute Journal, March-April 1983, pp.21-49.

1.17 "Engineering Features of the San Fernando Earthquake, February 9, 1971", Editor P.C. Jennings, Earthquake Engineering Research Laboratory, California Institute of Technology, 512pp.

1.18 MOREEL, B., "The Place and Function of Steel in Concrete Columns", Engineering News-Record, Vol. 114, March 21, 1935.

1.19 RICHART, F.E., BRANDTZAEG, A. and BROWN, R.L., "A Study of the Failure of Concrete under Combined Compression Stresses", University of Illinois, Engineering Experimental Station Bulletin 185, November 1929.

1.20 KLOPPEL, K. and GODER, W., "Collapse Load Tests on Concrete Filled Steel Tubes and Derivation of Design Formula", Translation from Der Stahlbau, January-February 1957.

1.21 SALANI, H.J. and SIMS, J.R., "Behaviour of Mortar Filled Steel Tubes in Compression", Proceedings of ACI, Vol. 61, No. 10, p.1271, October 1964.

1.22 GARDNER, N.J. and JACOBSON, E.R., "Structural Behaviour of Concrete Filled Steel Tubes", Proceedings of ACI, Vol. 64, No. 7, July 1967.

1.23 FURLONG, R.W., "Strength of Steel Encased Concrete Beam-Columns", Proceedings ASCE Structural Division, ST5, Vol. 93, Paper No. 5492, October 1967.

1.24 KNOWLES, R.B. and PARK, R., "Strength of Concrete Filled Steel Tubular Columns", Proceedings ASCE Structural Division, Vol. 95, No. ST12, Paper 6936, 1969.

1.25 NEOGI, P.K., SEN, H.K. and CHAPMAN, J.C., "Concrete-Filled Tubular Steel Columns under Eccentric Loading", The Structural Engineer, Vol. 47, No. 5, 1969.

1.26 TOMII, M., YOSHIMURA, K. and MORISHITA, Y., "Experimental Studies on Concrete Filled Steel Tubular Stub Columns under Concentric Loads", International Colloquium on Stability of Structures under Static and Dynamic Loads, May 17-19, 1977, Washington D.C., U.S.A.

1.27 CARTER, D.P., "A Non-Linear Soil Model for Predicting Lateral Pile Response", Report Number 359, Department of Civil Engineering, University of Auckland, August 1984, 137pp. and Appendices.

1.28 PRIESTLEY, M.J.N., "Mangere Bridge Foundation Cylinder Load Tests", Report No. 488, Central Laboratories, Lower Hutt, Ministry of Works and Development, New Zealand, July 1974, 47pp. and Appendices.

1.29 REESE, L.C., COX, W.R. and KOOP, F.D., "Analysis of Laterally Loaded Piles in Sand", Proceedings of the Sixth Annual Offshore Technology Conference, Houston, Texas, Paper No. OTC2080, 1974, pp.473-483.

1.30 SCOTT, R.F., "Analysis of Centrifuge Pile Tests; Simulation of Pile Driving", Research Report, American Petroleum Institute, OSAPR Project 13, California Institute of Technology, Pasadena, California, June 1980.

1.31 PARKER, F. and REESE, L.C., "Experimental and Analytical Study of Behaviour of Single Piles in Sand under Lateral and Axial Loading", Research Report No. 117-2, Center for Highway Research, University of Texas, Austin, Texas, November 1970.

1.32 PENDER, M.J. and MATUSCHKA, T., "NIMT Electrification:Field Trial Testing of Foundations for Traction Poles", unpublished report prepared by Tonkin and Taylor, Consulting Engineers, for the New Zealand Railways, 1983.

1.33 GOLDSMITH, P.R., "Aspects of Soil-Pile Interaction under Static Loads", Report No. 212, Department of Civil Engineering, University of Auckland, November 1979, 693pp.

1.34 FENDALL, H.D.W., "Laterally Loaded Pile Groups", Report No. 251, Department of Civil Engineering, University of Auckland, October 1980, 223pp.

1.35 SCHOFIELD, A.N., "Cambridge Geotechnical Centrifuge Operations", Géotechnique, Vol. 30, No. 3, 1980, pp.227-266.

1.36 SCOTT, R.F., "Centrifuge Studies of Cyclic Lateral Load-Displacement Behaviour of Single Piles", Research Program for American Petroleum Institute, OSAPR Project 8, California Institute of Technology, 1976-77.

1.37 REESE, L.C., "Laterally Loaded Piles:Program Documentation", Journal of the Geotechnical Engineering Division, Proceedings ASCE, Vol. 103, No. GT4, April 1977, pp.287-305.

1.38 "Comparisons of United States and New Zealand Seismic Design Practices for Highway Bridges", Applied Technology Council, California, August 1982, 270pp.

1.39 "Earthquake Resistance of Highway Bridges", Proceedings of a Workshop, Applied Technology Council, California, November 1979, 625pp.

CHAPTER 2

2.1 TOMII, M., YOSHIMURA, K. and MORISHITA, Y., "Experimental Studies on Concrete-Filled Steel Tubular Stub Columns under Concentric Loading", International Colloquium on Stability of Structures under Static and Dynamic Loads, Washington, D.C., May 17-19, 1977, pp.718-741.

2.2 MANDER, J.B., PRIESTLEY, M.J.N. and PARK, R., "Seismic Design of Bridge Piers", Research Report 84-2, Department of Civil Engineering, University of Canterbury, Christchurch, New Zealand, February 1984, 483pp.

2.3 SCOTT, B.D., PARK, R. and PRIESTLEY, M.J.N., "Stress-Strain Relationships for Confined Concrete:Rectangular Sections", Research Report 80-6, Department of Civil Engineering, University of Canterbury, Christchurch, New Zealand, February 1980, 106pp.

2.4 LORENZ, R., "Achsymmetrische Verzerrungen in dunwandigen Hohlzylinder", Zeitschrift des Vereins Deutscher Ingenenierus, Vol. 52, 1908, p1706 (in German).

2.5 TROITSKY, M.S., "Tubular Steel Structures - Theory and Design", The James F. Lincoln Arc Welding Foundation, 1982, 350 pp.

2.6 WILSON, W.M. and NEWMARK, N.M., "The Strength of Thin Cylindrical Shells as Columns", Bulletin Number 255, University of Illinois, February 1933.

2.7 McGUIRE, W., "Steel Structures", Prentice-Hall, London, 1968, 1112pp.

2.8 MENDELSON, A., "Plasticity - Theory and Applications", Macmillan, New York, 1968, 352pp.

2.9 SMITH, J.O. and SIDEBOTTOM, O.M., "Inelastic Behaviour of Load Carrying Members", John Wiley and Sons, New York, 1965.

2.10 PARK, R. and PAULAY, T., "Reinforced Concrete Structures", John Wiley and Sons, New York, 1975, 769pp.

2.11 KUPFER, H. and GERSTLE, K., "Behaviour of Concrete under Biaxial Stress", Journal of the Engineering Mechanics Division, ASCE, Vol. 99, No. EM4, Proceedings Paper 9917, August 1973, pp.852-866.

2.12 LIU, C.Y., NILSON, A.H. and SLATE, F.O., "Biaxial Stress-Strain Relations for Concrete", Journal of the Structural Division, ASCE, Vol. 98, No. ST5, Proceedings Paper 8095, May 1972, pp.1025-1034.

2.13 PALANISWAMY, R. and SHAH, S.P., "Fracture and Stress-Strain Relation of Concrete under Triaxial Compression", Journal of the Structural Division, ASCE, Vol. 100, No. ST5, Proceedings Paper 10547, May 1974, pp.901-916.

2.14 ELWI A.A. and MURRAY, D.W., "A 3D Hypoelastic Constitutive Relationship", Journal of the Engineering Mechanics Division, ASCE, Vol. 105, No. EM4, August 1979, Proceedings Paper 14746, pp.623-641.

2.15 CEDOLIN, L., CRUTZEN, Y.R.J. and DEI POLI S., "Triaxial Stress-Strain Relationship for Concrete", Journal of the Engineering Mechanics Division, ASCE, Vol. 103, No. EM3, June 1977, Proceedings Paper 12969, pp. 423-439.

2.16 CHEN, A.C.T. and CHEN, W.F., "Constitutive Relations for Concrete", Journal of the Engineering Mechanics Division, ASCE, Vol. 101, No. EM4, Proceedings Paper 11529, August 1975, pp.465-481.

2.17 BAZANT, Z.P. and BHAT, P.D., "Endochronic Theory of Inelasticity and Failure of Concrete", ASCE, Vol. 102, No. EM4, April 1976, pp.701-722.

2.18 BAZANT, Z.P. and BHAT, P.D., "Prediction of Hysteresis of Reinforced Concrete Members", ASCE, Vol. 103, No. ST1, January 1977.

2.19 BAZANT, Z.P. and SHIEH, C-L, "Endochronic Model for Nonlinear Triaxial Behaviour of Concrete", Nuclear Engineering and Design, 1978, pp.305-315.

2.20 BAZANT, Z.P. and BURROW, M.C., "Confinement Effect in Flexural Ductility of Concrete, 3D Analysis", Vol. 13, No. 76, Materiaux et Constructions.

2.21 LESLIE, P.D. and PARK, R., "Ductility of Reinforced Concrete Bridge Piers", Research Report, Civil Engineering Department, University of Canterbury, Christchurch, New Zealand, 1974, 147pp plus Appendices.

2.22 DESAYI, P., IYENGAR, K.T.S.R. and REDDY, T.S., "Equations for Stress-Strain Curve of Concrete Confined in Circular Steel Spiral", Materiaux et Constructions, September/October 1978, pp.339-345.

2.23 MOREEL, W., "The Place and Function of Steel in Composite Columns", Engineering-News Record, Vol. 114, p.410, March 21, 1935.

2.24 RICHART, F.E., BRANDTZAEG, A. and BROWN, R.L., "A Study of the Failure of Concrete under Combined Compressive Stresses", University of Illinois Engineering Experimental Station Bulletin 185, November 1929.

2.25 BALMER, G.G., JONES, V. and McHENDRY, D., "Shearing Strength of Concrete under High Triaxial Stress - Computation of Mohr's Envelope as a Curve", Structures Research Laboratory, Report No. SP-23, Research and Geology Division, U.S. Dept. of Interior, Bureau of Reclaimation, Denver, Colorado, October 28, 1949.

2.26 POPOVICS, S., "A Numerical Approach to the Complete Stress-Strain Curves of Concrete", Cement and Concrete Research, Vol. 3, No. 5, September 1973, pp.583-599.

2.27 KLOPPEL, K. and GODER, W., "Collapse Load Tests on Concrete-Filled Steel Tubes and Derivation of Design Formula", Translation from Der Stahlbau, January-February 1957.

2.28 SALANI, H.J. and SIMS, J.R., "Behaviour of Mortar-Filled Steel Tubes in Compression", Proceedings A.C.I., Vol. 61, No. 10, p1271, October 1964.

2.29 GARDNER, N.J. and JACOBSON, E.R., "Structural Behaviour of Concrete Filled Steel Tubes", Proceedings A.C.I., Vol. 64, No. 7, July 1967.

2.30 KNOWLES, R.B. and PARK, R., "Strength of Concrete Filled Tubular Columns", Journal of the Structural Division, ASCE, Vol. 95, No. ST12, December 1969.

2.31 NEOGI, P.K., SEN, H.K. and CHAPMAN, J.C., "Concrete-filled tubular steel columns under eccentric loading", The Structural Engineer, No. 5, Vol. 47, May 1969, pp.187-195.

2.32 FURLONG, R.W., "Strength of Steel-Encased Concrete Beam-Columns", Journal of the Structural Division, ASCE, Vol. 93, No. ST5, October 1967.

2.33 SEN, H.K., "Triaxial Effects in Concrete-Filled Tubular Steel Columns", Ph.D. Thesis, Imperial College, University of London, 1969.

2.34 SEN, H.K., CHAPMAN, J.C. and NEOGI, P.K., "Concrete-filled tubular steel columns - triaxial effects in circular stub columns under concentric loading", Technical Note 39, Construction Industry Research and Information Association, London, June 1972, 54pp.

2.35 BELENYA, E.I., "Investigation of Concrete Filled Steel Tubular Structures in the USSR", Proceedings of the International Specialty Conference on Concrete Filled Steel Tubular Structures, Harbin, China, August 1985, pp.7-11.

2.36 ZHONG SHAN-TONG, "Behaviour and Strength Index of Concrete Filled Steel Tube as Composite Material under First Compression", Proceedings of the International Specialty Conference on Concrete Filled Steel Tubular Structures, Harbin, China, August 1985, pp.32-39.

2.37 STOROZHENKO, L.I., "Strength and Deformation of Concrete Filled Steel Tubular Elements", Proceedings of the International Specialty Conference on Concrete Filled Steel Tubular Structures, Harbin, China, August 1985, pp.48-51.

2.38 CAI SHAO-HUAI, JIAO ZHAN-SHUAN, GU WAN-LI, and DI XIAO-TAN, "Limit Analysis of Concrete Filled Steel Tubular Columns", Proceedings of the International Specialty Conference on Concrete Filled Steel Tubular Structures, Harbin, China, August 1985, pp.59-66.

2.39 JIANG JIA-FEN, TANG GUAN-ZUO, and ZHAO BING-QUAN, "The Calculation of Ultimate Bearing Capacity of Concrete Filled Steel Tubular Columns under Axial and Eccentric Load", Proceedings of the International Specialty Conference on Concrete Filled Steel Tubular Structures, Harbin, China, August 1985, pp.67-73.

2.40 WANG ZHANG-AO and YANG SHANG-ZHANG, "Experimental Research of Comprehensive Strength and Comprehensive Modulus of Elasticity of Concrete Filled Steel Tube", Proceedings of the International Specialty Conference on Concrete Filled Steel Tubular Structures, Harbin, China, August 1985, pp.74-80.

2.41 SAKINO, K., TOMII, M. and WATANABE, K., "Sustaining Load Capacity of Plain Concrete Stub Columns Confined by Circular Steel Tube", Proceedings of the International Specialty Conference on Concrete Filled Steel Tubular Structures, Harbin, China, August 1985, pp.112-118.

2.42 ZHOU GUANG-SHI and LIU DIAN-ZHONG, "Calculation of Load Carrying Capacity for Stability of Concrete Filled Steel Tubular Members under Eccentric Loading", Proceedings of the International Specialty Conference on Concrete Filled Steel Tubular Structures, Harbin, China, August 1985, pp.140-146.

2.43 "Design Manual for SHS Concrete Filled Columns", British Steel Corporation, Tubes Division, 1983.

2.44 "Code of Practice for the Design of Concrete Structures", NZS 3101:1982, Standards Association of New Zealand, 127pp. plus Commentary.

2.45 VECCHIO, F. and COLLINS, M.P., "The Response of Reinforced Concrete to In-Plane Shear and Normal Stresses", University of Toronto, Department of Civil Engineering, Publication No. 82-03, March 1982, 332pp.

CHAPTER 3

3.1 "Code of Practice for the Design of Concrete Structures", NZS 3101: 1982, Standards Association of New Zealand, Wellington, 127pp plus Commentary.

3.2 MANDER, J.B., PRIESTLEY, M.J.N. and PARK, R., "Seismic Design of Bridge Piers", Research Report 84-2, Department of Civil Engineering, University of Canterbury, Christchurch, New Zealand, February 1984, 483pp.

3.3 PRIESTLEY, M.J.N., "Analysis and Design of Prestressed Concrete Storage Tanks", Journal of the Prestressed Concrete Institute, July/August 1985.

3.4 SHANLEY, F.R., "Inelastic Column Theory", Journal of the Aeronautical Sciences, Vol. 14, No. 5, May 1947, pp261-268.

3.5 MONTAGUE-BEART, A., "The Pan Book of Mathematical Tables", Pan Books, London, 1965, 176pp.

3.6 VECCHIO, F. and COLLINS, M.P., "The Response of Reinforced Concrete to In-Plane Shear and Normal Stresses", University of Toronto, Department of Civil Engineering, Publication No. 82-03, March 1982, 332pp.

CHAPTER 4

4.1 GERARD, G. and BECKER, H., "Handbook of Structural Stability, Part III, Buckling of Curved Plates and Shells", Technical Note No. 3783, National Advisory Commission for Aeronautics, Washington, D.C., August 1957.

4.2 BRAZIER, L.G., "On the Flexure of Thin Cylindrical Shells and Other Thin Sections", Proceedings of the Royal Society of London, Series A, Vol. 116, 1927, ppl04-114.

4.3 CHWALLA, E., "Reine Beigung Schlanker, dunwandiger Rohr mit gerader Achse", Z. Angin.Math. u. Mech., Vol. 13, No. 1, 1933, pp45-48 (in German).

4.4 FLUGGE, W., "Die Stabilitat der Kreiszylinderschule", Ingenieru-Archiv, Vol. 3, No. 5, 1932, p.463 (in German).

4.5 DINNIK, A.N., "Collected Works", Vol. III, Academy of Sciences, Ukrainian S.S.R., Kiev, 1956, pp88-90. (in Russian).

4.6 SCHILLING, C.G., "Buckling Strength of Circular Tubes", Journal of the Structural Division, ASCE, Vol. 91, No. ST5, October 1965, pp325-349.

4.7 LITTLE, G.H., "Design curves for the bending strength of circular and octagonal steel tubes, including the effect of a hole", The Structural Engineer, Volume 62B, No. 3, September 1984, pp53-59.

4.8 SHERMAN, D.R., "Tests of Circular Steel Tubes in Bending", Journal of Structural Division, ASCE, Vol. 102, No. ST11, Nov. 1976, pp2181-2195.

4.9 BABAN, S.A. and LITTLE, G.H., "Tests on the bending strength of circular and octagonal steel tubes, including the effect of a hole", The Structural Engineer, Vol. 62B, No. 3, September 1984, pp45-52.

4.10 POTANGAROA, R.T., PRIESTLEY, M.J.N. and PARK, R., "Ductility of Spirally Reinforced Concrete Columns under Seismic Loading", Research Report 79-8, Department of Civil Engineering, University of Canterbury, February 1979, 116pp.

4.11 GILL, W.D., PARK, R. and PRIESTLEY, M.J.N., "Ductility of Rectangular Reinforced Concrete Columns with Axial Load", Research Report 79-1, Department of Civil Engineering, University of Canterbury, February 1979, 136pp.

4.12 ANG BENG GHEE, PRIESTLEY, M.J.N. and PARK, R., "Ductility of Reinforced Concrete Bridge Piers under Seismic Loading", Research Report 81-3, Department of Civil Engineering, University of Canterbury, February 1981, 109pp.

4.13 MANDER, J.B., PRIESTLEY, M.J.N. and PARK, R., "Seismic Design of Bridge Piers", Research Report 84-2, Department of Civil Engineering, University of Canterbury, February 1984, 483pp.

4.14 ZAHN, F.A., PARK, R. and PRIESTLEY, M.J.N., "Strength and Ductility of Reinforced Concrete Piers - A Summary Report", Research Report 83-7, Department of Civil Engineering, University of Canterbury, December 1983, 43pp.

4.15 FALCONER, T.J. and PARK, R., "Ductility of Prestressed Concrete Piles under Seismic Loading", Research Report 82-6, Department of Civil Engineering, University of Canterbury, February 1982, 121pp.

4.16 PAM HOAT JOEN and PARK, R., "Ductility of Prestressed Concrete Piles Subjected to Simulated Seismic Loading", Research Report 84-4, Department of Civil Engineering, University of Canterbury, February 1984, 169pp.

4.17 "Code of Practice for the Design of Concrete Structures", NZS 3101: 1982, Parts 1 and 2, Standards Association of New Zealand, Wellington, New Zealand.

4.18 BRIDGE, R.Q., "Factors Affecting the Behaviour of Composite Steel and Concrete Columns", Ph.D. Thesis, University of Sydney, Australia, 1974, 582pp.

4.19 FURLONG, R.W., "Strength of Steel-Encased Concrete Beam-Columns", Journal of the Structural Division, ASCE, Vol. 93, No. ST5, October 1967, ppl13-124.

4.20 KNOWLES, R.B., "Steel Tube Columns Infilled with Concrete", M.E. Thesis, Department of Civil Engineering, University of Canterbury, 1967, 341pp.

4.21 NEOGI, P.K., SEN H.K. and CHAPMAN, J.C., "Concrete-filled Tubular Steel Columns under Eccentric Loading", The Structural Engineer, Vol. 47, No. 5, May 1969.

4.22 FURLONG, R.W., "Design of Steel-Encased Concrete Beam-Columns", Journal of the Structural Division, ASCE, Vol. 94, No. ST1, January 1968, pp267-281.

4.23 "Design Manual for SHS CONCRETE FILLED COLUMNS", British Steel Corporation Tubes Division, 1984, 134pp.

4.24 PARK, R.J.T., PRIESTLEY, M.J.N. and WALPOLE, W.R., "The Seismic Performance of Steel Encased Reinforced Concrete Bridge Piles", Research Report 82-12, Department of Civil Engineering, University of Canterbury, February 1982, 158pp.

4.25 BERRILL, J.B., PRIESTLEY, M.J.N. and CHAPMAN, H.E., "Design Earthquake Loading and Ductility Demand", Bulletin of the New Zealand National Society for Earthquake Engineering, Vol. 13, No. 3, September 1980, pp232-241.

4.26 "Code of Practice for General Structural Design and Design Loadings for Buildings", NZS 4203:1976, Standards Association of New Zealand, Wellington, New Zealand.

4.27 PARK, R. and PAULAY, T., "Reinforced Concrete Structures", John Wiley, New York, 1975, 769pp.

4.28 "Concrete Construction", NZS 3109, Standards Association of New Zealand, Wellington, New Zealand.

4.29 "Code of Design for Steel Structures", NZS 3404-1977, Standards Association of New Zealand, Wellington, New Zealand.

4.30 "Building Code Requirements for Reinforced Concrete", ACI318-83, American Concrete Institute, Detroit, 1983.

4.31 MATTOCK, A.H., KRIZ, L.B. and HOGNESTAD, E., "Rectangular Stress Distribution in Ultimate Strength Design", Journal ACI, Vol. 57, No. 8, February 1961.

4.32 ANG BENG GHEE, PRIESTLEY, M.J.N. and PAULAY, T., "Seismic Shear Strength of Circular Bridge Piers", Research Report 85-5, Department of Civil Engineering, University of Canterbury,, July 1985, 408pp.

4.33 PRIESTLEY, M.J.N. and PARK, R., "Strength and Ductility of Bridge Substructures", Road Research Unit Bulletin 71, National Roads Board, Wellington, New Zealand, 1984, 120pp.

4.34 ERASMUS, L.A. and PUSSEGODA, L.N., "Safe Bend Radii for Deformed Reinforcing Bars to Avoid Failure by Strain Age Embrittlement", New Zealand Engineering - The Journal of the New Zealand Institute of Engineers, Vol. 33, No. 8, 15 August 1978, ppl70-177.

4.35 PUSSEGODA, L.N., "Strain Age Embrittlement in Reinforcing Bars", Ph.D. Thesis, Mechanical Engineering Department, University of Canterbury, Christchurch, New Zealand, 1978, 172pp and Appendices.

4.36 ZANZA, T.M., "The Behaviour of Lapped Splices Subjected to Reversed Cyclic Loading", Master of Engineering Report, University of Canterbury, Christchurch, New Zealand, 1981.

4.37 VIRDI, K.S. and DOWLING, P.J., "Bond Strength in Concrete-Filled Steel Tubes", IABSE Proceedings P-33/80, ppl25-139.

4.38 MORISHITA, Y., TOMII, M. and YOSHIMURA, K., "Experimental Studies on Bond Strength in Concrete Filled Circular Steel Tubular Columns Subjected to Axial Loads", Transactions of the Japan Concrete Institute, 1979, pp351-358.

4.39 SATO, M., KATO, C. and MIYOSHI, H., "Mechanical Characteristics of Concrete-Filled Steel Pipes with Checkered Projections", Transactions of the Japan Concrete Institute, Vol. 3, 1981, pp431-438.

4.40 TOMII, M., YOSHIMURA, K. and MORISHITA, Y., "A Method of Improving Bond Strength between Steel Tube and Concrete Core Cast in Circular Steel Tubular Columns", Transactions of the Japan Concrete Institute, Vol. 2, 1981, pp319-326.

CHAPTER 5

5.1 BLAKELEY, R.W.G., "Ductility of Prestressed Concrete Frames under Seismic Loading", Ph.D. Thesis, University of Canterbury, Christchurch, New Zealand, 1971, 230pp and Appendices.

5.2 THOMPSON, K.J., "Ductility of Concrete Frames under Seismic Loading", Ph.D. Thesis, University of Canterbury, Christchurch, New Zealand, 1975, 341pp and Appendices.

5.3 FALCONER, T.J. and PARK, R., "Ductility of Prestressed Concrete Piles under Seismic Loading", Research Report 82-6, Department of Civil Engineering, University of Canterbury, Christchurch, New Zealand, February 1982, 121pp.

5.4 PAM HOAT JOEN and PARK, R., "Ductility of Prestressed Concrete Piles Subjected to Simulated Seismic Loading", Research Report 84-4, Department of Civil Engineering, University of Canterbury, Christchurch, New Zealand, February 1984, 169pp.

5.5 KENT, D.C., "Inelastic Behaviour of Reinforced Concrete Members with Cyclic Loading", Ph.D. Thesis, University of Canterbury, Christchurch, New Zealand, 1969, 246pp.

5.6 ZAHN, F.A., "Ductility of Bridge Piers", Ph.D. Thesis, Department of Civil Engineering, University of Canterbury, Christchurch, New Zealand, 1985.

5.7 PARK, R.J.T., PRIESTLEY, M.J.N. and WALPOLE, W.R., "The Seismic Performance of Steel-Encased Reinforced Concrete Bridge Piles", Research Report 82-12, Department of Civil Engineering, University of Canterbury, Christchurch, New Zealand, February 1982, 158pp.

5.8 AOYAMA, H., Unpublished Master of Engineering Course in Structural Concrete, Civil Engineering Department, University of Canterbury, Christchurch, New Zealand, 1979.

5.9 AL-NOURY, S.I. and CHEN, W.F., "Behaviour and Design of Reinforced and Composite Concrete Sections", ASCE, Vol. 108, No. ST6, June 1982, pp1266-1284.

5.10 MANDER, J.B., PRIESTLEY, M.J.N. and PARK, R., "Seismic Design of Bridge Piers", Research Report 84-2, Department of Civil Engineering, University of Canterbury, Christchurch, New Zealand, February 1984, 483pp.

CHAPTER 6

6.1 REESE, L.C., COX, W.R. and KOOP, F.D., "Analysis of Laterally Loaded Piles in Sand", Proceedings of the Offshore Technology Conference, Houston, U.S.A, Vol. 2, Paper No. OTC 2080, 1974.

6.2 WOODWARD, R.J., GARDNER, W.S. and GREER, D.M., "Drilled Pier Foundations", McGraw-Hill, New York, 287pp, 1974.

6.3 EDMONDS, F.D., CARR, A.J., GOLDSMITH, P.R., NORTH, P.J., WOOD, J.H. and PRESTON, R.L., "Bridge Foundations", Bulletin of the N.Z. National Society for Earthquake Engineering, Vol. 13, No. 3, September 1980, pp248-261.

6.4 POULOS, H.G. and DAVIS, E.H., "Elastic Solutions for Soil and Rock Mechanics", John Wiley and Sons Inc, 1974.

6.5 GOLDSMITH, P.R., "Aspects of Soil-Pile Interaction Under Static Loads", Report No. 212, Department of Civil Engineering, University of Auckland, November 1979, 694pp.

6.6 FENDALL, H.D.W., "Laterally Loaded Pile Groups", Report No. 251, Department of Civil Engineering, University of Auckland, October 1980, 223pp.

6.7 PECK, R.B., HANSON, W.E. and THORBURN, T.H., "Foundation Engineering", 2nd edition, Wiley International Edition, 1974, 514pp.

6.8 BERRILL, J.B., PRIESTLEY, M.J.N. and CHAPMAN, H.E., "Design Earthquake Loading and Ductility Demand", Bulletin of the N.Z. National Society for Earthquake Engineering, Vol. 13, No. 3, September 1980, pp232-241.

6.9 CLOUGH, R.W. and PENZIEN, J., "Dynamics of Structures", McGraw-Hill, 1975, 634pp.

6.10 JENNINGS, D.N., THURSTON, S.J. and EDMONDS, F.D., "Static and Dynamic Lateral Loading of Two Piles", Proceedings of the Eighth World Conference on Earthquake Engineering, Prentice-Hall, San Francisco, 1984.

6.11 FUKUSHIMA, S. and TATSUOKA, F., "Strength and Deformation Characteristics of Saturated Sands at Extremely Low Pressures", Soils and Foundations, Vol. 24, No.4,pp30-48, December 1984, Japanese Society of Soil Mechanics and Foundation Engineering.

6.12 PONCE, V.M. and BELL, J.M., "Shear Strength of Sand at Extremely Low Pressures", Journal of Soil Mechanics and Foundation Engineering, Proceedings of ASCE, Vol. 97, No. SM4, April 1971, pp625-638.

6.13 SCOTT, R.F., "Centrifuge Studies of Cyclic Lateral Load-Displacement Behaviour of Single Piles", Soil Mechanics Laboratory, Division of Engineering and Applied Science, California Institute of Technology, Pasadena, California, 1978, 46pp and appendix.

6.14 PRIESTLEY, M.J.N., "Mangere Bridge, Foundation Cylinder Load Tests", Report No. 488, Central Laboratories, Ministry of Works and Development, 1974, 47pp and appendices.

6.15 DORN, W.S. and McCRACKEN, D.D., "Numerical Methods and Fortran IV Case Studies", Wiley International Edition, 1972, 447pp.

6.16 SCOTT, R.F., "Analyses of Centrifuge Pile Tests, Simulation of Pile Driving", Soil Mechanics Laboratory, Division of Engineering and Applied Science, California Institute of Technology, Pasadena, California, 1979.

6.17 GERALD, C.F., "Applied Numerical Analysis", 1973, 340pp.

6.18 BROMS, B.B., "Lateral Resistance of Piles in Cohesionless Soils", Journal of the Soil Mechanics and Foundation Engineering Division, ASCE, Vol. 90, SM3, May 1964.

6.19 PRIESTLEY, M.J.N. and PARK, R., "Strength and Ductility of Bridge Substructures", Road Research Unit Bulletin 71, National Roads Board, Wellington, New Zealand, 120pp, 1984.

6.20 FISHER, R.W., LANIGAN, A.G. and STOCKWELL, M.J., "Small Bridges", Bulletin of the N.Z. National Society for Earthquake Engineering, Vol. 13, No. 3, September 1980, pp269-273.

CHAPTER 7

7.1 CARTER, D.P., "A Non-Linear Soil Model for Predicting Lateral Pile Response", Report Number 359, Department of Civil Engineering, University of Auckland, August 1984, 137pp and Appendices.

7.2 TOAN, D.V. and PIDGEON, A., "Computer Program for the Elasto-Plastic Analysis of Pile Groups", Beca, Carter, Hollings and Ferner Limited, Consulting Engineers, Auckland, 1978.

7.3 POULOS, H.G. and DAVIS, E.H., "Pile Foundation Analysis and Design", New York, Wiley, 1980.

7.4. REESE, L.C., "Laterally Loaded Piles : Program Documentation", Journal of the Geotechnical Engineering Division, ASCE, April 1977, pp287-305.

7.5 REESE, L.C., COX, W.R. and KOOP, F.D., "Analysis of Laterally Loaded Piles in Sand", Paper # OTC 2080, presented at the 1974 Fifth Annual Offshore Technology Conference, held at Houston, Texas.

7.6 EDMONDS, F.D., CARR, A.J., GOLDSMITH, P.R., NORTH, P.J., WOOD, J.H. and PRESTON, R.L., "Bridge Foundations", Bulletin of the N.Z. National Society for Earthquake Engineering, Vol. 13, No.3, September 1980, pp248-261.

7.7 PRIESTLEY, M.J.N. and PARK, R., "Strength and Ductility of Bridge Substructures", Road Research Unit Bulletin 71, National Roads Board, Wellington, New Zealand, 1984, 120pp.

7.8 PARK, R. and PAULAY, T., "Reinforced Concrete Structures", John Wiley and Sons, New York, 1975, 769pp.

7.9 BERRILL, J.B., PRIESTLEY, M.J.N., and CHAPMAN, H.E., "Design Earthquake Loading and Ductility Demand", Bulletin of the New Zealand National Society for Earthquake Engineering, Vol. 13, No. 3, September 1980, pp.232-241.

Classn:

SEISMIC PERFORMANCE OF STEEL-ENCASED CONCRETE PILES

R.J.T. Park

ABSTRACT: A theoretical and experimental investigation into the seismic performance of steel-encased reinforced concrete piles is presented. Constitutive models to describe the composite behaviour of tube and concrete were developed and calibrated against test data. Strength, ductility and energy-dissipating characteristics were found to be similar or superior to those of conventionally designed ductile reinforced concrete members. Lateral load tests of model piles embedded in sand indicated a large reserve of soil hysteretic damping, long plastic hinge lengths and lateral interaction and rocking of piles in a twin-pile bent.

Department of Civil Engineering, University of Canterbury,
Doctor of Philosophy Thesis, 1986.